

**Influences of Reduced Sulfur on
Arsenic and Antimony Mobility and Binding to
Natural Organic Matter**

Dissertation

zur Erlangung des akademischen Grades
eines Doktors der Naturwissenschaften (Dr. rer. nat.)
in der Bayreuther Graduiertenschule für Mathematik und Naturwissenschaften
(BayNAT)
der Universität Bayreuth

vorgelegt von:

Johannes Besold
(M.Sc. Geoökologie)

geboren in Eschenbach i. d. Opf.

Bayreuth, Januar 2020

Die vorliegende Arbeit wurde in der Zeit von Oktober 2015 bis Januar 2020 in Bayreuth an der Professur für Umweltgeochemie unter Betreuung von Frau Professorin Dr. Britta Planer-Friedrich angefertigt.

Vollständiger Abdruck der von der Bayreuther Graduiertenschule für Mathematik und Naturwissenschaften (BayNat) der Universität Bayreuth genehmigten Dissertation zur Erlangung des akademischen Grades eines Doktors der Naturwissenschaften (Dr. rer. Nat.)

Dissertation eingereicht am: 16.01.2020

Zulassung durch das Leitungsgremium: 05.02.2020

Wissenschaftliches Kolloquium: 16.07.2020

Amtierender Direktor: Professor Dr. Markus Lippitz

Prüfungsausschuss:

Prof. Dr. Britta Planer-Friedrich (Gutachterin)

Prof. Dr. Martin Obst (Gutachter)

Prof. Dr. Johanna Pausch (Vorsitz)

Prof. Dr. Stefan Peiffer

Weitere Gutachter: Dr. Andreas Vögelin, (Eawag, Schweiz)

Für meinen Bruder Markus

Acknowledgements

First of all, I would like to thank my doctoral advisor Britta Planer-Friedrich, who gave me the opportunity to start my PhD project after returning from one year of absence from science. Britta, thanks for supporting me throughout this journey called PhD with all your knowledge, curiosity and enthusiasm. I am thankful for the scientific discussions, the hours of thinking and rewriting manuscripts – I learned so much! – but also about all the “ölf” and “Göld” sounds entering my office door. Thanks also for always supporting me with finding my own way, may it be going abroad to the US or starting my “little” second job called “GreenCampus”. You have been the best “doctoral mum” I could imagine.

I acknowledge the financial support from the German Research Foundation for my PhD project. Moreover, I thank the University of Bayreuth Graduate School for their support in form of the 3-month “Feuerwehrfonds” as well as travel grants to the Goldschmidt Conference 2017 in Paris and the “Tools in Biogeochemistry” workshop in Tübingen. Further, I would like to thank the German Academic Exchange Service for the personal 6-month scholarship to Stanford University and the travel grant, which enabled me and several others from our group to conduct work at Stanford Synchrotron Radiation Lightsource and to travel to the Goldschmidt Conference 2018 in Boston. I would also like to thank for the financial support from the “Bayerische Forschungsallianz” which enabled the field work in the Finnish peatland and the European Union, which supported our work at the European Synchrotron Radiation Facility.

Many thanks to all the collaborators, without your help this thesis would not have been possible. Special thanks to Scott Fendorf for hosting me at Stanford University and for all your personal and scientific support. Thanks to Ashis Biswas, Naresh Kumar, and Vincent Noël for your support during laboratory experiments, XAS data collection and during manuscript preparations. Many thanks also to the team from Grenoble for their support in answering all my detailed XAS questions after learning the basis of this fascinating technique in theory and by hands-on training by Ruben Kretzschmar, Jon Petter Gustafsson, and Carin Sjöstedt. Thanks to the “beamline fire fighter” Juan Lezama Pacheco, who rescued us several times in the middle of the night by fixing all our problems. Also many thanks for their support, especially in field work, to Elke Suess, Christian Mikutta, Katharina Kujala, and Anne Eberle.

I would like to thank all my present and former colleagues from the Environmental Geochemistry Group in Bayreuth, who accompanied me during the time of my PhD. Many thanks go to Jiajia Wang, Kerstin Hockmann, Samer Bachmaf, Jörg Schaller, José Miguel Leon, Andrea Colina Blanco, and Alan Nicol for their support and helpful advices as well as for their interest in my work. I thank Inge Täuber for helping with all the administrative obstacles during the last year. Thanks go to Stefan Will for help in the laboratory. Special thanks go to my former master student and colleague Anne Eberle as well as to Carlin Kerl, and Judith Mehlhorn. Working with you at all times of a day was always great fun. Thanks also to my supervised bachelor students Constantin Heitzer and Madeleine Steeb, as well as my Hiwi Julian Graubner for washing the “brown gold”.

I am thankful to my colleague Leon Haupt and our Hiwis from GreenCampus for the great last year. Leon, thanks for your upright and collegial nature, making it possible to combine both worlds.

Furthermore, I thank my colleagues and friends from the extended Soil and Environmental Biogeochemistry Group at Stanford, especially Marie Mühe, Naresh Kumar, Vincent Noël, Sarah Fakhreddine, Alandra Lopez, Andrew Hennig, and Randall Holmes for all the scientific discussions, laboratory support, and general help, making those six months an unforgettable time of my life.

Moreover, I am grateful to the numerous people, who contributed to this work by providing equipment or access to instruments, conducting analyses, or helping with data interpretation, namely Martin Obst from the Experimental Biogeochemistry department, Silke Hammer, Martina Rohr, Jutta Eckert, and Heidi Zier from the Hydrology department, Peter Schmidt and Gerhard Gebhardt from the Geo workshop, Egbert Matzner and Karin Söllner from the Soil Ecology department, Dorothea Wiesner and Tiziana Boffa Ballaran from Bayreuth Geo-Institute, Thomas and Anna-Maria Dietel from the Inorganic Chemistry II department, Renée Siegel and Beate Bojer from the Inorganic Chemistry III department, the beamline scientists and technical staff from SSRL and ESRF, and finally Guangchao Li and Douglas Turner from Stanford University.

For proof-reading, I am thankful to Judith Mehlhorn, Marie Mühe, and Naresh Kumar.

Finally, I would like to thank my family and friends, but especially my parents, who always supported me on this long journey. Thanks that you were always there. To express my thanks to you, Sophie, is almost impossible. Thanks for your patience, the power and perspectives that you gave me during the last years.

Abstract

The fate of the potentially toxic metalloids arsenic (As) and antimony (Sb) in the environment is mainly controlled by iron (Fe) (oxyhydr)oxide minerals, which act as the main sinks for both elements under oxic conditions. In sub- to anoxic organic-rich environments like peatlands, Fe (oxyhydr)oxides are only thermodynamically stable at the oxic surfaces, but undergo reductive dissolution with increasing depth, accompanied by a release of adsorbed As and Sb. Simultaneously, sulfate-reduction produces reduced sulfur (S) species like dissolved sulfide, which interact with abundant solid natural organic matter (NOM), forming surface associated zero-valent S and thiol groups. Formation of As(III)-thiol bonds with solid NOM can sequester As in deep peat layers. Only little is known about the behavior of Sb in similar systems. Further, inorganic aqueous As(V)-S and Sb(V)-S species, so called thioarsenates and thioantimonates, have been found under sulfate-reducing conditions in geothermal waters and other terrestrial environments, but so far have never been reported in peatlands.

The aim of the present thesis was to investigate the occurrence of aqueous thioarsenates in peatlands and to elucidate the influence of reduced S on their formation, mobility, and binding to solid NOM in comparison to As oxoanions. A similar behavior is hypothesized for Sb, and therefore, we aimed to study Sb binding and mobility in a combination of laboratory and field experiments, to get new insights into the fate of Sb in sub- to anoxic organic-rich environments.

The first two studies investigated the occurrence of inorganic thioarsenates in a naturally As-contaminated peatland and its consequences for As mobility. Up to 93% of aqueous As species were thioarsenates and the dominant species found, monothioarsenate (MTAs(V)), likely formed from reaction of arsenite with surface associated zero-valent S. Incubation experiments of MTAs(V), arsenate, and arsenite with model peat rich in oxygen (O)-containing (carboxyl and phenol) functional groups, demonstrated only little adsorption of MTAs(V) and arsenate to peat at slightly acidic to neutral pH. Arsenite substantially complexed via As(III)-O-organic carbon (C_{org}) bonds. Incubations of MTAs(V) and arsenite with thiol-rich model peat confirmed strong As(III)-S- C_{org} complexation of arsenite, increasing from slightly alkaline to slightly acidic conditions. For MTAs(V), As adsorption was observed from neutral to slightly acidic pH and was attributed to adsorption of arsenite, formed by acid-catalyzed dissociation of MTAs(V), which in turn had a high affinity to thiol groups of peat. At pH 8.5, when MTAs(V) was stable, no complexation of MTAs(V) with thiol groups was observed. Thus, MTAs(V) and arsenate were very mobile, while arsenite showed high affinity to carboxyl/phenol and thiol groups of peat.

The following two studies focused on As mobilization potential by reduced S, when As(III) was previously bound to NOM within model peat and within organic-rich aquifer lenses. Addition of sulfide or polysulfides caused substantial As retention within peat compared to controls at acidic pH. Significant As mobilization occurred via thioarsenate formation in similar quantities at neutral to slightly alkaline pH. Spectroscopic analyses confirmed a decrease in As(III)-O- C_{org} binding, suggesting mobilization to proceed via arsenite

desorption, reaction with reduced S, and formation of thioarsenates. Formed thioarsenates remained in solution without (re)adsorption to peat. Similarly, As mobilization downstream of organic-rich lenses within aquifer sands was observed compared to control columns without lenses. Sulfate-reduction drove production of sulfide and zero-valent S. Thiol groups partitioned As via As(III)-S-C_{org} bond formation to the solid phase within the lenses, while zero-valent S mobilized As again by thioarsenate formation under slightly alkaline experimental pH conditions.

The fifth and sixth study explored binding mechanisms of antimonite to organic functional groups of model peat and under field conditions in a mine water impacted peatland. Incubation experiments showed strong antimonite adsorption to peat by formation of Sb(III)-O-C_{org} bonds as revealed by spectroscopic analyses. Antimonite adsorption strongly increased with increasing peat thiol-group content. Spectroscopic data revealed that Sb adsorption occurred via Sb(III)-S-C_{org} coordination and inorganic Sb-S phases could be excluded. Solid-phase Sb speciation in a mine water impacted peatland confirmed the high affinity of antimonite to O-containing functional groups and Sb(III)-S-C_{org} coordination strongly increased with increasing peat depth. No organically complexed Sb(V) was found. Aqueous Sb speciation was dominated by antimonate and antimonite concentrations were low. No thioantimonates were found. Hence, antimonate was very mobile while antimonite exhibited a very high affinity to peat functional groups.

Overall, our findings imply that reduced S has complex influences on As and Sb mobility in organic-rich environmental systems. While thiol-bond formation and ultimately sulfide mineral precipitation of As and Sb under anoxic conditions and at acidic pH efficiently sequester arsenite and antimonite, formation of highly mobile thioarsenates with reduced S can turn solid NOM from an As sink to a source at already circumneutral pH. This knowledge has important implications for the safe and long-term management of contaminated peatlands and other organic-rich environments to keep As and Sb partitioned to the solid phase.

Zusammenfassung

Das Verhalten der potenziell toxischen Metalloide Arsen (As) und Antimon (Sb) in der Umwelt wird hauptsächlich durch Eisen (Fe)-(Hydr)oxid-Mineralen kontrolliert, die unter oxidischen Bedingungen als die wichtigsten Senken dieser beiden Elemente fungieren. Bei sub- bis anoxischen Bedingungen und hohem Organikgehalt, wie etwa in Mooren vorhanden, sind Fe-(Hydr)oxide nur an den oxidischen Oberflächen thermodynamisch stabil, lösen sich aber mit zunehmender Tiefe auf. Dies hat die initiale Freisetzung von adsorbiertem As und Sb zur Folge. Gleichzeitig werden durch Sulfatreduktion reduzierte Schwefel (S)-Spezies wie gelöstes Sulfid gebildet, die mit organischem Festphasenmaterial reagieren können und oberflächenassoziierten nullwertigen S und Thiol-Gruppen bilden. Die Bildung von As(III)-Thiol-Verbindungen mit organischem Festphasenmaterial kann As in tiefen Torfschichten festlegen. Über das Verhalten von Sb in ähnlichen Systemen ist nur wenig bekannt. Weiterhin wurden anorganische gelöste As(V)-S- und Sb(V)-S-Spezies, so genannte Thioarsenate und Thioantimonate, unter sulfatreduzierenden Bedingungen in Geothermalmgewässern und anderen terrestrischen Umweltsystemen entdeckt, aber bisher noch nie in Mooren nachgewiesen.

Das Ziel der vorliegenden Arbeit war es, das Vorkommen von gelösten Thioarsenaten in Mooren zu untersuchen und den Einfluss von reduziertem S auf ihre Bildung, Mobilität und Bindung an organisches Festphasenmaterial im Vergleich zu As-Oxoanionen aufzuklären. Ein ähnliches Verhalten wurde für Sb angenommen, und deshalb wurden ebenfalls das Sb-Bindungsverhalten und die Sb-Mobilität in einer Kombination von Labor- und Feldexperimenten untersucht, um neue Erkenntnisse über den Verbleib von Sb in sub- bis anoxischen, organikreichen Umweltsystemen zu erhalten.

Die ersten beiden Studien untersuchten das Vorkommen von anorganischen Thioarsenaten in einem natürlich As-kontaminierten Mooregebiet und die daraus resultierenden Erkenntnisse für die As-Mobilität. Bis zu 93% der löslichen As-Spezies waren Thioarsenate und die dominante detektierte Spezies, Monothioarsenat (MTAs(V)), entstand wahrscheinlich durch Reaktion von Arsenit mit oberflächenassoziiertem nullwertigen S. Inkubationsexperimente von MTAs(V), Arsenat und Arsenit mit sauerstoff(O)-haltigen Carboxyl- und Phenolgruppen eines Modelltorfs zeigten bei leicht saurem bis neutralem pH-Wert nur eine geringe Adsorption von MTAs(V) und Arsenat. Arsenit wurde substantiell über die Bindung As(III)-O-organischer Kohlenstoff (C_{org}) komplexiert. Inkubationen von MTAs(V) und Arsenit mit thiolreichem Modelltorf bestätigten eine starke As(III)-S- C_{org} -Komplexierung von Arsenit, die von schwach alkalischen zu schwach sauren Bedingungen zunahm. Für MTAs(V) wurde eine As-Adsorption von neutralem zu leicht saurem pH-Wert beobachtet und auf die Adsorption von Arsenit zurückgeführt, das durch säurekatalysierte Dissoziation von MTAs(V) gebildet wurde, und wiederum eine hohe Affinität zu Thiolgruppen von Torf hatte. Bei pH 8,5, wenn MTAs(V) stabil war, wurde keine Komplexierung von MTAs(V) mit Thiolgruppen beobachtet. Somit waren MTAs(V) und Arsenat sehr mobil, während Arsenit eine hohe Affinität zu Carboxyl-/Phenol- und Thiolgruppen von Torf zeigte.

Die folgenden beiden Studien konzentrierten sich auf das As-Mobilisierungspotential durch reduzierten S, wenn As(III) zuvor an NOM innerhalb von Modelltorf und in organikreichen Aquiferlinsen gebunden war. Im Vergleich zu Kontrolleexperimenten verursachte die Zugabe von Sulfid oder Polysulfiden bei saurem pH-Wert eine erhebliche As-Retention im Torf. Signifikante As-Mobilisierung erfolgte durch Thioarsenatbildung, in ähnlich hohen Mengen bei neutralem wie leicht alkalischem pH-Wert. Spektroskopische Analysen bestätigten eine Abnahme der As(III)-O-C_{org}-Bindung, was darauf hindeutete, dass die As-Mobilisierung über Arsenit-Desorption, Reaktion mit reduziertem S und Bildung von Thioarsenaten erfolgte. Die gebildeten Thioarsenate blieben ohne (Re)adsorption an Torf in Lösung. In ähnlicher Weise wurde eine As-Mobilisierung stromabwärts von organikreichen Linsen in Aquifersanden im Vergleich zu Kontrollsäulenexperimenten ohne Linsen beobachtet. Die stattfindende Sulfatreduktion produzierte Sulfid und nullwertigen S. Innerhalb der Linsen verlagerten Thiolgruppen As über die Bildung von As(III)-S-C_{org}-Bindungen zunächst in die Festphase, während nullwertiger S As durch Thioarsenatbildung unter den leicht alkalischen experimentellen Bedingungen wieder mobilisierte.

Die fünfte und sechste Studie untersuchte die Bindungsmechanismen von Antimonit mit organischen funktionellen Gruppen von Modelltorf und unter Feldbedingungen in einem mit Grubenwasser beaufschlagten Moor. Inkubationsexperimente zeigten starke Antimonit-Adsorption an Torf durch die Bildung von Sb(III)-O-C_{org}-Bindungen, was durch spektroskopischen Analysen bestätigt wurde. Die Antimonit-Adsorption nahm mit zunehmendem Thiolgehalt im Torf stark zu. Spektroskopische Daten zeigten, dass die Sb-Adsorption über eine Sb(III)-S-C_{org}-Koordinierung erfolgte und anorganische Sb-S-Phasen dabei ausgeschlossen werden konnten. Die Sb-Festphasenspezifizierung in dem mit Grubenwasser beeinflussten Moor bestätigte die hohe Affinität von Antimonit zu O-haltigen funktionellen Gruppen. Die Sb(III)-S-C_{org}-Koordinierung nahm mit zunehmender Torftiefe stark zu. Es wurde kein organisch komplexiertes Sb(V) gefunden. Die Sb-Flüssigphasenspezifizierung im Oberflächen- und Porenwasser wurde von Antimonat dominiert und die Antimonitkonzentration war allgemein gering. Es wurden keine Thioantimonate gefunden. Antimonat war daher sehr mobil, während Antimonit eine sehr hohe Affinität zu den funktionellen Gruppen des Torfes zeigte.

Insgesamt implizieren die Ergebnisse, dass reduzierter S komplexe Einflüsse auf die As und Sb-Mobilität in organikreichen Umweltsystemen hat. Während die Thiolbindung mit und schließlich die Sulfidmineralfällung von As und Sb unter anoxischen Bedingungen und bei saurem pH-Wert As und Sb effizient sequestrieren, kann die Bildung hochmobiler Thioarsenate durch Reaktion von Arsenit mit reduziertem S organisches Festphasenmaterial bereits ab quasineutralem pH-Wert von einer As-Senke zu einer As-Quelle machen. Das hier erlangte Wissen ist wichtig für die sichere und langfristige Bewirtschaftung kontaminierter Moore und anderer organikreicher Umweltsysteme, um As und Sb in der Festphase gebunden zu halten.

Table of Contents

Acknowledgements.....	vii
Abstract.....	ix
Zusammenfassung	xi
Table of Contents.....	xiii
List of Abbreviations	xv
List of Figures	xvii
Extended Summary.....	1
1 Introduction	1
1.1 Arsenic and antimony occurrence and fate in the environment	1
1.2 Natural organic matter in the environment	5
1.3 Interactions of natural organic matter with arsenic and antimony.....	8
1.4 Objectives	10
2 Methods.....	13
2.1 General practices and analytical methods	13
2.2 Occurrence of thioarsenates in the minerotrophic peatland Gola di Lago and its implications for arsenic mobility in peatlands (study 1)	16
2.3 Mechanisms of arsenic complexation with O-containing functional groups of model peat (study 2)	16
2.4 Influence of reduced S on the fate of As during sulfurization of As-bearing model peat (study 3)	17
2.5 Influence of reduced S on the fate of As in sulfate-rich, alluvial aquifer sediments with high-organic matter interlayers (study 4)	17
2.6 Laboratory study: spectroscopic investigations of antimony complexation with thiol and carboxyl/phenol groups of model peat (study 5)	18
2.7 Field study: investigation of the Sb binding environments in a mine water impacted peatland (study 6)	18
3 Results and Discussion.....	21
3.1 Occurrence of thioarsenates in the peatland Gola di Lago and its consequences for As mobility in peat (studies 1 and 2).....	21
3.2 Influence of reduced S on the fate of As during sulfurization of As-bearing model peat and in alluvial aquifer sediments with high-organic matter interlayers.....	24
3.3 Binding mechanisms of antimonite to organic functional groups of model peat and under field conditions in a mine water impacted peatland (studies 5 and 6)	28
4 Conclusions	33
References	35
Contributions to Studies 1-6.....	47

Appendix: Studies 1-6.....	51
Study 1: Monothioarsenate transformation kinetics determining arsenic sequestration by sulfhydryl groups of peat	53
Study 2: Complexation of Arsenite, Arsenate, and Monothioarsenate with Oxygen-Containing Functional Groups of Natural Organic Matter: An XAS Study.....	93
Study 3: Arsenic Fate in Peat Controlled by pH-dependent Role of Reduced Sulfur	129
Study 4: Redox Heterogeneities Promote Thioarsenate Formation and Release into Groundwater from Low Arsenic Sediments	163
Study 5: Antimonite Complexation with Thiol and Carboxyl/Phenol Groups of Peat Organic Matter....	187
Study 6: Antimonite Binding to Natural Organic Matter: Spectroscopic Evidence from a Mine Water Impacted Peatland.....	221
List of Publications	281
Supervised Bachelor and Master Theses.....	282
(Eidesstattliche) Versicherungen und Erklärungen	283

List of Abbreviations

DOC	dissolved organic carbon
DTAs(V)	dithioarsenate
EXAFS	extended X-ray absorption fine structure
Fh	ferrihydrite
FT	Fourier-transform
FT-IR	Fourier-transform infrared spectroscopy
ICP-MS	inductively coupled plasma mass spectrometry
ICP-OES	inductively coupled plasma optical emission spectrometry
ITFA	iterative transformation factor analysis
LCF	linear combination fitting
MTAs(V)	monothioarsenate
NMR	nuclear magnetic resonance
NOM	natural organic matter
PCA	principal component analysis
pH _{PZC}	point of zero charge
PS	polysulfide
S(0)-species	zero-valent sulfur-containing species
SEM-EDS	scanning electron microscopy energy-dispersive X-ray spectroscopy
SOM	soil organic matter
TetraTAs(V)	tetrathioarsenate
TriTAs(V)	trithioarsenate
TT	target-transform testing
WHO	World Health Organization
XANES	X-ray absorption near edge structure
XAS	X-ray absorption spectroscopy
XRD	X-ray powder diffraction
XRF	X-ray fluorescence spectrometry

List of Figures

- Figure 1:** Overview of arsenic and antimony oxoacids and simplified model for formation of inorganic thioarsenates (adapted from Planer-Friedrich *et al.*⁴⁰). For simplicity, all species are depicted fully protonated. Abbreviations: MTAs(V) = monothioarsenate, DTAs(V) = Dithioarsenate, TriTAs(V) = trithioarsenate, TetraTAs(V) = tetrathioarsenate.....3
- Figure 2:** Comparison of arsenate and arsenite sorption edges on goethite as presented by Dixit and Hering⁴⁹. The total arsenic concentrations shown are 100 μM (circles) and 50 μM (squares). Open symbols represent arsenate and closed symbols arsenite.4
- Figure 3:** Polyhedral representations of arsenate ($\text{As}^{\text{V}}\text{O}_4$) (A) and antimonate ($\text{Sb}^{\text{V}}\text{O}_6$) (B) inner-sphere sorption geometries on a goethite model (geometries are analogous for $\text{As}^{\text{III}}/\text{Sb}^{\text{III}}\text{O}_3$ complexes). Sorption complexes are: ¹V = monodentate, ²C = corner-sharing, bidentate binuclear, ²E = edge-sharing bidentate mononuclear, ³C = tridentate over structural vacancies. Models were adapted from Sherman *et al.*⁶¹ after Foster and Kim⁴⁶ (A) and Scheinost *et al.*⁷ (B).5
- Figure 4:** Model “humic compound” which represents many functional groups of natural organic matter (slightly modified) as presented by Sundararajan *et al.*⁹⁰.....6
- Figure 5:** Suggested conceptual model showing summarized and simplified processes investigated in studies 1-6 (green arrows) in accordance with current literature knowledge^{7,40,46,65,67,68,76-79,81,83,115,121,164} (black arrows) of (A) As and (B) Sb (bio)geochemistry in an organic-rich environment like a peatland. Only directly important processes of Fe and S chemistry for As and Sb behavior are depicted. Initial formation of thioarsenites from dissolved sulfide and arsenite is excluded, since they are regarded as instable intermediates directly reacting to thioarsenates.^{38,39} Dotted lines illustrate general inner-sphere coordination of the respective species but no specific coordination environments.....34

Extended Summary

1 Introduction

1.1 Arsenic and antimony occurrence and fate in the environment

Arsenic (As) and antimony (Sb) are potentially toxic trace elements that occur ubiquitously in the environment. The average crustal abundances in the lithosphere of As and Sb are 2 and 0.2 mg kg⁻¹, respectively. From the lithosphere, they are released into ground- and surface water, soils, and the atmosphere by mineral weathering or during volcanic emissions. Thereby, As background concentrations are generally much higher than the corresponding values for Sb in soils and sediments (As ~6.0 mg kg⁻¹ vs. Sb ~1 mg kg⁻¹), while elevated concentrations are comparable.¹

Arsenic is or was used industrially in the manufacture of numerous products like semiconductors, glass, paint as well as ceramics, and in the latter half of the 20th century as pesticide, herbicide and for wood preservation.¹ Antimony also has a wide range of uses including the production of, among others, flameproof retardants, tracer bullets as well as automobile brake linings. Antimony is further used as catalyst in plastics synthesis.² World production for As is considerably lower than that of Sb. In 2019 the estimated As mine output was 35,000 t compared to 140,000 t for Sb, whereby the latter steadily increased over the last 20 years.³

Environmental enrichments of both metalloids occur naturally in areas of geological mineralization, but also due to anthropogenic action.^{1,2} However, the majority of Sb contamination originates from mining and smelting as well as industrial emission sources including shooting ranges.⁴⁻⁷ In contrast, next to anthropogenic contamination, the best known exposure pathway of humans toward As is the consumption of As-rich drinking water from geogenic sources in South and Southeast Asian countries.^{8,9} Arsenic-contaminated drinking water is therefore considered the cause of “the largest poisoning of a population in history”.¹⁰ Based on large-scale groundwater surveys, up to 100 million people are exposed to drinking water with As levels higher than 10 µg As L⁻¹, the threshold value set by the World Health Organization (WHO).^{9,11} The use of As-rich groundwater for the irrigation of rice paddies and the fact that rice is an efficient accumulator of As, with transfer of the metalloid up into the grains, adds an additional thread to millions of people.¹² Further, the contamination of paddy soils from industrial and mining activity exposes people not only to a health risk of As but also of Sb.^{12,13}

While it is known that long-term chronic exposure to As causes skin, kidney, lung, bladder cancer, and other severe diseases,¹⁴ to date no clear evidence exists^{15,16} for the carcinogenicity of chronic Sb exposure by the oral route.¹⁷ The derivation of guideline values for Sb is therefore somehow unclear with respect to As. The United States Environmental Protection Agency,¹⁸ Health Canada¹⁶ and the European Union¹⁹ use 6, 6, and 5 µg Sb L⁻¹, respectively, while the WHO¹⁷ drinking water threshold for Sb is set to 20 µg Sb L⁻¹.

In general, for a thorough evaluation of the (eco-)toxicity of both elements, the exposure to specific As or

Sb species in their respective redox state has to be considered, whereby trivalent species are generally considered more toxic than their pentavalent counterparts.^{2,20-24} Therefore, understanding the key factors and biogeochemical processes controlling the fate of As and Sb species in environmental systems is crucial for assessing the risks these metalloids pose to people living in contaminated regions around the world.

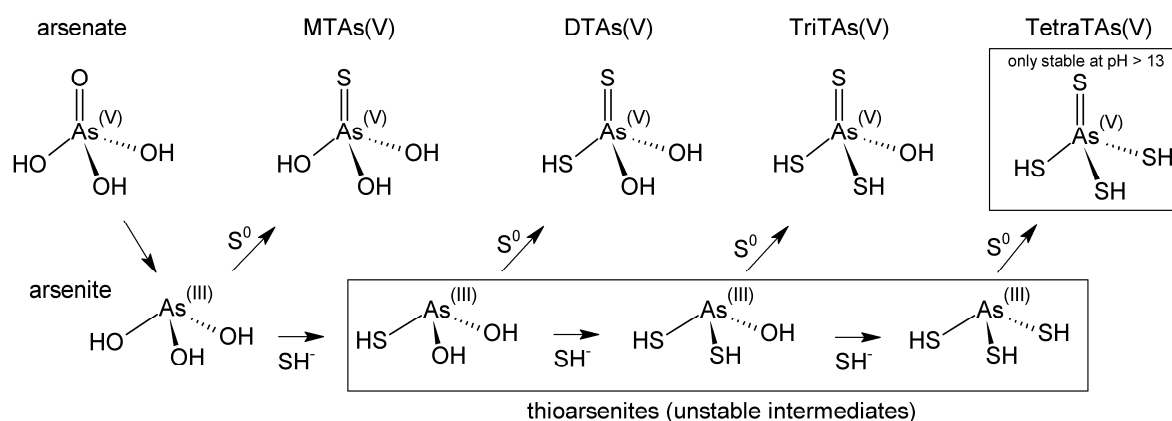
Both elements are members of group 15 in the periodic table and are situated below phosphorus (P), thus similarly having five valence electrons in a s^2p^3 electron configuration and possible oxidation states between -III and +V. Arsenic and Sb are chalcophile and siderophile and further have a high affinity for binding to oxygen (O). Therefore, they form many oxide, sulfide and mixed As/Sb-Fe oxide minerals at ambient pressure-temperature conditions, like As_2O_3 (arsenolite), $FeAsO_4 \cdot 2H_2O$ (scorodite), Sb_2O_3 (valentinite) and $FeSbO_4$ (triphyte) and the sulfides $FeAsS$ (arsenopyrite), As_2S_3 (orpiment), and Sb_2S_3 (stibnite).^{20,25}

In aqueous solutions with environmentally relevant pH conditions (pH ~3-10), As forms the trivalent oxoacid arsenite ($H_xAs^{III}O_3^{x-3}$, $x = 0-3$, $pK_{a1} = 9.17$) under moderately reducing to moderately oxidizing conditions and the pentavalent arsenate ($H_xAs^V O_4^{x-3}$, $x = 0-3$, $pK_{a1} = 2.30$, $pK_{a2} = 6.99$, $pK_{a3} = 11.80$) under oxidizing conditions.²⁶ Antimony reacts similar to As in aqueous solutions, however, still some ambiguity on the exact hydrolysis reactions exist.²⁷⁻³⁰ In general, under reducing conditions, the trivalent oxoacid antimonite ($H_xSb^{III}O_3^{x-3}$, $x = 0-3$, $pK_{a1} = 11.82$) is predicted to prevail, while at oxidizing conditions, the pentavalent antimonate ($H_xSb^V(OH)_6^{x-1}$, $x = 0-1$, $pK_{a1} = 2.72$) dominates the aqueous speciation. The octahedral configuration of Sb(V) compared to the tetrahedral coordination of P(V) or As(V) with O is explained by its larger ionic radius and lower charge density.³¹ Abiotic redox reactions of As and Sb species, respectively, which are thermodynamically feasible, are often slow and most often kinetically catalyzed directly or indirectly by microorganisms in the environment.³²

Under reducing and circumneutral to alkaline pH conditions, As and Sb thioacids can form in S-rich environments by reaction of arsenite or antimonite with reduced sulfur (S) species.³³⁻³⁷ Thereby, thioarsenates ($H_xAs^V S^{II}_n O_{4-n}^{x-3}$, $n = 1-4$, $x = 0-3$) are proposed to form in two steps from arsenite. First, at conditions of excess SH over OH, ligand exchange leads to the formation of thioarsenites ($H_xAs^{III} S^{II}_n O_{3-n}^{x-3}$, $n = 1-3$, $x = 0-3$) as unstable intermediates.^{38,39} Second, addition of zero-valent S transforms thioarsenites to thioarsenates.⁴⁰ Only the formation of monothioarsenate ($H_xAs^V S^{II} O_3^{x-3}$; $x = 0-3$; MTAs(V)) does not require excess sulfide, because it forms directly from arsenite and zero-valent S or zero-valent-S-containing species (hereafter denoted as S(0)-species) as, for example, colloidal elemental S or polysulfides⁴⁰ (Figure 1). Also, reactions of surface associated S(0)-species with arsenite are proposed to form MTAs(V).⁴¹ Thioantimonates were suggested to form in a similar way,³⁷ but their occurrence and formation pathways are much less studied. A recent study, for example, proposed that direct SH/OH⁻ ligand exchange at the pentavalent antimonate, with a maximum at neutral pH, is also possible.⁴² By direct comparison, for example in geothermal systems, ~80% of total aqueous As were thioarsenates,

whereas only ~40% of total Sb accounted for thioantimonates, suggesting higher affinity of As toward reduced S in aqueous solutions.³⁷ Microorganisms, algae, plants, and animals produce volatile and non-volatile methylated As and Sb species as well as more complex structures like arsenobetaine, arsenocholine and arsenosugars.^{20,43} Abiotic reactions of sulfide with methylated As oxoacids can even form methylated thioarsenates under slightly acidic conditions in environmental systems.^{44,45} To date no observations about methylated thioantimonates have been made.

Arsenic oxo- and thioacids



Antimony oxoacids

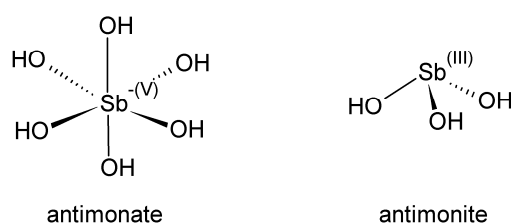


Figure 1: Overview of arsenic and antimony oxoacids and simplified model for formation of inorganic thioarsenates (adapted from Planer-Friedrich *et al.*⁴⁰). For simplicity, all species are depicted fully protonated. Abbreviations: MTAs(V) = monothioarsenate, DTAs(V) = Dithioarsenate, TriTAs(V) = trithioarsenate, TetraTAs(V) = tetrathioarsenate.

In environmental systems with low amounts of natural organic matter (NOM), aqueous As and Sb are primarily retained by adsorption reactions to the surfaces of fine-grained fractions of primary and secondary minerals. Sorption on mineral surfaces has therefore been extensively studied in the last decades,^{46,47} and thus, only the most important findings will be summarized in the following.

The major sorbents in those systems are iron (Fe), aluminum (Al) and manganese (Mn) (oxyhydr)oxides, which possess reactive ≡OH surface sites with variable charges mostly depending on pH and ionic strength as well as an inherent point of zero charge (pH_{PZC}).⁴⁸ Due to primarily electrostatic (Coulomb) interactions in outer-sphere complexations, negatively charged oxoanions, for example arsenate, adsorb strongly to positively charged goethite ≡OH₂⁺ surfaces at low pH and sorption rapidly decreases with increasing pH (Figure 2). Competition with other negatively charged ions can strongly influence outer-sphere sorption. Additionally, arsenate can form inner-sphere complexes with goethite. Arsenite stays uncharged over a

wide pH-range ($pK_{a1} = 9.17$) but still has a high sorption affinity, which can mostly be attributed to inner-sphere surface complexation⁴⁹ resulting in energetically favorable strong covalent bonds. The same mechanisms apply for antimonate and antimonite sorption to goethite.⁵⁰

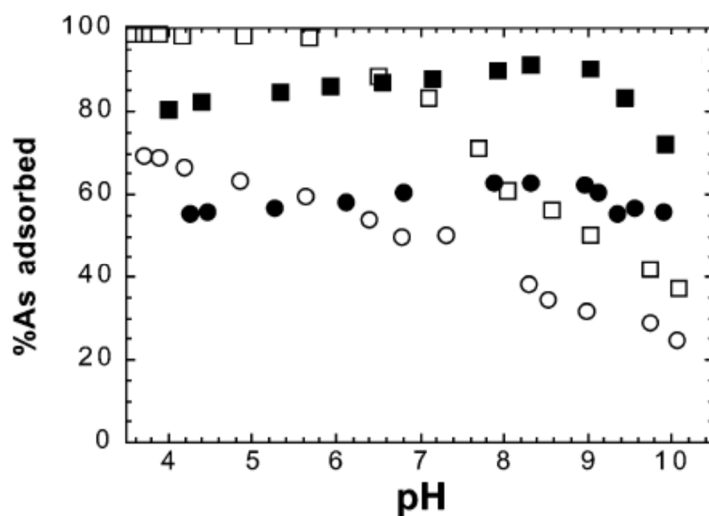


Figure 2: Comparison of arsenate and arsenite sorption edges on goethite as presented by Dixit and Hering⁴⁹. The total arsenic concentrations shown are 100 μM (circles) and 50 μM (squares). Open symbols represent arsenate and closed symbols arsenite. Copyright (2020), with permission from American Chemical Society.

Especially for inner-sphere complexation, each As and Sb species has its own specific sorption characteristics to the different minerals. For example, Fendorf *et al.*⁵¹ suggested a monodentate (¹V), a bidentate binuclear (²C), and a bidentate mononuclear (²E) complex for inner-sphere complexation of arsenate to goethite, while for arsenite, Manning *et al.*⁵² found a bidentate binuclear (²C) complex by use of extended X-ray absorption fine-structure (EXAFS) spectroscopy. Arsenite and arsenate can also form inner-sphere complexes to other Fe (oxyhydr)oxides,⁵³ Al (oxyhydr)oxides⁵⁴ and Mn oxides, however, As(III) will be oxidized to As(V) on the Mn oxide surfaces before sorption.^{55,56} Similar observations were made for antimonate, with mono- and bidentate inner-sphere surface complexation to Fe, Al and Mn (oxyhydr)oxides and for antimonate on Fe and Al (oxyhydr)oxides.^{7,57-60} Figure 3 summarizes possible geometries of surface complexes of arsenate and antimonate on Fe (oxyhydr)oxide surfaces.

Only little is known about the sorption behavior of thioarsenates on Fe and Al (oxyhydr)oxides. Couture *et al.*⁶² found MTAs(V) and TetraTAs(V) bound via a monodentate inner-sphere complex to ferrihydrite (Fh) and goethite, while in the presence of Fe sulfides, both thioarsenates were unstable and transformed to arsenite. Sorption experiments of MTAs(V) to amorphous Al oxyhydroxide revealed a bidentate binuclear complexation at higher pH and a partial reduction to arsenite at low pH.⁶³ In each case, the extent of adsorbed As was lower for thioarsenates compared to arsenate or arsenite, which suggests a higher mobility of these species in the environment.⁶²⁻⁶⁴

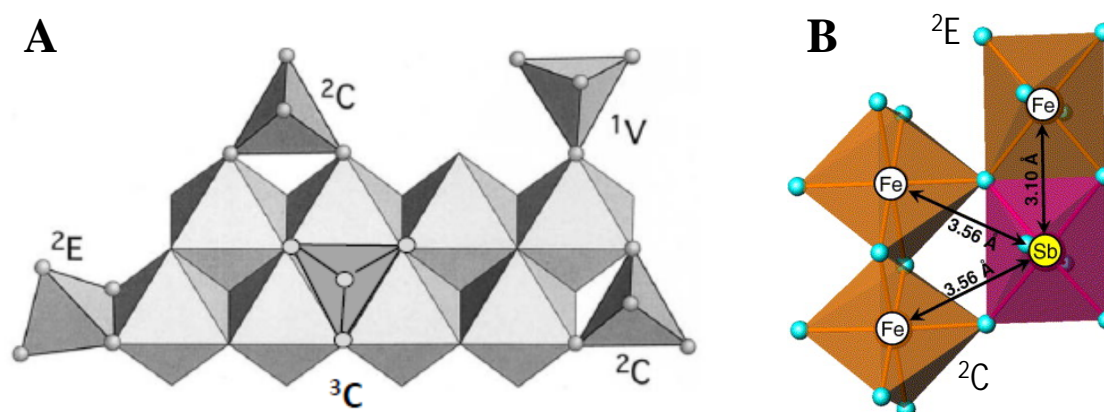


Figure 3: Polyhedral representations of arsenate ($\text{As}^{\text{V}}\text{O}_4$) (A) and antimonate ($\text{Sb}^{\text{V}}\text{O}_6$) (B) inner-sphere sorption geometries on a goethite model (geometries are analogous for $\text{As}^{\text{III}}/\text{Sb}^{\text{III}}\text{O}_3$ complexes). Sorption complexes are: ^1V = monodentate, ^2C = corner-sharing, bidentate binuclear, ^2E = edge-sharing bidentate mononuclear, ^3C = tridentate over structural vacancies. Models were adapted from Sherman *et al.*⁶¹ after Foster and Kim⁴⁶ (A) and Scheinost *et al.*⁷ (B). Copyright (2020), with permission from Elsevier.

While sorption to (oxyhydr)oxides is dominant at mostly oxic conditions, reductive dissolution of for example Fe (oxyhydr)oxide minerals,⁶⁵ induced by soil flooding and microbial activity,⁶⁶ can lead to As and Sb release.^{67,68} Consequentially, the metalloids can be mobilized into the aqueous phase or repartitioned between not reduced Fe (oxyhydr)oxides and freshly precipitated secondary mineral phases. In sulfate-rich environments, microbially mediated sulfate reduction generates dissolved sulfide,⁶⁹ which can lead to the formation of Fe sulfide minerals like mackinawite (FeS)⁷⁰ and finally pyrite (FeS_2), with capacities for As/Sb incorporation, surface complexation, or surface precipitation.⁷¹⁻⁷⁴ High levels of Fe(II) and dissolved sulfide may induce homogenous precipitation of As with Fe and S, resulting in the formation of arsenopyrite or As-rich (arsenian) pyrite.⁷⁵ In environments where Fe(II) is titrated out by Fe sulfides, the remaining sulfide can precipitate at acidic to neutral pH as amorphous As/Sb sulfides^{76,77} and subsequently form more stable phases like orpiment, realgar or stibnite.^{20,25} However, reaction of dissolved sulfide with Fe (oxyhydr)oxides leads in part to sulfide oxidation to form solid-phase associated S(0)-species, as well as to overall Fe mineral transformation.^{78,79} At circumneutral to alkaline pH, previously adsorbed As can then react with reduced S (S(0)-species and sulfide) to form thioarsenates, which can lead to overall As mobilization in such systems.^{34,80-82} For Sb, however, sulfidization of Sb-bearing Fh only led to minor formation and mobilization of thioantimonates.⁸³

1.2 Natural organic matter in the environment

Natural organic matter refers to a complex mixture of different organic compounds and is formed in both terrestrial and aquatic environments through chemical and microbial decomposition of plant litter as well as animal and microbial biomass.^{84,85} Due to the immense number of different chemical constituents of NOM, it is not practically feasible to characterize it simply based on individual compounds. Indeed, the formation mechanisms and its long-term stability are under ongoing debate.⁸⁶ For example, there still exists some ambiguity on whether NOM is chemically a true macromolecular entity⁸⁷ or just consists of self-assembled aggregates of small compounds held together by relatively weak noncovalent interactions

(primarily electrostatic and hydrogen (H) bonding) thereby mimicking large macromolecules (Lehmann and Kleber⁸⁶ and references therein).

In general, multiple environmental dynamics are affecting the decomposition of NOM such as time, climate, topography, minerals as well as parent material, and the microbial community available, and thus control the degree of its accumulation in the environment. These factors result in a range of soil NOM contents from ≤ 1 weight-% in the mineral horizons of some tropical and sandy soils to nearly 100 weight-% in ombrotrophic peat bogs, where the decomposition of organic material is slowed down under anoxic and often cold conditions.^{85,88} The average elemental composition of NOM reveals that it is primarily composed of carbon (C) (55-57%), O (34-36%), H (4-6%), nitrogen (N) (0.9-3%), and S (0.4-1.8%).⁸⁴ Despite NOM being a complex mixture with unknown exact composition, it possesses unique combinations of carboxylic, phenolic, esteric, quinone, aliphatic hydroxylic, amino, nitroso, and thiol functional groups, as well as nonpolar aliphatic and aromatic structural units.^{84,89} An example for a model “humic compound”, to demonstrate possible units and functional groups of NOM, is depicted in Figure 4.

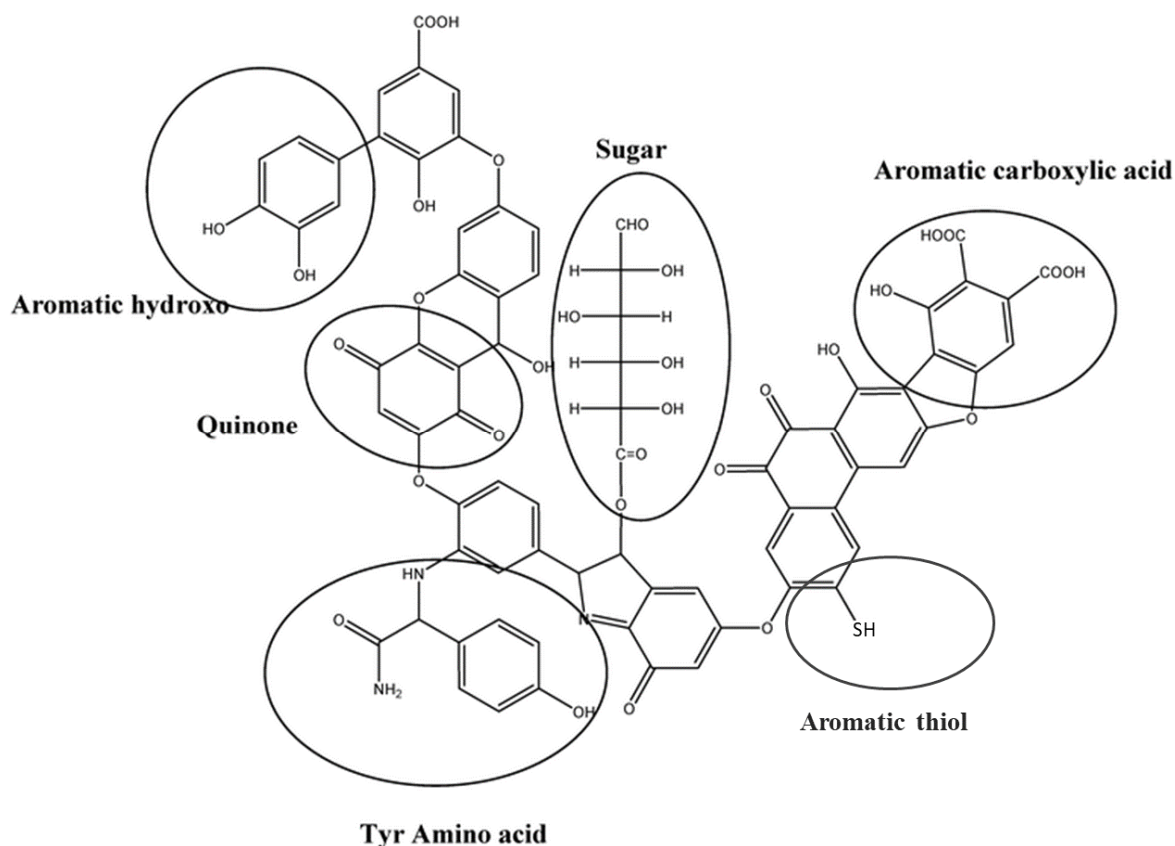


Figure 4: Model “humic compound” which represents many functional groups of natural organic matter (slightly modified) as presented by Sundararajan *et al.*⁹⁰ Copyright (2020), with permission from Royal Society of Chemistry.

There are several inherent properties to NOM which gives it a central role in aqueous and terrestrial biogeochemistry. Primarily due to its ubiquitous quinone functional groups, NOM is redox-active⁹¹ and can influence the biogeochemistry of trace metal(loid)s and other (organic) contaminants.⁹²⁻⁹⁵ Further, it is known to act as microbial electron shuttle in reductive dissolution processes^{95,96} and can for example be used by microorganisms as a terminal electron acceptor (in reversible redox cycles) during anaerobic

respiration.^{95,97,98}

Moreover, NOM possesses variable charges which originate mostly from deprotonated carboxylic (R-COOH) and phenolic (R-OH) groups (Brønsted acids) with proton dissociation constants (pK_a) of ~3 to ~5 and ~7 to ~10, respectively. To a lesser extent, also sulfhydryl (thiol) groups (R-SH, pK_a ~5 to ~11) contribute to the negative charge of NOM. Next to acidic groups, NOM features base groups like the amino group (R-NH₂) which are able to accept protons and consequently are positively charged. However, the concentration of these groups is low compared to the acid groups, which results in an overall net-negative charge of NOM at circumneutral pH.^{48,99}

As a consequence of their net negative charge, NOM can influence the (trans)formation, structure and reactivity of many minerals. Dissolved NOM can, for example, effect the formation (biomineralization) of Fe and Mn minerals through complexation and solubilization of the metal ions and by sorption to the mineral surface, generally causing the formation of less crystalline minerals.¹⁰⁰⁻¹⁰² Mineral-organic associations can lower the pH_{PZC} of particularly Fe minerals and therefore directly influence nutrient and contaminant mobility.^{48,103,104} Additionally, by conveying negative charge to mineral surfaces, NOM can stabilize mineral colloids,^{105,106} and thus facilitate their transport in the environment. Further, dissolved NOM competes especially with anionic (contaminant) species for sorption sites on minerals, contributing to their overall higher mobility.¹⁰⁷⁻¹⁰⁹ Strong mineral-organic associations or NOM occlusion during mineral formation prevent biodegradation and mineralization of C and are recognized as critically important to the long-term stabilization of organic C in soils and marine sediments.^{86,110,111}

The mostly anionic (Coulomb) interactions of NOM with variable charges from mineral surfaces, as described before, can be generalized for metal cations by the concept of “hard” and “soft” acids and bases. Therein, “hard” applies to species which have a high charge density and are weakly polarizable, whereas “soft” species have a lower charge density and are strongly polarizable. These characteristics have implications for binding site strength, and also for competition among metals. For example, Ca(II), which is abundant in natural waters, may compete effectively with Cd(II) at carboxylic sites, but hardly at thiol sites.⁹⁹ However, the binding preferences explained by this concept are not exclusive as shown for Cd(II) binding on humic acid (HA) under varying redox conditions.¹¹²

Moreover, complexation of NOM with redox-active cations can stabilize them against reduction/oxidation. For example, through binding of carboxylic or phenolic groups to Fe(III),¹¹³ the redox potential of the Fe(II)/Fe(III) redox couple is lowered¹¹⁴ and consequentially Fe in NOM-rich environments is stabilized in its oxidized redox state over a broad range of redox conditions. This mechanism can explain the occurrence of Fe(III) in reduced, water-saturated histosols.^{115,116} It is further worth noting that the high affinity between metals and certain functionalities of dissolved as well as solid NOM can result in a complex interplay in the environment. Mehlhorn *et al.*¹¹⁷, for example, investigated a NOM and redox gradient at a mofette site and found copper (Cu) immobilized and mainly bound to solid NOM at the anoxic center of the mofette

and at an oxic reference soil. Under suboxic conditions in between these two extremes, pore water Cu concentration, however, was elevated due to the increased complexation of Cu with dissolved NOM.

Among the non-metallic minor components of NOM (N, P, and S), S is exceptional. Additionally to the assimilation by plants and microbes, it can be incorporated into the NOM structure during early diagenesis, which is known to occur in many environmental systems such as peatlands, wetlands, deep groundwaters, as well as marine, estuarine, and lake sediments.^{118,119} The exact mechanisms of diagenetic S incorporation are still under debate, but generally require functional groups containing π -bonds (Hoffmann *et al.*¹²⁰ and references therein). The reaction of dissolved sulfide (for example originating from microbial sulfate reduction) with solid and dissolved NOM under anoxic conditions results in the formation of surface associated S(0)-species and various organic S functional groups, mainly thiols as well as organic disulfides, or S heterocycles.¹²⁰⁻¹²² Therefore, depending on the prevalent redox conditions, reduced organic S constitutes about 10-30% of total S in soils, whereas it can increase up to ~75% in NOM-rich soils.¹²³⁻¹²⁵

The formation of As and Sb complexes with S- and also O-containing functional groups of dissolved as well as solid NOM influences the metalloids` cycling in the environment and will therefore be introduced in more detail in the following part.

1.3 Interactions of natural organic matter with arsenic and antimony

There are many properties of NOM, described above in detail, which also can have direct or indirect influence on As and Sb mobility, such as redox active quinones,^{92,126-128} NOM-mineral interactions^{109,129} or dissolved NOM in the role as competitor for sorption sites.^{108,130-132} In most of these processes dissolved NOM leads to an increase in As and Sb mobility in systems with low general NOM content (mineral-dominated environments), but when solid NOM becomes a main sorbent, for example in high-organic wetland soils, it has been shown that NOM can sequester As and Sb.

Several studies already observed an association of As with solid NOM in peatlands¹³³⁻¹³⁵ or high-organic aquifer sediments.^{136,137} Especially in oxic zones, ternary complex formation, where polyvalent cations such as Ca(II) or Fe(III) can serve as bridges between negatively charged As species and NOM, have been suggested by correlations between As, C, and Fe from field¹³⁸⁻¹⁴¹ and laboratory studies^{142,143} and have finally been proven by EXAFS spectroscopy for arsenate^{144,145} and arsenite.¹⁴⁶

The direct complexation of arsenite and arsenate with O-containing organic ligands (mostly carboxylic and phenolic groups) has so far been investigated only in a few studies with HA, which showed generally only low binding affinities.^{143,147-150} Buschmann *et al.*¹⁴⁷ estimated from experiments with Aldrich HA that under environmentally relevant conditions ~10% of arsenite and arsenate can be complexed by dissolved NOM in aquatic environments. They hypothesized that an OH ligand exchange reaction between As species and hydroxylic (R-OH) groups of NOM could be a mechanism of such binary As binding. In investigations with Fe spiked model peat NOM, Hoffmann *et al.*¹⁴⁶ had to include a C-path at 2.70-2.77 Å in addition to

an Fe-path in the second shell during EXAFS shell-fitting in order to achieve reasonable results. They estimated that at least 27% of total arsenite was bound via phenolic NOM groups. Similarly, Guénet *et al.*¹⁵¹ provided XAS-based evidence for the complexation of arsenate and arsenite mixtures with NOM by As-O-C_{org} coordination, in addition to As binding to Fe nanoparticles during oxidation of reduced floodplain soil suspensions, further demonstrating that binary As coordination could have been so far underestimated in high-organic matter systems.

In contrast, the high affinity of As for reduced organic S was shown by Langner *et al.*¹¹⁵, who gave first spectroscopic evidence that As(III) was mainly 3-fold coordinated at 2.26 Å with thiol groups of NOM in deep layers of the naturally As contaminated peatland Gola di Lago, Switzerland. These findings were experimentally confirmed with EXAFS shell-by-shell fitting by Hoffmann *et al.*¹²⁰, who equilibrated arsenite with sulfide-reacted (thiol-rich) model peat NOM. They showed that a passive sorption mechanism, next to As uptake and active detoxification by plants via phytochelatin,¹⁵² can exist in peatlands, where arsenite reacts with thiol groups of plant debris and their degradation products.

Similar to the sulfidization of Fe (oxyhydr)oxides, ThomasArrigo *et al.*⁴¹ found thioarsenate formation upon sulfidization of As-bearing organic freshwater flocs from the Gola di Lago peatland at pH 7, where As was initially bound to Fe phases in the peat. Moreover, aqueous As mobilization from alluvial peat sediments in South-East Asia was observed,^{137,153} where As was primarily bound via thiol groups or incorporated in pyrite within the peat layer.¹³⁷ As elaborated before, biogenic sulfide can efficiently react with NOM. Next to the formation of As(III) sequestering groups like thiols, this process also forms surface associated S(0)-species, thus, the concentrations of dissolved sulfide in peatlands are generally low.^{118,154,155} Whether thioarsenates can also form under natural low-sulfide conditions in peatlands like Gola di Lago and whether their mobility is influenced by binding to O-containing or thiol groups of peat NOM is unknown. Further it is not clear, whether thioarsenate formation can only occur by reaction with S(0)-species associated to Fe phases or whether reactions on NOM surfaces may also be involved. Therefore, the overall question appears, whether organic sediments rich in thiol groups, are only a sink or also can become a source for As under certain conditions.

In contrast to As, the association of Sb with solid NOM has so far only been shown in a few field studies, including studies from peat bogs in Switzerland and the United Kingdom, where a strong association of atmospheric anthropogenic Sb depositions with NOM was observed.^{134,156-158} Further, Fawcett *et al.*¹⁵⁹ revealed the association of Sb with solid NOM in aquatic sediments residing adjacent to a former mining site.

In laboratory experiments, the complexation of antimonite and antimonate with O-containing ligands in aquatic solutions was studied in presence of low-molecular aliphatic and aromatic compounds and different HA, all containing different abundances of carboxylic, aliphatic hydroxyl, and aromatic hydroxyl functional groups.^{127,160-163} From these experiments, complexation of antimonate with dissolved NOM in natural

waters was estimated to be ~40% at pH ~2, where the neutral $\text{Sb}(\text{OH})_5^0$ species prevails, but is negligible at pH values >4 due to the dominance of the $\text{Sb}(\text{OH})_6^-$ ion and most probable electrostatic repulsions with the net negatively charged NOM.^{160,162} For the charge-neutral antimonite, an organic complexation of 30-35% was estimated in natural waters. A maximum of this Sb(III)-humic acid complexation was found at a pH value of ~6 and EXAFS showed Sb-C distances of 2.85-3.03 Å, depending on carboxylic or phenolic functionalities and chelation.^{127,161} Whether the low affinity of antimonate to NOM and the relatively high complexation of antimonite with O-containing ligands is also reflected in environments where solid NOM can be the major sorbent is, however, unknown to date.

First suggestions for Sb(III) complexation with thiol groups in organic-rich environments were made by Fawcett *et al.*¹⁵⁹ who found Sb(III)-S phases in organic sediments close to a former mining site. In another study, Arsic *et al.*¹⁶⁴ reported the formation of an Sb(III)-S phase in contaminated wetland soil mesocosm experiments. With organic-rich sediments from the same wetland, Bennett *et al.*⁷⁶ showed by use of EXAFS spectroscopy that up to 44% of total Sb was 3-fold coordinated to S at a distance of 2.46 Å, indicative for Sb-thiol coordination. Since such a coordination environment is common in amorphous Sb-sulfide precipitates, Sb-thiol complexes as well as in disordered SbS_3 formed via reaction of antimonite with FeS^{71} , unequivocal attribution to one of these Sb species could not be made. Thus, the existence and the role for potential Sb sequestration by thiol-bound Sb(III) in Sb contaminated high-organic wetlands is still unclear. Similar to As, also nothing is known about the existence of thioantimonate species in such environments.

1.4 Objectives

The overall aim of this thesis was to investigate influences of reduced S on As and Sb mobility and binding to solid NOM. To accomplish this aim, several studies were conducted with the emphasis to connect evidence from laboratory experiments with results from field analyses to achieve deeper insights in the mobility of these potentially toxic trace metalloids in anoxic, organic-rich environmental systems. The first study investigated the aqueous As speciation and species distribution in a naturally As-contaminated minerotrophic peatland. The species information obtained from these analyses was then used in study 1 and 2 to conduct laboratory experiments with different types of model peat to get new insights in the binding affinity and thus mobility of MTAs(V), the As species identified as dominant in this peatland. In order to get a better understanding of As mobilization processes from solid NOM through reduced S species, the third study focused on pH-dependent mobilization mechanisms of As from model peat after sulfurization. The fourth study additionally investigated As mobilization from sulfate-rich alluvial aquifer sediments with different numbers of reducing, high-organic matter interlayers using column experiments. The focus of study 5 was to elucidate with spectroscopic techniques whether Sb only forms precipitates of inorganic Sb sulfide in wetland soils or also has a high affinity to organic thiol and other groups of solid NOM. These theoretical insights from study 5 could be connected with study 6, where the binding environment of Sb in a peatland, which is anthropogenically influenced by high loads of Sb and sulfate from mining wastewaters, was investigated. Studying the fate of As and Sb in organic-rich systems influenced by reduced S will, on

the one hand, help to obtain deeper mechanistical knowledge about binding and mobilization processes, which can eventually be incorporated into geochemical models. On the other hand, the new insights can directly influence the (risk) management of constructed and non-constructed wetlands used for purification processes of these potentially toxic metalloids.

The specific objectives presented in this thesis were to:

- (1) explore the occurrence of inorganic thioarsenates in an As-contaminated peatland and consequently to study binding mechanisms of monothioarsenate, the dominant species found, to organic functional groups of (model) peat (study 1: Besold *et al.* (2018) and study 2: Biswas, Besold, *et al.* (2019))
- (2) investigate the influence of reduced S on the fate of As during sulfurization of As-bearing (model) peat and in alluvial aquifer sediments with high-organic matter interlayers (study 3: Eberle, Besold *et al.* (2020), study 4: Kumar, Noël, Planer-Friedrich, Besold *et al.* (2020))
- (3) determine the binding mechanisms of antimonite to organic functional groups of (model) peat and under field conditions in a mine water impacted peatland (study 5: Besold *et al.* (2019), study 6: Besold *et al.* (2019))

2 Methods

2.1 General practices and analytical methods

Various methods were used to investigate soil and pore water parameters which are relevant for metal(loid) binding and mobility. The most important methods will be mentioned in the following. Analytical details can be found in the method sections of the individual studies added in the appendix.

2.1.1 Sampling and laboratory practices

Due to the focus of all studies on O-limited environments, the influence of atmospheric O on samples was minimized in order to keep the redox integrity of the samples undisturbed. Soil samples were collected in the field with various types of soil and peat core samplers and were either immediately frozen on dry ice or cooled (4°C) under inert (helium (He)) atmosphere and then transported to the laboratory for further processing.

Pore water in study 6 was sampled using equilibrium dialysis samplers (peepers) as described by Hesslein¹⁶⁵ after installing the peepers at least for four weeks to guarantee equilibrium conditions. In study 1, pore water was obtained by manually squeezing water saturated peat samples in N₂-filled bags on-site. Afterwards, water samples were stabilized accordingly (as required by the targeted analysis) or were immediately flash-frozen and transported to the laboratory under cooled or frozen conditions.

For all experiments and sample preparations, doubly-deionized water and analytical grade reactants were used. All O-sensitive (field) samples were treated and all redox-sensitive experiments were conducted under inert atmosphere in a glove bag (95% N₂/5% H₂, Coy). Soil and peat samples were freeze-dried, ground and stored under dark conditions in the glovebag until further analyses.

2.1.2 Preparation of model peat

Model peat was used in studies 1, 2 3, and 5 to exemplary investigate the binding behavior of As and Sb species to organic functional groups of solid NOM. To prepare the model peat, peat taken from the Federseemoor, Bad Buchau, Germany,¹²⁰ was wet-sieved to a size fraction of 63-250 µm. This peat fraction was then washed once with 0.1 M HCl, to decrease the content of potentially As/Sb-complexing polyvalent metal cations (for example Fe(III) and Al(III)), followed by washing several times with doubly-deionized water, until the pH value returned to the initial pH of 4.5. The washed peat was freeze-dried, homogenized, and stored in the dark inside a glovebag until further use. Total element composition as well as functional groups of this peat were characterized in order to work under defined conditions (methods are described in chapter 2.1.4 and detailed results are reported in the Supporting Information (SI) of study 1). This peat-derived solid NOM is defined as model peat throughout this thesis.

2.1.3 Aqueous-phase analyses

Redox potential, pH, and electrical conductivity were determined directly in solution or soil suspension

after sampling in laboratory experiments or on-site in the field. Total aqueous S, Fe, As and Sb concentrations from pore water or other aqueous phase samples were determined by inductively coupled plasma mass-spectrometry (ICP-MS, X-Series 2, Thermo-Fisher) in stabilized (0.5% (v/v) H₂O₂, 0.8% (v/v) HNO₃) samples. Original samples were filtered (0.2 µm cellulose acetate or nylon) and diluted accordingly before analysis. Total dissolved organic carbon (DOC) and N were analyzed in filtrates (0.45 µm, polyamide) by use of thermo-catalytic oxidation with a TOC-VCPN Analyzer (Shimadzu).

Arsenite, arsenate, and thioarsenate species as well as sulfate and thiosulfate were determined by anion-exchange chromatography (AEC, ICS- 3000, Dionex; column: IonPac AS-16/AG-16 4-mm) coupled to an ICP-MS (XSeries2, Thermo- Fisher) after thawing the shock-frozen samples in a glovebag. Aqueous Sb speciation (Sb(III) or Sb(V) species) was either analyzed with an AEC (column AG, AS 16) coupled to an ICP-MS following the protocol of Hockmann *et al.*⁶⁷ (shock-frozen samples) or with an AEC (column: PRPX-100, 250 x 4.1 mm, 10 µm, Hamilton) coupled to an ICP-MS using an isocratic elution with 10 mM NH₄NO₃, 10 mM NH₄H₂PO₄, and 1.3 mM Na₂-EDTA at a flow rate of 1.0 mL/min (0.2% (v/v) HCl stabilized samples). Internal standards and reference materials were included in every analytical run to ensure data accuracy.

Dissolved sulfide was quantified using the methylene blue method¹⁶⁶ and ferrous iron (Fe(II)) as well as total dissolved iron (Fe(tot)) were measured using the phenanthroline method¹⁶⁷. In the field, sulfide as well as Fe(II) and Fe(tot) were determined with a portable photometer (LASA 100, Dr. Lange) at wavelengths of 605 nm and 480 nm, respectively. In the laboratory, these species were analyzed at an absorption wavelength of 650 nm and 570 nm, respectively, using a multiplate reader (Infinite 200 PRO, Tecan).

Zero-valent S (S(0)-species) was determined in ZnAc stabilized samples after chloroform (CHCl₃) extraction by high-performance liquid chromatography (HPLC, LaChrom Elite, L-2130 pump, L-2200 autosampler, L-2420 UV-Vis detector, Merck Hitachi) using a reversed phase C₁₈ column (Luna, 3µm, 150 x 2.0 mm, Phenomenex) following the method published by ThomasArrigo *et al.*⁴¹.

2.1.4 Solid-phase analyses

Total element contents of S, Fe, As, and Sb within freeze-dried and homogenized samples were either determined by ICP-MS or by inductively coupled plasma optical emission spectrometry (ICP-OES, ICAP 6300 Duo View, Thermo-Fisher) after microwave digestion (MARSXpress, CEM) using a 5:3 ratio of 30% (v/v) H₂O₂ and 65% (v/v) HNO₃. All samples were filtered (0.2 µm cellulose acetate) and diluted accordingly before analysis.

In study 6, the depth distributions of many other major and trace elements in peat were analyzed by an energy dispersive X-ray fluorescence spectrometer (XEPOSTM, Spectro X Lab) calibrated with a NIST 2711 certified reference material. Total organic C and N contents were analyzed with a TOC/TN analyzer (multi N/C 2100, Analytik Jena). The absence of carbonate was tested with 10% (v/v) HCl.

In study 4, chemical extractions targeting the reactive Fe(II) pool (HCl-extraction) and total acid-extractable As and Fe were performed on subsamples from all solid phase samples. Total metal(loid) contents in filtered (0.2 μm , cellulose-acetate) and diluted extracts were determined by ICP-MS (As) or ICP-OES (Fe).

Coordination chemistry and redox states of the elements S, Fe, As, and Sb in the solid phase were investigated using various X-ray absorption spectroscopy techniques, in particular X-ray absorption near-edge structure (XANES) and extended X-ray absorption fine-structure (EXAFS) spectroscopy of bulk samples. All spectra were collected at beamlines of the European Synchrotron Radiation Facility (ESRF), Grenoble, France (The Rossendorf Beamline, ROBL) or of the Stanford Synchrotron Radiation Lightsource (SSRL), Stanford, USA (beamlines 4-1, 4-3, 6-2, 7-3, 9-3, and 11-2) at cryogenic temperatures (Fe, As, and Sb) or under ambient temperature but inert He (<0.1% (v/v) O₂) atmosphere (S). A combination of several techniques was used to analyze the collected sample spectra. Normalized XANES and EXAFS spectra were analyzed by principal component analysis (PCA) combined with target-transform testing (TT) and subsequent linear combination fitting (LCF) for solid-phase speciation of Fe, As, and Sb. Further, iterative transformation factor analysis (ITFA) of normalized XANES and EXAFS spectra was used, especially to evaluate small spectral differences between several Sb phases. Gaussian peak fitting on normalized XANES spectra was performed to study the redox speciation of S. Shell-by-shell fitting of *k*-weighted EXAFS spectra, partly in combination with Morlet wavelet transform analysis was used to investigate the coordination chemistry of As and Sb. Details about spectra collection, data evaluation and analysis can be found in the respective studies.

In order to investigate the mineralogy of peat samples (study 6), selected samples were examined by scanning electron microscopy (SEM) using a Leo Gemini 1530 (Carl Zeiss, Germany) with a Schottky emitter. Elemental composition analysis was conducted by energy-dispersive X-ray spectrometry (EDS, Oxford X-Max 20, Oxford Instruments). Peat soil mineralogy in study 6 was moreover investigated by synchrotron X-ray powder diffraction at beamline 11-3 (SSRL), however, high organic matter background distortions hindered detailed interpretations (data not shown).

Confirmation of amorphous Sb-S phases in study 5 and characterization of soil mineralogy in study 4 were done by a laboratory powder XRD machine (Rigaku Miniflix 600 X-ray diffractometer equipped with a Cu-K _{α} radiation).

Organic functional groups of selected model peat samples were characterized by ¹³C NMR with an Avance III HD Spectrometer (Bruker) and by Fourier-transform infrared spectroscopy (FT-IR) with a Vector 22 spectrometer (Bruker Optik).

2.2 Occurrence of thioarsenates in the minerotrophic peatland Gola di Lago and its implications for arsenic mobility in peatlands (study 1)

Study 1 investigated with state-of-the-art methods the aqueous arsenic speciation in the peatland Gola di Lago and how the mobility of MTAs(V), the dominant aqueous arsenic species detected, is affected by thiol-groups in peat. Surface- and porewaters as well as peat samples from 5 peat profiles were sampled up to 210 cm depth close to sampling locations already described earlier.¹¹⁵ Pore water was collected by manually squeezing the water saturated peat samples in N₂-filled bags on-site and then immediately removing them from the bags for further analyses and preservation. Since aqueous arsenic speciation of peat pore water samples revealed MTAs(V) to be the dominant As species in most samples, laboratory incubations with (thiol-rich) model peat were conducted in order to elucidate MTAs(V) binding behavior in comparison to arsenite. To form thiol-rich model peat, as shown by Hoffmann *et al.*¹²⁰, model peat suspensions (0.2 M C) were reacted with 3.0 mM sulfide (S(-II)) solution (15 mmol S(-II) mol⁻¹ C) in a 30 mM NaCl electrolyte under anoxic conditions and shaken in the dark for 24 h. The respective pH (± 0.2) was adjusted using anoxic HCl and NaOH. Sodium azide (NaN₃, 0.75 mmol mol⁻¹ C) was added to prevent microbial growth. After reaction for 24 h to reach equilibrium, the suspensions were filtered and the remaining peat filter residues were subsequently washed with electrolyte to remove dissolved sulfide. A wet weight equivalent of 100 mg dry sulfide-reacted peat (0.2 M C) was then equilibrated with 50 μ M MTAs(V) or arsenite at pH 4.5, 7.0, and 8.5 in anoxic electrolyte, respectively (always in triplicates). The samples were incubated for a maximum time of 984 h (41 days) at room temperature and in the dark. Sampling of the sacrificing butyl rubber capped serum bottles was done at 13 (MTAs(V) incubations) and 7 (arsenite incubations) sampling times during the experiment. X-ray absorption spectra (XANES and EXAFS) of freeze-dried samples were collected at the As K-edge to follow As solid-phase speciation over time. Similarly, aqueous As speciation was determined by AEC-ICP-MS for every sampling point.

2.3 Mechanisms of arsenic complexation with O-containing functional groups of model peat (study 2)

Study 2 explored molecular binding mechanisms of different arsenic species with O-containing functional groups of model peat. Therefore, an equilibrium sorption experiment was conducted for the As species arsenite, arsenate and MTAs(V) at pH 4.5 and 7.0 in triplicates, respectively. For this experiment, ~ 0.2 g of dry model peat were incubated for 96 h with variable concentrations (0-1000 μ M) (0-4.6 mmol As mol⁻¹ C) of each As species in 46 mL anoxic background electrolytic solution of 30 mM NaCl (to fix the ionic strength) containing 0.15 mM NaN₃ (to inhibit microbial activity). The relatively high concentrations of As compared to those commonly observed in the environment were chosen to ensure sufficient spectra quality for subsequent EXAFS shell-fitting. Conditional distribution coefficients (K_{OC}) (L kg⁻¹ C) of As were determined as $K_{OC} = C_P/C_S$, where C_P and C_S represent the As concentration in peat (μ g kg⁻¹ C) and the As concentration in solution (μ g L⁻¹) after equilibration, respectively. The C_S value was determined by subtracting the amount of As sequestered into peat from that initially present in the equilibrated solution. Organic matter functional group characterization was done by ¹³C NMR and FT-IR.

X-ray absorption spectra (XANES and EXAFS) of freeze-dried samples were collected at the As *K*-edge in high quality to enable EXAFS shell-by-shell modeling.

2.4 Influence of reduced S on the fate of As during sulfurization of As-bearing model peat (study 3)

Study 3 focused on the potential mobilization of As from model peat binding sites induced by reduced inorganic aqueous S species. In a first step, model peat (0.2 M C) was reacted with 3.0 mM dissolved sulfide at pH 4.5, 7.0 and 8.5 under the same conditions as described in study 1. In a second step, wet sulfide-reacted model peat (0.2 M C equivalent) was equilibrated with 50 μ M arsenite at pH 4.5, 7.0, and 8.5 for 96 h, respectively. The filter residues of this procedure (As-loaded model peat) were then used as starting material for desorption experiments investigating As mobilization. Incubation experiments to monitor As desorption over time (180 h) were conducted at pH 4.5, 7.0, and 8.5 with three different treatments (no S, polysulfide (PS), and dissolved sulfide addition) and similar conditions as described above. For the two treatments with reduced S, PS was selected to represent a reduced S species including zero-valent S. Dissolved sulfide was used to distinguish the effect of zero-valent S from the effect of S(-II) (in PS) on potential desorption of As from model peat. A control was kept without S addition. The amount of PS addition was calculated by referring the zero-valent S concentration added with PS solution to the As concentration of As-loaded model peat with a nominal 10-fold excess of zero-valent S compared to As. The sulfide concentration in the dissolved sulfide treatments was then matched to the concentrations of added S(-II) within PS in the PS treatments. Next to various geochemical parameters, the total As concentrations (solid and aqueous phase) as well as aqueous As speciation were monitored over the course of the experiment. X-ray absorption spectra of freeze-dried samples from pH 7.0 experiments (180 h) were collected at the As *K*-edge (XANES and EXAFS) and the S *K*-edge (only XANES) to follow solid-phase speciation changes.

2.5 Influence of reduced S on the fate of As in sulfate-rich, alluvial aquifer sediments with high-organic matter interlayers (study 4)

Study 4 investigated how reduced S formed by redox heterogeneities, for example in organic matter-rich reductive zones, can mobilize As in naturally low-arsenic sediments. Twelve columns (30 cm long, 7 cm diameter) were filled with natural sediments, collected ~2 weeks prior from the Wind River-Little Wind River floodplain outside of Riverton, Wyoming, USA. Triplicate columns were set-up with 0 (control), 1, 2, or 3 reduced lens(es) (~3 cm diameter, 17-20 g dry weight each) embedded in aquifer sand (1.2 ± 0.4 mg As kg^{-1}) at increasing distances (with each additional reduced lens) from the influent (bottom) groundwater port and run for 10 weeks. The reduced lenses consisted of organic-rich, fine-grained, sulfidic sediments (0.7 ± 0.1 mg As kg^{-1}) collected from an oxbow lake on the floodplain. Porewater samplers were inserted into the sand (advective zone) and the reductive (diffusive) zones to enable sampling of groundwater before, within, and after the reduced lens(es) along the flowpath. All columns were fed with artificial groundwater (pH 8) made to have a chemical composition representative of average concentrations of the major solutes,

except DOC, measured in Riverton groundwater over the past 2 years. Total aqueous concentrations of As, S, and Fe from the different ports were determined during the course of the experiment. Dissolved sulfide and Fe(II) concentrations were measured as redox proxies. Further, aqueous As speciation was analyzed for a set of end-point samples. Chemical extractions targeting the reactive Fe(II) pool (HCl-extraction) and total acid-extractable As and Fe were performed on subsamples from all solid phase samples. To prevent biases in mineral composition and element speciation that could arise from drying and precipitation of evaporite salts and minerals due to the high salt content of the groundwater, selected samples for solid-phase speciation were treated with glycerol. Then, XANES spectra of the glycerol-preserved samples were collected at the As and S *K*-edge, respectively, to determine solid-phase speciation changes. Further, XRD spectra of end-point samples compared to initial materials were recorded to evaluate changes in soil mineralogy.

2.6 Laboratory study: spectroscopic investigations of antimony complexation with thiol and carboxyl/phenol groups of model peat (study 5)

Study 5 probed potential molecular-level binding mechanisms of the reduced Sb species antimonite to thiol and O-containing functional groups of model peat organic matter. In order to provide different concentrations of thiol groups as potential sorption sites, model peat suspensions (0.1 M C) were reacted with five different concentrations of dissolved sulfide (0-30 mM) at pH 6.0 and otherwise similar conditions as described in studies 2, 3, and 4. Afterwards, a wet weight equivalent of 200 mg dry untreated or sulfide-reacted model peat (0.1 M C) was equilibrated with 50 μ M antimonite at pH 6.0 in anoxic electrolyte for 96 h, respectively, using the same experimental conditions as described before. The organic C-normalized partition coefficients (K_{OC}) [$L\ kg^{-1}\ C$] of Sb were determined as described in study 2. Potential changes in aqueous Sb speciation were analyzed by AEC-ICP-MS. A thiol-rich synthetic organic model sorbent (Ambersep GT74, Rohm & Haas) and three Sb(III)-glutathione (GSH) complexes in molar ratios of GSH:Sb(III) of 1:1, 2:1, and 3:1 were synthesized as reference standards for XAS analysis. Additionally, an amorphous Sb(III) sulfide standard was synthesized. XANES spectra at the S *K*-edge were recorded to follow S solid-phase speciation of model peat after reaction with dissolved sulfide. Moreover, XANES and EXAFS spectra of freeze-dried model peat samples and synthesized reference standards were collected at the Sb *K*-edge in high quality in order to model the Sb binding environment ($\leq 5\ \text{\AA}$) and to investigate small spectral differences between organic and inorganic Sb-S phases.

2.7 Field study: investigation of the Sb binding environments in a mine water impacted peatland (study 6)

Study 6 focused on the aqueous and solid-phase speciation of antimony in natural peat and pore water samples of a mine water impacted peatland to explore the governing Sb binding mechanisms. Peat profiles were sampled at three different locations (B1-B3) along the water flow from near to the inflow to close to the outflow of a treatment peatland in Finnish Lapland. Peat pore water was sampled using equilibrium dialysis samplers (peepers) with a total length of 80 cm. After collection, peepers were transported in argon-

filled bags to avoid redox-induced sample changes to the close-by provisional field laboratory for further sample stabilization and processing. Within a radius of ~30 cm to each peeper location, peat cores were sampled up to a maximum sampling depth of 80 cm using a Russian Peat Borer. Then, the peat cores were separated into 10 cm sections to match the pore water information obtained from peepers. Special attention was paid to preserve redox integrity of all samples. General parameters as redox potential, pH, electrical conductivity, dissolved sulfide, and Fe(II) were directly determined on-site. Total aqueous Sb concentrations were analyzed by ICP-MS and aqueous Sb speciation by AEC-ICP-MS. Total solid-phase Sb, S, and Fe contents were determined by ICP-MS or ICP-OES. Peat mineralogy was explored on selected freeze-dried peat samples with SEM-EDS. X-ray absorption spectra at the Sb and Fe (XANES and EXAFS, respectively) as well as S (XANES) *K*-edge of freeze-dried peat samples were collected in order to elucidate the solid-phase speciation of Sb and its governing binding environment.

3 Results and Discussion

3.1 Occurrence of thioarsenates in the peatland Gola di Lago and its consequences for As mobility in peat (studies 1 and 2)

Total aqueous As in the slightly acidic (pH 5.2 to 6.1) surface and porewaters of the Gola di Lago peatland ranged from 1.8 to 180 $\mu\text{g L}^{-1}$. Arsenic initially entering the peatland via an intermittent inflow (IF), was mainly arsenate (study 1, Figure 1a). With increasing lateral distance to the IF, the percentage of arsenate decreased while thioarsenates increased (profiles B1L < B2L and B1R < B2R < B3R in Figure 1a, study 1). The percentage of arsenite remained comparatively low (2-30%) in surface water samples. At greater depth (~90 cm), arsenite increased to 25-80% of total As (study 1, Figure 1b). Overall, the maximum percentage of thioarsenates reached 93% of total As (profile B3R, 60 cm depth). Concentration and fraction of thioarsenates did not show a correlation with any of the aqueous parameters such as pH, redox potential, or concentration of total As and S in the solid phase. Mostly, the dominant species in all profiles was MTAs(V) with up to 91% of total As followed by significantly lower fractions of TriTAs(V) and DTAs(V) (median 3% and 2%, respectively), whereas TetraTAs(V) was instable at these low pH values.¹⁶⁸ It is important to note that the speciation data presented here only reflects a single-point observation from November; a seasonally changing water table or increased microbial activity in the summer half-year may lead to a slightly different As speciation, especially in the most affected shallow peat layers.

The significant fractions of MTAs(V) observed in Gola di Lago versus a complete lack of information on the effect of MTAs(V) formation on overall As mobility in reduced S and organic carbon-rich environments were the basis for several laboratory sorption studies.

In time series experiments with 3 mM sulfide-reacted model peat, total As sorption upon 50 μM MTAs(V) addition increased in the order pH 8.5 < 7.0 < 4.5, whereby sorption at pH 4.5 (32 $\mu\text{mol As mol}^{-1}\text{ C}$) was ~5 times higher than at pH 8.5 (7 $\mu\text{mol As mol}^{-1}\text{ C}$, study 1, Figure 2). The same trend occurred for arsenite, but the difference between As sorption at pH 4.5 (29 $\mu\text{mol As mol}^{-1}\text{ C}$) and 8.5 (14 $\mu\text{mol As mol}^{-1}\text{ C}$) was only a factor of 2. Compared to arsenite, the initial sorption of total As was slower in experiments where we added MTAs(V), but after 984 h (41 days), the extent of sorption was comparable, at least for pH 4.5 and 7.0. For pH 8.5, the amount of total As adsorbed remained at only ~50% of that observed in the arsenite experiments.

Aqueous As speciation analysis for the MTAs(V) experiments showed, in contrast to the arsenite experiments, significant transformations of MTAs(V) to mainly arsenite (study 1, Figure 3). Transformation rates decreased with increasing pH from half-lives of ~35 to ~470 h at pH 4.5 and 7.0, respectively, to almost no transformation at pH 8.5 over the duration of the experiment (study 1, Figure 3a,c,e). In a blank experiment with background electrolyte and NaN_3 only minor transformation of MTAs(V) to arsenite at pH 4.5 occurred after 120 h and no transformation at pH 7.0 and 8.5 was observed (study 1, Figure SI-9). Furthermore, no significant increase in S oxidation products (sulfate and thiosulfate) occurred during our sorption experiments confirming anaerobic conditions and indicating no obvious

microbial influence. The transformation of MTAs(V) was therefore not driven by pH or ionic strength but clearly triggered by the presence of sulfide-reacted model peat.

As described before, MTAs(V) is in equilibrium with arsenite and S(0)-species. Low pH will drive the equilibrium toward arsenite and S(0)-species,¹⁶⁹ but kinetics in solution are usually so slow that any MTAs(V) transformation is not likely to be observed over several days (study 1, Figure SI-9). However, previous reports^{115,120} and our own experiments (study 1, Figure 2) show that arsenite adsorbs strongly to thiol-rich NOM, particularly at low pH. This is consistent with the observed order of MTAs(V) transformation kinetics. We conclude that arsenite sorption drives the chemical equilibrium toward arsenite and S(0)-species, therefore accelerating MTAs(V) transformation. Sorption of S(0)-species would have the same effect.

While aqueous As speciation already implied that arsenite sorption is an important mechanism in the MTAs(V) experiments, it could not answer the question whether sorption observed in the MTAs(V) experiments occurred exclusively as arsenite or also included direct sorption of MTAs(V) to sulfide-reacted model peat. Thus, we analyzed normalized As *K*-edge XANES spectra by ITFA in order to follow As solid-phase speciation from selected sampling points of the time series experiments. The three standards “arsenite adsorbed via thiol-S to peat” (As(III)-S-NOM), “arsenite reacted with untreated peat” (As(III)-NOM), and “arsenate reacted with untreated peat” (As(V)-NOM) were found to be the statistically most plausible components in our system. MTAs(V) was not detected on the solid phase even if present in high aqueous concentrations at pH 8.5. This finding was further confirmed by EXAFS shell-fitting of resin spectra from MTAs(V) solutions reacted with the thiol-rich Ambersep GT74 resin at pH 7.5 and 8.0. MTAs(V) was stable in the aqueous solution at both pH values and no contribution of a double-bond S (typically 2.13-2.18 Å³⁸) was observed on the solid phase. Instead, As was 3-fold coordinated at each pH to S with a distance of 2.26 Å, indicating typical bond lengths of arsenite bound via thiol-S.¹²⁰

The ITFA calculations revealed an increase of As(III) fractions with decreasing pH in the same manner as MTAs(V) transformation to arsenite in the aqueous phase (study 1, Figures 3 and 4). Hereby, a systematically higher portion of As was complexed via thiol-S to model peat at pH 4.5 compared to pH 7.0. No thiol complexation higher than the detection limit (5%) was observed at pH 8.5 (study 1, Figure 4). The solid-phase speciation data clearly show that there was no significant MTAs(V) sorption to sulfide-reacted model peat via thiol groups. Probably, the reason for MTAs(V) showing no detectable sorption to S-NOM is that MTAs(V) has pK_a values of 3.30 (pK_{a1}), 7.20 (pK_{a2}), and 11.0 (pK_{a3}) and was therefore single- or double-negatively charged under our experimental conditions (pH 4.5-8.5). The negative charge causes a strong electrostatic repulsion with the negatively charged sulfide-reacted model peat, thus excluding MTAs(V) sorption, regardless of the pH value and S content (study 1, Figure 4) and thus renders MTAs(V) mobile in the S-NOM system.

However, arsenate with very similar pK_a values²⁶ showed, though to a very low extent, sorption in the

presence of sulfide-reacted model peat (study1, Figure 2 and 4). Further, relatively high fractions of arsenite, originally reacted with untreated model peat, were found in the sulfide-reacted peat solid phase. For both As species, as well as for MTAs(V), extent of sorption and underlying sorption mechanisms to untreated peat (low to no reduced S content) were still elusive and are thus addressed in the following.

Highest sorption to untreated model peat after incubation for 96 h was observed for arsenite, followed by MTAs(V) and arsenate, even though the difference between the extent of MTAs(V) and arsenate sorption was small (study 2, Figure 1). Earlier studies reported higher sorption of arsenate to HA compared to arsenite,^{147,148,170} but did not consider potential ternary complex formation of arsenate with Fe in their investigations.¹⁴⁴ In agreement with earlier studies,^{147-150,170} sorption of arsenite and arsenate was stronger at pH 7.0 than at pH 4.5. However, for MTAs(V), sorption was stronger at pH 4.5, which can be attributed to the partial transformation of MTAs(V) to arsenite, as revealed by the As *K*-edge XANES spectra (study 2, Figure SI-7). This finding suggests that the acid-assisted transformation will be feasible in the presence of any sorbent that adsorbs arsenite more strongly than MTAs(V), not only in presence of thiol groups as shown before.

The calculated $\log K_{OC}$ (L kg⁻¹ C) at pH 7.0 were 0.83-1.01 for arsenite, 0.40-0.56 for MTAs(V), and 0.34-0.41 for arsenate; at pH 4.5, corresponding values were 0.73-0.85, 0.44-0.66, and 0.31-0.38 (study 2, Figure SI-3). While the extent of sorption for arsenate and MTAs(V) was considerably low, complexation of arsenite with O-containing functional groups of model peat ($\log K_{OC}$: 0.83-1.01) was comparable with binding through Fe(III)-bridged ternary complexes ($\log K_{OC}$: 1.2-1.5)¹⁴⁶, but ranged clearly below As(III)-S-C_{org} coordination ($\log K_{OC}$: 0-2.9)¹²⁰ at pH 7.0.

Shell-by-shell fitting of the As *K*-edge EXAFS spectra revealed a significant As-O-C_{org} coordination for all three As species (study 2, Figure 2 and Table 1). In the arsenite-treated model peat samples, the average As-O distance was 1.79±0.01 Å for both pH values, consistent with reported As-O bond lengths in the AsO₃ pyramid.^{53,171} The As-C distances were 2.73±0.01 Å and lay between As-C distances of 2.77-2.86 Å^{172,173} (study 2, Table SI-2), representative for hydroxyl coordination, and 2.58-2.68 Å,¹⁷¹ representative for carboxyl coordination, suggesting a mixed coordination between both functionalities. Because of the higher oxidation state of arsenate, the average As-O distance was considerably shorter (1.69±0.01 Å) compared to that of arsenite.¹⁴⁴ The fitted As-C paths for both pH values were 2.83±0.01 Å and therefore longer than that in the arsenite-treated model peat. Guénet *et al.*¹⁵¹ determined comparable As-C distances (2.85-2.86 Å) for a mixture of arsenate and arsenite during oxidation of reduced organic-rich floodplain soil, similar with our results pointing to complexation with organic hydroxyl groups. In the MTAs(V)-treated model peat at pH 7.0, the fitted As-O path with 1.72±0.01 Å was longer than the As-O distance in arsenate- but shorter than in arsenite-treated model peat. The As-S distance was determined as 2.10±0.02 Å, indicating that S was double-bound to As.³⁸ Despite the same oxidation state of As, the longer As-O in the AsSO₃ compared to that in AsO₄ can be attributed to the less positive partial charge on the central As atom, because of replacement of the double-bonded O with less electronegative double-bonded S. The fitted As-C distances

were $2.80 \pm 0.02 \text{ \AA}$ and thus between arsenite- and arsenate-treated model peat.

The assumed underlying mechanism of these chemical reactions is the nucleophilic attack by carboxylic and/or hydroxyl groups to the partially positively charged As atom.¹⁴⁷ The partial positive charge of the central As atom is highest in arsenate, followed by MTAs(V) and arsenite, because of the double-bonded O of arsenate compared to arsenite and the replacement of O with the less electronegative S in MTAs(V). Thus, the expected order of complexation would be arsenate > MTAs(V) > arsenite. However, the order was exactly the opposite (study 2, Figure 1), which may be explained by the electrostatic repulsion between negatively charged, deprotonated carboxyl and hydroxyl groups of peat (study 2, Figure SI-1) and the As species. While arsenite ($pK_{a1} = 9.17$) is neutrally charged at pH 4.5-7.0 and adsorbed most, arsenate ($pK_{a1} = 2.30$, $pK_{a2} = 6.99$) and MTAs(V) ($pK_{a1} = 3.30$, $pK_{a2} = 7.20$) are negatively charged, and electrostatic repulsion probably predominated over the effect of higher partial positive charge of the As center in these two species. Despite electrostatic repulsion, the driving force for complexation of As species to NOM is attributed to the energetic stability gained by donation of the negative charge of the carboxylate ($R-COO^-$) and hydroxyl ($R-O^-$) ions to the partially positively charged As atom and/or additional chelation and H bonding with nearby functional groups.¹⁴⁷ We hypothesize that the energy gain forming covalent bonds together with the increased nucleophilicity of hydroxyl groups at higher pH 7.0 overcame the effect of electrostatic repulsion between arsenate or MTAs(V) and peat functional groups, however, resulting in a lower extent of sorption and relatively longer As-C bonds compared to neutral arsenite (study 2, Table 1).

Thus, our results demonstrate that compared to the K_{OC} values of ternary As(III)-O-Fe- C_{org} complexation and in addition to the reported As(III)-O- C_{org} contributions of other studies^{146,151} and our study 1, O-containing functional groups can be an important alternative or additional binding mechanism for arsenite in anoxic, organic-rich systems. The low complexation of arsenate and MTAs(V) with O-containing groups and the lack of MTAs(V) binding in systems with high thiol-group-contents, underline the high mobilization potential of arsenate and especially MTAs(V), in reduced S and organic-rich systems.

3.2 Influence of reduced S on the fate of As during sulfurization of As-bearing model peat and in alluvial aquifer sediments with high-organic matter interlayers

During our sulfurization experiments, As was desorbed from As-loaded model peat in all treatments, demonstrated consistently by both total As solid-phase (study 3, Figure 1b) and solution data (study 3, Figure 2a-c). In control experiments without addition of reduced S (as PS or dissolved sulfide), 35%, 32%, and 20% of initial As content remained adsorbed at pH 4.5, 7.0 and 8.5, respectively, after 180 h. Upon sulfurization of model peat, the proportion of As desorption was altered. Under acidic conditions, more than half of the As (56% and 54%) was still found in the solid phase for the sulfide and PS treatment, respectively, compared to only 35% in controls without S addition. This observation matches the findings from study 1 (study 1, Figure 2, Figure SI-18) that arsenite sorption to thiols is increased at slightly acidic pH. In contrast to acidic conditions, reduced S significantly increased As desorption compared to the controls at neutral to alkaline pH. The proportions of solid-phase As in sulfurized treatments were overall

between 9% and 14%. No significant differences were observed between pH 7.0 and 8.5, which suggests that a maximum of S-induced As desorption was already reached at neutral pH. The As desorption was slightly but consistently higher in PS compared to sulfide experiments. These differences can be attributed to the additional zero-valent S in the PS treatment, as the sulfide concentrations over time were nearly identical in all sulfurized treatments (study 3, Figure SI-8).

The As *K*-edge XAS solid-phase speciation of the initial As-loaded peat revealed that 42% of As were bound via thiol groups and 58% via O-containing groups at pH 7.0 (study 3, Figure 3). With sulfide and PS addition, the As(III)-S fraction increased to 55% and 58%, respectively, whereas the As(III)-O fraction decreased correspondingly, indicating stronger relative binding via As(III)-S bonds. In control experiments, the As(III)-S fraction stayed almost constant and As(III)-O appeared to be partially oxidized to As(V)-O after equilibration with S-free solution, indicating that arsenite bound via O-containing groups is less stable than thiol-bound As. The suggested weaker binding of As(III)-O moieties indicates that arsenite was likely the species desorbed from the solid phase rather than As-S species. Furthermore, surface complexation of stable thioarsenates with peat, by reaction of aqueous reduced S species with As(III) bound to NOM, is unlikely on the basis of our shell-fitting results. Fitted As-S bond-lengths of 2.24-2.27 Å (study 3, Table SI-7) were significantly longer than the typical bond distances observed in thioarsenates (2.13-2.18 Å).³⁸ Moreover, no As-S minerals could be fitted to the XAS spectra, showing low probability of precipitation of mineral phases in the incubation experiments.

Our aqueous As speciation showed that in control experiments without addition of reduced S, arsenite was the dominant species at all pH values (study 3, Figure 4). Addition of sulfide or PS yielded similar effects on As desorption and similar As speciation patterns. At all pH values, thioarsenate formation increased significantly upon sulfurization compared to controls. Under acidic conditions, arsenite remained the dominant species. After 12 h of reaction, a maximum of 26% and 38% thioarsenates was observed with PS and sulfide addition, respectively. However, the contribution of thioarsenates decreased again to 4% and 6% of total As after 180 h, confirming their instability at acidic pH.^{40,168}

At neutral and alkaline conditions, thioarsenates dominated As speciation throughout the experiment (study 3, Figure 4). At the start of the experiment (0 h), and for both pH 7.0 as well as pH 8.5, 77 and 74-79% of As (0.72-0.80 and 0.85-87 µM) were present as thioarsenates in sulfide and PS treatments, respectively. A maximum concentration of thioarsenates was reached after 4-12 h, remaining at a constant level of 1.3±0.2 and 1.2±0.1 µM, respectively, until the end of the experiment. Until thioarsenates reached a constant concentration, arsenite was present in low concentrations (until 12 h) and started to increase thereafter, reaching similar concentrations as thioarsenates at pH 7.0 (~1.1 µM), but only less than half the amount at pH 8.5 (~0.5 µM). Since the concentrations of thioarsenates showed no decreasing trend (only minor influence of arsenate), the increasing arsenite concentrations seemed to originate directly from a release from peat surfaces.

Arsenic release from the solid to the aqueous phase may result from arsenite desorption from relatively weak O-containing groups like carboxylic or phenolic groups (see study 2) or desorption of As bound via thiol groups, either by breaking the bond between S and C or between As and S. Due to the higher stability of thiol bound As in comparison with As bound to O-containing groups, as discussed above, arsenite desorption from As-O-C_{org} is considered the more likely pathway. This assumption is also consistent with the increase in aqueous arsenite concentrations and no observed transformation of thioarsenates over time. The larger fraction of the released arsenite likely formed thioarsenates spontaneously by reaction with aqueous or surface-associated reduced S species similarly at pH 7.0 and 8.5 shifting the equilibrium toward thioarsenates. After reaching their steady-state concentration, only arsenite concentrations increased thereon over time (study 3, Figure 4). The overall similar concentrations of S(0)-species in both sulfurization treatments may explain the comparable total As desorption and speciation patterns over time for both neutral and alkaline conditions (study 3, Figure 2, Figure 4), additionally suggesting that low amounts of S(0)-species are sufficient for thioarsenate formation and an excess of S(0)-species does not necessarily lead to an increase in thioarsenate concentrations. A dominance of higher thiolated As species in the sulfurization experiments (TriTAs(V) > DTAs(V) > MTAs(V)), and the observations in Gola di Lago (study 1), where MTAs(V) was the most abundant species and dissolved sulfide was below detection limit, could be explained by the high dissolved sulfide concentrations in the present experiments. This observation fits the current theory that high amounts of free dissolved sulfide are necessary to form higher thiolated thioarsenates.^{39,40}

While the results of study 3 showed enhanced mobilization of As upon sulfurization of As-bearing peat organic matter at neutral to alkaline pH, study 4 had a closer look onto potential As mobilization mechanisms from sulfate-rich alluvial aquifer sediments, where high-organic matter reductive zones were embedded in otherwise naturally low arsenic aquifer sand.

Within column experiments fed with artificial groundwater (pH 8), where 1, 2, or 3 organic-rich, sulfidic lenses were embedded in natural aquifer sand, aqueous As, Fe, and sulfide concentrations in aquifer ports (groundwater samples) increased as a function of time until day 40 of the experiment (study 4, Figure 1). Concentrations were considerably higher in ports immediately downstream from an organic-rich, sulfidic lens (max. ~600 nM As, ~40 μM Fe, ~18 μM sulfide). After day 40, concentrations of As, Fe, and sulfide decreased again, particularly in ports directly downstream of the lenses. Sulfide and As concentrations always increased directly after an organic-rich lens, but then decreased with increasing distance from lenses. In contrast, aqueous Fe concentrations remained elevated independent of the distance from, or the number of, lenses. Concentrations of As, Fe, and S in control columns only showed little increase over time or remained close to, or below, the detection limit throughout the experiment (study 4, Figure SI-3). In contrast to groundwater samples, pore water from inside the lenses exhibited low aqueous Fe concentrations (<5 μM) and lower As concentrations (~200 nM) but high sulfide (up to 60 μM) concentrations, which were sustained until the end of the experiment (study 4, Figure SI-4). Aqueous As speciation of end-point

groundwater samples downstream of the lenses (ports 3, 5, and 7) showed that ~30-40% of total aqueous As were thioarsenates, with MTAs(V) being most abundant (study 4, Figure 2). Arsenite and arsenate, were also present in these samples, with the relative fraction of arsenate generally increasing with distance away from reducing lenses.

Bulk As *K*-edge XANES spectra taken from samples of the glycerol-preserved column with 3 lenses (study 4, Figure 4) showed that thiol-bound As(III) was the only species exhibiting a clear change in relative abundance within lenses compared to the initial material. Both As(III) and As(V) were further adsorbed to FeS in the reducing lenses. Interestingly, the As speciation in the aquifer material shifted dramatically along the flow path and compared to the initial aquifer material, where As(V) adsorbed to Fh was dominating in addition to a small pool of As(III) adsorbed to Fh (Figure 4). Before the first fine-grained reducing lens, mineral As(III)S (realgar) dominated, thereafter As(III) adsorbed to FeS and As(V)-Fh were the dominant species with a small (but increasing along the flow path) pool of S-complexed As (represented by MTA) adsorbed to FeS. Notably, the decreasing pool of As(V) remained adsorbed to Fh, whereas the increasing pool of As(III) was adsorbed to FeS in the ports upstream from the reduced lenses.

Also S exhibited major shifts in solid-phase speciation (study 4, Figure 5). Before the first lens (port 1), some S(0) was detected, but no sulfide minerals were present. After the first lens, no S(0) was detected anymore; instead, the relative abundance of FeS increased and that of sulfate decreased after each lens (ports 3 and 5). The lenses themselves also exhibited a shift in inorganic S species. The original material contained S(0)-species together with FeS and sulfate, while sulfate dominated along the flow path, probably translocated from the upstream aquifer material. However, sulfate decreased again from lens 1 to 3, while FeS and small portions of thiol-S increased.

The combined results of aqueous and solid phase speciation of As, Fe, and S reveal that the fate of As was governed by redox processes. It appears that high sulfate concentrations in the groundwater, together with the abundance of microbially available organic carbon within reducing lenses, stimulated sulfate reduction within and along the edges of lenses to produce dissolved sulfide that dispersed within the groundwater (study 4, Figure 1). The sustained sulfide supply drove reductive dissolution of Fe(III)-oxides to aqueous Fe(II), producing S(0)-species, as shown before,^{78,79} and releasing adsorbed As. On the influent (upstream) side of the first lens, however, aqueous Fe(II)-concentrations were too low to precipitate FeS (study 4, Figure 1). Instead, the relative lack of aqueous Fe(II) (sulfide:Fe ratios >1) induced precipitation of realgar (study 4, Figure 4), thus keeping the aqueous As concentrations relatively low.

Similarly, within the organic-rich lenses, sulfide concentrations were consistently higher than the aqueous Fe concentrations (study 4, Figure SI-4). However, reaction of dissolved sulfide with NOM leads to formation of S(0)-species and thiol groups¹²¹, as discussed before, and consequently surface As(III)-S-C_{org} complexes could form, in contrast to precipitation of realgar. Probably dissolved sulfide and the slightly alkaline pH 8 induced the formation of thioarsenates and their mobilization downstream of the reduced

lenses (study 4, Figure 2). These observations are consistent with recent findings of mobile thioarsenates in the vicinity of organic-rich reduced zones in lake sediments,¹⁷⁴ in a Bangladeshi groundwater aquifer,¹⁵³ and probably also with observed As mobilization from an As-bearing alluvial aquifer peat-layer.¹³⁷ The formation of FeS precipitates downstream the organic-rich lenses (study 4, Figures 1, 5 and Figure SI-4), where aqueous Fe concentrations were constantly higher than the aqueous sulfide concentrations (Fe:sulfide ratios >1), did not hinder thioarsenate mobility, as observed before.⁷³

Our results reveal that organic-rich phases not only lead to the retention of As, but reduced sulfur species can also mobilize As through formation of thioarsenates under certain conditions in a broader range of solid NOM-containing systems than previously known. At slightly acidic to circumneutral pH and in presence of reduced S, solid NOM acts as a sink for As via formation of stable As-S-C_{org} bonds. Increases in pH in the presence of reduced S, from near-neutral to slightly alkaline pH, can turn NOM from an As sink into a source, and demonstrate the pH as a sensitive variable for As retention in sulfidic, organic-rich systems.

3.3 Binding mechanisms of antimonite to organic functional groups of model peat and under field conditions in a mine water impacted peatland (studies 5 and 6)

Though being the direct neighbor of As in the periodic table and possessing the same redox states, the behavior of Sb in organic-rich, sulfidic systems is far less studied. Therefore, the following section addresses the influence of reduced sulfur on antimonite binding with model peat and field samples of a mine water impacted peatland.

Similar to the study of Hoffmann *et al.*¹²⁰, the total S content in model peat increased monotonously after incubation with 0-30 mM sulfide at pH 6.0 from 0.60±0.02 to a maximum of 8.34±0.28 mmol S mol⁻¹ C (study 5, Figure 1a). The S *K*-edge XANES spectra of (sulfide-reacted) model peat samples showed a simultaneous increase of resonance peaks in the energy range from 2471 to 2475 eV summarized as “reduced S”, whereby the peak assigned to exocyclic/ elemental S (~2473 eV, including thiol moieties) increased the most with increasing total S (study 5, Figure 1b,c). Thus, the strong increase in reduced S functionalities from 0.4 to 7.6 mmol S mol⁻¹ C in the model peat with increasing sulfide addition could be assigned to the incorporation of sulfide into the structure of model peat, most likely as thiol S.

The untreated model peat adsorbed 84.5±0.2% (493±1 μmol Sb mol⁻¹ C) of the initial 50 μM antimonite added and sorption increased monotonously with increasing S content to a maximum of 97.8±0.2% (571±1 μmol Sb mol⁻¹ C) (study 5, Figure 2a). Under almost similar experimental conditions, antimonite’s structural analogue arsenite showed significantly different results with no sorption to untreated model peat and a maximum sorption of ~150 μmol As mol⁻¹ C at comparable S content.¹²⁰ From biological systems it is known that Sb(III) possesses a high affinity toward thiol groups.^{175,176} Depending on the backbone structure, reduced, strongly nucleophilic organic monosulfides have p*K*_a values ranging from ~5 to 11¹⁷⁷ and Sb(III)-thiol bonds are known to be stronger than Sb(III)-O bonds.^{175,178,179} These observations support the hypothesized Sb-thiol coordination during the incubation with sulfide-reacted model peat in our

experiment.

In the untreated model peat, the proportion of reduced S groups was lower than in all sulfide-reacted model peat samples (study 5, Figure 1c). Yet, $84.5 \pm 0.2\%$ ($493 \pm 1 \mu\text{mol Sb mol}^{-1} \text{C}$) of total Sb was already adsorbed. This observation indicates that there was at least one more binding mechanism in addition to Sb-thiol binding. Indeed, when plotting the adsorbed Sb as a function of the C-normalized ratio of $S_{\text{binitial}}/S_{\text{peat}}$ (study 5, Figure SI-9) an additional binding mechanism became clear. All model peat samples with sulfide loadings plotted on a line with negative slope, whereas the untreated model peat did not. Moreover, stronger binding sites seem to be involved at lower $S_{\text{binitial}}/S_{\text{peat}}$ ratios, resulting from presumed thiol complexation, since Sb sorption increased linearly and was highest at the lowest $S_{\text{binitial}}/S_{\text{peat}}$ ratio. Calculated $\log K_{\text{OC}}$ values ranged from 3.4 to 4.3 and were slightly lower than the ones from Buschmann and Sigg¹²⁷ (4-5, pH 6), who investigated the binding of antimonite to different commercial HA, but used ~ 190 times lower Sb/C ratios than that of our study.

To confirm our macroscopic observations about antimonite binding also from a molecular-level perspective, we used both Sb *K*-edge XANES and EXAFS spectra of model peat samples and reference standards, together with a set of (statistical) modeling tools. The edge positions of normalized Sb *K*-edge XANES spectra of the model peat decreased almost linearly with increasing S content from 30,491.8 to 30,490.9 eV, and comparison with Sb(III) and Sb(V) reference standards shows no oxidation in the solid-phase during our experiments (Figure 2b). All model peat samples were characterized by two major peaks in the Fourier-transform (FT) of EXAFS spectra in the 1.5-2.0 Å $R+\Delta R$ -range, which occur at the same positions as for the reference standards Sb(III)-(GSH)₁₋₃ and Sb(III)-S-Resin (study 5, Figure 2d). The first FT peak at ~ 1.5 Å $R+\Delta R$ corresponds to O atoms in the first coordination shell and decreased with increasing S content of model peat samples. Conversely, the second FT peak at ~ 2.0 Å $R+\Delta R$, which corresponds to S atoms in the first or higher coordination shells of Sb, increased with increasing S content.

The use of ITFA on model peat samples and reference spectra confirmed that this Sb(III) organic matter series constituted of only two statistical components, which were identified as the untreated model peat sample and the Sb(III)-S-Resin standard (study 5, Figure 3). All other samples were linear combinations of these two samples (study 5, Table 2). With shell-by-shell fitting of the Sb(III)-S-Resin sample, we were able to fit an Sb-S path at a distance of 2.45 Å, indicative of thiol-bound Sb (study 5, Figure 4, Table 1).^{76,180} No contribution of O was observed. Moreover, the inclusion of an Sb-C(S) path at a distance of 3.33 Å¹⁸⁰ improved the model fit significantly. The fitted Sb-S and Sb-C(S) coordination numbers of 3.4 and 4.1, respectively, suggest that Sb was 3-fold coordinated to thiol groups. The untreated model peat sample could be best fit with an Sb-O path at 2.02 Å and an Sb-C(O) path at 2.90 Å, showing that Sb was directly coordinated to NOM via Sb-O-C_{org} functionalities.^{161,181}

The results shown before demonstrate a clear relation between thiol-coordination of Sb in model peat and increasing S content. However, as recently discussed in the literature,^{6,76,164} it is difficult to discriminate

between organic thiol and inorganic Sb-S phases like amorphous Sb-sulfide (study 5, Table 1) or disordered Sb(III)-S on FeS⁷¹ solely based on Sb-S bond lengths, because they are all very similar (2.45-2.48 Å). Thus, in order to distinguish between these three phases, we used again ITFA with three different approaches, namely the Malinowski indicator values (study 5, Table SI-4), a VARIMAX rotation (study 5, Figure 3), as well as the normalized sum of squared residues and standard deviations between experimental and reproduced spectra within the ITFA-PCA analysis (study 5, Figure SI-10). In combination, these three approaches, together with the fact that we were able to shell-fit an Sb-C(S) path to the samples from the Sb(III) organic matter series (study 5, Table 1) and an Sb-Sb path to the amorphous Sb(III) sulfide sample (study 5, Figure 4, Table 1) reveal that disordered inorganic Sb-S phases can be discriminated from thiol-bound Sb in our experiments by using ITFA.

Hence, our results provide spectroscopic evidence that increasing content of “reduced S” (most likely thiol-S) in the model peat leads to increasing complexation of Sb(III) with peat thiol moieties at slightly acidic pH 6; they further show the importance of O-containing (phenol/ carboxyl) groups in Sb binding by untreated model peat. To which extent our laboratory results are of relevance under field conditions was studied in a Finnish mine water impacted peatland and will be elucidated in the following.

Geochemical parameters of the peatland revealed a slightly acidic to circumneutral pH (5.8-7.4) and oxic to suboxic redox conditions (148-454 mV). High total aqueous S concentrations (10.4±2.3 mmol L⁻¹, study 6, Table SI-1) mainly contributed to the electrical conductivity (study 6, Figure SI-3) of the peatland and originated from oxidation of sulfide ores to dissolved sulfate (study 6, Table SI-2) during the mining process.¹³⁵ Antimony contents ranged from <0.1 to 2.2 mmol kg⁻¹ (study 6, Figure 1). They were highest close to the peat surface in all profiles and decreased with increasing depth. Iron exhibited a similar distribution pattern to Sb, whereas the contents of S only slightly decreased and the contents of C_{org} slightly increased with depth. Total aqueous Sb in surface waters was highest close to the inflow location (1566 nmol L⁻¹) and only slightly decreased toward the outflow zone to 1439 nmol L⁻¹. Within the peat profiles, total aqueous Sb concentrations ranged from 63 to 2275 nmol L⁻¹ and showed a similar pattern as for solid-phase Sb (study 6, Figure 1a). Aqueous Sb speciation revealed solely the presence of antimonate in surface waters and only in profile B2, we observed a slight increase in the proportion of antimonite with increasing depth (study 6, Figure SI-11). No thioantimonates were detected in any of the profiles. Calculated Pourbaix diagrams for the Sb-O-H-S system and insertion of respective pH-E_h-values from peat profiles B1-B3 in the Pourbaix diagram generally confirmed our aqueous Sb speciation (study 6, Table SI-1).

In order to study the potential Sb-governing phases, solid-phase Fe and S speciation were analyzed by XAS. The solid-phase Fe speciation showed that up to 43% of Fe was present as phyllosilicates in the upper peat layers (study 6, Figure 2) which was additionally supported by the SEM-EDS results (study 6, Figure SI-4, Table SI-4). Organic Fe(III) complexes (up to 47%) generally decreased with increasing peat depth, whereas Fe(II)-NOM complexes (up to 48%) increased. No Fe (oxyhydr)oxides could be fitted to the

sample spectra in significant percentages (>10%). Nonetheless, the existence of at least small amounts of Fe (oxyhydr)oxides was demonstrated by SEM-EDS, where a particle with FeOOH stoichiometry was observed. Additionally, with increasing depth and subsequently increasing reducing conditions, the presence of (authigenic) Fe mono sulfides (FeS) increased and dominated the Fe speciation in deeper peat layers (up to 71%). Here, our SEM-EDS analysis was also consistent with the presence of FeS precipitates (study 6, Figure SI-4, Table SI-4). Solid-phase S speciation demonstrated that the fractions of oxidized S, which dominated all spectra at the peat surfaces (27-41%), decreased with increasing peat depth to 20-27%, whereas the reduced S fractions increased and dominated deep peat layers (66-71%) (study 6, Figure 3, Table SI-14). Within reduced S fractions, the exocyclic/elemental S fraction, often represented as thiol-S in organic-rich sediments,¹⁸² prevailed in deep peat layers (32-35%) followed by inorganic (mono) sulfides (20-27%) (study 6, Figure SI-6). Formation of organic thiol groups and/or inorganic (mono) sulfides in deeper peat layers is often linked to (microbial) sulfate reduction,¹⁸² although in all measured samples, dissolved sulfide concentrations were low (max. 3.6 $\mu\text{mol L}^{-1}$, study 6, Table SI- 1).

Solid-phase Sb speciation showed that several similar Sb depth trends were observed in all peat profiles. With fractions from Sb *K*-edge EXAFS LCF of 22-25%, Sb(V) associated with Fe solely existed in the uppermost peat layers and only in one sample, a significant fraction of Sb(III) associated with Fe (18%) could be fitted; despite the general correlation between down-core total Sb and Fe contents and a minimum molar Fe:Sb ratio of 64 in all profiles (study 6, Figure 1 and 4). A similar observation was made for As by Mikutta and Rothwell¹⁸³ in British peat bogs.

With 63-100% (\bar{x} = 82%), organically coordinated Sb(III) was the dominant fraction in every peat profile and across all depths (study 6, Figure 4). Hereby, Sb(III) associated with O-containing groups, abundant in peat NOM, showed the highest percentages (52-64%, \bar{x} = 60%). High affinity of antimonite to O-containing groups has already been demonstrated in our study 5. Although Sb-C distances derived in study 5 were slightly longer (2.90 Å) than the fitted Sb-C distance of our best-fit Sb(III)-O-C_{org} reference compound (2.83 Å, study 6, Figure SI-8, Table SI-20), both reside in the range of published Sb-C distances of ~2.85-~2.92 Å.^{161,181} We further verified the presence of an Sb-C(O) backscatterer in peat samples by shell-fitting of the Sb-C(O) path and by systematic exclusion of the Sb(III)-O-C_{org} reference within linear combination test fits. The test fits without the Sb(III)-O-C_{org} reference lead to clearly worse fit qualities in all peat samples and therefore suggest the Sb(III)-O-C_{org} reference to be a true component. Further, our shell-fitting approach revealed an Sb-C(O) path at a distance of 2.82 Å (study 6, Figure SI-9, Table SI-22), a similar distance as in our LCF Sb(III)-O-C_{org} reference with 2.83 Å. Both lines of evidence therefore corroborate the high contributions of O-containing groups for Sb(III) complexation in peat. With increasing depth, Sb(III) was increasingly bound to thiol groups of NOM (14-37%, \bar{x} = 22%) and therefore showed a similar depth pattern as the exocyclic/elemental S fraction fitted to the S XANES spectra as described before (study 6, Figure 3). In one case, an Sb(III) sulfide phase composing 37% of the spectrum was fitted to sample B2 60 cm (study 6, Figure 4). Shell-by-shell fitting of Sb-S distances of 2.45±0.01 Å for thiol-bonds

and a fitted Sb-S distance of 2.48 Å for the Sb(III) sulfide containing sample confirmed our LCF results (study 6, Figure SI-10 and Table SI-23).

Our Sb speciation results suggest that organically complexed Sb can dominate solid-phase Sb in peatlands, even in the presence of Fe phases. Progressive formation of thiol-bound Sb with increasing peat depth correlated with the thiol group content in peat, thus indicating efficient Sb sequestration via reduced S in deep peat layers. The fact that only organically-bound Sb(III) was found to bind to peat, while almost exclusively antimonate in peat surface and pore waters were detected, suggests that antimonite has a very high affinity to organic functional groups of peat. Our results further imply that antimonate is very mobile in organic-rich systems,^{108,160} probably because of electrostatic repulsions between the negatively charged antimonate oxoanion ($\text{Sb}(\text{OH})_6^-$) and the net negative surface charge of peat NOM. The mobilization potential via thioantimonate formation is considered low. Efficient (microbially mediated) reduction of antimonate to antimonite in such systems would increase overall Sb sequestration by peat functional groups.

4 Conclusions

This thesis elucidated various influences of reduced S on the fate of As and Sb in anoxic systems, where solid NOM becomes a main sorbent. The main outcomes from studies 1-6, together with the current literature knowledge are summarized as a conceptual model for As in Figure 5a and for Sb in Figure 5b.

Both pentavalent oxoacids arsenate and antimonate showed low to no tendency to bind to functional groups of peat NOM (studies 2 and 6). Thus, solid NOM does not act as a sink for those two species. In real environmental systems like peatlands, however, Fe (oxyhydr)oxides dominate at the oxic surface layers and both oxoanions are strongly partitioned to these surfaces, keeping the overall aqueous As and Sb concentrations low.

After reductive dissolution of Fe (oxyhydr)oxides and release of adsorbed arsenate and antimonate, arsenite and antimonite can form via (microbially mediated) reduction in deeper peat layers. We found spectroscopic evidence for both species to establish stable As(III)/Sb(III)-O-C_{org} bonds to O-containing (carboxyl or phenol) groups of peat NOM at slightly acidic to neutral pH conditions (studies 2, 5 and 6). The affinity to O-containing groups and hence the extent of sorption differed strongly between arsenite and antimonite. Antimonite showed a 30 times higher extent of sorption to O-containing groups than arsenite at similar experimental conditions. This high affinity was also reflected under natural environmental conditions in a Finnish peatland, where Sb(III)-O-C_{org} coordination was significant in all peat layers while no As(III)-O-C_{org} coordination has been verified so far under natural conditions. Thiol groups of solid NOM are highly reactive toward arsenite.^{115,120} Our results for antimonite demonstrate even a 4 times higher reactivity toward these reduced S species compared to arsenite at similar experimental conditions. With increasing availability of thiol groups Sb(III)-O-C_{org} coordination was replaced by Sb(III)-S-C_{org} coordination in laboratory experiments as well as under natural conditions in a peatland, demonstrating the high affinity of Sb(III) toward thiol groups (studies 5 and 6). We were further able to exclude the presence of Sb-sulfide precipitates in our laboratory experiments. Thus, carboxyl/phenol and especially thiol groups of solid NOM clearly act as important sinks for arsenite and antimonite at slightly acidic to neutral pH conditions.

Our results from field and laboratory experiments indicate that reaction of arsenite with S(0)-species associated with solid NOM surfaces leads to formation of aqueous MTAs(V). Higher concentrations of (free) dissolved sulfide induce higher thiolation to form DTAs(V) and TriTAs(V). These reaction mechanisms were deduced from the high fraction of MTAs(V) in shallow to mid depth peat layers of the peatland Gola di Lago, where dissolved sulfide concentrations were below detection limit (study 1). Further, at the redox interface of sulfidic, organic-rich lenses within alluvial aquifer sands, MTAs(V) still dominated next to higher thiolated arsenates at mid-sulfide conditions (study 4). After sulfidization of As-bearing peat NOM, TriTAs(V) next to DTAs(V) were major As species at high-sulfide conditions (study 3). Formation of thioarsenates was always observed at circumneutral to alkaline pH conditions in organic-rich systems. No formation of thioantimonates was observed in any of our experiments.

We found that reduced sulfur (PS or sulfide) can mobilize As by thioarsenate formation from previously organically bound As(III) within peat NOM and organic-rich lenses within alluvial aquifer sands (studies 3 and 4). The mobilization potential was the same at pH 7 compared to pH 8.5, while a net retention after reduction to arsenite and formation of stable As(III)-S-C_{org} bonds was observed at slightly acidic pH 4.5 conditions. Our studies show that solid NOM can also become a source for As through formation of thioarsenates, with a maximum of up to ~80% thioarsenates at already neutral pH.

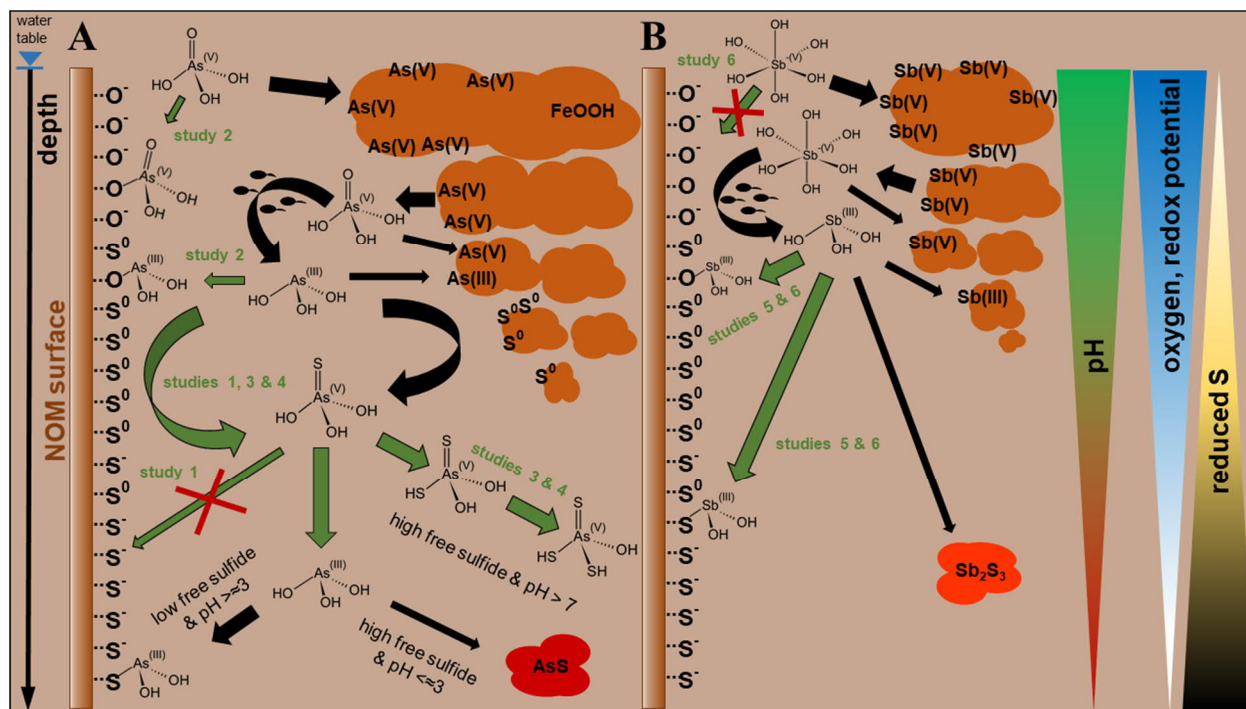


Figure 5: Suggested conceptual model showing summarized and simplified processes investigated in studies 1-6 (green arrows) in accordance with current literature knowledge^{7,40,46,65,67,68,76-79,81,83,115,121,164} (black arrows) of (A) As and (B) Sb (bio)geochemistry in an organic-rich environment like a peatland. Only directly important processes of Fe and S chemistry for As and Sb behavior are depicted. Initial formation of thioarsenites from dissolved sulfide and arsenite is excluded, since they are regarded as instable intermediates directly reacting to thioarsenates.^{38,39} Dotted lines illustrate general inner-sphere coordination of the respective species but no specific coordination environments.

Once formed, thioarsenates are very mobile in anoxic, organic-rich systems. MTAs(V) showed only very minor affinity via As(III)-O-C_{org} coordination toward peat NOM and no coordination of thioarsenates with thiol groups at all was found with our XAS techniques (studies 1, 2, and 3). Solid NOM, hence, cannot only become a source for As, but also the mobilized thioarsenates could potentially be transported long distances within those environments.

This thesis demonstrated that reduced S has complex influences on As and Sb mobility in organic-rich environments. While thiol-bond formation and ultimately sulfide mineral precipitation of As and Sb under anoxic conditions and at acidic pH efficiently sequester arsenite and antimonite, formation of highly mobile thioarsenates with reduced S already at circumneutral pH, can turn solid NOM from an As sink to a source, thereby jeopardizing drinking water resources. This mechanistic knowledge can be transferred into geochemical models and has implications for the safe and long-term management of contaminated peatlands and other organic-rich environments to keep As and Sb partitioned to the solid phase.

References

1. Wilson, S. C.; Lockwood, P. V.; Ashley, P. M.; Tighe, M., The chemistry and behaviour of antimony in the soil environment with comparisons to arsenic: A critical review. *Environ. Pollut.* **2010**, *158*, (5), 1169-1181.
2. Filella, M.; Belzile, N.; Chen, Y.-W., Antimony in the environment: a review focused on natural waters: I. Occurrence. *Earth Sci. Rev.* **2002**, *57*, (1), 125-176.
3. USGS, Mineral Commodity Summaries 2019. U.S. Geological Survey: Washington, 2019.
4. Telford, K.; Maher, W.; Krikowa, F.; Foster, S.; Ellwood, M. J.; Ashley, P. M.; Lockwood, P. V.; Wilson, S. C., Bioaccumulation of antimony and arsenic in a highly contaminated stream adjacent to the Hillgrove Mine, NSW, Australia. *Environ. Chem.* **2009**, *6*, (2), 133-143.
5. Okkenhaug, G.; Zhu, Y.-G.; Luo, L.; Lei, M.; Li, X.; Mulder, J., Distribution, speciation and availability of antimony (Sb) in soils and terrestrial plants from an active Sb mining area. *Environ. Pollut.* **2011**, *159*, (10), 2427-2434.
6. Warnken, J.; Ohlsson, R.; Welsh, D. T.; Teasdale, P. R.; Chelsky, A.; Bennett, W. W., Antimony and arsenic exhibit contrasting spatial distributions in the sediment and vegetation of a contaminated wetland. *Chemosphere* **2017**, *180*, 388-395.
7. Scheinost, A. C.; Rossberg, A.; Vantelon, D.; Xifra, I.; Kretzschmar, R.; Leuz, A.-K.; Funke, H.; Johnson, C. A., Quantitative antimony speciation in shooting-range soils by EXAFS spectroscopy. *Geochim. Cosmochim. Acta* **2006**, *70*, (13), 3299-3312.
8. Fendorf, S.; Michael, H. A.; van Geen, A., Spatial and Temporal Variations of Groundwater Arsenic in South and Southeast Asia. *Science* **2010**, *328*, (5982), 1123-1127.
9. Ravenscroft, P.; Brammer, H.; Richards, K., Arsenic Pollution: A Global Synthesis. Wiley-Blackwell: 2009.
10. Smith, A. H.; Lingas, E. O.; Rahman, M., Contamination of drinking-water by arsenic in Bangladesh: a public health emergency. *Bull. World Health Organ.* **2000**, *78*, (9), 1093-1103.
11. Sharma, A. K.; Tjell, J. C.; Sloth, J. J.; Holm, P. E., Review of arsenic contamination, exposure through water and food and low cost mitigation options for rural areas. *Appl. Geochem.* **2014**, *41*, 11-33.
12. Meharg, A. A.; Zhao, F.-J., *Arsenic & rice*. Springer Science & Business Media: 2012.
13. Okkenhaug, G.; Zhu, Y.-G.; He, J.; Li, X.; Luo, L.; Mulder, J., Antimony (Sb) and Arsenic (As) in Sb Mining Impacted Paddy Soil from Xikuangshan, China: Differences in Mechanisms Controlling Soil Sequestration and Uptake in Rice. *Environ. Sci. Technol.* **2012**, *46*, (6), 3155-3162.
14. Hopenhayn, C., Arsenic in Drinking Water: Impact on Human Health. *Elements* **2006**, *2*, (2), 103-107.
15. Poon, R.; Chu, I.; Lecavalier, P.; Valli, V. E.; Foster, W.; Gupta, S.; Thomas, B., Effects of antimony on rats following 90-day exposure via drinking water. *Food Chem. Toxicol.* **1998**, *36*, (1), 21-35.
16. HealthCanada, Guidelines for Canadian Drinking Water Quality. Health Canada: 1997.
17. WHO, Guidelines for drinking-water quality. World Health Organization: 2011.
18. USEPA, National Primary Drinking Water Regulations. US Environmental Protection Agency: 2019.
19. EU, COUNCIL DIRECTIVE 98/83/EC on the quality of water intended for human consumption. European Union: 1998.

20. Smedley, P. L.; Kinniburgh, D. G., A review of the source, behaviour and distribution of arsenic in natural waters. *Appl. Geochem.* **2002**, *17*, (5), 517-568.
21. Hinrichsen, S.; Geist, F.; Planer-Friedrich, B., Inorganic and Methylated Thioarsenates Pass the Gastrointestinal Barrier. *Chem. Res. Toxicol.* **2015**, *28*, (9), 1678-1680.
22. Naranmandura, H.; Iyata, K.; Suzuki, K. T., Toxicity of Dimethylmonothioarsinic Acid toward Human Epidermoid Carcinoma A431 Cells. *Chem. Res. Toxicol.* **2007**, *20*, (8), 1120-1125.
23. O'Day, P. A., Chemistry and Mineralogy of Arsenic. *Elements* **2006**, *2*, (2), 77-83.
24. Gebel, T., Arsenic and antimony: comparative approach on mechanistic toxicology. *Chem. Biol. Interact.* **1997**, *107*, (3), 131-144.
25. Roper, A. J.; Williams, P. A.; Filella, M., Secondary antimony minerals: Phases that control the dispersion of antimony in the supergene zone. *Geochemistry* **2012**, *72*, 9-14.
26. Nordstrom, D. K.; Archer, D. G., Arsenic thermodynamic data and environmental geochemistry. In *Arsenic in Ground Water: Geochemistry and Occurrence*, Springer: Boston, MA, 2003; pp 1-25.
27. Filella, M.; May, P. M., Computer simulation of the low-molecular-weight inorganic species distribution of antimony(III) and antimony(V) in natural waters. *Geochim. Cosmochim. Acta* **2003**, *67*, (21), 4013-4031.
28. Filella, M.; Belzile, N.; Chen, Y.-W., Antimony in the environment: a review focused on natural waters: II. Relevant solution chemistry. *Earth Sci. Rev.* **2002**, *59*, (1), 265-285.
29. Zakaznova-Herzog, V. P.; Seward, T. M., Antimonous acid protonation/deprotonation equilibria in hydrothermal solutions to 300°C. *Geochim. Cosmochim. Acta* **2006**, *70*, (9), 2298-2310.
30. Baes, C. F.; Mesmer, R. S., *The Hydrolysis of Cations*. John Wiley & Sons, Ltd: New York, 1976.
31. Pauling, L., The Formulas of Antimonic Acid and the Antimonates. *J. Am. Chem. Soc.* **1933**, *55*, (5), 1895-1900.
32. Oremland, R. S.; Stolz, J. F., The Ecology of Arsenic. *Science* **2003**, *300*, (5621), 939.
33. Stauder, S.; Raue, B.; Sacher, F., Thioarsenates in Sulfidic Waters. *Environ. Sci. Technol.* **2005**, *39*, (16), 5933-5939.
34. Stucker, V. K.; Silverman, D. R.; Williams, K. H.; Sharp, J. O.; Ranville, J. F., Thioarsenic Species Associated with Increased Arsenic Release during Biostimulated Subsurface Sulfate Reduction. *Environ. Sci. Technol.* **2014**, *48*, (22), 13367-13375.
35. Planer-Friedrich, B.; London, J.; McCleskey, R. B.; Nordstrom, D. K.; Wallschläger, D., Thioarsenates in Geothermal Waters of Yellowstone National Park: Determination, Preservation, and Geochemical Importance. *Environ. Sci. Technol.* **2007**, *41*, (15), 5245-5251.
36. Wallschläger, D.; Stadey, C. J., Determination of (Oxy)thioarsenates in Sulfidic Waters. *Anal. Chem.* **2007**, *79*, (10), 3873-3880.
37. Planer-Friedrich, B.; Scheinost, A. C., Formation and Structural Characterization of Thioantimony Species and Their Natural Occurrence in Geothermal Waters. *Environ. Sci. Technol.* **2011**, *45*, (16), 6855-6863.
38. Suess, E.; Scheinost, A. C.; Bostick, B. C.; Merkel, B. J.; Wallschlaeger, D.; Planer-Friedrich, B., Discrimination of Thioarsenites and Thioarsenates by X-ray Absorption Spectroscopy. *Anal. Chem.* **2009**, *81*, (20), 8318-8326.

39. Planer-Friedrich, B.; Suess, E.; Scheinost, A. C.; Wallschläger, D., Arsenic Speciation in Sulfidic Waters: Reconciling Contradictory Spectroscopic and Chromatographic Evidence. *Anal. Chem.* **2010**, *82*, (24), 10228-10235.
40. Planer-Friedrich, B.; Härtig, C.; Lohmayer, R.; Suess, E.; McCann, S. H.; Oremland, R., Anaerobic Chemolithotrophic Growth of the Haloalkaliphilic Bacterium Strain MLMS-1 by Disproportionation of Monothioarsenate. *Environ. Sci. Technol.* **2015**, *49*, (11), 6554-6563.
41. ThomasArrigo, L. K.; Mikutta, C.; Lohmayer, R.; Planer-Friedrich, B.; Kretzschmar, R., Sulfidization of Organic Freshwater Floccs from a Minerotrophic Peatland: Speciation Changes of Iron, Sulfur, and Arsenic. *Environ. Sci. Technol.* **2016**, *50*, (7), 3607-3616.
42. Ye, L.; Chen, H.; Jing, C., Sulfate-Reducing Bacteria Mobilize Adsorbed Antimonate by Thioantimonate Formation. *Environ. Sci. Technol. Lett.* **2019**, *6*, (7), 418-422.
43. Bentley, R.; Chasteen, T. G., Microbial Methylation of Metalloids: Arsenic, Antimony, and Bismuth. *Microbiol. Mol. Biol. Rev.* **2002**, *66*, (2), 250.
44. Fan, C.; Liu, G.; Long, Y.; Rosen, B.; Cai, Y., Thiolation in arsenic metabolism: a chemical perspective. *Metallomics* **2018**, *10*, (10), 1368-1382.
45. Wallschläger, D.; London, J., Determination of Methylated Arsenic-Sulfur Compounds in Groundwater. *Environ. Sci. Technol.* **2008**, *42*, (1), 228-234.
46. Foster, A. L.; Kim, C. S., Arsenic Speciation in Solids Using X-ray Absorption Spectroscopy. *Rev. Mineral. Geochem.* **2014**, *79*, (1), 257-369.
47. Hockmann, K.; Schulin, R., Leaching of Antimony from Contaminated Soils. In *Competitive sorption and transport of heavy metals in soils and geological media*, CRC Press: 2012.
48. Blume, H.-P.; Brümmer, G. W.; Horn, R.; Kandeler, E.; Kögel-Knabner, I.; Kretzschmar, R.; Stahr, K.; Wilke, B.-M., *Scheffer/Schachtschabel: Lehrbuch der Bodenkunde*. Springer-Verlag: 2016.
49. Dixit, S.; Hering, J. G., Comparison of Arsenic(V) and Arsenic(III) Sorption onto Iron Oxide Minerals: Implications for Arsenic Mobility. *Environ. Sci. Technol.* **2003**, *37*, (18), 4182-4189.
50. Leuz, A.-K.; Mönch, H.; Johnson, C. A., Sorption of Sb(III) and Sb(V) to Goethite: Influence on Sb(III) Oxidation and Mobilization. *Environ. Sci. Technol.* **2006**, *40*, (23), 7277-7282.
51. Fendorf, S.; Eick, M. J.; Grossl, P.; Sparks, D. L., Arsenate and Chromate Retention Mechanisms on Goethite. 1. Surface Structure. *Environ. Sci. Technol.* **1997**, *31*, (2), 315-320.
52. Manning, B. A.; Fendorf, S. E.; Goldberg, S., Surface Structures and Stability of Arsenic(III) on Goethite: Spectroscopic Evidence for Inner-Sphere Complexes. *Environ. Sci. Technol.* **1998**, *32*, (16), 2383-2388.
53. Ona-Nguema, G.; Morin, G.; Juillot, F.; Calas, G.; Brown, G. E., EXAFS Analysis of Arsenite Adsorption onto Two-Line Ferrihydrite, Hematite, Goethite, and Lepidocrocite. *Environ. Sci. Technol.* **2005**, *39*, (23), 9147-9155.
54. Arai, Y.; Elzinga, E. J.; Sparks, D. L., X-ray Absorption Spectroscopic Investigation of Arsenite and Arsenate Adsorption at the Aluminum Oxide–Water Interface. *J. Colloid Interface Sci.* **2001**, *235*, (1), 80-88.
55. Foster, A. L.; Brown, G. E.; Parks, G. A., X-ray absorption fine structure study of As(V) and Se(IV) sorption complexes on hydrous Mn oxides. *Geochim. Cosmochim. Acta* **2003**, *67*, (11), 1937-1953.
56. Manning, B. A.; Fendorf, S. E.; Bostick, B.; Suarez, D. L., Arsenic(III) Oxidation and Arsenic(V) Adsorption Reactions on Synthetic Birnessite. *Environ. Sci. Technol.* **2002**, *36*, (5), 976-981.

57. van Genuchten, C. M.; Peña, J., Antimonate and arsenate speciation on reactive soil minerals studied by differential pair distribution function analysis. *Chem. Geol.* **2016**, *429*, 1-9.
58. Essington, M. E.; Stewart, M. A., Adsorption of Antimonate by Gibbsite: Reversibility and the Competitive Effects of Phosphate and Sulfate. *Soil Sci. Soc. Am. J.* **2016**, *80*, (5), 1197-1207.
59. Guo, X.; Wu, Z.; He, M.; Meng, X.; Jin, X.; Qiu, N.; Zhang, J., Adsorption of antimony onto iron oxyhydroxides: Adsorption behavior and surface structure. *J. Hazard. Mater.* **2014**, *276*, 339-345.
60. Ilgen, A. G.; Trainor, T. P., Sb(III) and Sb(V) Sorption onto Al-Rich Phases: Hydrrous Al Oxide and the Clay Minerals Kaolinite KGa-1b and Oxidized and Reduced Nontronite NAu-1. *Environ. Sci. Technol.* **2012**, *46*, (2), 843-851.
61. Sherman, D. M.; Randall, S. R., Surface complexation of arsenic(V) to iron(III) (hydr)oxides: structural mechanism from ab initio molecular geometries and EXAFS spectroscopy. *Geochim. Cosmochim. Acta* **2003**, *67*, (22), 4223-4230.
62. Couture, R. M.; Rose, J.; Kumar, N.; Mitchell, K.; Wallschläger, D.; Van Cappellen, P., Sorption of Arsenite, Arsenate, and Thioarsenates to Iron Oxides and Iron Sulfides: A Kinetic and Spectroscopic Investigation. *Environ. Sci. Technol.* **2013**, *47*, (11), 5652-5659.
63. Xiao, F.; Wang, S.; Xu, L.; Wang, Y.; Yuan, Z.; Jia, Y., Adsorption of monothioarsenate on amorphous aluminum hydroxide under anaerobic conditions. *Chem. Geol.* **2015**, *407-408*, 46-53.
64. Suess, E.; Planer-Friedrich, B., Thioarsenate formation upon dissolution of orpiment and arsenopyrite. *Chemosphere* **2012**, *89*, (11), 1390-1398.
65. Schwertmann, U., Solubility and dissolution of iron oxides. *Plant Soil* **1991**, *130*, (1), 1-25.
66. Li, Y.-L.; Vali, H.; Yang, J.; Phelps, T. J.; Zhang, C. L., Reduction of Iron Oxides Enhanced by a Sulfate-Reducing Bacterium and Biogenic H₂S. *Geomicrobiol. J.* **2006**, *23*, (2), 103-117.
67. Hockmann, K.; Lenz, M.; Tandy, S.; Nachtegaal, M.; Janousch, M.; Schulin, R., Release of antimony from contaminated soil induced by redox changes. *J. Hazard. Mater.* **2014**, *275*, 215-221.
68. Hamon, R. E.; Lombi, E.; Fortunati, P.; Nolan, A. L.; McLaughlin, M. J., Coupling Speciation and Isotope Dilution Techniques To Study Arsenic Mobilization in the Environment. *Environ. Sci. Technol.* **2004**, *38*, (6), 1794-1798.
69. Wieder, R. K.; Yavitt, J. B.; Lang, G. E., Methane production and sulfate reduction in two Appalachian peatlands. *Biogeochemistry* **1990**, *10*, (2), 81-104.
70. Gramp, J. P.; Bigham, J. M.; Jones, F. S.; Tuovinen, O. H., Formation of Fe-sulfides in cultures of sulfate-reducing bacteria. *J. Hazard. Mater.* **2010**, *175*, (1), 1062-1067.
71. Kirsch, R.; Scheinost, A. C.; Rossberg, A.; Banerjee, D.; Charlet, L., Reduction of antimony by nanoparticulate magnetite and mackinawite. *Mineral. Mag.* **2008**, *72*, (1), 185-189.
72. Bostick, B. C.; Fendorf, S., Arsenite sorption on troilite (FeS) and pyrite (FeS₂). *Geochim. Cosmochim. Acta* **2003**, *67*, (5), 909-921.
73. Vega, A. S.; Planer-Friedrich, B.; Pastén, P. A., Arsenite and arsenate immobilization by preformed and concurrently formed disordered mackinawite (FeS). *Chem. Geol.* **2017**, *475*, 62-75.
74. Burton, E. D.; Johnston, S. G.; Kocar, B. D., Arsenic Mobility during Flooding of Contaminated Soil: The Effect of Microbial Sulfate Reduction. *Environ. Sci. Technol.* **2014**, *48*, (23), 13660-13667.
75. Savage, K. S.; Tingle, T. N.; O'Day, P. A.; Waychunas, G. A.; Bird, D. K., Arsenic speciation in pyrite and secondary weathering phases, Mother Lode Gold District, Tuolumne County, California. *Appl. Geochem.* **2000**, *15*, (8), 1219-1244.

76. Bennett, W. W.; Hockmann, K.; Johnston, S. G.; Burton, E. D., Synchrotron X-ray absorption spectroscopy reveals antimony sequestration by reduced sulfur in a freshwater wetland sediment. *Environ. Chem.* **2017**, *14*, (6), 345-349.
77. Helz, G. R.; Tossell, J. A.; Charnock, J. M.; Pattrick, R. A. D.; Vaughan, D. J.; David Garner, C., Oligomerization in As (III) sulfide solutions: Theoretical constraints and spectroscopic evidence. *Geochim. Cosmochim. Acta* **1995**, *59*, (22), 4591-4604.
78. Wan, M.; Shchukarev, A.; Lohmayer, R.; Planer-Friedrich, B.; Peiffer, S., Occurrence of Surface Polysulfides during the Interaction between Ferric (Hydr)Oxides and Aqueous Sulfide. *Environ. Sci. Technol.* **2014**, *48*, (9), 5076-5084.
79. Kumar, N.; Lezama Pacheco, J.; Noel, V.; Dublet, G.; Brown, G. E., Sulfidation mechanisms of Fe(III)-(oxyhydr)oxide nanoparticles: a spectroscopic study. *Environ. Sci.: Nano* **2018**, *5*, (4), 1012-1026.
80. Sun, J.; Quicksall, A. N.; Chillrud, S. N.; Mailloux, B. J.; Bostick, B. C., Arsenic mobilization from sediments in microcosms under sulfate reduction. *Chemosphere* **2016**, *153*, 254-261.
81. Burton, E. D.; Johnston, S. G.; Planer-Friedrich, B., Coupling of arsenic mobility to sulfur transformations during microbial sulfate reduction in the presence and absence of humic acid. *Chem. Geol.* **2013**, *343*, 12-24.
82. Kocar, B. D.; Borch, T.; Fendorf, S., Arsenic repartitioning during biogenic sulfidization and transformation of ferrihydrite. *Geochim. Cosmochim. Acta* **2010**, *74*, (3), 980-994.
83. Hockmann, K.; Planer-Friedrich, B.; Johnston, S. G.; Peiffer, S.; Burton, E. D., Antimony mobility and iron mineral transformations during sulfidization of ferrihydrite: Effect of pH, sulfide concentration and colloid formation. *Geochim. Cosmochim. Acta* **2020**, *282*, 276-296
84. Adusei-Gyamfi, J.; Ouddane, B.; Rietveld, L.; Cornard, J.-P.; Criquet, J., Natural organic matter-complexation and its impact on water treatment: A critical review. *Water Res.* **2019**, *160*, 130-147.
85. Stevenson, F. J., *Humus chemistry: genesis, composition, reactions*. John Wiley & Sons: 1994.
86. Lehmann, J.; Kleber, M., The contentious nature of soil organic matter. *Nature* **2015**, *528*, 60.
87. LeBoeuf, E. J.; Weber, W. J., Macromolecular Characteristics of Natural Organic Matter. 1. Insights from Glass Transition and Enthalpic Relaxation Behavior. *Environ. Sci. Technol.* **2000**, *34*, (17), 3623-3631.
88. Kirk, G., *The biogeochemistry of submerged soils*. John Wiley & Sons: 2004.
89. Stevenson, F., Extraction, fractionation, and general chemical composition of soil organic matter. In: *Humus chemistry: Genesis, composition, reactions*. John Wiley & Sons: **1982**, pp 26-54.
90. Sundararajan, M.; Rajaraman, G.; Ghosh, S. K., Speciation of uranyl ions in fulvic acid and humic acid: a DFT exploration. *Phys. Chem. Chem. Phys.* **2011**, *13*, (40), 18038-18046.
91. Aeschbacher, M.; Sander, M.; Schwarzenbach, R. P., Novel Electrochemical Approach to Assess the Redox Properties of Humic Substances. *Environ. Sci. Technol.* **2010**, *44*, (1), 87-93.
92. Qin, W.; Wang, Y.; Fang, G.; Wu, T.; Liu, C.; Zhou, D., Evidence for the generation of reactive oxygen species from hydroquinone and benzoquinone: Roles in arsenite oxidation. *Chemosphere* **2016**, *150*, 71-78.
93. Bauer, I.; Kappler, A., Rates and Extent of Reduction of Fe(III) Compounds and O₂ by Humic Substances. *Environ. Sci. Technol.* **2009**, *43*, (13), 4902-4908.

94. Fulda, B.; Voegelin, A.; Maurer, F.; Christl, I.; Kretzschmar, R., Copper Redox Transformation and Complexation by Reduced and Oxidized Soil Humic Acid. 1. X-ray Absorption Spectroscopy Study. *Environ. Sci. Technol.* **2013**, *47*, (19), 10903-10911.
95. Lovley, D. R.; Coates, J. D.; Blunt-Harris, E. L.; Phillips, E. J. P.; Woodward, J. C., Humic substances as electron acceptors for microbial respiration. *Nature* **1996**, *382*, (6590), 445-448.
96. Kappler, A.; Benz, M.; Schink, B.; Brune, A., Electron shuttling via humic acids in microbial iron(III) reduction in a freshwater sediment. *FEMS Microbiol. Ecol.* **2004**, *47*, (1), 85-92.
97. Klüpfel, L.; Piepenbrock, A.; Kappler, A.; Sander, M., Humic substances as fully regenerable electron acceptors in recurrently anoxic environments. *Nat. Geosci.* **2014**, *7*, 195.
98. Roden, E. E.; Kappler, A.; Bauer, I.; Jiang, J.; Paul, A.; Stoesser, R.; Konishi, H.; Xu, H., Extracellular electron transfer through microbial reduction of solid-phase humic substances. *Nat. Geosci.* **2010**, *3*, (6), 417-421.
99. Tipping, E., *Cation Binding by Humic Substances*. Cambridge University Press: Cambridge, 2002.
100. Jones, A. M.; Collins, R. N.; Rose, J.; Waite, T. D., The effect of silica and natural organic matter on the Fe(II)-catalysed transformation and reactivity of Fe(III) minerals. *Geochim. Cosmochim. Acta* **2009**, *73*, (15), 4409-4422.
101. Eusterhues, K.; Wagner, F. E.; Häusler, W.; Hanzlik, M.; Knicker, H.; Totsche, K. U.; Kögel-Knabner, I.; Schwertmann, U., Characterization of Ferrihydrite-Soil Organic Matter Coprecipitates by X-ray Diffraction and Mössbauer Spectroscopy. *Environ. Sci. Technol.* **2008**, *42*, (21), 7891-7897.
102. Thomas-Arrigo, L. K.; Byrne, J. M.; Kappler, A.; Kretzschmar, R., Impact of Organic Matter on Iron(II)-Catalyzed Mineral Transformations in Ferrihydrite–Organic Matter Coprecipitates. *Environ. Sci. Technol.* **2018**, *52*, (21), 12316-12326.
103. Kaiser, K.; Guggenberger, G.; Haumaier, L.; Zech, W., Dissolved organic matter sorption on sub soils and minerals studied by ¹³C-NMR and DRIFT spectroscopy. *Eur. J. Soil Sci.* **1997**, *48*, (2), 301-310.
104. Filius, J. D.; Meeussen, J. C. L.; Lumsdon, D. G.; Hiemstra, T.; van Riemsdijk, W. H., Modeling the binding of fulvic acid by goethite: the speciation of adsorbed FA molecules. *Geochim. Cosmochim. Acta* **2003**, *67*, (8), 1463-1474.
105. Kretzschmar, R.; Holthoff, H.; Sticher, H., Influence of pH and Humic Acid on Coagulation Kinetics of Kaolinite: A Dynamic Light Scattering Study. *J. Colloid Interface Sci.* **1998**, *202*, (1), 95-103.
106. Tipping, E.; Higgins, D. C., The effect of adsorbed humic substances on the colloid stability of haematite particles. *Colloids Surf.* **1982**, *5*, (2), 85-92.
107. Borch, T.; Kretzschmar, R.; Kappler, A.; Cappellen, P. V.; Ginder-Vogel, M.; Voegelin, A.; Campbell, K., Biogeochemical Redox Processes and their Impact on Contaminant Dynamics. *Environ. Sci. Technol.* **2010**, *44*, (1), 15-23.
108. Verbeeck, M.; Warrinnier, R.; Gustafsson, J. P.; Thiry, Y.; Smolders, E., Soil organic matter increases antimonate mobility in soil: An Sb(OH)₆ sorption and modelling study. *Appl. Geochem.* **2019**, *104*, 33-41.
109. Gustafsson, J. P., Arsenate adsorption to soils: Modelling the competition from humic substances. *Geoderma* **2006**, *136*, (1), 320-330.
110. Kaiser, K.; Guggenberger, G., The role of DOM sorption to mineral surfaces in the preservation of organic matter in soils. *Organ. Geochem.* **2000**, *31*, (7), 711-725.
111. Lalonde, K.; Mucci, A.; Ouellet, A.; Gélinas, Y., Preservation of organic matter in sediments promoted by iron. *Nature* **2012**, *483*, (7388), 198-200.

112. Maurer, F.; Christl, I.; Hoffmann, M.; Kretzschmar, R., Reduction and Reoxidation of Humic Acid: Influence on Speciation of Cadmium and Silver. *Environ. Sci. Technol.* **2012**, *46*, (16), 8808-8816.
113. Milne, C. J.; Kinniburgh, D. G.; van Riemsdijk, W. H.; Tipping, E., Generic NICA–Donnan Model Parameters for Metal-Ion Binding by Humic Substances. *Environ. Sci. Technol.* **2003**, *37*, (5), 958-971.
114. Harrington, J. M.; Crumbliss, A. L., The redox hypothesis in siderophore-mediated iron uptake. *BioMet.* **2009**, *22*, (4), 679-689.
115. Langner, P.; Mikutta, C.; Kretzschmar, R., Arsenic sequestration by organic sulphur in peat. *Nat. Geosci.* **2012**, *5*, (1), 66-73.
116. Langner, P.; Mikutta, C.; Suess, E.; Marcus, M. A.; Kretzschmar, R., Spatial Distribution and Speciation of Arsenic in Peat Studied with Microfocused X-ray Fluorescence Spectrometry and X-ray Absorption Spectroscopy. *Environ. Sci. Technol.* **2013**, *47*, (17), 9706-9714.
117. Mehlhorn, J.; Besold, J.; Lezama Pacheco, J. S.; Gustafsson, J. P.; Kretzschmar, R.; Planer-Friedrich, B., Copper Mobilization and Immobilization along an Organic Matter and Redox Gradient—Insights from a Mofette Site. *Environ. Sci. Technol.* **2018**, *52*, (23), 13698-13707.
118. Spratt, H. G.; Morgan, M. D., Sulfur cycling in a cedar-dominated, freshwater wetland. *Limnol. Oceanogr.* **1990**, *35*, (7), 1586-1593.
119. Urban, N. R.; Ernst, K.; Bernasconi, S., Addition of sulfur to organic matter during early diagenesis of lake sediments. *Geochim. Cosmochim. Acta* **1999**, *63*, (6), 837-853.
120. Hoffmann, M.; Mikutta, C.; Kretzschmar, R., Bisulfide Reaction with Natural Organic Matter Enhances Arsenite Sorption: Insights from X-ray Absorption Spectroscopy. *Environ. Sci. Technol.* **2012**, *46*, (21), 11788-11797.
121. Yu, Z.-G.; Peiffer, S.; Göttlicher, J.; Knorr, K.-H., Electron Transfer Budgets and Kinetics of Abiotic Oxidation and Incorporation of Aqueous Sulfide by Dissolved Organic Matter. *Environ. Sci. Technol.* **2015**, *49*, (9), 5441-5449.
122. Yu, Z.-G.; Göttlicher, J.; Steininger, R.; Knorr, K.-H., Organic sulfur and organic matter redox processes contribute to electron flow in anoxic incubations of peat. *Environ. Chem.* **2016**, *13*, (5), 816-825.
123. Tabatabai, M. A., Sulfur in soils. In *Encyclopedia of Soils in the Environment*, Hillel, D., Ed. Elsevier: Oxford, 2005; pp 76-85.
124. Karlsson, T.; Persson, P.; Skyllberg, U., Extended X-ray Absorption Fine Structure Spectroscopy Evidence for the Complexation of Cadmium by Reduced Sulfur Groups in Natural Organic Matter. *Environ. Sci. Technol.* **2005**, *39*, (9), 3048-3055.
125. Prietzel, J.; Thieme, J.; Tyufekchieva, N.; Paterson, D.; McNulty, I.; Kögel-Knabner, I., Sulfur speciation in well-aerated and wetland soils in a forested catchment assessed by sulfur K-edge X-ray absorption near-edge spectroscopy (XANES). *J. of Plant Nutr. Soil Sci.* **2009**, *172*, (3), 393-403.
126. Jiang, J.; Bauer, I.; Paul, A.; Kappler, A., Arsenic Redox Changes by Microbially and Chemically Formed Semiquinone Radicals and Hydroquinones in a Humic Substance Model Quinone. *Environ. Sci. Technol.* **2009**, *43*, (10), 3639-3645.
127. Buschmann, J.; Sigg, L., Antimony(III) Binding to Humic Substances: Influence of pH and Type of Humic Acid. *Environ. Sci. Technol.* **2004**, *38*, (17), 4535-4541.
128. Wu, T.-l.; Qin, W.-x.; Alves, M. E.; Fang, G.-d.; Sun, Q.; Cui, P.-x.; Liu, C.; Zhou, D.-m.; Wang, Y.-j., Mechanisms of Sb(III) oxidation mediated by low molecular weight phenolic acids. *Chem. Eng. J.* **2019**, *356*, 190-198.

129. Hiemstra, T.; Mia, S.; Duhaut, P.-B.; Molleman, B., Natural and Pyrogenic Humic Acids at Goethite and Natural Oxide Surfaces Interacting with Phosphate. *Environ. Sci. Technol.* **2013**, *47*, (16), 9182-9189.
130. Grafe, M.; Eick, M. J.; Grossl, P. R., Adsorption of Arsenate (V) and Arsenite (III) on Goethite in the Presence and Absence of Dissolved Organic Carbon. *Soil Sci. Soc. Am. J.* **2001**, *65*, (6), 1680-1687.
131. Bauer, M.; Blodau, C., Mobilization of arsenic by dissolved organic matter from iron oxides, soils and sediments. *Sci. Total Environ.* **2006**, *354*, (2-3), 179-190.
132. Redman, A. D.; Macalady, D. L.; Ahmann, D., Natural Organic Matter Affects Arsenic Speciation and Sorption onto Hematite. *Environ. Sci. Technol.* **2002**, *36*, (13), 2889-2896.
133. González A, Z. I.; Krachler, M.; Cheburkin, A. K.; Shotyk, W., Spatial Distribution of Natural Enrichments of Arsenic, Selenium, and Uranium in a Minerotrophic Peatland, Gola di Lago, Canton Ticino, Switzerland. *Environ. Sci. Technol.* **2006**, *40*, (21), 6568-6574.
134. Rothwell, J. J.; Taylor, K. G.; Chenery, S. R. N.; Cundy, A. B.; Evans, M. G.; Allott, T. E. H., Storage and Behavior of As, Sb, Pb, and Cu in Ombrotrophic Peat Bogs under Contrasting Water Table Conditions. *Environ. Sci. Technol.* **2010**, *44*, (22), 8497-8502.
135. Palmer, K.; Ronkanen, A.-K.; Kløve, B., Efficient removal of arsenic, antimony and nickel from mine wastewaters in Northern treatment peatlands and potential risks in their long-term use. *Ecol. Eng.* **2015**, *75*, 350-364.
136. Anawar, H. M.; Akai, J.; Komaki, K.; Terao, H.; Yoshioka, T.; Ishizuka, T.; Safiullah, S.; Kato, K., Geochemical occurrence of arsenic in groundwater of Bangladesh: sources and mobilization processes. *J. Geochem. Expl.* **2003**, *77*, (2), 109-131.
137. Asta, M. P.; Wang, Y.; Fruttschi, M.; Viacava, K.; Loreggian, L.; Le Pape, P.; Le Vo, P.; Fernández, A. M.; Morin, G.; Bernier-Latmani, R., Microbially Mediated Release of As from Mekong Delta Peat Sediments. *Environ. Sci. Technol.* **2019**, *53*, (17), 10208-10217.
138. Neubauer, E.; von der Kammer, F.; Knorr, K. H.; Peiffer, S.; Reichert, M.; Hofmann, T., Colloid-associated export of arsenic in stream water during stormflow events. *Chem. Geol.* **2013**, *352*, 81-91.
139. Huang, J.-H.; Matzner, E., Biogeochemistry of Organic and Inorganic Arsenic Species in a Forested Catchment in Germany. *Environ. Sci. Technol.* **2007**, *41*, (5), 1564-1569.
140. Kalbitz, K.; Wennrich, R., Mobilization of heavy metals and arsenic in polluted wetland soils and its dependence on dissolved organic matter. *Sci. Total Environ.* **1998**, *209*, (1), 27-39.
141. Rothwell, J. J.; Taylor, K. G.; Ander, E. L.; Evans, M. G.; Daniels, S. M.; Allott, T. E. H., Arsenic retention and release in ombrotrophic peatlands. *Sci. Total Environ.* **2009**, *407*, (4), 1405-1417.
142. Ritter, K.; Aiken, G. R.; Ranville, J. F.; Bauer, M.; Macalady, D. L., Evidence for the Aquatic Binding of Arsenate by Natural Organic Matter–Suspended Fe(III). *Environ. Sci. Technol.* **2006**, *40*, (17), 5380-5387.
143. Sharma, P.; Ofner, J.; Kappler, A., Formation of Binary and Ternary Colloids and Dissolved Complexes of Organic Matter, Fe and As. *Environ. Sci. Technol.* **2010**, *44*, (12), 4479-4485.
144. Mikutta, C.; Kretzschmar, R., Spectroscopic Evidence for Ternary Complex Formation between Arsenate and Ferric Iron Complexes of Humic Substances. *Environ. Sci. Technol.* **2011**, *45*, (22), 9550-9557.
145. Mikutta, C.; Frommer, J.; Voegelin, A.; Kaegi, R.; Kretzschmar, R., Effect of citrate on the local Fe coordination in ferrihydrite, arsenate binding, and ternary arsenate complex formation. *Geochim. Cosmochim. Acta* **2010**, *74*, (19), 5574-5592.

146. Hoffmann, M.; Mikutta, C.; Kretzschmar, R., Arsenite Binding to Natural Organic Matter: Spectroscopic Evidence for Ligand Exchange and Ternary Complex Formation. *Environ. Sci. Technol.* **2013**, *47*, (21), 12165-12173.
147. Buschmann, J.; Kappeler, A.; Lindauer, U.; Kistler, D.; Berg, M.; Sigg, L., Arsenite and Arsenate Binding to Dissolved Humic Acids: Influence of pH, Type of Humic Acid, and Aluminum. *Environ. Sci. Technol.* **2006**, *40*, (19), 6015-6020.
148. Warwick, P.; Inam, E.; Evans, N., Arsenics Interaction with Humic Acid. *Environ. Chem.* **2005**, *2*, (2), 119-124.
149. Liu, G.; Cai, Y., Complexation of arsenite with dissolved organic matter: Conditional distribution coefficients and apparent stability constants. *Chemosphere* **2010**, *81*, (7), 890-896.
150. Lenoble, V.; Dang, D. H.; Loustau Cazalet, M.; Mounier, S.; Pfeifer, H. R.; Garnier, C., Evaluation and modelling of dissolved organic matter reactivity toward AsIII and AsV – Implication in environmental arsenic speciation. *Talanta* **2015**, *134*, 530-537.
151. Guénet, H.; Davranche, M.; Vantelon, D.; Bouhnik-Le Coz, M.; Jardé, E.; Dorcet, V.; Demangeat, E.; Jestin, J., Highlighting the wide variability in arsenic speciation in wetlands: A new insight into the control of the behavior of arsenic. *Geochim. Cosmochim. Acta* **2017**, *203*, 284-302.
152. Schmöger, M. E. V.; Oven, M.; Grill, E., Detoxification of Arsenic by Phytochelatins in Plants. *Plant Physiol.* **2000**, *122*, (3), 793.
153. Planer-Friedrich, B.; Schaller, J.; Wismeth, F.; Mehlhorn, J.; Hug, S. J., Monothioarsenate Occurrence in Bangladesh Groundwater and Its Removal by Ferrous and Zero-Valent Iron Technologies. *Environ. Sci. Technol.* **2018**, *52*, (10), 5931-5939.
154. Shotyk, W., Review of the inorganic geochemistry of peats and peatland waters. *Earth Sci. Rev.* **1988**, *25*, (2), 95-176.
155. Steinmann, P.; Shotyk, W., Ion chromatography of organic-rich natural waters from peatlands IV. Dissolved free sulfide and acid-volatile sulfur. *J. Chromatogr. A* **1995**, *706*, (1), 287-292.
156. Shotyk, W.; Krachler, M.; Chen, B., Antimony in recent, ombrotrophic peat from Switzerland and Scotland: Comparison with natural background values (5,320 to 8,020 14C yr BP) and implications for the global atmospheric Sb cycle. *Global Biogeochem. Cycles* **2004**, *18*, (1), 1-13.
157. Cloy, J. M.; Farmer, J. G.; Graham, M. C.; MacKenzie, A. B., Retention of As and Sb in Ombrotrophic Peat Bogs: Records of As, Sb, and Pb Deposition at Four Scottish Sites. *Environ. Sci. Technol.* **2009**, *43*, (6), 1756-1762.
158. Cloy, J. M.; Farmer, J. G.; Graham, M. C.; MacKenzie, A. B.; Cook, G. T., A comparison of antimony and lead profiles over the past 2500 years in Flanders Moss ombrotrophic peat bog, Scotland. *J. Environ. Monit.* **2005**, *7*, (12), 1137-1147.
159. Fawcett, S. E.; Jamieson, H. E.; Nordstrom, D. K.; McCleskey, R. B., Arsenic and antimony geochemistry of mine wastes, associated waters and sediments at the Giant Mine, Yellowknife, Northwest Territories, Canada. *Appl. Geochem.* **2015**, *62*, 3-17.
160. Tella, M.; Pokrovski, G. S., Stability and structure of pentavalent antimony complexes with aqueous organic ligands. *Chem. Geol.* **2012**, *292-293*, 57-68.
161. Tella, M.; Pokrovski, G. S., Antimony(III) complexing with O-bearing organic ligands in aqueous solution: An X-ray absorption fine structure spectroscopy and solubility study. *Geochim. Cosmochim. Acta* **2009**, *73*, (2), 268-290.

162. Tella, M.; Pokrovski, G. S., Antimony(V) complexing with O-bearing organic ligands in aqueous solution: an X-ray absorption fine structure spectroscopy and potentiometric study. *Mineral. Mag.* **2008**, *72*, (1), 205-209.
163. Pilarski, J.; Waller, P.; Pickering, W., Sorption of antimony species by humic acid. *Water Air Soil Poll.* **1995**, *84*, (1), 51-59.
164. Arsic, M.; Teasdale, P. R.; Welsh, D. T.; Johnston, S. G.; Burton, E. D.; Hockmann, K.; Bennett, W. W., Diffusive Gradients in Thin Films Reveals Differences in Antimony and Arsenic Mobility in a Contaminated Wetland Sediment during an Oxic-Anoxic Transition. *Environ. Sci. Technol.* **2018**, *52*, (3), 1118-1127.
165. Hesslein, R. H., An in situ sampler for close interval pore water studies. *Limnol. Oceanogr.* **1976**, *21*, (6), 912-914.
166. Cline, J. D., Spectrophotometric determination of hydrogen sulfide in natural waters. *Limnol. Oceanogr.* **1969**, *14*, (3), 454-458.
167. Fortune, W.; Mellon, M., Determination of iron with o-phenanthroline: a spectrophotometric study. *Ind. Eng. Chem. Anal. Ed.* **1938**, *10*, (2), 60-64.
168. Planer-Friedrich, B.; Wallschläger, D., A Critical Investigation of Hydride Generation-Based Arsenic Speciation in Sulfidic Waters. *Environ. Sci. Technol.* **2009**, *43*, (13), 5007-5013.
169. Thilo, E.; Hertzog, K.; Winkler, A., Über Vorgänge bei der Bildung des Arsen(V)-sulfids beim Ansäuern von Tetrathioarsenatlösungen. *Z. anorg. allg. Chem.* **1970**, *373*, (2), 111-121.
170. Thanabalasingam, P.; Pickering, W. F., Arsenic sorption by humic acids. *Environ. Pollut.* **1986**, *12*, (3), 233-246.
171. Kamenar, B.; Bruvo, M.; Butumović, J., Structures involving unshared electron pair. The Crystal Structures of $\text{As}(\text{OCOCH}_3)_3$ and $\text{As}_2\text{O}(\text{OCOCH}_3)_4$. *Z. anorg. allg. Chem.* **1993**, *619*, (5), 943-946.
172. Dinger, M. B.; Scott, M. J., Sterically Crowded, Rigid, C₃ Symmetric Phosphites: Synthesis, Structure, and Preparation of Metal Complexes. *Inorg. Chem.* **2001**, *40*, (5), 856-864.
173. Said, M. A.; Kumara Swamy, K. C.; Veith, M.; Huch, V., First Structural Study of a Stable Arsorane Containing 1,3,2-Dioxarsenane Rings and an N→As Donor–Acceptor Bond: Arsenic vs Phosphorus Chemical Behavior. *Inorg. Chem.* **1996**, *35*, (22), 6627-6630.
174. Couture, R.-M.; Wallschläger, D.; Rose, J.; Van Cappellen, P., Arsenic binding to organic and inorganic sulfur species during microbial sulfate reduction: a sediment flow-through reactor experiment. *Environ. Chem.* **2013**, *10*, (4), 285-294.
175. Sun, H.; Yan, S. C.; Cheng, W. S., Interaction of antimony tartrate with the tripeptide glutathione. *Eur. J. Biochem.* **2000**, *267*, (17), 5450-5457.
176. Yan, S.; Ding, K.; Zhang, L.; Sun, H., Complexation of Antimony(III) by Trypanothione. *Angew. Chem. Int. Ed.* **2000**, *39*, (23), 4260-4262.
177. Martell, A.; Smith, R. M., *Critical stability constants - Volume 3: Other Organic Ligands*. Springer: New York, 1977; Vol. 3.
178. Anderegg, G.; Malik, S., Die Komplexbildungstendenz des dreiwertigen Antimons in wässriger Lösung. *Helv. Chim. Acta* **1970**, *53*, (3), 577-600.
179. Anderegg, G.; Malik, S., Komplexe XLIII. Die Komplexe des dreiwertigen Antimons mit Polyaminocarboxylaten. *Helv. Chim. Acta* **1970**, *53*, (3), 564-569.

180. Peters, M.; Saak, W.; Pohl, S., Neutrale Thiolate und ein Iodidthiolat von Antimon(III). Die Kristallstrukturen von $\text{Sb}(\text{SC}_6\text{H}_5)_3$, $\text{Sb}(\text{SC}_6\text{H}_2\text{Me}_3\text{-}2,4,6)_3$ und $\text{SbI}(\text{SC}_6\text{H}_2\text{Me}_3\text{-}2,4,6)_2$. *Z. anorg. allg. Chem.* **1996**, 622, (12), 2119-2123.
181. Horley, G. A.; Mahon, M. F.; Molloy, K. C.; Venter, M. M.; Haycock, P. W.; Myers, C. P., Structures of $\text{Sb}(\text{OC}_6\text{H}_3\text{Me}_2\text{-}2,6)_3$ and $\text{Sb}(\text{OEt})_5 \cdot \text{NH}_3$: The First Authenticated Monomeric $\text{Sb}(\text{OR})_n$ ($n = 3, 5$). *Inorg. Chem.* **2002**, 41, (6), 1652-1657.
182. Werne, J. P.; Hollander, D. J.; Lyons, T. W.; Sinninghe Damsté, J. S., Organic sulfur biogeochemistry: Recent advances and future research directions. *Spec. Pap. Geol. Soc. Am.* **2004**, 379, (135).
183. Mikutta, C.; Rothwell, J. J., Peat Bogs as Hotspots for Organoarsenical Formation and Persistence. *Environ. Sci. Technol.* **2016**, 50, (8), 4314-4323.

Contributions to Studies 1-6

STUDY 1: Monothioarsenate Transformation Kinetics Determining Arsenic Sequestration by Sulfhydryl Groups of Peat

Johannes Besold	60%	development of research concept, laboratory work, analyses and data interpretation, preparation of manuscript
Ashis Biswas	5%	assistance with laboratory work and XAS data acquisition, comments on manuscript
Elke Suess	5%	field and laboratory work, comments on manuscript
Andreas C. Scheinost	5%	assistance with XAS analysis, comments on manuscript
André Rossberg	2.5%	assistance with XAS analysis, comments on manuscript
Christian Mikutta	2.5%	field and laboratory work, comments on manuscript
Ruben Kretzschmar	2.5%	field site selection, comments on manuscript
Jon Petter Gustafsson	2.5%	assistance with XAS data discussion, comments on manuscript
Britta Planer-Friedrich	15%	development of research concept, discussion of results, contribution to manuscript writing and comments on manuscript

STUDY 2: Complexation of Arsenite, Arsenate, and Monothioarsenate with Oxygen-Containing Functional Groups of Natural Organic Matter: An XAS Study

Ashis Biswas	55%	development of research concept, laboratory work, analyses and data interpretation, preparation of manuscript
Johannes Besold	25%	assistance with laboratory and XAS work, comments on manuscript
Carin Sjöstedt	5%	assistance with XAS analysis, comments on manuscript
Jon Petter Gustafsson	2.5%	assistance with XAS analysis, comments on manuscript
Andreas C. Scheinost	2.5%	Morlet wavelet analysis, comments on manuscript
Britta Planer-Friedrich	10%	development of research concept, discussion of results, comments on manuscript

STUDY 3: Arsenic Fate in Peat Controlled by pH-dependent Role of Reduced Sulfur

Anne Eberle	50%	laboratory work, analyses and data interpretation, preparation of manuscript
Johannes Besold	30%	assistance with development of research concept, XAS analysis, discussion of results, contribution to manuscript writing and comments on manuscript
Carolin F. Kerl	5%	assistance with laboratory work, comments on manuscript
Juan S. Lezama-Pacheco	2.5%	assistance with XAS data acquisition
Scott Fendorf	2.5%	assistance with XAS data discussion, comments on manuscript
Britta Planer-Friedrich	10%	development of research concept, discussion of results, contribution to manuscript writing and comments on manuscript

STUDY 4: Redox Heterogeneities Promote Thioarsenate Formation and Release into Groundwater from Low Arsenic Sediments

Naresh Kumar	50%	development of research concept, field and laboratory work, analyses and data interpretation, preparation of manuscript
Vincent Noël	10%	assistance with laboratory work and XAS analysis, comments on manuscript
Britta Planer-Friedrich	5%	ICP-MS data processing, comments on manuscript
Johannes Besold	5%	assistance with data interpretation, comments on manuscript
Juan Lezama Pacheco	2.5%	XRD analyses and interpretation
John R. Bargar	2.5%	field site selection, comments on manuscript
Gordon E. Brown	2.5%	assistance with data interpretation, comments on manuscript
Scott Fendorf	2.5%	assistance with data interpretation, comments on manuscript
Kristin Boye	20%	development of research concept, field and laboratory work, analyses and data interpretation, preparation of manuscript

STUDY 5: Antimonite Complexation with Thiol and Carboxyl/Phenol Groups of Peat Organic Matter

Johannes Besold	80%	development of research concept, laboratory work, analyses and data interpretation, preparation of manuscript
Naresh Kumar	5%	assistance with laboratory work, comments on manuscript
Andreas C. Scheinost	5%	assistance with XAS analysis, comments on manuscript
Juan Lezama Pacheco	2.5%	assistance with XAS data acquisition
Scott Fendorf	2.5%	assistance with XAS data discussion, comments on manuscript
Britta Planer-Friedrich	5%	development of research concept, discussion of results, comments on manuscript

STUDY 6: Antimonite Binding to Natural Organic Matter: Spectroscopic Evidence from a Mine Water Impacted Peatland

Johannes Besold	65%	development of research concept, laboratory work, analyses and data interpretation, preparation of manuscript
Anne Eberle	5%	field and laboratory work, comments on manuscript
Vincent Noël	5%	assistance with Fe XAS analysis, comments on manuscript
Katharina Kujala	5%	assistance with field work, comments on manuscript
Naresh Kumar	2.5%	assistance with laboratory work, comments on manuscript
Andreas C. Scheinost	2.5%	assistance with Sb XAS analysis, comments on manuscript
Juan Lezama Pacheco	2.5%	assistance with XAS data acquisition
Scott Fendorf	2.5%	assistance with XAS data discussion, comments on manuscript
Britta Planer-Friedrich	10%	development of research concept, field work, discussion of results, comments on manuscript

Appendix: Studies 1-6

STUDY 1

Besold, J.; Biswas, A.; Suess, E.; Scheinost, A. C.; Rossberg, A.; Mikutta, C.; Kretzschmar, R.; Gustafsson, J. P.; Planer-Friedrich, B., Monothioarsenate transformation kinetics determining arsenic sequestration by sulfhydryl groups of peat. *Environ. Sci. Technol.* **2018**, 52, (13), 7317-7326.

STUDY 2

Biswas, A.; Besold, J.; Sjöstedt, C.; Gustafsson, J. P.; Scheinost, A. C.; Planer-Friedrich, B., Complexation of arsenite, arsenate, and monothioarsenate with oxygen-containing functional groups of natural organic matter: An XAS Study. *Environ. Sci. Technol.* **2019**, 53, (18), 10723-10731.

STUDY 3

Eberle, A.; Besold, J.; Kerl, C. F.; Lezama Pacheco, J.; Fendorf, S.; Planer-Friedrich, B., Arsenic fate in peat controlled by ph-dependent role of reduced sulfur. *Environ. Sci. Tech.* **2020**, 54, (11), 6682-6692.

STUDY 4

Kumar, N.; Noël, V.; Planer-Friedrich, B.; Besold, J.; Lezama Pacheco, J.; Bargar, J. R.; Brown, G. E. Jr.; Fendorf, S.; Boye, K., redox heterogeneities promote thioarsenate formation and release into groundwater from low arsenic sediments. *Environ. Sci. Tech.* **2020**, 54, (6), 3237-3244.

STUDY 5

Besold, J.; Kumar, N.; Scheinost, A. C.; Lezama Pacheco, J.; Fendorf, S.; Planer-Friedrich, B., Antimonite complexation with thiol and carboxyl/phenol groups of peat organic matter. *Environ. Sci. Technol.* **2019**, 53, (9), 5005-5015.

STUDY 6

Besold, J.; Eberle, A.; Noël, V.; Kujala, K.; Kumar, N.; Scheinost, A. C.; Pacheco, J. L.; Fendorf, S.; Planer-Friedrich, B., Antimonite binding to natural organic matter: spectroscopic evidence from a mine water impacted peatland. *Environ. Sci. Technol.* **2019**, 53, (18), 10792-10802.

Study 1: Monothioarsenate transformation kinetics determining arsenic sequestration by sulfhydryl groups of peat

Johannes Besold, Ashis Biswas, Elke Suess, Andreas C. Scheinost, Andree Rossberg, Christian Mikutta, Ruben Kretzschmar, Jon Petter Gustafsson and Britta Planer-Friedrich

Reprinted with permission from

Environmental Science & Technology

Copyright 2020 American Chemical Society

Monothioarsenate Transformation Kinetics Determining Arsenic Sequestration by Sulfhydryl Groups of Peat

Johannes Besold,[†] Ashis Biswas,^{†,‡} Elke Suess,[§] Andreas C. Scheinost,^{○,||} André Rossberg,^{○,||} Christian Mikutta,[⊥] Ruben Kretzschmar,[#] Jon Petter Gustafsson,[¶] and Britta Planer-Friedrich^{*,†,||}

[†]Department of Environmental Geochemistry, Bayreuth Center for Ecology and Environmental Research (BAYCEER), Bayreuth University, 95440 Bayreuth, Germany

[‡]Department of Earth and Environmental Sciences, Indian Institute of Science Education and Research (IISER) Bhopal, Bhopal Bypass Road, Bhauri, Madhya Pradesh 462066, India

[§]Eawag, Swiss Federal Institute of Aquatic Science and Technology, 8600 Dübendorf, Switzerland

[○]The Rossendorf Beamline (ROBL) at ESRF, 38043 Grenoble, France

^{||}Institute of Resource Ecology, Helmholtz-Zentrum Dresden-Rossendorf (HZDR), Bautzner Landstraße 400, 01328 Dresden, Germany

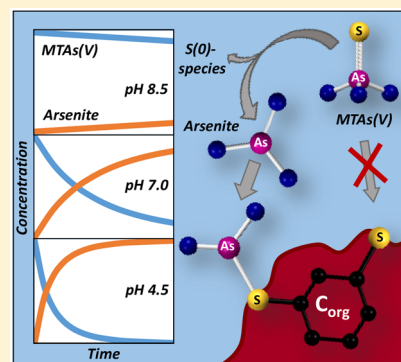
[⊥]Soil Mineralogy, Institute of Mineralogy, Gottfried Wilhelm Leibniz Universität Hannover, Callinstr. 3, 30167 Hannover, Germany

[#]Institute of Biogeochemistry and Pollutant Dynamics, Department of Environmental Systems Science, ETH Zurich, CHN, CH-8092 Zurich, Switzerland

[¶]Department of Soil and Environment, Swedish University of Agricultural Sciences, Box 7014, 750 07, Uppsala, Sweden

Supporting Information

ABSTRACT: In peatlands, arsenite was reported to be effectively sequestered by sulfhydryl groups of natural organic matter. To which extent porewater arsenite can react with reduced sulfur to form thioarsenates and how this affects arsenic sequestration in peatlands is unknown. Here, we show that, in the naturally arsenic-enriched peatland *Gola di Lago*, Switzerland, up to 93% of all arsenic species in surface and porewaters were thioarsenates. The dominant species, monothioarsenate, likely formed from arsenite and zerovalent sulfur-containing species. Laboratory incubations with sulfide-reacted, purified model peat showed increasing total arsenic sorption with decreasing pH from 8.5 to 4.5 for both, monothioarsenate and arsenite. However, X-ray absorption spectroscopy revealed no binding of monothioarsenate via sulfhydryl groups. The sorption observed at pH 4.5 was acid-catalyzed dissociation of monothioarsenate, forming arsenite. The lower the pH and the more sulfhydryl sites, the more arsenite sorbed which in turn shifted equilibrium toward further dissociation of monothioarsenate. At pH 8.5, monothioarsenate was stable over 41 days. In conclusion, arsenic can be effectively sequestered by sulfhydryl groups in anoxic, slightly acidic environments where arsenite is the only arsenic species. At neutral to slightly alkaline pH, monothioarsenate can form and its slow transformation into arsenite and low affinity to sulfhydryl groups suggest that this species is mobile in such environments.



INTRODUCTION

Arsenic (As) is a toxic metalloid whose speciation and thus mobility is strongly affected by (microbially triggered) redox transformations.^{1–3} In most terrestrial environments, inorganic arsenite ($H_xAs^{III}O_3^{3-x}$, $x = 1–3$) and arsenate ($H_xAs^VO_4^{3-x}$, $x = 1–3$) dominate aqueous As speciation;¹ hence, their sorption behavior to many environmentally relevant mineral phases has been extensively studied.⁴ In particular, natural organic matter (NOM), for example, in peatlands has been recognized as an important sink for As in recent years.^{5–8} Contrarily, complexation to dissolved or colloidal organic matter can lead to (re)mobilization of As in organic rich surface-, pore-, and groundwaters.^{9–11}

Several inner-sphere complexation mechanisms of As to NOM have been shown by X-ray absorption spectroscopy (XAS). Ternary complex formation between As oxoacids and iron (Fe, (III))–NOM complexes^{9,12,13} has been revealed by XAS for both, arsenite¹⁴ and arsenate.¹⁵ Moreover, direct coordination with phenolate groups of NOM has at first been postulated for arsenite and arsenate by Buschmann et al.¹⁶ and has recently been verified for arsenite by Hoffmann et al.¹⁴ Additionally, coordination of trivalent As with sulfhydryl groups

Received: March 22, 2018

Revised: May 30, 2018

Accepted: May 31, 2018

Published: May 31, 2018

of NOM, presumably provided by organic sulfur (S) from plant debris, was identified as prevailing sequestration mechanism in deep layers of the minerotrophic peatland *Gola di Lago*, Switzerland,^{17,18} and in a laboratory study using XAS.¹⁹

Although arsenite generally dominates aqueous As speciation under reducing conditions, multiple studies showed that thioarsenates ($H_xAs^V S^{II} O_{4-n}^{3-x}$; $n = 1-4$; $x = 1-3$) can form and dominate in sulfidic²⁰⁻²⁵ environments and even in the presence of high ferrous iron concentrations.²⁶ Thioarsenates are proposed to form in two steps from arsenite: First, at conditions of excess SH^- over OH^- , ligand exchange leads to formation of thioarsenites ($H_xAs^{III} S^{II} O_{3-n}^{3-x}$; $n = 1-3$; $x = 1-3$) as unstable intermediates.^{27,28} Second, addition of zerovalent sulfur transforms thioarsenites to thioarsenates.²⁹ Only formation of monothioarsenate ($H_xAs^V S^{II} O_3^{3-x}$; $x = 1-3$; MTAs(V)) does not require excess sulfide, because it forms directly from arsenite and zerovalent sulfur or zerovalent sulfur-containing species (thereafter abbreviated as S(0)-species) as, e.g., colloidal elemental sulfur or polysulfides²⁹ at neutral to alkaline pH. At acidic pH (<4.0), MTAs(V) can form as an intermediate species via a nucleophilic attack of sulfide with arsenate, eventually resulting in arsenite.^{25,30} Although sulfate-reducing conditions can prevail in peatlands, free sulfide concentrations are commonly low³¹⁻³³ since sulfide can be effectively incorporated into NOM as organic thiols and polysulfides^{31,34} or can form surface associated polysulfides during reduction of ferric (hydr)oxides.^{35,36} A recent study observed thioarsenate formation after sulfidization of organic freshwater flocs from the *Gola di Lago* peatland and related this to an excess of surface-bound S(0)-species.³⁷ The authors postulated thioarsenates to be common porewater constituents in the As-enriched *Gola di Lago* peatland; however, direct evidence is still missing. Further, nothing is known about their mobility in sulfidic, organic rich systems, although sorption behavior of MTAs(V) and tetrathioarsenate ($H_xAs^V S^{II} O_4^{3-x}$; $x = 1-3$; TetraTAs(V)) to iron (oxy)hydroxides and -sulfides has been studied before^{38,39} and often showed higher mobility of thioarsenates compared to As oxoacids.

The purpose of this study therefore was (i) to investigate the natural occurrence of thioarsenates in surface and porewaters of several peat profiles in the As-enriched peatland *Gola di Lago* and (ii) to compare the sorption behavior of MTAs(V), which was found to be the dominant species in *Gola di Lago*, with that of arsenite to sulfide-reacted peat at different pH values and sulfide spike concentrations, in order to elucidate the As retention processes in peatlands under different pH regimes.

MATERIALS AND METHODS

Field Site and Sampling. Peat cores, surface- and porewaters were collected as a single-point observation in November 2012 in the minerotrophic peatland *Gola di Lago*, Switzerland.^{5,17} In total, five peat profiles were sampled close to the sampling sites already visited in 2009.^{17,18} Peat cores were sampled up to 210 cm using a HUMAX drilling system.¹⁷ The sample cores were immediately removed from the plastic liners, packed into N_2 -filled sampling bags, and further processed in a field laboratory close to the peatland. Porewater was obtained by manually squeezing the water saturated peat samples in the N_2 -filled bags on-site and then quickly removing them from the bags for further analyses and preservation. A detailed description of the field site, sample handling, and analyses can be found in the [Supporting Information](#).

Materials. All reagents used were of analytical grade and purchased from Fluka, Alfa Aesar, or Sigma-Aldrich. Because of a lack of a commercially available standard, MTAs(V) was synthesized as $Na_3AsO_3 \cdot 7H_2O$ as described previously.²⁷ Considering exact molecular weight ($Na_3AsO_3 \cdot 4H_2O$, 296.01 g/mol) and purity (90%; 5% arsenite, 5% arsenate) of the synthesis product, the exact concentrations of MTAs(V) used in the experiments were 53 μM where nominal concentrations of 50 μM were declared. All solutions were prepared with doubly deionized (DDI) water (Milli-Q, Millipore, $\geq 18.2 M\Omega cm$), and all glassware was treated with acid before use.

Peat was collected from the ombrotrophic *Federseemoor* peatland near Bad Buchau, Germany.¹⁹ This peat was chosen as a model sorbent for NOM because it has already a naturally low metal(loid) content compared to minerotrophic peatlands such as the *Gola di Lago* peatland (ash content $\sim 10-80\%$).⁵ These low amounts enabled us to exclude the influence of elements which could act as bridging agent between organic functional groups of peat and arsenic (e.g., Fe) to study the influence of solely organic (thiol) groups on the behavior of MTAs(V) at different pH values. The peat was wet-sieved to a size fraction of 63–250 μm and, after an initial washing step with 0.1 M HCl to solve potentially interfering metal(loid)s, washed several times with DDI water until a starting pH of ~ 4.5 was reached. After washing, the Fe content in our model peat was 829 mg/kg (Table SI-2) in comparison to Fe contents between 4960 and 35 100 mg/kg in the *Gola di Lago* peat.¹⁸ Afterward, the peat was freeze-dried, homogenized, and stored in a glovebag ($pO_2 < 1 ppm$) in the dark until use. In this paper, the term peat is used when referring to the before described 63–250 μm ¹⁹ size fraction. After microwave digestion (MARS Xpress, CEM) using a 5:3 ratio of 30% H_2O_2 and 65% HNO_3 , the elemental composition was analyzed by inductively coupled plasma mass-spectrometry (ICP-MS, XSeries2, Thermo-Fisher).²¹ Carbon, S, and N contents of the peat were determined with a Thermo Quest, Flash EA 1112 analyzer. For functional group characterization, Fourier transform infrared (FT-IR) spectroscopy and ¹³C cross-polarization/magic-angle spinning–nuclear magnetic resonance (CP/MAS–NMR) spectroscopy were used. All described methods confirm similar chemical composition and functional groups as in a previous study of Hoffmann et al.,¹⁹ enabling direct comparison of results. A detailed description of the methods and their results can be found in the [Supporting Information](#). Furthermore, the Ambersep GT74 resin (Rohm & Haas) was used as a sulfhydryl-rich synthetic organic model adsorbent. After purchase, the resin was washed several times with anoxic DDI water and stored under anoxic conditions in a glovebag until use. A detailed chemical characterization of the resin can be found elsewhere.⁴⁰

Arsenic Sorption to Sulfide-Reacted Peat. An MTAs(V) and arsenite time-resolved sorption experiment (0–984 h) on sulfide-reacted peat was conducted at pH 4.5, 7.0, and 8.5, respectively. The peat suspensions (0.2 M C) were reacted with 3.0 mM sulfide (S(-II)) solution (15 mmol S(-II)/mol C) in a 30 mM NaCl electrolyte under anoxic conditions ($pO_2 < 1 ppm$) and shaken in the dark for 24 h. The respective pH (± 0.2) was adjusted using anoxic HCl and NaOH. Sodium azide (NaN_3 , 0.75 mmol/mol C) was added to prevent microbial growth. After reaction for 24 h to reach equilibrium,¹⁹ the suspensions were filtered off (12 μm , cellulose acetate) and the remaining peat filter residues were subsequently washed

with electrolyte to remove dissolved sulfide. A wet weight equivalent of 100 mg dry sulfide-reacted peat (0.2 M C) was equilibrated with 50 μM MTAs(V) or arsenite at pH 4.5, 7.0, and 8.5 in anoxic electrolyte, respectively. The samples were incubated for a maximum time of 984 h (41 days) at room temperature and in the dark. Sampling of sacrificing butyl-rubber capped serum bottles (triplicates) was done at 13 (MTAs(V) incubations) and 7 (arsenite incubations) sampling times during the experiment. At every sampling time, the peat suspensions were filtered (0.2 μm , Nylon) and an aliquot of the filtrate was immediately shock-frozen on dry ice. Another aliquot was stabilized in 0.5% H_2O_2 and 0.8% HNO_3 prior to analysis of total aqueous As and S with ICP-MS. After freeze-drying the peat filter residues, one part of the solid phase was used for XAS analysis and another sample aliquot was microwave-digested as described before. The pH dependency of S content in peat was similar compared to Hoffmann et al.¹⁹ assuming equal incorporation as sulfhydryl-S (Figure SI-11). The total amount of As sorbed was determined by analyzing the digests with ICP-MS. The pH and the redox potential (E_h) were monitored during the experiment.

Additionally, an experiment where peat suspensions (0.2 M C) were equilibrated with sulfide spike concentrations of 0.3, 3, and 30 mM (1.5, 15, and 150 mmol S(-II)/mol C) was performed at pH 4.5, 7.0, and 8.5 with 50 μM MTAs(V) addition for 96 h to examine the influence of sulfide spike concentrations on MTAs(V) affinity to sulfide-reacted peat. Otherwise, the experimental protocol was identical to the one described before. Monothioarsenate stability in the NaCl and NaN_3 electrolyte solution was tested prior to experiments at pH 4.5, 7.0, and 8.5 (Figure SI-9d).

Arsenic Sorption to Ambersep GT74 Resin. In order to examine the potential of MTAs(V) binding to sulfhydryl groups, 100 mg of washed resin was equilibrated with 200–250 μM MTAs(V) and arsenite for 96 h, respectively. The pH was adjusted to ~ 7 (arsenite) and 7.5 or 8.5 (MTAs(V)). Otherwise, the experimental setup was the same as the one described before.

Aqueous Arsenic and Sulfur Speciation. After thawing the shock-frozen samples in a glovebag, arsenite, arsenate, and thioarsenate species as well as sulfate and thiosulfate were determined by anion-exchange chromatography (AEC, ICS-3000, Dionex) coupled to an ICP-MS (XSeries2, Thermo-Fisher).²¹ Calibration standards were prepared from sodium arsenate dibasic-heptahydrate ($\text{Na}_2\text{HAsO}_4 \cdot 7\text{H}_2\text{O}$), sodium (meta)arsenite (NaAsO_2), ammonium sulfate ($(\text{NH}_4)_2\text{SO}_4$), and sodium thiosulfate ($\text{Na}_2\text{S}_2\text{O}_3$). Due to a lack of commercially available standards, thioarsenates were quantified via the arsenate calibration curve.²¹

Arsenic Solid-Phase Speciation. Arsenic K-edge (11 867 eV) X-ray absorption near-edge structure (XANES) and extended X-ray absorption fine-structure (EXAFS) spectra were collected at The Rossendorf Beamline (ROBL) at the European Synchrotron Radiation Facility (ESRF), Grenoble, France, and at beamline 4-1 of the Stanford Synchrotron Radiation Lightsource (SSRL), Stanford, USA. Always anoxically kept peat and resin samples were freeze-dried, homogenized, filled into sample holders, and sealed with Kapton tape. All sample measurements were performed in fluorescence mode using Ge array fluorescence detectors and a liquid He cryostat at 15 K to avoid beam damage and minimize thermal disorder. Spectra of As reference compounds were analyzed in transmission/fluorescence mode or were taken

from Suess et al.²⁷ Details on standards preparation, measurements, data reduction, and analyses are provided in the Supporting Information.

RESULTS AND DISCUSSION

Thioarsenates in Surface and Porewater of Gola di Lago Peatland. Total aqueous As in the slightly acidic (pH 5.2 to 6.1) surface and porewaters of Gola di Lago peatland ranged from 1.8 to 180 $\mu\text{g/L}$. Arsenic initially entering the peatland via the intermittent inflow (IF) was mainly arsenate (Figure 1a). With increasing lateral distance to the IF, the

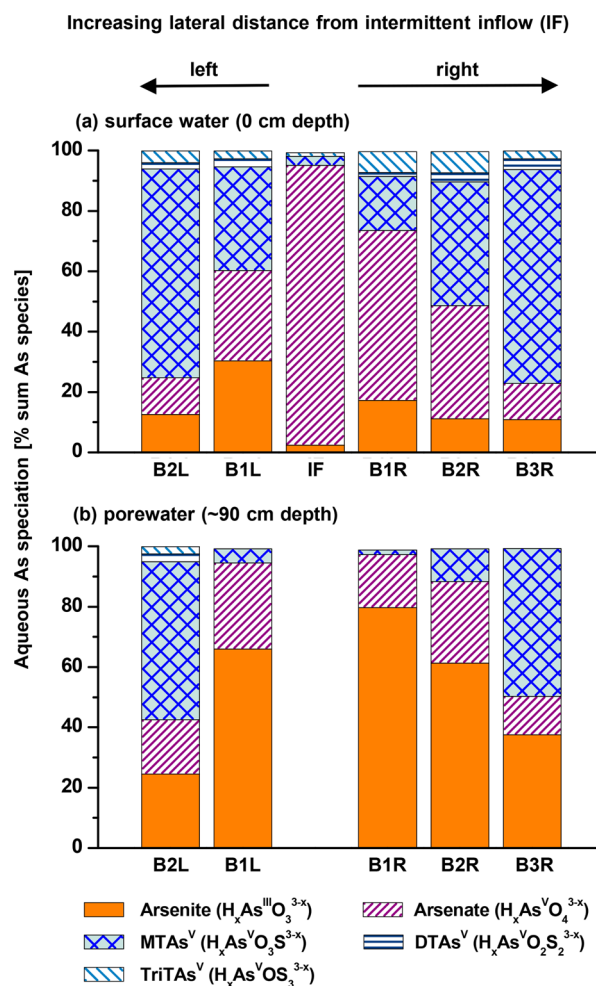


Figure 1. Aqueous As speciation [% of sum As species] of sampling profiles B2L, B1L, intermittent inflow (IF), B1R, B2R, and B3R at the surface (a) and in ~ 90 cm depth (b) from Gola di Lago peatland. Note: for B2R, results are depicted for 60 cm depth because this was the greatest depth achieved for that core. Details regarding sampling depths can be found in Table SI-1. Lateral distances of profiles from IF do not increase on the linear scale. Aqueous As speciation in ~ 90 cm comprises porewater plus an easily mobilizable soil-bound fraction. The detection limit for a single As species was 0.1 $\mu\text{g/L}$.

percentage of arsenate decreased while thioarsenates increased (profiles B1L < B2L and B1R < B2R < B3R in Figure 1a; Figures SI-2–6). The percentage of arsenite remained comparatively low (2–30%) in surface water samples. At greater depth (~ 90 cm), arsenite increased to 25–80% of total As (Figure 1b). Overall, the maximum percentage of thioarsenates reached 93% of total As (profile B3R, 60 cm

depth, Figure SI-6). Concentration and fraction of thioarsenates did not show a correlation with any of the aqueous parameters such as pH, redox potential, or concentration of total As and S in the solid phase (Figures SI-2–6, Table SI-1). Mostly, the dominant species in all profiles was MTAs(V) with up to 91% of total As followed by significantly lower fractions of tri- and dithioarsenate (median 3% and 2%, respectively). Tetrathioarsenate is instable at these low pH values.⁴¹ Note that this speciation data reflects conditions during a single point sampling in November 2012. A seasonally changing water table or increased microbial activity in the summer half-year may lead to a slightly different As speciation, especially in the mostly affected shallow peat layers. To our knowledge,^{5,7,8,17,18} this is the first report of thioarsenates in porewaters of peatlands. Unsuitable preservation and analytical methods probably prevented their detection before.

The significant fractions of MTAs(V) observed in *Gola di Lago* versus a complete lack of information on the effect of MTAs(V) formation on the overall As mobility in S and organic carbon-rich environments were the basis for the following laboratory sorption studies.

Total As Sorption upon Monothioarsenate versus Arsenite Addition to Sulfide-Reacted Peat. In the time series experiments with 3 mM sulfide-reacted peat, total As sorption upon MTAs(V) addition increased in the order pH 8.5 < 7.0 < 4.5, whereby sorption at pH 4.5 (32 $\mu\text{mol As/mol C}$) was ~ 5 times higher than at pH 8.5 (7 $\mu\text{mol As/mol C}$, Figure 2). The same trend occurred for arsenite, but the

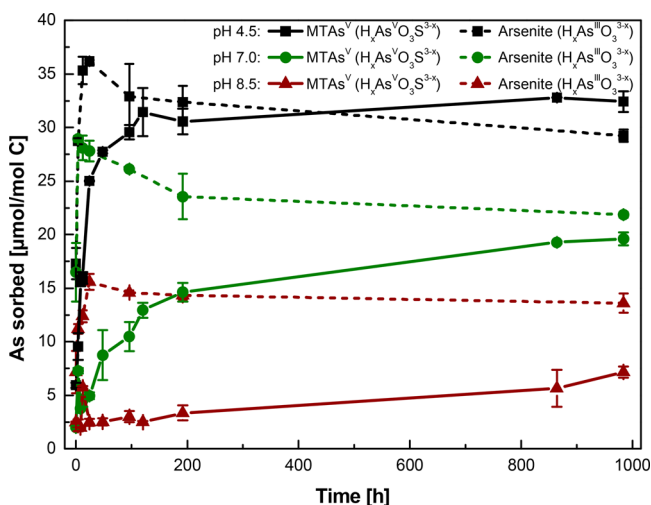


Figure 2. Time series of total As sorbed in experiments where MTAs(V) (straight lines) or arsenite (dashed lines) was added to sulfide-reacted (3 mM sulfide) peat suspensions (0.2 M C) at pH 4.5, 7.0, and 8.5. Conversion factor to [$\mu\text{g/g}$]: $\times 3.4308$. Error bars represent standard deviations of triplicates. Straight or dashed lines serve to guide the eye.

difference between As sorption at pH 4.5 (29 $\mu\text{mol As/mol C}$) and 8.5 (14 $\mu\text{mol As/mol C}$) was only a factor of 2. Compared to arsenite, the initial sorption of total As was slower in experiments where we added MTAs(V), but after 984 h (41 days), the extent of sorption was almost comparable, at least for pH 4.5 and 7.0. For pH 8.5, the amount of total As sorbed remained at only $\sim 50\%$ of that observed in the arsenite experiments (Figure 2).

Comparing the influence of 0.3, 3, and 30 mM sulfide spike concentrations after 96 h (MTAs(V) experiments), a strong

increase of total As sorbed with increasing sulfide spikes was observed at pH 4.5 (6 up to 85 $\mu\text{mol As/mol C}$), while at pH 7.0 and 8.5 almost no influence of sulfide spikes was detected. However, sorption of As at pH 7.0 was always higher than at pH 8.5 (Figure SI-14).

Arsenite Sorption to Sulfide-Reacted Peat. Aqueous As speciation analysis showed that over 41 days of incubation no As species other than arsenite occurred in solution (except for transformations to arsenate (<18%) and dithioarsenate (<11%) at pH 8.5, Figure 3). Compared to a previous study by Hoffmann et al.,¹⁹ the extent of arsenite sorption at pH 7.0 after 96 h (7.3 $\mu\text{mol As/mmol S}$) was lower but generally comparable. A remarkable difference was, however, observed for arsenite sorption at lower pH.

In their study, Hoffmann et al.¹⁹ also used sulfide-reacted humic acid at pH 5.0 (besides sulfide-reacted peat at pH 7.0) and found that, at a given S content, arsenite sorption was lower at lower pH. They explained the difference with sulfhydryl groups having a wide range of proton dissociation constants ($\text{p}K_a$) from 5 to 11,⁴² obtaining increasing nucleophilicity and hence reactivity with increasing pH.

In our experiments, the arsenite sorption strongly increased with lower pH (4.5 > 7.0 > 8.5) as shown before (Figure 2). These findings indicate that a high abundance of sulfhydryl groups with lower $\text{p}K_a$ values seem to be present in the peat, acting as strong nucleophiles. This observation is in general accordance with the proposed acid-catalyzed reaction of sulfide to unsaturated carbon bonds in Hoffmann et al.¹⁹ (Figure SI-7 and Figure SI-8). Additionally, the peak at $\sim 1715 \text{ cm}^{-1}$ in the FT-IR spectrum (Figure SI-7) indicates that significant amounts of aryl ketones were present in the peat, which can form sulfhydryl groups with lower $\text{p}K_a$ values (e.g., thiobenzoic acid, $\text{p}K_a$ 3.6), compared to other organic groups with thiol moieties, after acid catalyzed reaction with sulfide.⁴³

However, also if sulfhydryl groups with lower $\text{p}K_a$ values were present, their nucleophilicity usually increases with increasing pH, which should lead to higher sorption at higher pH, but As sorption was higher at lower pH, even at similar S contents for pH 4.5 and 7.0 (Figure SI-11b). Also, differences in released total S over time (Figure SI-11a) between pH 4.5 and 7.0 cannot fully explain higher As sorption at low pH, since As sorption was already significantly higher at pH 4.5 at the early time steps, when total S release was similar for pH 4.5 and 7.0. In addition, no indications for amorphous As–S phases could be found (see below and Figure SI-16 and Figure SI-17). Maybe polar interactions and/or H-bridges support sorption of the uncharged arsenite ($\text{p}K_a = 9.17^{44}$) via sulfhydryl groups to an overall less negatively charged NOM⁴⁵ at lower pH. At pH 8.5, arsenite is partially negatively charged which may lead to stronger electrostatic repulsion due to increased deprotonation of organic functional groups at high pH and thus explains low sorption to sulfide-reacted peat.

Aqueous As Speciation upon Monothioarsenate Addition to Sulfide-Reacted Peat. Aqueous As speciation analysis for the MTAs(V) experiments with 3 mM sulfide spike concentrations showed, in contrast to the arsenite experiments described before, significant transformations of MTAs(V) to mainly arsenite (Figure 3; corresponding pH and E_h values can be found in Figure SI-10). Transformation rates decreased with increasing pH from half-lives of ~ 35 to ~ 470 h at pH 4.5 and 7.0, respectively, to almost no transformation at pH 8.5 over the duration of the experiment (984 h, Figure 3a,c,e). In DDI water, MTAs(V) was stable (Figure SI-9a) and addition of

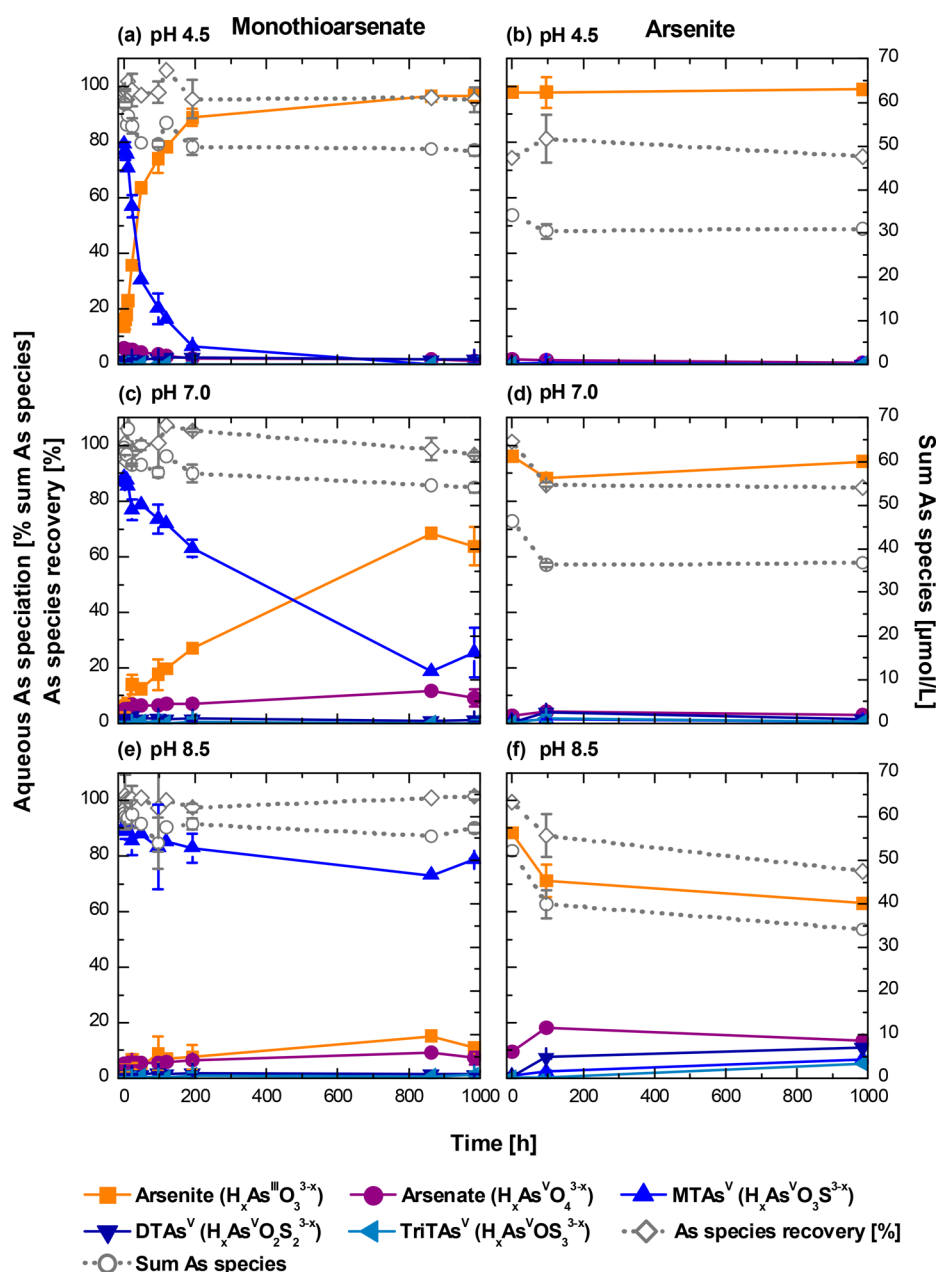


Figure 3. Aqueous As speciation [% of sum As species] of the time series experiments where MTAs(V) (left panel) or arsenite (right panel) was added to sulfide-reacted (3 mM sulfide) peat suspensions (0.2 M C) of pH 4.5 (a, b), pH 7.0 (c, d) and pH 8.5 (e, f). Aqueous As species recovery: 74–112%. Error bars represent standard deviations of triplicates for 4, 24, 96, 192, and 984 h. Otherwise, single data points. Straight or dotted lines serve to guide the eye.

background electrolyte or NaN_3 (Figure SI-9b,c), respectively, accelerated transformation of MTAs(V) only a little at pH 4.5. A blank experiment with background electrolyte and NaN_3 combined showed only minor transformation of MTAs(V) to arsenite at pH 4.5 (8%) and no species change at pH 7.0 and 8.5 after 120 h (Figure SI-9d) which is in line with previous observations on the stability of MTAs(V) in solution after acidification⁴¹ or aeration⁴⁶ or in the absence of S(0)-species.²⁹ Furthermore, no significant increase in S oxidation products (sulfate and thiosulfate) occurred during these experiments (Figure SI-12) confirming anaerobic conditions and indicating no microbial influence. The transformation of MTAs(V) was therefore not driven by pH or ionic strength but clearly triggered by the presence of sulfide-reacted peat.

One possible explanation is that sulfide was released from sulfide-reacted peat to solution and this drove MTAs(V) transformation to arsenite. From their experiments on arsenate reduction by sulfide where MTAs(V) was observed as byproduct, Rochette et al.³⁰ postulated such an acid-catalyzed (no reaction at pH 7.0), sulfide-driven MTAs(V) reduction via formation of dithioarsenate (DTAs(V)), reduction to MTAs(V), and finally hydrolyzation to arsenite. In our experiments, we could not determine whether there were significant amounts of free sulfide in solution. Although we washed our sulfide-reacted peat in order to remove any dissolved sulfide before the As sorption experiments, we observed some further release of S to the aqueous phase during the experiment (Figure SI-11a). The fraction of sulfide of this total S was impossible to

Time series with fixed 3 mM sulfide spike concentration

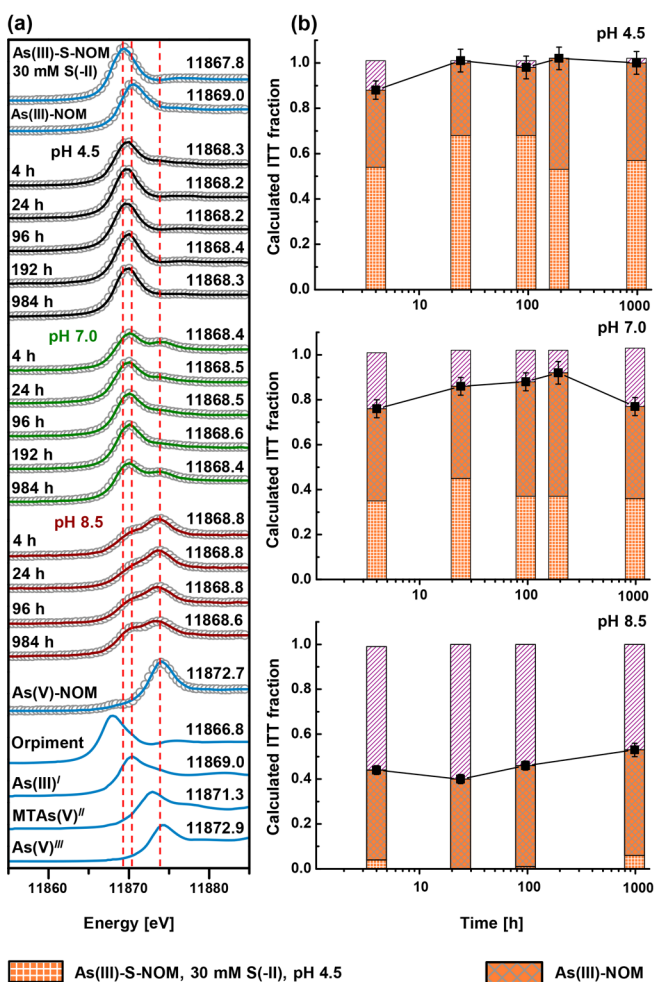


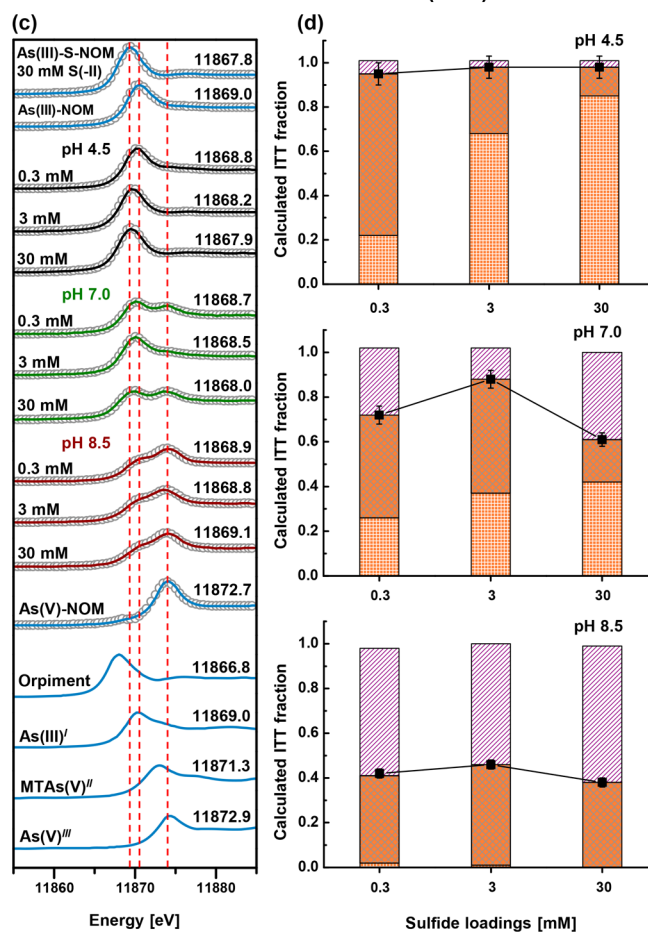
Figure 4. Normalized As K-edge XANES spectra and their respective edge-energies (eV) from the MTAs(V) time series experiment (4, 24, 96, 192, and 984 h) with fixed sulfide spike concentrations (3 mM) (a) and variable sulfide spike concentrations (0.3, 3, and 30 mM) but fixed time (c) and their respective ITT calculations (b, d). Straight lines represent experimental data, the reconstruction of the whole series (experimental spectra from (a) and (c)) are shown as circles. The vertical lines indicate the white line positions of the three identified components As(III)-S-NOM, As(III)-NOM, and As(V)-NOM. Abbreviations: As(III), trivalent As; As(V), pentavalent As. The S in As(III)-S-NOM is sulfhydryl-S. Sum As(III) fractions = As(III)-S-NOM + As(III)-NOM. Standards for comparison: I, sodium (meta)arsenite; II, $\text{Na}_3\text{AsO}_3 \cdot 7\text{H}_2\text{O}$; III, disodium arsenate. For the ITT calculation of relative species concentrations, the concentrations of the three identified references were fixed at 100%, while the concentrations of the mixtures were calculated without constraints; i.e., they were not normalized to 100%. Error bars represent general error of the ITFA procedure of about 5% of relative concentrations. Straight lines in (b) and (d) serve to guide the eye.

determine using the methylene blue method⁴⁷ due to strong interferences with DOC. However, if a reaction of this kind with potentially dissolved or even surface-bound sulfide would have occurred, then a DTAs(V) peak would have appeared during aqueous As analysis, which was not the case. The facts that DTAs(V) occurred only in trace amounts (max. ~2.5% of As species, Figure 3) and that Rochette et al.³⁰ found no transformation at pH 7.0 make this reaction pathway unlikely.

Another explanation is that the presence of the solid phase (sulfhydryl-S on peat) itself drives MTAs(V) transformation. As described before, MTAs(V) is in equilibrium with arsenite and S(0)-species. Low pH will drive the equilibrium toward arsenite and S(0)-species⁴⁸ (eq 1), but kinetics in solution are so slow that any MTAs(V) transformation is not likely to be observed over several days (Figure SI-9a).



Variable sulfide spike concentrations with fixed reaction time (96 h)



However, both previous reports^{17,19} and our own experiments (Figure 2) show that arsenite sorbs strongly to sulfhydryl-rich NOM, particularly at low pH. This is consistent with the observed order of MTAs(V) transformation kinetics. We therefore conclude that arsenite sorption drives the chemical equilibrium toward arsenite and S(0)-species, therefore accelerating MTAs(V) transformation. Sorption of S(0)-species^{35–37,49} would have the same effect.

Figure SI-14 shows aqueous As speciation and total As sorption of peat reacted with different amounts of sulfide (3 mM in comparison to 0.3 and 30 mM; 96 h) at pH 4.5, 7.0, and 8.5, and total S content is depicted in Figure SI-15b. At pH 8.5, MTAs(V) remained stable regardless of the sulfide spike concentrations, probably stabilized by the low proton concentration and lower sorption affinity of arsenite at high pH. Total As sorption increased strongly with S content at low pH and only tententially at pH 7.0, which shows a clear

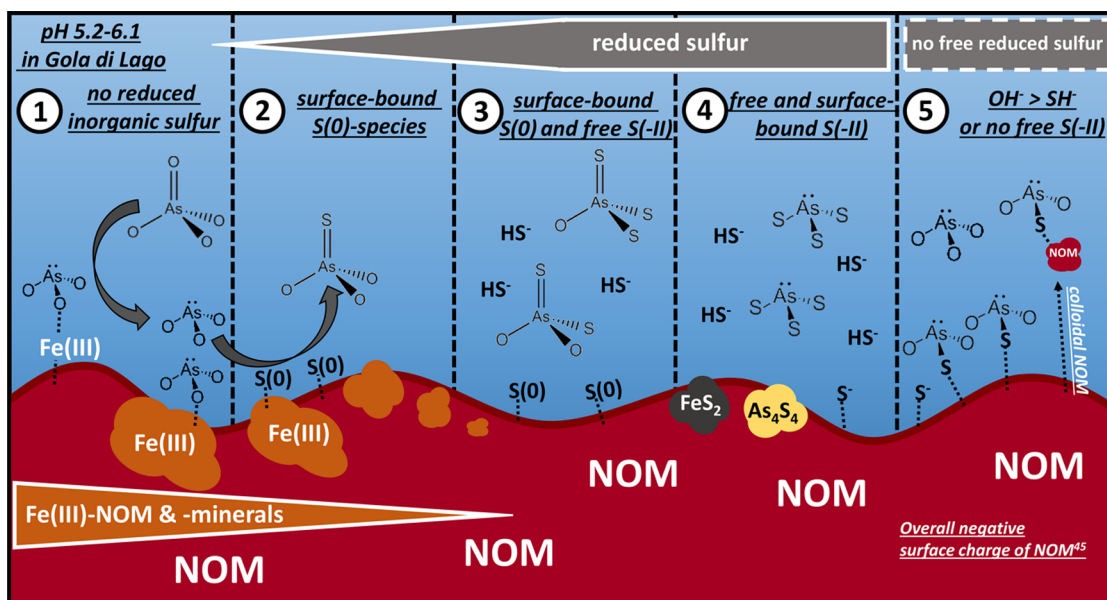


Figure 5. Suggested conceptual model for As–S chemistry in *Gola di Lago* peatland. Scenario 1: arsenate and arsenite prevail as long as no reduced inorganic sulfur is present. Scenario 2: monothioarsenate formation from arsenite and surface-bound zerovalent sulfur species. Scenario 3: formation of higher thiolated arsenates from monothioarsenate under conditions of available free sulfide. Scenario 4: thioarsenite formation and eventually FeS_2 and As_4S_4 precipitation in sulfide-rich, strongly reducing microenvironments or during sulfide-rich times. Scenario 5: arsenite sorption to sulfhydryl groups of peat or colloidal NOM. Scenarios 3 and 4 seem to be rather unlikely in *Gola di Lago* peatland since no free sulfide was detected. Information about mineralogy was taken from Langner et al.^{17,18} Dotted lines illustrate general inner-spheric coordination of the respective species but no specific coordination environments.

influence of sulfide spike concentrations on MTAs(V) transformation and As sorption, particularly at pH 4.5. But pH seems to be the rate-controlling variable, since MTAs(V) transformation was significantly higher at low pH, with peat possessing similar S contents at pH 4.5 and 7.0 (0.3 and 3 mM sulfide spike concentrations experiments, Figure SI-14 and Figure SI-15b). No increased shift of MTAs(V) toward arsenite was observed between 3 and 30 mM sulfide spike concentrations at pH 4.5 and 7.0, despite significantly higher S contents on the peat when higher amounts of sulfide were used (Figure SI-15b). The lack of correlation might be due to small increases of pH (max. 0.7 pH units) during incubation (Table SI-5) since no special buffers were used in order to not change organic functional groups of the peat. In general, all results show that extent and kinetics of MTAs(V) transformation strongly depended on pH because of the pH-dependent removal of arsenite through sorption.

While aqueous As speciation already implied that arsenite sorption is an important mechanism in the MTAs(V) experiments, it could not answer the question whether sorption observed in the MTAs(V) experiments occurred exclusively as arsenite or also included direct sorption of MTAs(V) to sulfide-reacted peat, which is addressed in the next section.

Solid-Phase As Speciation upon Monothioarsenate Addition to Sulfide-Reacted Peat. In order to follow As solid-phase speciation over a wide range of concentrations (8–280 ppm), we used principal component analysis (PCA) and iterative transformation factor analysis (ITFA)⁵⁰ of normalized As K-edge XANES spectra. The 20 spectra from selected sampling points of the time series and sulfide spike concentrations experiments could be reproduced by only three principle components, as indicated by a minimum of the Malinowski indicator value and 99.9% of the variance in the data set explained. This observation was confirmed by the

almost perfect reproduction of the experimental spectra by these three PCs (Figure 4). Further, target transform testing revealed that with the following three standards excellent to good empirical Malinowski SPOIL values (0.8–2.5) were achieved. These standards were the already described arsenite sorbed via sulfhydryl-S to peat (As(III)-S-NOM¹⁹) and arsenite directly sorbed to untreated peat (As(III)-NOM).¹⁴ Arsenate reacted with untreated peat was suitable as third standard (As(V)-NOM). Inclusion of these spectra in the experimental series and reanalysis with PCA and subsequent ITFA did not increase the number of statistically significant components and confirmed the standards indeed as end-member components. Aqueous and solid thioarsenate standards did not give acceptable SPOIL values and showed an increased number of PCs. The structure of As(III)-S-NOM was resolved and confirmed by EXAFS shell fitting (Figure SI-16, Table SI-6), and by using wavelet transform analysis,⁵¹ we excluded any influence of amorphous As–S precipitates⁵² (Figure SI-17). Finally, species distribution of the experimental spectra was calculated with iterative target transformation (ITT) giving an average sum of species of $100 \pm 1\%$ without using any constraints (Figure 4).

The ITFA calculations revealed that the solid phase contained one arsenate and two arsenite end-members without any contribution of MTAs(V) binding to sulfide-reacted peat. The general error of this kind of calculations is $\pm 5\%$ of relative concentration;²⁷ however, MTAs(V) was not detected on the solid phase even if present in high aqueous concentrations at pH 4.5–8.5 (Figure 3 and Figure SI-14). This finding was further confirmed by EXAFS shell-fitting of resin spectra from MTAs(V) solutions reacted with the sulfhydryl-rich Ambersep GT74 resin at pH 7.5 and 8.0 (Figure SI-19 and Figure SI-20). Though MTAs(V) was stable in the aqueous solution at both pHs (Figure SI-19), no contribution of a double-bound S

(typically 2.13–2.18 Å²⁷) was observed (Table SI-7, Figure SI-20) on the solid phase. Instead, As was 3-fold coordinated at each pH to S with distances of 2.26 Å, indicating typical bond lengths of arsenite bound via sulfhydryl-S.⁴⁰ This finding was confirmed by a control experiment with arsenite showing similar coordination numbers (CN) and atomic distances (Figure SI-20, Table SI-7).

Thus, in the experiments where MTAs(V) was added, sorption extent and kinetics (Figure 2 and Figure SI-14) were all determined by the behavior of the arsenite newly formed from MTAs(V). The ITT calculations revealed an increase of As(III) fractions with decreasing pH in the same manner as MTAs(V) transformation to arsenite (Figures 4 and 3). Hereby, a systematically higher portion of As was complexed via sulfhydryl-S to peat at pH 4.5 compared to pH 7.0. No sulfhydryl complexation higher than the detection limit (5%) was observed at pH 8.5 (Figure 4). These findings are in close agreement with the behavior of arsenite sorption discussed in the previous section, and recalculation of ITFA including the XANES spectra from arsenite sorption experiments (96 h) confirmed the same trend of ITT fractions (Figure SI-18). Increasing sulfide spike concentrations at pH 4.5 increased MTAs(V) transformation through increased arsenite complexation via sulfhydryl-S and therefore As sorption to peat. The lower reactivity of arsenite toward sulfide-reacted peat at higher pH, as discussed before, is further confirmed by the sulfide spike concentrations experiments at pH 7.0 and 8.5 (Figure 4 and Figure SI-14).

In summary, the solid-phase speciation data clearly show that there was no significant MTAs(V) sorption to sulfide-reacted peat via sulfhydryl groups. Probably, the reason for MTAs(V) showing no detectable sorption to S-NOM is that MTAs(V) has pK_a values of 3.30 (pK_{a1}), 7.20 (pK_{a2}), and 11.0 (pK_{a3})⁴⁸ and was therefore single- or double-negatively charged under our experimental conditions (pH 4.5–8.5). The negative charge causes a strong electrostatic repulsion with the negatively charged sulfide-reacted peat, thus excluding MTAs(V) sorption regardless of the pH value and S content (Figure 4). However, arsenate with very similar pK_a values⁴⁴ showed, though to a very low extent (Figure 2), sorption to sulfide-reacted peat (Figure 4). Buschmann et al.¹⁶ hypothesized that arsenate sorption to NOM can occur via deprotonated phenolic groups reacting with the formal positively charged electrophilic metal center of arsenate (+V) under release of water and stabilized by additional chelation by other functional groups and/or H-bridges. Also, we cannot completely exclude the influence of ternary complex formation of arsenate with traces of organically bound ferric iron¹⁵ that remained in the peat (Table SI-2). Both sorption mechanisms could have occurred in our study. Nothing is known about MTAs(V) sorption to phenolic groups or ternary complex formation. However, we did not find any indication for MTAs(V) sorption to our sulfide-reacted peat during solid-phase analysis.

Environmental Implications. Combining all information from the field site, our laboratory study, and the current literature, we propose the following conceptual model for As–S chemistry specifically in the *Gola di Lago* peatland (Figure 5) but also for similar As-enriched sulfidic environments. Such environments could be both, peatlands and swamps naturally enriched in As, as well as engineered wetlands used for removal of As and other metal(loid)s from mining effluents.

As long as there is no reduced inorganic S, As prevails as arsenate or arsenite (Scenario 1, Figure 5). Under more

reducing conditions, MTAs(V) forms from arsenite and S(0)-species as reported elsewhere²⁹ (Scenario 2, Figure 5). Zerovalent sulfur species can occur either as dissolved polysulfides or associated with solid phases. For *Gola di Lago*, S(0)-species have been reported to be primarily associated with the surfaces of organic iron flocs after sulfidation.³⁷ Furthermore, ferric (hydr)oxides have been shown to dominate the iron solid phase at the shallow layers of this peatland,^{17,18} which may be even more effective than the organic iron flocs in sorbing S(0)-species on their surfaces.^{35,36} Further reduction of S(0)-species to sulfide could lead to the formation of higher thiolated arsenates²⁹ (Scenario 3, Figure 5), formation of thioarsenites,^{27,28} and eventually precipitation of As–S mineral phases (Scenario 4, Figure 5). Even though realgar (As₄S₄) has been described for *Gola di Lago* before,^{17,18} its coexistence with ferric (hydr)oxides indicates its intermittent formation in sulfide-rich, strongly reducing microenvironments or during sulfide-rich times, e.g., of high flooding and persistence because of slow oxidation kinetics rather than equilibrium conditions with excess sulfide.^{18,53} However, the fact that no free dissolved sulfide was detected in any of the porewater samples (detection limit 0.3 μM) explains the overall low proportion of higher thiolated arsenates (Scenario 3, Figure 5) and renders the occurrence of thioarsenites unlikely (Scenario 4, Figure 5; thioarsenites can currently not be detected at environmentally relevant concentrations).²⁸

At greater depths, arsenite forms at the expense of MTAs(V). This transformation is possibly the kinetically constrained acid-catalyzed MTAs(V) transformation reaction to arsenite and its subsequent sorption to sulfhydryl groups as shown in our laboratory experiments with the model peat. Occurrence of sulfhydryl groups, which sequester arsenite, has previously been described in deeper peat layers of *Gola di Lago* (pH ~ 5.8)^{17,18} and agrees with the proposed conceptual model (Scenario 5, Figure 5). Complexation of arsenite to sulfhydryl groups of dissolved or colloidal NOM can lead to (re)mobilization of As, but considering the greater abundance of particulate NOM in peatlands, (re)mobilization of As by the dissolved or colloidal NOM fractions seems to be comparably small.^{7,10,19}

The dominance of MTAs(V) (besides arsenite) in peatlands versus higher thiolated arsenates in S-rich environments with less organic carbon^{21,41,46} can therefore be explained by the high sorption affinity of reduced S species to organic matter, causing aqueous As–S speciation presumably to be controlled mostly by reactions at solid-phase surfaces.

■ ASSOCIATED CONTENT

📄 Supporting Information

The Supporting Information is available free of charge on the ACS Publications website at DOI: 10.1021/acs.est.8b01542.

Field site description, sampling methods and geochemical characterization of *Gola di Lago* peatland, characterization of *Federseemoor* peat, monothioarsenate stability experiments, chemical background information for monothioarsenate and arsenite sorption to sulfide-reacted peat, a detailed methods description of As K-edge XAS analyses, and shell fits of As K-edge EXAFS spectra of reference standards including respective wavelet transformation analysis and monothioarsenate and arsenite sorption to Ambersep GT74 resin (PDF)

AUTHOR INFORMATION

Corresponding Author

*Phone: +49-921-553999; fax: +49-921-552334; e-mail: b.planer-friedrich@uni-bayreuth.de.

ORCID

Andreas C. Scheinost: 0000-0002-6608-5428

Britta Planer-Friedrich: 0000-0002-0656-4283

Notes

The authors declare no competing financial interest.

ACKNOWLEDGMENTS

This work was funded by the German Research Foundation Grant PL 302/20-1. A. Biswas received a Postdoc stipend from the Alexander-von-Humboldt Foundation. We acknowledge the help from R. Siegel and H. Zier for collecting the NMR and FT-IR spectra of the peat. Arsenic K-edge XAS experiments were performed at the European Synchrotron Radiation Facility (ESRF), Grenoble, France, and the Stanford Synchrotron Radiation Lightsource (SSRL), a Directorate of SLAC National Accelerator Laboratory and an Office of Science User Facility operated for the US Department of Energy, Office of Science, Office of Basic Energy Sciences under Contract No. DE-AC02-76SF00515. In this regard, we would like to thank R. Davis (SSRL) and J. Lezama Pacheco (Soil and Environmental Biogeochemistry group, Stanford University) for their support in using beamline 4-1.

REFERENCES

- (1) Smedley, P. L.; Kinniburgh, D. G. A review of the source, behaviour and distribution of arsenic in natural waters. *Appl. Geochem.* **2002**, *17*, 517–568.
- (2) Borch, T.; Kretzschmar, R.; Kappler, A.; Cappellen, P. V.; Ginder-Vogel, M.; Voegelín, A.; Campbell, K. Biogeochemical redox processes and their impact on contaminant dynamics. *Environ. Sci. Technol.* **2010**, *44*, 15–23.
- (3) Ravenscroft, P.; Brammer, H.; Richards, K. *Arsenic pollution: A global synthesis*; Wiley-Blackwell: Malden, MA, 2009.
- (4) Wang, S.; Mulligan, C. N. Speciation and surface structure of inorganic arsenic in solid phases: A review. *Environ. Int.* **2008**, *34*, 867–879.
- (5) González A, Z. I.; Krachler, M.; Cheburkin, A. K.; Shoty, W. Spatial distribution of natural enrichments of arsenic, selenium, and uranium in a minerotrophic peatland, Gola di Lago, Canton Ticino, Switzerland. *Environ. Sci. Technol.* **2006**, *40*, 6568–6574.
- (6) Lizama A, K.; Fletcher, T. D.; Sun, G. Removal processes for arsenic in constructed wetlands. *Chemosphere* **2011**, *84*, 1032–1043.
- (7) Palmer, K.; Ronkanen, A.-K.; Kløve, B. Efficient removal of arsenic, antimony and nickel from mine wastewaters in northern treatment peatlands and potential risks in their long-term use. *Ecol. Eng.* **2015**, *75*, 350–364.
- (8) Rothwell, J. J.; Taylor, K. G.; Chenery, S. R. N.; Cundy, A. B.; Evans, M. G.; Allott, T. E. H. Storage and behavior of As, Sb, Pb, and Cu in ombrotrophic peat bogs under contrasting water table conditions. *Environ. Sci. Technol.* **2010**, *44*, 8497–8502.
- (9) Liu, G.; Fernandez, A.; Cai, Y. Complexation of arsenite with humic acid in the presence of ferric iron. *Environ. Sci. Technol.* **2011**, *45*, 3210–3216.
- (10) Neubauer, E.; von der Kammer, F.; Knorr, K. H.; Peiffer, S.; Reichert, M.; Hofmann, T. Colloid-associated export of arsenic in stream water during stormflow events. *Chem. Geol.* **2013**, *352*, 81–91.
- (11) Anawar, H. M.; Tareq, S. M.; Ahmed, G. Is organic matter a source or redox driver or both for arsenic release in groundwater? *Phys. Chem. Earth* **2013**, *58–60*, 49–56.
- (12) Sharma, P.; Ofner, J.; Kappler, A. Formation of binary and ternary colloids and dissolved complexes of organic matter, Fe and As. *Environ. Sci. Technol.* **2010**, *44*, 4479–4485.
- (13) Ritter, K.; Aiken, G. R.; Ranville, J. F.; Bauer, M.; Macalady, D. L. Evidence for the aquatic binding of arsenate by natural organic matter—suspended Fe(III). *Environ. Sci. Technol.* **2006**, *40*, 5380–5387.
- (14) Hoffmann, M.; Mikutta, C.; Kretzschmar, R. Arsenite binding to natural organic matter: Spectroscopic evidence for ligand exchange and ternary complex formation. *Environ. Sci. Technol.* **2013**, *47*, 12165–12173.
- (15) Mikutta, C.; Kretzschmar, R. Spectroscopic evidence for ternary complex formation between arsenate and ferric iron complexes of humic substances. *Environ. Sci. Technol.* **2011**, *45*, 9550–9557.
- (16) Buschmann, J.; Kappeler, A.; Lindauer, U.; Kistler, D.; Berg, M.; Sigg, L. Arsenite and arsenate binding to dissolved humic acids: Influence of pH, type of humic acid, and aluminum. *Environ. Sci. Technol.* **2006**, *40*, 6015–6020.
- (17) Langner, P.; Mikutta, C.; Kretzschmar, R. Arsenic sequestration by organic sulphur in peat. *Nat. Geosci.* **2012**, *5*, 66–73.
- (18) Langner, P.; Mikutta, C.; Suess, E.; Marcus, M. A.; Kretzschmar, R. Spatial distribution and speciation of arsenic in peat studied with microfocused X-ray fluorescence spectrometry and X-ray absorption spectroscopy. *Environ. Sci. Technol.* **2013**, *47*, 9706–9714.
- (19) Hoffmann, M.; Mikutta, C.; Kretzschmar, R. Bisulfide reaction with natural organic matter enhances arsenite sorption: Insights from X-ray absorption spectroscopy. *Environ. Sci. Technol.* **2012**, *46*, 11788–11797.
- (20) Stauder, S.; Raue, B.; Sacher, F. Thioarsenates in sulfidic waters. *Environ. Sci. Technol.* **2005**, *39*, 5933–5939.
- (21) Planer-Friedrich, B.; London, J.; McCleskey, R. B.; Nordstrom, D. K.; Wallschläger, D. Thioarsenates in geothermal waters of Yellowstone National Park: Determination, preservation, and geochemical importance. *Environ. Sci. Technol.* **2007**, *41*, 5245–5251.
- (22) Wallschläger, D.; Stacey, C. J. Determination of (oxy)-thioarsenates in sulfidic waters. *Anal. Chem.* **2007**, *79*, 3873–3880.
- (23) Stucker, V. K.; Williams, K. H.; Robbins, M. J.; Ranville, J. F. Arsenic geochemistry in a biostimulated aquifer: An aqueous speciation study. *Environ. Toxicol. Chem.* **2013**, *32*, 1216–1223.
- (24) Stucker, V. K.; Silverman, D. R.; Williams, K. H.; Sharp, J. O.; Ranville, J. F. Thioarsenic species associated with increased arsenic release during biostimulated subsurface sulfate reduction. *Environ. Sci. Technol.* **2014**, *48*, 13367–13375.
- (25) Kong, L.; Peng, X.; Hu, X. Mechanisms of UV-light promoted removal of As(V) by sulfide from strongly acidic wastewater. *Environ. Sci. Technol.* **2017**, *51*, 12583–12591.
- (26) Suess, E.; Wallschläger, D.; Planer-Friedrich, B. Stabilization of thioarsenates in iron-rich waters. *Chemosphere* **2011**, *83*, 1524–1531.
- (27) Suess, E.; Scheinost, A. C.; Bostick, B. C.; Merkel, B. J.; Wallschläger, D.; Planer-Friedrich, B. Discrimination of thioarsenites and thioarsenates by X-ray absorption spectroscopy. *Anal. Chem.* **2009**, *81*, 8318–8326.
- (28) Planer-Friedrich, B.; Suess, E.; Scheinost, A. C.; Wallschläger, D. Arsenic speciation in sulfidic waters: Reconciling contradictory spectroscopic and chromatographic evidence. *Anal. Chem.* **2010**, *82*, 10228–10235.
- (29) Planer-Friedrich, B.; Härtig, C.; Lohmayer, R.; Suess, E.; McCann, S. H.; Oremland, R. Anaerobic chemolithotrophic growth of the haloalkaliphilic bacterium strain MLMS-1 by disproportionation of monothioarsenate. *Environ. Sci. Technol.* **2015**, *49*, 6554–6563.
- (30) Rochette, E. A.; Bostick, B. C.; Li, G.; Fendorf, S. Kinetics of arsenate reduction by dissolved sulfide. *Environ. Sci. Technol.* **2000**, *34*, 4714–4720.
- (31) Spratt, H. G.; Morgan, M. D. Sulfur cycling in a cedar-dominated, freshwater wetland. *Limnol. Oceanogr.* **1990**, *35*, 1586–1593.
- (32) Steinmann, P.; Shoty, W. Ion chromatography of organic-rich natural waters from peatlands IV. Dissolved free sulfide and acid-volatile sulfur. *J. Chromatogr. A* **1995**, *706*, 287–292.

- (33) Shoty, W. Review of the inorganic geochemistry of peats and peatland waters. *Earth-Sci. Rev.* **1988**, *25*, 95–176.
- (34) Yu, Z.-G.; Göttlicher, J.; Steininger, R.; Knorr, K.-H. Organic sulfur and organic matter redox processes contribute to electron flow in anoxic incubations of peat. *Environ. Chem.* **2016**, *13*, 816–825.
- (35) Wan, M.; Shchukarev, A.; Lohmayer, R.; Planer-Friedrich, B.; Peiffer, S. Occurrence of surface polysulfides during the interaction between ferric (hydr)oxides and aqueous sulfide. *Environ. Sci. Technol.* **2014**, *48*, 5076–5084.
- (36) Kumar, N.; Lezama Pacheco, J.; Noel, V.; Dublet, G.; Brown, G. E. Sulfidation mechanisms of Fe(III)-(oxyhydr)oxide nanoparticles: a spectroscopic study. *Environ. Sci.: Nano* **2018**, *5*, 1012–1026.
- (37) ThomasArrigo, L. K.; Mikutta, C.; Lohmayer, R.; Planer-Friedrich, B.; Kretzschmar, R. Sulfidization of organic freshwater flocs from a minerotrophic peatland: speciation changes of iron, sulfur, and arsenic. *Environ. Sci. Technol.* **2016**, *50*, 3607–3616.
- (38) Couture, R. M.; Rose, J.; Kumar, N.; Mitchell, K.; Wallschläger, D.; Van Cappellen, P. Sorption of arsenite, arsenate, and thioarsenates to iron oxides and iron sulfides: A kinetic and spectroscopic investigation. *Environ. Sci. Technol.* **2013**, *47*, 5652–5659.
- (39) Suess, E.; Planer-Friedrich, B. Thioarsenate formation upon dissolution of orpiment and arsenopyrite. *Chemosphere* **2012**, *89*, 1390–1398.
- (40) Hoffmann, M.; Mikutta, C.; Kretzschmar, R. Arsenite binding to sulfhydryl groups in the absence and presence of ferrihydrite: A model study. *Environ. Sci. Technol.* **2014**, *48*, 3822–3831.
- (41) Planer-Friedrich, B.; Wallschläger, D. A critical investigation of hydride generation-based arsenic speciation in sulfidic waters. *Environ. Sci. Technol.* **2009**, *43*, 5007–5013.
- (42) Martell, A.; Smith, R. M. *Critical stability constants - Vol. 3: Other Organic Ligands*; Springer: New York, 1977; Vol. 3.
- (43) Noble, P.; Tarbell, D. S. Thiobenzoic acid. *Org. Synth.* **1952**, *32*, 101.
- (44) Nordstrom, D. K.; Archer, D. G. Arsenic thermodynamic data and environmental geochemistry. In *Arsenic in Ground Water: Geochemistry and Occurrence*; Springer: Boston, MA, 2003.
- (45) Catrouillet, C.; Davranche, M.; Dia, A.; Bouhnik-Le Coz, M.; Pédrot, M.; Marsac, R.; Gruau, G. Thiol groups controls on arsenite binding by organic matter: New experimental and modeling evidence. *J. Colloid Interface Sci.* **2015**, *460*, 310–320.
- (46) Planer-Friedrich, B.; Fisher, J. C.; Hollibaugh, J. T.; Süß, E.; Wallschläger, D. Oxidative transformation of trithioarsenate along alkaline geothermal drainages—abiotic versus microbially mediated processes. *Geomicrobiol. J.* **2009**, *26*, 339–350.
- (47) Cline, J. D. Spectrophotometric determination of hydrogen sulfide in natural waters. *Limnol. Oceanogr.* **1969**, *14*, 454–458.
- (48) Thilo, E.; Hertzog, K.; Winkler, A. Über Vorgänge bei der Bildung des Arsen(V)-sulfids beim Ansäuern von Tetrathioarsenatlösungen. *Z. Anorg. Allg. Chem.* **1970**, *373*, 111–121.
- (49) Liu, R.; Yang, Z.; He, Z.; Wu, L.; Hu, C.; Wu, W.; Qu, J. Treatment of strongly acidic wastewater with high arsenic concentrations by ferrous sulfide (FeS): Inhibitive effects of S(0)-enriched surfaces. *Chem. Eng. J.* **2016**, *304*, 986–992.
- (50) Roßberg, A.; Reich, T.; Bernhard, G. Complexation of uranium(VI) with protocatechuic acid—application of iterative transformation factor analysis to EXAFS spectroscopy. *Anal. Bioanal. Chem.* **2003**, *376*, 631–638.
- (51) Funke, H.; Scheinost, A. C.; Chukalina, M. Wavelet analysis of extended x-ray absorption fine structure data. *Phys. Rev. B: Condens. Matter Mater. Phys.* **2005**, *71*, 94–110.
- (52) Helz, G. R.; Tossell, J. A.; Charnock, J. M.; Patrick, R. A. D.; Vaughan, D. J.; David Garner, C. Oligomerization in As (III) sulfide solutions: Theoretical constraints and spectroscopic evidence. *Geochim. Cosmochim. Acta* **1995**, *59*, 4591–4604.
- (53) Langner, P.; Mikutta, C.; Kretzschmar, R. Oxidation of organosulfur-coordinated arsenic and realgar in peat: Implications for the fate of arsenic. *Environ. Sci. Technol.* **2014**, *48*, 2281–2289.

Supporting Information to

“Monothioarsenate transformation kinetics determines arsenic sequestration by sulfhydryl groups of peat”

*Johannes Besold¹, Ashis Biswas^{1,2}, Elke Suess³, Andreas C. Scheinost⁴, André Rossberg⁴, Christian Mikutta⁵, Ruben Kretzschmar⁶, Jon Petter Gustafsson⁷ and Britta Planer-Friedrich^{*1}*

¹Department of Environmental Geochemistry, Bayreuth Center for Ecology and Environmental Research (BAYCEER), Bayreuth University, 95440 Bayreuth, Germany

²Department of Earth and Environmental Sciences, Indian Institute of Science Education and Research (IISER) Bhopal, Bhopal Bypass Road, Bhauri 462066, MP, India

³Eawag, Swiss Federal Institute of Aquatic Science and Technology, 8600 Dübendorf, Switzerland

⁴The Rossendorf Beamline (ROBL) at ESRF, 38043 Grenoble, France and Helmholtz-Zentrum Dresden-Rossendorf (HZDR), Institute of Resource Ecology, Bautzner Landstraße 400, 01328 Dresden, Germany

⁵Soil Mineralogy, Institute of Mineralogy, Gottfried Wilhelm Leibniz Universität Hannover, Callinstr. 3, 30167 Hannover, Germany

⁶Institute of Biogeochemistry and Pollutant Dynamics, Department of Environmental Systems Science, ETH Zurich, CHN, CH-8092 Zurich, Switzerland

⁷Department of Soil and Environment, Swedish University of Agricultural Sciences, Box 7014, 750 07, Uppsala, Sweden

(27 pages, 7 tables, 20 figures)

Table of contents

1	Minerotrophic peatland <i>Gola di Lago</i> : Field site, sampling methods and geochemical characterization in terms of arsenic	2
2	General chemical characterization of the Federseemoor peat	8
3	Monothioarsenate stability experiments in electrolyte background solutions.....	12
4	Arsenic <i>K</i> -edge X-ray absorption spectroscopy	13
5	Monothioarsenate and arsenite sorption to NOM	15
6	Monothioarsenate and arsenite sorption to Ambersep GT74 resin	24
7	References	26

* Corresponding author's email: b.planer-friedrich@uni-bayreuth.de

Phone: +49-921-553999; Fax: +49-921-552334

S1

1 Minerotrophic peatland *Gola di Lago*: Field site, sampling methods and geochemical characterization in terms of arsenic

Field site and sampling

Peat cores, stream and porewaters were collected in November 2012 in the carex-dominated minerotrophic peatland *Gola di Lago*, Ticino, Switzerland.^{1,2} The sampling locations were chosen close to our initial sampling points of 2009^{1,3} as well as the intermittent inflow (IF) in the south east of the sampling field (Figure SI-1). The peat cores were collected with a HUMAX drilling system^{1,3} to various depths (Table SI-1) for element characterization and extraction of porewaters. The sample cores were quickly removed out of the plastic liners, packed into sampling bags with N₂-atmosphere and processed in our field laboratory approximately 100 m away from the peatland.

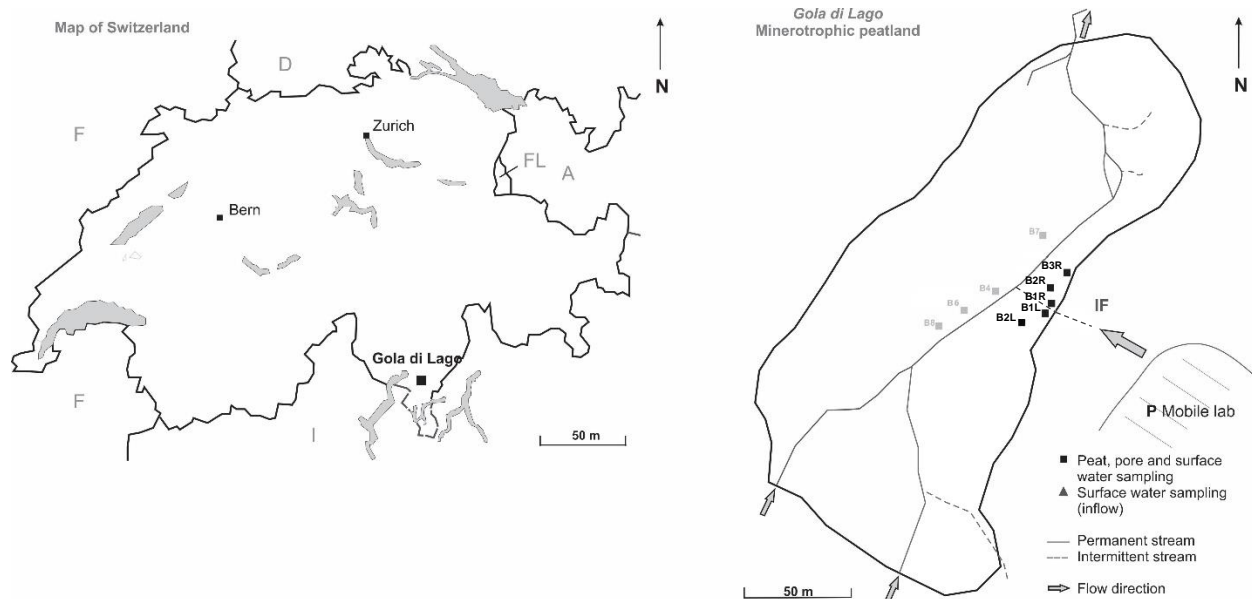


Figure SI-1: Map of the *Gola di Lago* field site with sampling locations. Notations for sampling locations were adjusted for this publication but can be compared with Langner *et al.* 2012, 2013^{1,3} as follows: B1L=B5, B2L=B1, B1R=B10, B2R=B9 and B3R=B3a.

The porewater was squeezed out of the water saturated peat material in the N₂-filled bags and then quickly removed for further analyses and preservation. For field moist or dry samples, the “porewater” was retrieved by extraction of the peat in nitrogen-purged DDI water (Milli-Q, Millipore, 18.2 MΩ·cm, Table SI-1). For that, a volume of 250 mL fresh peat was mixed with 500 mL nitrogen-purged DDI water in SCHOTT DURAN® bottles and constantly purged with nitrogen over a time of 2 h. The resulting solution contained any remaining porewater plus all easily mobilizable elements that were bound loosely to the peat before.

The peat material in the SCHOTT DURAN® bottles was immediately flash-frozen in liquid N₂, transported on dry-ice to the soil chemistry facilities of ETH Zurich, and extracted within 24 h. One part of the remaining peat material was used for the determination of on-site parameters (conductivity, pH, redox potential, and temperature). The rest of the material as well as the remaining peat from purging were stored in the dark at 4 °C for further characterization performed in the soil chemistry laboratory. In addition to the peat sampling, surface waters were collected with a 500 mL polyethylene (PE)-beaker at each peat sampling point as well as the inflow and immediately preserved for arsenic (As) speciation analyses.

Surface and porewater processing and analyses

Immediately after its collection from squeezing or after the 2 h anoxic extraction, the porewaters were processed. Aliquots were filtered through 0.2 μm cellulose nitrate (CN) filters for on-site photometrical determination of sulfide (methylene blue method) and iron(II) (ferrozine method). Free sulfide was not detectable in any of the samples (<0.3 μM). Dissolved organic carbon (DOC, 0.45 μm filtered in glass vials) was analyzed with an DIMATOC 2000, DIMATEC TOC-analyzer. Elemental analyses with ICP-MS (7500ce, Agilent) and ICP-OES (Vista MPX, Varian) were performed after acidifying the samples to pH < 2 with suprapure HNO₃. Simultaneously, samples for As-S speciation were collected by use of a nitrogen rinsed and filled syringe (PE, 10 mL) whereby 1 mL was disposed and the rest directly filtered (0.2 μm, CN) over a septum in nitrogen filled air-tight 50-mL glass bottles. These samples were immediately flash-frozen in liquid nitrogen, stored on dry-ice, and analyzed 10 days later for As-S speciation by AEC-ICP-MS coupling at Bayreuth University.⁴

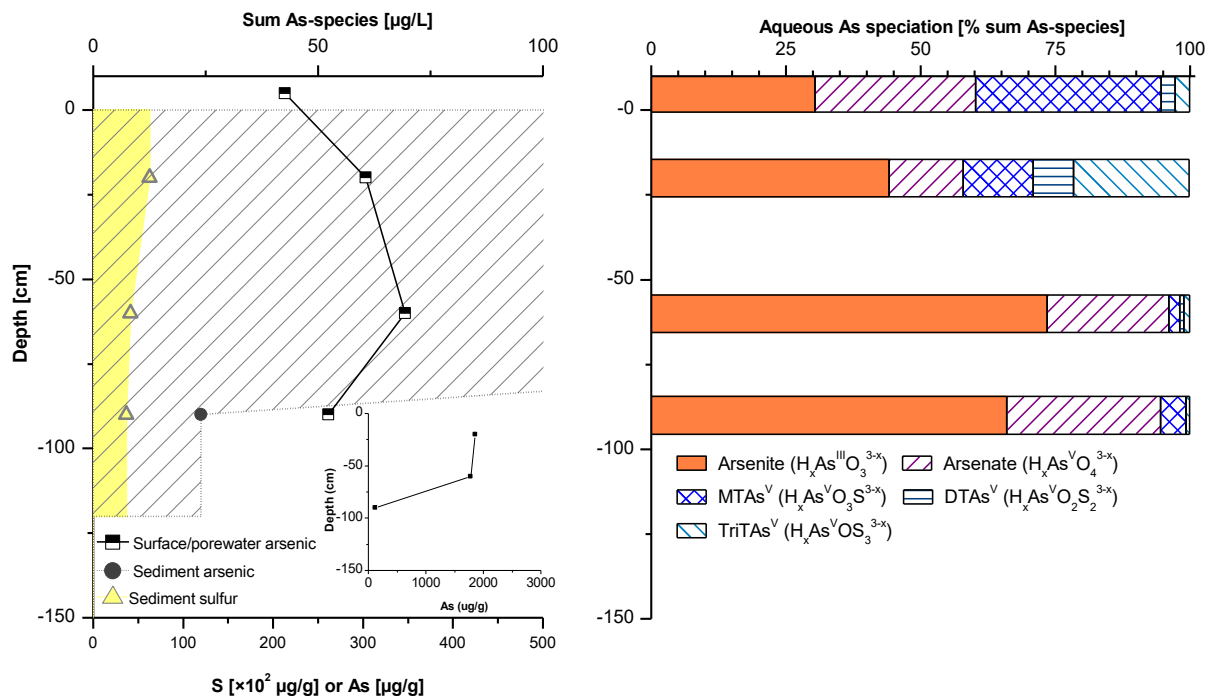


Figure SI-2: Total (aqueous and sediment) As and S distribution (left) as well as aqueous As speciation (right) of sampling profile B1L. Shaded area represents total sediment As. Small insert diagram illustrates As sediment contents higher than 500 µg/g. The detection limit for a single As species was 0.1 µg/L.

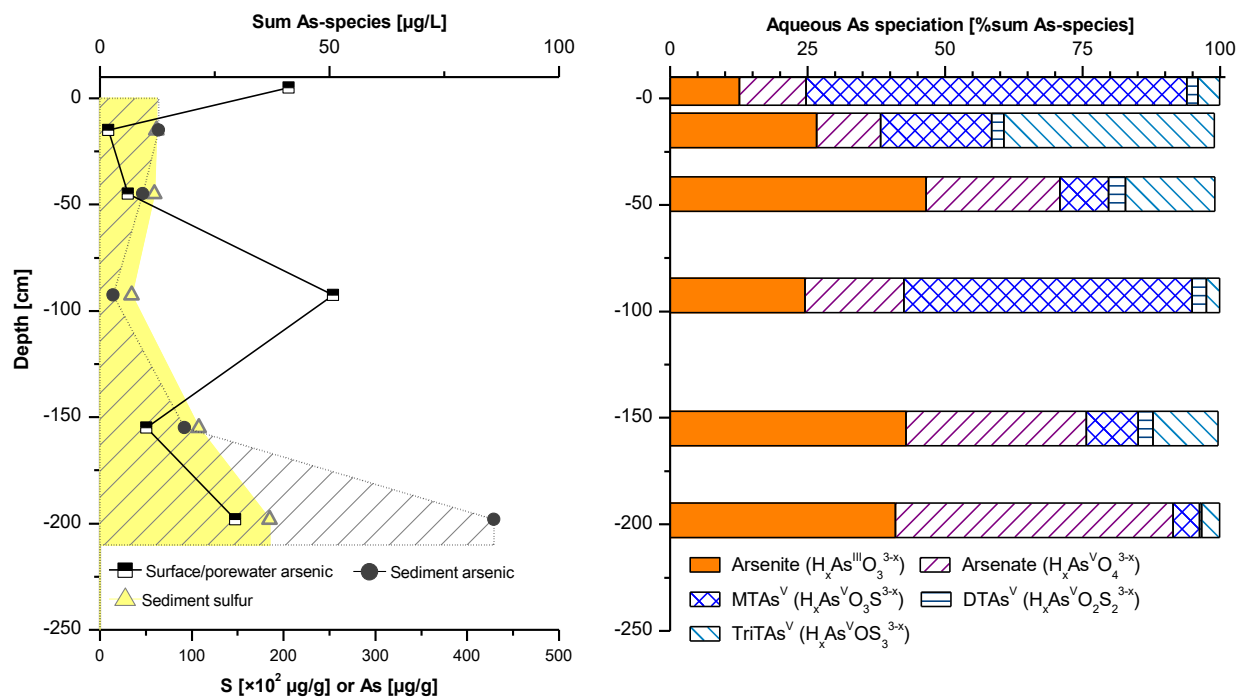


Figure SI-3: Total (aqueous and sediment) As and S distribution (left) as well as aqueous As speciation (right) of sampling profile B2L. Shaded area represents total sediment As. The detection limit for a single As species was 0.1 µg/L.

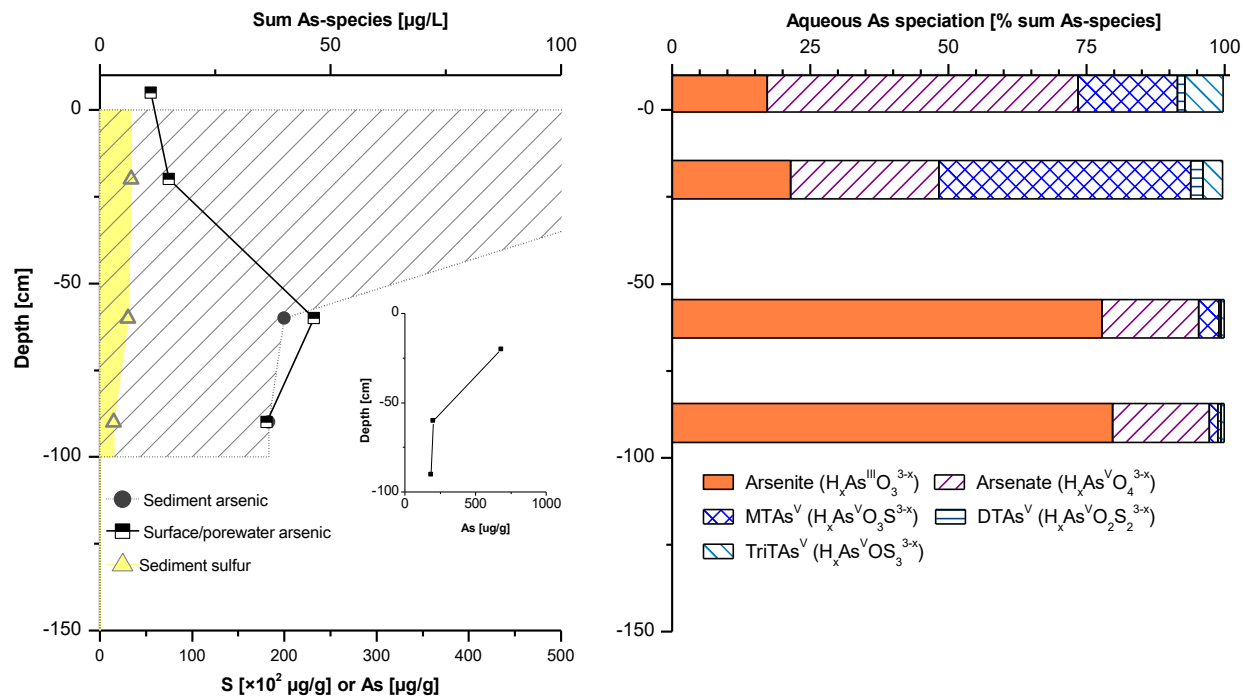


Figure SI-4: Total (aqueous and sediment) As and S distribution (left) as well as aqueous As speciation (right) of sampling profile B1R. Shaded area represents total sediment As. Small insert diagram illustrates As sediment contents higher than 500 $\mu\text{g/g}$. The detection limit for a single As species was 0.1 $\mu\text{g/L}$.

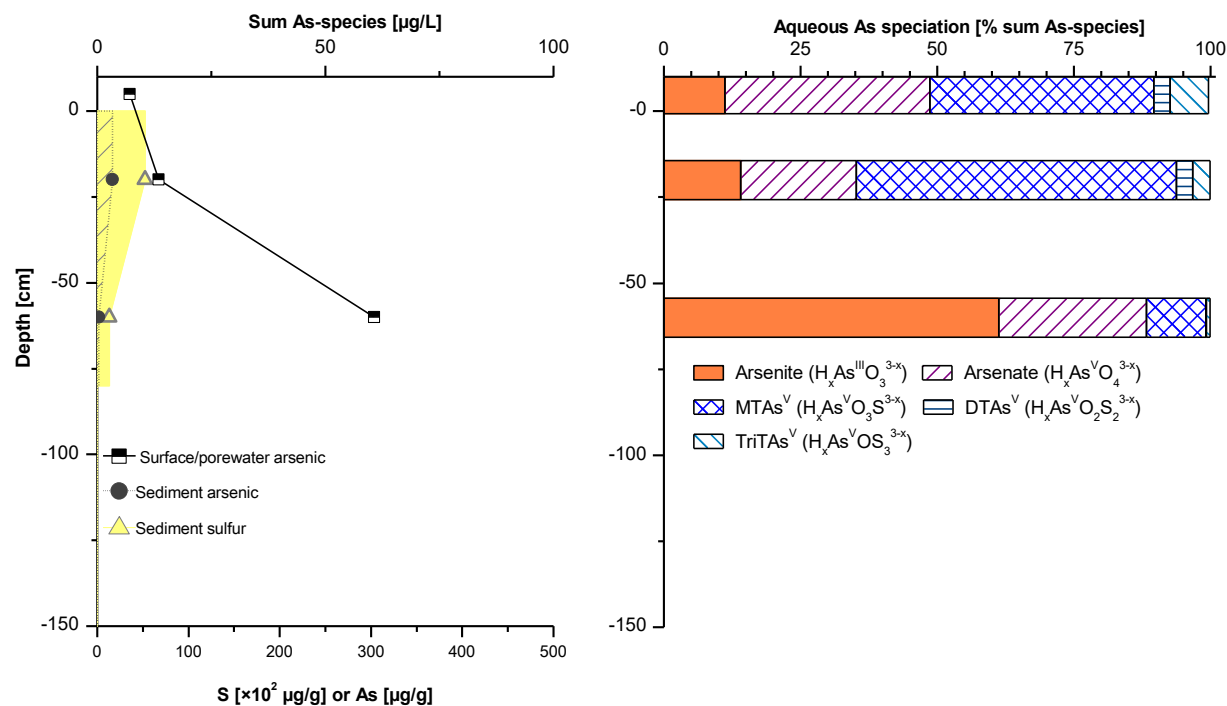


Figure SI-5: Total (aqueous and sediment) As and S distribution (left) as well as aqueous As speciation (right) of sampling profile B2R. Shaded area represents total sediment As. The detection limit for a single As species was 0.1 $\mu\text{g/L}$.

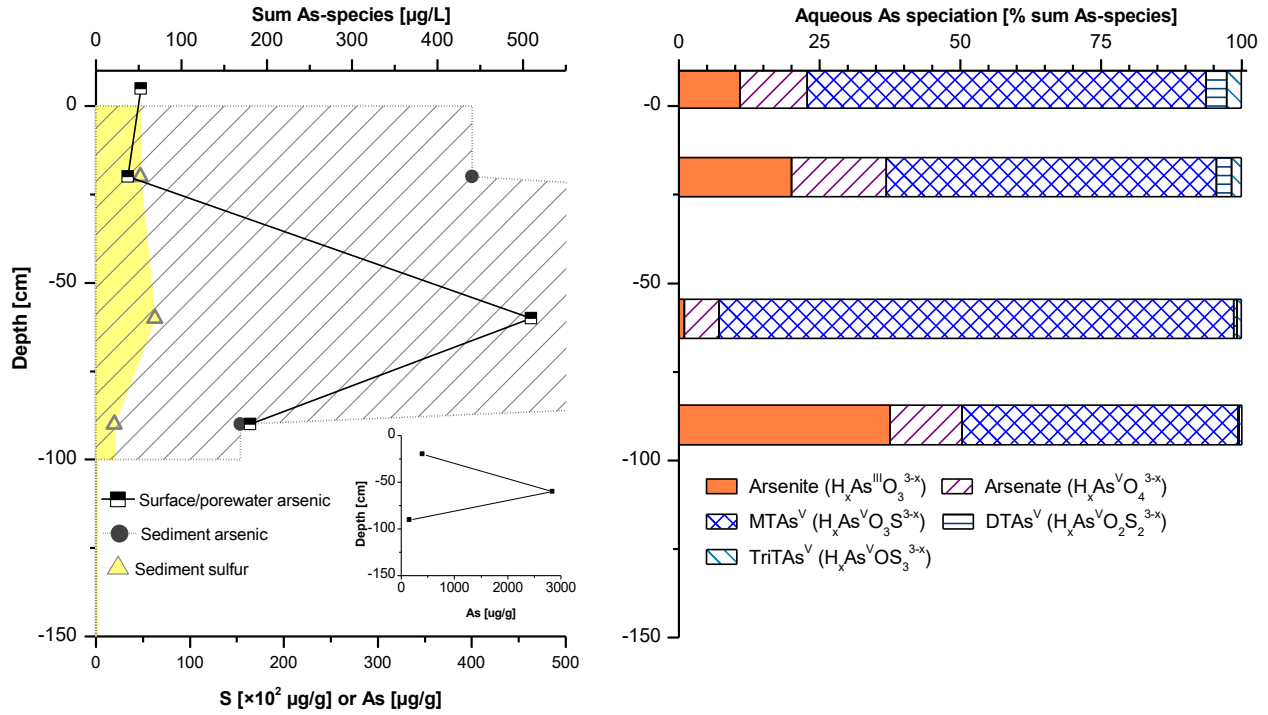


Figure SI-6: Total (aqueous and sediment) As and S distribution (left) as well as aqueous As speciation (right) of sampling profile B3R. Shaded area represents total sediment As. Small insert diagram illustrates As sediment contents higher than 500 µg/g. The detection limit for a single As species was 0.1 µg/L.

Table SI-1: Sample and sampling site overview

Sample name	Depth	Mean Depth	E_h	pH	EC	Fe(II)	O₂	TOC
	[cm]	[cm]	[mV]		[μS/cm]	[mg/L]	[mg/L]	[mgC/L]
IF								
IF	0		402	6.9	181	<0.01	9.7	7.85
B1L								
B1L-0	0	0						
B1L-1	0-40	20	73	5.8	365	7.2	-	35.39
B1L-2 ^a	40-80	60	-47	5.8	330	2.6	0.3	19.16
B1L-3 ^a	80-120	90	13	5.3	75	0.08	0.2	16.32
B2L								
B2L-0	0	0	71	5.99	420	1.31	1.6	
B2L-1	0-30	15	23	5.45	450	17.2	-	59.27
B2L-2	30-60	45	53	5.8	390	2.88	-	45.65
B2L-3 ^a	60-125	92.5	43	5.4	190	0.56	0.3	35.94
B2L-4 ^a	125-185	155	3	5.4	500	0.28	-	22.58
B2L-5 ^a	185-210	197.5	13	5.5	470		0.7	9.00
B1R								
B1R-0	0	0						
B1R-1	0-40	20	-87	5.86	300	1.18	-	34.85
B1R-2 ^a	40-80	60	133	5.7	303	1.04	0.2	20.19
B1R-3 ^a	80-100	90	-7	6.03	237	0.24	0.2	22.14
B2R								
B2R-0	0	0						
B2R-1	0-40	20	78	5.8	250	2.22	-	16.60
B2R-2 ^a	40-80	60	-177	5.74	235	0.52	-	19.54
B3R								
B3R-0	0	0						
B3R-1	0-40	20	374	5.6	364	0.34	-	47.03
B3R-2	40-80	60	-87	5.6	343	7.0	-	31.90
B3R-3 ^a	80-100	90	13	5.85	200	0.84	-	18.61

^a porewater plus easily mobilizable soil-bound fraction

2 General chemical characterization of the *Federseemoor* peat

Table SI-2: Elemental composition peat

[mg/kg]	Mean^a	SD
C^b	55,0	0,03
N^b	2,18	0,02
S^b	0,22	0,006
Fe	829	14,9
Mg	22,9	4,49
Al	1749	208
P	602	31,2
K	116	28,5
Cr	5,06	0,30
Mn	2,23	0,30
Co	0,39	0,03
Ni	3,39	0,16
Cu	6,08	1,96
Zn	13,7	0,71
Se	0,41	0,05
As	1,53	0,03
Mo	0,31	0,03
Cd	<LOQ	
Sb	0,43	0,13
Pb	12,5	0,30
Ash content^b	2,51	0,03
Water content^b	85,1	0,04
Molar C/N	29,0	0,28

^a n = 6

^b [wt.-%]

Characterization of the peat with FT-IR spectroscopy

Method:

FT-IR analysis was performed with a Bruker Vector 22 spectrometer. For the analysis, 2 mg freeze-dried peat were mixed with 200 mg KBr and pressed into pellets prior to analysis. Up to 32 spectra were recorded in transmission mode, co-added and background-corrected by subtracting the spectrum of pure KBr. Absorption band assignments are based on Artz *et al.*,⁵ Rennert *et al.*,⁶ and Pretsch *et al.*⁷

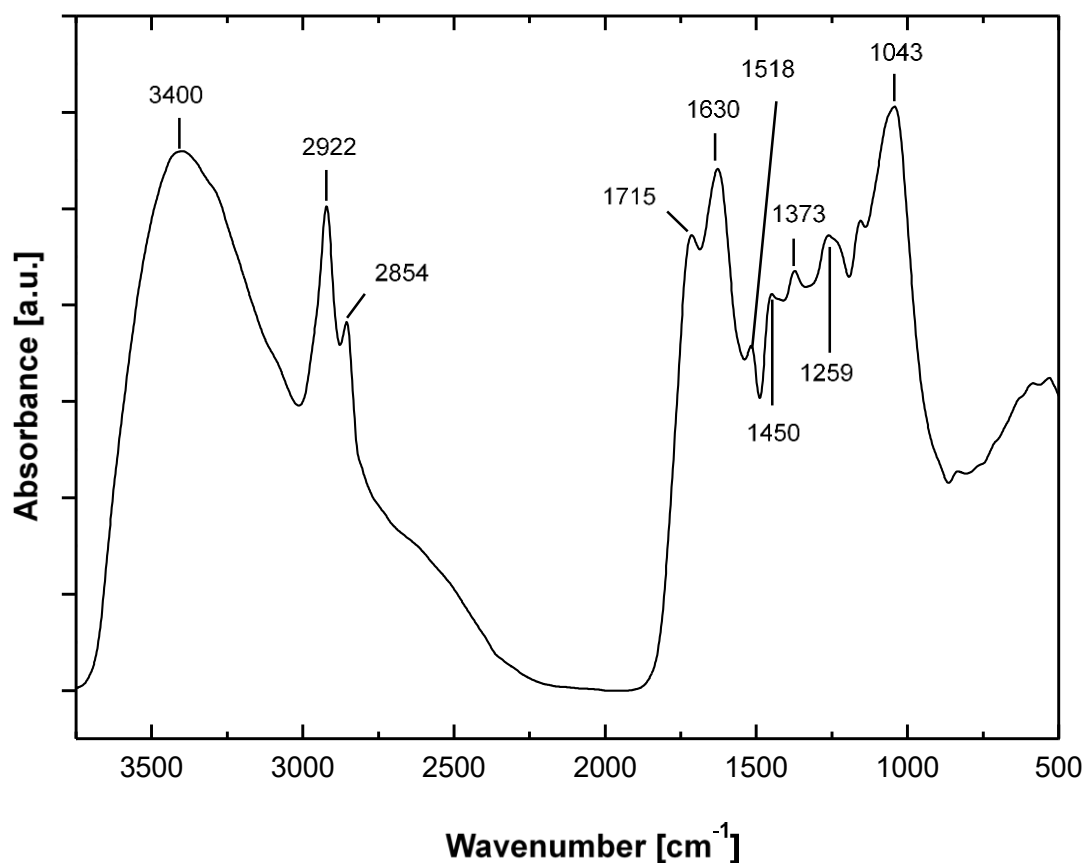


Figure SI-7: FT-IR spectrum of the washed and homogenized *Federseemoor* peat.

The broad intense band at about 3400-3300 cm⁻¹ with a maximum ~3340 cm⁻¹ results from stretching vibrations of hydroxyl (OH) groups which are indicative for cellulose and/or the N-H stretching of secondary amines. The bands at ~2922 and ~2854 cm⁻¹ can be assigned to antisymmetric and symmetric stretching of aliphatic C-H bonds of fats, wax or lipids. Stretching vibrations at ~1715 cm⁻¹ belong to the C=O group of carboxylic acids or other carbonyl groups like aromatic esters or aryl ketones. The intense band at 1630 cm⁻¹ in combination with that at 1518 cm⁻¹ is an indicator of skeletal vibrations of aromatics

(lignin backbone structures). Rennert *et al.*⁶ interprets the peak at 1630 cm^{-1} simply as residual H_2O but since the sample was freeze dried and kept sealed until analysis, this interpretation can most likely be excluded. The absorption bands at 1450 and 1373 cm^{-1} can be assigned for C-H deformations of phenolic (lignin) and aliphatic structures. Alcoholic functionalities are verified by the broad bands around 1259 cm^{-1} (phenolic groups) and 1043 cm^{-1} (aliphatic OH groups).

Characterization of the peat with ^{13}C CP/MAS-NMR

Method:

The ^{13}C CP/MAS-NMR spectrum of the peat was recorded on an Avance III HD spectrometer (Bruker) at a B_0 field 9.4 T . $^{13}\text{C}\{^1\text{H}\}$ (100.6 MHz). MAS spectra were obtained using a ramped cross-polarization (CP) experiment, where the nutation frequency ν_{nut} on the proton channel was varied linearly by 50%. The samples were spun at 12.5 kHz in a 4 mm MAS double resonance probe (Bruker). The corresponding ν_{nut} on the ^{13}C channel and the contact time were adjusted to 70 kHz and 3 ms , respectively. During acquisition proton broadband decoupling was applied using a spinal-64 sequence with $\nu_{\text{nut}} = 70\text{ kHz}$. ^{13}C spectra are referenced indirectly with respect to tetramethylsilane (TMS) using adamantane as secondary reference. For data analysis, the spectrum was divided into chemical shift regions assigned to the chemical group classes: aliphatic C ($0\text{--}60\text{ ppm}$), heteroaliphatic C ($60\text{--}90\text{ ppm}$), acetal C ($90\text{--}110\text{ ppm}$), aromatic C ($110\text{--}165\text{ ppm}$), carboxyl C ($165\text{--}190\text{ ppm}$), and carbonyl C ($190\text{--}220\text{ ppm}$).⁸ The relative intensity of these regions was determined by means of integration.

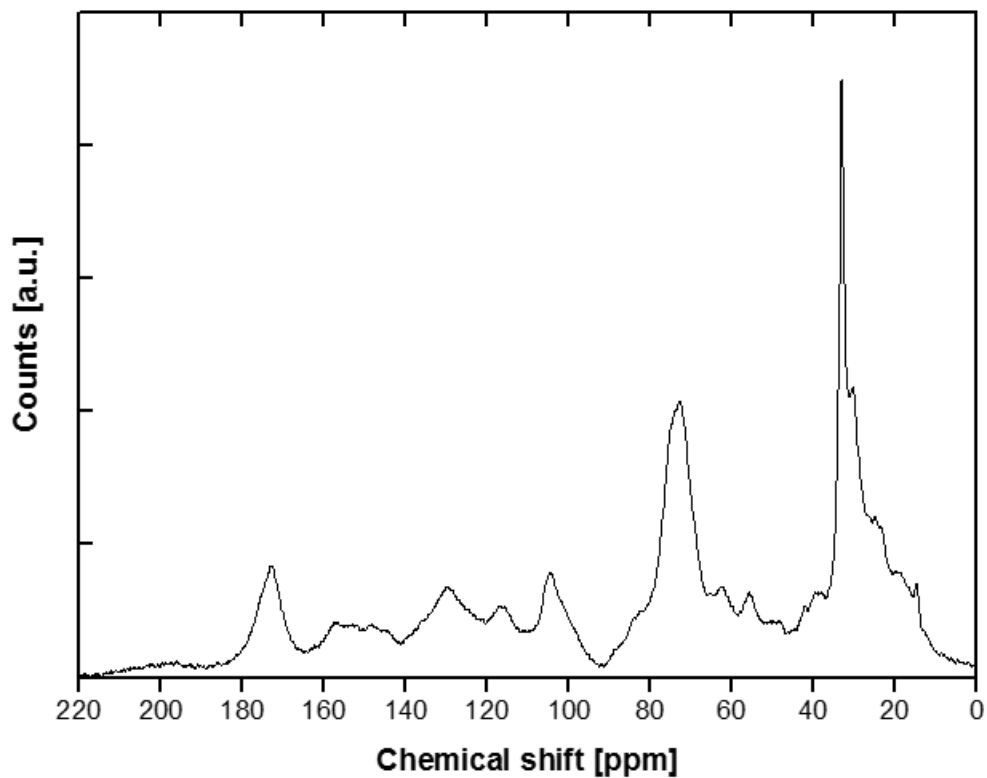


Figure SI-8: ^{13}C CP/MAS-NMR spectrum of the *Federseemoor* peat. The integrated peak intensities are summarized in Table SI-3.

Table SI-3: ^{13}C CP/MAS-NMR estimates of the C distribution in peat

	Carbonyl	Carboxyl	Aromatic	Acetal	Hetero- aliphatic	Aliphatic
	220-190 ppm	190-165 ppm	165-110 ppm	110-90 ppm	90-60 ppm	60-0 ppm
Peat (this publication)	1	7	21	7	24	40
Peat (Hoffmann et al. ⁸)	1	4	11	7	32	45

3 Monothioarsenate stability experiments in electrolyte background solutions

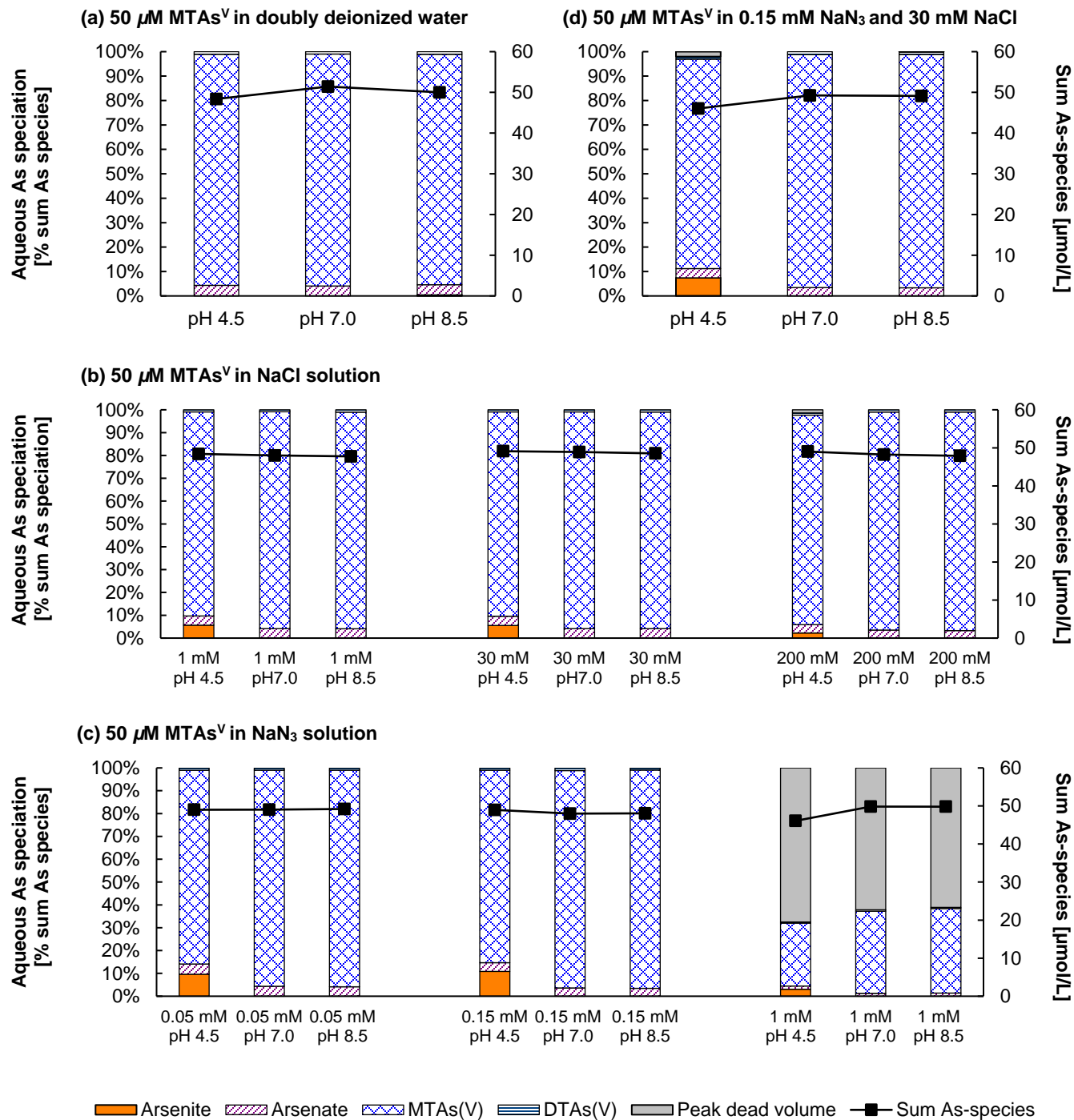


Figure SI-9: Blank experiments to test the stability of 50 μM MTAs(V) in (a) doubly deionized water, (b) different concentrations of NaCl solution, (c) different concentrations of NaN₃ solution and (d) 0.15 mM NaN₃ and 30 mM NaCl solution for pH 4.5, 7.0 and 8.5, respectively. Duration of experiments was 120 h. Straight lines serve to guide the eye.

4 Arsenic K-edge X-ray absorption spectroscopy

Details on XAS analyses

Arsenic K-edge X-ray absorption near-edge structure (XANES) and extended x-ray absorption fine-structure (EXAFS) spectra were collected at The Rossendorf Beamline (ROBL) at the European Synchrotron Radiation Facility (ESRF), Grenoble, France and at beamline 4-1 of the Stanford Synchrotron Radiation Lightsource (SSRL), Stanford, USA. Therefore, always anoxically kept peat and resin samples were freeze-dried, homogenized, filled into sample holders and sealed with Kapton tape. The beamlines were equipped with Si(111) (ROBL) and Si(220) (4-1) double crystal monochromators, which were calibrated to the L₃-edge of an Au foil (energy: 11919 eV). The absorption edge of the Au foil was monitored during all sample scans. To reduce higher-order harmonics, we detuned the monochromator to 65% of the maximum beam intensity at 4-1, or made use of two, 1.2-m and 1.4-m long, Pt mirrors at 2.5 mrad grazing incidence (ROBL). All sample measurements were performed in fluorescence mode using Ge array fluorescence detectors and He cryostats at 15 K to avoid beam damage and thermal disorder. Spectra of As reference compounds were analyzed in transmission/ fluorescence mode or were taken from Suess *et al.*⁹ Between 2 and 18 scans were collected per sample. Normalized XAS spectra were extracted from the raw data using the software codes SixPack¹⁰ and Athena.¹¹ For spectra normalization, the pre-edge region was consistently fitted with a linear function and the post-edge region also with linear function (XANES analysis) or a quadratic polynomial (EXAFS analysis). The E₀ positions of XANES were determined from the 2 points-smoothed maximum of the first derivative spectra. The background was removed using the Autobk algorithm incorporated in Athena. A Hanning window with a sill width of 1 Å⁻¹ was used for Fourier transformation. Shell-fit analysis of k³-weighted EXAFS spectra were performed in R-space employing the software Artemis. Theoretical scattering paths were calculated with FEFF6¹² based on the crystal structures of arsenolite¹³ and tris(phenylthio)arsine.¹⁴ Wavelet transform (WT) analysis of the k²-weighted EXAFS spectra¹⁵ was performed to distinguish between lighter (e.g. C, O) and heavier (e.g. Fe) back-scatterers using Morlet wavelets tuned to the region of interest (η=6 for a region around 3 Å). Principal component analysis (PCA) and iterative transformation factor analysis (ITFA) of normalized XANES spectra were performed with the ITFA software package.¹⁶

Arsenic reference compounds

Supplementary Table SI-4 provides an alphabetic list and details about their the origin of As reference compounds that were analysed by XAS and used in the ITFA analysis of the sulfide-reacted peat samples (see Figure 4).

Table SI-4: Arsenic reference compounds analysed by XAS.

Compound	Chemical formula	Source/synthesis	Synthesis information
As(III)-NOM	$\text{As}(\text{C}_x\text{H}_x\text{O}_{1+x})_2(\text{OH})_1^a$	synthetic	pure peat NOM (after Hoffmann et al. 2013 ¹⁷)
As(III)-S-NOM, 30 mM S(-II)	$\text{As}(\text{C}_x\text{O}_x\text{H}_x\text{S}_{1+x})_2(\text{OH})_1^a$	synthetic	peat NOM pre-equilibrated with 30 mM S(-II) (after Hoffmann et al. 2012 ⁸)
As(V)-NOM	n.d.	synthetic	pure peat NOM (after Hoffmann et al. 2013 ¹⁷)
dithioarsenate aqueous	$\text{H}_x\text{AsS}_2\text{O}_2^{3-x}$; $x=1-3^a$	synthetic	from Suess et al. 2009 ⁹
dithioarsenate solid	$\text{Na}_2\text{AsO}_2\text{S}_2 \cdot x\text{H}_2\text{O}^a$	synthetic	from Suess et al. 2009 ⁹
monothioarsenate aqueous	$\text{H}_x\text{AsSO}_3^{3-x}$; $x=1-3^a$	synthetic	from Suess et al. 2009 ⁹
monothioarsenate solid	$\text{Na}_3\text{AsO}_3\text{S} \cdot 7\text{H}_2\text{O}^b$	synthetic	from Suess et al. 2009 ⁹
Orpiment	As_2S_3	commercial (Alfa Aesar)	
Realgar	As_4S_4	commercial (Alfa Aesar)	
Sodium arsenate dibasic heptahydrate	$\text{Na}_2\text{HAsO}_4 \cdot 7\text{H}_2\text{O}$	commercial (Fluka)	
Sodium(meta)arsenite	NaAsO_2	commercial (Sigma-Aldrich)	
tetrathioarsenate aqueous	$\text{H}_x\text{AsS}_4^{3-x}$; $x=1-3^a$	synthetic	from Suess et al. 2009 ⁹
tetrathioarsenate solid	$\text{Na}_3\text{AsS}_4 \cdot 8\text{H}_2\text{O}^b$	synthetic	from Suess et al. 2009 ⁹

^a estimated by XAS^b XRD confirmed

5 Monothioarsenate and arsenite sorption to NOM

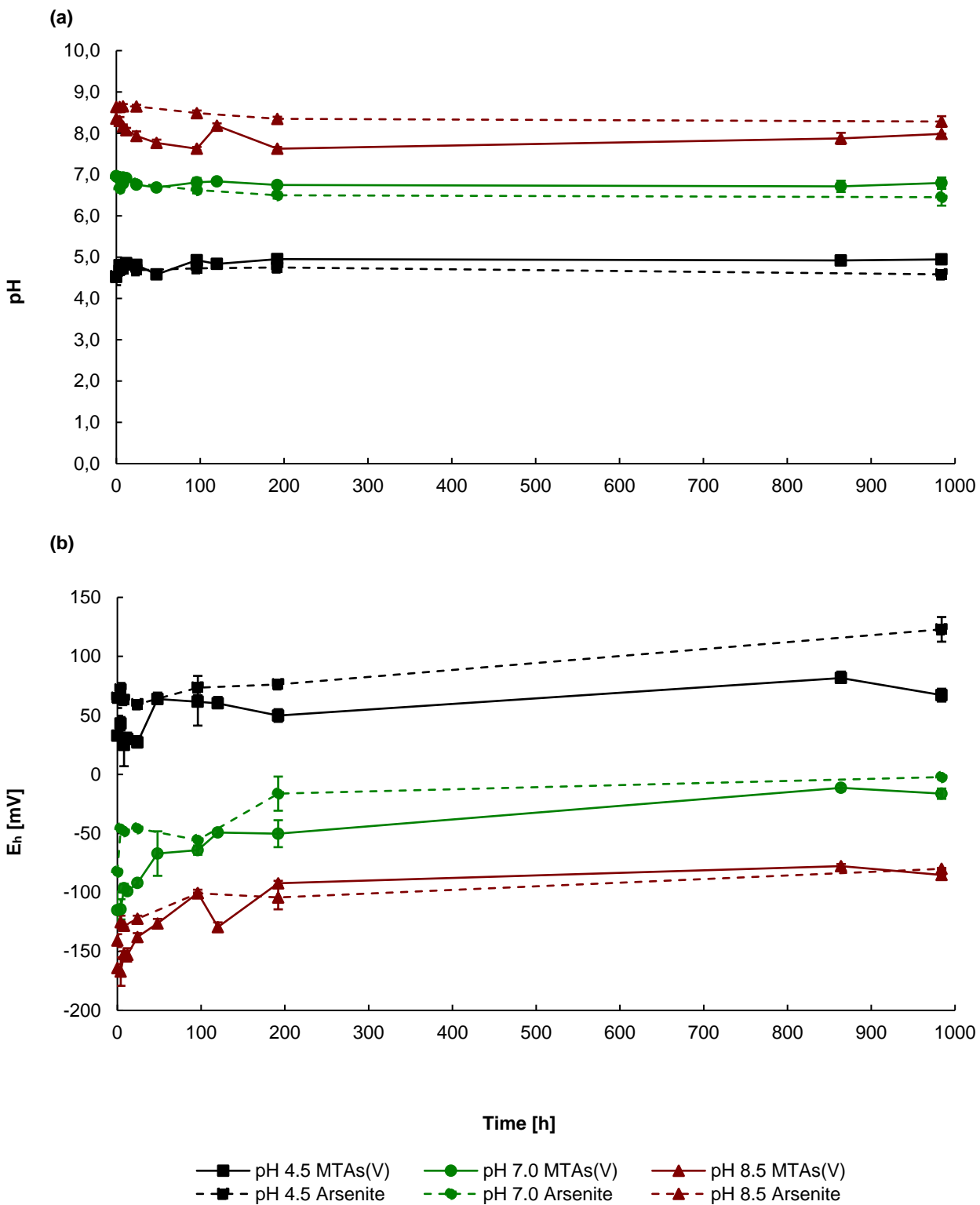


Figure SI-10: Solution pH (a) and E_h (b) of MTAs(V) and arsenite kinetic experiment for pH 4.5, 7.0 and 8.5, respectively. Mean and standard deviation of 3 replicates. Straight or dashed lines serve to guide the eye.

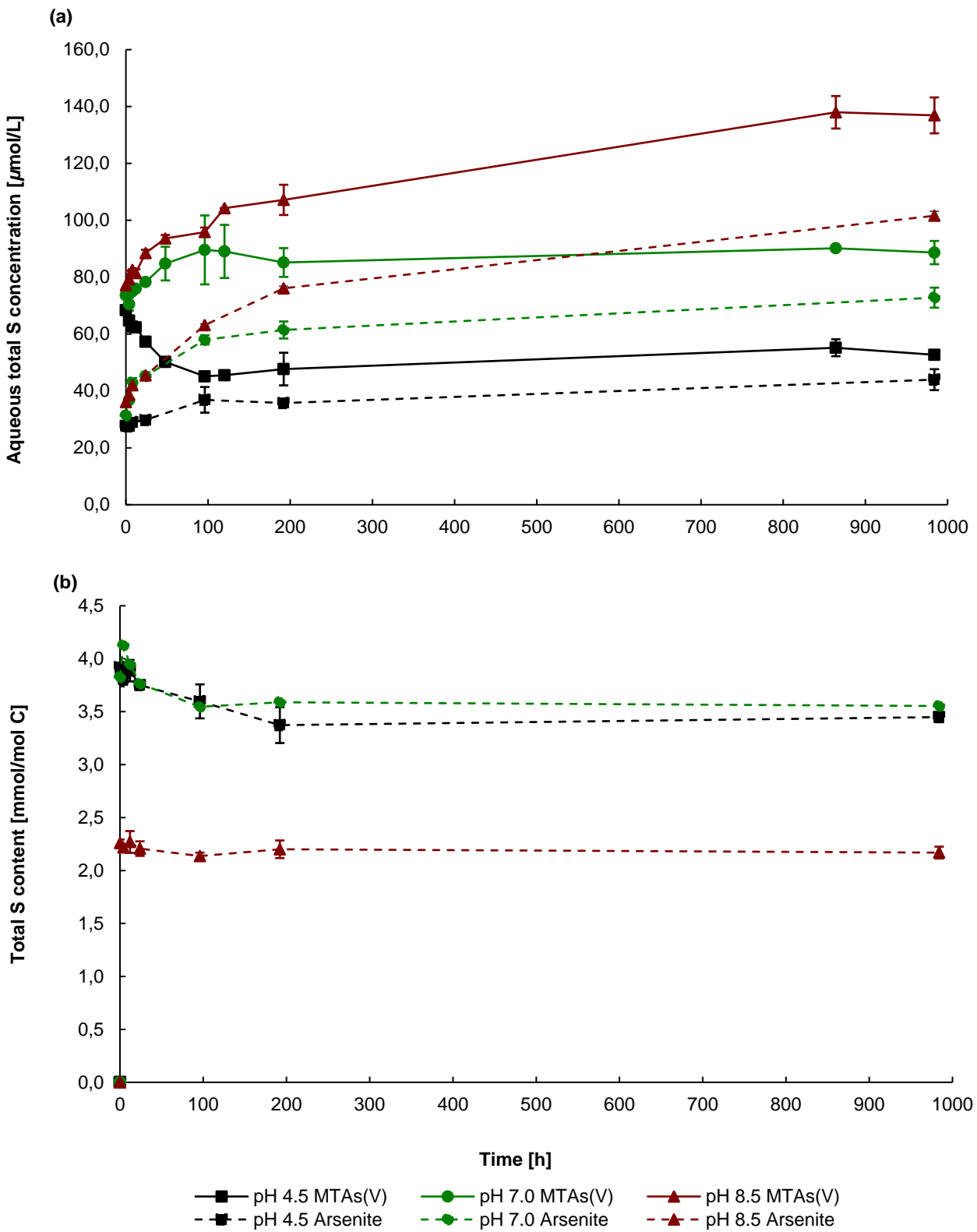


Figure SI-11: Aqueous total S concentrations (a) and total S solid-phase content (b) of MTAs(V) and arsenite kinetic experiment for pH 4.5, 7.0 and 8.5, respectively. Mean and standard deviation of 3 replicates. Straight or dashed lines serve to guide the eye.

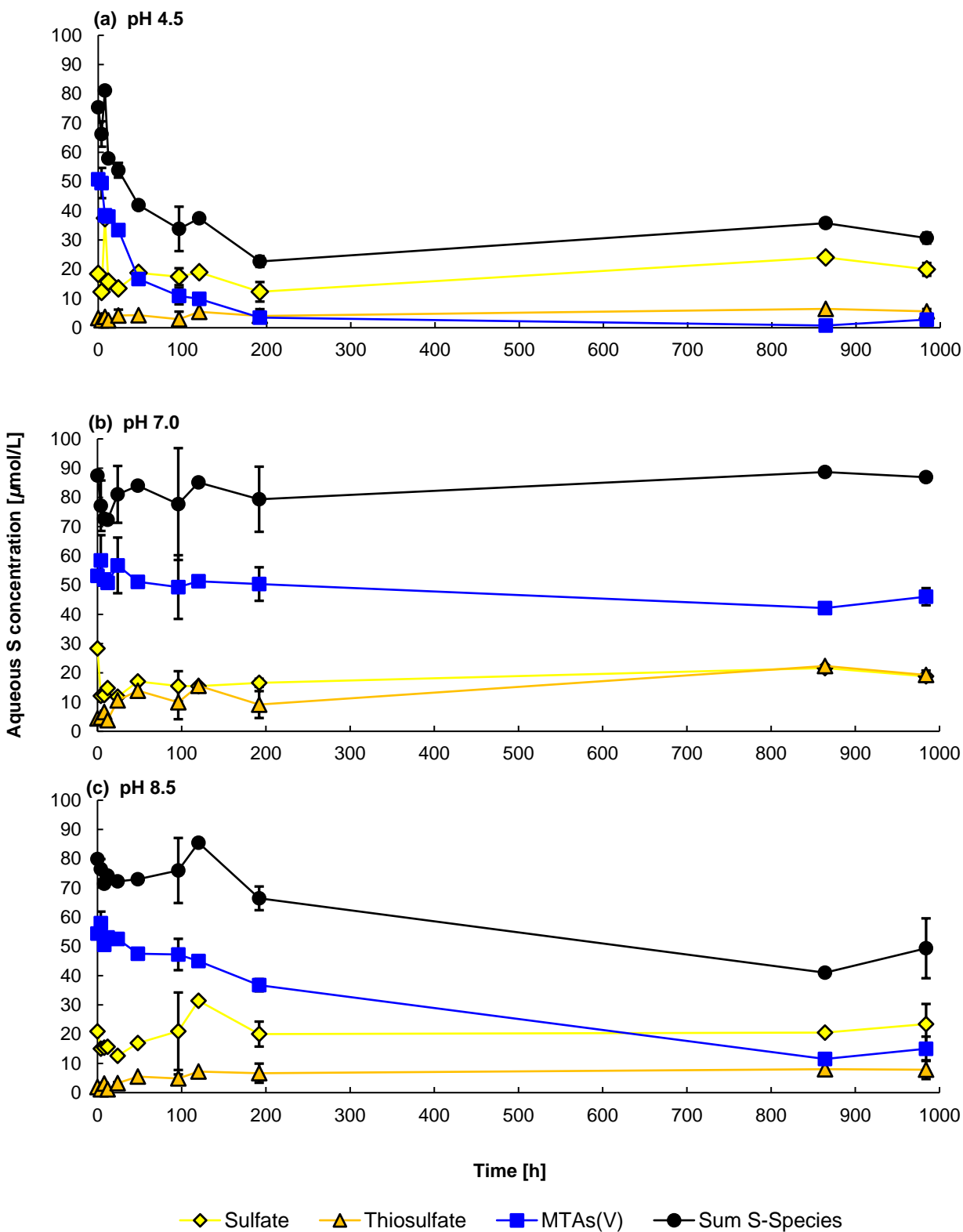


Figure SI-12: Aqueous S speciation detected with AEC-ICP-MS of MTAs(V) kinetic experiment for pH 4.5 (a), 7.0 (b) and 8.5 (c), respectively. Mean and standard deviation of 3 replicates for 4, 24, 96, 192 and 984 h. Otherwise, single data points. Straight or dashed lines serve to guide the eye.

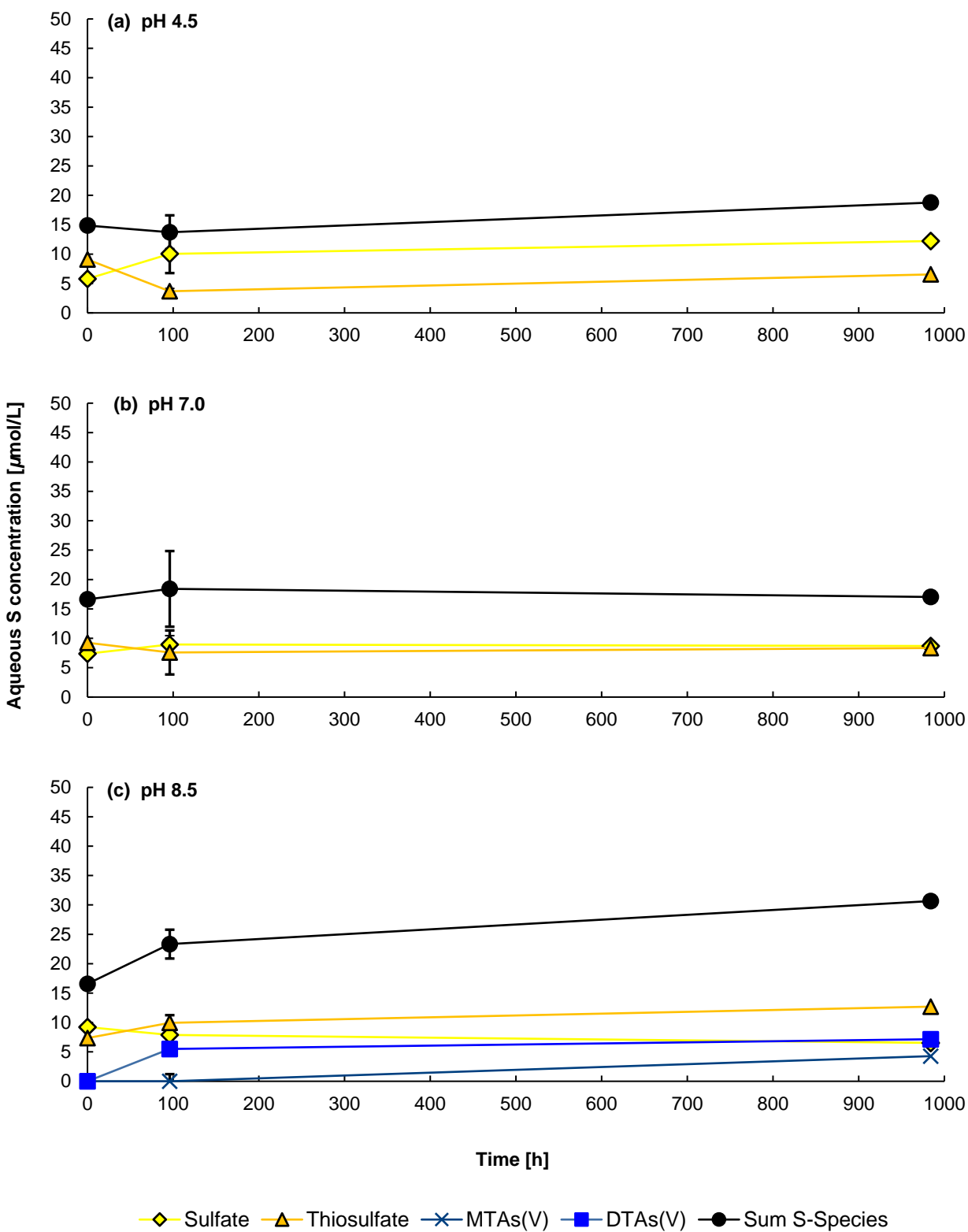


Figure SI-13: Aqueous S speciation detected with AEC-ICP-MS of arsenite kinetic experiment for pH 4.5 (a), 7.0 (b) and 8.5 (c), respectively. Mean and standard deviation of 3 replicates for 96 h. Otherwise, single data points. Straight or dashed lines serve to guide the eye.

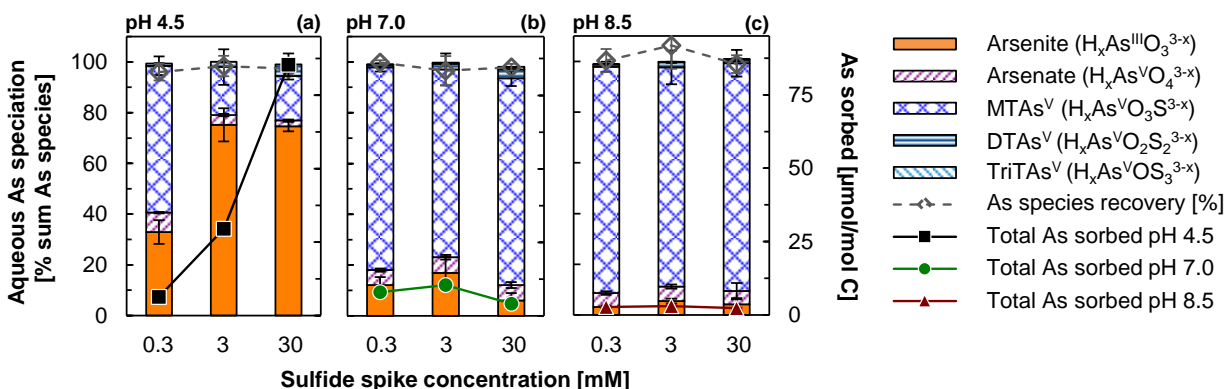


Figure SI-14: Total As sorption (straight lines) and aqueous As speciation in [%] (bars) of MTAs(V) sorbed to peat (0.2 mol C/L peat suspensions) reacted with 0.3, 3, or 30 mM sulfide for pH 4.5 (a), pH 7.0 (b), and pH 8.5 (c) and an incubation time of 96 h. Aqueous As species recovery: 81–106%). Error bars represent standard deviations of triplicates. Straight or dashed lines serve to guide the eye.

Table SI-5: Solution pH and E_h of MTAs(V) experiments with different nominal S(-II) spike concentrations on NOM (96 h) for pH 4.5, 7.0 and 8.5, respectively.

Nominal pH	S(-II)-I [mM]	Actual pH		E_h [mV]	
		Mean ^a	SD	Mean ^a	SD
4.5	0.3	4.65	0.07	133.20	2.33
	3	4.54	0.07	76.97	5.86
	30	5.06	0.06	9.37	2.54
7.0	0.3	6.13	0.05	74.30	6.47
	3	6.84	0.03	-63.30	1.82
	30	7.76	0.09	-137.03	3.26
8.5	0.3	7.21	0.09	31.60	4.52
	3	7.90	0.03	-138.27	33.98
	30	9.14	0.01	-179.83	1.05

^a n=3

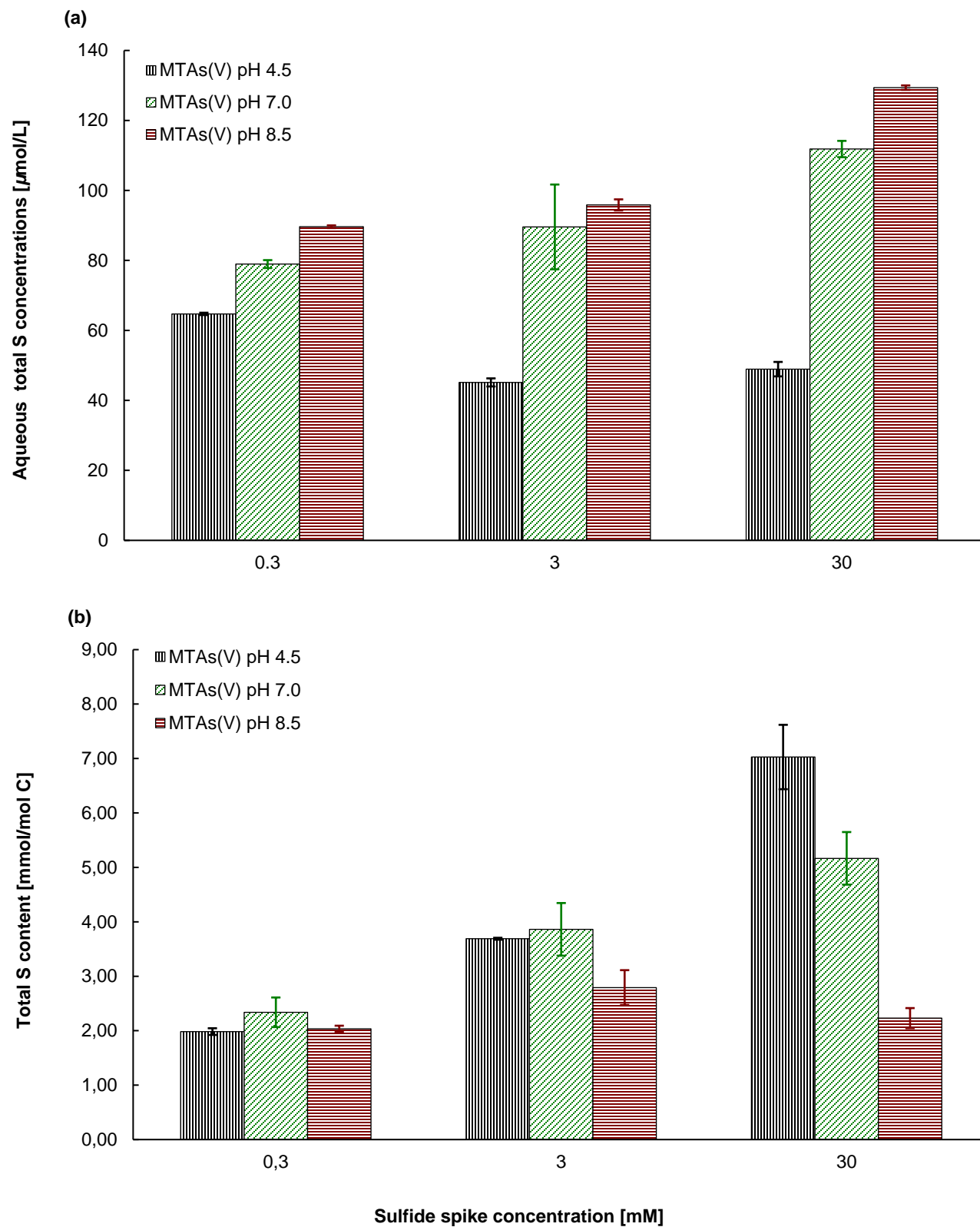


Figure SI-15: Aqueous total S concentrations (a) and total S solid-phase content (b) of MTAs(V) experiments with different nominal S(-II) spike concentrations on NOM (96 h) for pH 4.5, 7.0 and 8.5, respectively. Mean and standard deviation of 3 replicates.

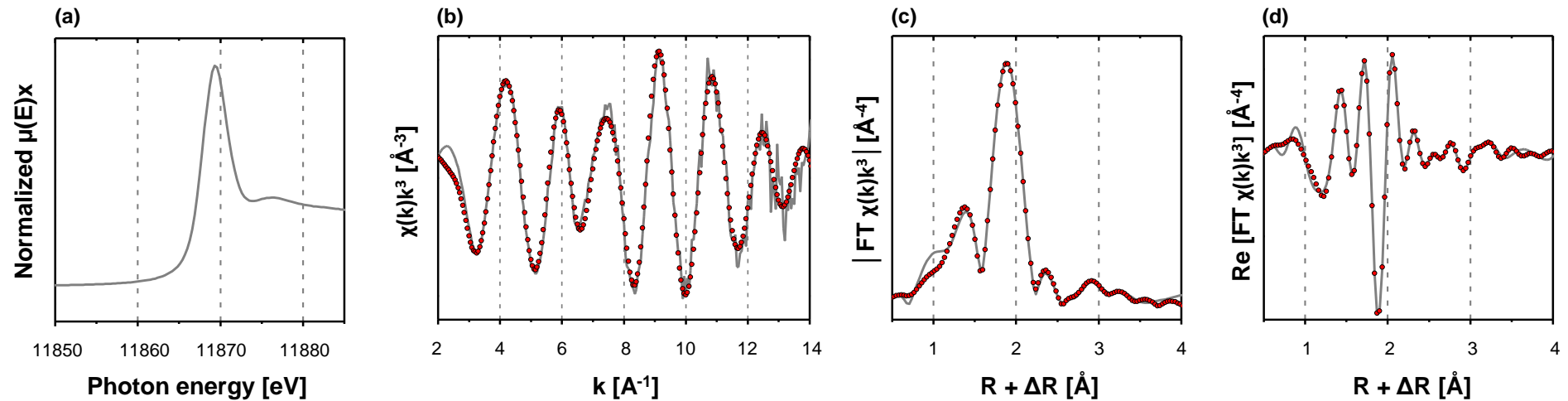


Figure SI-16: Arsenic *K*-edge XANES-spectra (a), k^3 -weighted EXAFS spectra (b), Fourier-transform magnitudes (c), and real parts of the Fourier transforms (d) of sulfide-reacted NOM (30 mM S(-II) spike concentration) equilibrated with 50 μ M arsenite solution. Grey lines represent experimental data and the fits are shown as red dashed lines.

Table SI-6: E_0 energy and EXAFS parameters determined by shell-fitting of As *K*-edge EXAFS spectra of sulfide-reacted NOM (30 mM S(-II) spike concentrations) equilibrated with 50 μ M arsenite solution.^a

Sample	E_0 [eV] ^b	Path	CN ^c	$R[\text{\AA}]$ ^d	σ^2 [\AA^2] ^e	ΔE_0 [eV] ^f	R-factor ^g	Red χ^2 ^h
As(III)-S-NOM, pH 4.5, 30 mM S(-II) spike	11867.8	As-O	1.1 (1)	1.80 (1)	0.0015 (3)	9.0 (5)	0.0057	48
		As-S	2.0 (1)	2.28 (1)	0.0027 (5)			
		As-C1	2.0 ⁱ	3.17 (2)	0.0052 (25)			
		As-C2	2.0 ⁱ	3.61 (3)	0.0052 ^j			

^a Fitting parameter uncertainties provided by *Artemis software* are given in parentheses for the last significant figure. The passive amplitude reduction factor S_0^2 was set to 0.9. ^b E_0 : maximum of first derivative of normalized XANES spectra, general error ± 0.3 eV. ^c Coordination number (path degeneracy), general error $\pm 25\%$. ^d Mean half path length, general error ± 0.02 \AA . ^e Debye-Waller parameter, general error ± 0.0005 \AA^2 . ^f Energy-shift parameter. ^g R -factor = $\sum_i (\text{data}_i - \text{fit}_i)^2 / \sum_i \text{data}_i^2$ and reduced $\chi^2 = (\text{N}_{\text{idp}}/\text{N}_{\text{pts}}) \sum_i (\text{data}_i - \text{fit}_i)^2 / \epsilon_i^2 (\text{N}_{\text{idp}} - \text{N}_{\text{var}})^{-1}$. N_{idp} : the number of independent points in the model fit, N_{pts} : the total number of data points, N_{var} : the number of variables in the fit, ϵ_i : the uncertainty of the i^{th} data point guessed by *Artemis software*. $\text{N}_{\text{idp}}/\text{N}_{\text{var}} = 19.4/10$, fit ranges: R-space: 0.85 – 3.8 \AA , K -space: 3.0 - 13.5 \AA^{-1} . ⁱ CN of As-C1 and As-C2 path were defined as CN As-S. ^j σ^2 of As-C2 path was defined as As-C1. The addition of the As-C2 path significantly improved the model (F-test: $\alpha=97.5\%$, after Downward et al.¹⁸). Test parameters: model with 2 C atoms: $\text{N}_{\text{var}}=10$, R-factor= 0.0057. Model with 1 C atom: $\text{N}_{\text{var}}=9$, R-factor= 0.0100.

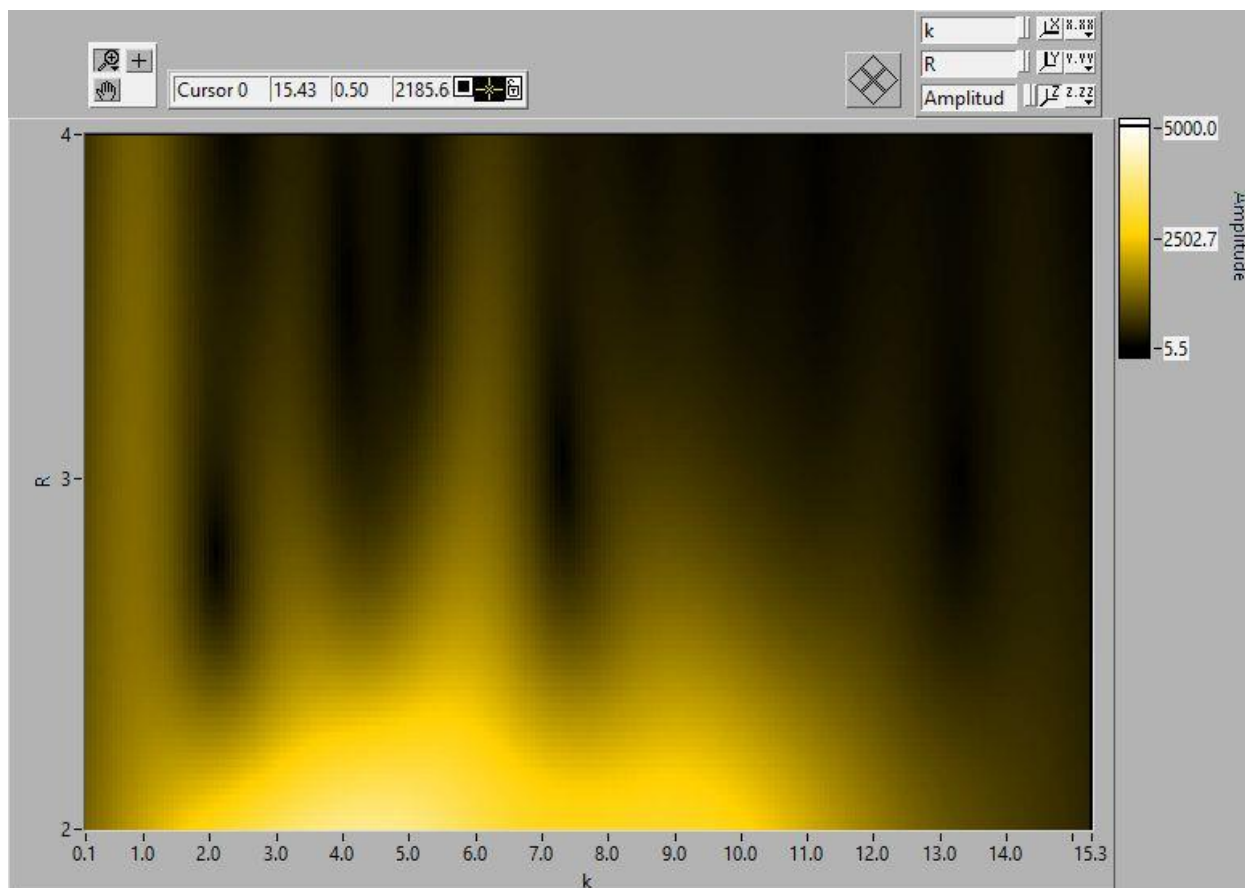


Figure SI-17: Morlet wavelets of k^2 -weighted As K -edge EXAFS spectra of As(III)-S-NOM, pH 4.5, 30 mM S(-II) spike sample ($\eta = 6$, $\sigma = 1$).

Wavelet transform analysis (WTA) was conducted to identify signals from possible heavier backscatters e.g. As-As waves of nanocrystalline As sulfide minerals at ~ 3.5 Å which show almost no features in the Fourier transformed spectrum after ~ 2.7 Å.¹⁹ Shell-by-shell fitting of Fourier transformed As K -edge EXAFS spectra of the As(III)-S-NOM, pH 4.5, 30 mM S(-II) spike sample (Table SI-6) suggested that As was entirely coordinated to sulfhydryl groups of the peat NOM. The WTA of the peat sample did not show any feature of heavy backscattering in that sample. All occurring signals originated from backscattering by low-Z elements (C/N/O) and/or multiple scattering and/or arbitrary signal (compare Funke et al.¹⁵). This points towards a direct binding between trivalent As and sulfhydryl groups of NOM where the WTA supports the absence of significant amounts of nanocrystalline As sulfide minerals in the peat sample. Consequently, this sample serves as an appropriate standard for trivalent As bound to sulfhydryl groups within the XANES ITFA of the kinetic and the sulfide spike concentrations experiment.

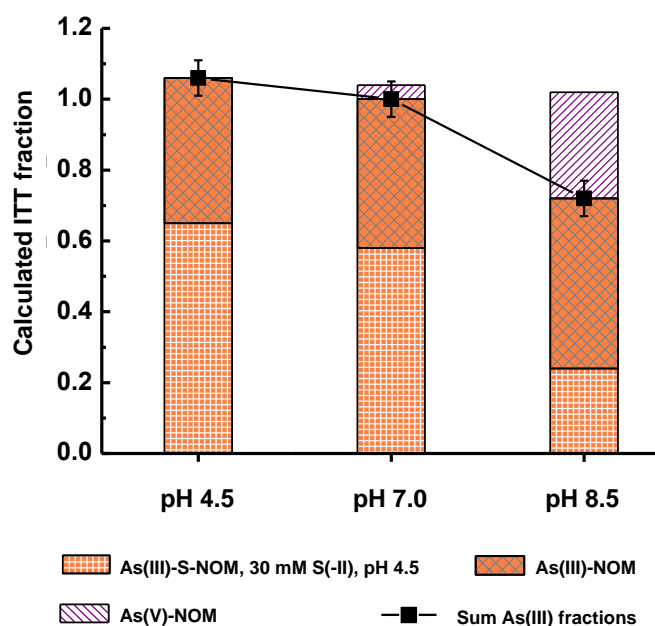


Figure SI-18: Calculated iterative target transformation (ITT) fractions of normalized As *K*-edge XANES spectra from arsenite time series experiment (96 h) with 3 mM sulfide spike concentrations. Abbreviations: As(III): tri-valent As, As(V): penta-valent As. The S in As(III)-S-NOM is sulfhydryl S. Sum As(III) fractions = As(III)-S-NOM + As(III)-NOM. For the ITT calculation of relative species concentrations, the concentrations of the three identified references were fixed at 100%, while the concentrations of the mixtures were calculated without constraints; i.e., they were not normalized to 100%. Error bars represent general error of ITFA procedure of about 5% of relative concentrations. That means contributions of components $\leq 5\%$ may not be considered. Straight lines serve to guide the eye.

It is noteworthy, that the fraction of As(III)-S-NOM does not directly represent As-S coordination but has to be multiplied by $(2/3 \cdot 3 = 2)$ since the CN of the reference standard was fitted as CN 2.0 (Table SI-6). Cross-checking with published spectra from Hoffmann *et al.*⁸ confirmed this approach (error ± 0.1 CN, data not shown).

6 Monothioarsenate and arsenite sorption to Ambersep GT74 resin

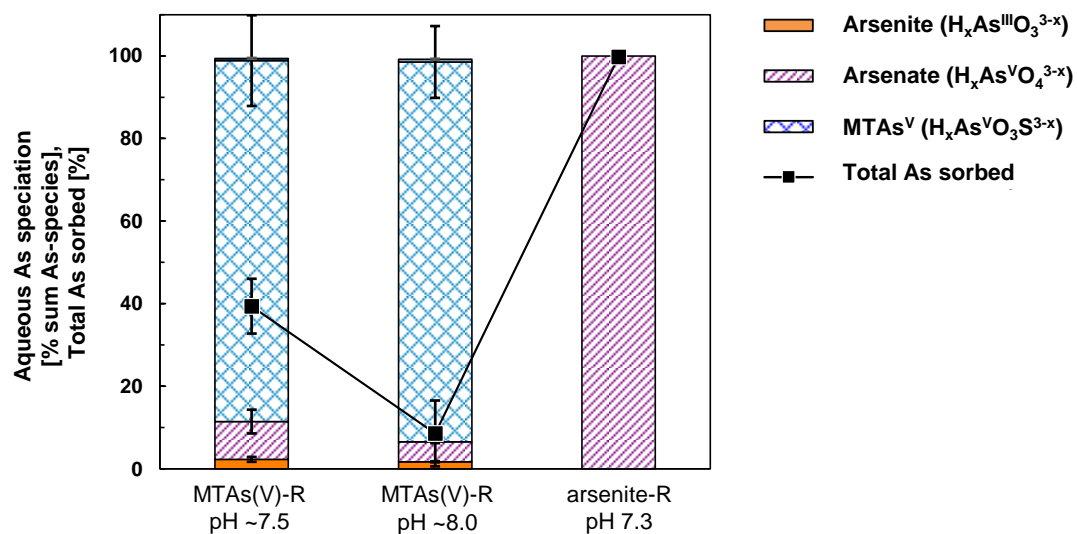


Figure SI-19: Aqueous As speciation and total As sorbed to Ambersep GT74 resin equilibrated with 200 μM (pH~7.5) and 250 μM (pH ~ 8.0) MTAs(V) as well as 250 μM (pH 7.3) arsenite solutions. Mean and standard deviation of 3 replicates for MTAs(V)-R, pH~7.5 and MTAs(V)-R, pH ~8.0. Otherwise, single data points.

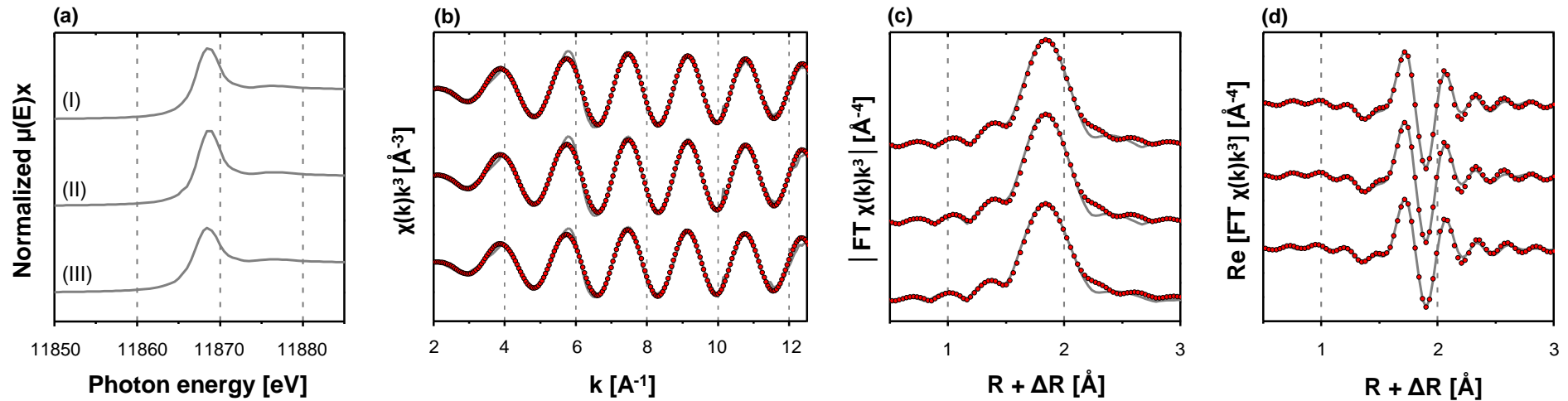


Figure SI-20: Arsenic *K*-edge XANES-spectra (a), k^3 -weighted EXAFS spectra (b), Fourier-transform magnitudes (c), and real parts of the Fourier transforms (d) of MTAs(V) – Resin, pH ~7.5 (I), MTAs(V) – Resin, pH ~8.0 (II) and Arsenite, pH 7.3 (III). Grey lines represent experimental data and the fits are shown as red dashed lines.

Table SI-7: E_0 energies and EXAFS parameters determined by shell-fitting of As *K*-edge EXAFS spectra of Ambersep GT74 resin equilibrated with MTAs(V) and arsenite solutions^a

Sample	E_0 [eV] ^b	Path	CN ^c	$R[\text{Å}]^d$	σ^2 [Å ²] ^e	ΔE_0 [eV] ^f	R-factor ^g	Red χ^2 ^h
MTAs(V) – Resin, pH ~7.5	11867.0	As–S	3.0 (2)	2.26 (1)	0.0020 (7)	2.1 (9)	0.009	1363
MTAs(V) – Resin, pH ~8.0	11867.1	As–S	3.1 (3)	2.26 (1)	0.0021 (8)	2.0 (10)	0.011	964
Arsenite - Resin, pH 7.3	11867.0	As–S	2.7 (2)	2.26 (1)	0.0018 (8)	2.1 (9)	0.009	1052

^a Fitting parameter uncertainties provided by Artemis software are given in parentheses for the last significant figure. The passive amplitude reduction factor S_0^2 was set to 0.9 for all samples. ^b E_0 : maximum of first derivative of normalized XANES spectra, general error ± 0.3 eV. ^c Coordination number (path degeneracy), general error $\pm 25\%$. ^d Mean half path length, general error ± 0.02 Å. ^e Debye–Waller parameter, general error ± 0.0005 Å². ^f Energy-shift parameter. ^g ^h R-factor = $\sum_i(\text{data}_i - \text{fit}_i)^2 / \sum_i \text{data}_i$ and reduced $\chi^2 = (\text{N}_{\text{idp}}/\text{N}_{\text{pts}}) \sum_i(\text{data}_i - \text{fit}_i)^2 / \varepsilon_i^2 (\text{N}_{\text{idp}} - \text{N}_{\text{var}})^{-1}$. N_{idp} : the number of independent points in the model fit, N_{pts} : the total number of data points, N_{var} : the number of variables in the fit, ε_i : the uncertainty of the i^{th} data point guessed by Artemis software. $\text{N}_{\text{idp}}/\text{N}_{\text{var}} = 8/4$, fit ranges: R-space: 1.0 - 2.3 Å, *K*-space: 2.5 - 12.5 Å⁻¹ (same parameters for all fitted samples).

7 References

- Langner, P.; Mikutta, C.; Suess, E.; Marcus, M. A.; Kretzschmar, R. Spatial distribution and speciation of arsenic in peat studied with microfocused X-ray fluorescence spectrometry and X-ray absorption spectroscopy. *Environ. Sci. Technol.* **2013**, *47*, 9706-9714.
- González A, Z. I.; Krachler, M.; Cheburkin, A. K.; Shotyk, W. Spatial distribution of natural enrichments of arsenic, selenium, and uranium in a minerotrophic peatland, Gola di Lago, Canton Ticino, Switzerland. *Environ. Sci. Technol.* **2006**, *40*, 6568-6574.
- Langner, P.; Mikutta, C.; Kretzschmar, R. Arsenic sequestration by organic sulphur in peat. *Nat. Geosci.* **2012**, *5*, 66-73.
- Planer-Friedrich, B.; London, J.; McCleskey, R. B.; Nordstrom, D. K.; Wallschläger, D. Thioarsenates in geothermal waters of Yellowstone National Park: Determination, preservation, and geochemical importance. *Environ. Sci. Technol.* **2007**, *41*, 5245-5251.
- Artz, R. R. E.; Chapman, S. J.; Jean Robertson, A. H.; Potts, J. M.; Laggoun-Défarge, F.; Gogo, S.; Comont, L.; Disnar, J.-R.; Francez, A.-J. FTIR spectroscopy can be used as a screening tool for organic matter quality in regenerating cutover peatlands. *Soil Biol. Biochem.* **2008**, *40*, 515-527.
- Rennert, T.; Eusterhues, K.; Pfanz, H.; Totsche, K. U. Influence of geogenic CO₂ on mineral and organic soil constituents on a mofette site in the NW Czech Republic. *Europ. J. Soil Sci.* **2011**, *62*, 572-580.
- Pretsch, E.; Bühlmann, P.; Badertscher, M. *Structure Determination of Organic Compounds: Tables of Spectral Data*. Springer-Verlag: Berlin, 2009.
- Hoffmann, M.; Mikutta, C.; Kretzschmar, R. Bisulfide reaction with natural organic matter enhances arsenite sorption: Insights from X-ray absorption spectroscopy. *Environ. Sci. Technol.* **2012**, *46*, 11788-11797.
- Suess, E.; Scheinost, A. C.; Bostick, B. C.; Merkel, B. J.; Wallschlaeger, D.; Planer-Friedrich, B. Discrimination of thioarsenites and thioarsenates by X-ray absorption spectroscopy. *Anal. Chem.* **2009**, *81*, 8318-8326.
- Webb, S. M. SIXpack: a graphical user interface for XAS analysis using IFEFFIT. *Phys. Scr.* **2005**, 1011.
- Ravel, B.; Newville, M. ATHENA, ARTEMIS, HEPHAESTUS: data analysis for X-ray absorption spectroscopy using IFEFFIT. *J. Synchrotron Radiat.* **2005**, *12*, 537-541.
- Zabinsky, S. I.; Rehr, J. J.; Ankudinov, A.; Albers, R. C.; Eller, M. J. Multiple-scattering calculations of x-ray-absorption spectra. *Phys. Rev. B* **1995**, *52*, 2995-3009.
- Ballirano, P.; Maras, A. Refinement of the crystal structure of arsenolite, As₂O₃. In *Z. Kristallogr. - New Cryst. Struct.* **2002**, 217,177.
- Pappalardo, G. C.; Chakravorty, R.; Irgolic, K. J.; Meyers, E. A. Tris(phenylthio)arsine, C₁₈H₁₅AsS₃. *Acta Crystallogr., Sect. C: Cryst. Struct. Commun.* **1983**, *39*, 1618-1620.
- Funke, H.; Scheinost, A. C.; Chukalina, M. Wavelet analysis of extended x-ray absorption fine structure data. *Phys. Rev. B.* **2005**, *71*, 94-110.
- Roßberg, A.; Reich, T.; Bernhard, G. Complexation of uranium(VI) with protocatechuic acid—application of iterative transformation factor analysis to EXAFS spectroscopy. *Anal. Bioanal. Chem.* **2003**, *376*, 631-638.
- Hoffmann, M.; Mikutta, C.; Kretzschmar, R. Arsenite binding to natural organic matter: Spectroscopic evidence for ligand exchange and ternary complex formation. *Environ. Sci. Technol.* **2013**, *47*, 12165-12173.

18. Downward, L.; Booth, C. H.; Lukens, W. W.; Bridges, F. A Variation of the F-test for determining statistical relevance of particular parameters in EXAFS fits. *AIP Conf. Proc.* **2007**, 882, 129-131.
19. Helz, G. R.; Tossell, J. A.; Charnock, J. M.; Patrick, R. A. D.; Vaughan, D. J.; David Garner, C. Oligomerization in As (III) sulfide solutions: Theoretical constraints and spectroscopic evidence. *Geochim. Cosmochim. Ac.* **1995**, 59, 4591-4604.

Study 2: Complexation of Arsenite, Arsenate, and Monothioarsenate with Oxygen-Containing Functional Groups of Natural Organic Matter: An XAS Study

Ashis Biswas, Johannes Besold, Carin Sjöstedt, Jon Petter Gustafsson, Andreas C. Scheinost and

Britta Planer-Friedrich

Reprinted with permission from

Environmental Science & Technology

Copyright 2020 American Chemical Society

Complexation of Arsenite, Arsenate, and Monothioarsenate with Oxygen-Containing Functional Groups of Natural Organic Matter: An XAS Study

Ashis Biswas,^{*,†,‡,§} Johannes Besold,[†] Carin Sjöstedt,[§] Jon Petter Gustafsson,[§] Andreas C. Scheinost,^{||,⊥} and Britta Planer-Friedrich[†]

[†]Department of Environmental Geochemistry, Bayreuth Center for Ecology and Environmental Research (BAYCEER), Bayreuth University, 95440 Bayreuth, Germany

[‡]Department of Earth and Environmental Sciences, Indian Institute of Science Education and Research (IISER) Bhopal, Bhopal Bypass Road, 462066 Bhaury, Madhya Pradesh, India

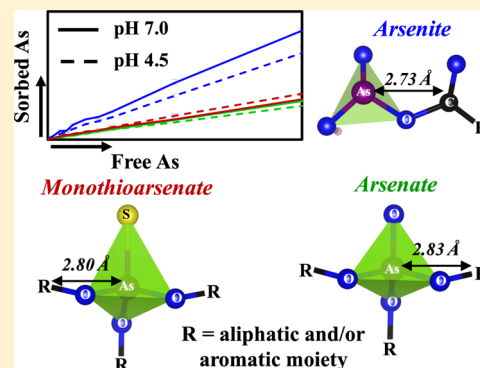
[§]Department of Soil and Environment, Swedish University of Agricultural Sciences, Box 7014, 750 07 Uppsala, Sweden

^{||}The Rossendorf Beamline (ROBL) at ESRF, 38043 Grenoble, France

[⊥]Institute of Resource Ecology, Helmholtz-Zentrum Dresden-Rossendorf (HZDR), Bautzner Landstraße 400, 01328 Dresden, Germany

Supporting Information

ABSTRACT: Arsenic (As) is reported to be effectively sorbed onto natural organic matter (NOM) via thiol coordination and polyvalent metal cation-bridged ternary complexation. However, the extent of sorption via complexation with oxygen-containing functional groups of NOM is poorly understood. By equilibrating arsenite, arsenate, and monothioarsenate with purified model-peat, followed by As K-edge X-ray absorption spectroscopic analysis, this study shows that complexation with oxygen-containing functional groups can be an additional or alternative mode of As sorption to NOM. The extent of complexation was highest for arsenite, followed by monothioarsenate and arsenate. Complexation was higher at pH 7.0 compared to 4.5 for arsenite and arsenate and vice versa for monothioarsenate because of partial transformation to arsenite at pH 4.5. Modeling of the As K-edge extended X-ray absorption fine structure data revealed that As···C interatomic distances were relatively longer in arsenate- ($2.83 \pm 0.01 \text{ \AA}$) and monothioarsenate-treated peat ($2.80 \pm 0.02 \text{ \AA}$) compared to arsenite treatments ($2.73 \pm 0.01 \text{ \AA}$). This study suggests that arsenite was predominantly complexed with carboxylic groups, whereas arsenate and monothioarsenate were complexed with alcoholic groups of the peat. This study further implies that in systems, where NOM is the major sorbent, arsenate and monothioarsenate can have higher mobility than arsenite.



INTRODUCTION

During the last four decades, natural and anthropogenic occurrences of elevated concentrations of arsenic (As) in surface waters, groundwaters, and agricultural soils have been highlighted as a potential environmental concern in many parts of the world.^{1–3} It is estimated that only in Southeast Asia more than 100 million people are at risk of chronic As toxicity from drinking water and food consumption.⁴ Therefore, it is necessary to characterize different biogeochemical processes that regulate the mobility of As in aquatic and terrestrial ecosystems.

Formation and interconversion of different As species determine the extent of its mobility in the environment.¹ Two most commonly reported inorganic As species are pentavalent arsenate and trivalent arsenite, which predominate under strongly oxidizing conditions and moderately oxidizing

to moderately reducing conditions, respectively.¹ After recent advances in analytical speciation techniques, it has become evident that under anoxic sulfidic conditions thiolated pentavalent As species, so-called thioarsenates ($\text{H}_x\text{AsS}_n\text{O}_{4-n}^{3-x}$; $n = 1–3$; $x = 1–3$), can also be formed in significant quantities under diverse natural settings.^{5–10} The extent of sorption of these As species onto different mineral phases, especially metal oxyhydroxides in soils and sediments, is identified as one of the key regulating processes for their mobility in the environment.^{1,11–13} Recently, a series of studies highlighted the importance of natural organic matter (NOM)

Received: May 21, 2019

Revised: August 14, 2019

Accepted: August 22, 2019

Published: August 22, 2019

as an alternative or additional sorbent for As and its regulatory role in As mobilization and transport in surface and subsurface environments.^{14–20}

Natural organic matter, being the decomposition product of animal, plant, and soil biomass is abundant in aquatic and terrestrial ecosystems.¹⁵ It has a complex structure with a variety of functional groups, such as carboxylic, alcoholic, esteric, quinone, amino, nitroso, thiol, hydroxyl, and so forth, which are mostly negatively charged at near-neutral pH.¹⁵ Several mechanisms for binding of arsenate and arsenite to NOM have been put forward. One spectroscopically well-characterized mechanism is the formation of ternary complexes through polyvalent metal cations (e.g., Fe³⁺, Al³⁺, Ca²⁺, etc.) bridging between negatively charged or neutral As species and negatively charged NOM (As–M–NOM; M represents polyvalent metal cations).^{16,21–25} Another mechanism is the direct binding of As species to specific functional groups of NOM. The most prominent site for such binary complexation can be organic thiol groups (–SH).^{20,26} By using X-ray absorption spectroscopy (XAS), Langner et al.²⁰ found almost 100% of arsenite to be bound to thiol groups in deep peat layers of a minerotrophic peat bog (Gola di Lago). A follow-up study showed that arsenite binding to thiol groups can compete with its binding to ferrihydrite.²⁷ Recently, Catrouillet et al.^{28,29} developed a geochemical model for arsenite complexation with NOM by thiol groups and via Fe²⁺ and Fe³⁺ bridging. Liu and Cai,³⁰ on the other hand, reported two types of binding sites (strong and weak sites) to be involved during binary complexation of arsenite with Aldrich humic acid (AHA), but without more specifically characterizing them.

Few studies have highlighted that As species can also be directly coordinated to oxygen-containing organic ligands. For example, Buschmann et al.¹⁷ in a dialysis experiment found that of the total spiked concentrations, 26% of arsenite and 62% of arsenate were bound to AHA. They estimated that under environmentally relevant conditions at least 10% of arsenate can be bound to dissolved organic carbon (DOC) in aquatic environments. They hypothesized that an OH[–] ligand exchange reaction between As species and alcoholic (–OH) groups of NOM could be the mechanism of such binding. Lenoble et al.³¹ investigated the interaction of arsenite and arsenate to Suwanee River humic acid (SRHA) in the absence and presence of Ca²⁺ by fluorescence spectroscopy. Based on sorption data and fluorescence-quenching phenomena of SRHA, they concluded the formation of only a binary complex for arsenite and a mixture of binary and Ca²⁺-bridged ternary complexes for arsenate. They determined the stability constant of these complexes assuming monodentate binding to carboxylic and alcoholic groups of SRHA. Furthermore, during modeling of As K-edge extended X-ray absorption fine structure (EXAFS) spectra of samples obtained by equilibrating arsenite with Fe-spiked peat, Hoffmann et al.²⁵ had to include C in addition to Fe for the second shell. They determined coordination numbers (CN) of 1.5–2.0 for C at a distance of 2.70–2.77 Å from As. However, because of the contribution from a Fe back-scatterer at a similar distance, the CN of C must be treated with caution. They also estimated that at least 27% of total arsenite was bound to phenolic groups, in addition to ternary complexation via Fe³⁺ bridging. Similarly, Guénet et al.³² provided XAS-based evidence for the complexation of arsenate and arsenite mixtures with the organic matter by As–O–C bond formation, in addition to As binding to Fe nanoparticle aggregates during oxidation of

reduced soil suspensions. However, to the best of our knowledge, the extent of arsenite and arsenate binding to NOM by complexation exclusively with oxygen-containing functional groups, with spectroscopic evidence of As–O–C bond formation, has never been investigated. The limited availability of this information obscures the potential importance of NOM to bind arsenite and arsenate in systems that have a low content of polyvalent metal cations for ternary complexation and low content of thiol groups to make significant thiol coordination. Also, the complexation of thioarsenate with NOM has not previously been investigated.

The objective of the present study was, therefore, to investigate the importance and determine the structural parameters for complexation of different As species (including monothioarsenate) with oxygen-containing functional groups of NOM. The objective was accomplished by equilibrating individual As species with low metal-containing purified peat (as a representative for NOM) under anoxic conditions, followed by determining the local coordination environment of As in the peat by As K-edge XAS analysis. The findings of this study will help to better constrain geochemical models for simulating the interaction of As species with NOM in aquatic and terrestrial environments. In general, this study will also develop our limited understanding of neutral to oxyanionic species complexation to NOM, a topic that is not as developed as metal cation complexation to NOM.¹⁷

■ MATERIALS AND METHODS

Materials. This study used purified peat as a model NOM compound. For details on the collection, purification, and characterization of this peat, see Besold et al.^{33,34} Briefly, the peat was collected from an ombrotrophic peatland near Bad Buchau, Germany (Federseemoor).²⁶ After collection, it was wet-sieved to a size fraction of 63–250 μm and washed once with 0.1 M HCl to decrease the mineral content, followed by washing several times with deionized water (Milli-Q, Millipore, ≥18.2 MΩ cm) until the pH value returned back to the initial pH of 4.5. The washed peat was freeze-dried, homogenized, and stored in the dark inside a glovebox (*p*_{O₂} < 1 ppm) until further use. The purified peat had carbon, sulfur, and ash contents of 55.0, 0.22, and 2.51 wt %, respectively. Concentrations of polyvalent metal cations (e.g., Fe³⁺, Al³⁺), that may facilitate ternary complexation between As species and peat, were low (<0.2 wt %). Fourier transform infrared spectroscopic analysis revealed the presence of aliphatic alcohol, phenol, and carboxyl C as the reactive functional moieties in the peat. ¹³C cross-polarization/magic-angle spinning-nuclear magnetic resonance (CP/MAS-NMR) spectroscopic analysis determined cellulose- and lignin-rich chemical backbone structure of the peat with carbonyl, alcoholic, and carboxylic groups to account for 2, 6, and 8% of the total NMR-active C, respectively. As the As sorption experiments were conducted at two pH values (presented in the following section), an attempt was made to determine the effect of the pH change (4.5–7.0) of the reaction medium on the molecular structure of the peat (Supporting Information Section 1). It was found that the pH change of the reaction medium did not change the overall structure of the peat, except it increased deprotonation of carboxylic and alcoholic groups with increasing pH (Supporting Information Figure SI-1).

Monothioarsenate was used as a representative thioarsenate species, since it is often reported as the major thioarsenic

species formed under diverse natural settings and is structurally analogous to arsenate.^{6,10,33,35} Because there is no commercial standard available, monothioarsenate was synthesized in the laboratory, with a purity of 90% (5% arsenate and 5% arsenite).³³ All other chemicals of analytical grade, including arsenite and arsenate standards, were purchased from Fluka, Alfa Aesar, or Sigma-Aldrich. All glassware used in this study was acid-washed, rinsed with deionized water (Milli-Q, Millipore, ≥ 18.2 M Ω cm), and dried before use.

Sorption Experiment. An independent equilibrium sorption experiment with three replicates was conducted for each As species at pH 4.5 (± 0.3) and 7.0 (± 0.3). For this experiment, ~ 0.2 g of dry peat was incubated with variable concentrations (0–1000 μ M) (0–4.6 mmol As/mol C) of each As species in 46 mL anoxic background electrolytic solution of 30 mM NaCl (to fix the ionic strength) containing 0.15 mM NaN₃ (to inhibit microbial activity).^{17,25,26,36} Relatively high concentrations of As compared to that commonly observed in the environment was chosen for the equilibration to ensure a sufficiently high concentration of As, required for the EXAFS study, to be present in the peat after the equilibration. Incubation was conducted for 96 h, as determined by a preliminary kinetic study (Supporting Information Section 2). An additional rationale for the 96 h incubation time was to make our results directly comparable to other As-NOM studies, which used the same peat before.^{25,26} The incubation procedure for the isotherm study was similar to that of the kinetic study, as detailed in the Supporting Information. After equilibration, the peat residue was freeze-dried, homogenized, and stored in the dark at the ambient temperature inside a glovebox until further analysis. Because the uncertainty was high with the quantification of As by ICP-MS in the solution after incubation, as observed during the kinetic study (Supporting Information Section 2), the amount of As sorbed to the peat in the equilibrium study was not determined by the difference in dissolved As concentration before and after equilibration. Instead, it was determined in the peat itself by microwave-assisted digestion with 65% HNO₃ and 30% H₂O₂ followed by quantification of As by ICP-MS (ICP-MS, XSeries2, Thermo-Fisher).^{6,33} The conditional distribution coefficient (K_{OC}) (L/kg C) of As was determined as $K_{OC} = C_p/C_s$, where C_p and C_s represent the As concentration in peat (μ g/kg C) and the As concentration in solution (μ g/L) after equilibration, respectively. C_s was determined by subtracting the amount of As sequestered into peat from that initially present in the equilibrated solution.

Arsenic K-Edge XAS Analysis. To determine the local coordination environment of As in the peat after equilibration, the As K-edge (11 867 eV) XAS analysis was performed at The Rossendorf Beamline (ROBL) at the European Synchrotron Radiation Facility (ESRF), Grenoble, France, and at the beamline 11-2 of the Stanford Synchrotron Radiation Light-source (SSRL), Stanford, USA. To aid the EXAFS modeling of the sample spectra, triethyl arsenite ((C₂H₅O)₃As) (TEA), purchased from Sigma-Aldrich, was measured as a reference standard at ROBL, ESRF. Samples were measured in fluorescence mode, while the TEA standard was measured in transmission mode. Samples and the standard were measured at about 15 K using a He cryostat to avoid beam damage and to minimize thermal disorder in the structure. Details on beamline setup, sample preparation, analysis, data reduction, and modeling are provided in the Supporting Information.

RESULTS AND DISCUSSION

Complexation of As Species with Peat. Amounts of As sorbed to peat at different equilibrated concentrations of the three As species at pH 4.5 and 7.0 are illustrated in Figure 1.

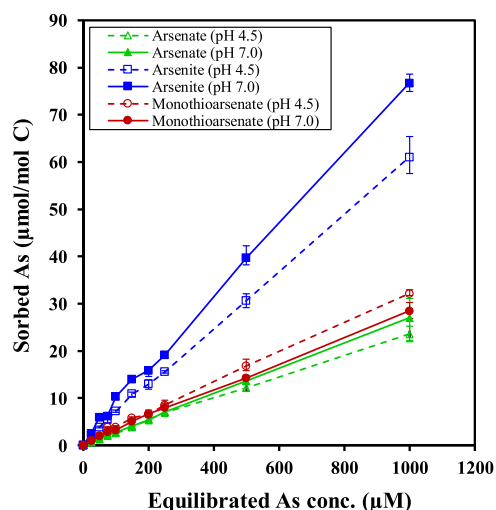


Figure 1. Sorption of three As species to peat at different equilibrated concentrations at pH 4.5 and 7.0. Symbols and error bars represent average and range of the replicates.

Among the three tested species, maximum sorption was observed for arsenite, followed by monothioarsenate and arsenate, even though the difference between the extent of monothioarsenate and arsenate sorption was small. Earlier studies have reported higher sorption of arsenate to AHA and SRHA compared to arsenite.^{17,21,37} The reason for the contradictory results is not clear so far. The maximum sorption capacity of the peat was not exhausted even with the highest equilibrated arsenite concentration of 1000 μ M (4.6 mmol As/mol C). In agreement with earlier studies,^{17,21,30,31,37} the sorption of arsenite and arsenate was stronger at pH 7.0 than at pH 4.5. The pH effect was more prominent for arsenite compared to arsenate. However, for monothioarsenate the sorption was stronger at pH 4.5, which can be attributed to the partial transformation of monothioarsenate to arsenite at this pH, as reflected in the XANES spectra discussed in the following section. The calculated $\log K_{OC}$ (L/kg C) at pH 7.0 were 0.83–1.01 (mean: 0.90) for arsenite, 0.40–0.56 (mean: 0.47) for monothioarsenate, and 0.34–0.41 (mean: 0.38) for arsenate; at pH 4.5, corresponding values were 0.73–0.85 (mean: 0.78), 0.44–0.66 (mean: 0.52), and 0.31–0.38 (mean: 0.35). Hoffmann et al. by equilibrating 0.275 mmol arsenite/mol C of the same peat at pH 7.0 did not observe any sorption of As in one set of experiments,²⁶ whereas in another set of experiments found a sorption of ~ 160 mg As/kg peat (46.7 μ mol As/mol C),²⁵ which provides a $\log K_{OC}$ value of 0.94, consistent with that found in the present study. In our study, the experimental uncertainty, presented by the error bar, was occasionally large; however, a general decreasing trend of $\log K_{OC}$ with the increase of the As/NOM ratio was observed in the system for all three As species at both pH values (Supporting Information Figure SI-3). Earlier studies have also reported a similar decreasing trend of distribution coefficients for arsenate and arsenite binding to NOM with increasing As/NOM ratios.^{17,30}

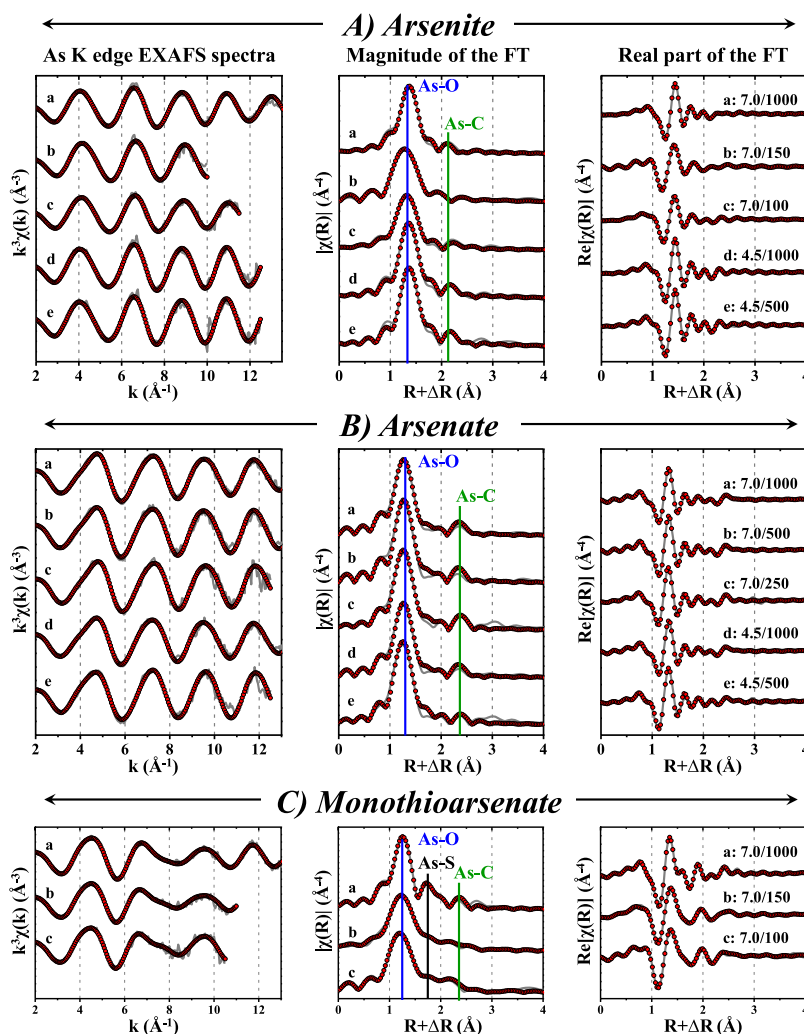


Figure 2. k^3 -weighted As K-edge EXAFS spectra and magnitude and real part of the FT of peat equilibrated with (A) arsenite, (B) arsenate, and (C) monothioarsenate. Gray lines and red dots represent data and best model fit, respectively. The position of peak corresponding to As–O, As–S, and As–C single scattering path in the magnitude of FT is shown by blue, black, and green solid vertical line, respectively. Sample labels represent equilibrated pH and As concentration.

EXAFS Modeling and Complexation Mechanisms.

Normalized As K-edge XANES spectra of peat after equilibration with arsenite, arsenate, and monothioarsenate at two pH values together with various reference standards are displayed in Supporting Information Figure SI-4. The edge energy (E_0) of the peat equilibrated with arsenite and arsenate at both pH values appeared at the respective position of arsenite ($\sim 11\,869$ eV) and arsenate ($\sim 11\,873$ eV) reference standards, indicating no species transformation during equilibration. Similarly, monothioarsenate was not transformed to other species at pH 7.0, as indicated by the similar E_0 of samples and reference standard at $\sim 11\,871$ eV. However, at pH 4.5, the spectra of the two monothioarsenate-treated peat samples showed two features at the position of monothioarsenate and arsenite standards, suggesting a partial transformation of monothioarsenate to arsenite during equilibration at this pH. Our earlier study³³ showed that monothioarsenate can be transformed into arsenite at acidic pH in the presence of S(II)-treated peat, which makes the transformation reaction kinetically feasible by sorbing arsenite (product of transformation) from the solution. The current study suggests that this acid-assisted transformation will be

feasible in the presence of any sorbent that sorbs arsenite more strongly than monothioarsenate. Based on the findings from the XANES analysis, EXAFS modeling was performed for all analyzed peat samples equilibrated with arsenite and arsenate at two pH values and monothioarsenate at pH 7.0; for the two peat samples equilibrated with monothioarsenate at pH 4.5, linear combination fitting (LCF) of the XANES spectra was performed.

The EXAFS spectrum of TEA was modeled first (Supporting Information Section 6) so that its structural parameters could be used to constrain different paths during the shell-fit analysis of the peat samples. The structural model for the shell-fit analysis of TEA included an As–O and an As \cdots C single-scattering (SS) path and a triangular As–O–C multiple-scattering (MS) path (path I, XI, and XIII, respectively in Supporting Information Table SI-1). The fitted interatomic distances (R) of the As–O and As \cdots C paths were 1.78 and 2.78 Å, respectively, while the fitted Debye–Waller parameters (σ^2) were 0.0021 and 0.0059 Å $^{-1}$, respectively (Supporting Information Table SI-2).

The k^3 -weighted As K-edge EXAFS spectra and their corresponding Fourier transforms (FT, magnitudes and real

Table 1. EXAFS Parameters Determined by Shell-Fit Analysis of the As K-edge EXAFS Spectra of the Peat Equilibrated with Different Concentrations of Arsenite and Arsenate at pH 4.5 and 7.0 and Monothioarsenate at pH 7.0 Only

As species	sample label	k-range	path	CN ^a	R ^b (Å)	σ^2 ^c (Å ²)	ΔE_0 ^d (eV)	R-factor ^e (%)	red χ^2 ^f
arsenite	7.0/1000	2.2–13.0	As–O	3.0^g	1.80(0 ^h)	0.0022(3)	0.9(6)	1.5	362
			As···C	1.7(4)	2.74(3)	0.0059ⁱ			
	7.0/150	2.2–9.5	As–O	3.0	1.78(0)	0.0023(3)	1.6(7)	0.6	60
			As···C	1.0(3)	2.73(4)	0.0059			
	7.0/100	2.2–11.0	As–O	3.0	1.79(0)	0.0031(3)	1.4(6)	1.0	62
			As···C	1.4(3)	2.73(3)	0.0059			
4.5/1000	2.2–12.0	As–O	3.0	1.80(0)	0.0010(4)	1.1(7)	1.7	144	
		As···C	2.1(5)	2.73(3)	0.0059				
4.5/500	2.2–12.0	As–O	3.0	1.80(1)	0.0006(4)	1.4(8)	2.2	122	
		As···C	2.4(5)	2.74(3)	0.0059				
arsenate	7.0/1000	2.2–12.5	As–O	4.0	1.69(0)	0.0016(4)	1.7(8)	1.7	407
			As···C	3.2(10)	2.84(2)	0.0059			
	7.0/500	2.2–12.5	As–O	4.0	1.69(1)	0.0009(5)	1.3(11)	3.4	372
			As···C	3.4(14)	2.82(3)	0.0059			
	7.0/250	2.2–12.0	As–O	4.0	1.68(1)	0.0011(4)	2.1(9)	2.3	110
			As···C	3.1(11)	2.82(3)	0.0059			
	4.5/1000	2.2–12.5	As–O	4.0	1.69(1)	0.0017(4)	0.9(9)	2.1	315
			As···C	3.0(10)	2.82(3)	0.0059			
	4.5/500	2.2–12.0	As–O	4.0	1.68(1)	0.0006(5)	(–)0.8(9)	3.2	260
Monothioarsenate	7.0/1000	2.2–12.5	As–O	3.0	1.71(0)	0.0034(4)	1.0(6)	0.7	171
			As–S	1.0	2.08(1)	0.0042(9)			
			As···C	2.6(5)	2.78(2)	0.0059			
	7.0/150	2.2–10.5	As–O	3.0	1.72(1)	0.0045(5)	1.6(7)	0.6	60
			As–S	1.0	2.10(1)	0.0048(10)			
			As···C	2.9(5)	2.82(2)	0.0059			
	7.0/100	2.2–10.0	As–O	3.0	1.72(1)	0.0031(5)	1.0(9)	0.8	33
			As–S	1.0	2.11(1)	0.0027(11)			
			As···C	3.4(7)	2.81(2)	0.0059			

^aCoordination number (path degeneracy). ^bInteratomic distance or mean half path length (bond distance for atom in the first-shell). ^cDebye–Waller parameter. ^dEnergy-shift parameter, was the same for all paths. ^eR-factor = $\sum_i(\text{data}_i - \text{fit}_i)^2 / \sum_i \text{data}_i$. ^fred χ^2 = $(N_{\text{idp}}/N_{\text{pts}}) \sum_i ((\text{data}_i - \text{fit}_i)/\epsilon_i)^2 / (N_{\text{idp}} - N_{\text{var}})^{-1}$, where N_{idp} : the number of independent points in the model fit, N_{pts} : the total number of data points, N_{var} : the number of variables in the fit, ϵ_i : the uncertainty in the i th data point. ^gValues in bold were fixed in the fit. ^hValues in parenthesis represent uncertainty in the last significant figure of the fitted parameters. ⁱThis value was determined by fitting the TEA (reference standard) spectrum. Various multiple scattering paths (see text for details) were included in the fit and constrained in terms of three single scattering paths (Table SI-1). Passive amplitude reduction factor (S_0^2) was set to 1.0 for shell-fit analysis of all the samples.

parts) of peat samples equilibrated with arsenite and arsenate at two pH values and monothioarsenate at pH 7.0 are shown in Figure 2. Morlet wavelet transforms analysis³⁸ of the respective As K-edge EXAFS spectra did not indicate the presence of any heavy back-scatterer (e.g., Fe) up to 3 Å distance from the As atom, similar to TEA (Supporting Information Figure SI-6). The FT of the k^3 -weighted EXAFS spectra of arsenite-, arsenate-, and monothioarsenate-treated peat samples were characterized by two peaks: a major peak at $R + \Delta R \approx 1.3$ Å for all three As species and a small peak at $R + \Delta R \approx 2.2$ Å for arsenite (Figure 2A) and at ~ 2.3 Å for arsenate and monothioarsenate (Figure 2B,C). Similar to TEA, these peaks were assigned to the nearest-neighbor O atom in the first shell and C atom in the second shell, respectively. For the monothioarsenate-treated peat samples, an additional peak appeared at $R + \Delta R \approx 1.8$ Å (Figure 2C), which can be attributed to S in the first shell.³⁵ Accordingly, the structural model used for the shell-fit analysis of the arsenite-treated peat samples included an As–O and As···C SS path. In addition, a triangular As–O–O MS path with the AsO₃ pyramid was necessary for the peat equilibrated with 150 μM arsenite at pH 7.0. Similarly, for the arsenate-treated peat samples, the model

included an As–O and As···C SS path (except for the peat equilibrated with 500 μM arsenate at pH 4.5) and three MS paths within the AsO₄ tetrahedron. For the monothioarsenate-treated peat samples, in addition to an As–O and As···C SS path and two MS paths within the AsSO₃ tetrahedron, an As–S SS path was also required for the analysis. The design of these structural models is discussed in details in Supporting Information Section 8. Furthermore, as the peat used in our experiments had a sulfur content of 0.22 wt %, alternative structural models were tested to assess the possibility of As sorption to the peat through complexation with inherent thiol groups (Supporting Information Section 9). However, as these alternative models could not provide meaningful fit results, this possibility was discarded. The final fits for arsenite-, arsenate-, and monothioarsenate-treated peat samples are displayed in Figure 2 and EXAFS parameters are listed in Table 1.

In the arsenite-treated peat samples, the average $R_{\text{As–O}}$ was 1.79 ± 0.01 Å (\pm std. dev.) (range: 1.78–1.80 Å), consistent with reported As–O bond lengths in the AsO₃ pyramid.^{39,40} For As···C path, the fitted R was 2.73 ± 0.01 Å (2.73–2.74 Å) with CN of 1.7 ± 0.6 (1.0–2.4). The fitted $R_{\text{As···C}}$ values are consistent with the bindings of arsenite to the oxyg-

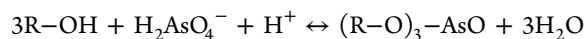
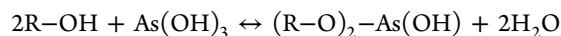
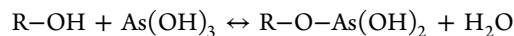
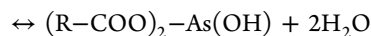
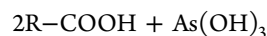
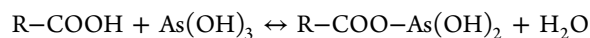
containing functional groups of the peat. For example, in TEA, where the AsO_3 pyramids are complexed to alcoholic groups, the $R_{\text{As}\cdots\text{C}}$ value was determined as 2.78 Å (Table SI-2). A previous study³⁹ showed that when AsO_3 pyramids are complexed to carboxylic groups, relatively shorter $R_{\text{As}\cdots\text{C}}$ values (2.58–2.68 Å) are expected due to possible hydrogen bonding between the H atom of the arsenite molecule and carbonyl O of the carboxyl group. The intermediate $R_{\text{As}\cdots\text{C}}$ values in peat possibly suggest that AsO_3 pyramids were complexed to both carboxylic and alcoholic groups (aliphatic and/or aromatic), resulting in average intermediate values for $R_{\text{As}\cdots\text{C}}$. The complexation of AsO_3 pyramids with carboxylic and alcoholic groups in peat is consistent with their increased deprotonation (Supporting Information Figure SI-1) and therefore increased nucleophilicity, which resulted in higher sorption of arsenite with increasing pH (Figure 1). The effect of increased nucleophilicity of peat with increasing pH on the As binding to peat is discussed in more detail in the following section. Because carboxylic groups ($\text{p}K_{\text{a}}$: ~3.0 to ~5.0)^{41,42} are expected to be more deprotonated compared to alcoholic groups ($\text{p}K_{\text{a}}$: ~8.5 to ~9.5)^{41,42} at the studied pH values (4.5 and 7.0), we anticipate that arsenite was predominantly complexed to carboxylic rather than alcoholic groups of the peat. The study by Hoffmann et al.²⁵ determined similar $R_{\text{As}\cdots\text{C}}$ (R : 2.70–2.77 Å) and $\text{CN}_{\text{As}\cdots\text{C}}$ (CN : 1.5–2.0) when arsenite was equilibrated with Fe-spiked peat at pH 7.0, 8.4, and 8.8 and attributed As bindings due to the binary complexation to phenolic groups of the peat, in addition to the ternary complexation through Fe bridging. Considering that the uncertainty associated with the determination of CN by the fitting of EXAFS data is ~25%, it was not possible to determine with certainty whether each AsO_3 pyramid in arsenite-treated peat was attached to one or two carboxylic and alcoholic groups. A change of equilibrium pH and arsenite concentrations did not have a significant impact on fitted EXAFS parameters (Table 1).

Because of the higher oxidation state of As in the arsenate-treated peat, the average $R_{\text{As}-\text{O}}$ was considerably shorter (1.69 ± 0.01 , 1.68–1.69 Å) compared to that in the arsenite-treated peat samples. These fitted $R_{\text{As}-\text{O}}$ values are similar to reported As–O bond lengths within the AsO_4 tetrahedron.⁴³ The fitted $R_{\text{As}\cdots\text{C}}$ and $\text{CN}_{\text{As}\cdots\text{C}}$ were 2.83 ± 0.01 Å (2.82–2.84 Å) and 3.2 ± 0.2 (3.0–3.4), respectively. Even for the peat equilibrated with 500 μM arsenate at pH 4.5, where the inclusion of the As \cdots C path in the model was not statistically required, the fitted R (2.79 Å) and CN (2.3) of this path were comparable to other samples. Guénet et al.³² determined comparable $R_{\text{As}\cdots\text{C}}$ (2.85–2.86 Å) and $\text{CN}_{\text{As}\cdots\text{C}}$ (1.7–2.1) for the mixture of arsenate and arsenite in 5–0.2 μm size fractions during oxidation of reduced soil suspensions. The fitted $R_{\text{As}\cdots\text{C}}$ values in the arsenate-treated peat are also consistent with the complexation of AsO_4 tetrahedra with the oxygen-containing functional groups of the peat. It is worth noting that in the arsenate-treated peat samples, $R_{\text{As}\cdots\text{C}}$ was relatively longer than that in the arsenite-treated peat (Table 1). To test whether variable k -ranges used for the fitting of EXAFS data (Table 1) was responsible for such difference in $R_{\text{As}\cdots\text{C}}$ values for the arsenite- and arsenate-treated peat, another fitting exercise was performed with a similar k -range of 2.2–9.5 (the lowest k -range fitted for any sample, Table 1) (Supporting Information Section 10). However, the comparison of this fitting results to that obtained with the variable k -ranges (Supporting Information Table SI-5) suggests that the use of variable k -

ranges for the EXAFS data fitting had a negligible influence on $R_{\text{As}\cdots\text{C}}$ values. We hypothesize that the longer $R_{\text{As}\cdots\text{C}}$ values in the arsenate-treated peat were due to the complexation of AsO_4 tetrahedra with predominantly alcoholic groups rather than carboxylic groups of the peat. Similar to arsenite treatment, there was no effect of equilibrium pH and As concentration on the fitted EXAFS parameters for the arsenate treatment (Table 1).

In the monothioarsenate-treated peat, the fitted $R_{\text{As}-\text{O}}$ was 1.72 ± 0.01 Å (1.71–1.72 Å), longer than $R_{\text{As}-\text{O}}$ in arsenate-treated peat but shorter than arsenite-treated peat. The $R_{\text{As}-\text{S}}$ was determined as 2.10 ± 0.02 Å (2.08–2.11 Å), indicating that S was double-bonded to As.³⁵ Suess et al.³⁵ determined $R_{\text{As}-\text{O}}$ and $R_{\text{As}-\text{S}}$ in a pure monothioarsenate standard by EXAFS modeling as 1.70 and 2.13 Å, respectively. Despite the same oxidation state of As, the longer $R_{\text{As}-\text{O}}$ in the AsSO_3 tetrahedron compared to that in the AsO_4 tetrahedron in peat can be attributed to the less positive partial charge on the central As atom because of replacement of the double-bonded O with double-bonded S, which is less electronegative. For the As \cdots C path, the fitted R and CN were 2.80 ± 0.02 Å (2.78–2.82 Å) and 3.0 ± 0.4 (2.6–3.4), respectively, closer to values obtained for the arsenate-treated peat. The fitted $R_{\text{As}\cdots\text{C}}$ values suggest that AsSO_3 tetrahedra were also complexed with oxygen-containing functional groups of the peat, possibly predominantly with the alcoholic groups, similar to arsenate. To the best of our knowledge, this is the first study that has determined the local coordination environment of As when monothioarsenate is complexed to NOM. The LCF analysis of the two peat samples equilibrated with monothioarsenate at the pH 4.5 (Supporting Information Figure SI-7) indicated that there was a mixture of almost equal proportion of monothioarsenate (44–58%) and arsenite (44–60%) complexed to peat with the above determined coordination environments (Supporting Information Table SI-5).

Factors Affecting the Complexation of As Species with NOM. Based on the above-presented modeling of the As K-edge EXAFS data, we suggest the following chemical reactions for the sorption of different As species to peat



The underlying mechanism of these chemical reactions is the nucleophilic attack by carboxylic and alcoholic groups to the partially positively charged As atom.¹⁷ Factors that can mutually influence the rate and thereby the extent of As complex formation are (i) the extent of partial positive charge on the central As atom in As species, (ii) the electrostatic interaction between As species and NOM, and (iii) the nucleophilicity of the carboxylic and alcoholic groups. These factors are discussed in the following.

Among the three tested As species, the partial positive charge on the central As atom is highest in arsenate, followed

by monothioarsenate and arsenite. This is because in arsenate there is an additional O double-bonded to As, compared to arsenite. In monothioarsenate, this double-bonded O is replaced by the less electronegative S. Therefore, considering the partial positive charge on the As atom, the expected order of complexation for three As species would be arsenate > monothioarsenate > arsenite. However, this order is found to be exactly opposite (Figure 1), which may be explained by the electrostatic repulsion between peat and As species. Because of the deprotonation of the carboxylic and alcoholic groups, peat was negatively charged at the studied pH of 4.5 and 7.0. Considering the pK_a values of three As species, at these pH values, the predominant species for arsenite should be neutral H_3AsO_3 , whereas for arsenate and monothioarsenate it should be negatively charged $H_2AsO_4^-$ and $H_2AsSO_3^-$, respectively.^{1,44} Therefore, when arsenate and monothioarsenate were equilibrated with peat, the effect of electrostatic repulsion between negatively charged peat and negatively charged As species predominated over the effect of higher partial positive charge on the As center in these two species, resulting in lower sorption. On the other hand, because the predominant arsenite species at the studied pH was neutral, the electrostatic repulsion between negatively charged peat and neutral As species would be low, resulting in higher complexation despite lower partial positive charge on the As center. This electrostatic repulsion could also be responsible for the predominant binding of arsenate and monothioarsenate to the relatively less deprotonated alcoholic groups with longer $R_{As...C}$ (even longer than in TEA) and higher $CN_{As...C}$ compared to more deprotonated carboxylic groups at the studied pH (Table 1). It is worth mentioning that in the study of Hoffmann et al.,²⁵ the $R_{As...C}$ in Fe-spiked peat equilibrated with arsenite was longer at pH ≥ 8.4 than at pH 7.0. This can also be due to the formation of more negatively charged $H_2AsO_3^-$ species at these pH, which are close to the pK_a of H_3AsO_3 (9.2),¹ resulting in increased electrostatic repulsion and therefore preferential bindings to alcoholic groups. Despite electrostatic repulsion, the driving force for complexation of As species to NOM is attributed to the stability gained by donation of the negative charge of the carboxylate ($-COO^-$) and alkoxide ($-O^-$) ions to the partially positively charged As atom and/or additional chelation and hydrogen bonding with nearby functional groups.¹⁷

Considering electrostatic repulsion between As species and peat, the complexation of arsenate and monothioarsenate is expected to be higher at pH 4.5 than at pH 7.0, which is also reflected in their reaction stoichiometry determined by EXAFS modeling. However, the complexation of arsenate was slightly higher at pH 7.0 (Figure 1). We hypothesize that the stronger complexation of arsenate at pH 7.0 might be because of an increased nucleophilicity of alcoholic groups due to the increased deprotonation with an increase of pH from 4.5 to 7.0 (Supporting Information Figure SI-1), which overcame the effect of electrostatic repulsion between arsenate and peat. The effect of increased nucleophilicity was more prominent for arsenite due to the involvement of neutral H_3AsO_3 in the complexation, resulting in considerably higher complexation at pH 7.0 compared to 4.5 (Figure 1). Few earlier studies have reported that complexation of arsenite and arsenate with NOM is highest around near-neutral pH.^{17,21} At moderate to high alkaline pH, hydroxyl ions of the reaction medium compete with carboxylic and alcoholic groups for the nucleophilic attack to the As center and thus decrease the binding of arsenite and

arsenate to carboxylic and alcoholic groups. Despite the increased nucleophilicity of the peat at pH 7.0, the higher complexation of monothioarsenate at pH 4.5 was due to its partial transformation to arsenite at this pH (Supporting Information Table SI-5) as discussed above. Guénet et al. highlighted the possibility of arsenate and arsenite complexation with biomolecules inherited from microbial activities through As–O–C bond formation. The involvement of microbes in the complexation of As species to peat in the current study could also make the complexation reactions less dependent on the pH of the bulk solution. However, considering that the peat was acid-washed, freeze-dried,³³ and NaN_3 was added to the reaction medium, it is expected that the involvement of microbes in the complexation of As species with the peat was negligible, if not completely removed.³⁶

Environmental Implication. This study shows that oxygen-containing functional groups of NOM can be a potential site for the sorption of As species to NOM-rich sediments with low contents of other As sorbents, such as different metal hydroxides. The extent of As sorption to NOM via complexation with the oxygen-containing functional groups can be compared to two other well-established sorption mechanisms (viz. binary complexation with thiol groups and ternary complexation via Fe^{3+} bridging) by accounting the results of Hoffmann et al.^{25,26} for arsenite. They determined the sorption of arsenite to NOM via these two mechanisms at pH 7.0 using the same peat after spiking with variable amounts of S(-II) and Fe^{3+} . Although the extent of binding through oxygen-containing functional groups is considerably lower (log K_{OC} : 0.83–1.01) compared to that through thiol groups (log K_{OC} : 0–2.9),²⁶ it is comparable to the binding through Fe^{3+} -bridged ternary complex formation (log K_{OC} : 1.2–1.5).²⁵ This comparison implies that oxygen-containing functional groups can constitute alternative or additional sites for bindings of different As species to NOM. The higher extent of arsenite sorption to organic thiol groups compared to oxygen-containing functional groups can be attributed to the high affinity of trivalent arsenite for sulfur to form a strong covalent complex due to the small electronegativity difference.⁴⁵ The complexation of As species to oxygen-containing functional groups can be a potential As sequestration process to the solid-phase in an anoxic sulfur-deficient ombrotrophic peat bog. However, similar complexation in the aqueous phase may increase the mobility of As species. For example, as suggested by Hoffmann et al.,²⁵ complexation to the oxygen-containing functional groups can explain the concomitant release of As and DOC in water from an ombrotrophic peat bog after the flood event⁴⁶ and wetland sediments,⁴⁷ association of arsenite with DOC in blackwater of the Great Dismal Swamp, Virginia, USA,⁴⁸ and complexation of arsenate and arsenite to humic and fulvic acids leached from the mangrove forest-floor sediments.⁴⁹ This study further implies that in systems, where NOM is the predominant sorbent for As species, arsenate and thioarsenates can have higher mobility than the arsenite. This is in contrast to the general assumption often made of arsenite being more mobile than arsenate in the environment.¹ Therefore, the interaction of As species with the oxygen-containing functional groups needs to be accounted to accurately predict the behavior of As in NOM-rich sediments.

■ ASSOCIATED CONTENT

Supporting Information

The Supporting Information is available free of charge on the ACS Publications website at DOI: 10.1021/acs.est.9b03020.

Additional experiments, interpretation of XANES and EXAFS spectra, tables, figures, and analytical methods (PDF)

■ AUTHOR INFORMATION

Corresponding Author

*E-mail: ashis@iiserb.ac.in. Phone: +91 755 269 1389.

ORCID

Ashis Biswas: 0000-0001-6285-1407

Andreas C. Scheinost: 0000-0002-6608-5428

Britta Planer-Friedrich: 0000-0002-0656-4283

Notes

The authors declare no competing financial interest.

■ ACKNOWLEDGMENTS

This research was funded by the Alexander von Humboldt Foundation, Germany, through a postdoctoral scholarship to A.B. B.P.-F. and J.B. acknowledge the funding by the Deutsche Forschungsgemeinschaft (DFG, German Research Foundation)—PL302/20. A.B. acknowledges the funding from the Indian Institute of Science Education and Research (IISER) Bhopal (INST/EES/2017081) and the Science and Engineering Research Board (SERB), Department of Science and Technology (DST), Govt. of India (ECR/2017/002353), during the preparation of the manuscript. Arsenic K-edge XAS analysis was performed at the ESRF, Grenoble, France, and the SSRL, a Directorate of SLAC National Accelerator Laboratory and an Office of Science User Facility operated for the US Department of Energy, Office of Science, Office of Basic Energy Sciences under contract no. DE-AC02-76SF00515. We are also thankful to C. Kerl and D. Halder (University of Bayreuth), A. Rossberg (ESRF), and R. Davis (SSRL) for their support during data collection at the ROBL and 11-2 beamlines.

■ REFERENCES

- (1) Smedley, P. L.; Kinniburgh, D. G. A review of the source, behaviour and distribution of arsenic in natural waters. *Appl. Geochem.* **2002**, *17*, 517–568.
- (2) Nordstrom, D. K. Enhanced: Worldwide Occurrences of Arsenic in Ground Water. *Science* **2002**, *296*, 2143–2145.
- (3) Brammer, H.; Ravenscroft, P. Arsenic in Groundwater: A Threat to Sustainable Agriculture in South and South-East Asia. *Environ. Int.* **2009**, *35*, 647–654.
- (4) Fendorf, S.; Michael, H. A.; Van Geen, A. Spatial and Temporal Variations of Groundwater Arsenic in South and Southeast Asia. *Science* **2010**, *328*, 1123–1127.
- (5) Stauder, S.; Raue, B.; Sacher, F. Thioarsenates in Sulfidic Waters. *Environ. Sci. Technol.* **2005**, *39*, 5933–5939.
- (6) Planer-Friedrich, B.; London, J.; McCleskey, R. B.; Nordstrom, D. K.; Wallschläger, D. Thioarsenates in Geothermal Waters of Yellowstone National Park: Determination, Preservation, and Geochemical Importance. *Environ. Sci. Technol.* **2007**, *41*, 5245–5251.
- (7) Suess, E.; Wallschläger, D.; Planer-Friedrich, B. Stabilization of Thioarsenates in Iron-Rich Waters. *Chemosphere* **2011**, *83*, 1524–1531.
- (8) Stucker, V. K.; Williams, K. H.; Robbins, M. J.; Ranville, J. F. Arsenic Geochemistry in a Biostimulated Aquifer: An Aqueous Speciation Study. *Environ. Toxicol. Chem.* **2013**, *32*, 1216–1223.

- (9) Stucker, V. K.; Silverman, D. R.; Williams, K. H.; Sharp, J. O.; Ranville, J. F. Thioarsenic Species Associated with Increased Arsenic Release during Biostimulated Subsurface Sulfate Reduction. *Environ. Sci. Technol.* **2014**, *48*, 13367–13375.

- (10) Planer-Friedrich, B.; Schaller, J.; Wismeth, F.; Mehlhorn, J.; Hug, S. J. Monothioarsenate Occurrence in Bangladesh Groundwater and Its Removal by Ferrous and Zero-Valent Iron Technologies. *Environ. Sci. Technol.* **2018**, *52*, 5931–5939.

- (11) Dixit, S.; Hering, J. G. Comparison of Arsenic (V) and Arsenic (III) Sorption onto Iron Oxide Minerals: Implications for Arsenic Mobility. *Environ. Sci. Technol.* **2003**, *37*, 4182–4189.

- (12) Couture, R.-M.; Rose, J.; Kumar, N.; Mitchell, K.; Wallschläger, D.; Van Cappellen, P. Sorption of Arsenite, Arsenate, and Thioarsenates to Iron Oxides and Iron Sulfides: A Kinetic and Spectroscopic Investigation. *Environ. Sci. Technol.* **2013**, *47*, 5652–5659.

- (13) Biswas, A.; Gustafsson, J. P.; Neidhardt, H.; Halder, D.; Kundu, A. K.; Chatterjee, D.; Berner, Z.; Bhattacharya, P. Role of Competing Ions in the Mobilization of Arsenic in Groundwater of Bengal Basin: Insight from Surface Complexation Modeling. *Water Res.* **2014**, *55*, 30–39.

- (14) Redman, A. D.; Macalady, D. L.; Ahmann, D. Natural Organic Matter Affects Arsenic Speciation and Sorption onto Hematite. *Environ. Sci. Technol.* **2002**, *36*, 2889–2896.

- (15) Wang, S.; Mulligan, C. N. Effect of Natural Organic Matter on Arsenic Release from Soils and Sediments into Groundwater. *Environ. Geochem. Health* **2006**, *28*, 197–214.

- (16) Ritter, K.; Aiken, G. R.; Ranville, J. F.; Bauer, M.; Macalady, D. L. Evidence for the Aquatic Binding of Arsenate by Natural Organic Matter - Suspended Fe(III). *Environ. Sci. Technol.* **2006**, *40*, 5380–5387.

- (17) Buschmann, J.; Kappeler, A.; Lindauer, U.; Kistler, D.; Berg, M.; Sigg, L. Arsenite and Arsenate Binding to Dissolved Humic Acids: Influence of pH, Type of Humic Acid, and Aluminum. *Environ. Sci. Technol.* **2006**, *40*, 6015–6020.

- (18) Bauer, M.; Blodau, C. Arsenic Distribution in the Dissolved, Colloidal and Particulate Size Fraction of Experimental Solutions Rich in Dissolved Organic Matter and Ferric Iron. *Geochim. Cosmochim. Acta* **2009**, *73*, 529–542.

- (19) Sharma, P.; Rolle, M.; Kocar, B.; Fendorf, S.; Kappler, A. Influence of Natural Organic Matter on As Transport and Retention. *Environ. Sci. Technol.* **2011**, *45*, 546–553.

- (20) Langner, P.; Mikutta, C.; Kretzschmar, R. Arsenic Sequestration by Organic Sulphur in Peat. *Nat. Geosci.* **2012**, *5*, 66–73.

- (21) Thanabalasingam, P.; Pickering, W. F. Arsenic sorption by humic acids. *Environ. Pollut., Ser. B* **1986**, *12*, 233–246.

- (22) Sharma, P.; Ofner, J.; Kappler, A. Formation of Binary and Ternary Colloids and Dissolved Complexes of Organic Matter, Fe and As. *Environ. Sci. Technol.* **2010**, *44*, 4479–4485.

- (23) Mikutta, C.; Kretzschmar, R. Spectroscopic Evidence for Ternary Complex Formation between Arsenate and Ferric Iron Complexes of Humic Substances. *Environ. Sci. Technol.* **2011**, *45*, 9550–9557.

- (24) Liu, G.; Fernandez, A.; Cai, Y. Complexation of Arsenite with Humic Acid in the Presence of Ferric Iron. *Environ. Sci. Technol.* **2011**, *45*, 3210–3216.

- (25) Hoffmann, M.; Mikutta, C.; Kretzschmar, R. Arsenite Binding to Natural Organic Matter: Spectroscopic Evidence for Ligand Exchange and Ternary Complex Formation. *Environ. Sci. Technol.* **2013**, *47*, 12165–12173.

- (26) Hoffmann, M.; Mikutta, C.; Kretzschmar, R. Bisulfide Reaction with Natural Organic Matter Enhances Arsenite Sorption: Insights from X-Ray Absorption Spectroscopy. *Environ. Sci. Technol.* **2012**, *46*, 11788–11797.

- (27) Hoffmann, M.; Mikutta, C.; Kretzschmar, R. Arsenite Binding to Sulfhydryl Groups in the Absence and Presence of Ferrihydrite: A Model Study. *Environ. Sci. Technol.* **2014**, *48*, 3822–3831.

- (28) Catrouillet, C.; Davranche, M.; Dia, A.; Bouhnik-Le Coz, M.; Pédrot, M.; Marsac, R.; Gruau, G. Thiol Groups Controls on Arsenite

Binding by Organic Matter: New Experimental and Modeling Evidence. *J. Colloid Interface Sci.* **2015**, *460*, 310–320.

(29) Catrouillet, C.; Davranche, M.; Dia, A.; Bouhnik-Le Coz, M.; Demangeat, E.; Gruau, G. Does As(III) Interact with Fe(II), Fe(III) and Organic Matter through Ternary Complexes? *J. Colloid Interface Sci.* **2016**, *470*, 153–161.

(30) Liu, G.; Cai, Y. Complexation of Arsenite with Dissolved Organic Matter: Conditional Distribution Coefficients and Apparent Stability Constants. *Chemosphere* **2010**, *81*, 890–896.

(31) Lenoble, V.; Dang, D. H.; Loustau Cazalet, M.; Mounier, S.; Pfeifer, H.-R.; Garnier, C. Evaluation and Modelling of Dissolved Organic Matter Reactivity toward AsIII and AsV - Implication in Environmental Arsenic Speciation. *Talanta* **2015**, *134*, 530–537.

(32) Guénet, H.; Davranche, M.; Vantelon, D.; Bouhnik-Le Coz, M.; Jardé, E.; Dorcet, V.; Demangeat, E.; Jestin, J. Highlighting the Wide Variability in Arsenic Speciation in Wetlands: A New Insight into the Control of the Behavior of Arsenic. *Geochim. Cosmochim. Acta* **2017**, *203*, 284–302.

(33) Besold, J.; Biswas, A.; Suess, E.; Scheinost, A. C.; Rossberg, A.; Mikutta, C.; Kretzschmar, R.; Gustafsson, J. P.; Planer-Friedrich, B. Monothioarsenate Transformation Kinetics Determining Arsenic Sequestration by Sulfhydryl Groups of Peat. *Environ. Sci. Technol.* **2018**, *52*, 7317–7326.

(34) Besold, J.; Kumar, N.; Scheinost, A. C.; Lezama Pacheco, J.; Fendorf, S.; Planer-friedrich, B. Antimonite Complexation with Thiol and Carboxyl/Phenol Groups of Peat Organic Matter. *Environ. Sci. Technol.* **2019**, *53*, 5005–5015.

(35) Suess, E.; Scheinost, A. C.; Bostick, B. C.; Merkel, B. J.; Wall Schlaeger, D.; Planer-Friedrich, B. Discrimination of Thioarsenites and Thioarsenates by X-Ray Absorption Spectroscopy. *Anal. Chem.* **2009**, *81*, 8318–8326.

(36) Buschmann, J.; Canonica, S.; Lindauer, U.; Hug, S. J.; Sigg, L. Photoirradiation of Dissolved Humic Acid Induces Arsenic(III) Oxidation. *Environ. Sci. Technol.* **2005**, *39*, 9541–9546.

(37) Warwick, P.; Inam, E.; Evans, N. Arsenics Interaction with Humic Acid. *Environ. Chem.* **2005**, *2*, 119–124.

(38) Funke, H.; Scheinost, A. C.; Chukalina, M. Wavelet Analysis of Extended X-Ray Absorption Fine Structure Data. *Phys. Rev. B: Condens. Matter Mater. Phys.* **2005**, *71*, 094110.

(39) Kamenar, B.; Bruvo, M.; Butumović, J. Structures Involving Unshared Electron Pair. The Crystal Structures of As(OCOCH₃)₃ and As₂O(OCOCH₃)₄. *Z. Anorg. Allg. Chem.* **1993**, *619*, 943–946.

(40) Ona-Nguema, G.; Morin, G.; Juillot, F.; Calas, G.; Brown, G. E. EXAFS Analysis of Arsenite Adsorption onto Two-Line Ferrihydrite, Hematite, Goethite, and Lepidocrocite. *Environ. Sci. Technol.* **2005**, *39*, 9147–9155.

(41) Tipping, E. *Cation Binding by Humic Substances*; Cambridge University Press: Cambridge, 2002.

(42) Gondar, D.; Lopez, R.; Fiol, S.; Antelo, J. M.; Arce, F. Characterization and Acid – Base Properties of Fulvic and Humic Acids Isolated from Two Horizons of an Ombrotrophic Peat Bog. *Geoderma* **2005**, *126*, 367–374.

(43) Kitahama, K.; Kiriya, R.; Baba, Y. Refinement of the Crystal Structure of Scorodite. *Acta Crystallogr., Sect. B: Struct. Crystallogr. Cryst. Chem.* **1975**, *31*, 322–324.

(44) Thilo, E.; Hertzog, K.; Winkler, A. Über Vorgänge Bei Der Bildung Des Arsen(V)-Sulfids Beim Ansäuern von Tetrathioarsenatlösungen. *Z. Anorg. Allg. Chem.* **1970**, *373*, 111–121.

(45) O'Day, P. A. Chemistry and Mineralogy of Arsenic. *Elements* **2006**, *2*, 77–83.

(46) Rothwell, J. J.; Taylor, K. G.; Ander, E. L.; Evans, M. G.; Daniels, S. M.; Allott, T. E. H. Arsenic Retention and Release in Ombrotrophic Peatlands. *Sci. Total Environ.* **2009**, *407*, 1405–1417.

(47) Kalbitz, K.; Wennrich, R. Mobilization of Heavy Metals and Arsenic in Polluted Wetland Soils and Its Dependence on Dissolved Organic Matter. *Sci. Total Environ.* **1998**, *209*, 27–39.

(48) Haque, S. E.; Tang, J.; Bounds, W. J.; Burdige, D. J.; Johannesson, K. H. Arsenic Geochemistry of the Great Dismal

Swamp, Virginia, USA: Possible Organic Matter Controls. *Aquat. Geochem.* **2007**, *13*, 289–308.

(49) Mandal, S. K.; Ray, R.; Chowdhury, C.; Majumder, N.; Jana, T. K. Implication of Organic Matter on Arsenic and Antimony Sequestration in Sediment: Evidence from Sundarban Mangrove Forest, India. *Bull. Environ. Contam. Toxicol.* **2013**, *90*, 451–455.

Supporting Information

Complexation of arsenite, arsenate, and monothioarsenate with oxygen-containing functional groups of natural organic matter: An XAS Study

Ashis Biswas^{1,2*}, Johannes Besold¹, Carin Sjöstedt³, Jon Petter Gustafsson³, Andreas C. Scheinost^{4,5}, Britta Planer-Friedrich¹

¹*Department of Environmental Geochemistry, Bayreuth Center for Ecology and Environmental Research (BAYCEER), Bayreuth University, 95440 Bayreuth, Germany*

²*Department of Earth and Environmental Sciences, Indian Institute of Science Education and Research (IISER) Bhopal, Bhopal Bypass Road, Bhauri 462066, Madhya Pradesh, India*

³*Department of Soil and Environment, Swedish University of Agricultural Sciences, Box 7014, 750 07, Uppsala, Sweden*

⁴*The Rossendorf Beamline (ROBL) at ESRF, 38043 Grenoble, France*

⁵*Institute of Resource Ecology, Helmholtz-Zentrum Dresden-Rossendorf (HZDR), Bautzner Landstraße 400, 01328 Dresden, Germany*

***Contact and corresponding author: Ashis Biswas (phone: +91 755 269 1389; e-mail: ashis@iiserb.ac.in)**

(Pages: 25, Tables: 6, and Figures: 7)

Table of Contents

1. Effect of pH change of the reaction medium on the molecular structure of purified model-peat.....	2
2. Kinetic study for sorption of arsenite and monothioarsenate to the model-peat at pH of 4.5 and 7.0	4
3. Arsenic K-edge X-ray absorption spectroscopic analysis and EXAFS data modeling.....	6
4. Variation of log K _{oc} with equilibrated As concentration	8
5. Arsenic K-edge XANES spectra and edge energy.....	9
6. Fitting of the As K-edge EXAFS data of triethyl arsenite ((C ₂ H ₅ O) ₃ As) (TEA).....	10
7. Morlet wavelet transforms (WT) analysis	13
8. Designing of structural models for the shell-fit analysis of the As K-edge EXAFS spectra of peat samples equilibrated with arsenite and arsenate at pH 4.5 and 7.0 and for monothioarsenate at pH 7.0	14
9. Alternative shell-fit analysis to test the possibility of As species sorption to the peat through complexation with inherent thiol groups	16
10. Possible influences of variable <i>k</i> -ranges, used for the fitting of EXAFS data on fitted EXAFS parameters for the As-C path in arsenite-, arsenate-, and monothioarsenate-treated peat samples	20
11. Linear combination fitting (LCF) of As K-edge XANES spectra of the peat equilibrated with monothioarsenate at pH 4.5	21
12. References.....	23

1. Effect of pH change of the reaction medium on the molecular structure of purified model-peat

Since As sorption experiments were conducted at two pH values, an attempt was made to determine the effect of pH change of the reaction medium on the molecular structure of the peat. For this purpose, ~0.2 g of peat were incubated for 96 h at the pH values of 4.5, 6.0, and 7.0 in 46 ml anoxic background electrolytic solution of 30 mM NaCl containing 0.15 mM NaN₃ in glass septum bottles capped and sealed with butyl rubber stoppers and aluminum caps, in an end-over-end shaker in the dark at ambient temperature (similar as in As sorption experiments, but without adding any As species). After incubation, freeze-dried peat samples were analyzed with a Bruker Vector 22 FT-IR spectrometer¹ to determine any change in the molecular structure of the peat. Absorption bands were assigned to different functional groups based on Gondar et al.², Artz et al.³, and Rennert et al.⁴. FT-IR spectra normalized to 1 at 1450 cm⁻¹ for peat samples incubated at three pH values are displayed in SI Figure SI-1. Overall, the identical appearance of absorption bands and their positions (SI Figure SI-1a) suggest that the pH change of the reaction medium did not change the overall structure of the peat. However, with the increase of pH, the intensity of the characteristic absorption band of the carboxylic groups at 1720 cm⁻¹ was decreased with a concomitant increase of the band intensity of the carboxylate ion at 1630 cm⁻¹ and 1380 cm⁻¹. Similarly, the band intensity of the phenolic and aliphatic alcoholic group at the respective position of 1270 cm⁻¹ and 1040 cm⁻¹ was decreased with increase of pH. These results suggest that carboxylic and alcoholic groups in the peat were increasingly deprotonated with increase of pH.

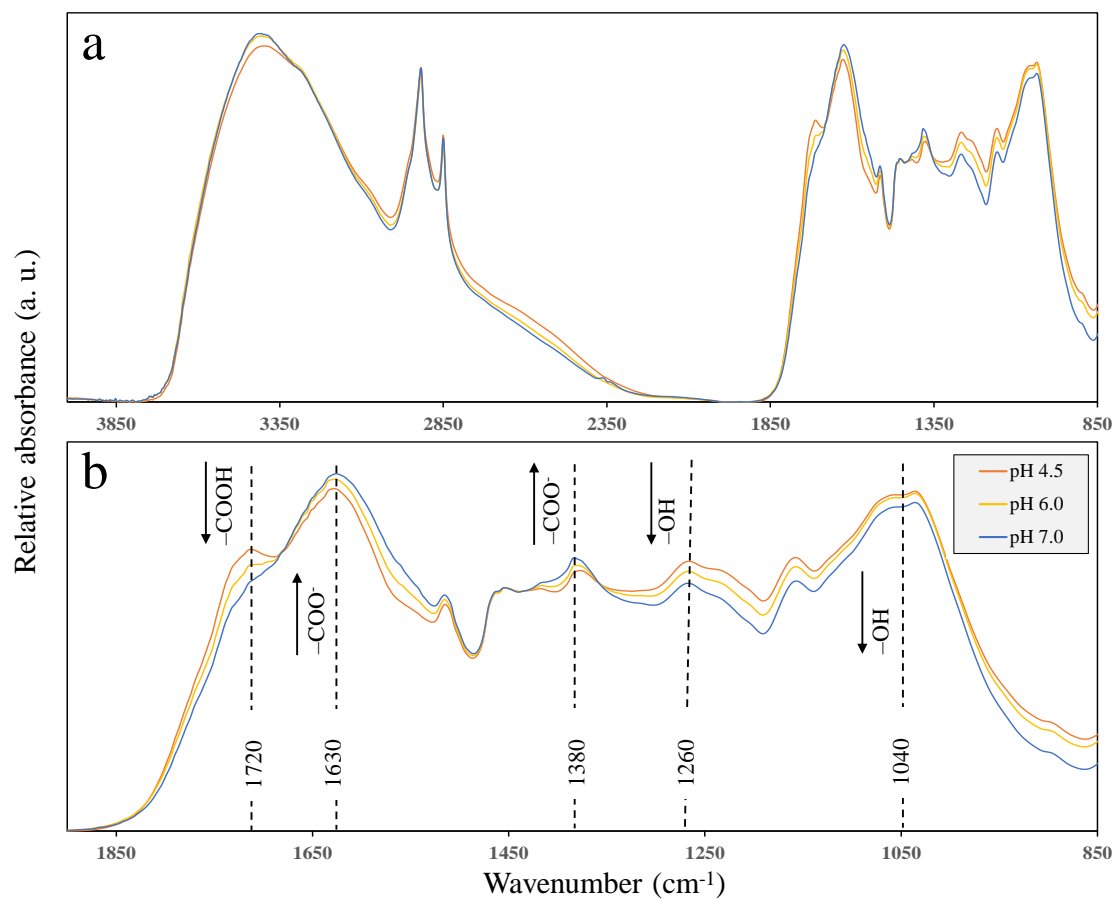


Figure SI-1: FT-IR spectra of purified-peat incubated for 96 h at pH 4.5, 6.0 and 7.0 in 30 mM NaCl and 0.15 mM NaN₃. Spectra were normalized to 1 at 1450 cm⁻¹. a) Spectra over the wavenumber range of 850 to 4000 cm⁻¹ and b) Same spectra over the wavenumber range of 850 to 2000 cm⁻¹. Arrows represent either increase or decrease of the specific absorption band.

2. Kinetic study for sorption of arsenite and monothioarsenate to the model-peat at pH of 4.5 and 7.0

A kinetic study was performed to determine the time required to reach equilibrium for sorption to the peat of arsenite at pH 4.5 (± 0.3) and 7.0 (± 0.3) and monothioarsenate at pH 7.0 (± 0.3) only. For monothioarsenate, the kinetic study was not conducted at pH 4.5, because a preliminary speciation study showed that at this pH it is partially converted to arsenite in the presence of peat (data not presented) (this is also reflected in the isotherm experiment of the current study presented in the main text). For the kinetic study, ~ 0.065 g of dry peat was incubated with 50 μM (0.25 mmol As/mol C) of arsenite and monothioarsenate in 15 mL anoxic background electrolytic solution of 30 mM NaCl in glass septum bottles capped and sealed with butyl rubber stoppers and aluminum caps. Incubation was conducted over a period of 0 to 192 h (eleven time steps) in an end-over-end shaker in the dark under anoxic conditions ($p\text{O}_2 < 1$ ppm) at ambient temperature. To inhibit microbial activity, 0.15 mM NaN_3 (0.70 mmol/mol C) was added to the reaction medium. Incubation was conducted in three replicates in sacrifice-bottles for each time step. The desired pH was adjusted with anoxic HCl and NaOH solutions. After equilibration, the peat-solution slurry was filtered through a 0.2 μm nylon filter using a vacuum filtration unit inside a glove box. An aliquot of 10 mL filtrate was stored with 30% H_2O_2 and 32.5% HNO_3 for the quantification of total As by inductively coupled plasma-mass spectrometry (ICP-MS, XSeries2, Thermo-Fisher).⁵ The amount of As sorbed to the peat after different time intervals were determined by the difference between the As concentration in solution before and after the incubation. Results show that the amount of As sorbed to the peat for three replicates of a particular time step varied largely as reflected by large error bars (SI Figure SI-2); this was because of the uncertainty associated with quantification of As in solution by ICP-MS, probably because of change in ionization conditions in the plasma due to variable contents of dissolved organic carbon released during incubation. With this range of experimental uncertainty, it was concluded that an incubation period of 96 h would be enough to reach equilibrium for the sorption of arsenite and monothioarsenate to the peat at the studied pH. Since arsenate is structurally analogous to monothioarsenate, it is expected that an incubation period of 96 h would also be enough for arsenate to reach equilibrium for sorption to the peat.

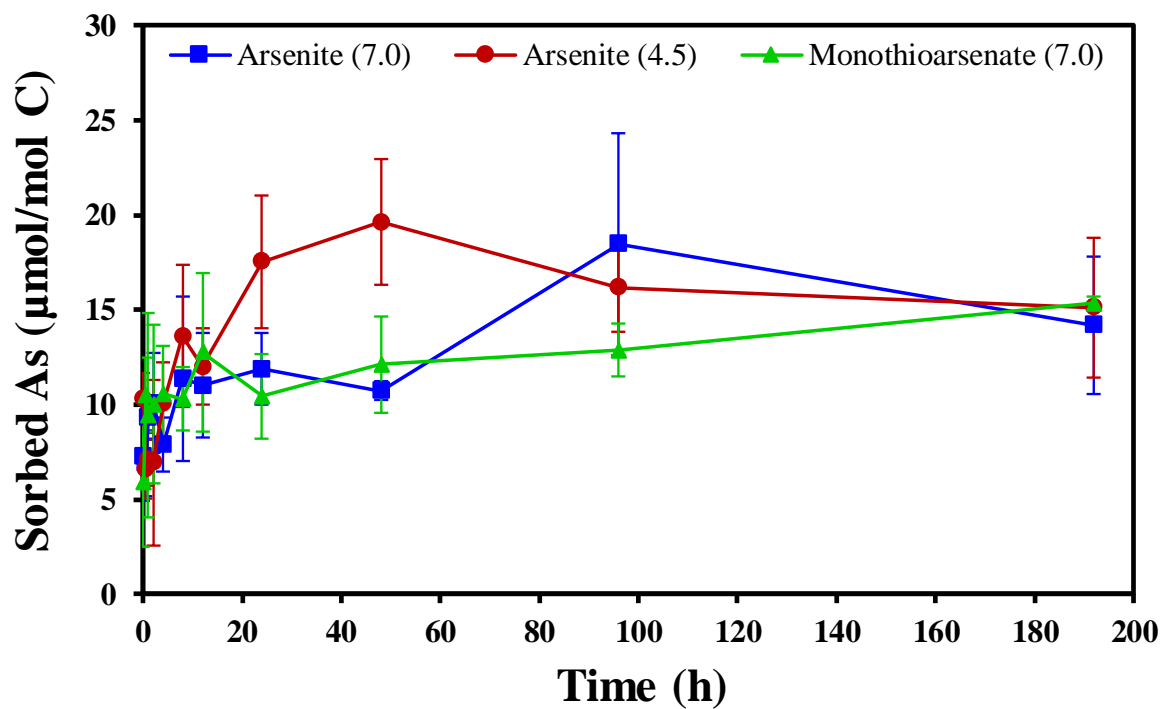


Figure SI-2: Sorption of arsenite and monothioarsenate to peat at pH 4.5 and 7.0 and 7.0, respectively at different time intervals. Symbols and error bars represent the average and standard deviation of three replicates.

3. Arsenic K-edge X-ray absorption spectroscopic analysis and EXAFS data modeling

Arsenic K-edge (11867 eV) X-ray absorption near edge structure (XANES) and extended X-ray absorption fine structure (EXAFS) spectra of the samples and reference standard were collected at the Rossendorf Beamline (ROBL) at the European Synchrotron Radiation Facility (ESRF), Grenoble, France and at the beamline 11-2 of the Stanford Synchrotron Radiation Lightsources (SSRL), Stanford, USA. To select particular energy from the incident whitebeam, these beamlines used either a Si(111) (ROBL) or a Si(220) double crystal monochromator, calibrated to the L₃-edge energy of Au foil (energy 11919 eV). To correct small energy drifts of the monochromator between scans, the Au foil was continuously monitored during data collection. Higher harmonics in the beam were rejected by using two 1.2 m and 1.4 m long Pt-coated mirrors (ROBL) and two 1 m long Rh-coated Si mirrors (11-2). For the collection of data, freeze-dried homogenized peat samples and the standard were loaded into sample holders and sealed with Kapton tape. Triethyl arsenite ((C₂H₅O)₃As) (TEA) was appropriately diluted with dry ethanol to avoid self-absorption. Samples were measured in fluorescence mode using solid-state Ge detectors, while the standard was measured in transmission mode using gas-filled ionization detectors. Measurements were conducted using He cryostats at 15 K to avoid beam damage and to minimize thermal disorder in the structure. To increase the signal-to-noise ratio in the data, multiple spectra of the same sample were collected and merged following standard procedures.⁶ Merged spectra were normalized with the software Athena,⁷ by fitting a linear function for the pre-edge region and a quadratic polynomial for the post-edge region. The edge energy (E₀) was defined as the energy at zero crossings of the second derivative of the XANES spectra. The background was subtracted from the normalized spectra by using the Autobk algorithm implemented in Athena, with R_{bkg} values set to 0.85 for arsenite- and 0.80 for arsenate- and monothioarsenate-treated peat samples and standard with *k*-weight set to 2. Normalized and background corrected *k*³-weighted EXAFS spectra were Fourier transformed using a Hanning window with a window parameter of 1 Å⁻¹. To extract structural parameters (CN: path degeneracy or coordination number, R: interatomic distance or mean half path length (bond length for first shell atom), and σ²: Debye – Waller parameter), least-square shell-fit analysis was performed in R-space within the fitting range of 0.85 – 4 Å for arsenite and 0.80 – 4 Å for arsenate and monothioarsenate samples, using the software Artemis.⁷ The amplitude reduction factor (S₀²) was set to 1.0 for the samples and the standard. Theoretical phase-shift and amplitude functions were calculated with FEFF v.6.0,⁸ implemented in Artemis, using the crystal structures of tris(acetate-O)-arsenic,⁹ scorodite,¹⁰ mapimite,¹¹ tris(phenylthio)arsine,¹²

and trisodium trioxothioarsenate dodecahydrate.¹³ The approach for all shell fit analysis was to build the structural model step-by-step, starting with the first shell (bottom-up approach). For any shell, a single scattering (SS) path was included in the model at first. In addition to checking the meaningfulness of the fitted parameters, a statistical F-Test was performed to judge whether inclusion of a particular SS path to the model improved the fit significantly with a confidence level of $\geq 67\%$.¹⁴ If a SS path turned out to be essential for the fit then its corresponding multiple scattering (MS) path was tested. The MS paths were always constrained in terms of an SS path to avoid an increase in the number of fit parameters and to check the robustness of the structural model. An MS path was considered to be significant when it decreased the reduced χ^2 ($\text{red}\chi^2$), a goodness-of-fit parameter, by at least 20%. Then SS path for the next shell was included in the fit and so on. The number of fit parameters in the final model for TEA and samples never exceed 44% of the independent data points, calculated by Stern's rule.¹⁵

4. Variation of log K_{OC} with equilibrated As concentration

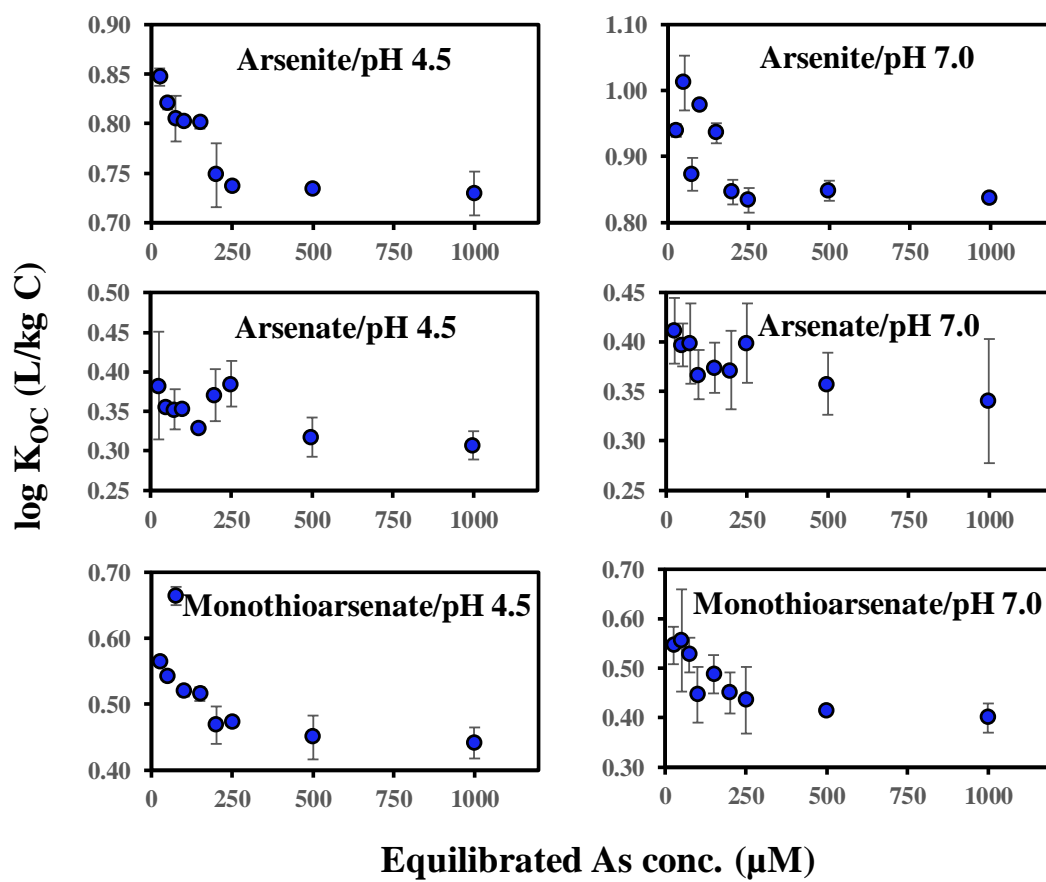


Figure SI-3: Variation of $\log K_{OC}$ with equilibrated As concentration, more specifically with equilibrated As/NOM ratio, as the amount of NOM was fixed to 0.2 g. Error bar represents $\pm 1 \sigma$.

5. Arsenic K-edge XANES spectra and edge energy

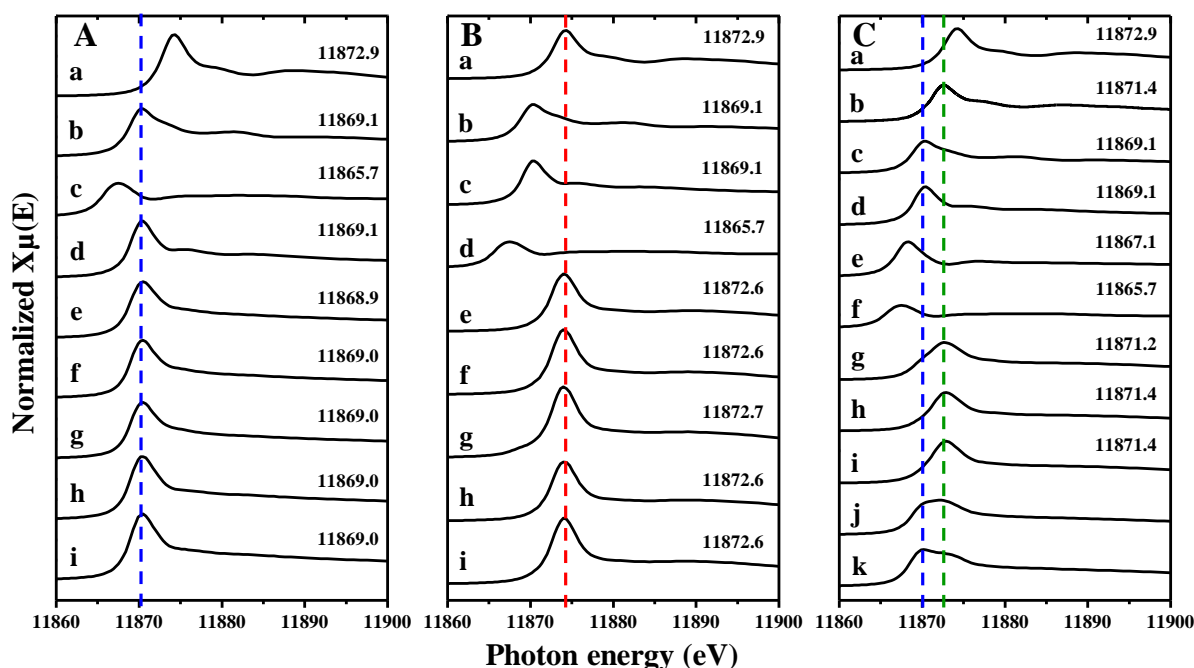


Figure SI-4: Arsenic K-edge normalized XANES spectra and edge energy of the reference standards and peat samples equilibrated with arsenite, arsenate, and monothioarsenate at pH 4.5 and 7.0: (A) a) disodium arsenate, b) sodium meta arsenite, c) arsenopyrite, d) triethyl arsenite (TEA), e, f, g) peat, respectively treated with 1000, 150, and 100 μM arsenite at pH 7.0, h, i) peat, respectively treated with 1000 and 500 μM arsenite at pH 4.5; (B) a) disodium arsenate, b) sodium meta arsenite, c) triethyl arsenite (TEA), d) arsenopyrite, e, f, g) peat, respectively treated with 1000, 500, and 250 μM arsenate at pH 7.0, h, i) peat, respectively treated with 1000 and 500 μM arsenate at pH 4.5; and (C) a) disodium arsenate, b) monothioarsenate, c) sodium meta arsenite, d) triethyl arsenite (TEA), e) orpiment, f) arsenopyrite, g, h, i) peat, respectively treated with 1000, 150, and 100 μM monothioarsenate at pH 7.0, j, k) peat, respectively treated with 1000 and 500 μM monothioarsenate at pH 4.5. Blue, red, and green dashed line represents white line peak position corresponding to arsenite, arsenate, and monothioarsenate, respectively.

6. Fitting of the As K-edge EXAFS data of triethyl arsenite ((C₂H₅O)₃As) (TEA)

The k^3 -weighted As K-edge EXAFS spectra and their corresponding FT (magnitudes and real parts) of TEA are presented in Figure SI-5. The major peak at $R+\Delta R \sim 1.3$ Å in the FT is due to the nearest neighbor O of the AsO₃ pyramid. This was followed by a small FT peak at $R+\Delta R \sim 2.2$ Å, which can be assigned to C in the second shell.^{9,16} Quantitative structural parameters of these two shells were determined by shell-fit analysis. The final model for TEA included an As-O and an As··C single-scattering (SS) path and a triangular As-O-C multiple-scattering (MS) path. The parameterization of these paths is presented in Table SI-1. The triangular As-O-O MS path within the AsO₃ pyramid (Table SI-1) was also tested but finally discarded, since it did not improve the fit significantly. Extracted structural parameters are listed in Table SI-2.

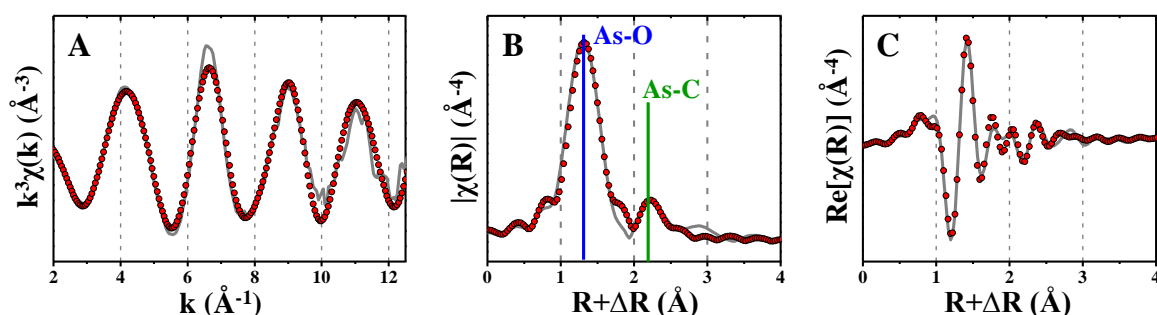


Figure SI-5: (A) k^3 -weighted As K edge EXAFS spectrum, (B) magnitude of Fourier transforms (FT), and (C) real part of FT of triethyl arsenite (TEA). Grey lines and red dots represent data and best model fit, respectively. The position of the peak corresponding to As-O and As-C single scattering path in the magnitude of FT is shown by blue and green solid vertical line, respectively.

Table SI-1: Parameterization of different paths in the final fitting model

S.N.	Path	CN	R	σ^2
I	As-O (AsO ₃)	3.0 ^a	R _{As-O}	σ^2_{As-O}
II	As-O (AsO ₄)	4.0	R _{As-O}	σ^2_{As-O}
III	As-O (AsSO ₃)	3.0	R _{As-O}	σ^2_{As-O}
IV	As-S	1.0	R _{As-S}	σ^2_{As-S}
V	Triangular As-O-O (AsO ₃)	6.0	$1.7568 \times R_{As-O}$	σ^2_{As-O}
VI	Triangular As-O-O (AsO ₄)	12.0	$(1 + (2/3)^{1/2}) \times R_{As-O}$	σ^2_{As-O}
VII	Colinear As-O-As-O (AsO ₄)	4.0	$2 \times R_{As-O}$	$4 \times \sigma^2_{As-O}$
VIII	Non-colinear As-O-As-O (AsO ₄)	12.0	$2 \times R_{As-O}$	$2 \times \sigma^2_{As-O}$
IX	Triangular As-O-O (AsSO ₃)	6.0	$(1 + (2/3)^{1/2}) \times R_{As-O}$	σ^2_{As-O}
X	Colinear As-O-As-O (AsSO ₃)	3.0	$2 \times R_{As-O}$	$4 \times \sigma^2_{As-O}$
XI	As...C (TEA)	3.0	R _{As...C}	$\sigma^2_{As...C}$
XII	As...C (Sample)	CN _{As...C}	R _{As...C}	$\sigma^2_{As...C}$
XIII	As-O-C	$2 \times CN_{As...C}$	$0.5(R_{As-O} + R_{As...C} + R_{O-C})$	$\sigma^2_{As...C}$

^aParameters in bold were fixed in the fit.

Table SI-2: EXAFS parameters determined by shell-fit analysis of the As K-edge EXAFS spectra of triethyl arsenite ((C₂H₅O)₃As) (TEA).

Sample	k -range	As-O			As-C			ΔE_0^a (eV)	R-factor ^b (%)	red χ^2 ^c
		CN ^d	R ^e (Å)	σ^{2f} (Å ²)	CN	R (Å)	σ^2 (Å ²)			
TEA	2.3-11.0	3.0 ^g	1.78(1 ^h)	0.0021(5)	3.0	2.78(2)	0.0059(30)	1.9(10)	2.2	469

^aEnergy-shift parameter, was the same for all paths. ^bR-factor = $\sum_i(\text{data}_i - \text{fit}_i)^2 / \sum_i \text{data}_i$. ^cred χ^2 = $(N_{\text{idp}}/N_{\text{pts}}) \sum_i ((\text{data}_i - \text{fit}_i)/\varepsilon_i)^2 (N_{\text{idp}} - N_{\text{var}})^{-1}$, where N_{idp} : the number of independent points in the model fit, N_{pts} : the total number of data points, N_{var} : the number of variables in the fit, ε_i : the uncertainty in the i^{th} data point. ^dCoordination number (path degeneracy). ^eInteratomic distance or mean half path length (bond distance for atom in the first-shell). ^fDebye – Waller parameter. ^gValues in bold were fixed in the fit. ^hValues in parenthesis represent uncertainty in the last significant figure of the fitted parameters. As-O-C MS path was included in the fit and constrained in terms of As-O and As-C SS paths (Table SI-1). Passive amplitude reduction factor (S_0^2) was set to 1.0.

7. Morlet wavelet transforms (WT) analysis

Wavelet transform (WT) analysis of the k^2 -weighted spectra of representative samples and TEA was performed to check possible contribution of heavy back-scatterers (e.g. Fe) in the region of $1.0 < R < 3.0$ by optimizing Morlet wavelets with $\eta = 4.0$ and $\sigma = 1.0$.¹⁷ The results of this analysis are displayed in the following figure:

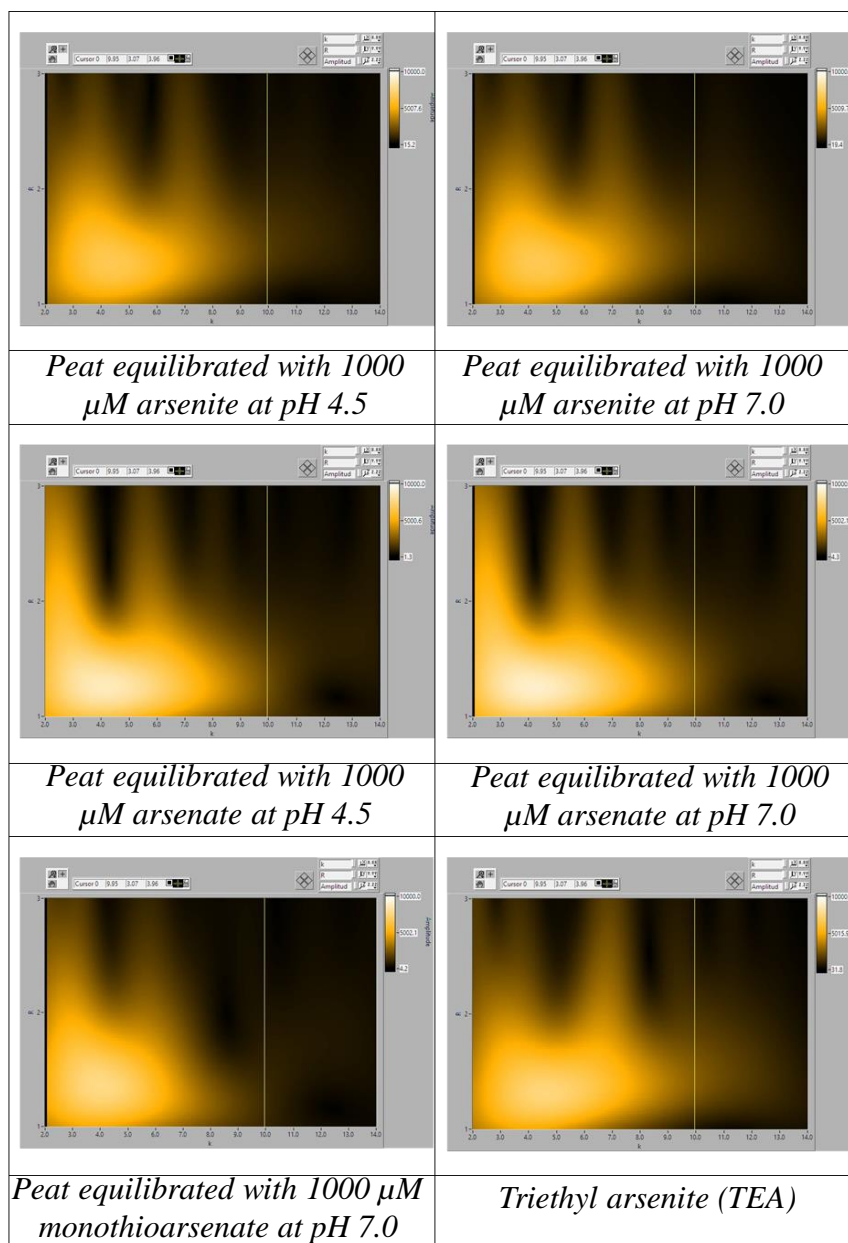


Figure SI-6: Morlet wavelet transforms (WT) analysis of As K-edge EXAFS spectra of the representative arsenite-, arsenate-, and monothioarsenate-treated peat samples and TEA ($\eta = 4.0$ and $\sigma = 1.0$).

8. Designing of structural models for the shell-fit analysis of the As K-edge EXAFS spectra of peat samples equilibrated with arsenite and arsenate at pH 4.5 and 7.0 and for monothioarsenate at pH 7.0

The k^3 -weighted As K-edge EXAFS spectra and their corresponding FT (magnitudes and real parts) of peat samples equilibrated with arsenite and arsenate at two pH values and monothioarsenate at pH 7.0 are shown in Figure 2 in the main text. The FT of the k^3 -weighted EXAFS spectra of arsenite-, arsenate-, and monothioarsenate-treated peat samples were characterized by two peaks: a major peak at $R+\Delta R \sim 1.3 \text{ \AA}$ and a small peak at $R+\Delta R \sim 2.2 \text{ \AA}$ for arsenite (Figure 2A) and $\sim 2.3 \text{ \AA}$ for arsenate and monothioarsenate (Figure 2B,C). Similar to TEA, these peaks were assigned to the nearest neighbor O in the first shell and C in the second shell, respectively. For the monothioarsenate-treated peat samples, an additional peak appeared at $R+\Delta R \sim 1.8 \text{ \AA}$ (Figure 2C), which can be attributed to S in the first shell.¹⁸ Accordingly, for all peat samples except that equilibrated with 500 μM arsenate at pH 4.5, the inclusion of As-O and As \cdots C SS paths (Table SI-1) in the structural model was essential to fit the sample spectra. For the three monothioarsenate-treated samples, an additional As-S SS path (Table SI-1) was also necessary for the fitting. For the peat equilibrated with 500 μM arsenate at pH 4.5, despite the small FT peak at $R+\Delta R \sim 2.3 \text{ \AA}$ the addition of As \cdots C SS path to the model after As-O SS path and MS paths within the AsO_4 tetrahedron (discussed latter) did not improve the fit significantly according to the F-Test (SI Section 3), although it decreased the R-factor.

Although the As-O-C MS path was essential to fit the TEA spectrum, this MS path (constrained similarly as for TEA, Table SI-1) did not improve the fit significantly for any sample according to the set criteria for the MS path (SI Section 3). For the arsenite-treated peat samples, the triangular As-O-O MS path within the AsO_3 pyramid (Table SI-1) was tested and found to be significant only for the peat equilibrated with 150 μM arsenite at pH 7.0, for which the $\text{red}\chi^2$ was decreased by 31% compared to the model that only contained the As-O SS path. However, for all arsenate-treated samples, when three MS paths within the AsO_4 tetrahedron, namely, triangular As-O-O, collinear As-O-As-O, and non-collinear As-O-As-O (Table SI-1) were included together in the fit, the $\text{red}\chi^2$ decreased on average by 52% (38-69%). Similarly, addition of triangular As-O-O and collinear As-O-As-O MS paths within the AsSO_3 tetrahedron (Table SI-1) decreased the $\text{red}\chi^2$ in the monothioarsenate-treated samples on average by 30% (23-36%), compared to the model with only As-O and As-S SS paths. Therefore, the final fit model included an As-O and an As \cdots C SS path for arsenite-treated

samples (in addition, a triangular As-O-O MS path for the peat equilibrated with 150 μM arsenite at pH 7.0); an As-O and an As...C (except the peat equilibrated with 500 μM arsenate at pH 4.5) SS path and three MS paths within the AsO_4 tetrahedron for arsenate-treated samples, and an As-O, an As-S, and an As...C SS path and two MS paths within the AsSO_3 tetrahedron for monothioarsenate-treated samples.

9. Alternative shell-fit analysis to test the possibility of As species sorption to the peat through complexation with inherent thiol groups

Since the used peat in our experiments has a sulfur content of 0.22 wt%, the possibility of As sorption to the peat through complexation with inherent thiol groups was tested. In the case of As species complexation to thiol groups, FT spectra of As-treated peat samples are expected to have one peak at $R+\Delta R \sim 1.8 \text{ \AA}$ (As-S SS path) and another peak at $\sim 2.8 \text{ \AA}$ (As...C SS path, where the C is bonded to the S: As-S-C), respectively.^{19,20} As mentioned before, the As-S SS peak was found only for the monothioarsenate-treated peat samples and the As...C SS peak at $\sim 2.8 \text{ \AA}$ was not found for any sample (Figure 2 in the main text), which possibly suggests that As species were not complexed to thiol groups. To further strengthen this interpretation, a shell-fit analysis was performed to test whether the inclusion of an As-S SS path in the first shell for the arsenite- and arsenate-treated peat and As...C SS path (at 2.8 \AA) in the second shell for the monothioarsenate-treated peat improve the fit significantly. It was found that for peat samples of all arsenite treatments and arsenate treatments at pH 4.5, the inclusion of an As-S SS path to the model was not possible due to very low to negative values for CN_{As-S} (Table SI-3). For samples of arsenate treatments at pH 7.0, either the CN_{As-S} was negative or the R_{As-S} was longer (SI Table SI-3) than that obtained for the same peat ($2.24\text{-}2.30 \text{ \AA}$)¹⁹ when treated with sulfide before equilibration with arsenite. Similarly, for monothioarsenate treatments at pH 7.0, either the $CN_{As...C}$ was negative or the $R_{As...C}$ was abnormal (very high or very low) (Table SI-4) compared to the expected value of 3.16 \AA determined for this peat.¹⁹ These results clearly suggest that complexation of As species to inherent thiol groups could not be a mechanism for their sorption to peat in our experiments.

Table SI-3: EXAFS parameters determined by shell-fit analysis of the As K-edge EXAFS spectra of the peat equilibrated with different concentrations of arsenite and arsenate at pH 4.5 and 7.0 considering two structural models: model 1 – contains only As-O single scattering (SS) path and model 2 – contains As-S SS path in addition to the As-O SS path.

As species	Sample label	k-range	N _{idp}	Model	N _{var}	As-O			As-S			ΔE_0^a (eV)	R-factor ^b (%)	red χ^2 ^c
						CN ^d	R ^e (Å)	σ^{2f} (Å ²)	CN	R (Å)	σ^2 (Å ²)			
Arsenite	7.0/1000	2.2-13.0	21	Model 1	3	3.2(1 ^g)	1.80(1)	0.002 ^{h,i}				0.0(6)	3.3	658
				Model 2	5	3.2(1)	1.80(1)	0.002	-0.1(1)	2.21(14)	0.003 ^j	0.1(9)	3.2	727
	7.0/150	2.2-9.5	14	Model 1	3	3.0(1)	1.78(1)	0.002				1.5(9)	1.6	148
				Model 2	5	3.0(1)	1.78(1)	0.002	0.1(1)	2.17(18)	0.003	1.2(15)	1.5	175
	7.0/100	2.2-11.0	17	Model 1	3	2.9(1)	1.79(1)	0.002				0.7(10)	3.1	206
				Model 2	5	2.9(1)	1.78(1)	0.002	0.1(1)	2.15(10)	0.003	0.2(14)	2.7	227
	4.5/1000	2.2-12.0	19	Model 1	3	3.6(1)	1.80(1)	0.002				0.1(8)	2.1	161
				Model 2	5	3.6(1)	1.80(1)	0.002	-0.1(1)	2.23(13)	0.003	0.1(9)	2.0	179
	4.5/500	2.2-12.0	19	Model 1	3	3.7(1)	1.80(1)	0.002				0.3(9)	2.5	125
				Model 2	5	3.8(1)	1.80(1)	0.002	-0.2(2)	2.10(6)	0.003	1.1(12)	2.7	135
Arsenate	7.0/1000	2.2-12.5	21	Model 1	3	4.4(2)	1.68(1)	0.002 ^k				-0.1(11)	3.7	1003
				Model 2	5	4.4(2)	1.69(1)	0.002	0.7(3)	2.42(3)	0.003	0.8(11)	3.2	832
	7.0/500	2.2-12.5	21	Model 1	3	4.8(2)	1.68(1)	0.002				-0.9(12)	3.9	502
				Model 2	5	4.9(3)	1.69(1)	0.002	-0.4(3)	2.14(5)	0.003	-0.9(13)	3.4	497
	7.0/250	2.2-12.0	20	Model 1	3	4.5(2)	1.68(1)	0.002				0.2(13)	4.0	253
				Model 2	5	4.6(2)	1.68(1)	0.002	0.8(3)	2.36(3)	0.003	1.5(12)	3.3	210
	4.5/1000	2.2-12.5	21	Model 1	3	4.4(2)	1.69(1)	0.002				-0.9(12)	4.0	743
				Model 2	5	4.5(2)	1.69(1)	0.002	-0.3(3)	2.15(7)	0.003	-0.9(13)	3.6	769
	4.5/500	2.2-12.0	20	Model 1	3	4.8(2)	1.68(1)	0.002				-1.3(12)	3.3	349
				Model 2	5	4.8(3)	1.68(1)	0.002	0.1(3)	1.96(13)	0.003	-1.8(19)	3.1	392

^aEnergy-shift parameter, was the same for all paths. ^bR-factor = $\sum_i(\text{data}_i - \text{fit}_i)^2 / \sum_i \text{data}_i$. ^cred $\chi^2 = (N_{\text{idp}}/N_{\text{pts}}) \sum_i ((\text{data}_i - \text{fit}_i) / \epsilon_i)^2 (N_{\text{idp}} - N_{\text{var}})^{-1}$, where N_{idp}: the number of independent points in the model fit, N_{pts}: the total number of data points, N_{var}: the number of variables in the fit, ϵ_i : the uncertainty in the ith data point. ^dCoordination number (path degeneracy). ^eInteratomic distance or mean half path length (bond distance for atom in the first-shell). ^fDebye – Waller parameter. ^gValues in parenthesis represent uncertainty in the last significant figure of the fitted parameters.

^hValues in bold were fixed in the fit. ⁱConstrained to σ^2 of TEA (reference standard). ^jConstrained to σ^2 of tris(phenyl)thioarsine as reported by Hoffmann et al.¹⁹. ^kConstrained to σ^2 of scorodite as reported by Halder et al.²¹ Passive amplitude reduction factor (S_0^2) was set to 1.0 for shell-fit analysis of all the samples.

Table SI-4: EXAFS parameters determined by shell-fit analysis of the As K-edge EXAFS spectra of the peat equilibrated with different concentrations of monothioarsenate at pH 7.0 considering three structural models: model 1 – contains As-O and As-S single scattering (SS) paths and two multiple scattering (MS) paths within the AsSO₃ tetrahedron (namely, triangular As-O-O and collinear As-O-As-O, constrained according to As-O SS path (Table SI-1)), model 2 – contains As···C(C bonded to S) SS path in addition to paths of the model 1, model 3 – contains As···C(C bonded to O) SS path in addition to paths of the model 1.

As species	Sample label	<i>k</i> -range	N _{idp}	Model	N _{var}	As-O			As-S			As···C(C bonded to O)			As···C(C bonded to S)			ΔE ^a ₀ (eV)	R-factor ^b (%)	redχ ^{2c}	
						CN ^d	R ^e (Å)	σ ^{2f} (Å ²)	CN	R (Å)	σ ² (Å ²)	CN	R (Å)	σ ² (Å ²)	CN	R (Å)	σ ² (Å ²)				
Monothioarsenate	7.0/1000	2.2-12.5	21	Model 1	5	3.0^g	1.70(1 ^h)	0.0034(5)	1.0	2.05(1)	0.0050(14)							(-)1.6(8)	1.7	379	
				Model 2	7	3.0	1.72(1)	0.0033(5)	1.0	2.09(1)	0.0036(11)				-2.7(7)	2.50(2)	0.011ⁱ		2.0(1)	1.3	299
				Model 3	7	3.0	1.71(0)	0.0034(4)	1.0	2.08(1)	0.0042(9)	2.6(5)	2.78(2)	0.0059^j					1.0(6)	0.7	171
	7.0/150	2.2-10.5	17	Model 1	5	3.0	1.71(1)	0.0049(8)	1.0	2.06(2)	0.0055(18)							(-)1.7(11)	1.7	166	
				Model 2	7	3.0	1.70(1)	0.0046(11)	1.0	2.05(2)	0.0051(22)				0.3(4)	0.89(6)	0.011	(-)2.8(21)	1.7	189	
				Model 3	7	3.0	1.72(1)	0.0045(5)	1.0	2.10(1)	0.0048(10)	2.9(5)	2.82(2)	0.0059					1.6(7)	0.6	60
	7.0/100	2.2-10.0	16	Model 1	5	3.0	1.70(1)	0.0033(9)	1.0	2.08(2)	0.0039(20)							(-)2.4(13)	2.3	89	
				Model 2	7	3.0	1.71(1)	0.0034(7)	1.0	2.09(2)	0.0039(16)				5.3(17)	3.66(4)	0.011	(-)1.1(9)	1.5	55	
				Model 3	7	3.0	1.72(1)	0.0031(5)	1.0	2.11(1)	0.0027(11)	3.4(7)	2.81(2)	0.0059					1.0(9)	0.8	33

^aEnergy-shift parameter, was the same for all paths. ^bR-factor = $\sum_i(\text{data}_i - \text{fit}_i)^2 / \sum_i \text{data}_i$. ^credχ² = $(N_{\text{idp}}/N_{\text{pts}}) \sum_i ((\text{data}_i - \text{fit}_i)/\epsilon_i)^2 (N_{\text{idp}} - N_{\text{var}})^{-1}$, where N_{idp}: the number of independent points in the model fit, N_{pts}: the total number of data points, N_{var}: the number of variables in the fit, ε_i: the uncertainty in the ith data point. ^dCoordination number (path degeneracy). ^eInteratomic distance or mean half path length (bond distance for atom in the first-shell). ^fDebye – Waller parameter. ^gValues in bold were fixed in the fit. ^hValues in parenthesis represent uncertainty in the last significant figure of the fitted parameters. ⁱConstrained to σ² of tris(phenyl)thioarsine as reported by Hoffmann et al.¹⁹. ^jConstrained to σ² of TEA (reference standard). Passive amplitude reduction factor (S₀²) was set to 1.0 for shell-fit analysis of all the samples.

10. Possible influences of variable k -ranges, used for the fitting of EXAFS data on fitted EXAFS parameters for the As··C path in arsenite-, arsenate-, and monothioarsenate-treated peat samples

The fitted $R_{As··C}$ was relatively longer in the arsenate- and monothioarsenate-treated peat than in the arsenite-treated peat (Table 1 in the main text). To test whether variable k -ranges used for the fitting of EXAFS data (Table 1 in the main text) was responsible for such difference in $R_{As··C}$ values, another fitting exercise was performed with a similar k -range of 2.2–9.5 (the lowest k -range fitted for any sample, Table 1). Comparison of these fitting results with that obtained with the variable k -ranges shows that the use of variable k -ranges had a negligible influence on the fitted EXAFS parameters of the As··C path (Table SI-5).

Table SI-5: Comparison of the EXAFS parameters determined by shell-fit analysis of the As K-edge EXAFS spectra of the arsenite-, arsenate-, and monothioarsenate-treated peat using the variable k -range (Table 1 in the main text) and the similar k -range of 2.2–9.5.

As species	Sample label	As··C (variable k -range, Table 1)			As··C (k -range:2.2–9.5)		
		CN	R (Å)	σ^2 (Å ²)	CN	R (Å)	σ^2 (Å ²)
As(III)	7.0/1000	1.7(4)	2.74(3)	0.0059	1.8(5)	2.74(3)	0.0059
	7.0/150	1.0(3)	2.73(4)	0.0059	1.0(3)	2.73(4)	0.0059
	7.0/100	1.4(3)	2.73(3)	0.0059	1.5(3)	2.75(3)	0.0059
	4.5/1000	2.1(5)	2.73(3)	0.0059	2.2(6)	2.74(4)	0.0059
	4.5/500	2.4(5)	2.74(3)	0.0059	2.5(6)	2.73(4)	0.0059
As(V)	7.0/1000	3.2(10)	2.84(2)	0.0059	3.0(11)	2.84(3)	0.0059
	7.0/500	3.4(14)	2.82(3)	0.0059	3.0(17)	2.83(4)	0.0059
	7.0/250	3.1(11)	2.82(3)	0.0059	2.7(12)	2.84(4)	0.0059
	4.5/1000	3.0(10)	2.82(3)	0.0059	2.7(13)	2.83(4)	0.0059
MTAs(V)	7.0/1000	2.6(5)	2.78(2)	0.0059	2.3(7)	2.77(2)	0.0059
	7.0/150	2.9(5)	2.82(2)	0.0059	2.7(6)	2.82(2)	0.0059
	7.0/100	3.4(7)	2.81(2)	0.0059	3.4(7)	2.81(2)	0.0059

11. Linear combination fitting (LCF) of As K-edge XANES spectra of the peat equilibrated with monothioarsenate at pH 4.5

For the two peat samples equilibrated with monothioarsenate at pH 4.5, linear combination fitting of the As K-edge normalized XANES spectra were performed by Athena.⁷ Fitting was conducted in the energy range between -20 to +30 eV with respect to the edge energy. Two peat samples equilibrated with 1000 μM monothioarsenate and arsenite at pH 7.0, were taken as the two end-members for the fitting. A smaller value of residual (R) factor indicates a better fit. Furthermore, as the sum of the two species (represented by ‘total’) determined by LCF analysis was not constrained to be 100, a value close to 100 will also suggest a fit to be reasonable. The fitting of the two samples is displayed in Figure SI-7 and results are summarized in Table SI-5.

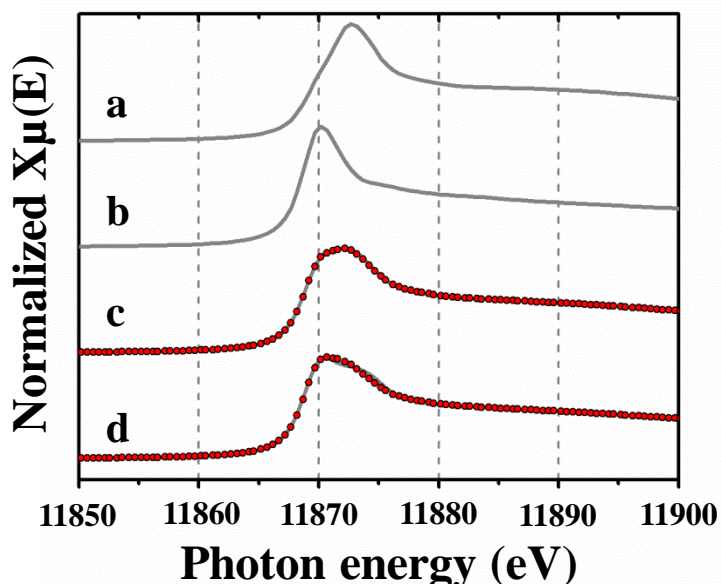


Figure SI-7: Linear combination fitting of As K-edge normalized XANES spectra of the peat equilibrated with monothioarsenate at pH 4.5: a) Peat equilibrated with 1000 μM monothioarsenate at pH 7.0, b) Peat equilibrated with 1000 μM arsenite at pH 7.0, c) Peat equilibrated with 1000 μM monothioarsenate at pH 4.5, and d) Peat equilibrated with 500 μM monothioarsenate at pH 4.5. Grey lines and red dots represent data and model fit, respectively.

Table SI-6: Results of LCF analysis of As K-edge normalized XANES spectra of the peat equilibrated with monothioarsenate at pH 4.5

Sample	%As species from LCF analysis of XANES spectra		Total (%)	R-factor (%)
	Peat equilibrated with 1000 μ M monothioarsenate at pH 7.0	Peat equilibrated with 1000 μ M arsenite at pH 7.0		
Peat equilibrated with 1000 μ M monothioarsenate at pH 4.5	58(0 ^a)	44(0)	102	0.01
Peat equilibrated with 500 μ M monothioarsenate at pH 4.5	44(1)	60(1)	104	0.18
Average	51	52		

^aValue in the parenthesis represents uncertainty in the last significant figure

12. References

- (1) Besold, J.; Kumar, N.; Scheinost, A. C.; Pacheco, J. L.; Fendorf, S.; Planer-friedrich, B. Antimonite Complexation with Thiol and Carboxyl/Phenol Groups of Peat Organic Matter. *Environ. Sci. Technol.* **2019**, *53*, 5005–5015.
- (2) Gondar, D.; Lopez, R.; Fiol, S.; Antelo, J. M.; Arce, F. Characterization and Acid – Base Properties of Fulvic and Humic Acids Isolated from Two Horizons of an Ombrotrophic Peat Bog. *Geoderma* **2005**, *126*, 367–374.
- (3) Artz, R. R. E.; Chapman, S. J.; Robertson, A. H. J.; Potts, J. M.; Laggoun-Defarge, F.; Gogo, S.; Comont, L.; Disnar, J.-R.; Francez, A.-J. FTIR Spectroscopy Can Be Used as a Screening Tool for Organic Matter Quality in Regenerating Cutover Peatlands. *Soil Biol. Biochem.* **2008**, *40*, 515–527.
- (4) Rennert, T.; Eusterhues, K.; Pfanzer, H.; Totsche, K. Influence of Geogenic CO₂ on Mineral and Organic Soil Constituents on a Mofette Site in the NW Czech Republic. *Eur. J. Soil Sci.* **2011**, No. 62, 572–580.
- (5) Planer-Friedrich, B.; London, J.; McCleskey, R. B.; Nordstrom, D. K.; Wallschläger, D. Thioarsenates in Geothermal Waters of Yellowstone National Park: Determination, Preservation, and Geochemical Importance. *Environ. Sci. Technol.* **2007**, *41* (15), 5245–5251.
- (6) Kelly, S.; Hesterberg, D.; Ravel, B. Analysis of Soils and Minerals Using X-Ray Absorption Spectroscopy. In *Methods of Soil Analysis. Part 5: Mineralogical Methods*; Soil Science Society of America: Madison, Wisconsin, 2008; pp 387–464.
- (7) Ravel, B.; Newville, M. ATHENA, ARTEMIS, HEPHAESTUS: Data Analysis for X-Ray Absorption Spectroscopy Using IFEFFIT. *J. Synchrotron Radiat.* **2005**, *12* (4), 537–541.
- (8) Zabinsky, S. I.; Rehr, J. J.; Ankudinov, A.; Albers, R. C.; Eller, M. J. Multiple-Scattering Calculations of x-Ray-Absorption Spectra. *Phys. Rev. B* **1995**, *52* (4), 2995–3009.
- (9) Kamenar, B.; Bruvo, M.; Butumović, J. Structures Involving Unshared Electron Pair. The Crystal Structures of As(OCOCH₃)₃ and As₂O(OCOCH₃)₄. *Zeitschrift für Anorg. und Allg. Chemie* **1993**, *619* (5), 943–946.

- (10) Kitahama, K.; Kiriya, R.; Baba, Y. Refinement of the Crystal Structure of Scorodite. *Acta Crystallogr. Sect. B* **1975**, *31* (1), 322–324.
- (11) Ginderow, D.; Cesbron, F. Structure de La Mapimite, $Zn_2Fe_3(AsO_4)_3(OH)_4 \cdot 10H_2O$. *Acta Crystallogr. Sect. B* **1981**, *37*, 1040–1043.
- (12) Pappalardo, G. C.; Chakravorty, R.; Irgolic, K. J.; Meyers, E. A. Tris(Phenylthio)arsine, $C_{18}H_{15}AsS_3$. *Acta Crystallogr. Sect. C* **1983**, *39* (12), 1618–1620.
- (13) Kempa, P. B.; Wiebcke, M.; Felsche, J. Structure of Trisodium Monothioarsenate Dodecahydrate. *Acta Crystallogr. Sect. C* **1990**, *46* (5), 729–732.
- (14) Downward, L.; Booth, C. H.; Lukens, W. W.; Bridges, F. A Variation of the F-Test for Determining Statistical Relevance of Particular Parameters in EXAFS Fits. *AIP Conf. Proc.* **2007**, *882* (2), 129–131.
- (15) Stern, E. A.; Newville, M.; Ravel, B.; Yacobi, Y.; Haskel, D. The UWXAFS Analysis Package - Philosophy and Details. *Phys. B* **1995**, *208 & 209*, 117–120.
- (16) Hoffmann, M.; Mikutta, C.; Kretzschmar, R. Arsenite Binding to Natural Organic Matter: Spectroscopic Evidence for Ligand Exchange and Ternary Complex Formation. *Environ. Sci. Technol.* **2013**, *47* (21), 12165–12173.
- (17) Funke, H.; Scheinost, A. C.; Chukalina, M. Wavelet Analysis of Extended X-Ray Absorption Fine Structure Data. *Phys. Rev. B* **2005**, *71* (9), 094110.
- (18) Suess, E.; Scheinost, A. C.; Bostick, B. C.; Merkel, B. J.; Wallschlaeger, D.; Planer-Friedrich, B. Discrimination of Thioarsenites and Thioarsenates by X-Ray Absorption Spectroscopy. *Anal. Chem.* **2009**, *81* (20), 8318–8326.
- (19) Hoffmann, M.; Mikutta, C.; Kretzschmar, R. Bisulfide Reaction with Natural Organic Matter Enhances Arsenite Sorption: Insights from X - Ray Absorption Spectroscopy. *Environ. Sci. Technol.* **2012**, *46*, 11788–11797.
- (20) Langner, P.; Mikutta, C.; Kretzschmar, R. Arsenic Sequestration by Organic Sulphur in Peat. *Nat. Geosci.* **2012**, *5* (1), 66–73.
- (21) Halder, D.; Lin, J.; Essilfie-Dughan, J.; Das, S.; Robertson, J.; Hendry, M. J. Implications of the Iron (II / III)-Arsenic Ratio on the Precipitation of Iron-Arsenic

Minerals from PH 2.5 to 10.5. *Appl. Geochemistry* **2018**, 98, 367–376.

Study 3: Arsenic Fate in Peat Controlled by pH-dependent Role of Reduced Sulfur

Anne Eberle, Johannes Besold, Carolin F. Kerl, Juan S. Lezama-Pacheco, Scott Fendorf and

Britta Planer-Friedrich

Reprinted with permission from

Environmental Science & Technology

Copyright 2020 American Chemical Society

Arsenic Fate in Peat Controlled by the pH-Dependent Role of Reduced Sulfur

Anne Eberle, Johannes Besold, Carolin F. Kerl, Juan S. Lezama-Pacheco, Scott Fendorf, and Britta Planer-Friedrich*



Cite This: *Environ. Sci. Technol.* 2020, 54, 6682–6692



Read Online

ACCESS |



Metrics & More

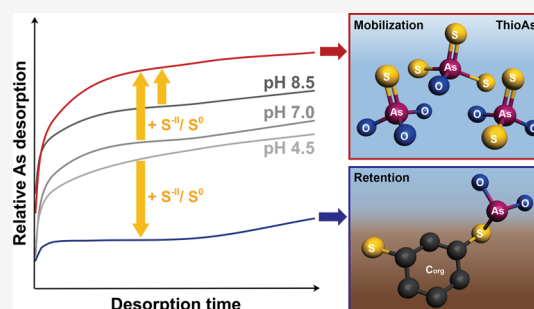


Article Recommendations



Supporting Information

ABSTRACT: Reduced sulfur (S) has a contrasting role in the fate of arsenic (As) in peatlands. Sulfur bridges provide efficient binding of As to organic carbon (C), but the formation of aqueous As–S species, so-called thioarsenates, leads to a low to no sorption tendency to organic C functional groups. Here, we studied how pH changes the role of reduced S in desorption and retention of presorbed As in model peat. Control desorption experiments without S addition revealed that As was mobilized, predominantly as arsenite, in all treatments with relative mobilization increasing with pH ($4.5 < 7.0 < 8.5$). Addition of sulfide or polysulfide caused substantial As retention at acidic conditions but significantly enhanced As desorption compared to controls at neutral to alkaline pH. Thioarsenates dominated As speciation at pH 7.0 and 8.5 (maximum, 79%) and remained in solution without (re)sorption to peat. Predominance of arsenite in control experiments and no evidence of surface-bound thioarsenates at pH 7.0 suggest mobilization to proceed via arsenite desorption, reaction with dissolved or surface-bound reduced S, and formation of thioarsenates. Our results suggest that natural or management-related increases in pH or increases in reduced S in near-neutral pH environments can turn organic matter from an As sink into a source.



INTRODUCTION

Peatlands, both natural and managed, are important sinks^{1–4} but also sources^{3–6} of the toxic metalloid arsenic (As). Immobilization can occur by precipitation of As-containing minerals^{2,7,8} or by inner-spheric and outer-spheric adsorption of the oxidized species arsenate ($H_xAs^V O_4^{x-3}$; $x = 0–3$) and the reduced species arsenite ($H_xAs^{III} O_3^{x-3}$; $x = 0–3$) to mineral surfaces in peat.^{6,11–13} Furthermore, As can be retained by peat through binding of arsenate via ternary complexes with Fe(III) bound to natural organic matter (NOM) surfaces^{9,10} or after reduction to arsenite through direct binding via thiol^{7,11,12} and/or phenolic/carboxylic groups to NOM^{13,14} as well as via ternary Fe(III)–NOM complexes.¹³ Strong impacts on the overall peatland regime, such as water table fluctuations, changing water chemistry, or changing redox conditions, can trigger As remobilization,^{3,4,6} in addition to export due to complexation with dissolved organic matter (DOM).^{4,15,16}

Sulfur (S) has a prominent, yet potentially contrasting, role in the fate of As in peatlands. Under strongly sulfidic conditions and acidic to neutral pH, As–S mineral precipitation limits aqueous As concentrations.^{7,8} Dissolved sulfide concentrations in peatlands are typically low^{5,17–19} but can be high at peaks of microbial sulfate reduction²⁰ in summer, with up to 300 $\mu\text{mol/L}$ reported from natural peatlands.^{21–23} Even higher concentrations are possible upon

high anthropogenic sulfate inputs to peatlands used for treatment of mine wastewater.³ However, in many peatlands, dissolved sulfide concentrations are too low to reach mineral supersaturation.^{5,11,17–19} Instead, reduced S is incorporated into NOM, forming thiol (R–SH) groups, which provide binding sites for As.¹¹ These As–S–C_{org} bonds form preferentially relative to As–S mineral precipitation in peat.^{7,8} At the Gola di Lago peatland in Switzerland, for example, covalent binding of trivalent As with thiol groups of NOM was identified as the main binding mechanism in deep peat layers.⁷ The same observation was made for a peat layer in alluvial sediments in the Mekong Delta, which exhibited the highest As contents in the sediment profile.²⁴ Hence, reduced S is able to efficiently retain As in the solid phase of peat. Further, the As–S–C_{org} bonds proved to be very stable, even in the presence of oxygen, and were able to compete with iron minerals for As complexation.^{11,25,26}

On the other hand, we have recently found that reduced S can play a key role in keeping As dissolved in peatland pore

Received: January 22, 2020

Revised: April 23, 2020

Accepted: April 29, 2020

Published: April 29, 2020



and surface water by the formation of highly mobile As–S complexes.⁵ Detailed pore water As speciation of the previously mentioned Gola di Lago peatland revealed that up to 93% of total As in surface and pore water was present as thioarsenates ($H_xAs^V S^{II} O_{4-n} x^{-3}$; $n = 1-4$, $x = 0-3$).⁵ Also, in an aquifer in Bangladesh, the highest share of thioarsenates was found in a well with a distinct peat layer.²⁷ These As–S species form by the reaction of arsenite with dissolved sulfide and/or zero-valent S;²⁸ the latter includes (colloidal) elemental S and inorganic polysulfide species ($[S_n^{0-} S^{II}]^{2-}$; $n = 1-7$).²⁹ Despite typically low dissolved reduced S concentrations in peatlands,^{5,17-19} sulfide incorporated into NOM as organic thiols or polysulfides^{17,30,31} and surface-associated polysulfides formed, for example, during reduction of ferric (hydr)oxides³²⁻³⁷ seem to be sufficient as a S supply for As thiolation. The dominant thiolated species observed both in the Gola di Lago peatland and the Bangladesh aquifer was monothioarsenate (MTAs^V), which is the only thioarsenate that can form directly from arsenite by the addition of zero-valent S (without excess dissolved sulfide)^{28,38} and shows little transformation under either alkaline or acidic conditions³⁹ or upon exposure to air.⁴⁰ Compared to the oxyarsenic species, arsenite and arsenate, all thioarsenates show lower tendencies for sorption to mineral surfaces, including those of iron.⁴¹⁻⁴³ Furthermore, MTAs^V has a low to no affinity for O-bearing and thiol groups of NOM.^{5,14} Hence, As–S complexation in solution seems to increase As mobility. In fact, an earlier study showed mobilization of As, which was bound to small iron-rich organic flocs occurring in the Gola di Lago peatland, upon sulfidization with up to 33% mobilized As being thioarsenates.³⁵

We hypothesize that apart from absolute reduced S concentrations, pH is the key factor in determining the net effect of S on the fate of As in peatlands, with acidic conditions causing As retention via binding to thiol groups and neutral to alkaline conditions causing As mobilization by thioarsenate formation. Changes in pH can occur in natural peatlands or aquifers with peat interlayers due to natural seasonal fluctuations; more typically, however, pH changes occur more extensively and frequently in treatment peatlands or remediated aquifers as consequence of management changes.³ Anthropogenic use of peatlands for treatment of pretreated neutral to alkaline mine wastewater,³ for example, can increase the pH of formerly acidic peatlands to circumneutral pH values.^{44,45}

Understanding the complex interplay between S and As at different pH conditions would be important not only to estimate long-term retention capacity of As in peatlands but also to understand the origin of previously reported high amounts of thioarsenates in natural peatland pore water⁵ or the influence of reduced S on potential mobilization of As from peat layers in neutral anoxic aquifers.²⁴

Therefore, in this study, we used As-loaded model peat and investigated As desorption in the presence and absence of reduced S species at pH 4.5, 7.0, and 8.5 covering conditions typical for natural bogs (pH 3.5–4.5)⁴⁶ and fens (pH 5.5–7.5),⁴⁶ including the upper limit in high carbonate fens with pH values up to 8.5,^{19,47,48} as well as conditions that can occur in managed peatlands^{44,45} and peat layers in pH-neutral aquifers.^{24,27} Although peatlands with different pH conditions would also differ in, for example, chemical composition and vegetation, we used the same peat material here for all pH conditions to specifically target the effects of pH and reduced S

on As mobility. A combination of solid- and aqueous-phase As and S quantification, aqueous As speciation by ion chromatography coupled to inductively coupled plasma mass spectrometry (IC-ICP-MS), and bulk As X-ray absorption spectroscopy (XAS) was used to reveal the net interaction between As and S at different pH values.

MATERIALS AND METHODS

Materials. All chemicals used were of analytical grade. Potassium (poly)sulfide (K_2S_n , $\geq 42\%$ K_2S basis, Sigma-Aldrich), characterized with high-performance liquid chromatography (HPLC) coupled to UV–vis photometry, had a composition of 42% K_2S and 58% K_2S_2 . Details about the characterization can be found in the Supporting Information.

Peat Organic Matter. Peat was taken from Federseemoor, an ombrotrophic peatland near Bad Buchau, Germany.¹¹ To obtain an NOM model sorbent, the peat was prepared as described elsewhere.^{5,11,13,49} In short, the peat was wet sieved to a size fraction of 63–250 μm , cleaned from metal(loid)s with 0.1 M HCl, and washed repeatedly using double deionized (DDI) water to reach the starting pH of ~ 4.5 . Subsequently, the peat organic matter (OM) was freeze-dried, homogenized, and stored in the dark under anoxic conditions in a glovebag (Coy, $pO_2 < 1$ ppm) until use. The same material was used by Besold et al.^{5,49} (C: 55 wt %, S: 0.22 wt %, Fe: 829 mg/kg, and As: 1.53 mg/kg); detailed composition and characterization of functional groups can be found there.^{5,49}

Preparation of Arsenic-Loaded Model Peat for Desorption Experiments. For the desorption experiments, As-loaded peat was needed. Previous studies^{5,11} have addressed sorption of arsenite via thiol groups or O-bearing groups at different pH conditions. Here, we took the protocols developed in these earlier studies to produce thiol-rich peat OM, which was subsequently loaded with arsenite (As-loaded model peat), as a starting point for our desorption experiments. Experiments were conducted at room temperature and under anoxic conditions in a glovebag. A background electrolyte containing 30 mM NaCl was used to establish stable ionic strength, and 0.15 mM sodium azide (0.75 mmol/mol C, NaN_3) was used to inhibit microbial growth in all experiments. All solutions were prepared with DDI water (Millipore, ≥ 18.2 M Ω cm) and purged with N_2 before use in anaerobic incubation experiments.^{5,11}

In the first step, to prepare the thiol-rich peat material, peat OM in suspension (0.2 M C) was equilibrated at pH 4.5, 7.0, and 8.5 in a 2 L Schott bottle for each pH condition with 3.0 mM dissolved sulfide in the background electrolyte. The pH was adjusted using small amounts of HCl and NaOH (± 0.2 pH units). After equilibration for 24 h in the dark, the produced thiol-rich peat OM of each pH treatment was filtered from solution (12 μm , cellulose nitrate) and washed with the electrolyte to remove excess dissolved sulfide. The resulting material will be referred to as model peat hereafter.

In the second step, the model peat (corresponding to the same C content of 0.2 M C in suspension) was equilibrated with 50 μM arsenite ($NaAsO_2$) in an electrolyte solution at pH 4.5, 7.0, and 8.5. In each treatment, the pH was again adjusted to the previous value; the suspension was shaken in the dark for 96 h. The produced As-loaded model peat was then filtered (12 μm , cellulose nitrate), and the filter residues were used for the following As desorption experiments immediately after preparation. To account for differences in pH-dependent initial sorption^{5,11} when comparing the results of the desorption

experiments, relative desorption in percent was calculated in addition to absolute As concentrations. Therefore, the amount of As in aqueous and solid phases at the end of the desorption experiment was normalized to the corresponding initial amount of As in the As-loaded model peat through mass balance, as explained in the Supporting Information.

Arsenic Desorption Experiments. Desorption experiments were conducted at pH 4.5, 7.0, and 8.5 using the As-loaded model peat of the respective pH with three different treatments (no S, polysulfide, and dissolved sulfide addition) and three replicates each, resulting in 27 batches. The incubations were conducted anoxically in 250 mL serum bottles with butyl rubber stoppers for 180 h, and the aqueous phase was sampled at seven time-steps during the experiment. Experiments were designed with a starting volume of 100 mL to keep the loss of solution due to sampling below 35% until the last sampling step. Similar to the batch sorption experiments, the concentration of peat in background electrolyte solution was 0.2 M C. For the two treatments with reduced S, polysulfide (PS) was selected to represent a reduced S species including zero-valent S. Dissolved sulfide was used to distinguish the effect of zero-valent S from the effect of S^{-II} (in polysulfide) on potential desorption of As from peat. The term “sulfurization” is used to summarize the addition of reduced S in the desorption experiments. A control was kept without S addition. The amount of polysulfide addition was calculated by referring the zero-valent S concentration added with polysulfide solution to the As concentration in 0.2 M C peat suspension with a nominal 10-fold excess (actual values, 9.3 ± 3.2) of zero-valent S compared to As. The sulfide concentration in the dissolved sulfide treatments was matched to the concentrations added with the polysulfide solution in the polysulfide treatments. Finally, the pH was adjusted to the target pH (± 0.02) of the incubation batch using anoxic HCl and NaOH. The bottles were shaken and kept in the dark for the duration of the experiment.

At each time-step of the experiment the suspensions of peat in electrolyte solution were sampled with a syringe and needle after shaking, to keep the solid-to-solution ratio constant, and filtered (0.2 μm , cellulose acetate). An aliquot of filtered aqueous-phase samples was immediately flash-frozen on dry ice for speciation analysis.⁵⁰ Another aliquot was stabilized for total element analysis by inductively coupled plasma mass spectrometry (ICP-MS) in 0.44% H₂O₂ and 0.78% HNO₃. For the determination of zero-valent S, 725 μL of filtered sample was stabilized by the addition of 25 μL of ZnAc (20% (w/v) ZnAc·2H₂O) and stored in a cool (4 °C) and dark place.

Samples for dissolved sulfide determination were processed immediately. The pH was determined at the start ($t = 0$ h) and end ($t = 180$ h) of the experiment. Changes of pH during the experiment were below 0.4 pH units. At the end of the incubation experiments, the peat material of each batch was recovered by filtration (12 μm , cellulose nitrate), frozen in liquid N₂, and freeze-dried. The dry samples were transferred back into the glovebag and homogenized with a mortar and pestle. An aliquot of each freeze-dried peat sample from the desorption experiment was stored anoxically for XAS analysis. A second aliquot was microwave-digested (soil-to-solution ratio, 1:160; Mars XPress, CEM) using a 5:3 ratio of 65% HNO₃ and 30% H₂O₂. Total element concentrations in aqueous-phase samples (As) and filtered digests (As and S) were determined by ICP-MS (XSeries2, Thermo Fisher) as AsO⁺ (m/z 91) and SO⁺ (m/z 48).

Aqueous Arsenic and Sulfur Speciation. Flash-frozen samples were thawed in a glovebag. Arsenite, arsenate, and thioarsenate species concentrations were determined by anion-exchange chromatography (ICS-3000, AG/AS 16 IonPac column, Dionex; 20–100 mM NaOH at a flow rate of 1.2 mL/min) coupled to ICP-MS.⁵⁰ Calibration standards were made from sodium arsenate dibasic heptahydrate (Na₂HAsO₄·7H₂O) and sodium (meta)arsenite (NaAsO₂) in DDI water. Due to a lack of commercially available standards, thioarsenates were quantified via the arsenate calibration curve, an approach evaluated previously.⁵⁰

Dissolved sulfide was quantified photometrically according to the methylene blue method⁵¹ at an absorption wavelength of 650 nm using a multiplate reader (Infinite 200 PRO, Tecan). Calibrations were prepared from sodium sulfide (Na₂S·9H₂O) in DDI water. Zero-valent S was determined according to the method of Kamysny et al.⁵² modified by ThomasArrigo et al.³⁵ Therefore, ZnAc-stabilized samples were extracted with 700 μL of chloroform (CHCl₃) while shaking for 1 h. Analysis was done by high-performance liquid chromatography (HPLC, LaChrom Elite, L-2130 pump, L-2200 autosampler, L-2420 UV-vis detector, Merck Hitachi) using a reversed-phase C18 column (Luna, 3 μm , 150 × 2.0 mm, Phenomenex). Samples were eluted with 100% methanol (CH₃OH) at a flow rate of 0.2 mL/min and detected at a wavelength of 254 nm. Calibration standards were prepared from elemental S (S⁰) dissolved in chloroform.

Solid-Phase Arsenic and Sulfur Speciation with X-ray Absorption Spectroscopy. Solid-phase speciation of As in peat samples was analyzed by As *K*-edge (11,867 eV) X-ray absorption near-edge structure (XANES) as well as extended X-ray absorption fine structure (EXAFS) and solid-phase S via *K*-edge (2472 eV) XANES spectroscopy. Arsenic *K*-edge XANES and EXAFS spectra from samples of the desorption experiment at pH 7.0 were collected at beamline 9-3 at the Stanford Synchrotron Radiation Lightsource (SSRL), Stanford, USA. Measurements were performed in the fluorescence mode using a 100-element solid-state Ge detector (Canberra) at about 15 K (He cryostat) to avoid beam damage and reduce thermal disorder. Principal component analysis (PCA), target-transform testing (TT), and linear combination fitting (LCF) of As *K*-edge XANES and EXAFS spectra were done in Athena⁵³ and SIXPack.⁵⁴ Shell-by-shell fitting of As *K*-edge EXAFS spectra was performed using the software Artemis.⁵³ In addition, S *K*-edge XANES spectra from all peat samples were collected at beamline 4-3. The samples were measured in the fluorescence mode with a 4-element solid-state Si drift detector (Hitachi HTA) under a constant He atmosphere (<0.1% (v/v) O₂) at ambient temperature. Sulfur species were quantified based on spectral S *K*-edge XANES deconvolution in Athena following the approach of Manceau and Nagy.⁵⁵ Details on data collection, reference compounds, data processing, and analyses are provided in the Supporting Information.

Statistics. Two-way ANOVA with a Tukey post-hoc test was performed separately on solid-phase As contents, S contents, absolute aqueous As concentrations as well as calculated relative As desorption values for the nine parallel treatments of the desorption experiment for the last time point ($t = 180$ h), using SigmaPlot 11.

RESULTS AND DISCUSSION

Characterization of As-Loaded Model Peat before the Start of Desorption Experiments. Desorption experi-

ments were initiated with As-loaded model peat at three different pH values. Solid-phase As and S concentrations at the start of the experiments were different due to different pH-dependent sorptions of As. The absolute As content was the highest at the lowest pH (with 2.4 mmol/kg at pH 4.5 compared to 0.9 and 0.8 mmol/kg at pH 7.0 and 8.5, respectively; Figure 1a), similar to the chemical composition received at the end of our previously published sorption experiments with the same peat OM.⁵ The underlying mechanism of pH dependency (higher abundance of thiol groups with lower pK_a values, the presence of aryl ketones, and polar interactions or H bridges supporting sorption of uncharged arsenite at lower pH) has been discussed before but remains unresolved.⁵ Binding of As via thiol and O-bearing groups of NOM, as observed earlier,^{5,11} was confirmed by As *K*-edge LCF (see later discussion, Figure 3, and shell-by-shell fitting in Figure SI-2). In addition, a fraction of As may have been bound in outer-sphere complexes. The total S content in As-loaded model peat was the highest at pH 4.5 and 7.0 with about 170 mmol/kg S, likely due to acid-catalyzed sulfide addition,¹¹ while at alkaline conditions, the S content was considerably lower with 94 mmol/kg (Figure SI-5). Gaussian curve fitting (GCF) of S *K*-edge XANES spectra revealed comparable S speciation for pH 4.5 and 7.0, with a dominance of reduced S, whereas at pH 8.5, proportionally more oxidized S (organic and inorganic) and less reduced S were found (Figure SI-5). Arsenic-to-sulfur ratios (14, 6, and 8 $\mu\text{mol As/mol S}$ for pH 4.5, 7.0, and 8.5, respectively) were similar to those reported before.^{5,11}

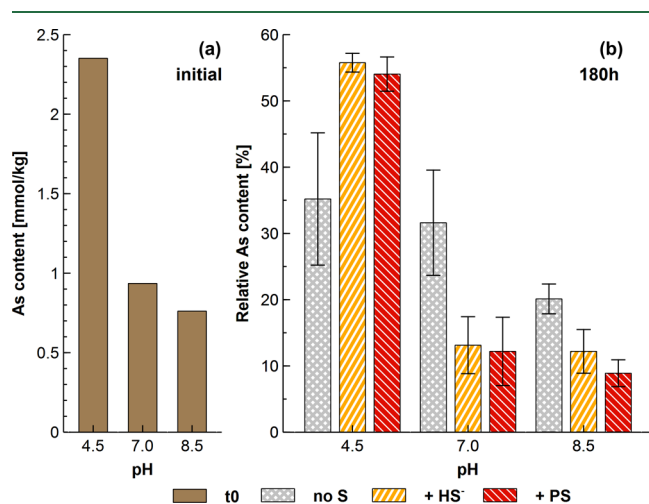


Figure 1. (a) Initial total As content in As-loaded model peat at different pH conditions. (b) Relative As content after 180 h of desorption in relation to the initial As content for the controls without S addition (no S) and with sulfide (+HS⁻) and polysulfide (+PS) treatments at different pH values of 4.5, 7.0, and 8.5. Note: since As-loaded model peat showed different initial As contents depending on pH (see panel a), solid As contents were normalized to initial As content and reported in %; error bars represent the standard deviation of experimental triplicates.

Arsenic Desorption Dependency on pH. Arsenic was released (via desorption) from As-loaded model peat in all treatments, demonstrated consistently by both solid-phase (Figure 1b) and solution data (Figure 2a–c). In control experiments without the addition of reduced S in solution, 6.4, 2.7, and 2.4 μM total As ($p < 0.001$; Figure SI-18) were

released into solution after 180 h from the As-loaded model peat at pH 4.5, 7.0, and 8.5, respectively (Figure SI-3). The absolute amount of As released reflects equilibration in As-free solution and was the highest under acidic conditions because of the highest initial solid-phase As loading and the highest As/C ratio, whereas ratios were similar at pH 7.0 and 8.5 (51 $\mu\text{mol As/mol C}$ in comparison to 20 and 17 $\mu\text{mol As/mol C}$ for pH 7.0 and 8.5, respectively). The reverse tendency was observed in relative proportion of As desorption (normalized to initial solid-phase As content), which increased with increasing pH. Aqueous As concentrations reveal that 62, 65, and 73% of initially sorbed As were released to solution after 180 h (Figure 2a–c and Tables SI-8 and SI-19: $p = 0.069$ for pH 4.5 vs 7.0 and $p < 0.001$ for pH 4.5/7.0 vs 8.5). Matching this observation, solid-phase analysis illustrates that 35, 32, and 20% of initial As content remained sorbed at pH 4.5, 7.0, and 8.5, respectively (Figure 1b and Table SI-15: $p \leq 0.031$). The high degree of desorption questions the overall stability of As–NOM binding (more broadly discussed in the following section).

Effect of Sulfurization on pH-Dependent Arsenic Desorption. Upon sulfurization of the peat, the proportion of As desorption was altered. However, addition of sulfide or polysulfide did not result in different relative desorption within a pH treatment (Table SI-17). Under acidic conditions, more than half of As (56 and 54%; Figure 1b) was still found in the solid phase for the sulfide and polysulfide treatments, respectively, compared to only 35% in the control without S addition. Relative proportions of As in the aqueous phase were 43 and 40% in the sulfide and polysulfide treatments ($p = 0.083$; Table SI-17), respectively, in comparison to 62% in the control (Figure 2a–c; $p < 0.001$; Table SI-17), showing decreased As desorption in the presence of S. The decreased As release from the solid with reduced S addition in comparison to controls without S addition at acidic conditions could be due to less desorption of As or secondary adsorption of As by thiol groups of peat. We cannot distinguish between those two processes in our experiments and will therefore use the term “retention” in the following discussion. The observed retention is consistent with the findings of Hoffmann et al.,¹¹ who showed high As sorption via thiol groups of peat at slightly acidic to neutral pH. Arsenic binding via S groups is also consistent with slightly greater As retention in polysulfide compared to sulfide treatments and correspondingly higher S contents in the solid phase (130% vs 95% of S content in original As-loaded model peat with $p < 0.001$; Figure SI-7 and Table SI-11), which could be caused by higher affinity of polysulfides toward NOM compared to pure sulfide.

In contrast to acidic conditions, reduced S led to significantly increased As desorption compared to the controls without S addition at neutral to alkaline pH ($p < 0.001$, Table SI-17). The proportions of solid-phase As in sulfurized treatments were between 9 and 14% (Figure 1b) after 180 h of desorption, and aqueous As proportions ranged from 79 to 85% (Figure 2). No significant differences were observed between pH 7.0 and 8.5 ($p > 0.1$; Tables SI-13 and SI-17), which suggests that the maximum of S-induced As desorption was already reached. The net effect of reduced S on As desorption compared to controls without S addition was lower for pH 8.5 than for pH 7.0 (Figure 2). This difference might be explained by the fact that pH 8.5 controls already contained higher dissolved sulfide concentrations released from the solid phase than pH 7.0 controls (Figure SI-8), and thus, S spikes

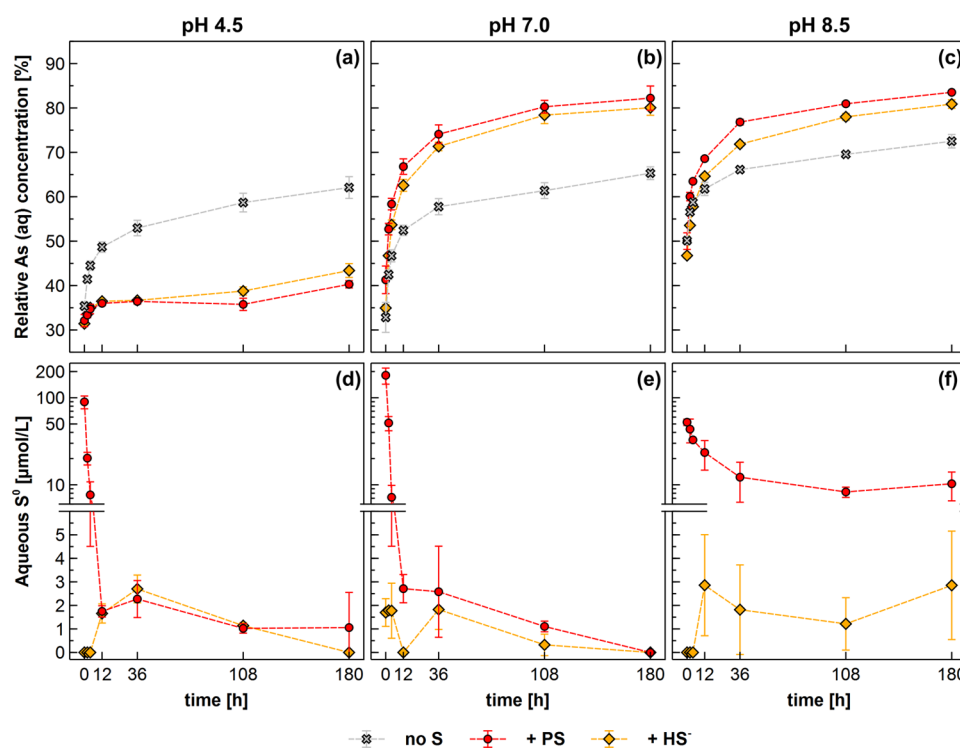


Figure 2. (a–f) Relative aqueous As and total aqueous zero-valent S concentrations over desorption time at pH (a, d) 4.5, (b, e) 7.0, and (c, f) 8.5 in controls without S addition (no S) and with sulfide (+HS⁻) and polysulfide (+PS) addition. Since As-loaded model peat showed different initial As contents depending on pH (see Figure 1a), aqueous As concentrations were normalized to initial As content and reported in %; time series of total aqueous As concentrations can be found in the Supporting Information (Figure SI-3). Zero-valent S concentrations are not presented for controls without S addition because no zero-valent S was detected in any of the samples; the lower part of the y-axis is linear (up to 6 μmol/L), and the upper part is logarithmic (log₁₀) (from 6 μmol/L). Error bars represent standard deviations of experimental triplicates.

had less additional impact on As desorption. Comparing polysulfide and sulfide experiments, there is a slight but consistent shift to higher As desorption in polysulfide experiments. These differences between polysulfide and sulfide treatments can be attributed to the additional zero-valent S in the polysulfide treatment as the sulfide concentrations over time were nearly identical in all sulfurized treatments (Figure SI-8). Solid S contents in the polysulfide treatments after 180 h were, again, significantly higher than those in sulfide experiments and showed a comparable percentage increase to those observed at pH 4.5 (Figure SI-7 and Tables SI-10 and SI-11: $p < 0.005$). Changes in overall solid-phase S speciation during the experiment were only minor in all treatments, apart from a considerable increase in reduced S in the polysulfide treatment of pH 8.5 (Figure SI-6). Considering the high S contents in combination with nearly unchanged speciation, neither differences between polysulfide and sulfide experiments nor the desorption of As observed at neutral to alkaline pH can be attributed to a lack of S-containing binding sites.

Changes in Solid-Phase Arsenic Speciation. Changes in bulk As speciation due to different treatments of As-loaded model peat at pH 7.0 were evaluated by LCF of k^2 -weighted As K-edge EXAFS and XANES spectra (Figure 3). The LCF results of XANES and EXAFS were consistent and are summarized in Tables SI-4 and SI-5, respectively.

The As speciation of the initial As-loaded model peat revealed that 42% As was bound via thiol groups and 58% via O-bearing groups (Figure 3). With sulfide and polysulfide addition, the As(III)–S fraction increased to 55 and 58%, respectively, whereas the As(III)–O fraction decreased correspondingly, indicating stronger relative binding via

As(III)–S bonds because this occurs simultaneously with a decrease in the total As content in the peat material. Our shell-by-shell fitting approach confirmed this observation, showing increased As–S coordination numbers with reduced S (Table SI-7). Interestingly, in the control experiments, the As(III)–S fraction stayed almost constant and As(III)–O appears to be partially oxidized to As(V)–O after equilibration with S-free solution (Tables SI-4 and SI-5), indicating that arsenite bound via O-bearing groups is less stable and more prone to oxidation than thiol-bound As. Thus, As binding via O-bearing groups to peat seems to be more labile and therefore more easily desorbed from the solid.

The suggested weaker binding of As(III)–O moieties indicates that arsenite was likely the species desorbed from the solid phase rather than As–S species. Furthermore, the formation of stable thioarsenates on the surface of NOM by the reaction of aqueous reduced S species with As bound to NOM is unlikely on the basis of the shell-by-shell fitting that revealed As–S bond lengths of 2.24–2.27 Å (Table SI-7), which are significantly longer than the typical bond distances in thioarsenates (2.13–2.18 Å).⁵⁶ No As–S minerals could be fitted to the XAS spectra, showing low probability of precipitation of mineral phases in the incubation experiments.

Aqueous Arsenic Speciation in Experiments without Sulfur Addition. More detailed insights into the adsorption–desorption processes of As from peat were gained from aqueous As speciation data (Figure 4). In experiments without the addition of reduced S (control experiments), arsenite was the dominant species at all pH values (Figure 4, left panel). At acidic and neutral pH, arsenite (81–89%) was followed by arsenate and hardly any thioarsenates were found (<1% and

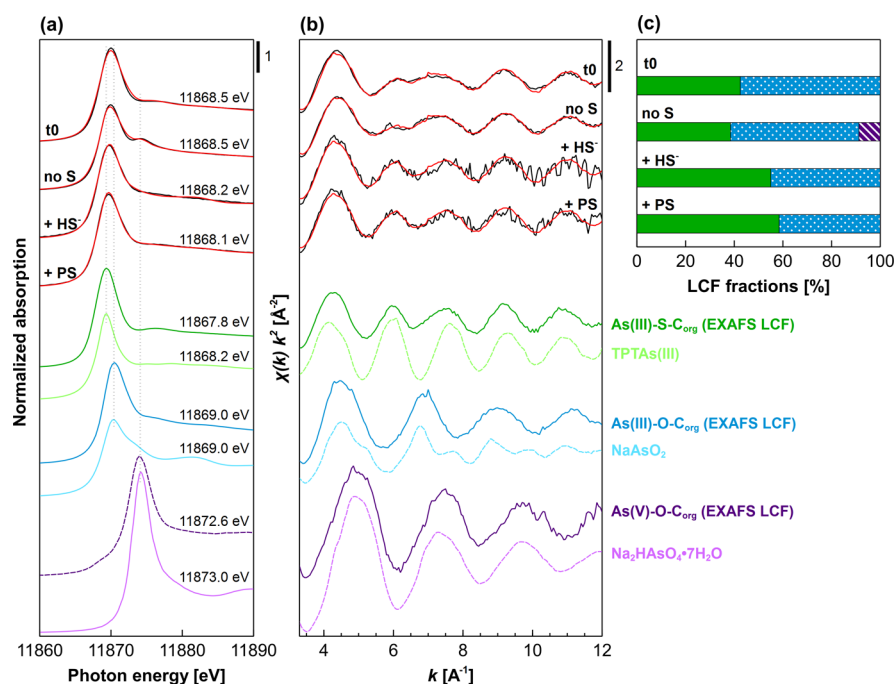


Figure 3. Arsenic solid-phase speciation in As-loaded model peat at pH 7.0 before use in desorption experiments (t0) and at the end of the desorption experiment after subjection to different S treatments for 180 h (no S, +HS⁻, and +PS addition). (a) Linear combination fits (LCF) of normalized As K-edge XANES spectra from peat samples (t0, no S, +HS⁻, and +PS) and reference spectra. For each spectrum, the respective edge energy (eV) is shown, and white line positions of reference spectra are marked with dotted vertical lines. (b) LCFs of k²-weighted As K-edge EXAFS spectra from peat samples (t0, no S, +HS⁻, and +PS) and reference spectra. Experimental data and LCFs are represented by black and red lines, respectively. Reference spectra used in the LCF of XANES or EXAFS are shown as solid lines; dashed lines represent excluded references. Fit references: As(III)-S-C_{org} = As(III) bound via thiol groups to peat NOM and TPTAs(III) = tris(phenylthio)arsine, As(III)-O-C_{org} = As(III) bound via O-bearing groups to peat NOM and NaAsO₂ = sodium (meta)arsenite, and As(V)-O-C_{org} = As(V) bound via O-bearing groups to peat NOM and Na₂HAsO₄·7H₂O = sodium arsenate dibasic heptahydrate. (c) Calculated LCF fractions for EXAFS spectra. The fitted fractions were normalized to a sum of 100%. Calculated LCF fractions for XANES spectra confirmed EXAFS results and are shown together with detailed EXAFS results in the Supporting Information.

≤7% at pH 4.5 and 7.0, respectively). At alkaline conditions, thioarsenates were the second most prominent As species, ranging from 25 to 38%, and the formation of thioarsenates at pH 8.5 could explain the increased relative desorption compared to acidic and neutral controls.

Zero-valent S was not detected in solution, but with increasing pH and time, an increasing release of dissolved sulfide into solution was observed. High sulfide concentrations ($4.9 \pm 1.4 \mu\text{M}$) could explain thioarsenate formation at high pH, and low sulfide concentrations ($1.7 \pm 0.4 \mu\text{M}$) could explain the predominance of arsenite at low pH. However, the exact pathways of sulfide release from peat remain unknown. Examining arsenite binding to sulfide-reacted peat, Besold et al.⁵ found a similar pH pattern of thioarsenate formation, with hardly any formation at acidic to neutral conditions and low formation at pH 8.5. Our observations are consistent with previous observations⁵ that even without detectable zero-valent S in solution, thioarsenate formation took place at high pH.

Aqueous Speciation of Arsenic upon Sulfurization. Addition of sulfide (Figure 4, middle panel) or polysulfide (Figure 4, right panel) yielded similar effects on As desorption and similar As speciation patterns. At all pH values examined, thioarsenate formation increased significantly upon sulfurization compared to controls.

Under acidic conditions, arsenite remained the dominant species. After 12 h of reaction, maximum values of 26 and 38% thioarsenates were observed with polysulfide and sulfide addition, respectively. The contribution of thioarsenates

decreased again to 4 and 6% of total As after 180 h; the same pattern of increase and decrease can also be found in total As concentrations. The decrease in thioarsenate concentrations toward the end of the experiment suggests that thioarsenates were only an intermediate species at acidic pH, which fits the reported instability of thioarsenates due to transformation to arsenite under acidic conditions.^{5,28,39}

At neutral and alkaline conditions, thioarsenates dominated As speciation throughout the experiment. At the start of the experiment (0 h), 77 and 79% As (0.72 and 0.85 μM) were present as thioarsenates in sulfide and polysulfide treatments at pH 7.0, respectively. The maximum concentration of thioarsenates was reached after 4–12 h, remaining at a constant level of $1.3 \pm 0.2 \mu\text{M}$ in all sulfurized treatments thereafter until the end of the experiment (Figure 4). At pH 8.5, about 77 and 74% As were initially present as thioarsenates (0.80 and 0.87 μM) in sulfide and polysulfide treatments, respectively. Again, a constant level of thioarsenates of $1.2 \pm 0.1 \mu\text{M}$ could be found from 4 to 12 h onward in all sulfurization treatments. Until thioarsenates reached a constant concentration, arsenite was present in low concentrations (until 12 h) and started to increase thereafter, reaching similar concentrations to thioarsenates at pH 7.0 ($\sim 1.1 \mu\text{M}$), but only less than half the amount at pH 8.5 ($\sim 0.5 \mu\text{M}$). Since the concentrations of thioarsenates did not decrease, the increasing arsenite concentrations in solution seem to originate due to a release from peat surfaces, which fits the observations in controls where arsenite was the dominant species. Arsenate

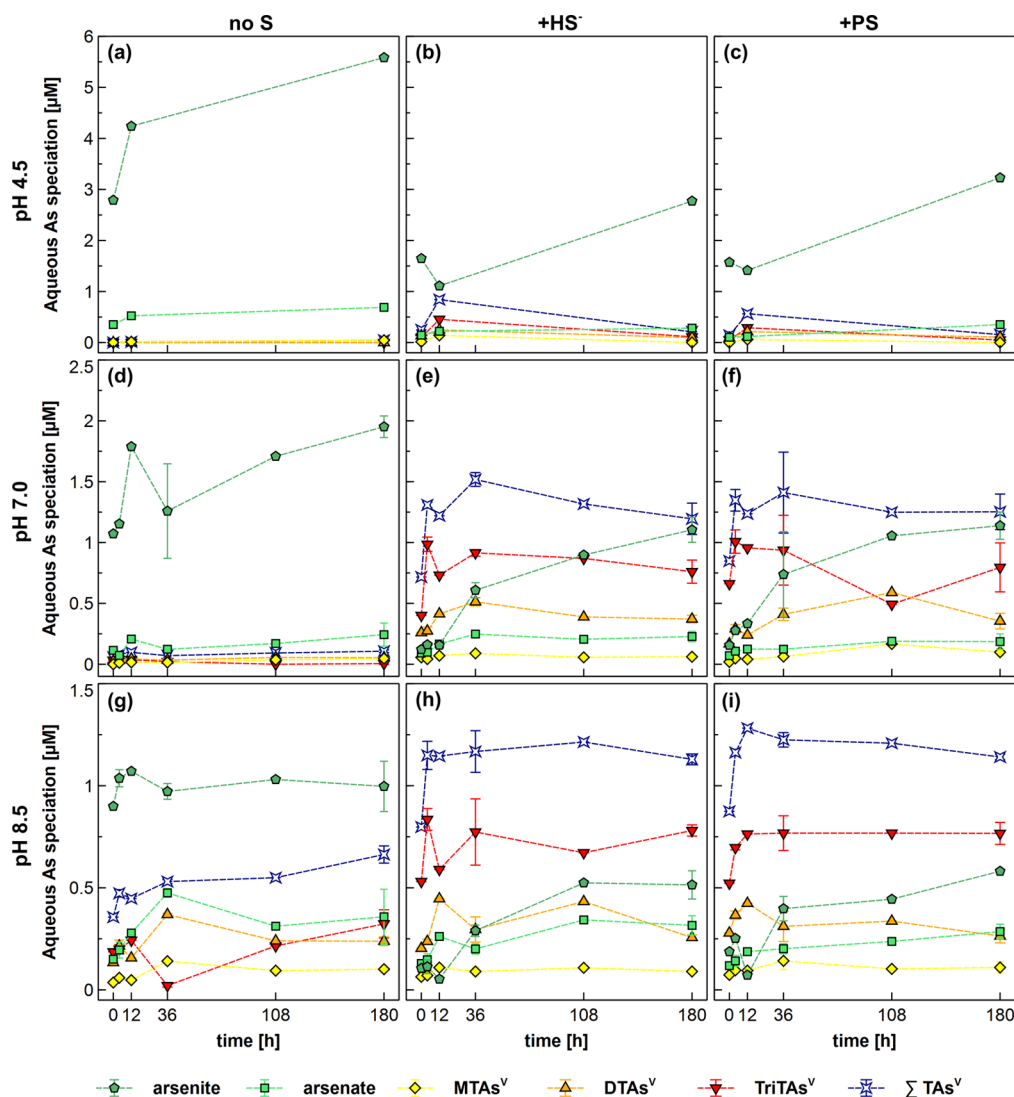


Figure 4. (a–i) Time series of aqueous As speciation in μM at pH (a–c) 4.5, (d–f) 7.0, and (g–i) 8.5 in controls without S addition (left panel), with addition of sulfide (middle panel), and with addition of polysulfide (right panel) as reduced S species. Recovery of aqueous As species was $76 \pm 10\%$. Arsenic speciation was analyzed in triplicates only for $t = 4, 36,$ and 180 h at pH 7.0 and 8.5, error bars show the standard deviation, and all other points represent single data points.

only occurred as a minor species, and its concentrations remained rather constant throughout the experiment.

Arsenic release from the solid to the aqueous phase may result from arsenite desorption from weak O-bearing groups like carboxylic or phenolic groups of NOM¹⁴ or desorption of As bound via thiol groups of NOM. Due to the higher stability of thiol-bound As in comparison with As bound to O-bearing groups, as discussed above, arsenite desorption from As–O–C_{org} is considered the dominant pathway. Arsenite desorption from As–S–C_{org} could also occur but only to a lower extent as it would not resorb to the peat after transformation to thioarsenates. This assumption is also consistent with the increase in aqueous arsenite concentrations and no observed transformation of thioarsenates over time, and it is consistent with a release of mainly arsenite in control experiments.

The larger fraction of the released arsenite likely formed thioarsenates by the reaction with aqueous or surface-associated S species probably immediately after desorption (Figure 4). Interestingly, maximum desorption resulted in similar concentrations of thioarsenates in both sulfurization

treatments at pH 7.0 and 8.5. During thioarsenate formation from released arsenite, the condition was shifted toward less arsenite in solution, inducing further desorption. When thioarsenates reached their steady-state concentration, only arsenite concentrations increased over time. Therefore, the preferential formation of thioarsenates under neutral to alkaline conditions in combination with their stability,^{40,50} removing arsenite from solution and shifting the equilibrium toward more desorption, can result in the enhanced desorption of As upon sulfurization at neutral to alkaline pH. Appreciable amounts of thioarsenates were formed without S addition at pH 8.5, affecting As mobilization and thus diminishing the impact of excess S addition on As dynamics at alkaline conditions.

Parallel to thioarsenate formation, aqueous zero-valent S was found in all S addition treatments (Figure 2). After a substantial decrease of zero-valent S within polysulfide treatments at acidic and neutral conditions, where polysulfides are known to be rather unstable and dissociate into sulfide and S⁰ upon acidification,⁵⁷ low zero-valent S concentrations

occurred in solution of all sulfurization treatments after 12 h ($<3 \mu\text{M}$) (Figure 2d,e). Part of the decrease in zero-valent S concentration could also be potentially explained by consumption of the reduced S species by thioarsenate formation or binding to the NOM surface. At pH 8.5, zero-valent S is more stable than at low pH⁵⁷ and therefore occurred in higher concentrations ($\sim 10 \mu\text{M}$) (Figure 2f) compared to the other pH conditions and the sulfide treatment.

The similar concentrations of zero-valent S in both sulfurization treatments may also explain the comparable total As desorption and speciation patterns over time for both neutral and alkaline conditions (Figures 2 and 4), additionally suggesting that low amounts of zero-valent S are sufficient for thioarsenate formation and an excess of zero-valent S does not necessarily lead to an increase in thioarsenate concentrations. Even though no zero-valent S was detectable in the controls, considerable amounts of thioarsenates were formed at pH 8.5. Therefore, the species of S causing thioarsenate formation are likely not limited to aqueous zero-valent S; they may include solid-phase-associated S species, reaction with sulfide, or the possibility that low concentrations of zero-valent S occurred, which were kept below the detection limit due to rapid consumption by reactions such as thioarsenate formation.

A dominance of higher thiolated As species in the sulfurization experiments ($\text{TriTAs}^{\text{V}} > \text{DTAs}^{\text{V}} > \text{MTAs}^{\text{V}}$), in contrast to the observations by Besold et al.,⁵ where MTAs^{V} was the most abundant species and dissolved sulfide was below the detection limit, is attributed to the high dissolved sulfide concentrations in the present experiments. This observation fits the current theory that high amounts of dissolved sulfide are necessary to form higher thiolated thioarsenates.^{28,58}

Environmental Implications. At present, there are contradictory reports on the effects of reduced S on As chemistry in peat, specifically its partitioning between the solid and aqueous phases. Often, reduced S is believed to retain As either by mineral precipitation or by promoting sorption to organic matter. Here, we demonstrate that reduced S can indeed lead to retention of As, but enhanced retention is largely restricted to acidic pH conditions (our pH 4.5 experiments). At near-neutral and alkaline pH values, reduced S promotes As desorption through thioarsenate formation. Therefore, in the presence of reduced S, a change in pH from acidic to neutral/alkaline transitions organic matter from a sink to a source of As.

Arsenic mobilization caused by thioarsenate formation is relevant for numerous environments from peatlands to aquifers rich in organic materials. Thereby, As mobilization can be observed either in environments where pH increases naturally or due to anthropogenic impact, crossing the point where S switches its role in the fate of As, or in environments with stable neutral to alkaline conditions and changes in reduced S content. Such changes in reduced S content could be induced by natural fluctuations such as melt water inputs, water table changes, or seasonal changes in microbial sulfate reduction as well as by changes in treatment or remediation measures of managed peatlands or aquifers.

For managed peatlands, environmental regulations typically define requirements for pretreatment of wastewater prior to discharge into the environment. Commonly used methods involve an increase in the pH (for precipitation reactions) generating neutral to alkaline wastewater.⁵⁹ One such example is a formerly acidic peatland used for treatment of mine

wastewater at a gold mine in northern Finland,³ which received pretreated water with neutral to alkaline pH and high concentrations of sulfate; the resulting reduced S and higher pH values may lead organic matter to change from being a sink to a source of As. The absolute As release in this peatland could be especially high because, based on the observed pH dependency of sorption, the original, acidic peat should have initially accumulated higher amounts of As compared to the same peat at neutral conditions. Based on the results of our laboratory experiments, the intended preclean-up could reduce As retention potential or even lead to long-term As mobilization from the peatland, especially in conjunction with the additional input of high sulfate concentrations, promoting thioarsenate formation upon microbial reduction to sulfide.

Small, natural changes or naturally prevailing neutral pH conditions may also favor As mobilization. In minerotrophic fens with naturally occurring neutral pH conditions, for example, a pool of reduced S in the aqueous or solid phase as well as fluctuations due to seasonal microbial sulfate reduction controlling thioarsenate formation may play an important role in As mobilization. In addition, even in slightly acidic natural wetlands, such as Gola di Lago peatland (pH 5.3–6.0),⁵ thiolation via interaction of As with surface-associated S or nondetectable concentration of reduced S in solution may mobilize As. High aqueous As pore water concentrations and a dominance of MTAs^{V} , which is also stable under acidic conditions, demonstrate continuous As release likely due to lack of sorption and consequent built-up of MTAs^{V} in solution over time.

The high potential for As mobilization at neutral pH conditions is further relevant to aquifers containing peat layers, which are common in, for example, Southeast Asia.^{24,27,60} A recent study on Mekong Delta sediments discovered high proportions of thiol-bound As (along with arsenian pyrite) in peat layers highly enriched in As compared to the surrounding low C sediment.²⁴ Zero-valent S, on NOM surfaces or in solution, may be formed in the sediments during pyrite oxidation²⁴ or the reaction of dissolved sulfide with NOM,⁶¹ and consequently, thioarsenates may be mobilized. This would match well-water observations made in Bangladesh, where the highest proportion of MTAs^{V} occurred at a depth where a distinct peat layer was found.²⁷ Therefore, thioarsenate formation in aquifer peat layers could play a so far underestimated role in localized As mobilization. Further, the sea level rising due to global warming may drive biogeochemical reactions that change pH and reduced S levels in aquifers, wetlands, and peatlands in coastal lowland areas, potentially enhancing As mobilization from these environments.

Overall, our study demonstrates the importance of pH and reduced S for the mobility of As relevant for a wide range of environments, where abundant solid NOM has previously been thought to act predominantly as the sorbent for As.

■ ASSOCIATED CONTENT

SI Supporting Information

The Supporting Information is available free of charge at <https://pubs.acs.org/doi/10.1021/acs.est.0c00457>.

Characterization of potassium (poly)sulfide, detailed method description of As solid-phase speciation analyses with XAS and used reference standards, shell-fitting

results for As K-edge EXAFS spectra of samples at pH 7.0, comparison of As desorption calculated from solid-phase and aqueous-phase data, total aqueous As and Fe concentrations, details of S solid-phase speciation analyses with XAS as well as results of solid-phase S speciation, further data S solid-phase content and aqueous sulfide concentrations, and results of statistical analyses (PDF)

AUTHOR INFORMATION

Corresponding Author

Britta Planer-Friedrich – Department of Environmental Geochemistry, Bayreuth Center for Ecology and Environmental Research (BAYCEER), University of Bayreuth, 95440 Bayreuth, Germany; orcid.org/0000-0002-0656-4283; Phone: +49-921-553999; Email: b.planer-friedrich@uni-bayreuth.de; Fax: +49-921-552334

Authors

Anne Eberle – Department of Environmental Geochemistry, Bayreuth Center for Ecology and Environmental Research (BAYCEER), University of Bayreuth, 95440 Bayreuth, Germany

Johannes Besold – Department of Environmental Geochemistry, Bayreuth Center for Ecology and Environmental Research (BAYCEER), University of Bayreuth, 95440 Bayreuth, Germany

Carolin F. Kerl – Department of Environmental Geochemistry, Bayreuth Center for Ecology and Environmental Research (BAYCEER), University of Bayreuth, 95440 Bayreuth, Germany

Juan S. Lezama-Pacheco – Department of Earth System Science, Stanford University, Stanford, California 94305, United States

Scott Fendorf – Department of Earth System Science, Stanford University, Stanford, California 94305, United States; orcid.org/0000-0002-9177-1809

Complete contact information is available at: <https://pubs.acs.org/10.1021/acs.est.0c00457>

Notes

The authors declare no competing financial interest.

ACKNOWLEDGMENTS

We acknowledge financial support by the German Research Foundation (grant no. DFG PL 302/20), a PhD student short-time stipend to Stanford University for J.B. (German Academic Exchange Service, DAAD 57314604) as well as a DAAD mobility grant (DAAD 57315737) for the USA to B.P.-F. Sulfur and As K-edge XAS experiments were performed at the Stanford Synchrotron Radiation Lightsource, SLAC National Accelerator Laboratory, supported by the U.S. Department of Energy, Office of Science, Office of Basic Energy Sciences under contract no. DE-AC02-76SF00515. We are grateful to Matthew Latimer and Erik Nelson for their support at beamlines 4-3 and 9-3. Further, we thank Christian Mikutta (Soil Mineralogy, Gottfried Wilhelm Leibniz Universität Hannover) for providing peat for the incubations and Lukas Gerber, Esther Breuning, Andreas Cramer, and Judith Mehlhorn for assistance during experiments.

REFERENCES

- (1) González, A. Z. I.; Krachler, M.; Cheburkin, A. K.; Shoty, W. Spatial distribution of natural enrichments of arsenic, selenium, and uranium in a minerotrophic peatland, Gola di Lago, Canton Ticino, Switzerland. *Environ. Sci. Technol.* **2006**, *40*, 6568–6574.
- (2) Lizama, K. A.; Fletcher, T. D.; Sun, G. Removal processes for arsenic in constructed wetlands. *Chemosphere* **2011**, *84*, 1032–1043.
- (3) Palmer, K.; Ronkanen, A.-K.; Kløve, B. Efficient removal of arsenic, antimony and nickel from mine wastewaters in Northern treatment peatlands and potential risks in their long-term use. *Ecol. Eng.* **2015**, *75*, 350–364.
- (4) Rothwell, J. J.; Taylor, K. G.; Ander, E. L.; Evans, M. G.; Daniels, S. M.; Allott, T. E. H. Arsenic retention and release in ombrotrophic peatlands. *Sci. Total Environ.* **2009**, *407*, 1405–1417.
- (5) Besold, J.; Biswas, A.; Suess, E.; Scheinost, A. C.; Rossberg, A.; Mikutta, C.; Kretzschmar, R.; Gustafsson, J. P.; Planer-Friedrich, B. Monothioarsenate Transformation Kinetics Determining Arsenic Sequestration by Sulfhydryl Groups of Peat. *Sci. Total Environ.* **2018**, *52*, 7317–7326.
- (6) Blodau, C.; Fulda, B.; Bauer, M.; Knorr, K.-H. Arsenic speciation and turnover in intact organic soil mesocosms during experimental drought and rewetting. *Geochim. Cosmochim. Acta* **2008**, *72*, 3991–4007.
- (7) Langner, P.; Mikutta, C.; Kretzschmar, R. Arsenic sequestration by organic sulphur in peat. *Nat. Geosci.* **2012**, *5*, 66.
- (8) Langner, P.; Mikutta, C.; Suess, E.; Marcus, M. A.; Kretzschmar, R. Spatial distribution and speciation of arsenic in peat studied with microfocused X-ray fluorescence spectrometry and X-ray absorption spectroscopy. *Sci. Total Environ.* **2013**, *47*, 9706–9714.
- (9) Mikutta, C.; Kretzschmar, R. Spectroscopic evidence for ternary complex formation between arsenate and ferric iron complexes of humic substances. *Sci. Total Environ.* **2011**, *45*, 9550–9557.
- (10) Sharma, P.; Ofner, J.; Kappler, A. Formation of binary and ternary colloids and dissolved complexes of organic matter, Fe and As. *Sci. Total Environ.* **2010**, *44*, 4479–4485.
- (11) Hoffmann, M.; Mikutta, C.; Kretzschmar, R. Bisulfide Reaction with Natural Organic Matter Enhances Arsenite Sorption: Insights from X-ray Absorption Spectroscopy. *Sci. Total Environ.* **2012**, *46*, 11788–11797.
- (12) Couture, R.-M.; Wallschläger, D.; Rose, J.; Van Cappellen, P. Arsenic binding to organic and inorganic sulfur species during microbial sulfate reduction: a sediment flow-through reactor experiment. *Environ. Chem.* **2013**, *10*, 285–294.
- (13) Hoffmann, M.; Mikutta, C.; Kretzschmar, R. Arsenite Binding to Natural Organic Matter: Spectroscopic Evidence for Ligand Exchange and Ternary Complex Formation. *Sci. Total Environ.* **2013**, *47*, 12165–12173.
- (14) Biswas, A.; Besold, J.; Sjöstedt, C.; Gustafsson, J. P.; Scheinost, A. C.; Planer-Friedrich, B. Complexation of Arsenite, Arsenate, and Monothioarsenate with Oxygen-Containing Functional Groups of Natural Organic Matter: An XAS Study. *Sci. Total Environ.* **2019**, *53*, 10723–10731.
- (15) Buschmann, J.; Kappeler, A.; Lindauer, U.; Kistler, D.; Berg, M.; Sigg, L. Arsenite and arsenate binding to dissolved humic acids: influence of pH, type of humic acid, and aluminum. *Sci. Total Environ.* **2006**, *40*, 6015–6020.
- (16) Liu, G.; Fernandez, A.; Cai, Y. Complexation of arsenite with humic acid in the presence of ferric iron. *Sci. Total Environ.* **2011**, *45*, 3210–3216.
- (17) Spratt, H. G., Jr.; Morgan, M. D. Sulfur cycling in a cedar-dominated, freshwater wetland. *Limnol. Oceanogr.* **1990**, *35*, 1586–1593.
- (18) Steinmann, P.; Shoty, W. Ion chromatography of organic-rich natural waters from peatlands IV. Dissolved free sulfide and acid-volatile sulfur. *J. Chromatogr. A* **1995**, *706*, 287–292.
- (19) Shoty, W. Review of the inorganic geochemistry of peats and peatland waters. *Earth-Sci. Rev.* **1988**, *25*, 95–176.
- (20) Stumm, W.; Morgan, J. J. *Aquatic chemistry: chemical equilibria and rates in natural waters*; John Wiley & Sons: 2012; Vol. 126.

- (21) Koretsky, C. M.; Haas, J. R.; Ndenga, N. T.; Miller, D. Seasonal variations in vertical redox stratification and potential influence on trace metal speciation in minerotrophic peat sediments. *Water, Air, and Soil Pollut.* **2006**, *173*, 373–403.
- (22) Koretsky, C. M.; Haveman, M.; Beuing, L.; Cuellar, A.; Shattuck, T.; Wagner, M. Spatial variation of redox and trace metal geochemistry in a minerotrophic fen. *Biogeochemistry* **2007**, *86*, 33–62.
- (23) Wieder, R. K.; Lang, G. E. Cycling of inorganic and organic sulfur in peat from Big Run Bog, West Virginia. *Biogeochemistry* **1988**, *5*, 221–242.
- (24) Asta, M. P.; Wang, Y.; Frutschi, M.; Viacava, K.; Loreggian, L.; Le Pape, P.; Le Vo, P.; Fernández, A. M.; Morin, G.; Bernier-Latmani, R. Microbially Mediated Release of As from Mekong Delta Peat Sediments. *Sci. Total Environ.* **2019**, *53*, 10208–10217.
- (25) Langner, P.; Mikutta, C.; Kretzschmar, R. Oxidation of organosulfur-coordinated arsenic and realgar in peat: Implications for the fate of arsenic. *Sci. Total Environ.* **2014**, *48*, 2281–2289.
- (26) Hoffmann, M.; Mikutta, C.; Kretzschmar, R. Arsenite Binding to Sulfhydryl Groups in the Absence and Presence of Ferrihydrite: A Model Study. *Sci. Total Environ.* **2014**, *48*, 3822–3831.
- (27) Planer-Friedrich, B.; Schaller, J.; Wismeth, F.; Mehlhorn, J.; Hug, S. J. Monothioarsenate Occurrence in Bangladesh Groundwater and Its Removal by Ferrous and Zero-Valent Iron Technologies. *Sci. Total Environ.* **2018**, *52*, 5931–5939.
- (28) Planer-Friedrich, B.; Härtig, C.; Lohmayer, R.; Suess, E.; McCann, S. H.; Oremland, R. Anaerobic Chemolithotrophic Growth of the Haloalkaliphilic Bacterium Strain MLMS-1 by Disproportionation of Monothioarsenate. *Sci. Total Environ.* **2015**, *49*, 6554–6563.
- (29) Kamysny, A., Jr.; Ferdelman, T. G. Dynamics of zero-valent sulfur species including polysulfides at seep sites on intertidal sand flats (Wadden Sea, North Sea). *Mar. Chem.* **2010**, *121*, 17–26.
- (30) Heitmann, T.; Blodau, C. Oxidation and incorporation of hydrogen sulfide by dissolved organic matter. *Chem. Geol.* **2006**, *235*, 12–20.
- (31) Yu, Z.-G.; Göttlicher, J.; Steininger, R.; Knorr, K.-H. Organic sulfur and organic matter redox processes contribute to electron flow in anoxic incubations of peat. *Environ. Chem.* **2016**, *13*, 816–825.
- (32) Hellige, K.; Pollok, K.; Larese-Casanova, P.; Behrends, T.; Peiffer, S. Pathways of ferrous iron mineral formation upon sulfidation of lepidocrocite surfaces. *Geochim. Cosmochim. Acta* **2012**, *81*, 69–81.
- (33) Poulton, S. W. Sulfide oxidation and iron dissolution kinetics during the reaction of dissolved sulfide with ferrihydrite. *Chem. Geol.* **2003**, *202*, 79–94.
- (34) Poulton, S. W.; Krom, M. D.; Raiswell, R. A revised scheme for the reactivity of iron (oxyhydr) oxide minerals towards dissolved sulfide. *Geochim. Cosmochim. Acta* **2004**, *68*, 3703–3715.
- (35) ThomasArrigo, L. K.; Mikutta, C.; Lohmayer, R.; Planer-Friedrich, B.; Kretzschmar, R. Sulfidization of organic freshwater flocs from a minerotrophic peatland: Speciation changes of iron, sulfur, and arsenic. *Sci. Total Environ.* **2016**, *50*, 3607–3616.
- (36) Wan, M.; Shchukarev, A.; Lohmayer, R.; Planer-Friedrich, B.; Peiffer, S. Occurrence of surface polysulfides during the interaction between ferric (hydr) oxides and aqueous sulfide. *Sci. Total Environ.* **2014**, *48*, 5076–5084.
- (37) Kumar, N.; Pacheco, J. L.; Noël, V.; Dublet, G.; Brown, G. E. Sulfidation mechanisms of Fe (III)-(oxyhydr) oxide nanoparticles: a spectroscopic study. *Environ. Sci.: Nano* **2018**, *5*, 1012–1026.
- (38) Stauder, S.; Raue, B.; Sacher, F. Thioarsenates in Sulfidic Waters. *Sci. Total Environ.* **2005**, *39*, 5933–5939.
- (39) Planer-Friedrich, B.; Wallschläger, D. A critical investigation of hydride generation-based arsenic speciation in sulfidic waters. *Sci. Total Environ.* **2009**, *43*, 5007–5013.
- (40) Planer-Friedrich, B.; Fisher, J. C.; Hollibaugh, J. T.; Süß, E.; Wallschläger, D. Oxidative transformation of trithioarsenate along alkaline geothermal drainages—abiotic versus microbially mediated processes. *Geomicrobiol. J.* **2009**, *26*, 339–350.
- (41) Burton, E. D.; Johnston, S. G.; Planer-Friedrich, B. Coupling of arsenic mobility to sulfur transformations during microbial sulfate reduction in the presence and absence of humic acid. *Chem. Geol.* **2013**, *343*, 12–24.
- (42) Couture, R.-M.; Rose, J.; Kumar, N.; Mitchell, K.; Wallschläger, D.; Van Cappellen, P. Sorption of arsenite, arsenate, and thioarsenates to iron oxides and iron sulfides: A kinetic and spectroscopic investigation. *Sci. Total Environ.* **2013**, *47*, 5652–5659.
- (43) Suess, E.; Planer-Friedrich, B. Thioarsenate formation upon dissolution of orpiment and arsenopyrite. *Chemosphere* **2012**, *89*, 1390–1398.
- (44) Khan, U. A.; Kujala, K.; Nieminen, S. P.; Räisänen, M. L.; Ronkanen, A.-K. Arsenic, antimony, and nickel leaching from northern peatlands treating mining influenced water in cold climate. *Sci. Total Environ.* **2019**, *657*, 1161–1172.
- (45) Besold, J.; Eberle, A.; Noël, V.; Kujala, K.; Kumar, N.; Scheinost, A. C.; Lezama-Pacheco, J. S.; Fendorf, S.; Planer-Friedrich, B. Antimonite Binding to Natural Organic Matter: Spectroscopic Evidence from a Mine Water Impacted Peatland. *Sci. Total Environ.* **2019**, *53*, 10792–10802.
- (46) Urban, N. R.; Bayley, S. E.; Eisenreich, S. J. Export of dissolved organic carbon and acidity from peatlands. *Water Resour. Res.* **1989**, *25*, 1619–1628.
- (47) Chesworth, W.; Cortizas, A. M.; García-Rodeja, E. Chapter 8 The redox–pH approach to the geochemistry of the Earth’s land surface, with application to peatlands. In *Developments in Earth Surface Processes*; Martini, I. P.; Martínez Cortizas, A.; Chesworth, W., Eds. Elsevier: 2006; Vol. 9, pp 175–195.
- (48) Bares, R. H.; Wali, M. K. Chemical relations and litter production of *Picea mariana* and *Larix laricina* stands on an alkaline peatland in Northern Minnesota. *Vegetatio* **1979**, *40*, 79–94.
- (49) Besold, J.; Kumar, N.; Scheinost, A. C.; Pacheco, J. L.; Fendorf, S.; Planer-Friedrich, B. Antimonite Complexation with Thiol and Carboxyl/Phenol Groups of Peat Organic Matter. *Sci. Total Environ.* **2019**, *53*, 5005–5015.
- (50) Planer-Friedrich, B.; London, J.; McCleskey, R. B.; Nordstrom, D. K.; Wallschläger, D. Thioarsenates in Geothermal Waters of Yellowstone National Park: Determination, Preservation, and Geochemical Importance. *Sci. Total Environ.* **2007**, *41*, 5245–5251.
- (51) Cline, J. D. Spectrophotometric determination of hydrogen sulfide in natural waters¹. *Limnol. Oceanogr.* **1969**, *14*, 454–458.
- (52) Kamysny, A., Jr.; Borkenstein, C. G.; Ferdelman, T. G. Protocol for quantitative detection of elemental sulfur and polysulfide zero-valent sulfur distribution in natural aquatic samples. *Geostand. Geoanal. Res.* **2009**, *33*, 415–435.
- (53) Ravel, B.; Newville, M. ATHENA, ARTEMIS, HEPHAESTUS: data analysis for X-ray absorption spectroscopy using IFEFFIT. *J. Synchrotron Radiat.* **2005**, *12*, 537–541.
- (54) Webb, S. M. SIXpack: a graphical user interface for XAS analysis using IFEFFIT. *Phys. Scr.* **2005**, *2005*, 1011.
- (55) Manceau, A.; Nagy, K. L. Quantitative analysis of sulfur functional groups in natural organic matter by XANES spectroscopy. *Geochim. Cosmochim. Acta* **2012**, *99*, 206–223.
- (56) Suess, E.; Scheinost, A. C.; Bostick, B. C.; Merkel, B. J.; Wallschläger, D.; Planer-Friedrich, B. Discrimination of thioarsenites and thioarsenates by X-ray absorption spectroscopy. *Anal. Chem.* **2009**, *81*, 8318–8326.
- (57) Rickard, D.; Morse, J. W. Acid volatile sulfide (AVS). *Mar. Chem.* **2005**, *97*, 141–197.
- (58) Planer-Friedrich, B.; Suess, E.; Scheinost, A. C.; Wallschläger, D. Arsenic speciation in sulfidic waters: reconciling contradictory spectroscopic and chromatographic evidence. *Anal. Chem.* **2010**, *82*, 10228–10235.
- (59) Johnson, D. B.; Hallberg, K. B. Acid mine drainage remediation options: a review. *Sci. Total Environ.* **2005**, *338*, 3–14.
- (60) McArthur, J. M.; Banerjee, D. M.; Hudson-Edwards, K.; Mishra, R.; Purohit, R.; Ravenscroft, P.; Cronin, A.; Howarth, R. J.; Chatterjee, A.; Talukder, T.; Lowry, D.; Houghton, S.; Chadha, D. K. Natural organic matter in sedimentary basins and its relation to arsenic in anoxic ground water: the example of West Bengal and its worldwide implications. *Appl. Geochem.* **2004**, *19*, 1255–1293.

(61) Yu, Z.-G.; Peiffer, S.; Göttlicher, J.; Knorr, K.-H. Electron Transfer Budgets and Kinetics of Abiotic Oxidation and Incorporation of Aqueous Sulfide by Dissolved Organic Matter. *Sci. Total Environ.* **2015**, *49*, 5441–5449.

Supporting Information to

“Arsenic Fate in Peat Controlled by the
pH-Dependent Role of Reduced Sulfur”

*Anne Eberle¹, Johannes Besold¹, Carolin F. Kerl¹, Juan S. Lezama-Pacheco², Scott Fendorf² and
Britta Planer-Friedrich*¹*

¹Department of Environmental Geochemistry, Bayreuth Center for Ecology and Environmental
Research (BAYCEER), University of Bayreuth, 95440 Bayreuth, Germany

²Department of Earth System Science, Stanford University, Stanford, California
94305, United States

(20 pages, 8 figures, 19 tables)

Table of contents

1	Characterization of Potassium (poly)sulfide	2
2	Arsenic Solid-Phase Speciation Analyses with X-ray Absorption Spectroscopy	3
3	Shell-fitting Results for As <i>K</i> -edge EXAFS Spectra of Peat Samples at pH 7.0	8
4	Comparison of Arsenic Desorption calculated from Solid-Phase and Aqueous-Phase Data	9
5	Total Aqueous Arsenic and Iron Concentrations	10
6	Sulfur Solid-Phase Speciation Analyses with X-ray Absorption Spectroscopy	11
7	Changes in Sulfur Solid-Phase Content and Aqueous Sulfide Concentrations	15
8	Statistics.....	16

* corresponding author: email: b.planer-friedrich@uni-bayreuth.de

phone +49 921 553999; fax: +49 921 52334

1 Characterization of Potassium (poly)sulfide

The potassium (poly)sulfide (K_2S_n , $\geq 42\%$ K_2S basis, Sigma-Aldrich) used to add zero-valent sulfur in a water soluble form, was characterized. A solution of 1 g/L was analyzed for its zero-valent sulfur and sulfide concentrations by high-performance liquid chromatography (HPLC, LaChrom Elite, L-2130 pump, L-2200 autosampler, L-2420 UV-vis detector, Merck Hitachi) using a reversed phase C18 column (Luna, $3\mu\text{m}$, 150×2.0 mm, Phenomenex) after extraction according to previously published methods.^{1,2} Sulfide was determined photometrically according to the methylene blue method³ at an absorption wavelength of 650 nm with a multiplate reader (Infinite 200 PRO, Tecan). The solution showed a zero-valent sulfur concentration of 1386 ± 214 $\mu\text{mol/L}$ ($n=6$) and a sulfide (S^{-II}) concentration of 2336 ± 287 $\mu\text{mol/L}$ ($n=6$). Assuming that K_2S_n is K_2S_2 , then K_2S_n contained equal amounts of zero-valent sulfur and S^{-II} (1386 $\mu\text{mol/L}$ of S^{-II} ($= c(S^0)$) originate from K_2S_2). Therefore, 950 $\mu\text{mol/L}$ out of 2336 $\mu\text{mol/L}$ S^{-II} are left for the free sulfide K_2S . The resulting 41% of K_2S are similar to what was indicated by the manufacturer. Hence, the polysulfide was characterized as 42% K_2S and 58% K_2S_2 .

2 Arsenic Solid-Phase Speciation Analyses with X-ray Absorption Spectroscopy

X-ray Absorption Spectroscopy. For X-ray absorption spectroscopy (XAS) analysis, anoxic freeze-dried and homogenized peat samples were filled into aluminum sample holders and sealed with Kapton tape. Arsenic K-edge spectra were collected at beamline 9-3 at the Stanford Synchrotron Radiation Lightsource (SSRL, Stanford, USA). The beamline was equipped with a liquid nitrogen-cooled Si(220) double-crystal monochromator, which was calibrated to the L₃-edge of a Au foil (11,919 eV). Absorption of Au was monitored in transmission mode simultaneously to all sample scans. Higher order harmonic X-rays were minimized through use of two 1.0 m and 1.2 m Rh-coated Si mirrors. Measurements were done in fluorescence mode using a 100-element solid-state Ge detector (Canberra) at 15 K achieved with a He-cryostat to avoid beam damage and thermal disorder. Soller slits and Al foil were used to filter Fe fluorescence and scattering contributions. A Ge-filter was installed to filter energies below As. Per sample 2-3 scans were collected and averaged. Arsenic reference compounds measured as described for the samples or published reference spectra¹⁻⁴ were used for data analyses. The arsenic reference compounds, their origin and literature references are listed in Table SI-1.

XAS Data Processing. All spectra were normalized using the software Athena.⁵ Background correction was performed by subtracting a linear function fit to the pre-edge region (-178.7 to -14.9 eV) and subsequently dividing by a third-order polynomial fit to the post-edge region (150 to 997 eV). The edge positions (E_0) of XANES were determined from the 2 points-smoothed maximum of the first derivative spectra. For EXAFS analysis, E_0 was fixed to 11,865 eV. The background spline of EXAFS spectra was adjusted using the Autobk algorithm incorporated in Athena (Rbkg=0.9; k -weight=3; k -range 0–13 Å⁻¹).

Principal Components Analysis, Target-Transform Testing and Linear Combination Fitting.

Spectra were tested for the minimum number of components by principal component analysis (PCA) based on the empirical indicator function⁶ and target-transform testing (TT) was done for the significant components against the references library using the program SIXpack.⁷ SPOIL, chi-squared and R-values as well as visual confirmation were used to evaluate whether a target was acceptable.^{6,8} Linear combination fitting (LCF) of the normalized XANES spectra in the energy

range 11,848.5-11,898.5 eV and of the k^2 -weighted EXAFS spectra in the k -range 3.2–11 Å⁻¹ was done in Athena.⁵

The suitability of reference spectra for LCF was determined by TT using the first three of four components calculated by PCA for XANES spectra and the first two of four components for EXAFS spectra (selected based on cumulative variance >99% and visual inspection, Table SI-2). The quality of the transformation was evaluated by the empirical SPOIL value categorized by Malinowski⁹: 0-1.5 excellent, 1.5-3 good, 3-4.5 fair, 4.5-6 acceptable, and >6 for an unacceptable reference spectrum. Only references with SPOIL values <4.2 were used for further LCF analyses. (Table SI-3: references in italic).

However, the obtained number of As reference spectra suitable for LCF analysis based on TT (9) was larger than the number of principal components determined by PCA (3). This may be due to (i) similar local As coordination environments in reference compounds identified by TT or (ii) the occurrence of several species in constant proportions in all analyzed spectra.¹⁰ Since we could not exclude the latter effect, LCF analyses were performed using all nine As references determined as suitable (Table SI-3). Each experimental spectrum was least-squares simulated in Athena by calculating all two- to five-component fits. The number of components included in the fit was successively increased and each additional component was retained in the fit when the reduced chi-square value decreased by at least 10%. The best fit LCF results for the peat As XANES spectra included two out of nine As reference spectra for the initial sample and sulfide treatment and four out of nine reference spectra for no sulfur addition and polysulfide treatment (Table SI-4). The best fit LCF results for the peat As EXAFS spectra included two out of nine As reference spectra for the initial sample and sulfur treatments and three out of nine reference spectra for the sample without sulfur addition (Table SI-5).

Shell-fit Analysis. A Kaiser-Bessel window with a sill width of 3 Å⁻¹ was used for Fourier transformation. Shell-fit analysis of k^2 -weighted EXAFS spectra were performed in R-space employing the software Artemis. Theoretical scattering paths were calculated with FEFF6¹¹ based on the crystal structures of arsenolite¹² and tris(phenylthio)arsine.¹³ Quality of the fits were evaluated based on the NSSR-value ($100 \times \sum_i (\text{data}_i - \text{fit}_i)^2 / \sum_i \text{data}_i^2$).

Table SI-1: Arsenic reference compounds used in PCA, TT and LCF analyses of XANES and EXAFS spectra with details about their origin and literature references.

Compound	Chemical formula	Source/synthesis	Reference
Arsenopyrite	FeAsS	natural	from Langner et al. 2012 ²
As(III)-Ambersep GT74 resin	n.d.	synthetic	from Besold et al. 2018 ³
As(III)-O-C _{org}	As(C _x H _x O _{1+x}) ₂ (OH) ₁ ^a	synthetic	from Biswas et al. 2019 ⁴
As(III)-S-C _{org} , 30 mM S(-II)	As(C _x O _x H _x S _{1+x}) ₂ (OH) ₁ ^a	synthetic	from Besold et al. 2018 ³
As(V)-O-C _{org}	As(C _x H _x O _{1+x}) ₃ (OH) ₁ ^a	synthetic	from Biswas et al. 2019 ⁴
Dithioarsenate aqueous	H _x AsS ₂ O ₂ ^{3-x} ; x=1-3 ^a	synthetic	from Suess et al. 2009 ¹
Glutamylcysteinylglycylthioarsenite	As(C ₁₀ H ₁₇ N ₅ O ₆ S) _{2.5} (OH) _{0.5}	synthetic	synthesized after Raab et al. 2004 ¹⁴ , this study
Monothioarsenate aqueous	H _x AsO ₃ ^{3-x} ; x=1-3 ^a	synthetic	from Suess et al. 2009 ¹
Orpiment	As ₂ S ₃	commercial (Alfa Aesar)	from Besold et al. 2018 ³
Realgar	As ₄ S ₄	commercial (Alfa Aesar)	from Besold et al. 2018 ³
Sodium arsenate dibasic heptahydrate	Na ₂ HAsO ₄ · 7H ₂ O	commercial (Fluka)	from Besold et al. 2018 ³
Sodium (meta)arsenite	NaAsO ₂	commercial (Sigma-Aldrich)	from Besold et al. 2018 ³
Tetrathioarsenate aqueous	H _x AsS ₄ ^{3-x} ; x=1-3 ^a	synthetic	from Suess et al. 2009 ¹
Tris(phenylthio)arsine	C ₁₈ H ₁₅ AsS ₃	commercial (Aldrich)	from Langner et al. 2012 ²

^aestimated by XAS**Table SI-2:** Results from principal component analysis (PCA) of 4 normalized peat sample XANES spectra (energy range: 11,848.5-11,898.5 eV) and 4 *k*²-weighted peat sample EXAFS spectra (*k*-range: 3.2–11 Å⁻¹).

Compound	PCA XANES			PCA EXAFS		
	Eigenvalue	Cum. Var. ^a	IND ^b	Eigenvalue	Cum. Var. ^a	IND ^b
1	1.909	0.995	0.00042	0.865	0.934	0.00265
2	0.006	0.998	0.00040	0.035	0.973	0.00369
3	0.002	0.999	4.59e-05	0.020	0.995	0.00435
4	4.59e-05	1.0	NA	0.004	1.0	NA

^acumulative variance^bindicator function

Table SI-3: Results of target transform (TT) analysis. Compounds in *italic* were not considered for further analysis.

Reference compound	SPOIL-value	chi-squared	R-value
As(III)-O-C _{org}	1.9924	13	0.14
Sodium (meta)arsenite	2.5636	10	0.22
Tris(phenylthio)arsine	3.4914	24	0.31
Glutamylcysteinylglycylthioarsenite	3.6109	19	0.35
As(III)-Ambersep GT74 resin	3.6687	20	0.37
Sodium arsenate dibasic heptahydrate	3.6943	134	0.52
Monothioarsenate aqueous	3.8125	60	0.49
As(III)-S-C _{org} , 30 mM S(-II)	4.1572	5	0.13
As(V)-O-C _{org}	4.1871	106	0.56
<i>Orpiment</i>	4.4212	27	0.45
<i>Realgar</i>	4.8435	18	0.50
<i>Dithioarsenate aqueous</i>	5.5509	46	0.55
<i>Arsenopyrite</i>	8.5079	24	0.76
<i>Tetrathioarsenate aqueous</i>	9.5113	138	0.70

Table SI-4: Linear Combination Fit results for normalized As *K*-edge XANES spectra of the peat samples from the desorption experiment at pH 7.0 before and after incubation with or without reduced sulfur species.^a

Sample	As(III)-S-C _{org} ^b [atomic%]	As(III)-O ^c [atomic%]	As(V)-O ^d [atomic%]	Initial fit sums [atomic%]	NSSR ^e [%]
pH 7.0, t0	50 (50/-)	50 (50/-)	-	96	0.20
pH 7.0, no S	50 (14/36)	43 (43/-)	7	100	0.10
pH 7.0, + HS ⁻	52 (52/-)	48 (-/48)	-	111	0.11
pH 7.0, PS	66 (42/23)	34 (18/16)	-	107	0.04

^a Fit range: 11,845-11,875 eV, E₀ = 11,865 eV. Fitted fractions were normalized to a component sum of 100%. Fitted fractions are accurate within ±10 atom% at best. Number of fitted components in one fit (N) is significantly different from fits with N-1 components and not significantly different from fits with N+1 components (Hamilton test, p < 0.05). Fit references: ^b As(III)-S-C_{org} = As(III) bound via thiol groups to organic carbon; values in parentheses: (As(III)-S-NOM = As(III) bound via thiol groups to peat NOM/ tris(phenylthio)arsine), ^c As(III)-O = As(III) bound via oxygen; values in parentheses: (As(III)-O-NOM = As(III) bound to O-bearing groups of peat NOM/ sodium (meta)arsenite), ^d As(V)-O = sodium arsenate dibasic heptahydrate, ^e Normalized sum of squared residuals (100 × Σ_i(data_i-fit_i)²/Σ_idata_i²).

Table SI-5: Linear Combination Fit results for *k*²-weighted As *K*-edge EXAFS spectra of the peat samples from the desorption experiment at pH 7.0 before and after incubation with or without reduced sulfur species.^a

Sample	As(III)-S-C _{org} ^b [atomic%]	As(III)-O-C _{org} ^c [atomic%]	As(V)-O-C _{org} ^d [atomic%]	Initial fit sums [atomic%]	NSSR ^e [%]
pH 7.0, t0	42	58	-	85	2.7
pH 7.0, no S	38	53	9	85	2.1
pH 7.0, + HS ⁻	55	45	-	92	13.9
pH 7.0, PS	58	42	-	88	10.6

^a Fit range: 3.2–11 Å⁻¹, E₀ = 11,865 eV. Fitted fractions were normalized to a component sum of 100%. Fitted fractions are accurate within ±10 atom% at best. Number of fitted components in one fit (N) is significantly different from fits with N-1 components and not significantly different from fits with N+1 components (Hamilton test, p < 0.05). Fit references: ^b As(III)-S-C_{org} = tris(phenylthio)arsine, ^c As(III)-O-C_{org} = As(III) bound to O-bearing groups of peat NOM, ^d As(V)-O-C_{org} = As(V) bound to peat NOM via O-bearing groups, ^e Normalized sum of squared residuals (100 × Σ_i(data_i-fit_i)²/Σ_idata_i²).

Synthesis and Characterization of As(III)-(GSH)₃ Reference Standard. An As(III)-glutathione complex with As(III)-(GSH)₃ stoichiometry was synthesized according to the following procedure slightly modified from Raab et al.¹⁴ A molar ratio of As(III) (sodium (meta)arsenite, Sigma-Aldrich, $\geq 90\%$) and GSH (L-glutathione, VWR, 98%) of 1:3 was dissolved within 6 mL of anoxic water in a glovebag ($pO_2 < 1$ ppm). The mixture was stirred for 12 h at room temperature in the glovebag and subsequently the formed As(III)-(GSH)₃ complex was precipitated with 25 mL of ethanol. The resulting precipitates were filtered using glass frits and a vacuum pump and dried within the glovebag in a desiccator over hygroscopic silica gel for several days. The As(III)-(GSH)₃ standard was carefully ground with mortar and pestle and stored in the glovebag until XAS analyses.

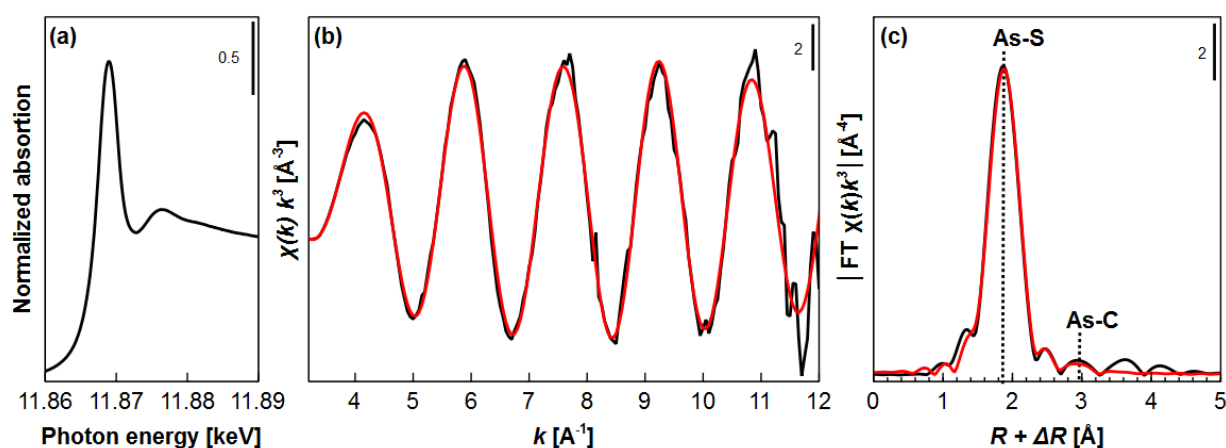


Figure SI-1: Arsenic *K*-edge XANES spectra (a), k^3 -weighted EXAFS spectra (b), and Fourier-transform magnitudes (c) of synthesized As(III)-(GSH)₃ standard. Black lines show experimental data and red lines represent the fits.

Table SI-6: E_0 -energy and EXAFS parameters determined by shell-fitting of As *K*-edge EXAFS spectra of synthesized As(III)-(GSH)₃.^a

Sample	E_0 [eV] ^b	Path	CN ^c	R [Å] ^d	σ^2 [Å ²] ^e	ΔE_0 [eV] ^f	NSSR [%] ^g
As(III)-(GSH) ₃	11,867.6	As-S	3.0	2.27	0.0018	9.2	0.66
		As-C	3.1	3.17	0.0089		

^aThe passive amplitude reduction factor S_0^2 was set to 0.82. ^b E_0 : maximum of the first derivative of normalized XANES spectra, general error ± 0.3 eV. ^cCoordination number (path degeneracy), general error $\pm 25\%$. ^dMean half path length, general error ± 0.02 Å. ^eDebye-Waller parameter, general error ± 0.0005 Å². ^fEnergy-shift parameter. ^gNormalized sum of squared residuals ($100 \times \sum_i(\text{data}_i - \text{fit}_i)^2 / \sum_i \text{data}_i^2$).

3 Shell-fitting Results for As *K*-edge EXAFS Spectra of Peat Samples at pH 7.0

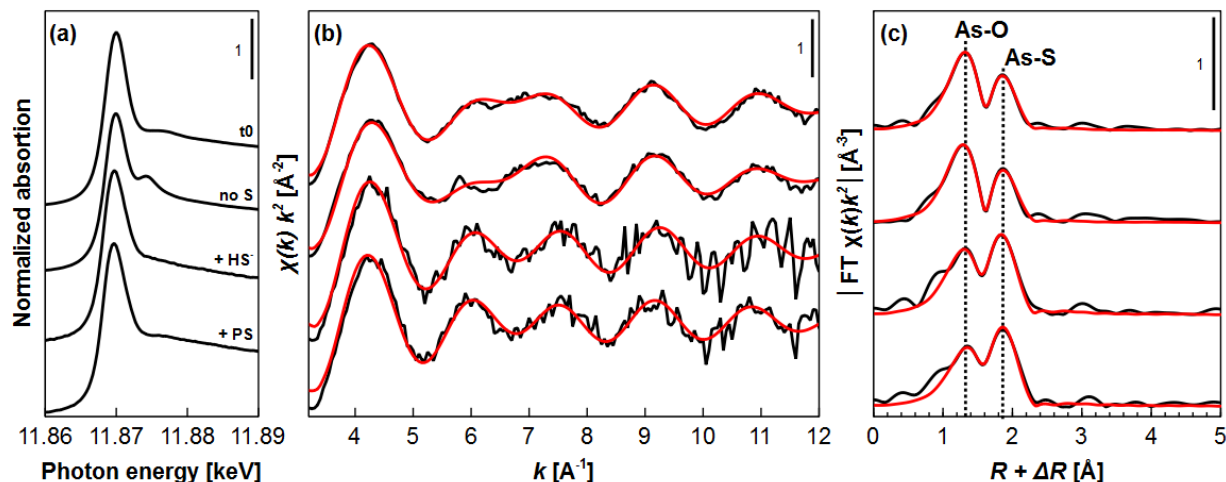


Figure SI-2: Arsenic *K*-edge XANES spectra (a), k^2 -weighted EXAFS spectra (b), and Fourier-transform magnitudes (c) of peat samples at the end of the desorption experiment at pH 7.0. Black lines show experimental data and red lines represent the fits.

Table SI-7: E_0 -energy and EXAFS parameters determined by shell-fitting of As *K*-edge EXAFS spectra of the studied peat samples from the desorption experiment at pH 7.0.^a

Sample	E_0 [eV] ^b	Path	CN ^c	R [Å] ^d	σ^2 [Å ²] ^e	ΔE_0 [eV] ^f	NSSR [%] ^g
pH 7.0, t0	11,868.5	As-S	1.5	2.24	0.0049	8.3	0.84
		As-O	2.2	1.79	0.0043		
pH 7.0, no S	11,868.5	As-S	1.3	2.27	0.0037	8.3	1.27
		As-O	2.5	1.77	0.0056		
pH 7.0, +HS ⁻	11,866.2	As-S	2.0	2.25	0.0042	9.8	1.46
		As-O	2.3	1.79	0.0078		
pH 7.0, +PS	11,866.2	As-S	2.0	2.27	0.0040	11.0	1.26
		As-O	2.0	1.79	0.0075		

^aThe passive amplitude reduction factor S_0^2 was set to 0.82. ^b E_0 : maximum of the first derivative of normalized XANES spectra, general error ± 0.3 eV. ^cCoordination number (path degeneracy), general error $\pm 25\%$. ^dMean half path length, general error ± 0.02 Å. ^eDebye-Waller parameter, general error ± 0.0005 Å². ^fEnergy-shift parameter. ^gNormalized sum of squared residuals ($100 \times \sum_i (\text{data}_i - \text{fit}_i)^2 / \sum_i \text{data}_i^2$).

4 Comparison of Arsenic Desorption calculated from Solid-Phase and Aqueous-Phase Data

Desorption (in percent) was calculated both from the difference in solid-phase As content before and at the end of the experiment, as well as from the concentration in solution referred to initial solid-phase content on the As-loaded model peat (Table SI-8). Arsenic desorption (in percent) from solid-phase data was calculated by dividing the difference between the solid-phase As content at the end and the beginning of the experiment by the initial solid-phase As content of the As-loaded model peat, and multiplication of this unit-free ratio by 100%. Using aqueous As concentrations, both aqueous As concentration and initial solid-phase As content were multiplied by the respective volume or mass used in the experiment to get absolute amount of substance in mol. Subsequently, the ratio between the amount of As in solution and the amount of As in the initial As-loaded model peat was calculated. This ratio multiplied by 100% gives the relative desorption in percent. Both methods resulted in similar percentages and trends between the treatments.

Table SI-8: Comparison of desorption results calculated from solid-phase and aqueous-phase data.

pH	treatment	As desorption [%] \pm SD [%]	As desorption [%] \pm SD [%]
		from solid-phase data	from aqueous-phase data
4.5	no S	65 \pm 5.4	62 \pm 2.4
	+ HS ⁻	44 \pm 1.8	43 \pm 1.6
	+ PS	46 \pm 3.0	40 \pm 0.8
7.0	no S	68 \pm 3.7	65 \pm 1.4
	+ HS ⁻	87 \pm 0.7	80 \pm 1.7
	+ PS	88 \pm 0.7	82 \pm 2.7
8.5	no S	80 \pm 0.6	73 \pm 1.5
	+ HS ⁻	88 \pm 0.5	81 \pm 1.0
	+ PS	91 \pm 0.2	83 \pm 0.3

5 Total Aqueous Arsenic and Iron Concentrations

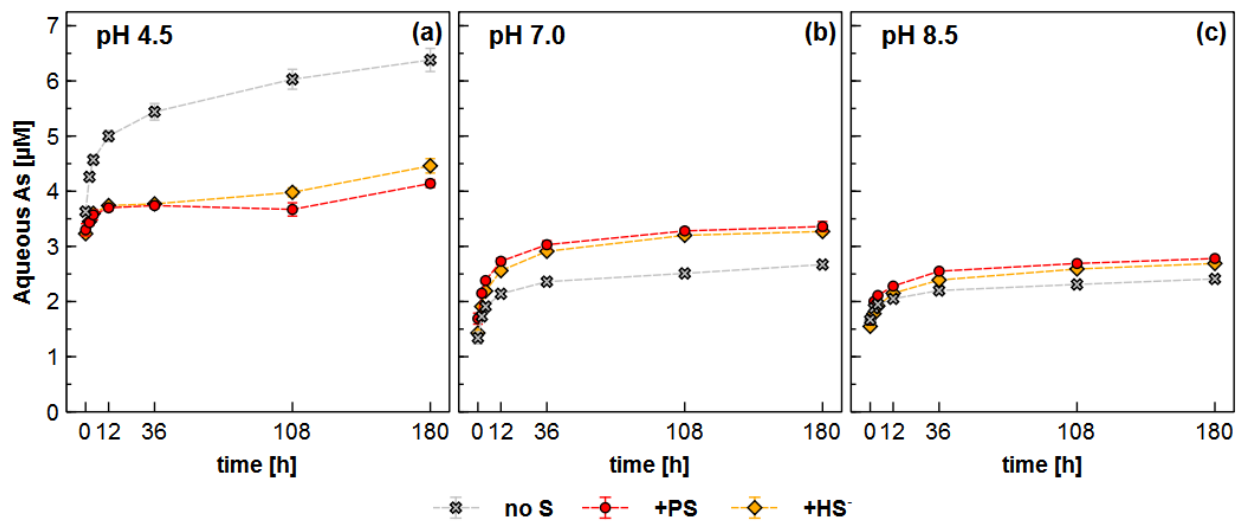


Figure SI-3: Time series of total aqueous As concentrations over 180h at pH 4.5 (a), 7.0 (b), and 8.5 (c) without sulfur addition (no S), with sulfide (+HS⁻) and polysulfide (+PS) addition. Concentrations at all time points were analyzed in triplicates, error bars represent the standard deviation.

Despite acid washing, low amounts of Fe remained in the model peat organic matter and were mobilized with a linear trend over time (Figure SI-4). The release was only pH dependent with about 5 μM under acidic conditions and <2 μM at neutral and alkaline conditions.

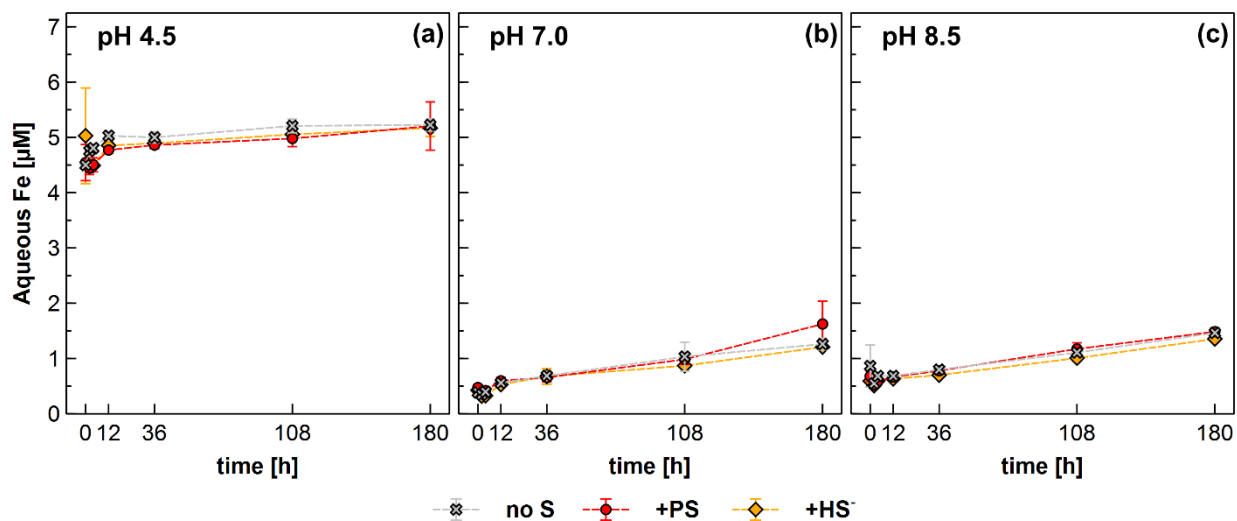


Figure SI-4: Time series of total aqueous Fe concentrations over 180h at pH 4.5 (a), 7.0 (b), and 8.5 (c) without sulfur addition (no S), with sulfide (+HS⁻) and polysulfide (+PS) addition. Concentrations at all time points were analyzed in triplicates, error bars represent the standard deviation.

6 Sulfur Solid-Phase Speciation Analyses with X-ray Absorption Spectroscopy

X-ray Absorption Spectroscopy. Anoxic freeze-dried, homogenized peat samples for S K-edge XANES analysis were prepared in aluminum multi-slot sample holders sealed with sulfur-free tape. When concentrations exceeded 2000 mg/kg, samples were diluted with boron nitride to reduce self-absorption effects.¹⁵ Sulfur K-edge XANES spectra were collected at beamline 4-3 at the Stanford Synchrotron Radiation Lightsource (SSRL, Stanford, USA). The beamline was equipped with a liquid nitrogen-cooled Si(111) double-crystal monochromator, which was calibrated relative to the white-line energy of a thiosulfate standard (2,472.02 eV). The standard was constantly monitored between two sample runs. Reduction of higher order harmonics was achieved by using a 1.0 m bare Si mirror (cutoff ~10.5 keV). All measurements were performed in under constant He stream (<0.1% (v/v) O₂) at room temperature in fluorescence mode using a 4-element solid-state Si drift detector (Hitachi HTA). Per sample up to four scans were recorded and averaged.

XAS Data Processing. All sulfur XANES spectra were normalized to the absorption at 2,490 eV in Athena.⁵ The edge positions (E_0) of XANES were determined from the 2 points-smoothed maximum of the first derivative spectra. Spectral deconvolution of normalized S K-edge spectra was done in Athena⁵ according to the fitting approach recommended by Manceau and Nagy.¹⁶ Deconvolution of the spectra was performed in the energy range 2,465-2,490 eV using two arctan functions (edge steps of reduced and oxidized S species) and six Gaussian functions representing S $s \rightarrow p$ transition peaks of exocyclic/elemental S, heterocyclic S, sulfoxide S, sulfone S, sulfonate S, and sulfate S. The step heights of the arctan functions were fitted, whereby their positions (energy of center) were fixed to 2,475.51 eV for reduced S and 2,482.91 eV for oxidized sulfur species, and their widths were fixed to 0.45 in all model fits. Likewise, the positions and areas of all Gaussians were fit, while keeping the sigma values (standard deviation of Gaussian) fixed in all model fits to values determined beforehand. Following the approach of Manceau and Nagy¹⁶, the position of the arctan (reduced species) was constrained to be located close to the Gaussian functions of the reduced sulfur functionalities (before the center of the sulfoxide Gaussian function) in order to obtain correct sulfur fractions. The fitted peak areas were corrected for the oxidation state dependent absorption cross-section of S using the generic equation of Manceau and Nagy.¹⁶ The atomic fraction of each S species in the peat samples was then calculated by dividing its corrected peak area by the total peak area sum. Please note that the intermediate oxidized fractions (sulfoxide and sulfone S) are likely to be overestimated due to post-edge absorption features of

reduced S species.¹⁶ The Gaussian fit envelopes and experimental spectra are displayed in Figure SI-5, a summary of detailed fit results and corrected atomic fractions can be found in Table SI-9.

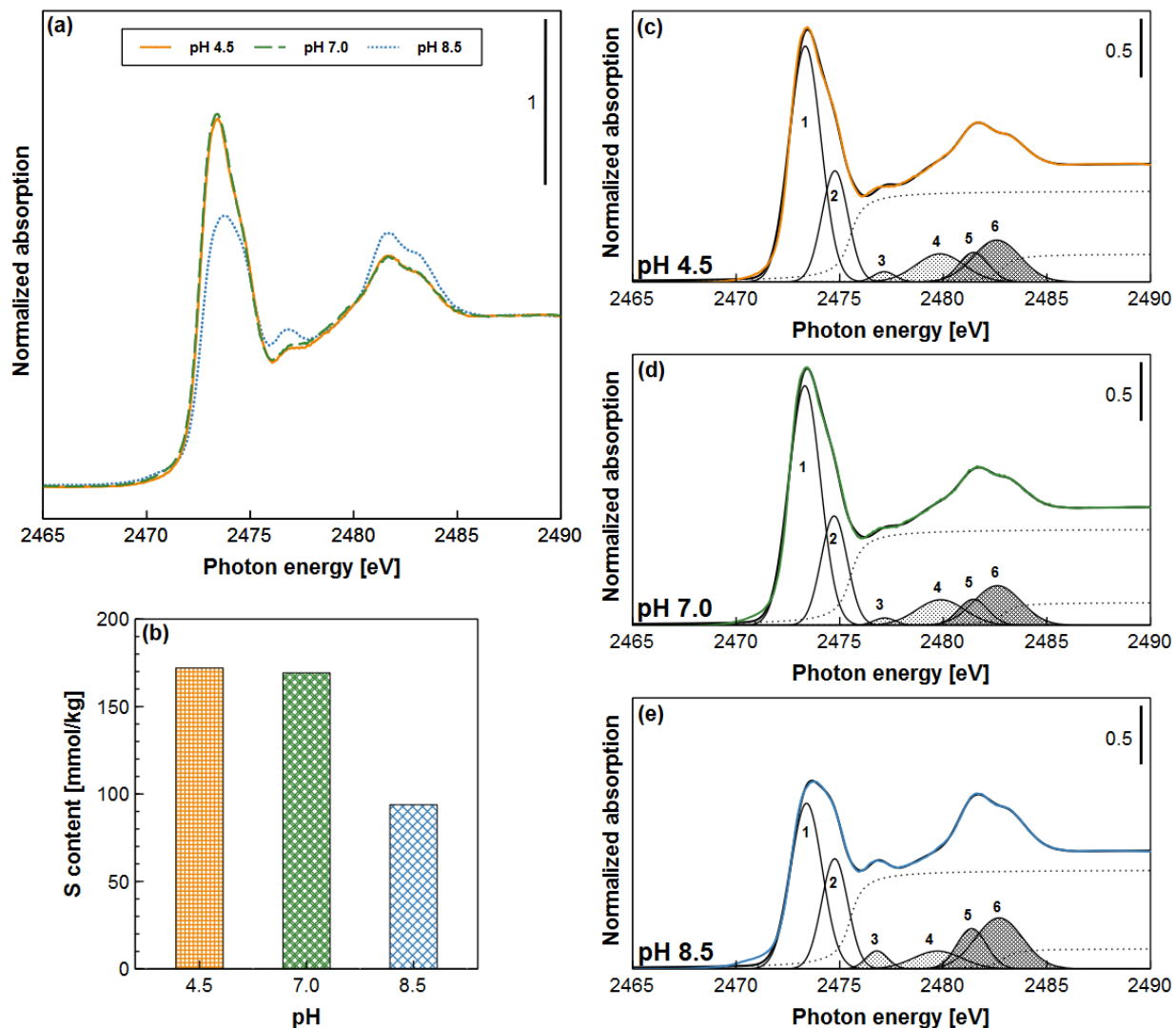


Figure SI-5: Characterization of As-loaded model peat samples before use in desorption experiments. (a) Sulfur K-edge XANES spectra of As-loaded model peat samples at pH 4.5, 7.0 and 8.5. (b) Total sulfur content in As-loaded model peat [mmol/kg]. (c-e) Gaussian curve fits of As-loaded model peat spectra. Experimental data is shown in color of the respective pH, fit envelopes as black lines. The spectral decomposition is illustrated for each spectrum. The two arctan functions are shown as dotted lines and the Gaussian peaks correspond to (from 1 to 6) exocyclic/elemental S (1), heterocyclic S (2), sulfoxide S (3), sulfone S (4), sulfonate S (5), and sulfate S (6). The fit parameters for all samples are reported in Table SI-9.

Table SI-9: Gaussian deconvolution of normalized S *K*-edge XANES spectra of the As-loaded model peat of all pH values. Parameters with identical numbers (in *italic*) were fixed during fitting.

Sample	Fitted functions	Energy ^a (center) [eV]	Width (arctan) or σ (Gaussian)	Step (arctan) or area (Gaussian)	Corrected area ^b	Fraction [atomic-%]	NSSR ^c
pH 4.5, t0	Arctan (red. S species)	<i>2475.51</i>	<i>0.45</i>	0.78	-	-	6.1
	Arctan (ox. S species)	<i>2482.91</i>	<i>0.45</i>	0.24	-	-	
	Exocyclic/ elemental S	2473.34	<i>0.76</i>	3.81	3.09	68.7	
	Heterocyclic S	2474.77	<i>0.85</i>	1.49	0.85	18.8	
	Sulfoxide S	2477.15	<i>0.52</i>	0.11	0.04	1.0	
	Sulfone S	2479.84	<i>1.17</i>	0.70	0.19	4.3	
	Sulfonate S	2481.46	<i>0.71</i>	0.45	0.11	2.4	
	Sulfate S	2482.58	<i>1.14</i>	1.02	0.22	4.9	
	pH 7.0, t0	Arctan (red. S species)	<i>2475.51</i>	<i>0.45</i>	0.82	-	
Arctan (ox. S species)		<i>2482.91</i>	<i>0.45</i>	0.20	-	-	
Exocyclic/ elemental S		2473.31	<i>0.76</i>	3.87	3.17	70.1	
Heterocyclic S		2474.73	<i>0.85</i>	1.47	0.84	18.7	
Sulfoxide S		2477.17	<i>0.52</i>	0.08	0.03	0.7	
Sulfone S		2479.88	<i>1.17</i>	0.64	0.17	3.9	
Sulfonate S		2481.45	<i>0.71</i>	0.40	0.09	2.1	
Sulfate S		2482.62	<i>1.14</i>	0.96	0.21	4.6	
pH 8.5, t0		Arctan (red. S species)	<i>2475.51</i>	<i>0.45</i>	0.84	-	-
	Arctan (ox. S species)	<i>2482.91</i>	<i>0.45</i>	0.17	-	-	
	Exocyclic/ elemental S	2473.40	<i>0.76</i>	2.68	2.13	59.4	
	Heterocyclic S	2474.76	<i>0.85</i>	1.48	0.84	23.5	
	Sulfoxide S	2476.79	<i>0.52</i>	0.20	0.08	2.2	
	Sulfone S	2479.72	<i>1.17</i>	0.44	0.12	3.4	
	Sulfonate S	2481.37	<i>0.71</i>	0.61	0.15	4.1	
	Sulfate S	2482.70	<i>1.14</i>	1.24	0.26	7.4	

^aEnergy of the white-line maximum. ^bArea after correction for the oxidation state-dependent absorption cross-section of S with the “generic equation” of Manceau and Nagy.¹⁶ ^cNormalized sum of squared residuals ($10^4 \cdot \sum_i (\text{data}_i - \text{fit}_i)^2 / \sum_i \text{data}_i^2$).

Sulfur *K*-edge XANES spectra of As-loaded model peat before the experiment and the respective Gaussian curve fits are shown in Figure SI-5, the spectra of the peat samples after subsection to different sulfurization treatments are displayed in Figure SI-6. The total sulfur content on the As-loaded model peat at each pH value was very high (Figure SI-5b). In contrast, the changes in speciation due to the experiment might have only affected a small fraction of the big sulfur pool, hence causing only minor changes in the sulfur *K*-edge XANES spectra. Therefore, it was difficult to interpret the changes apart from the decrease of reduced sulfur with simultaneous increase of sulfate at pH 4.5, likely an analytical artifact, and the increase of reduced sulfur in the polysulfide treatment of pH 8.5 possibly due to high affinity of polysulfide towards NOM.

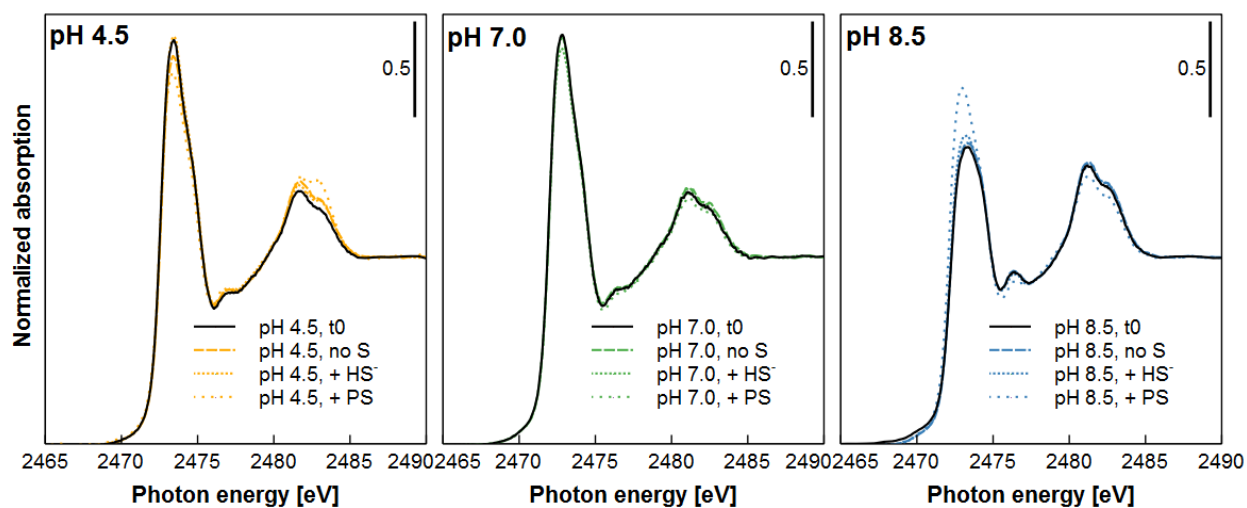


Figure SI-6: Sulfur *K*-edge XANES spectra of initial As-loaded model peat samples and model peat after the different reduced sulfur treatments at pH 4.5, 7.0 and 8.5.

7 Changes in Sulfur Solid-Phase Content and Aqueous Sulfide Concentrations

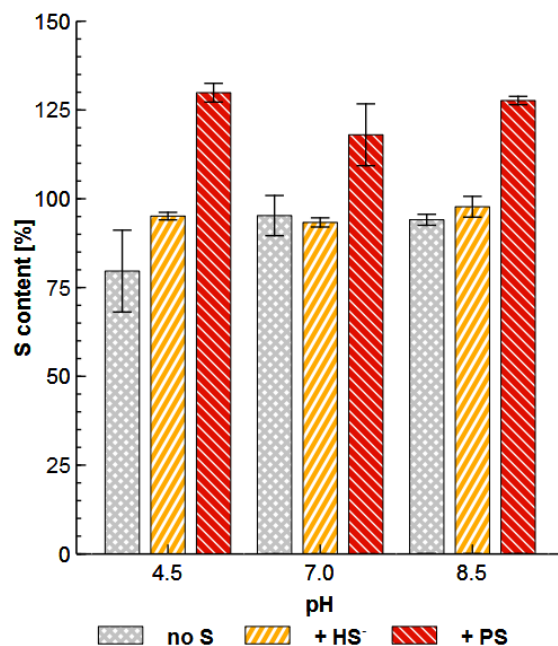


Figure SI-7: Sulfur content of solid-phase samples of As-loaded, thiol-rich model peat at the different pH conditions after 180h of desorption in percent of the original S content for the three sulfur treatments (no sulfur, HS⁻ and polysulfide (PS) addition) and pH values 4.5, 7.0 and 8.5. Error bars represent the standard deviation of triplicates.

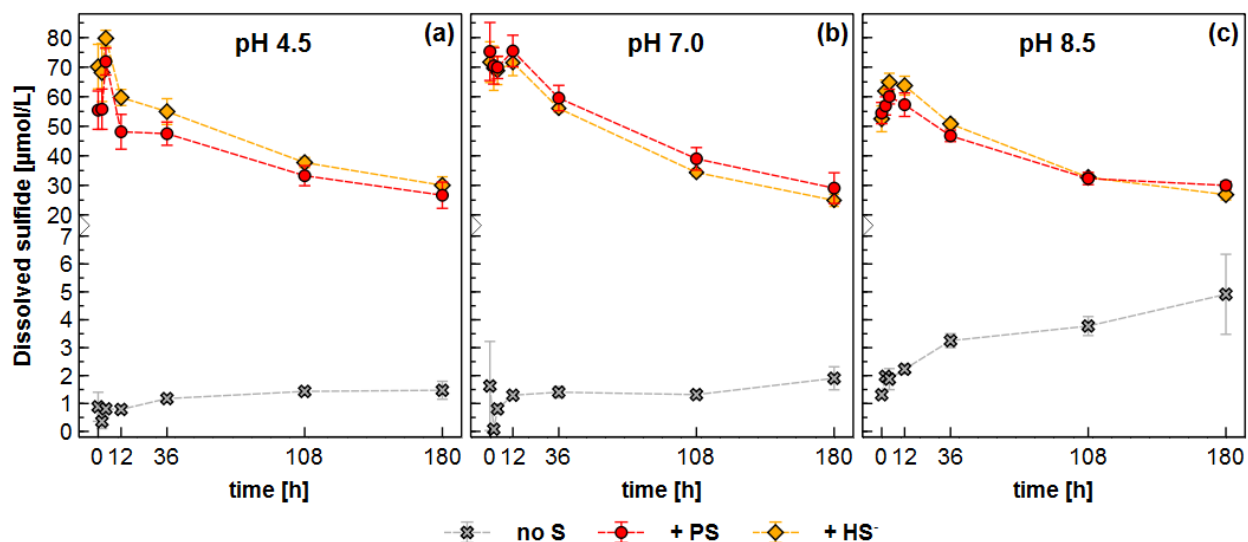


Figure SI-8: Time series of dissolved sulfide concentrations in treatments of pH 4.5 (a), 7.0 (b) and 8.5 (c) of the desorption experiment.

8 Statistics

Results of a two-way ANOVA with Tukey post-hoc test using SigmaPlot 11 are shown in the Tables SI-10 to SI-21. All statistical analyses were done for total contents or total concentrations and for the corresponding normalized contents or relative desorption. The results of tests on normalized contents and relative desorption exclude effects originating from pH dependent sorption during preparation of As-loaded model peat.

Table SI-10: P-values of a two-way ANOVA with Tukey post-hoc test comparing the total S contents of the As-loaded model peat material [mmol/kg] of different S treatments within pH conditions at the end of desorption experiments.

S [mmol/kg]	4.5			7			8.5		
	control	+ PS	+ HS ⁻	control	+ PS	+ HS ⁻	control	+ PS	+ HS ⁻
control		<0.001	0.008		<0.001	0.968		0.002	0.962
+ PS	<0.001		<0.001	<0.001		<0.001	0.002		0.005
+ HS ⁻	0.008	<0.001		0.968	<0.001		0.962	0.005	

Table SI-11: P-values of a two-way ANOVA with Tukey post-hoc test comparing the normalized S contents of the As-loaded model peat material at the end of desorption experiments [%] of different S treatments within pH conditions. Normalized S contents were calculated dividing total S contents by the initial S content of the corresponding As-loaded model peat.

S [%]	4.5			7			8.5		
	control	+ PS	+ HS ⁻	control	+ PS	+ HS ⁻	control	+ PS	+ HS ⁻
control		<0.001	0.01		<0.001	0.969		<0.001	0.969
+ PS	<0.001		<0.001	<0.001		<0.001	<0.001		<0.001
+ HS ⁻	0.01	<0.001		0.969	<0.001		0.969	<0.001	

Table SI-12: P-values of a two-way ANOVA with Tukey post-hoc test comparing the total As contents of the As-loaded model peat material [mmol/kg] of different S treatments within pH conditions at the end of desorption experiments.

As [mmol/kg]	4.5			7			8.5		
	control	+ PS	+ HS ⁻	control	+ PS	+ HS ⁻	control	+ PS	+ HS ⁻
control		<0.001	<0.001		<0.001	<0.001		0.018	0.124
+ PS	<0.001		0.416	<0.001		0.986	0.018		0.763
+ HS ⁻	<0.001	0.416		<0.001	0.986		0.124	0.763	

Table SI-13: P-values of a two-way ANOVA with Tukey post-hoc test comparing the normalized As contents of the As-loaded model peat material at the end of desorption experiments [%] of different S treatments within pH conditions. Normalized As contents were calculated dividing total As contents by the initial As content of the corresponding As-loaded model peat.

As [%]	4.5			7			8.5		
	control	+ PS	+ HS ⁻	control	+ PS	+ HS ⁻	control	+ PS	+ HS ⁻
control		<0.001	<0.001		<0.001	<0.001		<0.001	<0.001
+ PS	<0.001		0.552	<0.001		0.886	<0.001		0.083
+ HS ⁻	<0.001	0.552		<0.001	0.886		<0.001	0.083	

Table SI-14: P-values of a two-way ANOVA with Tukey post-hoc test comparing the total As contents of the As-loaded model peat material [mmol/kg] of different pH conditions within S treatments at the end of desorption experiments.

As [mmol/kg]	control			+ PS			+ HS ⁻		
	4.5	7	8.5	4.5	7	8.5	4.5	7	8.5
4.5		<0.001	<0.001		<0.001	<0.001		<0.001	<0.001
7	<0.001		<0.001	<0.001		0.196	<0.001		0.488
8.5	<0.001	<0.001		<0.001	0.196		<0.001	0.488	

Table SI-15: P-values of a two-way ANOVA with Tukey post-hoc test comparing the normalized As contents of the As-loaded model peat material at the end of desorption experiments [%] of different pH conditions within S treatments. Normalized As contents were calculated dividing total As contents by the initial As content of the corresponding As-loaded model peat.

As [%]	control			+ PS			+ HS ⁻		
	4.5	7	8.5	4.5	7	8.5	4.5	7	8.5
4.5		0.031	<0.001		<0.001	<0.001		<0.001	<0.001
7	0.031		<0.001	<0.001		0.049	<0.001		0.754
8.5	<0.001	<0.001		<0.001	0.049		<0.001	0.754	

Table SI-16: P-values of a two-way ANOVA with Tukey post-hoc test comparing the total desorption of As [$\mu\text{mol/L}$] at the last sampling time point (t6) of different S treatments within pH conditions.

t6, As [$\mu\text{mol/L}$]	4.5			7			8.5		
	control	+ PS	+ HS ⁻	control	+ PS	+ HS ⁻	control	+ PS	+ HS ⁻
control		<0.001	<0.001		<0.001	<0.001		0.003	0.022
+ PS	<0.001		0.009	<0.001		0.627	0.003		0.627
+ HS ⁻	<0.001	0.009		<0.001	0.627		0.022	0.627	

Table SI-17: P-values of a two-way ANOVA with Tukey post-hoc test comparing the relative desorption of As [%] at the last sampling time point (t6) of different S treatments within pH conditions.

t6, As [%]	4.5			7			8.5		
	control	+ PS	+ HS ⁻	control	+ PS	+ HS ⁻	control	+ PS	+ HS ⁻
control		<0.001	<0.001		<0.001	<0.001		<0.001	<0.001
+ PS	<0.001		0.083	<0.001		0.274	<0.001		0.152
+ HS ⁻	<0.001	0.083		<0.001	0.274		<0.001	0.152	

Table SI-18: P-values of a two-way ANOVA with Tukey post-hoc test comparing the total desorption of As [$\mu\text{mol/L}$] at the last sampling time point (t6) of different pH conditions within S treatments.

t6, As [$\mu\text{mol/L}$]	control			+ PS			+ HS ⁻		
	4.5	7	8.5	4.5	7	8.5	4.5	7	8.5
4.5		<0.001	<0.001		<0.001	<0.001		<0.001	<0.001
7	<0.001		0.035	<0.001		<0.001	<0.001		<0.001
8.5	<0.001	0.035		<0.001	<0.001		<0.001	<0.001	

Table SI-19: P-values of a two-way ANOVA with Tukey post-hoc test comparing the relative desorption of As [%] at the last sampling time point (t6) of different pH conditions within S treatments.

t6, As [%]	control			+ PS			+ HS ⁻		
	4.5	7	8.5	4.5	7	8.5	4.5	7	8.5
4.5		0.069	<0.001		<0.001	<0.001		<0.001	<0.001
7	0.069		<0.001	<0.001		0.608	<0.001		0.822
8.5	<0.001	<0.001		<0.001	0.608		<0.001	0.822	

References

1. Suess, E.; Scheinost, A. C.; Bostick, B. C.; Merkel, B. J.; Wallschlaeger, D.; Planer-Friedrich, B., Discrimination of thioarsenites and thioarsenates by X-ray absorption spectroscopy. *Analytical chemistry* **2009**, *81*, (20), 8318-8326.
2. Langner, P.; Mikutta, C.; Kretzschmar, R., Arsenic sequestration by organic sulphur in peat. *Nature Geoscience* **2012**, *5*, (1), 66.
3. Besold, J.; Biswas, A.; Suess, E.; Scheinost, A. C.; Rossberg, A.; Mikutta, C.; Kretzschmar, R.; Gustafsson, J. P.; Planer-Friedrich, B., Monothioarsenate Transformation Kinetics Determining Arsenic Sequestration by Sulfhydryl Groups of Peat. *Environmental Science & Technology* **2018**, *52*, (13), 7317-7326.
4. Biswas, A.; Besold, J.; Sjostedt, C.; Gustafsson, J. P.; Scheinost, A. C.; Planer-Friedrich, B., Complexation of arsenite, arsenate, and monothioarsenate with oxygen-containing functional groups of natural organic matter: An XAS Study. *Environmental Science & Technology* **2019**.
5. Ravel, B.; Newville, M., ATHENA, ARTEMIS, HEPHAESTUS: data analysis for X-ray absorption spectroscopy using IFEFFIT. *Journal of synchrotron radiation* **2005**, *12*, (4), 537-541.
6. Malinowski, E. R., Determination of the number of factors and the experimental error in a data matrix. *Anal. Chem.* **1977**, *49*, (4), 612-617.
7. Webb, S., SIXpack: a graphical user interface for XAS analysis using IFEFFIT. *Physica scripta* **2005**, *2005*, (T115), 1011.
8. Beauchemin, S.; Hesterberg, D.; Beauchemin, M., Principal component analysis approach for modeling sulfur K-XANES spectra of humic acids. *Soil Science Society of America Journal* **2002**, *66*, (1), 83-91.
9. Malinowski, E. R., Theory of error for target factor analysis with applications to mass spectrometry and nuclear magnetic resonance spectrometry. *Anal. Chim. Acta* **1978**, *103*, (4), 339-354.
10. Mancaeu, A.; Marcus, M. A.; Tamura, N., Quantitative Speciation of Heavy Metals in Soils and Sediments by Synchrotron X-ray Techniques. *Rev. Mineral. Geochem.* **2002**, *49*, (1), 341-428.
11. Zabinsky, S.; Rehr, J.; Ankudinov, A.; Albers, R.; Eller, M., Multiple-scattering calculations of X-ray-absorption spectra. *Physical Review B* **1995**, *52*, (4), 2995.
12. Ballirano, P.; Maras, A., Refinement of the crystal structure of arsenolite, As₂O₃. *Zeitschrift für Kristallographie-New Crystal Structures* **2002**, *217*, (1), 177-178.
13. Pappalardo, G.; Chakravorty, R.; Irgolic, K.; Meyers, E., Tris (phenylthio) arsine, C₁₈H₁₅AsS₃. *Acta Crystallographica Section C: Crystal Structure Communications* **1983**, *39*, (12), 1618-1620.
14. Raab, A.; Meharg, A. A.; Jaspars, M.; Genney, D. R.; Feldmann, J., Arsenic-glutathione complexes-their stability in solution and during separation by different HPLC modes. *J. Anal. At. Spectrom.* **2004**, *19*, (1), 183-190.
15. Prietzel, J.; Botzaki, A.; Tyufekchieva, N.; Brettholle, M.; Thieme, J.; Klysubun, W., Sulfur speciation in soil by SK-edge XANES spectroscopy: comparison of spectral deconvolution and linear combination fitting. *Environmental science & technology* **2011**, *45*, (7), 2878-2886.
16. Manceau, A.; Nagy, K. L., Quantitative analysis of sulfur functional groups in natural organic matter by XANES spectroscopy. *Geochimica et Cosmochimica Acta* **2012**, *99*, 206-223.

Study 4: Redox Heterogeneities Promote Thioarsenate Formation and Release into Groundwater from Low Arsenic Sediments

Naresh Kumar, Vincent Noël, Britta Planer-Friedrich, Johannes Besold, Juan Lezama Pacheco

John R. Bargar, Gordon E. Brown, Scott Fendorf and Kristin Boye

Reprinted with permission from

Environmental Science & Technology

Copyright 2020 American Chemical Society

floodplain is representative of alluvial aquifers globally, particularly within arid/semiarid environments. By embedding various numbers of organic-rich, fine-grained, sulfidic lenses in the aquifer sand at various distances along the length of the column, we were able to both determine the influence of reduced zones on the geochemical processes involving As and establish concentration thresholds of As, sulfide, and Fe that regulated the chemical speciation of As in solid and aqueous phases. Our results provide clear evidence of the importance of redox interfaces for controlling As behavior in groundwater aquifers with high S concentrations. Further, we demonstrate the significant influence that fine-grained lenses, which operate as reducing zones, can have on groundwater quality in otherwise coarse-grained, oxic aquifers.

MATERIALS AND METHODS

Column Design and Sediment Properties. Detailed descriptions of the column setup are provided in the Supporting Information (SI, pages 2–3), along with initial sediment properties (Supporting Information, pages 2–3 and 7–8, Tables SI-1 and SI-2 and Figure SI-5). Briefly, 12 columns (30 cm long, 7 cm diameter) were filled with natural sediments, collected ~2 weeks prior from the Wind River-Little Wind River floodplain outside of Riverton, WY (42°59'19.1"N, 108°23'58.6"W). Triplicate columns were set up with 0 (control), 1, 2, or 3 fine-grained, organic-rich, reducing lens(es) (~3 cm diameter, 17–20 g dry weight each) embedded in aquifer sand (1.3–1.4 kg dry sand per column) at increasing distances (with each additional lens) from the influent (bottom) groundwater port. The lenses consisted of organic-rich, fine-grained, sulfidic sediments collected underneath an oxbow lake on the floodplain and thoroughly homogenized to ensure consistent composition between different lenses. The As concentrations in aquifer sand and oxbow lake sediment materials were 1.2 ± 0.4 and 0.7 ± 0.1 mg As/kg sediment, respectively. Porewater samplers (Rhizon-Flex, 5 cm, 0.15 μm pore size, Rhizosphere Research Products, Wageningen, Netherlands) were inserted into the sand to enable sampling of groundwater (advective zone) before and after fine-grained lens(es) (and at increasing distances away from the reduced zones in columns with one or two lenses) along the flow path. Micro-rhizons (8 mm, 0.15 μm pore size, Rhizosphere Research Products, Wageningen, Netherlands) were inserted into the center of each lens to enable sampling of porewater from the reduced (diffusive) zones. All columns were fed artificial groundwater (by peristaltic pump at a flow rate of 90 mL/day, equivalent to ~1 pore volume exchange per 48 h) made to have a chemical composition similar in concentrations of the major solutes, except organic C, measured in Riverton floodplain groundwater at the site over the past 2 years (Supporting Information, Table SI-3). The sulfate concentrations in the groundwater at this site are high relative to elsewhere in the Riverton area,²¹ but we preferred to use a concentration representative of the site. The artificial groundwater was fully aerated (240–260 μM dissolved O_2) in the source container to achieve a dissolved oxygen concentration in the control columns (~50 μM) similar to that measured in the floodplain groundwater (average 87 μM , range 14–211 μM). Finally, the artificial groundwater had a pH of ~8, which is higher than that recently measured at the floodplain site, but within the normal range of groundwater in the area.²¹

Experimental Details. The column experiment was run for a total of 70 days. Porewater from the rhizons and micro-rhizons was sampled every 7 days using prerinsed 3 mL luer lock syringes. To flush the tubing, the first 1–3 mL of water extracted from rhizons was discarded. PEEK tubing connected to micro-rhizons was assumed to have minimal contribution to the porewater samples obtained from these ports. Dissolved sulfide was always analyzed on the second, freshly extracted sample from micro-rhizons (the first sample being used for total element concentrations).

Aqueous Phase Analyses. The aqueous phase in this study is defined as containing all colloidal and dissolved species <0.15 μm , by virtue of the pore size of the porewater samplers. Total aqueous concentrations of S and Fe were determined by inductively coupled plasma optical emission spectroscopy (ICP-OES, iCAP6000, Thermo Scientific, Cambridge, U.K.) and total aqueous As by inductively coupled plasma mass spectrometry (ICP-MS, XSERIES 2, Thermo Scientific, Cambridge, U.K.). All ICP analyses were conducted on samples diluted 1:20 with 2% nitric acid, and a reference standard with known S, As, and Fe concentrations was intercalated every 15 samples to monitor instrument drift and concentration retrieval accuracy. No interference from Ar–Cl on As concentrations was detected. Dissolved sulfide (HS^-) concentrations were measured, from day 35 onward, using the methylene blue method²² on freshly drawn samples that were immediately mixed with the first (stabilizing) reagent to minimize volatilization and exposure to oxygen. Total concentrations of aqueous Fe (from ICP-OES) were assumed to be equivalent to total aqueous Fe(II) because no increase in Fe(II) concentrations (as measured by the ferrozine method²³) was detected after reduction with hydroxylamine when we tested this for the first few and the final sampling steps (data not shown).

A set of end-point samples from the rhizons (ports 3, 5, and 7) from columns with reducing lenses were flash-frozen immediately after adding diethylene triamine pentaacetic acid (DTPA) (10 mM) to complex Fe(II) and kept at -80°C until analyzed for aqueous As speciation. Aqueous As species were separated by IC (Dionex ICS-3000) using an IonPac AS-16/AG-16 4 mm column (gradient program with 2.5–100 mM NaOH at a flow rate of 1.2 mL/min and 50 μL injection volume; without suppressor) and quantified by ICP-MS (XSERIES 2, Thermo-Fisher).¹⁰ It should be noted that the chromatographic analyses with NaOH prevent the detection of thioarsenites as they would experience a ligand-exchange ($-\text{OH}$ replacing $-\text{SH}$) and, thus, be transformed to the arsenite oxoanion.¹² Thus, there is a slight risk of overestimating the arsenite concentrations at the expense of thiolated As species. Further, we cannot fully exclude that what is measured as thioarsenates could originally have been thioarsenites that oxidized while sitting in capped vials for a few minutes on an autosampler in ambient air, as reported before.¹² More details about the aqueous As speciation methodology are provided in the Supporting Information.

Solid-Phase Sampling. After the final aqueous sampling time, six columns (two control, two with one reducing lens, one with two reducing lenses, and one with three reducing lenses) were disconnected from the peristaltic pump and immediately transferred into a glove bag (3–4% H_2 , balance N_2). Sediments from these columns were sampled around each rhizon and micro-rhizon present in the columns. Subsamples were taken to determine the water content (by weighing before

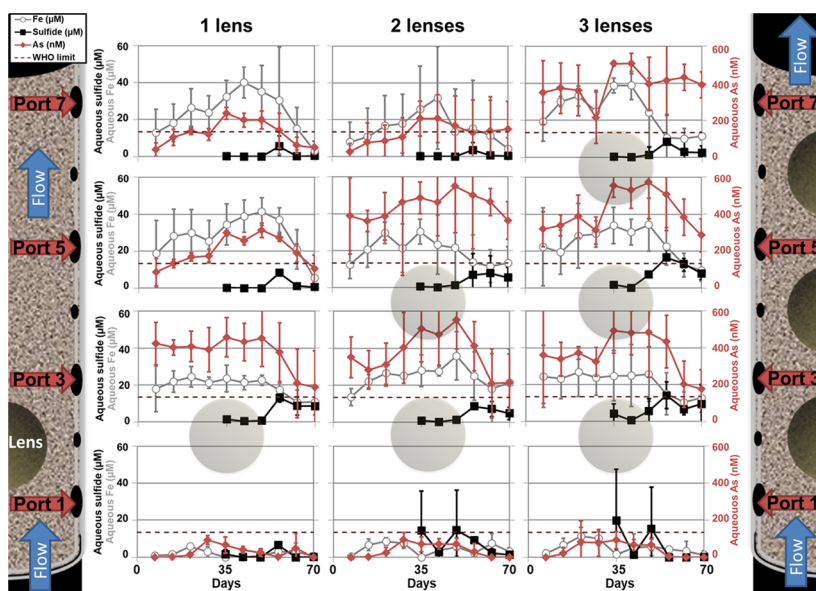


Figure 1. Temporal evolution of aqueous sulfide (μM) and Fe (μM) (both on left vertical axis) and aqueous As (nM, right vertical axis) in the groundwater (horizontal axes) and along the flow path (panels from bottom to top) in columns with 1, 2, or 3 fine-grained, reducing lenses (positions indicated by shaded circles). Values are averages of triplicate columns for each treatment and error bars denote the standard deviation from the mean for the triplicates. The dashed line indicates the WHO drinking water limit for As ($10 \mu\text{g/L} = 133.5 \text{ nM}$). To facilitate examining the evaluation of influence from fine-grained, reducing zones on groundwater concentrations, column depth profiles for aqueous As, Fe, and sulfide on days 35 and 70 in the Supporting Information (Figure SI-2).

and after drying at $105 \text{ }^\circ\text{C}$) and HCl-extractable Fe(II) (described below). The remainder of the sampled sediments from each port was dried at room temperature and used for HNO_3 digestions (see below).

One of the remaining columns with three reducing lenses was switched over from groundwater solution to glycerol and pumping continued until glycerol had passed through the entire column (i.e., had replaced the groundwater in the advective pores), at which point the column was immediately transferred into the glove bag. This glycerol treatment served to prevent biases in mineral composition and element speciation that could arise from drying and precipitation of evaporite salts. Glycerol preservation also allows for samples to be frozen (a prerequisite for the X-ray absorption analyses, (XAS)) without risking destructive ice formation. Sediment samples were taken around each rhizon and micro-rhizon sampler (as described above) and ground to a smooth paste using an agate mortar and pestle. Samples were stored in 2 mL cryovials inside sealed mason jars with oxygen scrubbers and kept at $-20 \text{ }^\circ\text{C}$ until XAS analyses.

Chemical Extractions. Chemical extractions targeting the reactive Fe(II) pool (HCl-extraction) and total acid-extractable As and Fe were performed on subsamples from all solid-phase samples (not preserved with glycerol).

Reactive Fe(II) Pool: HCl Extraction. Triplicate subsamples equivalent to 1–2 g of dry sediment were weighed into 15 mL centrifuge tubes containing 5 mL of 0.5 M HCl (trace metal grade). After shaking for 2 h, tubes were centrifuged and the supernatant filtered ($0.45 \mu\text{m}$) into a new 15 mL centrifuge tube. The HCl extracts were analyzed for total Fe concentration (ICP-OES) to compare the concentration of reactive Fe(II) in reducing lenses and aquifer sand before and after the experiment.

Total Acid-Extractable Fraction: Concentrated HNO_3 . About 0.2 g of dry sediment was weighed in Teflon tubes and 10 mL of concentrated nitric acid (70% HNO_3 , trace

metal grade) was added to each tube. Tubes were capped and sediments digested according to the United States EPA standard protocol for total digestion of soil in a CEM MarsXpress microwave digester (CEM, Matthews, NC). Extracts were transferred to acid-washed glass vials and a subsample was diluted 1:5 and analyzed for total Fe by ICP-OES and total As by ICP-MS.

X-ray Absorption Spectroscopy (XAS). *Arsenic X-ray Absorption Near-Edge Structure Spectroscopy (XANES).* Arsenic K-edge XANES spectra of glycerol-preserved endpoint samples and the initial aquifer and oxbow lake sediments were collected at BL 7-3 at the Stanford Synchrotron Radiation Lightsource (SSRL). A Si(220) double crystal monochromator was detuned by 50% to minimize higher-order harmonics, and the beam energy was calibrated by setting the first inflection point of a simultaneously measured Au L_{III} -edge to 11,919 eV (double transmission mode). All spectra were averaged and normalized using the Ifeffit 1.2.12 (Matt Newville) Demeter 0.9.25 Athena software (Bruce Ravel).²⁴ Linear combination least-squares (LC-LS) fitting of the normalized spectra was also performed in Athena. Good fits for all sample spectra were obtained using 2–4 of the following seven standard spectra (out of a comprehensive spectra database): realgar (AsS or As_4S_4), organically complexed As(III) S_3 (trisphenylthioarsine), arsenite sorbed to ferrihydrite (Fh) or to mackinawite (FeS), monothioarsenate sorbed to FeS, and arsenate sorbed to Fh or to FeS. More details regarding the As XANES data collection and processing procedures are provided in the Supporting Information.

Sulfur XANES Spectroscopy. Sulfur K-edge XANES spectroscopy was performed in a He atmosphere at SSRL BL 4-3 to compare the solid-phase speciation of S in the initial materials with that of the glycerol-preserved samples. A detailed description of the procedure is provided in the Supporting Information.

RESULTS AND DISCUSSION

Aqueous Phase Chemistry. Aqueous (<0.15 μm colloids and dissolved species) concentrations of As and Fe in aquifer ports (groundwater) increased as a function of time until day 42 of the experiment and were considerably higher in ports immediately downgradient from a fine-grained, reduced lens (Figure 1, Supporting Information Figure SI-2). After day 42, the concentrations of As and Fe decreased again, particularly in ports directly downgradient of reducing lenses. Sulfide was only measured from day 35 of the experiment but generally followed the same pattern as Fe and As. Sulfide and As concentrations always increased directly after a reducing lens, but then decreased with increasing distance from the lenses (Figures 1 and SI-2). In contrast, aqueous Fe concentrations remained elevated independent of the distance from, or the number of, reducing lenses (Figures 1 and SI-2). In an equivalent natural aquifer setting, the large increase in aqueous As from a few nM to >0.5 μM observed in the presence of reducing lenses would be equivalent to a transition from background levels to concentrations exceeding the World Health Organization (WHO) drinking water standard of 10 μg As/L (Figure 1).

In control columns (Supporting Information, Figure SI-3), aqueous concentrations of As in groundwater increased between days 28 and 40, but much less so than in columns with fine-grained, reducing lens(es) (cf. Figure 1). Both aqueous sulfide and Fe concentrations remained close to, or below, the detection limit throughout the experiment in control columns (Supporting Information, Figure SI-3). In contrast to groundwater samples, porewater from inside the lenses exhibited low aqueous Fe concentrations and lower As concentrations but high sulfide concentrations, which were sustained until the end of the experiment (Supporting Information, Figure SI-4).

End-point groundwater samples downgradient of fine-grained, reducing lenses (ports 3, 5, and 7) were analyzed for As speciation (Figure 2). Remarkably large proportions of the aqueous As were in thiolated forms (mono-, di-, and trithioarsenates were observed, with monothioarsenate being most abundant), comprising ~30–40% of total aqueous As in ports directly downgradient from a lens. Both oxoanions of As,

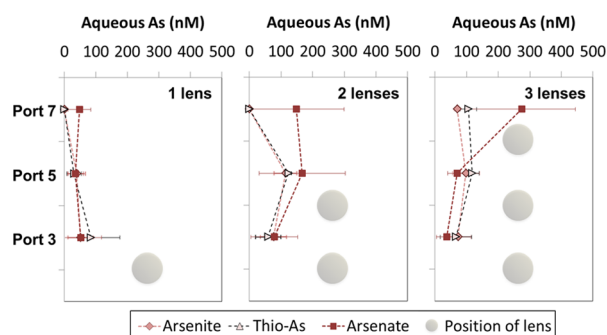


Figure 2. Aqueous concentration of As species (nM) in groundwater at the end of the experiment (day 70). Only water samples taken downgradient from lenses (lens positions are indicated by shaded circles) along the flow path were analyzed for aqueous As species. Values represent averages of triplicate columns for each treatment calculated from the relative distribution between species (normalized to total recovery) multiplied by total aqueous As concentration. Error bars denote the standard deviation of the mean. Thio-As includes mono-, di-, and trithioarsenate species.

arsenite (AsIII) and arsenate (AsV), were also present in these samples, with the relative abundance of arsenate generally increasing with distance away from the reducing lenses. In port 7 of columns with one or two lens(es), arsenate was the only As species detected (Figure 2).

Solid-Phase As, Fe, and S Speciation and Spatial Distribution. Acid extractions of the end-point solid-phase samples, as compared to the initial sediments, indicated that large mass transfers of both As and Fe had taken place between fine-grained, reducing lenses and the aquifer material (Figure 3). The HNO_3 digestions showed a net loss of As from all columns that increased with the number of lenses. However, the fine-grained, reducing lenses themselves accumulated As, indicating that aquifer sediment in proximity to lenses was responsible for the net As loss. A slightly different pattern was discerned for Fe, which unlike As was supplied at a low concentration (0.5 mg/L) in the influent groundwater and also was much more abundant in the initial lens material than in the aquifer material (Supporting Information, Table SI-1). Thus, only columns with three reducing lenses exhibited a net loss of Fe, mainly from the aquifer material. Columns with one or two reducing lenses instead experienced an increase in total acid (HNO_3)-extractable Fe, which was relatively homogeneously distributed between aquifer sediment and fine-grained, reducing lenses. However, the HCl-extractable pool of Fe shifted more dramatically than total Fe between the aquifer material and the lenses (Figure 3); fine-grained, reducing lenses exhibited a net loss of HCl-extractable Fe of 30–45%, whereas the aquifer materials immediately after a lens gained 23–69% of HCl-extractable Fe. In spite of these large shifts in HCl-extractable Fe, no differences in mineralogy were detected in X-ray diffraction (XRD) analyses of end-point samples compared to initial materials (Supporting Information Figure SI-5). This finding is consistent with the assumption that HCl-extractable Fe comprises redox-sensitive phases, such as surface-sorbed Fe(II) and poorly crystalline mackinawite, which is difficult to detect with XRD in quartz dominated materials.^{17,25}

Bulk As K-edge XANES spectra from the glycerol-preserved column with three fine-grained, reducing lenses (Figure 4) show that As(III) S_3 complexed with organics increased in relative abundance inside reducing lenses compared to the initial material and along the flow path, at the expense of As(V). Both As(III) and As(V) were present and adsorbed to FeS in the reducing lenses. Interestingly, the As speciation in the aquifer material shifted dramatically along the flow path and compared to the initial aquifer material, which was dominated by As(V) adsorbed to Fh, with a small pool of As(III) also adsorbed to Fh (Figure 4). Before the first fine-grained reducing lens, mineral As(III)S (as realgar, As_4S_4) dominated, thereafter, As(III) adsorbed to FeS and As(V)–Fh were the dominant species with a small (but increasing along the flow path) pool of S-complexed As (represented by MTA) adsorbed to FeS. Notably, the decreasing pool of As(V) remained adsorbed to Fh, whereas the increasing pool of As(III) was adsorbed to FeS in the ports upgradient from the reduced lenses.

Similar to As, S exhibited major shifts in speciation along the flow path in the aquifer material from the glycerol-preserved column with three reducing lenses (Figure 5, left panel). Before the first lens (port 1), some zero-valent S (S^0) was detected (possibly along with some pyrite from the initial material), but no divalent sulfur (i.e., monosulfide) minerals

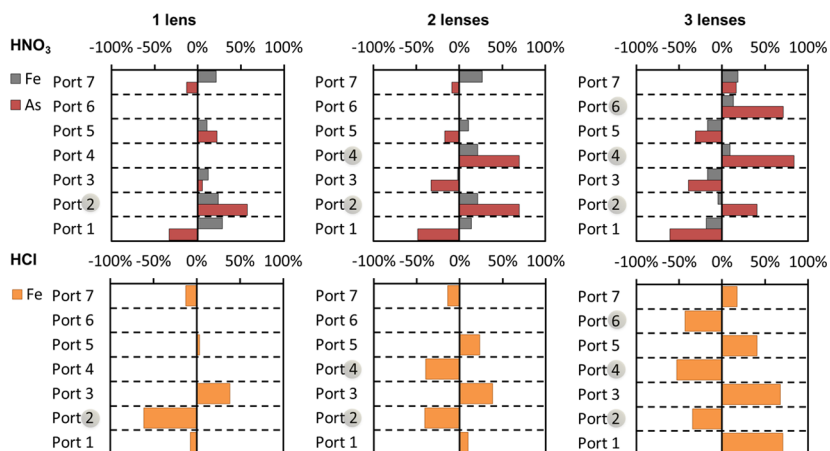


Figure 3. Estimated mass balances of total acid-extractable (70% HNO_3 digestions, top panels) Fe and As and HCl-extractable Fe (bottom panels) in columns at the end of the experiment relative to initial sediments (aquifer material for ports 1, 3, 5, and 7 and oxbow lake sediment for lenses at ports 2, 4, and 6). Estimates are based on averages for two one-lens columns and single column values for two- and three-lens columns. Positions of reducing lenses are indicated by shaded circles.

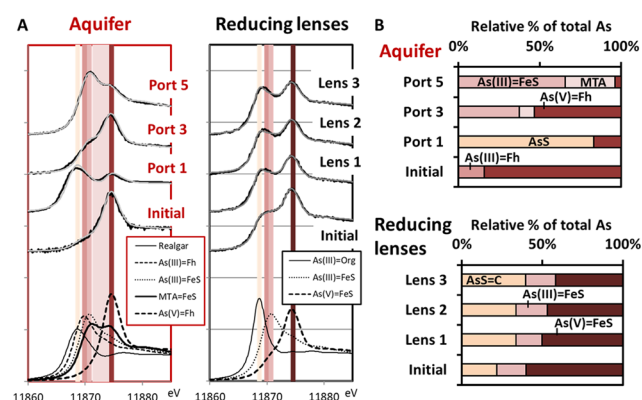


Figure 4. (A) Bulk As K-edge XANES analyses of samples from the glycerol-preserved column with three fine-grained, reducing lenses (black line) and LC-LS fits (gray line) using standard spectra (plotted at the bottom). (B) Relative distribution of As species (normalized to 100%) from the LC-LS fits; colors correspond to the vertical lines in A (indicating the absorption edge for the model compounds). Peak positions for reference spectra, data, and statistics from the fits are provided in the Supporting Information, Table SI-3.

were present. After the first lens, no S^0 was detected; instead, the relative abundance of mackinawite (FeS) increased and sulfate decreased after each fine-grained, reducing lens (ports 3 and 5). The lenses also exhibited a shift in inorganic S species from the original material containing S^0 along with FeS and sulfate to FeS and sulfate being the only detectable species at the end of the experiment and the relative abundance of FeS increasing in each lens along the flow path (Figure 5, right panel). It should be noted that there is always some uncertainty associated with the exact identification of S species from XANES, due to $\sim 5\%$ detection limit and multiple species exhibiting similar edge energies and spectral features. However, after taking careful consideration of the other geochemical data and comparisons of spectra from initial materials and endpoint samples, as well as along the flow path, we are confident that this interpretation of the S speciation is the most plausible.

Controls on As Behavior. The combined results of aqueous ($<0.15 \mu\text{m}$ colloids and dissolved species) and solid-phase speciation of As, Fe, and S reveal clear governance of redox interfaces and the relative concentrations of Fe/sulfide

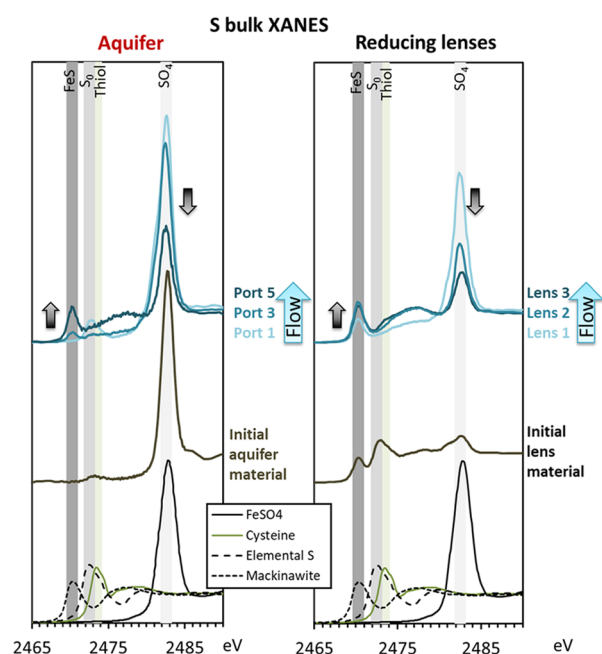


Figure 5. Sulfur K-edge XANES spectra of samples from the glycerol-preserved column with three fine-grained, reducing lenses and of initial aquifer material (left panel) and oxbow lake (lenses, right panel) materials. Arrows indicate the respective increase of mackinawite (FeS) and the decrease of sulfate along the flow path (and in relation to the initial materials). Model spectra for the dominant species are plotted at the bottom and their peak energies are indicated by vertical lines for reference: mackinawite, FeS (2470.3 eV), elemental S (S^0 , 2472.5 eV), cysteine (a thiol, $\text{C}_3\text{H}_7\text{NO}_2\text{S}$, 2473.4 eV), and FeSO_4 (2482.6 eV).

on the fate of As (conceptualized in the graphical abstract). A small fraction of As was likely mobilized due to the relatively high pH of the groundwater (Supporting Information, Table SI-1),^{26,27} as indicated by As release in control columns (Supporting Information, Figure SI-2). However, the shifts in As speciation in relation to fine-grained, reducing lenses indicate that As behavior was dominated by redox processes. It appears that high sulfate concentrations in the groundwater, together with the abundance of microbially available organic C

within fine-grained, reducing lenses (Supporting Information, Table SI-1), stimulated sulfate reduction within and along the edges of lenses to produce aqueous sulfide that dispersed within the groundwater (Figure 1). The sustained sulfide supply drove reductive dissolution of Fe(III) oxides to aqueous Fe(II), producing zero-valent S and releasing adsorbed As, as shown in previous studies.^{28–33} Zero-valent S is not very stable in the aqueous phase at pH 8, where it will likely react with sulfide to form polysulfides or with other species, such as As(III), unless it is partitioned to the solid phase (as seen in the aquifer sand before the first reducing lens in this study). On the influent (upstream) side of the first fine-grained, reducing lens, it appears that aqueous Fe(II) concentrations were too low to precipitate FeS (Figure 1). Instead, the relative lack of aqueous Fe(II) (sulfide/Fe ratios >1) induced precipitation of realgar (As(III)S, As₄S₄) and zero-valent S (Figures 4 and 5), thus keeping the aqueous As concentrations relatively low. Similarly, within the fine-grained, reducing lenses, sulfide concentrations were consistently higher than the aqueous Fe concentrations (Figure SI-4) and, consequently, As(III)S species formed (Figure 4). However, due to the presence of organic matter in the lenses, As(III)S was preferentially associated with organics, probably through sulfhydryl groups,^{9,34–36} and did not precipitate as realgar. This finding is consistent with the findings of Couture et al.³⁷ and supports the sulfurization of organics as a sink for As under sulfidic conditions.

Whether As(III)S precipitates in the mineral form or binds to sulfhydryl groups, our results show that As mobilization due to reductive dissolution is moderated when the aqueous Fe/sulfide ratio <1. Downstream of reducing lenses, aqueous Fe concentrations in the groundwater were consistently higher than the aqueous sulfide concentrations (Fe/sulfide ratios >1), which resulted in mackinawite (FeS) formation and aggregation (Figures 1, 5, and SI-4) and promoted the formation of aqueous thioarsenates (Figures 2 and 5).^{27,38–43} These observations are consistent with recent findings of thioarsenates in the vicinity of reduced zones in a Bangladeshi groundwater aquifer.¹¹

Although the thermodynamics and kinetics of thiolated As species and their formation are still being resolved,⁴⁴ it is clear that they (including thioarsenates) are dependent on pH and the aqueous concentrations and relative ratios of Fe, sulfide, and As.^{9,39,42,45–47} In this study, the pH remained around 8 in all sampling ports (data not shown), so we assume that the observed differences in As speciation result from factors other than the pH. Further, our As concentrations (<0.5 μM) and sulfide/As ratios (>20) are considerably lower and higher, respectively,^{45,46,48} than those considered in most previous studies. Thus, our findings of mixes of arsenate, arsenite, and thioarsenate species at pH 8 and in the presence of aqueous Fe(II) at molar concentrations exceeding those of sulfide are not fully consistent with published thermodynamics.^{42,45,46} This is not surprising, considering the complexity of redox interfaces and nonequilibrium conditions. Nevertheless, our results clearly show that thioarsenate species can form and remain stable under our experimental conditions, indicating that at pH 8, a mixture of aqueous thioarsenates form when sulfide is present at sulfide/As ratios <100 and sulfide/Fe(II) ratios <1. If sulfide/As ratios exceed 100 and sulfide/Fe(II) ratios exceed 1, As–S interactions instead partition As to the solid phase as realgar and/or organically complexed As(III)S. We found no evidence of orpiment

(As₂S₃) in the solid phase As K-edge XANES spectra (Figure 4), despite its common occurrence and thermodynamic stability over a wide range of conditions in comparison to realgar.^{45,46} However, orpiment does exhibit a higher solubility at neutral to alkaline pH⁴⁵ and realgar has previously been found in natural sediments^{34,40,49} and laboratory experiments.^{35,48,50} The precipitation of mineral As–S only at sulfide/As ratios above 100 is inconsistent with previous studies^{49,51} and is likely the result of the considerably higher pH in the current study where aqueous thioarsenates are more favorable.^{42,45,46,52}

The presence of S-complexed As species in both aqueous (thioarsenates) and solid (adsorbed to organics and FeS) phases in this experiment adds to the increasing evidence for the importance of these species in sulfidic environments.^{11,12,43} Further, the fact that thioarsenates were most abundant in samples with high aqueous As concentrations suggests that thiolation promotes As mobilization, as has been proposed by others.^{9,14,53} Thus, as previously found for bioamended sediments,²⁹ our results indicate that aquifers with low (<2 mg/kg) sediment concentrations of As may be at risk for groundwater As concentrations exceeding the drinking water standards (10 μg/L) if the formation of thiolated As species is favorable, i.e., under dominant Fe-reducing conditions with a low, but consistent, supply of sulfide and near-neutral pH.

Importantly, here the influence of sulfate-reducing zones on groundwater chemistry extended downgradient from the fine-grained, reducing lenses at distances up to four times the diameter of the lens itself. Although we only used one size and shape of reduced lenses, this suggests that relatively small layers or lenses of fine-grained, reducing material can have an outsized influence on otherwise oxic aquifers. Unfortunately, borehole samples and geology-based assessments that are performed prior to well installations are typically conducted on a scale where the presence of fine-grained, reducing lenses (i.e., redox heterogeneities) can easily be missed (or their presence is disregarded). Thus, future studies should investigate the relevance of dimensions and spacing of redox heterogeneities induced by fine-grained, reduced lenses on their influence on groundwater chemistry. Such data, and the data from this study, provide guidance for developing predictive groundwater quality models for aquifers exhibiting heterogeneous sediment composition (cf. ref 6).

■ ASSOCIATED CONTENT

Supporting Information

The Supporting Information is available free of charge at <https://pubs.acs.org/doi/10.1021/acs.est.9b06502>.

Schematic of column design; initial concentrations of relevant elements and particle size distribution in natural sediments used for the experiment; groundwater chemical composition; aqueous concentrations of As, Fe, and sulfide in groundwater ports (1, 3, 5, and 7) on day 35 and day 70 of the experiment; temporal evolution of aqueous sulfide, Fe, and As in the groundwater in control columns (without reducing lenses) and pore-water inside reducing lenses; diffractograms from initial and end-point samples of aquifer material and reducing lens material; details from As and SK-edge XANES analyses (PDF)

AUTHOR INFORMATION

Corresponding Author

Kristin Boye – Geochemistry and Biogeochemistry Group, SLAC National Accelerator Laboratory, Menlo Park, California 94025, United States; orcid.org/0000-0003-2087-607X; Email: kboye@slac.stanford.edu

Authors

Naresh Kumar – Department of Geological Sciences, Stanford University, Stanford, California 94305-2115, United States; Department of Environmental Geosciences, Centre for Microbiology and Environmental Systems Science, University of Vienna, 1090 Vienna, Austria

Vincent Noël – Geochemistry and Biogeochemistry Group, SLAC National Accelerator Laboratory, Menlo Park, California 94025, United States; orcid.org/0000-0002-5387-8664

Britta Planer-Friedrich – Environmental Geochemistry, Bayreuth Center for Ecology and Environmental Research (BayCEER), University of Bayreuth, D-95440 Bayreuth, Germany; orcid.org/0000-0002-0656-4283

Johannes Besold – Environmental Geochemistry, Bayreuth Center for Ecology and Environmental Research (BayCEER), University of Bayreuth, D-95440 Bayreuth, Germany

Juan Lezama-Pacheco – Department of Earth System Science, Stanford University, Stanford, California 94305-4216, United States

John R. Bargar – Geochemistry and Biogeochemistry Group, SLAC National Accelerator Laboratory, Menlo Park, California 94025, United States; orcid.org/0000-0001-9303-4901

Gordon E. Brown, Jr. – Department of Geological Sciences, Stanford University, Stanford, California 94305-2115, United States; Department of Photon Science, SLAC National Accelerator Laboratory, Menlo Park, California 94025, United States

Scott Fendorf – Department of Earth System Science, Stanford University, Stanford, California 94305-4216, United States; orcid.org/0000-0002-9177-1809

Complete contact information is available at: <https://pubs.acs.org/10.1021/acs.est.9b06502>

Notes

The authors declare no competing financial interest.

ACKNOWLEDGMENTS

This work was funded by the U.S. Department of Energy (DOE), Office of Science, Office of Biological and Environmental Research (BER), through the SLAC National Accelerator Laboratory scientific focus area (SFA) (Contract No. DE-AC02-76SF00515). Work by N.K. and G.E.B. was supported by the U.S. National Science Foundation and the U.S. Environmental Protection Agency under NSF Cooperative Agreement EF-0830093, to the Center for the Environmental Implications of NanoTechnology (CEINT), based at Duke University. Work by S.F. was supported by the U.S. DOE BER Subsurface Biogeochemistry Program (Award Number DE-SC0020205). B.P.F. and J.B. were supported by the German Research Foundation Grant PL 302/20-1. Use of the Stanford Synchrotron Radiation Lightsource, SLAC National Accelerator Laboratory, is supported by the U.S. DOE, Office of Science, Office of Basic Energy Sciences under Contract No. DE-AC02-76SF00515. This study could not have been completed without sampling and analytical efforts provided

by the following people: George Sims, Dustin Proctor (Central Wyoming College); Laura E. Spielman, Lilia Barragan, Guangchao Li, and Douglas Turner (Stanford University).

REFERENCES

- (1) Fakhreddine, S.; Dittmar, J.; Phipps, D.; Dadakis, J.; Fendorf, S. Geochemical triggers of arsenic mobilization during managed aquifer recharge. *Environ. Sci. Technol.* **2015**, *49*, 7802–7809.
- (2) Fendorf, S.; Nico, P. S.; Kocar, B. D.; Masue, Y.; Tufano, K. J. Arsenic Chemistry in Soils and Sediments. In *Developments in Soil Science*; Elsevier, 2010; Vol. 34, pp 357–378.
- (3) Smedley, P. L.; Kinniburgh, D. A review of the source, behaviour and distribution of arsenic in natural waters. *Appl. Geochem.* **2002**, *17*, 517–568.
- (4) Foster, A. L.; Kim, C. S. Arsenic speciation in solids using X-ray absorption spectroscopy. *Rev. Mineral. Geochem.* **2014**, *79*, 257–369.
- (5) Fendorf, S.; Michael, H. A.; van Geen, A. Spatial and Temporal Variations of Groundwater Arsenic in South and Southeast Asia. *Science* **2010**, *328*, 1123.
- (6) Fakhreddine, S.; Lee, J.; Kitanidis, P. K.; Fendorf, S.; Rolle, M. Imaging geochemical heterogeneities using inverse reactive transport modeling: An example relevant for characterizing arsenic mobilization and distribution. *Adv. Water Resour.* **2016**, *88*, 186–197.
- (7) Mirecki, J. E.; Bennett, M. W.; López-Baláez, M. C. Arsenic control during aquifer storage recovery cycle tests in the Floridan Aquifer. *Groundwater* **2013**, *51*, 539–549.
- (8) Prommer, H.; Stuyfzand, P. J. Identification of temperature-dependent water quality changes during a deep well injection experiment in a pyritic aquifer. *Environ. Sci. Technol.* **2005**, *39*, 2200–2209.
- (9) Besold, J.; Biswas, A.; Suess, E.; Scheinost, A. C.; Rossberg, A.; Mikutta, C.; Kretzschmar, R.; Gustafsson, J. P.; Planer-Friedrich, B. Monothioarsenate Transformation Kinetics Determining Arsenic Sequestration by Sulfhydryl Groups of Peat. *Environ. Sci. Technol.* **2018**, *52*, 7317–7326.
- (10) Planer-Friedrich, B.; London, J.; McCleskey, R. B.; Nordstrom, D. K.; Wallschläger, D. Thioarsenates in geothermal waters of Yellowstone National Park: determination, preservation, and geochemical importance. *Environ. Sci. Technol.* **2007**, *41*, 5245–5251.
- (11) Planer-Friedrich, B.; Schaller, Jr., Wismeth, F.; Mehlhorn, J.; Hug, S. J. Monothioarsenate Occurrence in Bangladesh Groundwater and Its Removal by Ferrous and Zero-Valent Iron Technologies. *Environ. Sci. Technol.* **2018**, *52*, 5931–5939.
- (12) Planer-Friedrich, B.; Suess, E.; Scheinost, A. C.; Wallschläger, D. Arsenic speciation in sulfidic waters: reconciling contradictory spectroscopic and chromatographic evidence. *Anal. Chem.* **2010**, *82*, 10228–10235.
- (13) Beak, D. G.; Wilkin, R. T. Performance of a Zerovalent iron reactive barrier for the treatment of arsenic in groundwater: Part 2. Geochemical modeling and solid phase studies. *J. Contam. Hydrol.* **2009**, *106*, 15–28.
- (14) Stucker, V. K.; Silverman, D. R.; Williams, K. H.; Sharp, J. O.; Ranville, J. F. Thioarsenic species associated with increased arsenic release during biostimulated subsurface sulfate reduction. *Environ. Sci. Technol.* **2014**, *48*, 13367–13375.
- (15) Boye, K.; Noël, V.; Tfaily, M. M.; Bone, S. E.; Williams, K. H.; Bargar, J. R.; Fendorf, S. Thermodynamically controlled preservation of organic carbon in floodplains. *Nat. Geosci.* **2017**, *10*, 415.
- (16) Janot, N.; Lezama Pacheco, J. S.; Pham, D. Q.; O'Brien, T. M.; Hausladen, D.; Noël, V.; Lallier, F.; Maher, K.; Fendorf, S.; Williams, K. H.; et al. Physico-chemical heterogeneity of organic-rich sediments in the Rifle aquifer, CO: Impact on uranium biogeochemistry. *Environ. Sci. Technol.* **2016**, *50*, 46–53.
- (17) Noël, V.; Boye, K.; Kukkadapu, R. K.; Bone, S.; Pacheco, J. S. L.; Cardarelli, E.; Janot, N.; Fendorf, S.; Williams, K. H.; Bargar, J. R. Understanding controls on redox processes in floodplain sediments of the Upper Colorado River Basin. *Sci. Total Environ.* **2017**, *603–604*, 663–675.

- (18) Noël, V.; Boye, K.; Lezama Pacheco, J. S.; Bone, S. E.; Janot, Nm.; Cardarelli, E.; Williams, K. H.; Bargar, J. R. Redox controls over the stability of U (IV) in floodplains of the Upper Colorado River Basin. *Environ. Sci. Technol.* **2017**, *51*, 10954–10964.
- (19) Campbell, K. M.; Kukkadapu, R. K.; Qafoku, N.; Peacock, A. D.; Leshner, E.; Williams, K. H.; Bargar, J. R.; Wilkins, M. J.; Figueroa, L.; Ranville, J.; et al. Geochemical, mineralogical and microbiological characteristics of sediment from a naturally reduced zone in a uranium-contaminated aquifer. *Appl. Geochem.* **2012**, *27*, 1499–1511.
- (20) Qafoku, N. P.; Kukkadapu, R. K.; McKinley, J. P.; Arey, B. W.; Kelly, S. D.; Wang, C.; Resch, C. T.; Long, P. E. Uranium in framboidal pyrite from a naturally bioreduced alluvial sediment. *Environ. Sci. Technol.* **2009**, *43*, 8528–8534.
- (21) Plafcan, M.; Eddy-Miller, C. A.; Ritz, G. F.; Holland Ii, J. P. R.; Stockdale, R. G. *Water Resources of Fremont County, Wyoming*; Water-Resources Investigations Report 95-4095, 1995.
- (22) Cline, J. D. Spectrophotometric determination of hydrogen sulfide in natural waters 1. *Limnol. Oceanogr.* **1969**, *14*, 454–458.
- (23) Viollier, E.; Inglett, P.; Hunter, K.; Roychoudhury, A.; Van Cappellen, P. The ferrozine method revisited: Fe (II)/Fe (III) determination in natural waters. *Appl. Geochem.* **2000**, *15*, 785–790.
- (24) Newville, M.; Ravel, B. HEPHAESTUS: data analysis for x-ray absorption spectroscopy using Ifeffit Ravel, B.; Newville, M. J. *Synchrotron Radiat.* **2005**, *12*, 537–541.
- (25) Noël, V.; Boye, K.; Kukkadapu, R. K.; Li, Q.; Bargar, J. R. Uranium storage mechanisms in wet-dry redox cycled sediments. *Water Res.* **2019**, *152*, 251–263.
- (26) Antelo, J.; Avena, M.; Fiol, S.; López, R.; Arce, F. Effects of pH and ionic strength on the adsorption of phosphate and arsenate at the goethite–water interface. *J. Colloid Interface Sci.* **2005**, *285*, 476–486.
- (27) Wolthers, M.; Charlet, L.; van Der Weijden, C. H.; van der Linde, P. R.; Rickard, D. Arsenic mobility in the ambient sulfidic environment: Sorption of arsenic(V) and arsenic(III) onto disordered mackinawite. *Geochim. Cosmochim. Acta* **2005**, *69*, 3483–3492.
- (28) Poulton, S. W.; Krom, M. D.; Raiswell, R. A revised scheme for the reactivity of iron (oxyhydr)oxide minerals towards dissolved sulfide. *Geochim. Cosmochim. Acta* **2004**, *68*, 3703–3715.
- (29) Smith, S.; Dupont, R. R.; McLean, J. E. Arsenic Release and Attenuation Processes in a Groundwater Aquifer During Anaerobic Remediation of TCE with Biostimulation. *Groundwater Monit. Rem.* **2019**, *39*, 61–70.
- (30) Kumar, N.; Lezama Pacheco, J.; Noël, V.; Dublet, G.; Brown, G. E. Sulfidation mechanisms of Fe(III)-(oxyhydr)oxide nanoparticles: a spectroscopic study. *Environ. Sci.: Nano* **2018**, *5*, 1012–1026.
- (31) Peiffer, S.; Wan, M. Reductive Dissolution and Reactivity of Ferric (Hydr)oxides: New Insights and Implications for Environmental Redox Processes. In *Iron Oxides: From Nature to Applications*; Wiley-VCH Verlag GmbH & Co. KGaA: Weinheim, Germany, 2016.
- (32) Hellige, K.; Pollok, K.; Laresca-Casanova, P.; Behrends, T.; Peiffer, S. Pathways of ferrous iron mineral formation upon sulfidation of lepidocrocite surfaces. *Geochim. Cosmochim. Acta* **2012**, *81*, 69–81.
- (33) Pyzik, A. J.; Sommer, S. E. Sedimentary iron monosulfides: kinetics and mechanism of formation. *Geochim. Cosmochim. Acta* **1981**, *45*, 687–698.
- (34) Langner, P.; Mikutta, C.; Kretzschmar, R. Arsenic sequestration by organic sulphur in peat. *Nat. Geosci.* **2012**, *5*, 66.
- (35) Langner, P.; Mikutta, C.; Suess, E.; Marcus, M. A.; Kretzschmar, R. Spatial Distribution and Speciation of Arsenic in Peat Studied with Microfocused X-ray Fluorescence Spectrometry and X-ray Absorption Spectroscopy. *Environ. Sci. Technol.* **2013**, *47*, 9706–9714.
- (36) Hoffmann, M.; Mikutta, C.; Kretzschmar, R. Bisulfide Reaction with Natural Organic Matter Enhances arsenite Sorption: Insights from X-ray Absorption Spectroscopy. *Environ. Sci. Technol.* **2012**, *46*, 11788–11797.
- (37) Couture, R.-M.; Wallschläger, D.; Rose, J.; Van Cappellen, P. Arsenic binding to organic and inorganic sulfur species during microbial sulfate reduction: a sediment flow-through reactor experiment. *Environ. Chem.* **2013**, *10*, 285–294.
- (38) Burton, E. D.; Johnston, S. G.; Bush, R. T. Microbial sulfidogenesis in ferrihydrite-rich environments: Effects on iron mineralogy and arsenic mobility. *Geochim. Cosmochim. Acta* **2011**, *75*, 3072–3087.
- (39) Vega, A. S.; Planer-Friedrich, B.; Pastén, P. A. arsenite and arsenate immobilization by preformed and concurrently formed disordered mackinawite (FeS). *Chem. Geol.* **2017**, *475*, 62–75.
- (40) O'Day, P. A.; Vlassopoulos, D.; Root, R.; Rivera, N. The influence of sulfur and iron on dissolved arsenic concentrations in the shallow subsurface under changing redox conditions. *Proc. Natl. Acad. Sci. U.S.A.* **2004**, *101*, 13703–13708.
- (41) Couture, R. M.; Rose, J.; Kumar, N.; Mitchell, K.; Wallschläger, D.; Van Cappellen, P. Sorption of arsenite, Arsenate, and Thioarsenates to Iron Oxides and Iron Sulfides: A Kinetic and Spectroscopic Investigation. *Environ. Sci. Technol.* **2013**, *47*, 5652–5659.
- (42) Couture, R.-M.; Van Cappellen, P. Reassessing the role of sulfur geochemistry on arsenic speciation in reducing environments. *J. Hazard. Mater.* **2011**, *189*, 647–652.
- (43) Stauder, S.; Raue, B.; Sacher, F. Thioarsenates in sulfidic waters. *Environ. Sci. Technol.* **2005**, *39*, 5933–5939.
- (44) Herath, I.; Vithanage, M.; Seneweera, S.; Bundschuh, J. Thiolated arsenic in natural systems: What is current, what is new and what needs to be known. *Environ. Int.* **2018**, *115*, 370–386.
- (45) Wilkin, R. T.; Wallschläger, D.; Ford, R. G. Speciation of arsenic in sulfidic waters. *Geochim. Trans.* **2003**, *4*, No. 1.
- (46) Helz, G. R.; Tossell, J. A. Thermodynamic model for arsenic speciation in sulfidic waters: A novel use of ab initio computations. *Geochim. Cosmochim. Acta* **2008**, *72*, 4457–4468.
- (47) Wood, S. A.; Tait, C. D.; Janecky, D. R. A Raman spectroscopic study of arsenite and thioarsenite species in aqueous solution at 25 C. *Geochim. Trans.* **2002**, *3*, 31.
- (48) Bostick, B. C.; Fendorf, S.; Brown, G. E. In situ analysis of thioarsenite complexes in neutral to alkaline arsenic sulphide solutions. *Mineral. Mag.* **2005**, *69*, 781.
- (49) Root, R. A.; Vlassopoulos, D.; Rivera, N. A.; Rafferty, M. T.; Andrews, C.; O'Day, P. A. Speciation and natural attenuation of arsenic and iron in a tidally influenced shallow aquifer. *Geochim. Cosmochim. Acta* **2009**, *73*, 5528–5553.
- (50) Gallegos, T. J.; Han, Y.-S.; Hayes, K. F. Model predictions of realgar precipitation by reaction of As (III) with synthetic mackinawite under anoxic conditions. *Environ. Sci. Technol.* **2008**, *42*, 9338–9343.
- (51) Rochette, E. A.; Bostick, B. C.; Li, G.; Fendorf, S. Kinetics of Arsenate Reduction by Dissolved Sulfide. *Environ. Sci. Technol.* **2000**, *34*, 4714–4720.
- (52) Planer-Friedrich, B.; Wallschläger, D. A critical investigation of hydride generation-based arsenic speciation in sulfidic waters. *Environ. Sci. Technol.* **2009**, *43*, 5007–5013.
- (53) Kumar, N.; Couture, R.-M.; Millot, R.; Battaglia-Brunet, F.; Rose, J. Microbial Sulfate Reduction Enhances Arsenic Mobility Downstream of Zerovalent-Iron-Based Permeable Reactive Barrier. *Environ. Sci. Technol.* **2016**, *50*, 7610–7617.

Supporting Information

Redox Heterogeneities Promote Thioarsenate Formation and Release into Groundwater from Low Arsenic Sediments

Naresh Kumar^{1,2}, Vincent Noël³, Britta Planer-Friedrich⁴, Johannes Besold⁴, Juan Lezama-Pacheco⁵, John R. Bargar³, Gordon E. Brown, Jr.^{1,6}, Scott Fendorf⁵, Kristin Boye^{3}*

¹Department of Geological Sciences, Stanford University, Stanford, CA 94305-2115, U.S.A.

²Department of Environmental Geosciences, Centre for Microbiology and Environmental Systems Science, University of Vienna, 1090 Vienna, AUSTRIA

³Geochemistry and Biogeochemistry Group, SLAC National Accelerator Laboratory, 2575 Sand Hill Road, Menlo Park, CA 94025, U.S.A

⁴Environmental Geochemistry, Bayreuth Center for Ecology and Environmental Research (BayCEER), University of Bayreuth, D-95440 Bayreuth, GERMANY

⁵Department of Earth System Science, Stanford University, Stanford, CA 94305-4216, U.S.A.

⁶Department of Photon Science, SLAC National Accelerator Laboratory, 2575 Sand Hill Road, Menlo Park, CA 94025, U.S.A.

Contents

Column Design and sediment properties

Figure SI-1: Schematic of column design

Table SI-1: Element concentrations in sediments

Table SI-2: Particle size distribution of sediments

Table SI-3: Chemical composition of artificial groundwater

Aqueous phase analyses

Aqueous As speciation analyses

Figure SI-2: Depth profiles of aqueous concentrations of As, Fe, and sulfide at days 35 and 70

Figure SI-3: Aqueous concentrations of As, Fe, and sulfide in control columns

Figure SI-4: Aqueous concentrations of As, Fe, and sulfide in lens porewater

Solid phase analyses

X-ray diffraction procedure and results

Figure SI-5: Diffractograms for initial and end-point materials

As K-edge x-ray absorption near-edge structure (XANES) spectroscopy details

Table SI-4: Statistics of linear combination fits for As XANES sample spectra

S K-edge XANES details

Column design and sediment properties

Twelve columns were fabricated from 30 cm long, 7 cm diameter Cast Acrylic Plexiglass tubes (ePlastics®, Ridout Plastics Co. Inc., San Diego, U.S.A.) with holes drilled into the side to enable insertion of porewater samplers (RhizonFlex, 5 cm, and MicroRhizon, 8 mm, both with 0.15 µm pore size, from Rhizosphere Research Products, Wageningen, Netherlands) (Fig. SI-1). Column ends were closed off with polyethylene caps equipped with pipette tips, filled with glass wool to prevent sediment loss, acting as connectors for influent and effluent groundwater tubing (Fisherbrand™ Tygon S3™ flexible tubing). All gaps around sampling ports and caps were sealed with silicone rubber (Dow Corning®, Midland, MI, U.S.A) to prevent leaks. A 1.5 cm layer of pure quartz sand (IOTA Quartz, 99.9% crystalline silica, Unimin corporation) was added to the bottom of each column to provide a level surface for sediments and prevent particles leaking into the groundwater tubing. The columns were then filled with natural sediments, which had been collected ~2 weeks prior from the Wind River-Little Wind River floodplain outside of Riverton, WY (42°59'19.1"N 108°23'58.6"W). Columns were filled with moist aquifer sand (equivalent to 1.3-1.4 kg dry sand per column) collected by digging down to the groundwater from a cut-bank close to the Little Wind River, where As concentrations were 1.2±0.4 mg/kg sediment. The sediment for the reducing lenses was collected from underneath an oxbow lake at the site; the sulfidic, fine-grained, and organic rich sediments are similar in character to so called 'Naturally Reduced Zones' (NRZs) documented in similar alluvial environments¹⁻⁶. Both the sand and the material for the lenses were thoroughly homogenized to ensure consistent composition between different columns and lenses. The lens material contained lower As concentrations (0.7±0.1 mg/kg sediment) than the aquifer sand. Sediment properties for the aquifer and lens materials are presented in Table SI-1 (element concentrations) and SI-2 (particle size distribution). The oxbow lake sediment was allowed to dry in a glovebag (3-4% H₂, balance N₂) to ~50% (w/w) water content in order to facilitate shaping and controlling the positioning of the spherical (ϕ 2.5 cm) lenses within the columns. Triplicate columns with 0 (control), 1, 2, or 3 lens(es) were packed from bottom to top with the first lens centered between the first and second rhizon sampler, the second (if present) between the second and the third rhizon etc. (Fig. SI-1). The columns were agitated slightly during filling to ensure homogeneous packing (packed volume corresponded to ~1000 mL and 20% porosity). Micro-rhizons were thereafter inserted into the center of each lens to enable sampling of pore-water from within lenses. Influent tubing was connected to a peristaltic pump adjusted to operate at a speed equivalent to roughly one pore volume exchange per 48 hours, corresponding to 90 mL per day or 6 mm/hr. All columns were fed artificial groundwater from the same source (20 L Teflon container) through 0.1 µm in-line filters (Corning®, USA). Groundwater was replenished every 7 days and was made to have a chemical composition representative of average concentrations of the major solutes, except organic C, measured in Riverton groundwater over the past 2 years (SI, Table SI-3). Bicarbonate (HCO₃⁻) and Ca concentrations had to be adjusted to slightly below the minimum concentrations observed at the site in order to obtain complete dissolution of all salts in the groundwater. The groundwater supply container was loosely covered with parafilm to maintain equilibrium with the atmosphere while preventing dust to enter the system. Dissolved oxygen concentrations in the groundwater supply were 240-260 µmol O₂/L, in order to achieve a dissolved oxygen concentration in the control columns (~50 µM) similar to that measured in the floodplain groundwater (average 87 µM, range 14-211 µM).

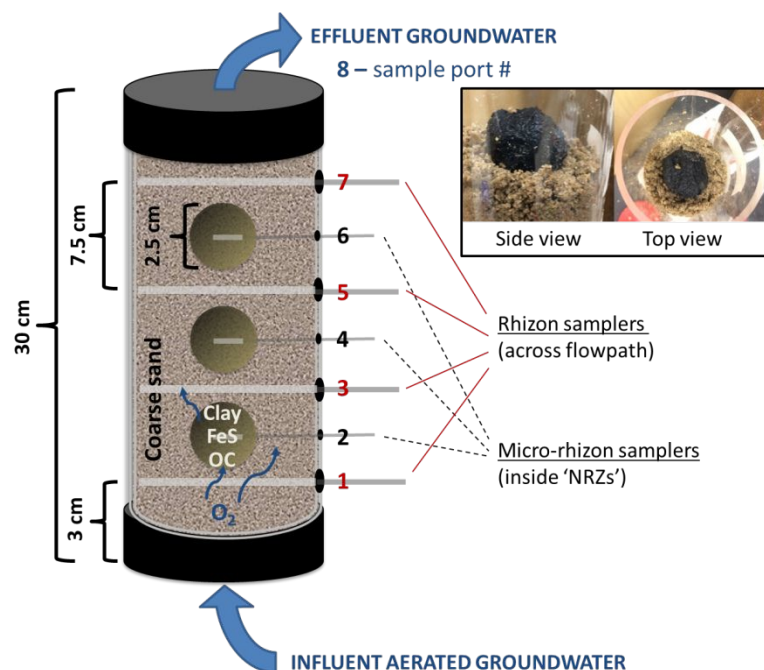


Figure SI-1. Schematic of column design.; all columns containing reducing lenses were equipped with rhizon samplers (5 cm) at ports 1, 3, 5, and 7, plus a micro-rhizon (8 mm) in each lens (*e.g.*, at ports 2, 4, and 6 for columns with 3 lenses). In columns with one lens (positioned at port 2) or two lenses (at ports 2 and 4) no micro-rhizons were used at ports without a lens (*i.e.* ports 4 and 6 for columns with one clay lens and port 6 for columns with two clay lenses). Control columns (no reducing lenses) were equipped with only one rhizon (5 cm) sampler at port number 5. Photo insert shows the laterally centered placement of reducing lenses inside the columns.

Table SI-1. Initial concentrations of relevant elements in natural sediments used for the experiment. All values are averages \pm standard deviation of triplicate measurements

Constituent	Lens material	Aquifer Sand
Total As ($\mu\text{g/g}$)	0.7 ± 0.1	1.2 ± 0.4
Total S (mg/g)	6.5 ± 0.4	0.65 ± 0.03
Total Fe (mg/g)	31 ± 2	7.1 ± 0.3
Total C (mg/g)	37.2 ± 0.2	0.28 ± 0.02
Organic C (mg/g)	27.7 ± 0.2	0.12^\dagger
Inorganic C (mg/g)	9.5 ± 0.2	0.16^\dagger
Total N (mg/g)	2.16 ± 0.04	B.D.

[†]Two of the triplicate measurements were below detection, so no standard deviation could be calculated

B.D. = below detection

Table SI-2. Particle size distribution in the oxbow lake sediment (lens material) and aquifer sand, as determined by U.S. standard sieve particle separation

Particle size fraction	Lens material	Aquifer Sand
1-2 mm (very coarse sand)	0%	8%
0.5-1 mm (coarse sand)	6%	39%
0.15-0.5 mm (medium to fine sand)	33%	49%
0.053-0.15 mm (very fine sand)	41%	3%
<0.053 mm (silt and clay)	19%	1%

Table SI-3. Chemical composition of artificial groundwater and average (min-max) concentrations (mg/L) measured in groundwater at 3 depths in a nearby well at the Riverton site in August each year from 2015 to 2017⁷.

Constituent	Artificial groundwater		Riverton groundwater	
	8 mM	mg/L	6.95	(6.78-7.18) mg/L
pH				
Ca	3.7	150	550	(380-710)
Na	10.4	2400	1967	(1600-2400)
Mg	18.5	450	419	(280-630)
Mn	0.03	1.5	2.12	(0.77-4.30)
K	0.5	20	22.8	(15.0-31.0)
Si [†]	0.3	8	13.7	(12.0-14.0)
Fe ^{††}	0.009	0.5	2.05	(0.36-3.00)
Mo	0.003	0.25	0.29	(0.25-0.34)
Cl	16.9	600	656	(380-1000)
SO ₄ ²⁻	62.2	6000	7678	(5100-11000)
HCO ₃ ⁻	7.5	450	527	(440-636)
NO ₃ ⁻	0.016 (0.16) ^{†††}	1 (10) ^{†††}	0.37	(0.17-0.578)
U	0 (0.008) ^{†††}	0 (2.0) ^{†††}	1.50	(0.86-2.00)
Br	0.02	1	N/A	
TDS		10,053	10,240*	

[†]Silicon was added as Na₂(SiO₃²⁻)·9H₂O

^{††}Iron was added as Fe(III)(NO₃)₃·9H₂O

^{†††}Values in brackets represent concentrations during the last 14 days of the experiment

*Calculated from measured electrical conductivity in 2017 of 16,000 μS/cm

Aqueous phase analyses

Aqueous As speciation analyses

The recovery rate for As-species compared to total ICP-MS values ranged between 19 and 109%, with an average of 69%. The lowest recovery rates (19-34%) were exclusively obtained from the last (furthest down-field) sampling point, which was the least reduced, and all samples with low recovery (5 out of 27 total) contained only arsenate. This may indicate the presence of small (<0.15 μm) particles of iron-(oxyhydr)oxides that could have aggregated and sorbed arsenate between the time of sampling and the time of IC-ICP-MS analyses. Nevertheless, the sum of As-species was linearly correlated with total As ($r^2=0.66$ for all ports, $r^2=0.84$ when excluding the last sampling port #7), so overall the relative distribution of species was assumed to be intact.

Note that with the chromatographic method we used, we cannot fully exclude that what is measured as thioarsenates could originally have been thioarsenites that oxidized while sitting in capped vials for a few minutes on an autosampler at ambient air, as reported before⁸. Thioarsenites have been shown to be necessary precursors for thioarsenate formation⁸, so it is likely that they were the first species to form from arsenite and sulfide also in this study. However, they are highly prone to oxidation and have been reported before to react rapidly with zero-valent sulfur (S₀) to form thioarsenates⁹. Since S₀ was also detected in our experiments (see below) we conclude that thioarsenates are not analytical artefacts, but the original species present inside the columns. The observed dominance of monothioarsenate is a further piece of evidence for its *in-situ* formation in the columns, as the precursor for monothioarsenite has so far never been observed in considerable amounts, whereas monothioarsenate is the dominant species to form from arsenite and S₀.

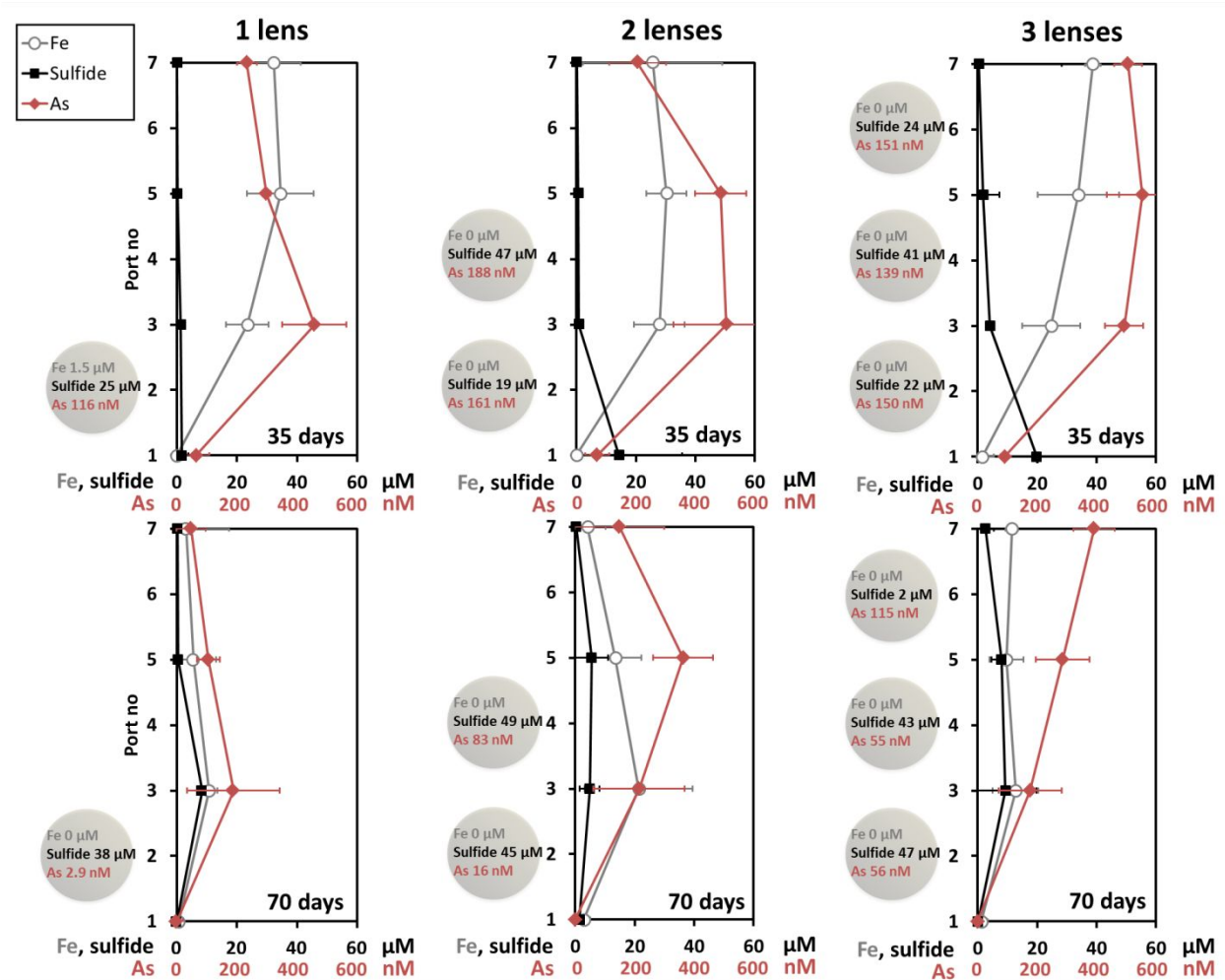


Figure SI-2. Aqueous concentrations of As (nM, red), Fe (μM , grey), and sulfide (μM , black) in groundwater ports (1, 3, 5, and 7) on day 35 (top panels) and day 70 (bottom panels) of the experiment. Positions of the reducing lenses are indicated by the shaded circles to the left of each plot. Porewater concentrations of As, Fe, and sulfide inside each lens is given in numbers in the corresponding circles. All numbers and values are averages for triplicate columns and error bars for groundwater concentrations denote the standard deviation of the mean for triplicate columns.

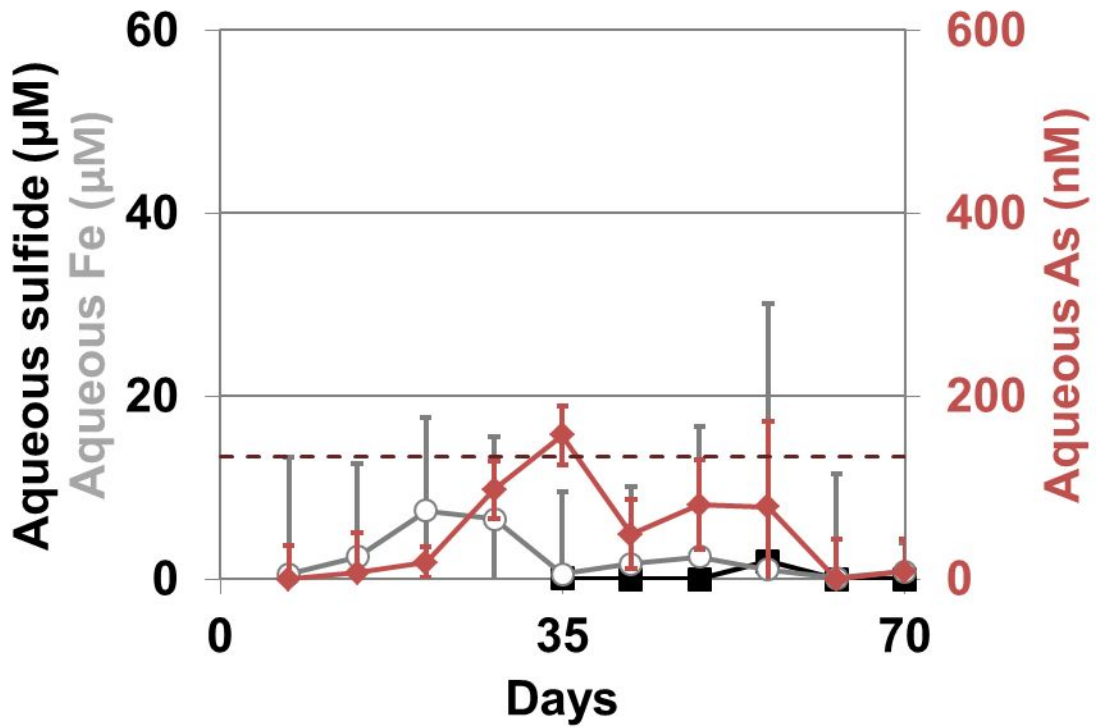


Figure SI-3. Temporal evolution of aqueous sulfide (μM) and Fe (μM) (both on left vertical axis) and aqueous As (nM, right vertical axis), in the groundwater in control columns (without reducing lenses). All values are averages of triplicate columns and error bars denote the standard deviation from the mean for the triplicates. The dotted line indicates the WHO drinking water limit for As ($10 \mu\text{g/L} = 133.5 \text{ nM}$).

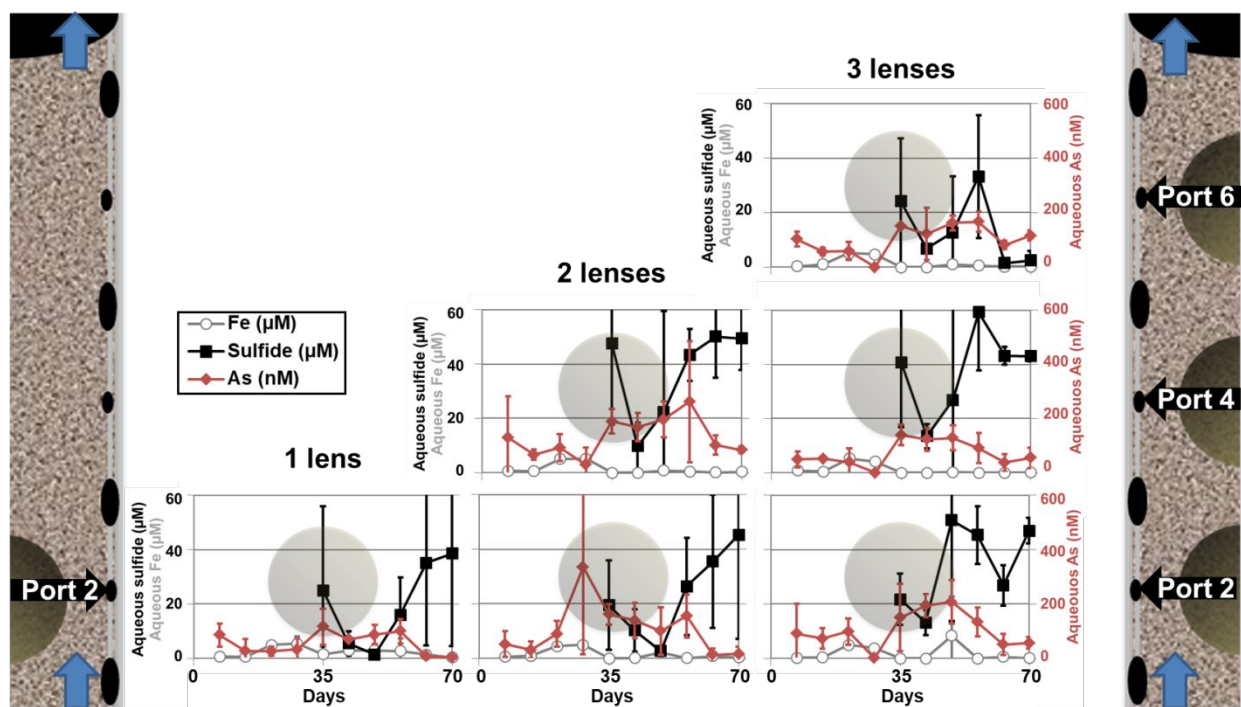


Figure SI-4. Temporal evolution of aqueous sulfide (μM) and Fe (μM) (both on left vertical axis) and aqueous As (nM, right vertical axis), in the pore water inside reducing lenses (horizontal axes). All values are averages of triplicate columns for each treatment and error bars denote the standard deviation from the mean for the triplicates.

Solid phase analyses

X-ray diffraction procedure and results

Subsamples of the initial aquifer sand and lens materials were dried and finely ground for x-ray diffraction (XRD) analyses of mineralogical phase composition. Additionally end-point samples were taken (from one of the columns with 3 reducing lenses) from the aquifer sand between reducing lenses (ports 3 and 5) and two of the reducing lenses (ports 4 and 6). The end-point samples were dried, finely ground, and loaded onto the anoxic XRD sample holders inside a glovebag and run on a Rigaku MiniFlex 600 Benchtop X-ray Diffraction System at the Cu wavelength ($\lambda=1.5406 \text{ \AA}$) and phase identification was performed by automatic search, using the Inorganic Crystal Structure Database (ICSD, ©2019 FIZ Karlsruhe GmbH). In order to account for slight differences in background signals from the sample holders, all diffractograms were normalized by setting the intensity of the main quartz peak ($2\theta \text{ CuK}\alpha=26.7^\circ$) to 1, thus enabling intensity comparisons between initial and end-point samples of the same material (assuming the quartz peak intensity for each material remained unchanged during the course of the experiment).

Overall, the diffractograms (Fig. SI-5) from end-point samples were very similar to the corresponding initial diffractogram. The aquifer sand mineralogy was dominated by quartz, along with some albite and calcium carbonate, whereas the lens material contained montmorillonite, quartz, calcium carbonate, and iron sulfate. There was a small change in the lens material diffractograms; all of the montmorillonite peaks of the end-point lens material were smaller than in the initial material, suggesting that some smectite clays were lost from the lenses during the course of the experiment. However, the first montmorillonite peak also exhibited a slightly smaller d-spacing ($2\theta=6.8-7.0^\circ$, $d=12.6-13.1 \text{ \AA}$) in the end-point material than the initial material ($2\theta=6.1^\circ$, $d=14.5 \text{ \AA}$). Thus, another option is that there was a change in the collapsed spacing of the layers of smectites, possibly due to a change in exchange cations.

Apart from the slight shift in the phyllosilicate minerals, the only other distinguishable difference between initial and end-point materials was found in the aquifer material sampled from port 5, which exhibited a peak at $2\theta=29.5^\circ$ ($d=3.0 \text{ \AA}$) that was not present in the initial aquifer material. This peak is consistent with calcium carbonate d-spacing and may indicate an accumulation of carbonate minerals along the flowpath during the experiment. Indeed, the other CaCO_3 -peaks were also smaller in the initial material than in the Port 5 end-point sample.

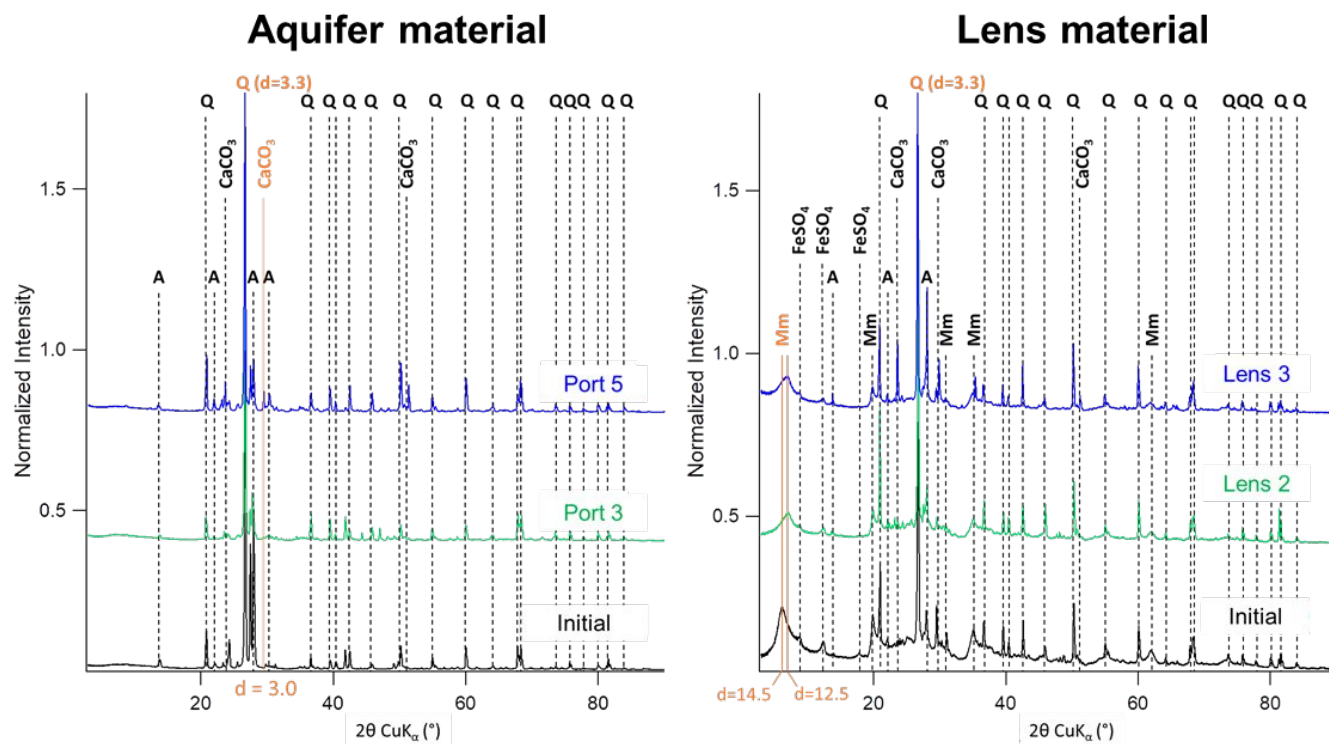


Figure SI-5. Diffractograms from initial and end-point samples of aquifer material (left) and reducing lens material (right). Orange vertical lines indicate peaks that exhibit clear differences between the initial and end-point samples of the same materials. Dashed vertical indicates the positions of the peaks for all identified phases (A=Albite, Q=Quartz, M=Muscovite, Mm=Montmorillonite). The quartz peak at $d=3.3$ was set to 1 for all spectra to account for slight differences in background signal from the Si-coated holders.

As K-edge XANES spectroscopy details

Arsenic K-edge XANES spectra were collected at 10 K (LHe cryostat) in fluorescence yield mode, using a 30 pixel germanium X-ray detector, on the 7-3 beamline at the Stanford Synchrotron Radiation Lightsource, SSRL. The Si(220) double crystal monochromator was detuned by 50% to minimize higher order harmonics. Glycerol-preserved samples were loaded inside the glovebag onto an Al sample holder with Kapton® windows. The mounted holder was transferred to the beamline in liquid N₂ and quickly inserted into a LHe cryostat placed under vacuum. Calibration was monitored by setting the first inflection point of a simultaneously measured Au L_{III}-edge to 11,919 eV (double transmission mode). Aluminum foils and Soller slits were used to increase the signal to noise ratio. For each sediment sample, 4 to 9 scans were recorded, depending on the total As concentration (0.7 to 3 µg/g As). In order to prevent beam damage, a motorized sample holder was used to illuminate a new spot on the sample for each acquisition scan and a shutter was used to minimize the exposure of the sample to the beam between each movement of the monochromator. As a consequence, no evidence of beam damage was detected between subsequent scans. All spectra were averaged and normalized using the Ifeffit 1.2.12 (© Matt Newville) Demeter 0.9.25 Athena software (© Bruce Ravel)¹⁰. Linear combination least squares (LC-LS) fitting of the normalized spectra was also performed in Athena. Our library of As reference spectra includes the oxoanions arsenite (As(III)O₃³⁻), arsenate (As(V)O₄³⁻) as sodium salts and adsorbed to Fe sulfides (FeS, FeS₂), ferrihydrite, and goethite, as well as mono- and tetrathioarsenates (synthesized from sodium arsenite) as salts and adsorbed to the same Fe sulfides and Fe oxides as the oxoanions, all of which have been published by Couture et al.¹¹. In addition, we included orpiment (As₂S₃) and realgar (AsS or As₄S₄) spectra from Besold et al.⁹, and organically complexed As(III)S₃ (As(III)-C₁₈H₁₅; trisphenylthioarsine) from Boye et al.¹². However, we found that the best fits (Table SI-4) were obtained using 2-4 of the following seven standard spectra: Realgar (AsS or As₄S₄) (in aquifer), As(III)S₃ complexed with organics (trisphenylthioarsine, As(III)S₃-C₁₈H₁₅) (in reducing lenses), As(III) adsorbed to ferrihydrite (As(III)=Fh) or to mackinawite (As(III)-FeS), S-complexed As sorbed to FeS (represented by monothiolated (MTA) As(V) adsorbed to mackinawite, MTA=FeS), and As(V) sorbed to ferrihydrite (As(V)=Fh, in aquifer) or to mackinawite (As(V)=FeS, in reducing lenses).

Table SI-4. Results from As k-edge XANES linear combination fitting, showing As speciation in the solid phase of aquifer and reducing lens samples from the glycerol preserved column (with 3 reducing lenses) and in the initial aquifer and lens materials from the field site. Column colors are consistent with the colors representing each species in Fig. 4 of the main text

Sample	% of total As (normalized to sum of 100%)							Fitted sum	NSSR [†]
	Realgar (As ₄ S ₄)	As(III) ≡Org	As(III) ≡Fh	As(III) ≡FeS	MTA≡FeS	As(V) ≡Fh	As(V) ≡FeS		
	11868.7 eV	11868.7 eV	11869.9 eV	11870.9 eV	11871.2 (11874.1) eV	11874.6 eV	11874.3 eV	%	%
Aquifer initial	–	–	16	–	–	84	–	75	2.4
Port 1	83	–	–	–	–	17	–	108	0.05
Port 3	–	–	–	37	9	53	–	89	0.57
Port 5	–	–	–	66	31	4	–	101	0.001
Lens initial	–	22	–	18	–	–	60	108	0.05
Lens 1	–	34	–	16	–	–	50	107	0.01
Lens 2	–	34	–	20	–	–	47	103	0.0001
Lens 3	–	40	–	19	–	–	42	106	0.02

[†]Normalized sum of squared residuals (NSSR) = $100\% \times \sum_i(\text{sample}_i - \text{fit}_i)^2 / \sum_i(\text{sample}_i)^2$

S K-edge XANES spectroscopy details

In order to examine the solid phase S speciation in NRZs and aquifer sand samples, we used the glycerol-preserved samples from the column with 3 reducing lenses (also used for As K-edge XANES). The sample paste was pressed into S-free tape covered windows of Al-holders and covered with Ultralene® XRF film (0.16 mm thick, SPEX SamplePrep, Metuchen, NJ, U.S.A.). Sample holders were transferred to Beam line 4-3 at the Stanford Synchrotron Radiation Lightsource (SSRL) in an airtight jar. Sample holders were inserted at a 45° angle in the sample chamber under He-atmosphere with the Ultralene covered side facing the incoming beam. The XANES spectra were collected in fluorescence yield mode under He atmosphere laminar flux at room temperature, using a Si (111) double crystal monochromator and a four element SiLi Vortex detector. The incoming beam was detuned by 35% to minimize the interference from Fe resonance. Energy calibration was performed by setting the K-edge of a freshly prepared Na-thiosulfate standard to 2472.02 eV. To fully capture the fine details in the structure of the XANES spectra, we increased the energy in 0.5 eV increments from 2440-2467 eV, 0.05 eV steps from 2467-2492 eV, 0.5 eV from 2492-2520 eV and finally in 3 eV steps from 2520-2593. Between 3 and 6 scans were performed for each sample, but there was evidence of significant beam oxidation of highly reduced S in some samples; as a consequence, only the first scan was used from any samples that exhibited a change in spectral features between the first and subsequent scans. All spectra were normalized using the Ifeffit 1.2.12 (© Matt Newville) Demeter 0.9.25 (© Bruce Ravel) Athena software⁷. Normalization was conducted by setting the edge energy (E_0) to the inflection point of the first major absorption peak for each sample, the pre-edge region was set to 2440-2460 eV and the post-edge (normalization) region was adjusted for each spectra to roughly transect the post-edge oscillations (after 2500 eV) at the inflection points.

References

1. Boye, K.; Noël, V.; Tfaily, M. M.; Bone, S. E.; Williams, K. H.; Bargar, J. R.; Fendorf, S., Thermodynamically controlled preservation of organic carbon in floodplains. *Nature Geoscience* **2017**, *10*, (6), 415.
2. Janot, N.; Lezama Pacheco, J. S.; Pham, D. Q.; O'Brien, T. M.; Hausladen, D.; Noël, V.; Lallier, F.; Maher, K.; Fendorf, S.; Williams, K. H., Physico-chemical heterogeneity of organic-rich sediments in the Rifle aquifer, CO: Impact on uranium biogeochemistry. *Environmental science & technology* **2015**, *50*, (1), 46-53.
3. Noël, V.; Boye, K.; Kukkadapu, R. K.; Bone, S.; Pacheco, J. S. L.; Cardarelli, E.; Janot, N.; Fendorf, S.; Williams, K. H.; Bargar, J. R., Understanding controls on redox processes in floodplain sediments of the Upper Colorado River Basin. *Science of the Total Environment* **2017**, *603*, 663-675.
4. Noël, V.; Boye, K.; Lezama Pacheco, J. S.; Bone, S. E.; Janot, N. m.; Cardarelli, E.; Williams, K. H.; Bargar, J. R., Redox controls over the stability of U (IV) in floodplains of the Upper Colorado River Basin. *Environmental science & technology* **2017**, *51*, (19), 10954-10964.
5. Campbell, K. M.; Kukkadapu, R. K.; Qafoku, N.; Peacock, A. D.; Leshner, E.; Williams, K. H.; Bargar, J. R.; Wilkins, M. J.; Figueroa, L.; Ranville, J., Geochemical, mineralogical and microbiological characteristics of sediment from a naturally reduced zone in a uranium-contaminated aquifer. *Applied geochemistry* **2012**, *27*, (8), 1499-1511.
6. Qafoku, N. P.; Kukkadapu, R. K.; McKinley, J. P.; Arey, B. W.; Kelly, S. D.; Wang, C.; Resch, C. T.; Long, P. E., Uranium in framboidal pyrite from a naturally bioreduced alluvial sediment. *Environmental science & technology* **2009**, *43*, (22), 8528-8534.
7. GEMS, Groundwater Quality by Location (GEMS100), Site: RVT01, Riverton Processing Site. <https://gems.lm.doe.gov/#>. REPORT DATE/TIME: 5/9/2018 12:06:23 PM.
8. Planer-Friedrich, B.; Suess, E.; Scheinost, A. C.; Wallschläger, D., Arsenic speciation in sulfidic waters: reconciling contradictory spectroscopic and chromatographic evidence. *Analytical chemistry* **2010**, *82*, (24), 10228-10235
9. Besold, J.; Biswas, A.; Suess, E.; Scheinost, A. C.; Rossberg, A.; Mikutta, C.; Kretzschmar, R.; Gustafsson, J. P.; Planer-Friedrich, B., Monothioarsenate Transformation Kinetics Determining Arsenic Sequestration by Sulfhydryl Groups of Peat. *Environmental Science & Technology* **2018**, *52*, (13), 7317-7326.
10. Athena, A., HEPHAESTUS: data analysis for x-ray absorption spectroscopy using IFEFFIT Ravel, B.; Newville, M. *Journal of Synchrotron Radiation* **2005**, *12*, (4), 537-541.
11. Couture, R. M.; Rose, J.; Kumar, N.; Mitchell, K.; Wallschläger, D.; Van Cappellen, P., Sorption of Arsenite, Arsenate, and Thioarsenates to Iron Oxides and Iron Sulfides: A Kinetic and Spectroscopic Investigation. *Environmental Science & Technology* **2013**, *47*, (11), 5652-5659.
12. Boye, K., Lezama Pacheco, J.S., Fendorf, S. (2017) Relevance of Reactive Fe:S Ratios for Sulfur Impacts on Arsenic Uptake by Rice. *Soils* *1*, 1. doi:10.3390/soils1010001

Study 5: Antimonite Complexation with Thiol and Carboxyl/Phenol Groups of Peat Organic Matter

Johannes Besold, Naresh Kumar, Andreas C. Scheinost, Juan Lezama Pacheco, Scott Fendorf and

Britta Planer-Friedrich

Reprinted with permission from

Environmental Science & Technology

Copyright 2020 American Chemical Society

Antimonite Complexation with Thiol and Carboxyl/Phenol Groups of Peat Organic Matter

Johannes Besold,[†] Naresh Kumar,^{‡,§} Andreas C. Scheinost,^{||} Juan Lezama Pacheco,[⊥] Scott Fendorf,[⊥] and Britta Planer-Friedrich^{*,†,||}

[†]Department of Environmental Geochemistry, Bayreuth Center for Ecology and Environmental Research (BAYCEER), Bayreuth University, 95440 Bayreuth, Germany

[‡]Department of Geological Sciences, School of Earth, Energy, and Environmental Sciences, Stanford University, Stanford, California 94305, United States

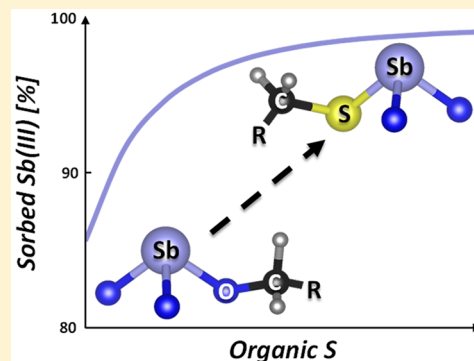
[§]Department of Environmental Geosciences, University of Vienna, 1090 Vienna, Austria

^{||}The Rossendorf Beamline (ROBL) at ESRF, 38043 Grenoble, France and Helmholtz-Zentrum Dresden-Rossendorf (HZDR), Institute of Resource Ecology, 01328 Dresden, Germany

[⊥]Department of Earth System Science, School of Earth, Energy, and Environmental Sciences, Stanford University, Stanford, California 94305, United States

Supporting Information

ABSTRACT: Peatlands and other wetlands with abundant natural organic matter (NOM) are important sinks for antimony (Sb). While formation of Sb(III) sulfide phases or Sb(III) binding to NOM are discussed to decrease Sb mobility, the exact binding mechanisms remain elusive. Here, we reacted increasing sulfide concentrations with purified model peat at pH 6, forming reduced organic sulfur species, and subsequently equilibrated the reaction products with 50 μM of antimonite under anoxic conditions. Sulfur solid-phase speciation and the local binding environment of Sb were analyzed using X-ray absorption spectroscopy. We found that 85% of antimonite was sorbed by untreated peat. Sulfide-reacted peat increased sorption to 98%. Shell-by-shell fitting of Sb *K*-edge X-ray absorption fine structure spectra revealed Sb in untreated peat bound to carboxyl or phenol groups with average Sb–carbon distances of ~ 2.90 Å. With increasing content of reduced organic sulfur, Sb was progressively coordinated to S atoms at distances of ~ 2.45 Å and Sb–carbon distances of ~ 3.33 Å, suggesting increasing Sb–thiol binding. Iterative target factor analysis allowed exclusion of reduced inorganic Sb–sulfur phases with similar Sb–sulfur distances. In conclusion, even when free sulfide concentrations are too low for formation of Sb–sulfur precipitates, peat NOM can sequester Sb in anoxic, sulfur-enriched environments.



INTRODUCTION

Antimony (Sb) is a potentially toxic^{1–3} metalloid, whose mobility and speciation is strongly influenced by its redox transformations.^{4,5} Under oxic to slightly reducing conditions, the pentavalent antimonate is the thermodynamically favored species, whereas the trivalent antimonite is predicted to dominate under anoxic conditions. Antimonate thereby prevails as negatively charged $\text{Sb}(\text{OH})_6^-$, whereas antimonite occurs as neutral oxoacid $\text{Sb}(\text{OH})_3$ at environmentally relevant pH values.⁴

In contrast to its group-five neighbor arsenic (As), the biogeochemistry of Sb is relatively poorly studied,^{6,7} despite pollution due to increased mining activities in the past years^{8,9} as well as broad industrial (flame retardants, catalyst in plastics synthesis, etc.)^{1,10} and military (ammunition)¹¹ use. The majority of research has been conducted on oxic environments^{11–14} with special focus on the role of iron and manganese (oxyhydr)oxides as well as clay minerals for the

mobility of Sb.⁵ However, there is little information on Sb aqueous- and solid-phase speciation under anoxic, partly sulfidic conditions with high abundances of solid natural organic matter (NOM). Such conditions prevail in peatlands and other wetlands.^{5,15} While natural antimony background concentrations, including values from pristine peatlands for comparison, are commonly low (0.008 – 0.3 mg kg^{-1}),^{16,17} high Sb contents have been reported from atmospheric deposition¹⁶ and from waste waters received from mining activities, principally gold¹⁷ and Sb^{12,18–20} mining (with resulting Sb concentrations up to $22\,000$ mg kg^{-1}).¹⁸

Several studies have demonstrated in recent years, particularly for As^{17,21–23} but also for other (radioactive)

Received: January 30, 2019

Revised: April 10, 2019

Accepted: April 11, 2019

Published: April 11, 2019

toxic trace metal(loid)s,^{24–28} that natural and engineered peatlands and wetlands can act as important contaminant sinks due to covalent binding to solid NOM. On the other hand, complexation with dissolved or colloidal organic matter could lead to (re)mobilization of metal(oids) in organic-rich surface-, pore-, and groundwaters.^{29–32} Based on current findings, although limited in number, Sb sequestration appears more important in organic carbon-rich environments compared to mobilization because complexation of antimonite with dissolved organic ligands was generally observed to be limited (<30% of total Sb).^{33–35}

In peatlands, iron and manganese (oxyhydr)oxides undergo reductive dissolution with increasing depth due to increasing water content and eventual saturation;^{36,37} additionally, (microbially triggered) sulfate-reduction leads to formation of dissolved sulfide with depth.³⁸ Released metal(oid)s such as Sb or As can then react with sulfide, forming authigenic amorphous As/Sb–S precipitates at low to neutral pH values.^{5,39} Despite generally sulfidic conditions, however, free sulfide concentrations in peatlands are commonly low^{40–43} since the produced sulfide can be effectively incorporated into NOM as organic thiols,^{40,44} often the dominant sulfur species in such systems.⁴⁵ Precipitation of Sb(III) sulfide phases may, therefore, play a minor role in peatlands compared to complexation by reduced organic sulfur (thiol) functional groups.

The association of Sb with solid NOM has so far only been shown in a few field studies, including studies from peat bogs in Switzerland¹⁶ and the United Kingdom^{46–48} where a strong association of atmospheric anthropogenic Sb depositions with NOM was observed. Further, Fawcett et al.²⁰ revealed the association of Sb with solid NOM, and the presence of Sb(III)–S phases in aquatic sediments residing adjacent to a former mining site. In a recent study, Arsic et al.⁴⁹ also reported the formation of an Sb(III)–S phase in contaminated wetland soil mesocosm experiments. They speculated the formation of authigenic Sb(III) sulfide or Sb(III) complexation with thiol functional groups, but were unable to distinguish between them. With organic-rich sediments from the same wetland, Bennett et al.⁵⁰ showed with bulk extended X-ray absorption fine-structure (EXAFS) spectroscopy that up to 44% of total Sb was 3-fold coordinated to sulfur at a distance of 2.46 Å, indicative for Sb–thiol coordination. Since such a coordination environment is common in both phases, Sb–thiol complexes as well as in disordered SbS₃ formed via reaction of antimonite with mackinawite (FeS),⁵¹ unequivocal attribution to one of these two Sb species could not be made.

The aim of the present work was hence two-fold. First, to determine the extent of antimonite sorption and its local binding environment (<5 Å) with NOM, we examined Sb sorption on untreated and thiol-rich model NOM under controlled laboratory conditions at slightly acidic pH 6.0, conditions typical for many peatlands. Second, we sought to distinguish the contributions of organic, thiol-bound Sb(III) from inorganic Sb(III)–S phases.

To fulfill our goals, we used S *K*-edge XANES spectroscopy to follow the solid-phase speciation of S upon reaction of sulfide with the model NOM, and we used Sb *K*-edge EXAFS spectroscopy to study the local Sb coordination environment. Iterative target factor analysis (ITFA) of Sb *K*-edge XANES and EXAFS spectra, a powerful means to discriminate small spectral differences,⁵² was used to differentiate between thiol- and inorganic disordered Sb–S phases.

MATERIALS AND METHODS

Materials. All reagents used were of analytical grade and purchased from Alfa Aesar, Sigma-Aldrich or VWR. All solutions were prepared with doubly deionized (DDI) water (Milli-Q, Millipore, ≥ 18.2 M Ω cm) and all glassware was treated with acid before use.

Model Natural Organic Matter. Peat, which was used as a model sorbent for NOM, was collected from the ombrotrophic *Federseemoor* peatland near Bad Buchau, Germany and prepared for the Sb sorption study as described elsewhere.^{23,43,53} In brief, the peat was wet-sieved to a size fraction of 63–250 μ m and, after an initial washing step with 0.1 M HCl to solve potentially interfering metal(loid)s, washed several times with anoxic DDI water until a starting pH of ~ 4.5 was reached. Afterward, the peat was freeze-dried, homogenized, and stored in a glovebag (Coy, pO₂ < 1 ppm) in the dark until use. In this paper, the term peat is used when referring to the 63–250 μ m size fraction.

Elemental composition analyses and functional group characterization with ¹³C cross-polarization/magic-angle spinning-nuclear magnetic resonance (CP/MAS NMR) spectroscopy for the washed and freeze-dried peat are described elsewhere.^{23,43} Fourier transform infrared (FT–IR) spectra of freeze-dried peat samples after incubation at pH 4.5, 6.0, and 7.0 for 96 h (same conditions as described for Sb sorption experiments below) were recorded to follow pH-dependent changes of functional groups. Further detailed descriptions of these methods and analyses are provided in the [Supporting Information \(SI\)](#).

Reaction of Peat with Sulfide. In order to provide different concentrations of thiol groups as potential sorption sites, peat suspensions (0.1 M C) were reacted with five different concentrations of dissolved sulfide (0–30 mM) in 30 mM NaCl background electrolyte solution under anoxic conditions (pO₂ < 1 ppm) and shaken at room temperature in the dark for 24 h. The pH value was adjusted to pH 6.0 \pm 0.2 using anoxic HCl and NaOH solutions. Sodium azide (NaN₃, 0.75 mmol/mol C) was added to prevent microbial growth. After reacting for 24 h to reach equilibrium,²³ the suspensions were filtered (12 μ m, cellulose acetate), and the remaining peat filter residues were subsequently washed with electrolyte to remove dissolved sulfide. A representative sample was then freeze-dried, homogenized, and analyzed for its total S content or stored for XAS analysis. Total S content analysis was done using inductively coupled plasma mass-spectrometry (ICP–MS, XSeries2, Thermo-Fisher, Waltham, MA) after microwave digestion (MARS Xpress, CEM) using a 5:3 ratio of 30% H₂O₂ and 65% HNO₃. Another sample aliquot was directly used in the antimonite sorption experiments without drying.

Antimonite Sorption Experiments. A wet weight equivalent of 200 mg of dry untreated or sulfide-reacted peat (0.1 M C) was equilibrated with 50 μ M antimonite at pH 6.0 \pm 0.2 in anoxic electrolyte for 96 h, using the same experimental conditions as described before. The 50 μ M antimonite solution was prepared by spiking an aliquot from an 8.26 mM antimonite stock solution (Sb₂O₃ dissolved in 2 M HCl) in 10 mM MES (2-(*N*-morpholino)ethanesulfonic acid, pK_a = 6.15) buffered electrolyte solution. After a 96 h reaction, the peat suspensions were filtered (0.2 μ m, nylon) and an aliquot of the filtrate was immediately shock-frozen on dry ice in order to avoid Sb species changes. After thawing the frozen

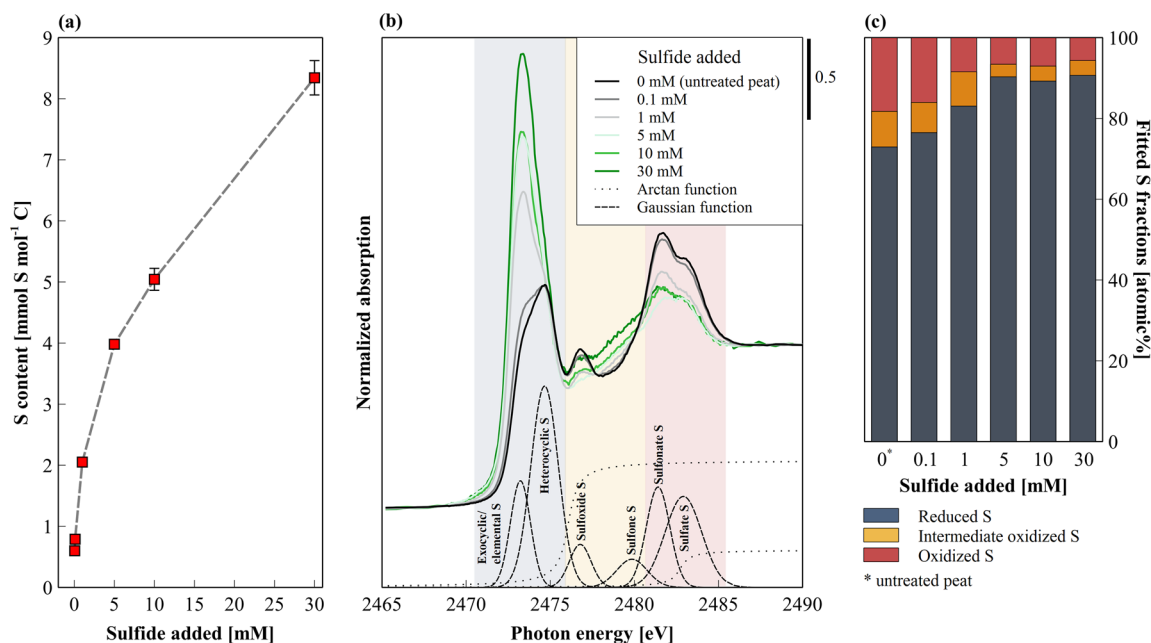


Figure 1. Results of model peat reacted with sulfide (0–30 mM sulfide, 0.1 M peat-C, 30 mM NaCl background electrolyte at pH 6.0 ± 0.2 (NaOH adjusted)). (a) Sulfur content in model peat as a function of added sulfide. (Error bars represent standard deviations of triplicates, and the dashed line serves to illustrate data trends). (b) Normalized S *K*-edge XANES spectra of untreated (0 mM sulfide added) and sulfide-reacted peat samples. Spectral decomposition is illustrated as an example for the untreated peat (with offset from the other spectra). The two arctan functions are shown as dotted lines and the Gaussian functions as dashed lines corresponding to **reduced S (oxidation states –II to +I)**: exocyclic/elemental S, heterocyclic S; **intermediate oxidized S (oxidation states > +I to +III)**: sulfoxide S, sulfone S, and **oxidized S (oxidation states > +III to +VI)**: sulfonate S, sulfate S. Gaussian function assigned to questionable inorganic sulfide was excluded. The experimental data and fit envelopes as well as all fit parameters for every sample can be found in SI Figure SI-5 and Table SI-3. (c) Sulfur solid-phase speciation results based on spectral XANES deconvolution. SI Figure SI-6 shows individual relative fractions of fitted Gaussian functions. Please note that the intermediate oxidized fractions (sulfoxide and sulfone S) are likely to be overestimated due to postedge absorption features of reduced S species.⁶¹

samples in a glovebag, aqueous Sb speciation was analyzed with anion-exchange chromatography (AEC, ICS-3000, Dionex) coupled to an ICP–MS (XSeries2, Thermo-Fisher) following the protocol of Hockmann et al.⁵⁴ In all cases, Sb(III), with only very minor fractions of Sb(V) (max. 0.5 μM), were detected in solution (SI Figure SI-8), which can be explained by oxidation of Sb(III) by disulfides or quinones of NOM as previously reported.^{33,55} Another aliquot was stabilized in 0.5% H_2O_2 and 0.8% HNO_3 prior to analysis of total aqueous Sb with ICP–MS. The amount of Sb sorbed was calculated as the difference between total and dissolved Sb. The organic C-normalized partition coefficients (K_{OC}) [$\text{L kg}^{-1} \text{C}$] of Sb were determined as $K_{\text{OC}} = C_p/C_s$; whereby C_p and C_s represent Sb contents in peat ($\mu\text{g kg}^{-1} \text{C}$) and Sb concentrations in solution ($\mu\text{g L}^{-1}$) after equilibration, respectively. After freeze-drying the peat filter residues, one part of the solid phase was used for XAS analysis and another sample aliquot was microwave-digested, as described before, to determine total S content.

Antimony Reference Compounds. The Ambersep GT74 resin (Rohm & Haas) was used as a sulfhydryl-rich synthetic organic model adsorbent. A detailed chemical characterization of the resin can be found elsewhere.⁵⁶ In order to examine the potential of antimonite binding to sulfhydryl groups, 100 mg of washed resin were equilibrated with 50 μM of antimonite for 96 h at pH 6.0 ± 0.2 following the experimental setup described earlier.

Further, three aqueous Sb(III)–glutathione (GSH) complexes were synthesized in a glovebag in molar ratios of GSH:Sb(III) of 1:1, 2:1, and 3:1 following an adapted protocol

of Sun et al.⁵⁷ and Raab et al.⁵⁸ and were subsequently precipitated with ethanol. The resulting precipitates were filtered using glass frits and a vacuum pump and dried within the glovebag in a desiccator over hygroscopic silica gel for several days. The Sb(III)–GSH standards were ground with mortar and pestle and stored in the glovebag until XAS analyses.

An amorphous Sb(III) sulfide standard was synthesized in order to evaluate spectral differences to organic Sb(III) standards. Equal volumes of 8 mM anoxic antimonite and 16 mM anoxic sulfide solution were mixed with gentle shaking in a 1 L wide-neck bottle (PET, Nalgene) inside the glovebag until orange-colored Sb sulfide precipitated. The precipitate was filtered and subsequently washed several times with DDI water. Afterward the precipitate was dried within the glovebag in a desiccator over hygroscopic silica gel for several days. After grinding, the fine-grained Sb sulfide was stored in the glovebag until phase identification with powder XRD and XAS analyses. Detailed descriptions of all syntheses and the diffraction pattern of amorphous Sb(III) sulfide are provided in the SI.

Solid-Phase Speciation with X-ray Absorption Spectroscopy. Bulk S *K*-edge (2472 eV) XANES spectra of untreated and sulfide-reacted peat samples, kept permanently under anoxic conditions, were collected at beamline 4–3 and Sb *K*-edge (30 491 eV) XANES and EXAFS spectra of samples equilibrated with antimonite were measured at beamline 4–1 at the Stanford Synchrotron Radiation Lightsource (SSRL), Menlo Park, CA. All measurements were performed in fluorescence mode. Samples for S XANES data were collected under inert He (<0.1% (v/v) O_2) atmosphere at ambient

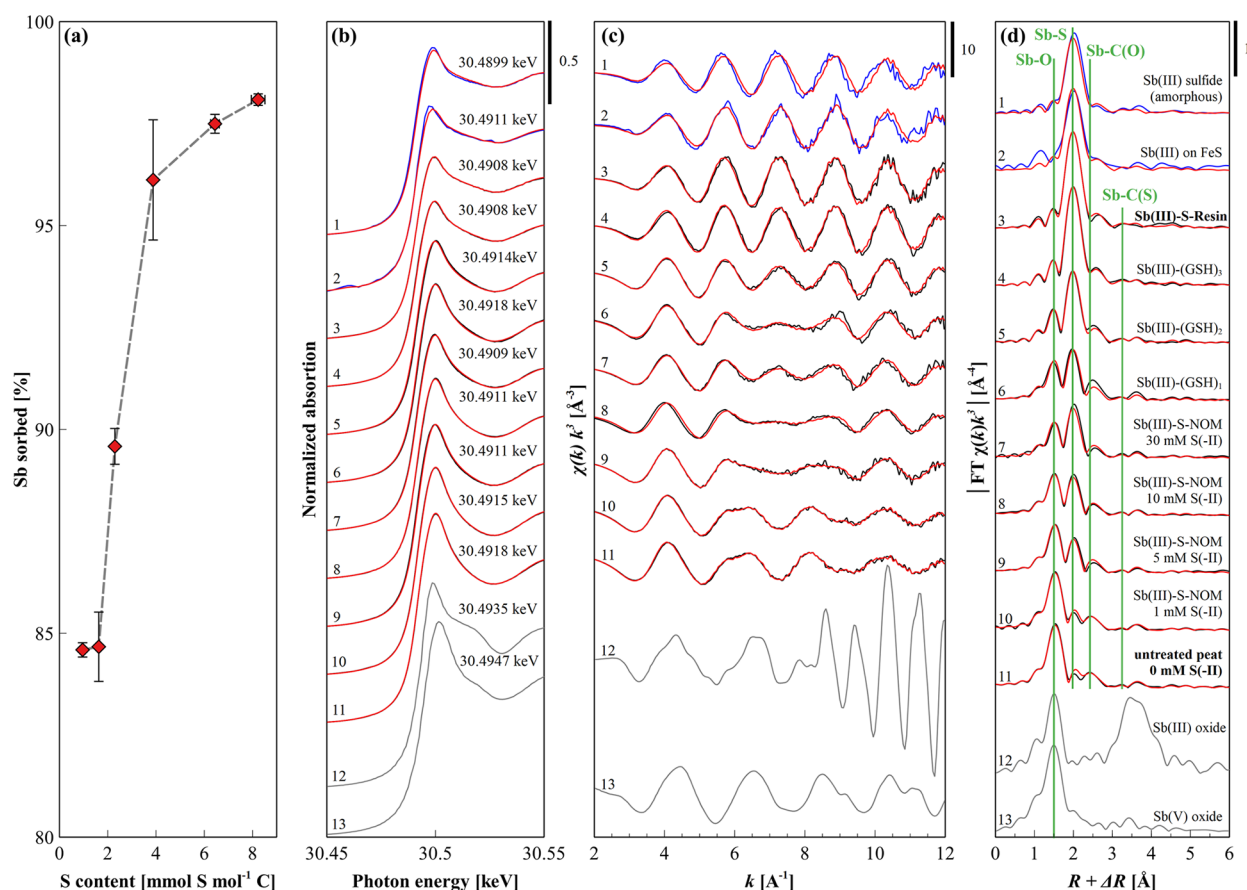


Figure 2. Results of antimonite sorption experiment with untreated and sulfide-reacted model peat. (a) Sorbed antimonite (50 μM antimonite solution, 0.1 M peat-C, 30 mM NaCl background electrolyte at pH 6.0 (MES buffered)) as a function of S content (Sb(III)–S–NOM experiment). (Error bars represent standard deviations of triplicates and the dashed line serves to illustrate data trends) The ordinate is shown as [% Sb sorbed], conversion factor to $\mu\text{mol Sb mol}^{-1}\text{ C} = 5.8391$. (b) Experimental normalized Sb K -edge XANES spectra, (c) k^3 -weighted EXAFS spectra and (d) corresponding Fourier-transform (FT) magnitudes of the Sb(III) organic matter series (black lines) and separately added Sb(III) sulfide (amorphous) and Sb(III) on FeS from Kirsch et al.⁵¹ (blue lines). The reconstruction of the whole series by two principal components is shown in red. End-member species (Sb(III)–S–Resin and untreated peat (0 mM S(-II))) are highlighted in bold. Reference spectra representing Sb(III) and Sb(V) species (Sb(III) oxide and Sb(V) oxide) are added for comparison (gray lines). Magnitudes of single scattering paths of Sb–O, Sb–S, Sb–C(O), and Sb–C(S) are marked with green lines at the respective positions in the FT.

temperature, and samples for Sb solid-phase speciation were analyzed using a liquid He cryostat maintaining a temperature of ~ 7 K under vacuum. Spectral deconvolutions of normalized S K -edge XANES spectra were done in Athena.⁵⁹ Principal component analysis (PCA) and iterative transformation factor analysis (ITFA) of normalized Sb K -edge XANES and EXAFS spectra were performed with the ITFA software package.⁶⁰ Evaluation of the quality of reconstructions calculated with principal components from PCA was done with the NSSR-value ($100 \times \sum_i (\text{data}_i - \text{reconstruction}_i)^2 / \sum_i \text{data}_i^2$) and the normalized standard deviations between data and reconstructions ($\text{SD} = (1/n) \times \sum (\text{data}_i - \text{reconstruction}_i)^2$; n = number of data points within spectrum). Shell-by-shell fitting of k^3 -weighted Sb K -edge EXAFS spectra was performed in R-space employing the software Artemis.⁵⁹ Details on XAS measurements, data reduction, and analyses are provided in the SI.

RESULTS AND DISCUSSION

Characterization of Untreated Peat. The peat contained ~ 55 wt % C and ~ 2200 mg kg^{-1} of total S. Concentrations of metals (e.g., Al, Fe) for potential ternary complex formation with Sb were relatively low (< 0.2 wt %).^{28,43,48} Further information on the elemental composition of untreated peat

has been described before⁴³ and is also summarized in SI Table SI-1.

In the ¹³C CP/MAS–NMR spectrum (SI Figure SI-1, Table SI-2) relative intensities of chemical shift regions were dominated by alkyl, O-alkyl and aromatic C functionalities (89%), representing a cellulose- and lignin-rich chemical backbone structure of the peat.²³ Carbonyl, phenolic and carboxylic groups accounted for 2%, 6%, and 8% of total NMR-active C, respectively. The FT–IR spectrum of peat incubated at the experimental pH 6.0 (SI Figure SI-2) showed absorptions bands typical for aliphatic alcohol, phenol, and carboxyl C moieties, besides bands indicative of a comparably unreactive chemical backbone structure (3850 cm^{-1} and ~ 2350 cm^{-1}).

Reaction of Peat with Sulfide. The total S content in peat increased monotonously after incubation with 0–30 mM sulfide from 0.60 ± 0.02 to a maximum of 8.34 ± 0.28 mmol S mol^{-1} C (Figure 1a). The results are comparable to a previous study of Hoffmann et al.²³ using the same peat, where nucleophilic addition of the S(-II) via the Michael mechanism and/or an acid-catalyzed addition to unsaturated carbon bonds lead to formation of reactive R-SH groups in the peat. Indeed, S K -edge XANES spectra of (sulfide-reacted) peat samples

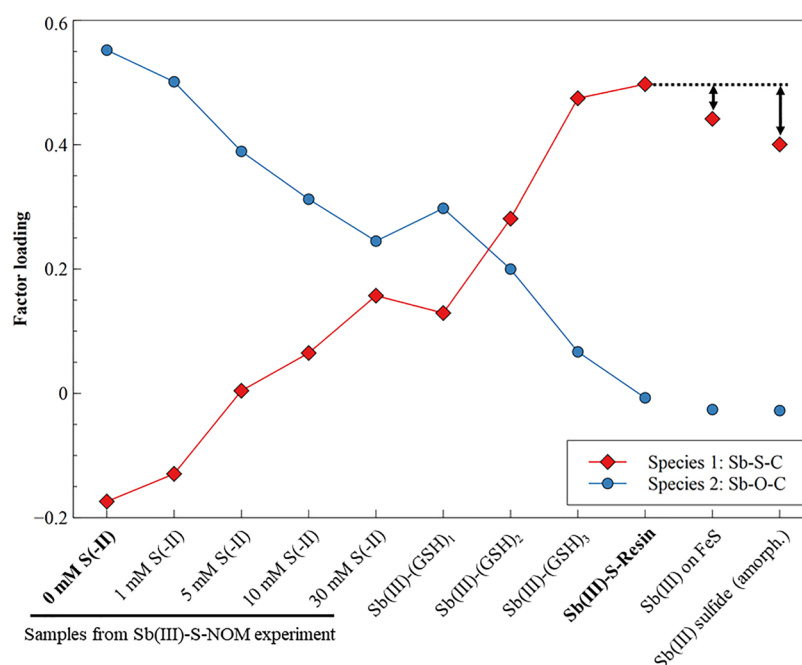


Figure 3. VARIMAX rotation with two factors from principal component analysis of k^3 -weighted EXAFS spectra. End-member species (Sb(III)–S–Resin and untreated peat (0 mM S(-II)) are highlighted in bold. Black dotted line and arrows illustrate that Sb(III) sulfide (amorphous) and Sb(III) on FeS are not members of the Sb(III) organic matter series. The information in Figure 3 can be used for qualitative conclusions but not for a quantitative determination of factor loadings.

showed a simultaneous increase of resonance peaks in the energy range from 2471 to 2475 eV summarized as “reduced S” with increasing total S content (Figure 1b). In this range, two Gaussian functions representing $s \rightarrow p$ transitions of exocyclic/elemental S (~ 2473 eV) and heterocyclic S (~ 2474 eV) could be fitted to the spectra (SI Figure SI-5, Table SI-3, and Figure SI-6), whereby the peak assigned to exocyclic/elemental S (including thiol moieties) increased the most with increasing total S.

A third (reduced S) Gaussian function at energies of 2471.7 ± 0.1 eV was necessary in order to reach good overall fit results and had contributions of <9 atomic% (SI Table SI-3). This fraction is probably an artifact, since comparing the spectral features of the rising edge of the peat sample with highest sulfide addition (30 mM) to a purely organic thiol-standard like 4-nitrobenzenethiol showed no difference (SI Figure SI-7). Further, the occurrence of inorganic mono- and disulfides, with white line positions typically lower in energy (FeS: 2470.7 ± 0.3 eV; FeS₂: 2471.1 ± 0.2 eV⁶²), seems to be unlikely.

Resonance peaks of the second major peak range from 2481 to 2485 eV (“oxidized S”) generally decreased with increasing sulfide addition and could be deconvoluted as organic sulfonate and inorganic sulfate S (Figure 1b, SI Table SI-3 and Figure SI-6). A simultaneous general increase of the fitted sulfone S fraction (~ 2479 eV) with increasing sulfide addition suggests the (partial) reduction of species from the “oxidized S” pool²³ (SI Figure SI-5). Further, a Gaussian function for sulfoxide S (~ 2277 eV), which accounts together with sulfone S to the “intermediate oxidized S” pool, had to be fitted to the peat samples with low to moderate S contents (Figure 1b, SI Figure SI-6).

Overall, the strong increase in reduced S functionalities from 0.4 to 7.6 mmol S mol⁻¹ C (Figure 1c) in the peat with increasing sulfide addition could be assigned to the

incorporation of sulfide into the structure of peat, most likely as thiol S.

Antimonite Sorption to Untreated and Sulfide-Reacted Peat. The sorption of antimonite to untreated and sulfide-reacted peat is illustrated in Figure 2a. The untreated peat sorbed $84.5 \pm 0.2\%$ (493 ± 1 $\mu\text{mol Sb mol}^{-1}$ C) of the initial 50 μM antimonite added and sorption increased monotonously with increasing S content to a maximum of $97.8 \pm 0.2\%$ (571 ± 1 $\mu\text{mol Sb mol}^{-1}$ C). Under almost similar experimental conditions, antimonite’s structural analogue arsenite showed significantly different results with no sorption to untreated peat and a maximum sorption of ~ 150 $\mu\text{mol As mol}^{-1}$ C at comparable S content.²³

As described before, S *K*-edge XANES analysis revealed that thiol moieties increased to the greatest extent with increasing S content, which are known to have a high affinity toward Sb(III).^{57,63,64} Depending on the backbone structure, reduced, strongly nucleophilic organic monosulfides have $\text{p}K_a$ values ranging from ~ 4 to 11⁶⁵ and Sb(III)–thiol bonds are known to be stronger than Sb(III)–oxygen bonds.^{63,66–68} These observations are consistent in supporting Sb–thiol coordination during the incubation with sulfide-reacted peat in our experiment.

In the untreated peat, the proportion of reduced S groups was lower than in all sulfide-reacted peat samples (Figure 1c). Yet, $84.5 \pm 0.2\%$ (493 ± 1 $\mu\text{mol Sb mol}^{-1}$ C) of total Sb were already sorbed. This observation indicates that there is at least one more binding mechanism in addition to Sb–thiol binding. Indeed, when plotting the sorbed Sb as a function of the C-normalized ratio of $\text{Sb}_{\text{initial}}/\text{S}_{\text{peat}}$ (SI Figure SI-9) an additional binding mechanism is clear. All peat samples with sulfide loadings plotted on a line with negative slope, whereas the untreated peat did not. Moreover, stronger binding sites seem to be involved at lower $\text{Sb}_{\text{initial}}/\text{S}_{\text{peat}}$ ratios, resulting from

presumed thiol complexation, since Sb sorption increased linearly and was highest at the lowest $S_{\text{initial}}/S_{\text{peat}}$ ratio.

Calculated $\log K_{\text{OC}}$ values ranged from 3.4 to 4.3 and were slightly lower than the ones from Buschmann and Sigg³³ (4–5, pH 6), who investigated the binding of antimonite to different humic acids, but used ~ 190 times lower Sb/C ratios than that of our study. The same study also proposed complexation of Sb with carboxylic and/or phenolic functionalities of humic substances by ligand exchange at the Sb center or formation of a negatively charged complex as main binding mechanisms. At the experimental pH of 6.0, antimonite occurs as uncharged oxoacid ($\text{p}K_a = 11.97$), and FT–IR analysis demonstrated that carboxylic groups of our untreated peat deprotonated between pH 4.5 and 7.0, whereas phenolic groups stay mostly protonated due to higher $\text{p}K_a$ values typically ranging between ~ 8.5 and ~ 9.5 .^{34,65,69} Thus, carboxylic groups likely provide additional sorption sites for antimonite, especially in the untreated peat with low amounts of reduced S. However, H-bridging or hydrophobic interactions may also be involved in Sb binding³³ and the influence of hydroxyl binding via its two free electron pairs cannot be fully excluded.

Antimony Solid-Phase Speciation of Untreated and Sulfide-Reacted Peat. The edge positions of normalized Sb *K*-edge XANES spectra of the peat decreased almost linearly with increasing S content from 30 491.8 to 30 490.9 eV, and comparison with Sb(III) and Sb(V) reference standards shows that no oxidation occurred in the solid-phase during our experiments (Figure 2b).

Figure 2c and d illustrate the k^3 -weighted Sb *K*-edge EXAFS spectra and the magnitudes of the corresponding Fourier transforms (FT) of peat and reference standards. All peat samples are characterized by two major FT peaks in the 1.5–2.0 Å $R + \Delta R$ -range, which occur at the same positions as for the reference standards Sb(III)–(GSH)_{1–3} and Sb(III)–S–Resin (Figure 2d). The first FT peak at ~ 1.5 Å $R + \Delta R$ corresponds to O atoms in the first coordination shell and decreased with increasing S content of peat samples. Conversely, the second FT peak at ~ 2.0 Å $R + \Delta R$, which corresponds to S atoms in the first or higher coordination shells of Sb, increased with increasing S content.

Performing principal component analysis (PCA) on the k^3 -weighted Sb *K*-edge EXAFS spectra of peat samples including Sb(III)–(GSH)_{1–3} samples as well as the Sb(III)–S–Resin sample (in the following called Sb(III) organic matter (OM) series) using the ITFA package revealed that the spectra of the Sb(III)–OM series could be reproduced by only two principal components (PCs). Two PCs are indicated by a minimum of the Malinowski indicator value (SI Table SI-4) and 98.3% of total variance explained in the data set. Further, this observation was confirmed by the almost perfect reproductions of the experimental EXAFS and also XANES spectra by two PCs (Figure 2b and c). VARIMAX rotation on the EXAFS spectra of the Sb(III)–OM series with two PCs revealed that Sb(III)–S–Resin (species 1) and untreated peat (0 mM S(-II)) (species 2) were the purest representatives for the respective PC (=species) and are therefore considered as end-members of the Sb(III)–OM series (Figure 3). Consequently, it was sufficient to shell-fit only the two end-members of the Sb(III)–OM series with the purest spectral features. All other samples thus are linear combinations of the Sb(III)–S–Resin and the untreated peat (0 mM S(-II)) sample.

Shell-by-shell fitting parameters and best-fit models of the k^3 -weighted EXAFS spectra of the Sb(III)–S–Resin and

untreated peat (0 mM S(-II)) sample are shown in Table 1 and Figure 4. For the Sb(III)–S–Resin sample, we were able

Table 1. EXAFS Parameters Determined from Shell-by-Shell Fitting of Sb *K*-Edge EXAFS Spectra of the Two End-Members of the Sb(III) Organic Matter Series (Sb(III)–S–Resin and Untreated Peat (0 mM S(-II)) as well as Sb(III) Sulfide (Amorphous)).^a

sample	path	CN ^b	R [Å] ^c	σ^2 [Å ²] ^d	ΔE^0 [eV] ^e	NSSR [%] ^f
Sb(III) sulfide (amorphous)	Sb–S	3.6	2.48	0.0051	14.2	7.7
	Sb–Sb	1.1	3.85	0.0083		
Sb(III)–S–resin (GT74)	Sb–S	3.4	2.45	0.0035	13.5	3.5
	Sb–C(S)	4.1	3.33	0.0100		
	C(O)					
untreated peat (0 mM S(-II))	Sb–O	3.0	2.02	0.0053	9.7	5.4
	Sb–S	0.4	2.36	0.0100		
	Sb–C(O)	2.8	2.90	0.0039		

^aThe amplitude reduction factor was set to 1.0 for all fits. Fits were carried out in *R*-space over an $R + \Delta R$ -range of 1.5–4.0 Å using a k -range of 3.2–12.5. ^bCoordination number (path degeneracy), error $\pm 25\%$. ^cMean half path length, error ± 0.01 Å. ^dDebye–Waller parameter, error ± 0.002 Å². ^eEnergy-shift parameter. ^fNSSR = $\sum_i (\text{data}_i - \text{fit}_i)^2 / \sum_i \text{data}_i$.

to fit an Sb–S path at a distance of 2.45 Å, indicative of thiol-bound Sb.^{50,70} No contribution of oxygen was observed. Moreover, the inclusion of an Sb–C(S) path at a distance of 3.33 Å⁷⁰ improved the model fit significantly. The fitted Sb–S and Sb–C(S) distances in combination with fitted Sb–S and Sb–C(S) coordination numbers of 3.4 and 4.1, respectively, suggest that Sb was 3-fold coordinated to thiol groups offered by the Ambersep resin.

The untreated peat sample could be best fit with an Sb–O path at 2.02 Å and an Sb–C(O) path at 2.90 Å, showing that Sb was directly coordinated to NOM via Sb–O–C functionalities.^{34,71} In contrast to what was expected from the characterization of functional groups in untreated peat with FT–IR spectroscopy, as described before, the fitted Sb–C(O) length of 2.90 Å suggests that Sb was coordinated to phenolic (2.85–2.92 Å)^{34,71} rather than to carboxylic (2.95–2.96 Å)³⁴ groups. Furthermore, the model improved significantly with inclusion of an additional Sb–S path at a distance of 2.36 Å and a small coordination number of 0.4, indicating that a small portion of Sb(III) was also bound via S in the untreated peat. Antimony-binding thiol moieties in the structure of “pure” NOM have also been previously discussed by Buschmann et al.³³

The relative contributions of thiol- and O–C-bound Sb in the Sb(III)–OM series were then calculated with iterative target transformation (ITT) giving an average sum of species of 99 ± 8 atomic% without using any constraints (Table 2). Calculated coordination numbers from the relative contributions (Table 2) showed that the Sb–S coordination clearly increased from CN 0.4 to 1.7 with increasing S content, whereas Sb–O coordination decreased from CN 3.0 to 1.4, suggesting an O to S ligand exchange. Also the Sb–S coordination in the synthesized Sb(III)–GSH complexes with nominal values of 1, 2, and 3 gave overall reasonable values of 1.7, 2.5, and 3.5, considering small deviations during

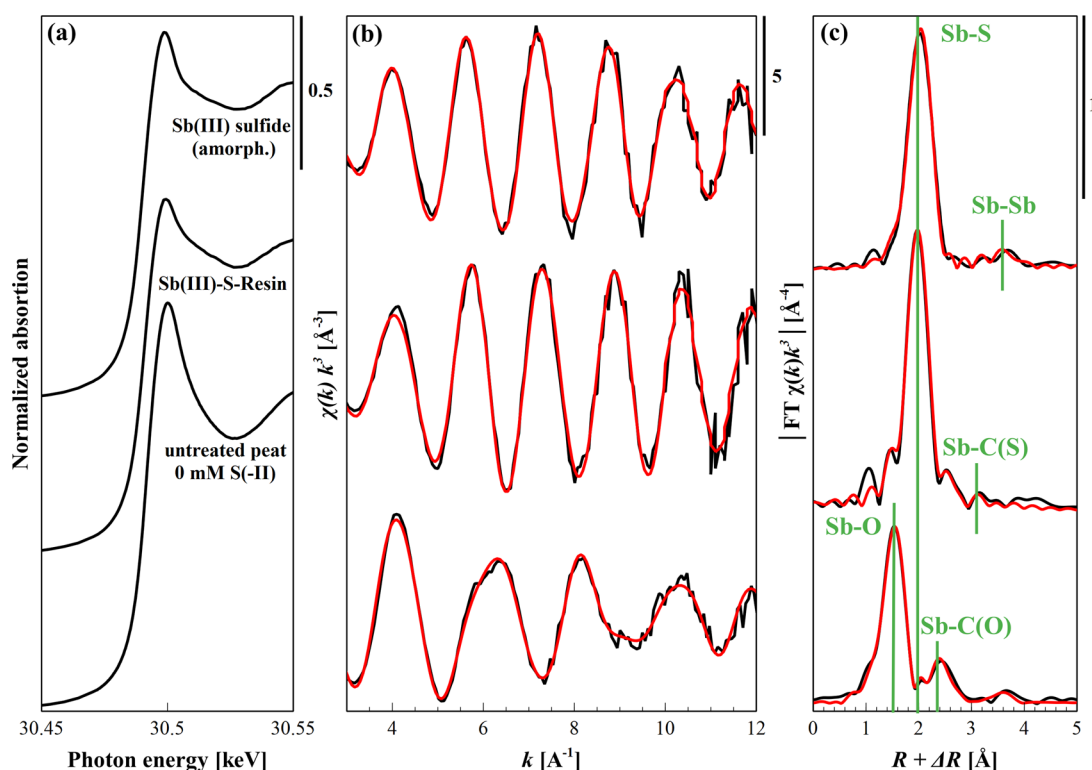


Figure 4. Antimony K -edge XANES-spectra (a), k^3 -weighted EXAFS spectra (b) and Fourier-transform magnitudes of Sb(III) sulfide (amorphous) and the two end-members of the Sb(III) organic matter series: Ambersep resin GT74 (Sb(III)–S–Resin) and untreated peat (0 mM S(-II)), both reacted with 50 μ M antimonite solution (pH 6.0). Black lines represent experimental data and the best fits are shown as red lines. Single scattering paths of Sb–O, Sb–C(O), Sb–S, Sb–C(S), and Sb–Sb are marked with green lines at the respective positions in the FT.

Table 2. ITT Calculation of Relative Species Concentrations and Derived from This, the Coordination Numbers of Sb for the Sb(III) Organic Matter Series.^a

sample name	species 1 (Sb–S–C)	species 2 (Sb–O–C)	sum	Sb–S	Sb–O	sum
	[atomic%]	[atomic%]	[atomic%]	CN	CN	CN
Sb(III)–resin	100	0	100	3.4	0.0	3.4
Sb(III)–(GSH) ₃	100	13	113	3.5	0.4	3.8
Sb(III)–(GSH) ₂	69	37	107	2.5	1.1	3.6
Sb(III)–(GSH) ₁	45	54	99	1.7	1.6	3.4
Sb–S–NOM 30 mM S(-II)	45	48	92	1.7	1.4	3.2
Sb–S–NOM 10 mM S(-II)	31	59	90	1.3	1.8	3.1
Sb–S–NOM 5 mM S(-II)	24	72	96	1.1	2.2	3.3
Sb–S–NOM 1 mM S(-II)	6	91	97	0.6	2.7	3.3
Sb–S–NOM 0 mM S(-II)	0	100	100	0.4	3.0	3.4

^aFor the ITT calculation of relative species concentrations, the concentrations of the two identified end-members were fixed at 100%, whereas the concentrations of the mixtures were calculated without constraints; i.e., they were not normalized to 100%. The general error of ITFA procedure is about 5% of relative concentrations. Coordination numbers were calculated from relative concentrations multiplied by the coordination numbers derived from shell-fitting of Sb(III)–S–Resin and untreated peat (0 mM S(-II)).

synthesis and a summarized general fit error of \sim 30%. Thus, these results provide spectroscopic evidence that increasing content of “reduced S” (most likely thiol-S) in the peat leads to increasing complexation of Sb(III) with peat thiol moieties; they further show the importance of O-bearing (phenol/carboxyl) groups in Sb binding by untreated peat.

Discrimination between Thiol- and Inorganic Disordered Sb–S Phases. The results presented above show a clear relation between thiol-coordination of Sb in peat and increasing S content. However, as recently discussed in the literature,^{18,49,50} it is difficult to discriminate between thiol- and inorganic Sb–S phases solely based on Sb–S bond lengths, because they are very similar. Thiol-bound Sb(III) has

Sb–S bond lengths of 2.45–2.46 Å (Table 1 and Bennett et al.⁵⁰) and our self-synthesized amorphous Sb(III) sulfide showed a fitted Sb–S length of 2.48 Å (Table 1, Figure 4), which is slightly lower than literature values for crystalline Sb₂S₃ (2.51–2.53 Å^{72,73}). Considering a general error of 0.01 Å of EXAFS shell-fitting procedure, a sound statistical discrimination may be questioned. Moreover, a disordered Sb(III)–S phase on mackinawite (FeS) from Kirsch et al.⁵¹ is reported with an Sb–S length of 2.46 Å. There, it was not possible to fit either an Sb–Sb or an Sb–Fe path, indicative of Sb sulfide precipitation or Sb–mackinawite sorption, respectively, to this spectrum. Thus, in order to discriminate between

these phases, we used again ITFA and tried three different approaches.

First, we added individually the EXAFS or XANES spectra of amorphous Sb(III) sulfide or of Sb(III) on FeS to the spectra of the Sb(III)–OM series and calculated the Malinowski indicator values (SI Table SI-4). By adding amorphous Sb(III) sulfide, the minimum indicator value increased from two (determined for the Sb(III)–OM series) to three, suggesting that Sb(III) sulfide is a third component not contained in the original spectral data set. Contrary, the number of statistically significant components remained at two when adding the spectrum of Sb(III) on FeS; however, the difference to three components was very small (SI Table SI-4). This method provides the first indications that Sb(III) sulfide can be discriminated from the Sb(III)–OM series. For Sb(III) on FeS, this method is not sensitive enough and further investigations were needed as described in the following.

Since any spectral differences should be visible by a third component added to the Sb(III)–OM series, we calculated a VARIMAX rotation as a second approach with two PCs including amorphous Sb(III) sulfide and Sb(III) on FeS (Figure 3). VARIMAX rotation thereby optimizes the factor loadings calculated by PCA and thus helps better interpreting the two significant PCs. As already indicated by the minimum indicator values, a clear difference between amorphous Sb(III) sulfide and the end-member of the Sb(III)–OM series Sb(III)–S–Resin was visible (black dotted line). Moreover, a smaller, but also clear difference from the Sb(III)–on–FeS spectra to the Sb(III)–OM series was observed.

A third way of revealing spectral variations was to evaluate the differences between the reproductions derived from two PCs of the Sb(III)–OM series and the two inorganic Sb–S phases. Visual differences can already be seen in Figure 2b–d but tend to be subjective. Therefore, we tried to objectify these differences by calculating the respective normalized sum of squared residues (NSSR) and standard deviations (SD) between experimental and reproduced spectra. SI Figure SI-10 shows that for the NSSR- as well as the SD-values and for both, EXAFS and XANES spectra, the spectra from the Sb(III)–OM series were clearly distinguishable from amorphous Sb(III) sulfide or Sb(III) on FeS. Again, the differences were smaller for Sb(III) on FeS than for amorphous Sb(III) sulfide. Recalculation of the NSSR- and the SD-values using reproductions with three components equalized the differences between amorphous Sb(III) sulfide or Sb(III) on FeS and the Sb(III)–OM series, respectively, implying indeed that a third component was required and thus that Sb(III) sulfide and Sb(III) on FeS are distinguishable from the Sb(III)–OM series.

In sum, these three lines of evidence, together with the fact that we were able to shell-fit an Sb–C(S) path to the samples from the Sb(III)–OM series (Table 1) and an Sb–Sb path to the amorphous Sb(III) sulfide sample (Table 1) show that disordered inorganic Sb–S phases can be discriminated from thiol-bound Sb in our experiments by using ITFA.

Environmental Implications. The biogeochemistry of Sb in the presence of NOM has been discussed previously mostly in terms of complexation with dissolved or colloidal organic ligands differing in molecular weight and structural complexity.^{4,5,7} Additionally, competition for sorption sites of Sb with dissolved NOM at mineral surfaces⁵ and the influence of NOM on the redox dynamics of Sb have been addressed.^{55,74–76} Although these processes are important

aspects of Sb biogeochemistry, understanding the fate of Sb in environments with high levels of solid NOM, such as peatlands or other wetlands, remained unresolved.

Here, we provide the first experimental and spectroscopic evidence illuminating the important role of carboxyl/phenol and thiol functional groups of peat NOM for the sequestration of Sb. In natural or Sb contaminated peatlands and other wetlands, Sb(III) will complex to carboxyl or phenol groups if the thiol content in peat is low and no metal (oxyhydr)oxides are available. After reductive dissolution of metal (oxyhydr)oxides and with higher thiol group content, for example with increasing peat depth, Sb(III) is suggested from our experiments to increasingly bind to thiol functional groups. If free sulfide concentrations are high, for example at hotspots of microbial sulfate reduction, Sb(III) can also precipitate as amorphous Sb(III) sulfides.

While it is known that organic Sb–thiol bonds are generally stronger than organic Sb–O bonds,^{63,66–68} there is a general lack of knowledge about the stability of thiol-bound Sb in comparison to inorganic Sb–S phases under changing hydrological or redox conditions.

Our studies further suggest that antimonite binding to thiol groups of dissolved or colloidal NOM, as shown for As,²³ could be an important aspect of Sb mobilization in the environment. However, given the greater abundance of solid NOM in peatlands and other wetlands compared to the dissolved NOM, similar K_{OC} values for antimonite sorption to peat and humic acids emphasize the key role of solid NOM in Sb sequestration under anoxic conditions. Therefore, our findings generally reveal that high amounts of free sulfide are not necessary to sequester Sb in sub- to anoxic, organic-rich peatlands and wetlands.

■ ASSOCIATED CONTENT

📄 Supporting Information

The Supporting Information is available free of charge on the ACS Publications website at DOI: 10.1021/acs.est.9b00495.

General chemical characterization of the *Federseemoor* model peat, Synthesis and characterization of Sb reference compounds, S solid-phase speciation analysis and results, Results of aqueous Sb speciation with AEC–ICP–MS, Sb solid-phase speciation analysis, and results (PDF)

■ AUTHOR INFORMATION

Corresponding Author

*Phone: +49-921-553999; fax: +49-921-552334; e-mail: b.planer-friedrich@uni-bayreuth.de.

ORCID

Andreas C. Scheinost: 0000-0002-6608-5428

Scott Fendorf: 0000-0002-9177-1809

Britta Planer-Friedrich: 0000-0002-0656-4283

Notes

The authors declare no competing financial interest.

■ ACKNOWLEDGMENTS

This work was funded by the German Research Foundation Grant PL 302/20-1, a PhD student short-time stipend to Stanford University for Johannes Besold (German Academic Exchange Service, DAAD 57314604) as well as a DAAD

mobility grant (DAAD 57315737) to Britta Planer-Friedrich. We thank Christian Mikutta for providing the peat material and Julian Graubner for his help with purifying the peat. Further we acknowledge help from Pablo Ingino, André Rossberg, and Vincent Noël for discussions on XAS data. Antimony and sulfur K-edge XAS experiments were performed at the Stanford Synchrotron Radiation Lightsource (SSRL), a Directorate of SLAC National Accelerator Laboratory and an Office of Science User Facility operated for the U.S. Department of Energy, Office of Science, Office of Basic Energy Sciences under Contract No. DE-AC02-76SF00515. We thank R. Davis for his support in using beamline 4-1 as well as Matthew Latimer and Eric Nelson for help at beamline 4-3.

REFERENCES

- (1) Filella, M.; Belzile, N.; Chen, Y.-W. Antimony in the environment: a review focused on natural waters: I. Occurrence. *Earth-Sci. Rev.* **2002**, *57* (1), 125–176.
- (2) Zhang, D.; Pan, X.; Mu, G.; Wang, J. Toxic effects of antimony on photosystem II of *Synechocystis* sp. as probed by in vivo chlorophyll fluorescence. *J. Appl. Phycol.* **2010**, *22* (4), 479–488.
- (3) Verdugo, M.; Ogra, Y.; Quiroz, W. Mechanisms underlying the toxic effects of antimony species in human embryonic kidney cells (HEK-293) and their comparison with arsenic species. *J. Toxicol. Sci.* **2016**, *41* (6), 783–792.
- (4) Filella, M.; Belzile, N.; Chen, Y.-W. Antimony in the environment: a review focused on natural waters: II. Relevant solution chemistry. *Earth-Sci. Rev.* **2002**, *59* (1), 265–285.
- (5) Hockmann, K.; Schulin, R., Leaching of Antimony from Contaminated Soils. In *Competitive Sorption and Transport of Heavy Metals in Soils*, **2012**, 119.
- (6) Filella, M.; Williams, P. A.; Belzile, N. Antimony in the environment: knowns and unknowns. *Environ. Chem.* **2009**, *6* (2), 95–105.
- (7) Wilson, S. C.; Lockwood, P. V.; Ashley, P. M.; Tighe, M. The chemistry and behaviour of antimony in the soil environment with comparisons to arsenic: A critical review. *Environ. Pollut.* **2010**, *158* (5), 1169–1181.
- (8) Brown, T. J.; Idoine, N. E.; Raycraft, E. R.; Shaw, R. A.; Deady, E. A.; Rippingale, J.; Bide, T.; Wrighton, C. E.; Rodley, J. *World Mineral Production 2008–2012*; British Geological Survey, 2014.
- (9) Brown, T. J.; Idoine, N. E.; Raycraft, E. R.; Shaw, R. A.; Hobbs, S. F.; Everett, P.; Deady, E. A.; Bide, T. *World Mineral Production 2012–2016*; British Geological Survey, 2018.
- (10) Krachler, M.; Emons, H.; Zheng, J. Speciation of antimony for the 21st century: promises and pitfalls. *TrAC, Trends Anal. Chem.* **2001**, *20* (2), 79–90.
- (11) Scheinost, A. C.; Rossberg, A.; Vantelon, D.; Xifra, I.; Kretzschmar, R.; Leuz, A.-K.; Funke, H.; Johnson, C. A. Quantitative antimony speciation in shooting-range soils by EXAFS spectroscopy. *Geochim. Cosmochim. Acta* **2006**, *70* (13), 3299–3312.
- (12) Hiller, E.; Lalinská, B.; Chovan, M.; Jurkovič, L.; Klimko, T.; Jankulár, M.; Hovorič, R.; Šottník, P.; Flaková, R.; Zenišová, Z.; Ondrejková, I. Arsenic and antimony contamination of waters, stream sediments and soils in the vicinity of abandoned antimony mines in the Western Carpathians, Slovakia. *Appl. Geochem.* **2012**, *27* (3), 598–614.
- (13) Okkenhaug, G.; Zhu, Y.-G.; Luo, L.; Lei, M.; Li, X.; Mulder, J. Distribution, speciation and availability of antimony (Sb) in soils and terrestrial plants from an active Sb mining area. *Environ. Pollut.* **2011**, *159* (10), 2427–2434.
- (14) Li, J.; Hou, H.; Hosomi, M. Sorption–desorption of Sb(III) in different soils: Kinetics and effects of the selective removal of hydroxides, organic matter, and humic substances. *Chemosphere* **2018**, *204*, 371–377.
- (15) Filella, M.; Williams, P. A. Antimony interactions with heterogeneous complexants in waters, sediments and soils: A review of binding data for homologous compounds. *Chem. Erde* **2012**, *72*, 49–65.
- (16) Shotyk, W.; Krachler, M.; Chen, B. Antimony in recent, ombrotrophic peat from Switzerland and Scotland: Comparison with natural background values (5,320 to 8,020 14C yr BP) and implications for the global atmospheric Sb cycle. *Global Biogeochem. Cycles* **2004**, *18* (1), 1–13.
- (17) Palmer, K.; Ronkanen, A.-K.; Kløve, B. Efficient removal of arsenic, antimony and nickel from mine wastewaters in Northern treatment peatlands and potential risks in their long-term use. *Ecol. Eng.* **2015**, *75*, 350–364.
- (18) Warnken, J.; Ohlsson, R.; Welsh, D. T.; Teasdale, P. R.; Chelsky, A.; Bennett, W. W. Antimony and arsenic exhibit contrasting spatial distributions in the sediment and vegetation of a contaminated wetland. *Chemosphere* **2017**, *180*, 388–395.
- (19) Okkenhaug, G.; Zhu, Y.-G.; He, J.; Li, X.; Luo, L.; Mulder, J. Antimony (Sb) and Arsenic (As) in Sb Mining Impacted Paddy Soil from Xikuangshan, China: Differences in Mechanisms Controlling Soil Sequestration and Uptake in Rice. *Environ. Sci. Technol.* **2012**, *46* (6), 3155–3162.
- (20) Fawcett, S. E.; Jamieson, H. E.; Nordstrom, D. K.; McCleskey, R. B. Arsenic and antimony geochemistry of mine wastes, associated waters and sediments at the Giant Mine, Yellowknife, Northwest Territories, Canada. *Appl. Geochem.* **2015**, *62*, 3–17.
- (21) Langner, P.; Mikutta, C.; Kretzschmar, R. Arsenic sequestration by organic sulphur in peat. *Nat. Geosci.* **2012**, *5* (1), 66–73.
- (22) Langner, P.; Mikutta, C.; Suess, E.; Marcus, M. A.; Kretzschmar, R. Spatial Distribution and Speciation of Arsenic in Peat Studied with Microfocused X-ray Fluorescence Spectrometry and X-ray Absorption Spectroscopy. *Environ. Sci. Technol.* **2013**, *47* (17), 9706–9714.
- (23) Hoffmann, M.; Mikutta, C.; Kretzschmar, R. Bisulfide Reaction with Natural Organic Matter Enhances Arsenite Sorption: Insights from X-ray Absorption Spectroscopy. *Environ. Sci. Technol.* **2012**, *46* (21), 11788–11797.
- (24) Reddy, K. R.; DeLaune, R. D. Metals/Metalloids. In *Biogeochemistry of Wetlands: Science and Applications*; CRC Press–Taylor & Francis: Boca Raton, FL, 2008.
- (25) Mikutta, C.; Langner, P.; Bargar, J. R.; Kretzschmar, R. Tetra- and Hexavalent Uranium Forms Bidentate-Mononuclear Complexes with Particulate Organic Matter in a Naturally Uranium-Enriched Peatland. *Environ. Sci. Technol.* **2016**, *50* (19), 10465–10475.
- (26) Skyllberg, U.; Xia, K.; Bloom, P. R.; Nater, E. A.; Bleam, W. F. Binding of Mercury(II) to Reduced Sulfur in Soil Organic Matter along Upland-Peat Soil Transects. *J. Environ. Qual.* **2000**, *29* (3), 855–865.
- (27) Gündoğan, R.; Acemioğlu, B.; Alma, M. H. Copper (II) adsorption from aqueous solution by herbaceous peat. *J. Colloid Interface Sci.* **2004**, *269* (2), 303–309.
- (28) González A, Z. I.; Krachler, M.; Cheburkin, A. K.; Shotyk, W. Spatial Distribution of Natural Enrichments of Arsenic, Selenium, and Uranium in a Minerotrophic Peatland, Gola di Lago, Canton Ticino, Switzerland. *Environ. Sci. Technol.* **2006**, *40* (21), 6568–6574.
- (29) Neubauer, E.; von der Kammer, F.; Knorr, K. H.; Peiffer, S.; Reichert, M.; Hofmann, T. Colloid-associated export of arsenic in stream water during stormflow events. *Chem. Geol.* **2013**, *352*, 81–91.
- (30) Jiskra, M.; Wiederhold, J. G.; Skyllberg, U.; Kronberg, R.-M.; Kretzschmar, R. Source tracing of natural organic matter bound mercury in boreal forest runoff with mercury stable isotopes. *Environ. Sci.: Processes Impacts* **2017**, *19* (10), 1235–1248.
- (31) Weng, L.; Fest, E. P. M. J.; Fillius, J.; Temminghoff, E. J. M.; Van Riemsdijk, W. H. Transport of Humic and Fulvic Acids in Relation to Metal Mobility in a Copper-Contaminated Acid Sandy Soil. *Environ. Sci. Technol.* **2002**, *36* (8), 1699–1704.
- (32) Anawar, H. M.; Tareq, S. M.; Ahmed, G. Is organic matter a source or redox driver or both for arsenic release in groundwater? *Phys. Chem. Earth* **2013**, *58–60*, 49–56.

- (33) Buschmann, J.; Sigg, L. Antimony(III) Binding to Humic Substances: Influence of pH and Type of Humic Acid. *Environ. Sci. Technol.* **2004**, *38* (17), 4535–4541.
- (34) Tella, M.; Pokrovski, G. S. Antimony(III) complexing with O-bearing organic ligands in aqueous solution: An X-ray absorption fine structure spectroscopy and solubility study. *Geochim. Cosmochim. Acta* **2009**, *73* (2), 268–290.
- (35) Pilarski, J.; Waller, P.; Pickering, W. Sorption of antimony species by humic acid. *Water, Air, Soil Pollut.* **1995**, *84* (1), 51–59.
- (36) Schwertmann, U. Solubility and dissolution of iron oxides. *Plant Soil* **1991**, *130* (1), 1–25.
- (37) Petrunic, B. M.; MacQuarrie, K. T. B.; Al, T. A. Reductive dissolution of Mn oxides in river-recharged aquifers: a laboratory column study. *J. Hydrol.* **2005**, *301* (1), 163–181.
- (38) Wieder, R. K.; Yavitt, J. B.; Lang, G. E. Methane production and sulfate reduction in two Appalachian peatlands. *Biogeochemistry* **1990**, *10* (2), 81–104.
- (39) Rittle, K. A.; Drever, J. I.; Colberg, P. J. S. Precipitation of arsenic during bacterial sulfate reduction. *Geomicrobiol. J.* **1995**, *13* (1), 1–11.
- (40) Spratt, H. G.; Morgan, M. D. Sulfur cycling in a cedar-dominated, freshwater wetland. *Limnol. Oceanogr.* **1990**, *35* (7), 1586–1593.
- (41) Steinmann, P.; Shoty, W. Ion chromatography of organic-rich natural waters from peatlands IV. Dissolved free sulfide and acid-volatile sulfur. *J. Chromatogr. A* **1995**, *706* (1), 287–292.
- (42) Shoty, W. Review of the inorganic geochemistry of peats and peatland waters. *Earth-Sci. Rev.* **1988**, *25* (2), 95–176.
- (43) Besold, J.; Biswas, A.; Suess, E.; Scheinost, A. C.; Rossberg, A.; Mikutta, C.; Kretzschmar, R.; Gustafsson, J. P.; Planer-Friedrich, B. Monothioarsenate transformation kinetics determines arsenic sequestration by sulfhydryl groups of peat. *Environ. Sci. Technol.* **2018**, *52* (13), 7317–7326.
- (44) Yu, Z.-G.; Göttlicher, J.; Steininger, R.; Knorr, K.-H. Organic sulfur and organic matter redox processes contribute to electron flow in anoxic incubations of peat. *Environ. Chem.* **2016**, *13* (5), 816–825.
- (45) Werne, J. P.; Hollander, D. J.; Lyons, T. W.; Sinninghe Damsté, J. S. Organic sulfur biogeochemistry: Recent advances and future research directions. *Special Paper Geological Society of America* **2004**, *379*, (135).135
- (46) Cloy, J. M.; Farmer, J. G.; Graham, M. C.; MacKenzie, A. B. Retention of As and Sb in Ombrotrophic Peat Bogs: Records of As, Sb, and Pb Deposition at Four Scottish Sites. *Environ. Sci. Technol.* **2009**, *43* (6), 1756–1762.
- (47) Cloy, J. M.; Farmer, J. G.; Graham, M. C.; MacKenzie, A. B.; Cook, G. T. A comparison of antimony and lead profiles over the past 2500 years in Flanders Moss ombrotrophic peat bog, Scotland. *J. Environ. Monit.* **2005**, *7* (12), 1137–1147.
- (48) Rothwell, J. J.; Taylor, K. G.; Chenery, S. R. N.; Cundy, A. B.; Evans, M. G.; Allott, T. E. H. Storage and Behavior of As, Sb, Pb, and Cu in Ombrotrophic Peat Bogs under Contrasting Water Table Conditions. *Environ. Sci. Technol.* **2010**, *44* (22), 8497–8502.
- (49) Arsic, M.; Teasdale, P. R.; Welsh, D. T.; Johnston, S. G.; Burton, E. D.; Hockmann, K.; Bennett, W. W. Diffusive Gradients in Thin Films Reveals Differences in Antimony and Arsenic Mobility in a Contaminated Wetland Sediment during an Oxidation-Anoxic Transition. *Environ. Sci. Technol.* **2018**, *52* (3), 1118–1127.
- (50) Bennett, W. W.; Hockmann, K.; Johnston, S. G.; Burton, E. D. Synchrotron X-ray absorption spectroscopy reveals antimony sequestration by reduced sulfur in a freshwater wetland sediment. *Environ. Chem.* **2017**, *14* (6), 345–349.
- (51) Kirsch, R.; Scheinost, A. C.; Rossberg, A.; Banerjee, D.; Charlet, L. Reduction of antimony by nano-particulate magnetite and mackinawite. *Mineral. Mag.* **2008**, *72* (1), 185–189.
- (52) Fröhlich, D. R.; Kremleva, A.; Rossberg, A.; Skerencak-Frech, A.; Koke, C.; Krüger, S.; Rösch, N.; Panak, P. J. Combined EXAFS spectroscopic and quantum chemical study on the complex formation of Am(III) with formate. *Inorg. Chem.* **2017**, *56*, 6820–6829.
- (53) Hoffmann, M.; Mikutta, C.; Kretzschmar, R. Arsenite Binding to Natural Organic Matter: Spectroscopic Evidence for Ligand Exchange and Ternary Complex Formation. *Environ. Sci. Technol.* **2013**, *47* (21), 12165–12173.
- (54) Hockmann, K.; Lenz, M.; Tandy, S.; Nachtegaal, M.; Janousch, M.; Schulin, R. Release of antimony from contaminated soil induced by redox changes. *J. Hazard. Mater.* **2014**, *275*, 215–221.
- (55) Wu, T.-l.; Qin, W.-x.; Alves, M. E.; Fang, G.-d.; Sun, Q.; Cui, P.-x.; Liu, C.; Zhou, D.-m.; Wang, Y.-j. Mechanisms of Sb(III) oxidation mediated by low molecular weight phenolic acids. *Chem. Eng. J.* **2019**, *356*, 190–198.
- (56) Hoffmann, M.; Mikutta, C.; Kretzschmar, R. Arsenite Binding to Sulfhydryl Groups in the Absence and Presence of Ferrihydrite: A Model Study. *Environ. Sci. Technol.* **2014**, *48* (7), 3822–3831.
- (57) Sun, H.; Yan, S. C.; Cheng, W. S. Interaction of antimony tartrate with the tripeptide glutathione. *Eur. J. Biochem.* **2000**, *267* (17), 5450–5457.
- (58) Raab, A.; Meharg, A. A.; Jaspars, M.; Genney, D. R.; Feldmann, J. Arsenic-glutathione complexes-their stability in solution and during separation by different HPLC modes. *J. Anal. At. Spectrom.* **2004**, *19* (1), 183–190.
- (59) Ravel, B.; Newville, M. ATHENA, ARTEMIS, HEPHAESTUS: data analysis for X-ray absorption spectroscopy using IFEFFIT. *J. Synchrotron Radiat.* **2005**, *12* (4), 537–541.
- (60) Roßberg, A.; Reich, T.; Bernhard, G. Complexation of uranium(VI) with protocathechuic acid—application of iterative transformation factor analysis to EXAFS spectroscopy. *Anal. Bioanal. Chem.* **2003**, *376* (5), 631–638.
- (61) Manceau, A.; Nagy, K. L. Quantitative analysis of sulfur functional groups in natural organic matter by XANES spectroscopy. *Geochim. Cosmochim. Acta* **2012**, *99* (Supplement C), 206–223.
- (62) Prietzel, J.; Botzaki, A.; Tyufekchieva, N.; Brettholle, M.; Thieme, J.; Klysubun, W. Sulfur Speciation in Soil by S K-Edge XANES Spectroscopy: Comparison of Spectral Deconvolution and Linear Combination Fitting. *Environ. Sci. Technol.* **2011**, *45* (7), 2878–2886.
- (63) Sun, H.; Yan, S. C.; Cheng, W. S. Interaction of antimony tartrate with the tripeptide glutathione. *Eur. J. Biochem.* **2000**, *267* (17), 5450–5457.
- (64) Yan, S.; Ding, K.; Zhang, L.; Sun, H. Complexation of Antimony(III) by Trypanothione. *Angew. Chem., Int. Ed.* **2000**, *39* (23), 4260–4262.
- (65) Martell, A.; Smith, R. M. *Critical Stability Constants - Vol. 3: Other Organic Ligands*; Springer: New York, 1977; Vol. 3.
- (66) Yan, S.; Li, F.; Ding, K.; Sun, H. Reduction of pentavalent antimony by trypanothione and formation of a binary and ternary complex of antimony(III) and trypanothione. *J. Biol. Inorg. Chem.* **2003**, *8* (6), 689–697.
- (67) Anderegg, G.; Malik, S. Die Komplexbildungstendenz des dreiwertigen Antimons in wässriger Lösung. *Helv. Chim. Acta* **1970**, *53* (3), 577–600.
- (68) Anderegg, G.; Malik, S. Komplexe XLIII. Die Komplexe des dreiwertigen Antimons mit Polyaminocarboxylaten. *Helv. Chim. Acta* **1970**, *53* (3), 564–569.
- (69) Gondar, D.; Lopez, R.; Fiol, S.; Antelo, J. M.; Arce, F. Characterization and acid–base properties of fulvic and humic acids isolated from two horizons of an ombrotrophic peat bog. *Geoderma* **2005**, *126* (3), 367–374.
- (70) Peters, M.; Saak, W.; Pohl, S. Neutrale Thiolate und ein Iodidthiolat von Antimon(III). Die Kristallstrukturen von Sb(SC₆H₅)₃, Sb(SC₆H₂Me₃-2,4,6)₃ und SbI(SC₆H₂Me₃-2,4,6)₂. *Z. Anorg. Allg. Chem.* **1996**, *622* (12), 2119–2123.
- (71) Horley, G. A.; Mahon, M. F.; Molloy, K. C.; Venter, M. M.; Haycock, P. W.; Myers, C. P. Structures of Sb(OC₆H₃Me₂-2,6)₃ and Sb(OEt)₅NH₃: The First Authenticated Monomeric Sb(OR)_n (n = 3, 5). *Inorg. Chem.* **2002**, *41* (6), 1652–1657.
- (72) Hofmann, W. Die Struktur der Minerale der Antimonitgruppe. *Z. Kristallogr. - Cryst. Mater.* **1933**, *86* (1–6), 225–245.

(73) Kyono, A.; Kimata, M. Structural variations induced by difference of the inert pair effect in the stibnite-bismuthinite solid solution series $(\text{Sb,Bi})_2\text{S}_3$. *Am. Mineral.* **2004**, *89* (7), 932–940.

(74) Nguyen, V. K.; Lee, J.-U. Isolation and Characterization of Antimony-Reducing Bacteria from Sediments Collected in the Vicinity of an Antimony Factory. *Geomicrobiol. J.* **2014**, *31* (10), 855–861.

(75) Buschmann, J.; Canonica, S.; Sigg, L. Photoinduced Oxidation of Antimony(III) in the Presence of Humic Acid. *Environ. Sci. Technol.* **2005**, *39* (14), 5335–5341.

(76) Borch, T.; Kretzschmar, R.; Kappler, A.; Cappellen, P. V.; Ginder-Vogel, M.; Voegelin, A.; Campbell, K. Biogeochemical Redox Processes and their Impact on Contaminant Dynamics. *Environ. Sci. Technol.* **2010**, *44* (1), 15–23.

Supporting Information to

“Antimonite complexation with thiol and carboxyl/phenol groups of peat organic matter”

*Johannes Besold¹, Naresh Kumar^{2,3}, Andreas C. Scheinost⁴, Juan Lezama Pacheco⁵, Scott Fendorf⁵ and Britta Planer-Friedrich*¹*

¹ Department of Environmental Geochemistry, Bayreuth Center for Ecology and Environmental Research (BAYCEER), Bayreuth University, 95440 Bayreuth, Germany

² Department of Geological Sciences, School of Earth, Energy, and Environmental Sciences, Stanford University, Stanford, CA 94305, USA.

³ Dept. of Environmental Geosciences, University of Vienna, 1090 Vienna, Austria

⁴ The Rossendorf Beamline (ROBL) at ESRF, 38043 Grenoble, France and Helmholtz-Zentrum Dresden-Rossendorf (HZDR), Institute of Resource Ecology, Bautzner Landstraße 400, 01328 Dresden, Germany

⁵ Department of Earth System Science, School of Earth, Energy, and Environmental Sciences, Stanford University, Stanford, CA 94305, USA

(20 pages, 4 tables, 10 figures)

Table of contents

1	General chemical characterization of the <i>Federseemoor</i> model peat.....	2
2	Synthesis and characterization of antimony reference compounds.....	7
3	Sulfur solid-phase speciation analyses and results.....	9
4	Antimony sorption to untreated anoxic and sulfide-reacted peat.....	15
5	Antimony solid-phase speciation analyses and results.....	16

* Corresponding author's email: b.planer-friedrich@uni-bayreuth.de

Phone: +49-921-553999; Fax: +49-921-552334

1 General chemical characterization of the *Federseemoor* model peat

Elemental composition of peat

Method:

After microwave digestion (MARS Xpress, CEM) using a 5:3 ratio of 30% H₂O₂ and 65% HNO₃, the elemental composition of the untreated peat was analyzed by inductively coupled plasma mass-spectrometry (ICP-MS, XSeries2, Thermo-Fisher).¹ Carbon, S, and N contents of the peat were determined with a Thermo Quest, Flash EA 1112 analyzer. Information in Table SI-1 has already been presented in Besold *et al.*² and is only illustrated here for further information.

Table SI-1: Elemental composition of the Federseemoor model peat

[wt.-%]	Mean ^a	SD
C	55.0	0.03
N	2.18	0.02
S	0.22	0.006
Ash content	2.51	0.03
Water content	85.1	0.04
Molar C/N	29.0	0.28
[mg kg ⁻¹]	Mean ^a	SD
Fe	829	14.9
Mg	22.9	4.49
Al	1749	208
P	602	31.2
K	116	28.5
Cr	5.06	0.30
Mn	2.23	0.30
Co	0.39	0.03
Ni	3.39	0.16
Cu	6.08	1.96
Zn	13.7	0.71
Se	0.41	0.05
As	1.53	0.03
Mo	0.31	0.03
Cd	<LOQ	
Sb	0.43	0.13
Pb	12.5	0.30

^an=6

Characterization of the peat with ^{13}C CP/MAS-NMR

Method:

The ^{13}C CP/MAS-NMR spectrum of the peat was recorded on an Avance III HD spectrometer (Bruker) at a B0 field 9.4 T. $^{13}\text{C}\{^1\text{H}\}$ (100.6 MHz). MAS spectra were obtained using a ramped cross-polarization (CP) experiment, where the nutation frequency ν_{nut} on the proton channel was varied linearly by 50%. The samples were spun at 12.5 kHz in a 4 mm MAS double resonance probe (Bruker). The corresponding ν_{nut} on the ^{13}C channel and the contact time were adjusted to 70 kHz and 3 ms, respectively. During acquisition proton broadband decoupling was applied using a spinal-64 sequence with $\nu_{\text{nut}} = 70$ kHz. ^{13}C spectra are referenced indirectly with respect to tetramethylsilane (TMS) using adamantane as secondary reference. For data analysis, the spectrum was divided into chemical shift regions assigned to the chemical group classes after Gondar *et al.*³: alkyl C (0–45 ppm), O-alkyl C (45–110 ppm), aromatic C (110–160 ppm), phenolic C (140–160 ppm), carboxyl C (160–185 ppm), and carbonyl C (185–220 ppm). The relative intensity of these regions was determined by means of integration. Figure SI-1 has already been presented in Besold *et al.*² but assignment of chemical shift regions has changed from Hoffmann *et al.*⁴ to Gondar *et al.*³ due to clearer differentiation of chemical group classes.

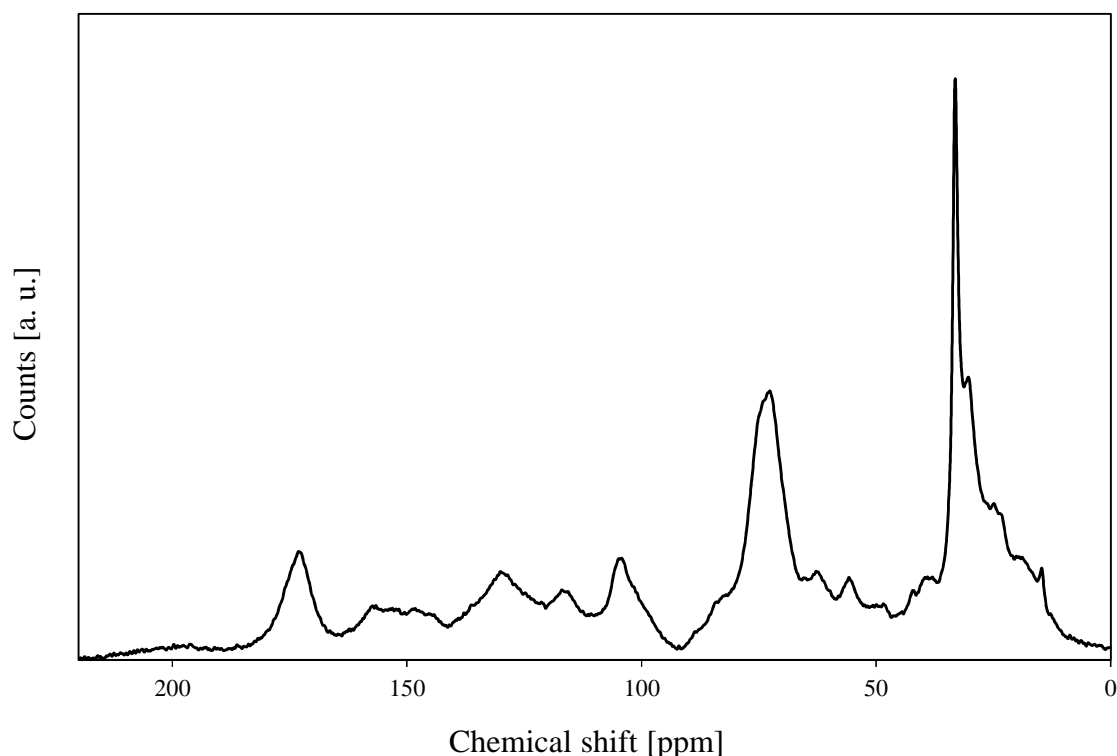


Figure SI-1: ^{13}C CP/MAS-NMR spectrum of the *Federseemoor* peat. The integrated peak intensities are summarized in Table SI-2.

Table SI-2: ^{13}C CP/MAS-NMR estimates of the C distribution in *Federseemoor* peat in [%].^a

	Alkyl C	O-alkyl	Aromatic C	Phenolic C	Carboxyl C	Carbonyl C
	0–45 ppm	45–110 ppm	110–160 ppm	140–160 ppm	160–185 ppm	185–220 ppm
Peat sample	33	37	19	6	8	2

^aChemical shift classification after Gondar *et al.*³

Characterization of the peat with FT-IR spectroscopy

Method:

FT-IR analysis was performed with a Bruker Vector 22 spectrometer. For the analysis, 2 mg freeze-dried untreated peat were mixed with 200 mg KBr and pressed into pellets prior to analysis. Up to 32 spectra were recorded in transmission mode, co-added and background-corrected by subtracting the spectrum of pure KBr. Absorption band assignments are based on Artz *et al.*⁵, Rennert *et al.*⁶, Pretsch *et al.*⁷ and Gondar *et al.*³

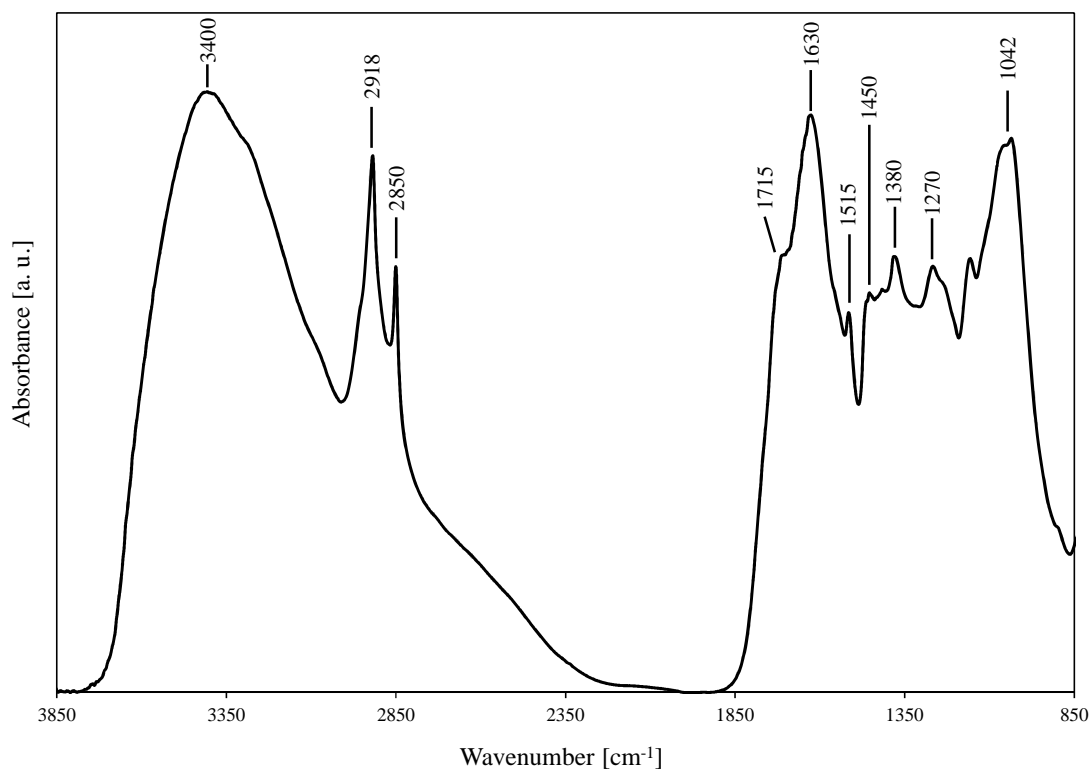


Figure SI-2: FT-IR spectrum of the untreated *Federseemoor* peat incubated for 96 h at pH 6.0.

The broad intense band at about 3400-3300 cm⁻¹ with a maximum ~3340 cm⁻¹ results from stretching vibrations of hydroxyl (OH) groups which are indicative for cellulose and/or the N-H stretching of secondary amines. The bands at ~2918 and ~2850 cm⁻¹ can be assigned to antisymmetric and symmetric stretching of aliphatic C-H bonds of fats, wax or lipids. Stretching vibrations at ~1715 cm⁻¹ belong to the C=O group of protonated carboxylic acids (COOH) or other carbonyl groups like aromatic esters or aryl ketones. The intense band at 1630 cm⁻¹ in combination with that at 1515 cm⁻¹ is an indicator of skeletal vibrations of aromatics (lignin backbone structures). Rennert *et al.*⁶ interprets the peak at 1630 cm⁻¹ simply as residual H₂O but since the sample was freeze dried and kept sealed until analysis, this interpretation can most likely be excluded. The absorption bands at 1450 and 1380 cm⁻¹ can be assigned to C-H deformations of phenolic (lignin) and aliphatic structures. Further, peaks at 1630 and 1380 cm⁻¹ represent also deprotonated carboxyl moieties (COO⁻). Alcoholic functionalities are verified by the broad bands around 1270 cm⁻¹ (phenolic groups) and 1042 cm⁻¹ (aliphatic OH groups).

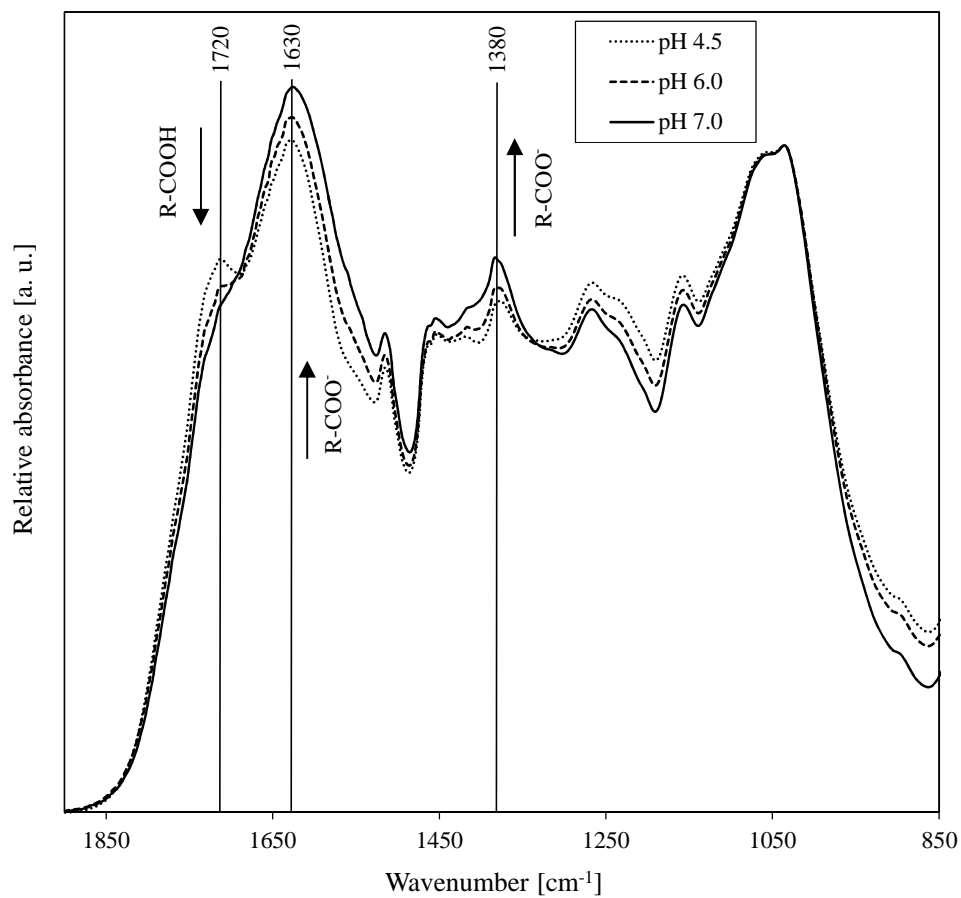


Figure SI-3: FT-IR spectra of the untreated *Federseemoor* peat incubated for 96 h at pH 4.5, 6.0 and 7.0 in 30 mM NaCl and 0.15 mM NaN₃. Spectra were normalized to 1 at 1042 cm⁻¹.

2 Synthesis and characterization of antimony reference compounds

Sb(III)-GSH reference standards

Sb(III)-GSH complexes with nominal Sb(III)-(GSH)₁, Sb(III)-(GSH)₂, Sb(III)-(GSH)₃ stoichiometry were synthesized according to the following procedure slightly modified from Sun *et al.*⁸ and Raab *et al.*⁹ A molar ratio of Sb(III) (Potassium antimonyl tartrate sesquihydrate, Acros Organics, ACS Reagent Grade) and GSH (L-glutathione, VWR, 98%) of 1:1, 1:2 and 1:3 was achieved by dissolving the chemicals within 6 mL of anoxic water in a glovebag (pO₂ < 1 ppm, Coy). The mixtures were stirred for 12 h at room temperature in the glovebag and then the formed Sb(III)-GSH complexes were precipitated with 25 mL of ethanol. The resulting precipitates were filtered using glass frits and a vacuum pump and dried within the glovebag in a desiccator over hygroscopic silica gel for several days. The Sb(III)-GSH standards were carefully ground with mortar and pestle and stored in the glovebag until XAS analyses.

Amorphous Sb(III) sulfide

Equal volumes (250 mL) of 8 mM anoxic antimonite and 16 mM anoxic sulfide solution were mixed by gentle shaking in a 1 L wide-neck bottle (PET, Nalgene) within an anoxic glovebag until orange-colored Sb sulfide was precipitated. The antimonite solution was prepared by dissolving Sb₂O₃ (Alfa) in 2 M anoxic HCl solution. The sulfide solution was prepared by dissolving Na₂S (Sigma-Aldrich) in anoxic DDI water. The precipitate was filtered with a “Büchner-Filter” (12 µm cellulose nitrate) by use of a vacuum unit and subsequently washed several times with DDI water. Afterwards the precipitate was dried within the glovebag in a desiccator over hygroscopic silica gel for several days. After grinding with mortar and pestle, the fine grained Sb sulfide was stored in the glovebag until powder XRD and XAS analyses.

XRD identification of amorphous Sb(III) sulfide

Method

X-ray diffraction analysis was performed using a Rigaku® Miniflix600 X-ray diffractometer equipped with Cu-K_α radiation source running at 40 KV voltage and 15 mA current and fitted with HyPix-400 MF 2D hybrid pixel array detector. Samples were placed on a zero-background silicon plate within an air tight sample holder under N₂ environment to keep the redox integrity before analysis for 2θ range of 5° to 80°. PDXL software (Rigaku), with International Center for Diffraction Data (ICDD) and PDF-2 database was used for phase identifications.

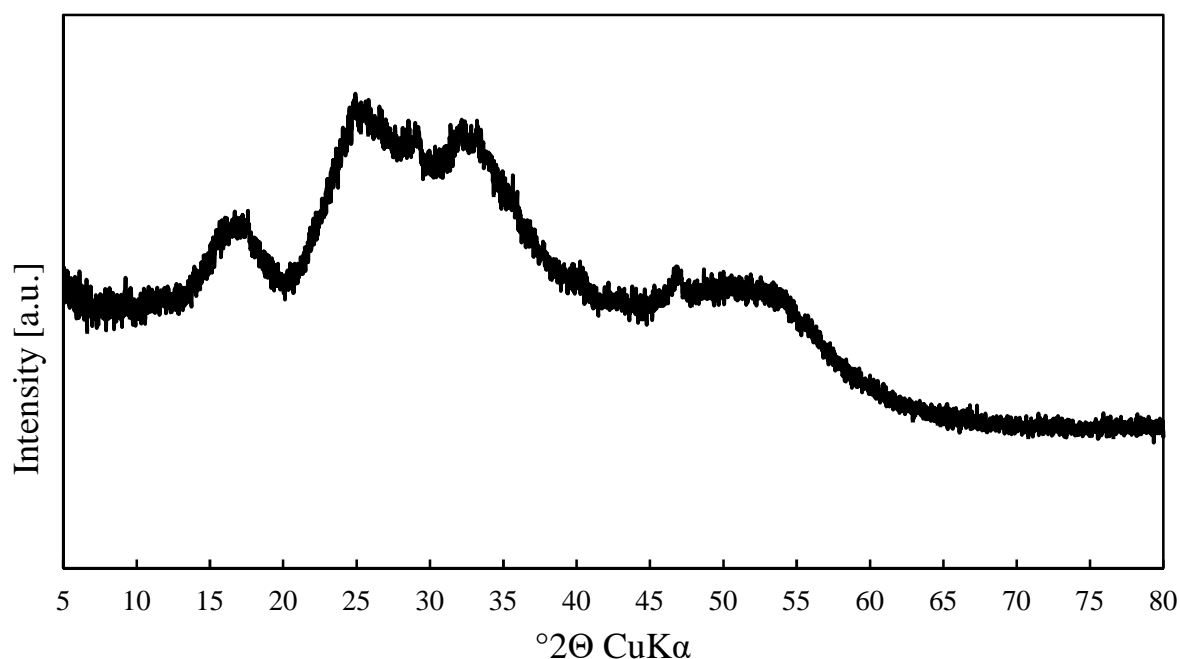


Figure SI-4: XRD pattern of the amorphous Sb(III) sulfide.

Sb(III)-Resin (Ambersep GT74)

For the Sb(III)-Resin standard, 120 mg (dry weight) pre-washed resin (Ambersep GT74) were equilibrated with 100 mL of 50 μ M antimonite solution (pH 6.0, 10 mM MES buffer) for 96 h. The antimonite solution was prepared by dissolving Sb_2O_3 (Alfa) in 2 M anoxic HCl solution and titrating the solution with NaOH until pH 6.0. After equilibration, the resin was filtered with a “Büchner-Filter” (12 μ m cellulose nitrate) by use of a vacuum unit and subsequently washed several times with DDI water. Then the resin was filled into cryo-tubes and shock-frozen within liquid nitrogen before freeze-drying. The resin standard was ground with mortar and pestle and stored in the glovebag until XAS analyses (overall same procedure as for Sb(III)-S-NOM samples).

3 Sulfur solid-phase speciation analyses and results

For S *K*-edge XANES analysis, homogenized peat samples were filled into multi-slot sample holders and sealed with Kapton tape. If necessary, the S concentration was adjusted to $\leq 2,000 \text{ mg kg}^{-1}$ with boron nitride in order to reduce self-absorption effects.¹⁰ Spectra were collected at beamline 4-3 at the Stanford Synchrotron Radiation Lightsource (SSRL), Stanford, USA. The Si(111) double crystal monochromator was calibrated relative to the white-line energy of a sodium thiosulfate standard (2,472.02 eV) which was constantly monitored between two sample runs. All measurements were performed at room temperature under constant He stream ($<0.1\%$ (v/v) O₂) in fluorescence mode using a 4-element solid-state Si drift detector (HTA Hitachi). Up to four scans per sample were recorded, averaged and normalized to the absorption at 2,490 eV using the software Athena.¹¹ Normalized S *K*-edge XANES spectra were deconvoluted in Athena following the fitting approach recommended by Manceau and Nagy.¹² Deconvolution of the spectra was performed in the energy range 2,465-2,490 eV using two arctan functions (edge steps of reduced and oxidized S species) and seven Gaussian functions representing S *s* → *p* transition peaks of inorganic sulfide, exocyclic/elemental S, heterocyclic S, sulfoxide S, sulfone S, sulfonate S, and sulfate S. The positions (energy of center), and step heights of the arctan functions were fitted, whereby their widths were fixed to 0.45 in all model fits. Likewise, the positions and areas of all Gaussians were fit, while keeping the sigma values (standard deviation of Gaussian) fixed in all model fits to values determined beforehand. Following the approach of Manceau and Nagy¹², the position of the arctan (reduced species) was constrained to be located close to the Gaussian functions of the reduced sulfur functionalities (before the center of the sulfoxide Gaussian function) in order to obtain correct sulfur fractions. The fitted peak areas were corrected for the oxidation state dependent absorption cross-section of S using the generic equation of Manceau and Nagy.¹² The atomic fraction of each S species in the peat samples was then calculated by dividing its corrected peak area by the total peak area sum. Please note that the intermediate oxidized fractions (sulfoxide and sulfone S) are likely to be overestimated due to post-edge absorption features of reduced S species.¹² Figure SI-5 illustrates the Gaussian fit envelopes and experimental spectra, Table SI-3 summarizes the detailed fit results and Figure SI-6 gives a visual overview of the corrected atomic fractions.

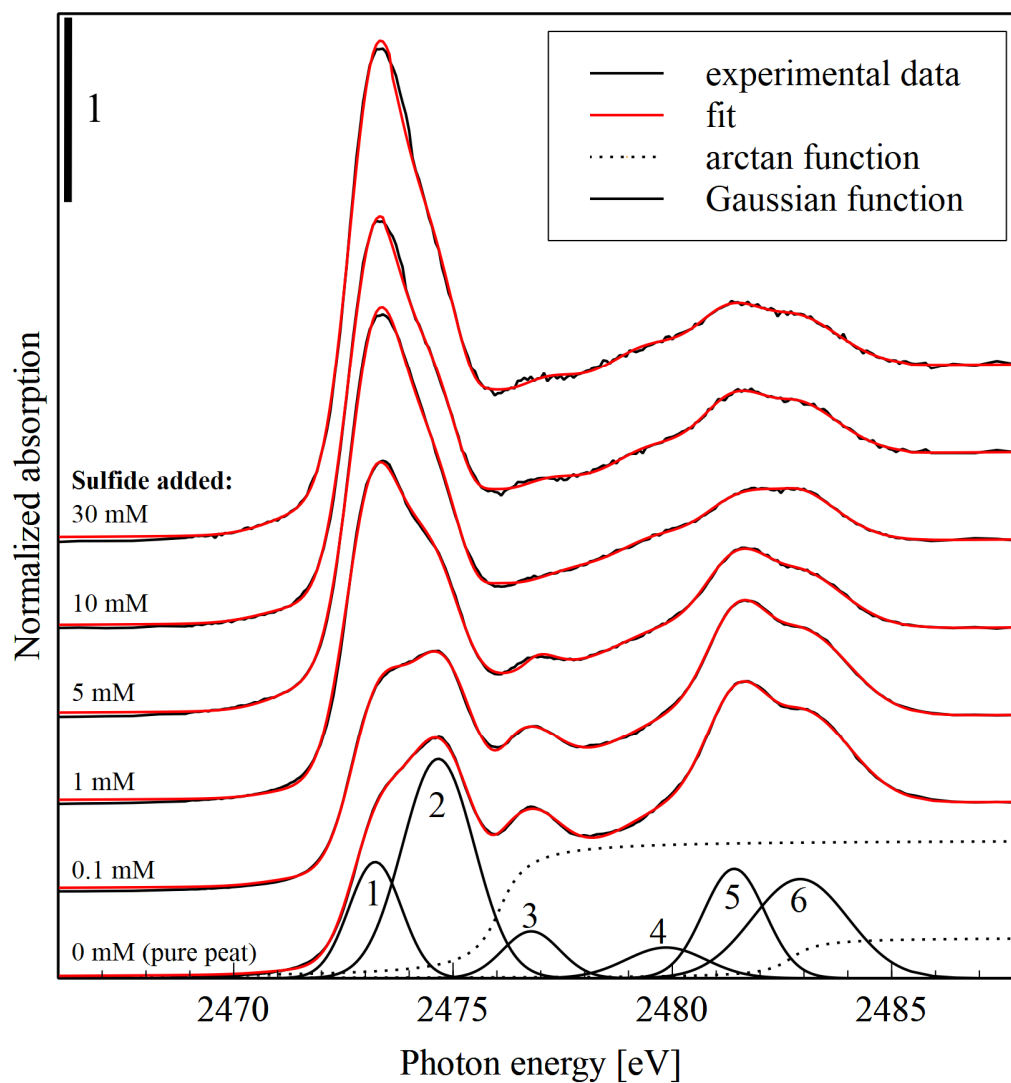


Figure SI-5: Gaussian curve fits of model peat spectra. Experimental data are shown as black and fit envelopes as red lines. The spectral decomposition is illustrated as an example for the untreated peat (0 mM sulfide) sample. The two arctan functions are shown as dotted lines and the Gaussian peaks correspond to (from 1 to 6) exocyclic/elemental S (1), heterocyclic S (2), sulfoxide S (3), sulfone S (4), sulfonate S (5), and sulfate S (6). The fit parameters for all samples are reported in Table SI-3. Gaussian function assigned to questionable inorganic sulfide was excluded.

Table SI-3: Gaussian deconvolution of normalized S *K*-edge XANES spectra of the model peat.

Sample	Fitted functions	Energy ^a	Width (arctan)	Step (arctan) or area (Gaussian)	Corrected area ^b	Fraction	NSSR ^c
		(center) [eV]	or sigma (Gaussian)				
0 mM sulfide (untreated peat)	Arctan (reduced S species)	2476.07	<i>0.45</i>	0.79	-	-	7.6
	Arctan (oxidized S species)	2482.72	<i>0.45</i>	0.23	-	-	
	<i>Inorganic sulfide?</i> Exocyclic/ elemental S	2471.76	<i>0.90</i>	0.05	0.08	2.4	
	Heterocyclic S	2473.18	<i>0.60</i>	0.99	0.84	25.8	
	Sulfoxide S	2474.67	<i>0.82</i>	2.55	1.48	45.3	
	Sulfoxide S	2476.78	<i>0.65</i>	0.43	0.17	5.3	
	Sulfone S	2479.86	<i>0.91</i>	0.40	0.11	3.3	
	Sulfonate S	2481.41	<i>0.70</i>	1.09	0.26	7.9	
	Sulfate S	2482.92	<i>1.09</i>	1.54	0.32	9.9	
0.1 mM sulfide	Arctan (reduced S species)	2476.16	<i>0.45</i>	0.82	-	-	7.2
	Arctan (oxidized S species)	2482.67	<i>0.45</i>	0.20	-	-	
	<i>Inorganic sulfide?</i> Exocyclic/ elemental S	2471.78	<i>0.90</i>	0.10	0.15	4.5	
	Heterocyclic S	2473.23	<i>0.60</i>	1.29	1.08	31.1	
	Sulfoxide S	2474.69	<i>0.82</i>	2.52	1.46	42.0	
	Sulfoxide S	2476.69	<i>0.65</i>	0.37	0.15	4.3	
	Sulfone S	2479.89	<i>0.91</i>	0.36	0.10	2.8	
	Sulfonate S	2481.43	<i>0.70</i>	1.01	0.24	6.9	
	Sulfate S	2482.92	<i>1.09</i>	1.39	0.10	8.4	
1 mM sulfide	Arctan (reduced S species)	2475.72	<i>0.45</i>	0.88	-	-	13.6
	Arctan (oxidized S species)	2482.77	<i>0.45</i>	0.13	-	-	
	<i>Inorganic sulfide?</i> Exocyclic/ elemental S	2471.76	<i>0.90</i>	0.12	0.19	4.2	
	Heterocyclic S	2473.11	<i>0.60</i>	2.19	1.90	42.4	
	Sulfoxide S	2474.45	<i>0.82</i>	2.74	1.67	37.2	
	Sulfoxide S	2476.32	<i>0.65</i>	0.66	0.283	6.3	
	Sulfone S	2479.77	<i>0.91</i>	0.29	0.08	1.8	
	Sulfonate S	2481.39	<i>0.70</i>	0.63	0.15	3.4	
	Sulfate S	2482.73	<i>1.09</i>	1.00	0.21	4.7	

^aEnergy of the white-line maximum. Parameters with identical numbers (in italic) were correlated during fitting. ^bArea after correction for the oxidation state-dependent absorption cross-section of S with the “generic equation” of Manceau and Nagy.¹²

^cNormalized sum of squared residuals ($10^5 \times \sum_i (\text{data}_i - \text{fit}_i)^2 / \sum_i \text{data}_i^2$).

Table SI-3: Continued.

Sample	Fitted functions	Energy ^a	Width (arctan) or sigma	Step (arctan) or area (Gaussian)	Corrected area ^b	Fraction	NSSR ^c
		(center) [eV]	(Gaussian)				
5 mM sulfide	Arctan (reduced S species)	2475.77	<i>0.45</i>	0.85	-	-	11.8
	Arctan (oxidized S species)	2482.70	<i>0.45</i>	0.17	-	-	
	<i>Inorganic sulfide?</i> Exocyclic/ elemental S	2471.86	<i>0.90</i>	0.28	0.41	8.7	
	Heterocyclic S	2473.17	<i>0.60</i>	2.58	2.20	46.3	
	Sulfoxide S	2474.39	<i>0.82</i>	2.78	1.71	36.1	
	Sulfone S	2477.70	<i>0.65</i>	0.05	0.02	0.4	
	Sulfonate S	2479.66	<i>0.91</i>	0.41	0.12	2.4	
	Sulfate S	2481.27	<i>0.70</i>	0.29	0.07	1.5	
		2482.50	<i>1.09</i>	1.00	0.22	4.6	
10 mM sulfide	Arctan (reduced S species)	2475.77	<i>0.45</i>	0.85	-	-	11.2
	Arctan (oxidized S species)	2482.70	<i>0.45</i>	0.16	-	-	
	<i>Inorganic sulfide?</i> Exocyclic/ elemental S	2471.56	<i>0.90</i>	0.19	0.32	6.6	
	Heterocyclic S	2473.15	<i>0.60</i>	2.72	2.34	48.1	
	Sulfoxide S	2474.44	<i>0.82</i>	2.81	1.71	35.2	
	Sulfone S	2477.21	<i>0.65</i>	0.11	0.04	0.9	
	Sulfonate S	2479.65	<i>0.91</i>	0.45	0.13	2.6	
	Sulfate S	2481.36	<i>0.70</i>	0.50	0.12	2.5	
		2482.68	<i>1.09</i>	0.94	0.20	4.1	
30 mM sulfide	Arctan (reduced S species)	2475.77	<i>0.45</i>	0.92	-	-	16.0
	Arctan (oxidized S species)	2482.70	<i>0.45</i>	0.10	-	-	
	<i>Inorganic sulfide?</i> Exocyclic/ elemental S	2471.76	<i>0.90</i>	0.28	0.42	7.5	
	Heterocyclic S	2473.17	<i>0.60</i>	3.22	2.75	48.3	
	Sulfoxide S	2474.41	<i>0.82</i>	3.30	2.03	35.6	
	Sulfone S	2477.18	<i>0.65</i>	0.14	0.05	0.9	
	Sulfonate S	2479.56	<i>0.91</i>	0.49	0.14	2.4	
	Sulfate S	2481.28	<i>0.70</i>	0.47	0.11	2.0	
		2482.71	<i>1.09</i>	0.87	0.19	3.3	

^aEnergy of the white-line maximum. Parameters with identical numbers (in italic) were correlated during fitting. ^bArea after correction for the oxidation state-dependent absorption cross-section of S with the “generic equation” of Manceau and Nagy.¹² ^cNormalized sum of squared residuals ($10^5 \times \sum_i (\text{data}_i - \text{fit}_i)^2 / \sum_i \text{data}_i^2$).

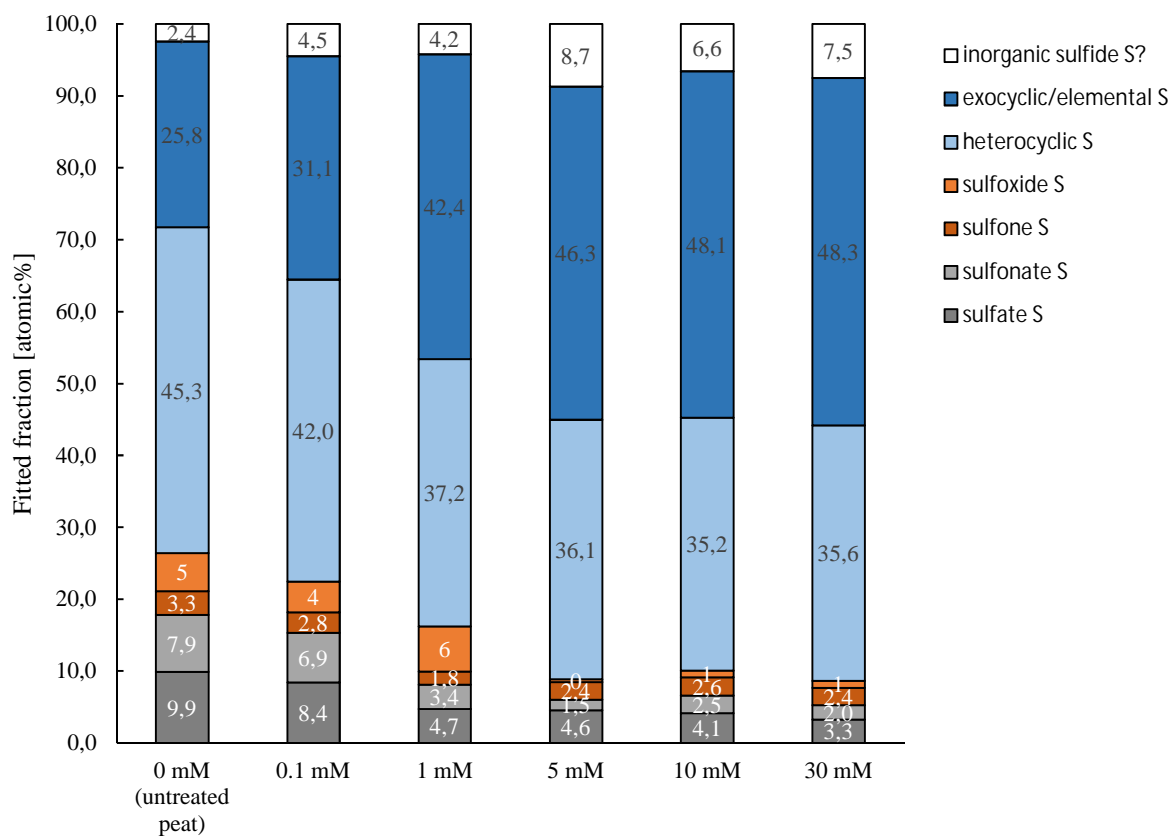


Figure SI-6: Corrected atomic fractions of Gaussian deconvolution of normalized S *K*-edge XANES spectra of model peat samples. Please note that the intermediate oxidized fractions (sulfoxide and sulfone S) are likely to be overestimated due to post-edge absorption features of reduced S species.¹² Fractions assigned to questionable inorganic sulfide are shown as white bars.

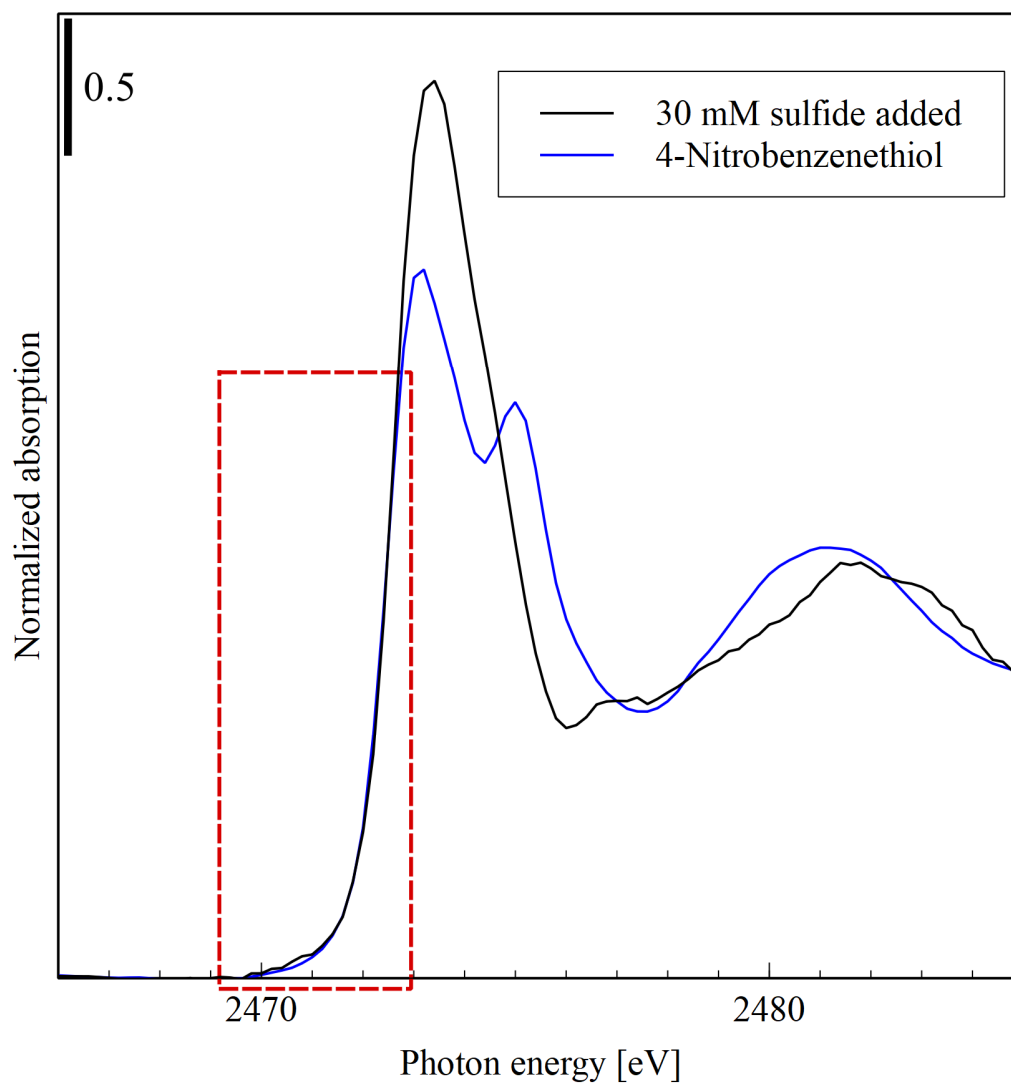


Figure SI-7: Similar rising edge of peat sample equilibrated with 30 mM sulfide (pH 6.0) and the solely organic thiol “4-Nitrobenzenethiol” (spectrum from Manceau and Nagy¹²) demonstrates that it is not necessary to include inorganic sulfides at energies of 2,471.7-2,471.9 eV. Other spectral features do not have to be similar, since peat sample is a mixture of many functional S groups.

4 Antimony sorption to untreated anoxic and sulfide-reacted peat

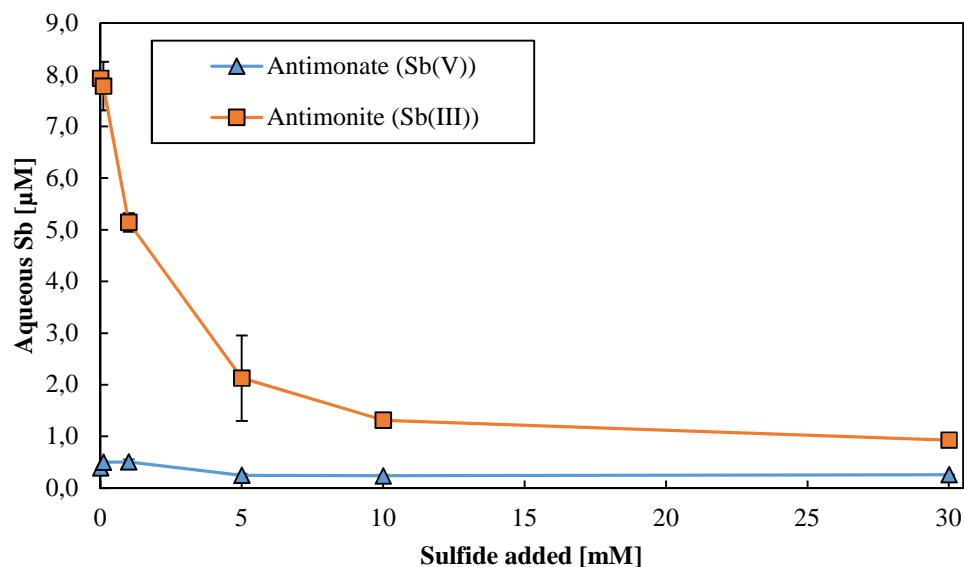


Figure SI-8: Aqueous antimony speciation of Sb(III)-S-NOM experiment after 96 h of incubation. Aqueous Sb species recovery ((Sum Sb species/ Sb totals) \times 100%): \bar{x} = 83% (39–112%). Error bars represent standard deviations of triplicates. Straight lines serve to guide the eye.

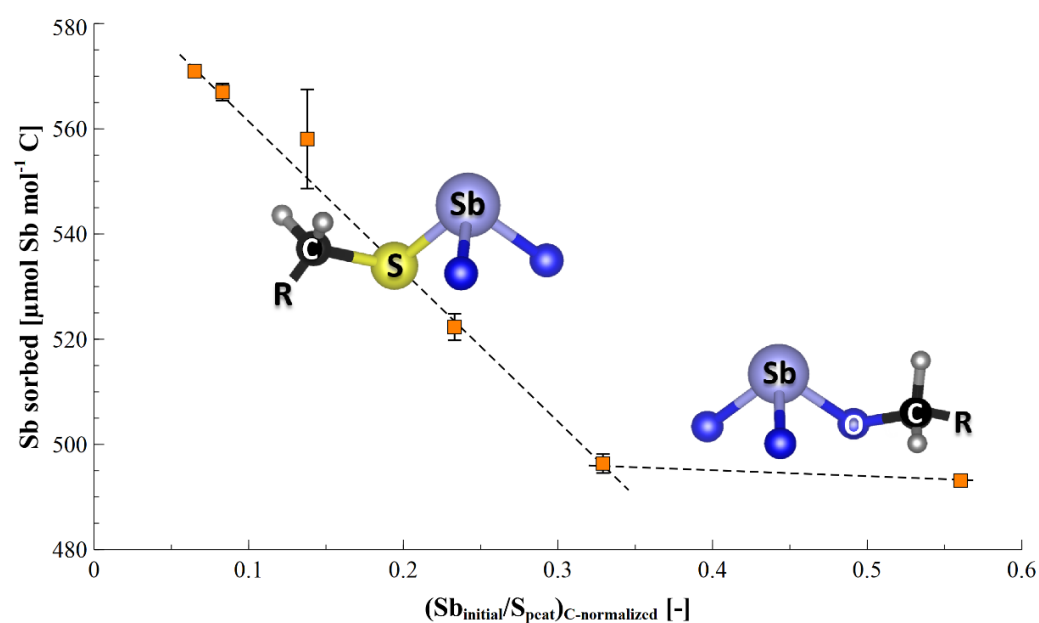


Figure SI-9: Sorption of Sb as a function of the C-normalized $Sb_{initial}/S_{peat}$ ratio. Initial ($t=0$) Sb concentration for experiments was 50 μM . S_{peat} : S content of peat after equilibration with 0–30 mM sulfide.

5 Antimony solid-phase speciation analyses and results

For Sb *K*-edge XAS analyses, homogenized anoxic samples were filled into aluminum sample holders, sealed with Kapton tape and analyzed at beamline 4-1 (SSRL). The beamline was equipped with a Si(220) double crystal monochromator, which was calibrated to the *K*-edge of an Sb foil (energy: 30,491 eV). The absorption edge of the Sb foil was monitored during all sample scans. To reduce higher-order harmonics, we detuned the monochromator to 80% of the maximum beam intensity. All sample measurements were performed in fluorescence mode using a 32-element Ge array fluorescence detector (Canberra) and a He cryostat at 7 K to minimize beam damage and thermal disorder. Spectra of Sb reference compounds were analyzed in fluorescence mode or were taken from Scheinost *et al.*¹³ Between 3 and 8 scans were collected per sample. Normalized XAS spectra were extracted from the raw data using the software codes SixPack¹⁴ and Athena. For spectra normalization, the pre-edge region was consistently fitted with a linear function and the post-edge region with a quadratic polynomial function. The edge positions of XANES were determined from the 2 points-smoothed maximum of the first derivative spectra. The background was removed using the Autobk algorithm incorporated in Athena. A Hanning window with a sill width of 1 Å⁻¹ was used for Fourier transformation. Shell-fit analysis of *k*³-weighted EXAFS spectra were performed in R-space employing the software Artemis. Theoretical scattering paths were calculated with FEFF6 based on the crystal structures of a modified kermesite model (Sb₂S₂O)¹⁵ and Sb(OC₆H₃Me_{2-2,6})₃.¹⁶ Principal component analysis (PCA) and iterative transformation factor analysis (ITFA) of normalized XANES and EXAFS spectra were performed with the ITFA software package.¹⁷ Evaluation of the quality of reconstructions calculated with principal components from PCA was done with the NSSR-value ($100 \times \sum_i (\text{data}_i - \text{reconstruction}_i)^2 / \sum_i \text{data}_i^2$) and the normalized standard deviations between data and reconstructions ($\text{SD} = (1/n) \times \sum (\text{data}_i - \text{reconstruction}_i)^2$; n = number of data points within spectrum).

Table SI-4: Malinowski indicator values.^a

Nr. of PC	EXAFS				XANES			
	Sb(III)-OM series	+ Sb(III) sulfide	+ Sb(III) on FeS	+ Sb(III) sulfide + Sb (III) on FeS.	Sb(III)-OM series	+ Sb(III) sulfide	+ Sb(III) on FeS	+ Sb(III) sulfide + Sb (III) on FeS
1	1.60E-02	1.30E-02	1.29E-02	1.06E-02	2.14E-04	1.86E-04	1.88E-04	1.59E-04
2	8.32E-03	8.21E-03	7.68E-03	7.04E-03	1.05E-04	1.04E-04	9.86E-05	8.71E-05
3	8.88E-03	6.72E-03	<i>7.91E-03</i>	6.69E-03	4.62E-05	3.75E-05	5.93E-05	5.50E-05
4	1.10E-02	7.94E-03	8.76E-03	<i>6.70E-03</i>	4.88E-05	3.53E-05	4.48E-05	3.55E-05
5	1.56E-02	1.03E-02	1.09E-02	7.90E-03	6.61E-05	4.60E-05	4.61E-05	3.38E-05
6	2.52E-02	1.53E-02	1.55E-02	1.02E-02	9.41E-05	6.36E-05	5.99E-05	4.30E-05
7	5.03E-02	2.48E-02	2.50E-02	1.51E-02	1.94E-04	9.07E-05	9.10E-05	5.77E-05
8	1.86E-01	5.03E-02	5.01E-02	2.45E-02	6.34E-04	1.93E-04	1.83E-04	8.71E-05
9		1.86E-01	1.86E-01	5.00E-02		6.31E-04	6.34E-04	1.81E-04
10				7.82E-02				6.57E-06

^aIndicator values of solely the Sb(III) organic matter (OM) series ordered after increasing number of principal components (PCs) are shown in column one for EXAFS and XANES, respectively. Column two and three show indicator values of the Sb(III)-OM series incl. amorphous Sb(III) sulfide or Sb(III) on FeS for EXAFS and XANES, respectively. Column four gives indicator values, where amorphous Sb(III) sulfide and Sb(III) on FeS were added to the Sb(III)-OM series simultaneously for EXAFS and XANES, respectively. Numbers in bold show minimum indicator values for the respective column. Numbers in blue and italic illustrate that these numbers are very close to the ones in bold in the respective column.

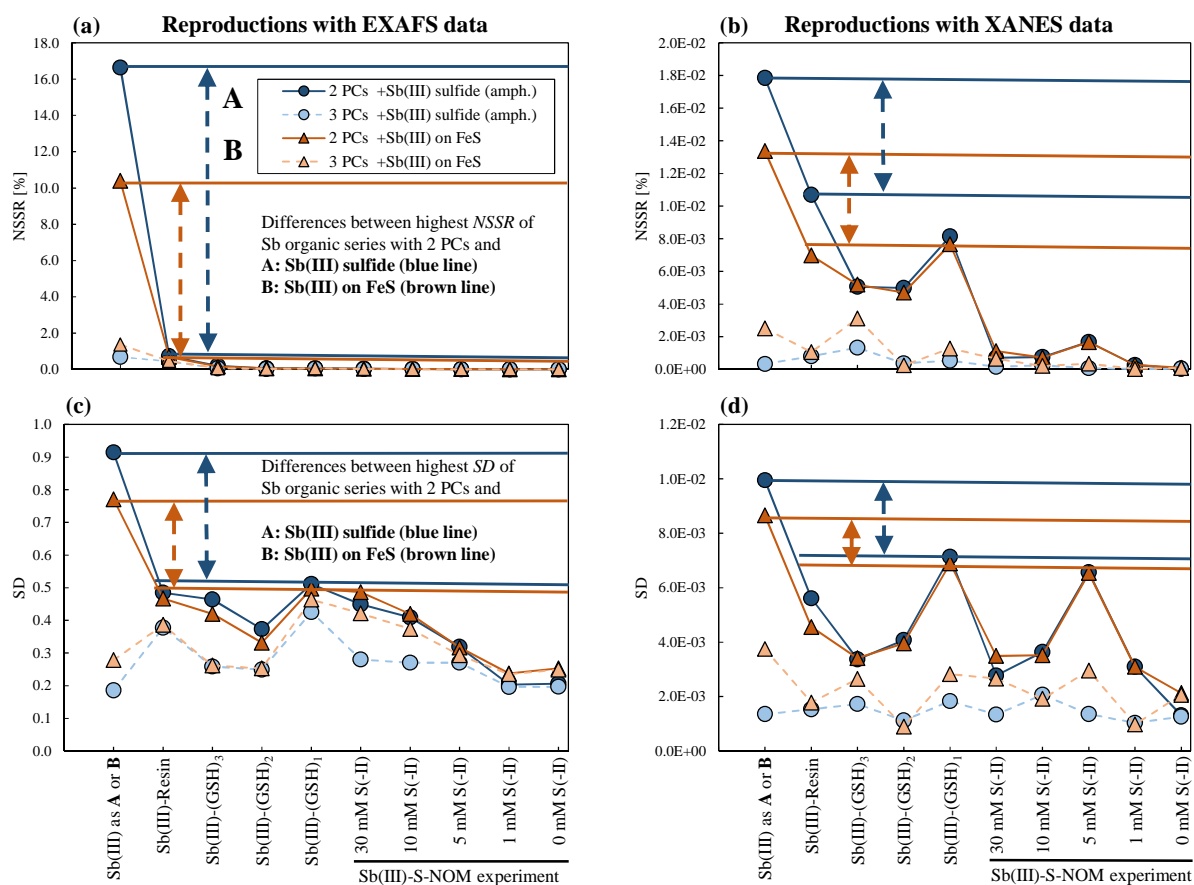


Figure SI-10: Deviations of reproductions of Sb(III) organic matter (OM) series incl. (A) amorphous Sb(III) sulfide or (B) Sb(III) on FeS for EXAFS data (a, c) and XANES data (b, d) expressed as NSSR-values (a, b) or normalized standard deviations (SD) (c, d). Dark colors show deviations of reproductions of respective series with two principal components (PCs) as suggested for the Sb(III)-OM series from the Malinowski indicator values. Light colors show deviations of reproductions with three PCs. Differences between highest deviation of reproductions with two PCs from a member of the Sb(III)-OM series and amorphous Sb(III) sulfide (blue lines) or Sb(III) on FeS (brown lines) are marked with blue or brown arrows, respectively.

References

1. Planer-Friedrich, B.; London, J.; McCleskey, R. B.; Nordstrom, D. K.; Wallschläger, D., Thioarsenates in Geothermal Waters of Yellowstone National Park: Determination, Preservation, and Geochemical Importance. *Environ. Sci. Technol.* **2007**, *41*, (15), 5245-5251.
2. Besold, J.; Biswas, A.; Suess, E.; Scheinost, A. C.; Rossberg, A.; Mikutta, C.; Kretzschmar, R.; Gustafsson, J. P.; Planer-Friedrich, B., Monothioarsenate Transformation Kinetics Determining Arsenic Sequestration by Sulfhydryl Groups of Peat. *Environ. Sci. Technol.* **2018**, *52*, (13), 7317-7326.
3. Gondar, D.; Lopez, R.; Fiol, S.; Antelo, J. M.; Arce, F., Characterization and acid–base properties of fulvic and humic acids isolated from two horizons of an ombrotrophic peat bog. *Geoderma* **2005**, *126*, (3), 367-374.
4. Hoffmann, M.; Mikutta, C.; Kretzschmar, R., Bisulfide Reaction with Natural Organic Matter Enhances Arsenite Sorption: Insights from X-ray Absorption Spectroscopy. *Environ. Sci. Technol.* **2012**, *46*, (21), 11788-11797.
5. Artz, R. R. E.; Chapman, S. J.; Jean Robertson, A. H.; Potts, J. M.; Laggoun-Défarge, F.; Gogo, S.; Comont, L.; Disnar, J.-R.; Francez, A.-J., FTIR spectroscopy can be used as a screening tool for organic matter quality in regenerating cutover peatlands. *Soil Biol. Biochem.* **2008**, *40*, (2), 515-527.
6. Rennert, T.; Eusterhues, K.; Pfanz, H.; Totsche, K. U., Influence of geogenic CO₂ on mineral and organic soil constituents on a mofette site in the NW Czech Republic. *Eur. J. Soil Sci.* **2011**, *62*, (4), 572-580.
7. Pretsch, E.; Bühlmann, P.; Badertscher, M., *Structure Determination of Organic Compounds: Tables of Spectral Data*. Springer-Verlag: Berlin, 2009.
8. Sun, H.; Yan, S. C.; Cheng, W. S., Interaction of antimony tartrate with the tripeptide glutathione. *Eur. J. Biochem.* **2003**, *267*, (17), 5450-5457.
9. Raab, A.; Meharg, A. A.; Jaspars, M.; Genney, D. R.; Feldmann, J., Arsenic-glutathione complexes—their stability in solution and during separation by different HPLC modes. *J. Anal. At. Spectrom.* **2004**, *19*, (1), 183-190.
10. Prietzel, J.; Botzaki, A.; Tyufekchieva, N.; Brettholle, M.; Thieme, J.; Klysubun, W., Sulfur Speciation in Soil by S K-Edge XANES Spectroscopy: Comparison of Spectral Deconvolution and Linear Combination Fitting. *Environ. Sci. Technol.* **2011**, *45*, (7), 2878-2886.
11. Ravel, B.; Newville, M., ATHENA, ARTEMIS, HEPHAESTUS: data analysis for X-ray absorption spectroscopy using IFEFFIT. *J. Synchrotron Radiat.* **2005**, *12*, (4), 537-541.
12. Manceau, A.; Nagy, K. L., Quantitative analysis of sulfur functional groups in natural organic matter by XANES spectroscopy. *Geochim. Cosmochim. Acta* **2012**, *99*, (Supplement C), 206-223.
13. Scheinost, A. C.; Rossberg, A.; Vantelon, D.; Xifra, I.; Kretzschmar, R.; Leuz, A.-K.; Funke, H.; Johnson, C. A., Quantitative antimony speciation in shooting-range soils by EXAFS spectroscopy. *Geochim. Cosmochim. Acta* **2006**, *70*, (13), 3299-3312.
14. Webb, S. M., SIXpack: a graphical user interface for XAS analysis using IFEFFIT. *Phys. Scr.* **2005**, *2005*, (T115), 1011.

15. Hybler, J.; Durovic, S., Kermesite, Sb₂S₂O: crystal structure revision and order-disorder interpretation. *Acta Crystallogr. Sect. B-Struct. Sci.* **2013**, *69*, 570-583.
16. Horley, G. A.; Mahon, M. F.; Molloy, K. C.; Venter, M. M.; Haycock, P. W.; Myers, C. P., Structures of Sb(OC₆H₃Me_{2-2,6})₃ and Sb(OEt)₅·NH₃: The First Authenticated Monomeric Sb(OR)_n (n = 3, 5). *Inorg. Chem.* **2002**, *41*, (6), 1652-1657.
17. Roßberg, A.; Reich, T.; Bernhard, G., Complexation of uranium(VI) with protocatechuic acid—application of iterative transformation factor analysis to EXAFS spectroscopy. *Anal. Bioanal.Chem.* **2003**, *376*, (5), 631-638.

Study 6: Antimonite Binding to Natural Organic Matter: Spectroscopic Evidence from a Mine Water Impacted Peatland

Johannes Besold, Anne Eberle, Vincent Noël, Katharina Kujala, Naresh Kumar, Andreas C. Scheinost

Juan Lezama Pacheco, Scott Fendorf and Britta Planer-Friedrich

Reprinted with permission from

Environmental Science & Technology

Copyright 2020 American Chemical Society

Antimonite Binding to Natural Organic Matter: Spectroscopic Evidence from a Mine Water Impacted Peatland

Johannes Besold,[†] Anne Eberle,[†] Vincent Noël,^{‡,§} Katharina Kujala,[§] Naresh Kumar,^{||,⊥} Andreas C. Scheinost,[#] Juan Lezama Pacheco,[∇] Scott Fendorf,[∇] and Britta Planer-Friedrich^{*,†,⊥}

[†]Department of Environmental Geochemistry, Bayreuth Center for Ecology and Environmental Research (BAYCEER), Bayreuth University, 95440 Bayreuth, Germany

[‡]Stanford Synchrotron Radiation Lightsource, SLAC National Accelerator Laboratory, Menlo Park, California 94025, United States

[§]Water Resources and Environmental Engineering Research Unit, University of Oulu, FI-90014, Oulu, Finland

^{||}Department of Geological Sciences, School of Earth, Energy, and Environmental Sciences, Stanford University, Stanford, California 94305, United States

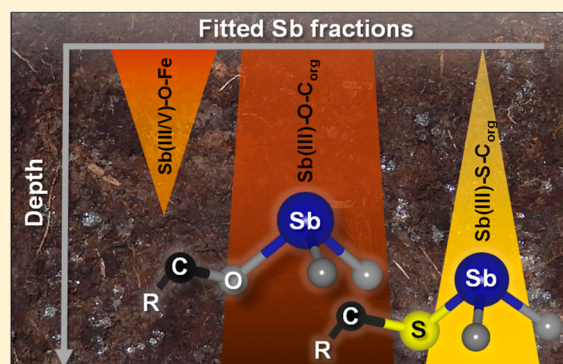
[⊥]Department of Environmental Geosciences, Centre for Microbiology and Environmental Systems Science, University of Vienna, 1090 Vienna, Austria

[#]The Rossendorf Beamline (ROBL) at ESRF, 38043 Grenoble, France and Helmholtz-Zentrum Dresden-Rossendorf (HZDR), Institute of Resource Ecology, Bautzner Landstraße 400, 01328 Dresden, Germany

[∇]Department of Earth System Science, School of Earth, Energy, and Environmental Sciences, Stanford University, Stanford, California 94305, United States

Supporting Information

ABSTRACT: Peatlands and other wetlands are sinks for antimony (Sb), and solid natural organic matter (NOM) may play an important role in controlling Sb binding. However, direct evidence of Sb sequestration in natural peat samples is lacking. Here, we analyzed solid phase Sb, iron (Fe), and sulfur (S) as well as aqueous Sb speciation in three profiles up to a depth of 80 cm in a mine water impacted peatland in northern Finland. Linear combination fittings of extended X-ray absorption fine structure spectra showed that Sb binding to Fe phases was of minor importance and observed only in the uppermost layers of the peatland. Instead, the dominant (to almost exclusive) sequestration mechanism was Sb(III) binding to oxygen-containing functional groups, and at greater depths, increasingly Sb(III) binding to thiol groups of NOM. Aqueous Sb speciation was dominated by antimonate, while antimonite concentrations were low, further supporting our findings of much higher reactivity of Sb(III) than Sb(V) toward peat surfaces. Insufficient residence time for efficient reduction of antimonate to antimonite currently hinders higher Sb removal in the studied peatland. Overall, our findings imply that Sb(III) binding to solid NOM acts as an important sequestration mechanism under reducing conditions in peatlands and other high-organic matter environments.



INTRODUCTION

Wetlands span more than 6% of the global ice-free land area¹ and among those, peatlands, with ~3% land cover, are the dominant group.² Peatlands have important ecological functions including long-term carbon storage, niche for threatened animal and plant species or regulation of the water budget.² In addition, they are also increasingly recognized as sinks for potentially toxic trace metal(loid)s^{3–7} and therefore are an important factor controlling surface water and groundwater quality.

Antimony (Sb) is a potentially toxic trace element, which has received increasing attention only during the last decades due to increased mining activities^{8,9} as well as increased

industrial use^{10–12} and proposed toxicity similar to arsenic (As).^{13,14} Moreover, Sb is a redox-active trace metalloid that prevails at environmentally relevant pH values as pentavalent aqueous antimonate ($\text{Sb}(\text{OH})_6^-$) under mostly oxic and as trivalent aqueous antimonite ($\text{Sb}(\text{OH})_3$) under mostly anoxic conditions.¹⁵ At high dissolved sulfide concentrations and neutral to alkaline pH, also thiolated Sb can form.^{16–18}

Received: July 2, 2019

Revised: August 20, 2019

Accepted: August 22, 2019

Published: August 22, 2019

The natural Sb background concentrations in soils and sediments ($<10 \text{ mg kg}^{-1}$)^{12,19} as well as in surface and pore waters ($<1 \text{ } \mu\text{g L}^{-1}$)¹² are generally low. However, anthropogenically impacted environments like shooting-range soils or mining impacted soils can reach Sb concentrations up to several thousand mg kg^{-1} , thereby jeopardizing water resources if they partition into the aqueous phase.^{20,21} Further, accumulation of Sb in peatlands or other wetlands rich in solid natural organic matter (NOM) has been reported in recent years.^{19,22–29} Antimony usually enters the peatlands or other wetlands either through atmospheric deposition related to smelter activities^{22–25} or through mining (typically of Sb or gold) where (pretreated) mining water contacts wetland soils.^{19,27,28}

In wetlands, Sb retention has been focused on two mechanisms. In shallow, oxic layers, Sb is typically oxidized to Sb(V) and can be retained, on iron (Fe) (III) and/or manganese (Mn) (III/IV) (oxyhydr)oxide surfaces.^{20,30} With increasing depth and associated increasing water content (and eventually saturation), limited oxygen (O) supply leads to anaerobic conditions that result in Fe and Mn (oxyhydr)oxide reductive dissolution^{31,32} and can be accompanied by a release of associated Sb.³³ Reduction (often microbially mediated),^{34,35} of Sb(V) to Sb(III) can then facilitate reaction with (biogenic) dissolved sulfide to form authigenic amorphous Sb-sulfur (S) precipitates at low to neutral pH values. Hence, the formation of sulfide precipitates has been considered as primary Sb retention mechanism in anoxic zones of wetlands.^{19,28,34,36}

As a potential third mechanism of Sb retention, we recently demonstrated with purified model peat NOM and by use of X-ray absorption spectroscopy (XAS) that Sb(III) can form inner-sphere complexes with O-bearing groups of peat NOM.³⁷ Further, increased thiol content in the peat NOM lead to increased Sb(III) complexation via thiol bonds, demonstrating the higher affinity of Sb(III) toward S-bearing organic moieties compared to O-bearing groups. These results suggest that retention of Sb in anoxic layers of peatlands may also be facilitated by direct complexation of Sb(III) with solid peat NOM, and high dissolved sulfide concentrations for Sb(III) sulfide precipitation are not necessarily required.

Indeed, measured dissolved sulfide concentrations in peatlands are commonly low^{38–41} since sulfide produced from, e.g., (microbially mediated) reduction of sulfate can be effectively incorporated into NOM as organic thiols.^{38,42} Thiol groups therefore often are the dominant S species in such systems.⁴³ Although a few studies have already observed a strong association of Sb with solid NOM,^{22–26,28} direct (e.g., spectroscopic) evidence for Sb binding to NOM from field samples is still lacking.

In order to study the fate of anthropogenic Sb in peatlands, we determined the speciation of Sb along with Fe and S, elements which often govern Sb biogeochemistry, in three different profiles of a mine water impacted treatment peatland located in Finnish Lapland (Figure SI-1 of the Supporting Information, SI).

The peatland ($\sim 17 \text{ ha}$) has been used for purification of pretreated drainage water from open pits and underground gold mining since 2006. Inflow to the peatland contains high levels of sulfate, nitrogen, phosphorus, and various metals and metalloids including nickel, As, and Sb. Previous water analyses showed that Sb inflow concentrations were higher than the

outflow concentrations, indicating that the peatland sequesters Sb.¹⁹

We hypothesize that solid NOM plays a crucial role in the fate of Sb in peatlands. Hence, the objective of our study was to identify the dominant Sb solid-phase binding mechanisms in natural peat impacted by Sb containing mine water. We examined three peat profiles distributed over the peatland and analyzed selected peat samples by means of bulk Sb, Fe, and S X-ray absorption spectroscopy. Additionally, we used aqueous Sb speciation complemented with thermodynamic calculations to further investigate Sb sequestration reactions occurring within the peatland.

MATERIALS AND METHODS

Field Work. Peat profiles were sampled at three different locations along the water flow from near to the inflow to close to the outflow of the peatland (B1–B3, Figure SI-1). Details about the field-site location and its characteristics have been previously reported¹⁹ and are summarized in the SI.

Peat pore water was sampled using equilibrium dialysis samplers (peepers) as described by Hesslein^{44,45} with a total length of 80 and 5 cm resolution for the first 20 and 10 cm resolution from 20 to 80 cm. Peepers were installed in mid-May 2017 and left in the peat for 4 weeks to guarantee equilibrium conditions.⁴⁵ After collection, peepers were transported in argon-filled bags to avoid redox-induced sample change to the close-by provisional field laboratory. There, pore water was sampled from the chambers of the peepers using syringe and needle. Samples were filtered ($0.2 \text{ } \mu\text{m}$, cellulose acetate), stabilized (as described in the following) and cooled ($\sim 4 \text{ } ^\circ\text{C}$) or analyzed directly on-site.

Within a radius of $\sim 30 \text{ cm}$ to each peeper location, peat cores were sampled up to a maximum sampling depth of 80 cm using a Russian Peat Borer.⁴⁶ Then, the peat cores were separated into 10 cm sections to match the pore water information obtained from peepers. Each sample section was immediately transferred to a separate argon-filled glass bottle (50 mL) and purged again with argon before closing with PTFE-sealed screw caps. Afterward, the bottles were transported under refrigerated conditions on ice packs to the laboratory in Bayreuth, Germany, where they were immediately processed within an anaerobic glovebag (Coy, N_2/H_2 95/5% (v/v), $\text{pO}_2 < 1 \text{ ppm}$). Further details about the pore water and peat core sampling procedure can be found in the SI.

Aqueous-Phase Analyses. Redox potential, pH, and electrical conductivity were determined directly after sampling the chambers using a setup designed to minimize redox changes and to handle small sample volumes (Figure SI-2). Dissolved sulfide was quantified using the methylene blue method⁴⁷ and ferrous iron (Fe(II)) as well as total dissolved iron (Fe(tot)) were measured using the phenanthroline method⁴⁸ with a portable photometer (LASA 100, Dr. Lange) at wavelengths of 605 and 480 nm, respectively. Total aqueous Sb and S concentrations were determined by inductively coupled plasma mass-spectrometry (ICP-MS, XSeries2, Thermo-Fisher) in stabilized pore water samples ($0.44\% \text{ (v/v) H}_2\text{O}_2$ (Fisher Scientific), $0.78\% \text{ (v/v) HNO}_3$ (Kraft)). Aqueous Sb speciation of samples stabilized in $0.2\% \text{ (v/v) HCl}$ (Kraft) was carried out with an anion-exchange chromatography (AEC, ICS-3000, Dionex; PRPX-100, $250 \times 4.1 \text{ mm}^2$, $10 \text{ } \mu\text{m}$, Hamilton) coupled to an ICP-MS using an isocratic elution with $10 \text{ mM NH}_4\text{NO}_3$, $10 \text{ mM NH}_4\text{H}_2\text{PO}_4$, and $1.3 \text{ mM Na}_2\text{-EDTA}$ at a flow rate of 1.0 mL/min .

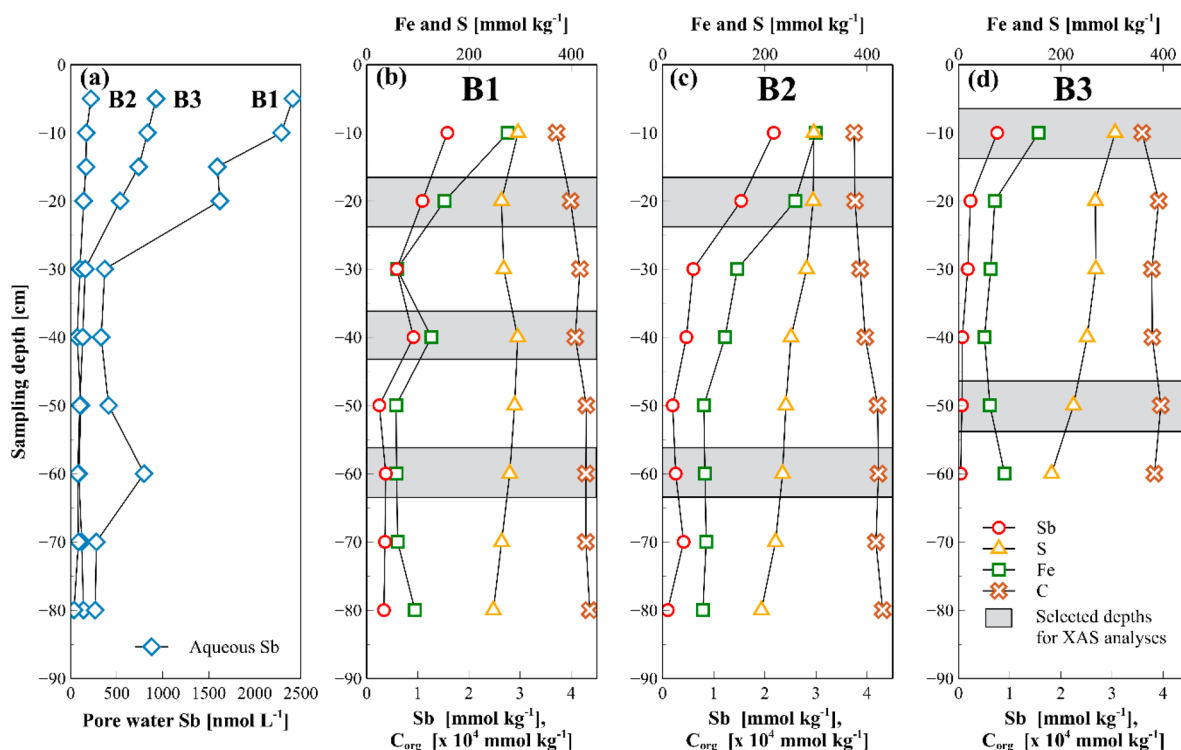


Figure 1. Vertical element distributions in peat samples for sampling points B1–B3. Total aqueous Sb concentrations (a) and down-core contents of Sb, S, Fe, and C_{org} for sampling points B1–B3, respectively (b–d). Element contents are given on dry-weight basis. Total C represents organic C (C_{org}) only because absence of carbonates was tested with 10% HCl. Depth resolution for aqueous Sb: 0–20 cm: 5 cm; 20–80 cm: 10 cm. Solid-phase element distribution resolution: 10 cm, whereby, e.g., 10 cm depth means an integrated sample from 0 to 10 cm. At sampling location B3, solid-phase sampling was only possible down to 60 cm. Please note that the scales differ between upper and lower x-axes.

Calibration standards were prepared from potassium antimony tartrate sesquihydrate (Acros) and potassium hexahydroantimonate (Fluka) stock solutions. Only antimonite and antimonate were detected with this method. Another sample stabilization (flash-freezing) and chromatographic method¹⁶ was used to screen for the occurrence of tri- and tetrathioantimonate, but none of these species were detected in any of the profiles.

Solid-Phase Analyses. Back in the laboratory in Bayreuth, the peat of each depth section was transferred into a 50 mL polyethylene tube (Sarstedt) inside a glovebag before freeze-drying following the approach of Ji et al.⁴⁹ One part of freeze-dried peat was stored anoxically, dry and in dark until solid-phase analyses, while another part was milled to <45 μm in a ball mill (MM2000, Retsch) for total element determination. Total Sb content was determined by ICP-MS and total Fe and S contents by inductively coupled plasma optical emission spectrometry (ICAP 6300 Duo View, Thermo-Fisher) after microwave digestion (MARS Xpress, CEM) using a 5:3 ratio of 30% H₂O₂ and 65% HNO₃. To get an overview of the depth distributions of many other major and trace elements, ground peat samples were analyzed by an energy dispersive X-ray fluorescence spectrometer (XEPOSTM, Spectro X Lab) calibrated with a NIST 2711 certified reference material. Total carbon (C) content was analyzed with a TOC analyzer (multi N/C 2100, Analytik Jena).

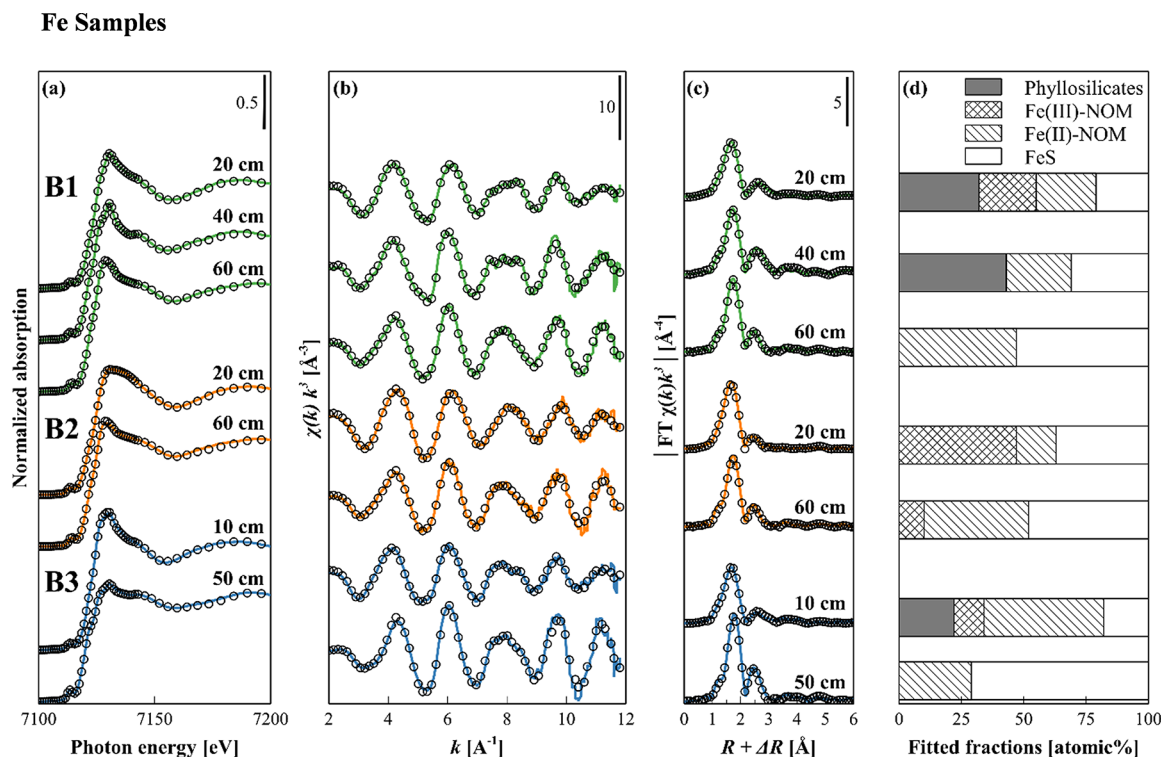
Selected peat samples were examined by scanning electron microscopy (SEM) using a Leo Gemini 1530 (Carl Zeiss, Germany) with a Schottky emitter and elemental composition analysis was conducted by energy-dispersive X-ray spectrometry (EDS, Oxford X-Max 20, Oxford Instruments). Therefore,

selected freeze-dried and homogenized peat samples were ground in a mortar, mounted on aluminum specimen stubs and coated with C before analysis.

For XAS measurements at the Stanford Synchrotron Radiation Lightsource (SSRL), Stanford, U.S.A., selected freeze-dried, homogenized, and ground peat samples from all three sample locations were filled into aluminum sample holders and sealed with Kapton tape for Fe and Sb analysis and with S-free tape for S analysis. Thereby, samples were always kept under anoxic conditions until the end of XAS experiments. Bulk Sb *K*-edge (30,491 eV), Fe *K*-edge (7,112 eV), and S *K*-edge (2,472 eV) XAS spectra were collected in fluorescence mode at beamlines 11–2 (Sb), 4–1 (Fe), and 4–3 (S) under cryogenic (10 K, 11–2 and 4–1) or ambient (inert He (<0.1% (v/v) O₂) atmosphere, 4–3) temperatures. The collected Fe *K*-edge X-ray absorption near edge structure (XANES) and extended X-ray absorption fine structure (EXAFS) spectra and Sb *K*-edge EXAFS spectra were analyzed by linear combination fitting (LCF) using a homemade software based on the Levenberg–Marquardt minimization algorithm^{50,51} and Athena,⁵² respectively, after principal component analysis and target-transform testing (PCA-TT) using SIXpack.⁵³ The Sb *K*-edge EXAFS shell-by-shell fitting analysis was performed using Artemis.⁵² Spectral deconvolutions of normalized S *K*-edge XANES spectra were performed using Athena.⁵⁹ Details on all XAS measurements, data reduction, and analyses are provided in the SI.

RESULTS AND DISCUSSION

General Geochemical Parameters and Vertical Element Distributions. Geochemical parameters of the peatland



Fe References

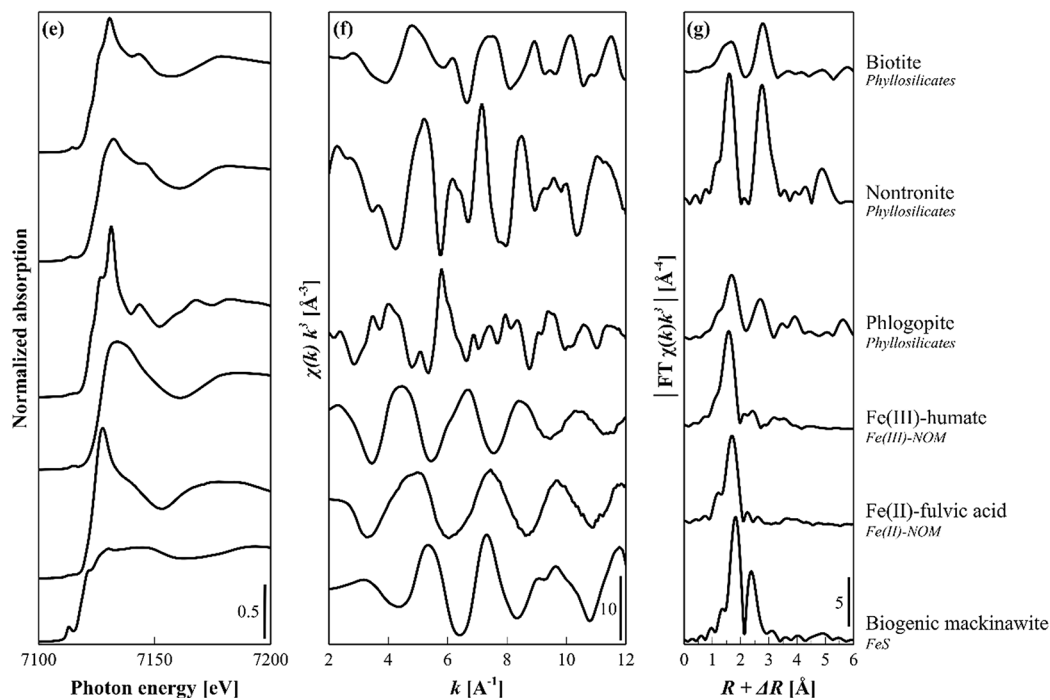


Figure 2. Normalized Fe *K*-edge XANES spectra (a, e), k^3 -weighted Fe *K*-edge EXAFS spectra (b, f) and their corresponding Fourier-transform (FT) magnitudes (c, g) of selected peat samples and Fe references. Best linear combination fits of Fe *K*-edge EXAFS peat spectra (d). The Fe EXAFS spectra are illustrated here as LCF results since similarities of XANES spectra for different iron sulfides and oxides do not appear for EXAFS spectra and make EXAFS LCF a more powerful method for Fe solid-phase speciation. Detailed results about Fe *K*-edge XANES and EXAFS best fit models can be found in [Tables SI-10 and SI-11](#). Individual fractions were constrained to values between 0 and 100%, the sum of fractions was not constrained in initial fits. For better comparison and visualization, fitted fractions were normalized to a component sum of 100% in [Figure 2d](#). Initial fit sums were 93–104% (\bar{x} = 98%). Linear combination fits of the samples are shown as black circles. Fit references: Phyllosilicates = \sum (Biotite, Nontronite, Phlogopite). Fe(III)-NOM = Fe(III)-humate. Fe(II)-NOM = Fe(II)-DOM (Suwannee River Fulvic Acid (SRFA)). FeS = biogenic mackinawite from microbial sulfate reduction.

revealed a slightly acidic to circumneutral pH (5.8–7.4) and oxic to suboxic redox conditions (148–454 mV). Both the pH and redox potential decreased with increasing depth in the peat profiles (Table SI-1). Electrical conductivity remained almost constant across the profile closest to the inflow (B1; 2.0 ± 0.2 mS cm⁻¹), but decreased with increasing depth in the other profiles. High total aqueous S concentrations (10.4 ± 2.3 mmol L⁻¹, Table SI-1) thereby mainly contributed to the electrical conductivity (Figure SI-3) of the peatland and originated from oxidation of sulfide ores to dissolved sulfate (Table SI-2) during the mining process.¹⁹

Depth distributions of total solid Sb, S, Fe, and C_{org} are illustrated in Figure 1, and distributions of additional major and trace elements are displayed in Table SI-3. Antimony contents ranged from <0.1 to 2.2 mmol kg⁻¹ ($\bar{x} = 0.6$ mmol kg⁻¹). They were highest close to the peat surface in all profiles and decreased with increasing depth. Iron exhibited a similar distribution pattern to Sb, whereas the contents of S only slightly decreased and the contents of C_{org} slightly increased with depth by maintaining minimum Fe:Sb, S:Sb, and C_{org}:Sb molar ratios of 64, 136, and 17 000, respectively.

Total aqueous Sb in surface waters was highest close to the inflow location (B1, 1566 nmol L⁻¹) and only slightly decreased toward the outflow zone (B3) to 1439 nmol L⁻¹. Within the peat profiles, total aqueous Sb concentrations ranged from 63 to 2275 nmol L⁻¹ ($\bar{x} = 480$ nmol L⁻¹) and showed a similar pattern as for solid-phase Sb (Figure 1a). However, aqueous Sb concentrations in location B2 were low (max. 380 nmol L⁻¹) throughout the profile, and solid-phase Sb contents were elevated in the first 40 cm, suggesting high Sb retention within the peat (Figure 1).

Iron and Sulfur Solid-Phase Speciation. Solid-phase Fe *K*-edge XANES and EXAFS spectra of peat samples as well as Fe reference compounds identified as peat compounds during spectra evaluation along with the Fe speciation results are illustrated in Figure 2 and summarized in Tables SI-10 and SI-11. Best LCF fit models for XANES and EXAFS spectra thereby were almost identical (Table SI-12).

Up to 43% of Fe occurred as phyllosilicates in the upper peat layers which was additionally supported by SEM-EDS results (Figure SI-4, Table SI-4). Phyllosilicates most probably originated from the underlying bedrock of greenschist⁵⁴ and presumably entered the peatland via the inflow of treated mine drainage water. Organic Fe(III) complexes (up to 47%) generally decreased with increasing peat depth, whereas Fe(II)-NOM complexes (up to 48%) increased. Organic Fe(III) complexes can form in substantial amounts, even at neutral pH values, in oxic layers of environments with abundant NOM such as peatlands and can even dominate over Fe (oxyhydr)oxides.⁵⁵ Although PCA-TT analysis of EXAFS spectra suggested that ferrihydrite, lepidocrocite, and/or schwertmannite, all representatives of Fe (oxyhydr)oxides, were suitable reference compounds (Tables SI-7 and SI-9), no Fe (oxyhydr)oxides could be fitted to the sample spectra in significant percentages (>10%).

Nonetheless, the existence of at least small amounts of Fe (oxyhydr)oxides could be demonstrated by SEM-EDS, where a particle with FeOOH stoichiometry was observed. This FeOOH polymorph was likely to be lepidocrocite or ferroxhyte, which are both Fe (oxyhydr)oxides forming through oxidation of aqueous Fe(II) e.g. induced through an oscillating water table^{56,57} Ferroxhyte, in particular, seems to be favored when Fe(II) oxidizes in the presence of Sb(V),⁵⁸

however, only in the absence of NOM. In the presence of high amounts of NOM and also Sb(V), aqueous Fe(II) is scavenged and therefore generally hinders or decelerates the formation of lepidocrocite.^{59–61}

The formation of substantial amounts of Fe(II)-NOM complexes in deeper peat layers further suggests that solid NOM plays an active role in (re)-sequestering aqueous Fe(II)⁶² (Table SI-1) after (microbially mediated) reductive dissolution of Fe (oxyhydr)oxides,³¹ Fe containing phyllosilicates^{63,64} or Fe(III)-NOM complexes.

Additionally, with increasing depth and subsequently increasing reducing conditions (Table SI-1), the presence of (authigenic) Fe mono sulfides (FeS) increased and dominated the Fe speciation in deeper peat layers (up to 71%). Here, our SEM-EDS analysis was also consistent with the presence of FeS precipitates (Figure SI-4, Table SI-4).

Sulfur *K*-edge XANES spectra of selected peat samples are shown in Figure 3 and the results from Gaussian

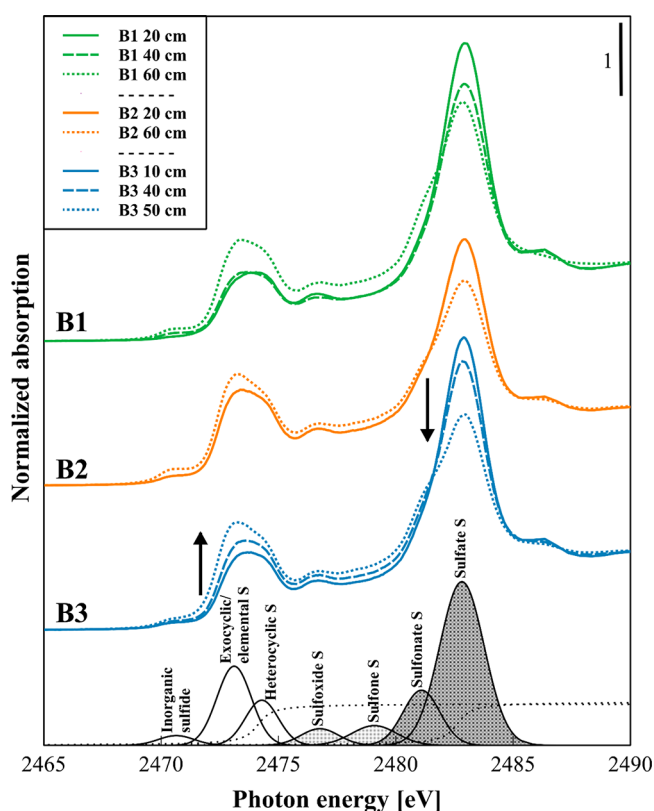
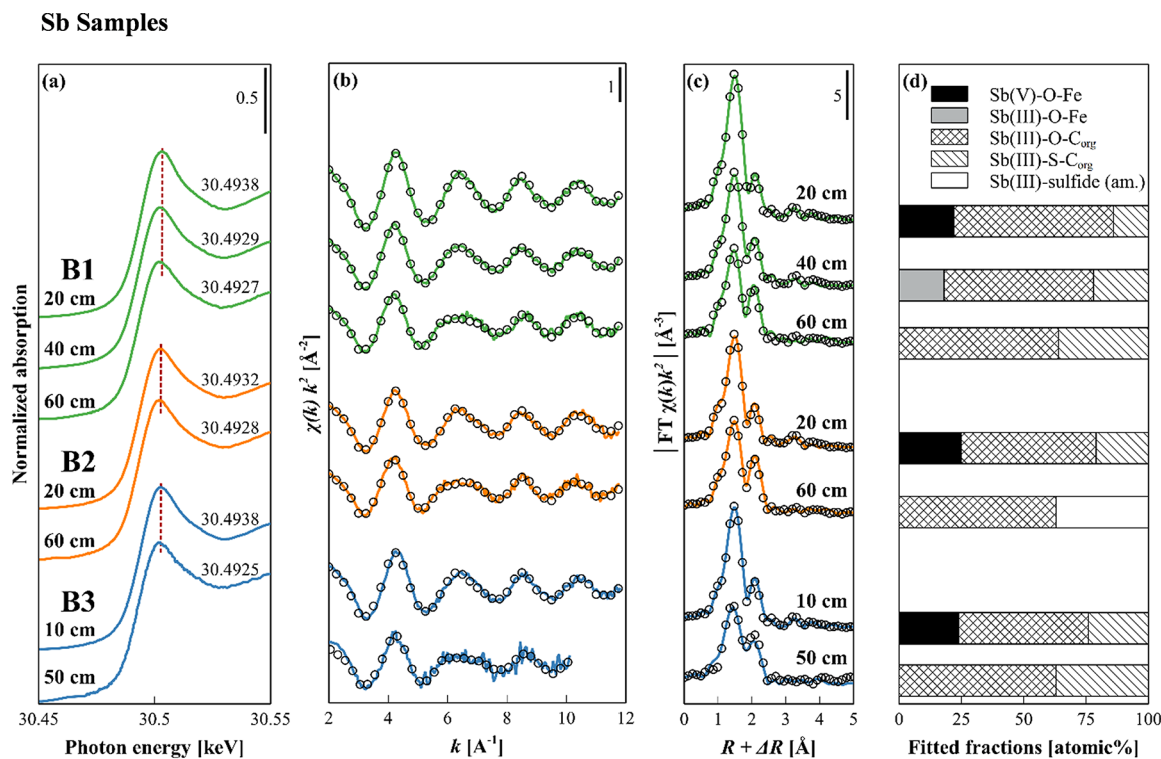


Figure 3. Sulfur solid-phase speciation of selected peat samples from sampling points B1–B3. The normalized S *K*-edge XANES spectra of peat are plotted as a function of sampling depth. Spectral decomposition is illustrated as an example for sample B3 50 cm (with offset from the other spectra). The two arctan functions are shown as dotted lines and the Gaussian functions as straight lines correspond to reduced S (oxidation states – II to + I; no shading): inorganic (mono) sulfide, exocyclic/elemental S, heterocyclic S; intermediate oxidized S (oxidation states > +I to + III; light gray shading): sulfoxide S, sulfone S and oxidized S (oxidation states > +III to + VI; dark gray shading): sulfonate S, sulfate S. The experimental data and fit envelopes as well as all fit parameters for every sample can be found in Figures SI-5 and SI-6 as well as Tables SI-13 and SI-14. Please note that the intermediate oxidized fractions (sulfoxide and sulfone S) are likely to be overestimated due to postedge absorption features of reduced S species.⁶⁵



Sb References

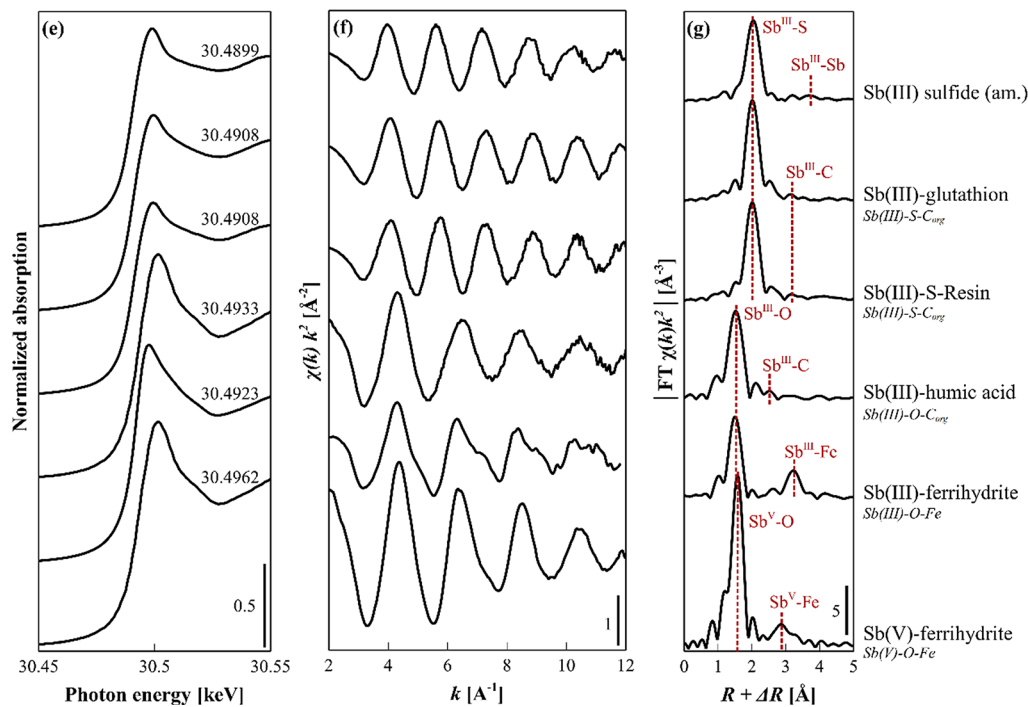


Figure 4. Normalized Sb *K*-edge XANES spectra and their respective edge-energies (keV) (a, e), *k*²-weighted Sb *K*-edge EXAFS spectra (b, f) and their corresponding Fourier-transform (FT) magnitudes (c, g) of selected peat samples and Sb references. Best linear combination fits of Sb *K*-edge EXAFS peat spectra (d). Detailed results can be found in Table SI-19. Individual fractions were constrained to values between 0 and 100%, the sum of fractions was not constrained in initial fits. For better comparison and visualization, fitted fractions were normalized to a component sum of 100% in Figure 4d. Initial fit sums were 85–100% (\bar{x} = 94%). Linear combination fits of the samples are shown as black circles. Fit references: Sb(V)–O–Fe = Sb(V) adsorbed to ferrihydrite, Sb(III)–O–Fe = Sb(III) adsorbed to ferrihydrite, Sb(III)–O–C_{org} = Sb(III) complexed with phenol groups of OM (Sb(III)-Aldrich humic acid), Sb(III)–S–C_{org} = Sb(III) complexed with thiol groups of OM: sum of Sb(III)-thiol resin (Ambersep GT74) and Sb(III)-glutathione, Sb(III) sulfide (am.) = amorphous Sb(III) sulfide. Vertical dashed lines in (a) represent white line positions of the uppermost peat sample of each profile and in (g) they illustrate main Sb single scattering paths of reference compounds.

deconvolutions, which represent $s \rightarrow p$ transitions of major S fractions, are illustrated in Figures SI-5 and SI-6 and Tables SI-13 and SI-14. The S XANES spectra could generally be divided into two main spectral regions. The first region (“reduced S”) with white line energies <2774.5 eV corresponded to inorganic (mono) sulfide, exocyclic/elemental S and heterocyclic S. The second region with white line energies >2780.6 eV (“oxidized S”) was characterized as sulfonate S and sulfate S. The region with energies in between ($2774.5 < x < 2780.6$ eV) and with only minor importance in our samples (max. 14% of fitted fractions) was summarized as “intermediate oxidized S” which was deconvoluted as sulfoxide S and sulfone S fractions and was likely to be overestimated due to postedge absorption features of reduced S species.⁶⁵

Two main depth trends were observed for S in each peat profile. The fractions of oxidized S, which dominated all spectra at the peat surfaces (27–41%), decreased with increasing peat depth to 20–27%, whereas the reduced S fractions increased and dominated deep peat layers (66–71%) (Figure 3, Table SI-14). The oxidized S fraction hereby was mainly represented through sulfate S (Figure SI-6), which most likely originated from the high sulfate inflow concentrations (Table SI-2) and at least partly precipitated as calcium sulfate (CaSO_4) during the freeze-drying process of peat samples (Figures SI-4 and SI-7, Table SI-4).

Within reduced S fractions, the exocyclic/elemental S fraction, often represented as thiol-S in organic-rich sediments,⁴³ prevailed in deep peat layers (32–35%) followed by inorganic (mono) sulfides (20–27%) (Figure SI-6). Both species are suitable entities for antimonite sequestration.^{37,66} Formation of organic thiol groups and/or inorganic (mono) sulfides in deeper peat layers often is linked to (microbial) sulfate reduction,⁴³ although in all measured samples, dissolved sulfide concentrations were low (max. $3.6 \mu\text{mol L}^{-1}$, Table SI-1). Inorganic (mono) sulfides were mostly present as FeS phases since their contents were very similar after multiplying the relative atomic fractions (%) derived from Fe and S XAS analysis with their respective total element contents (mmol kg^{-1}) (Table SI-15).

Overall, our solid-phase speciation results demonstrate that independent of the redox state of Fe and S, which followed the oxic-anoxic depth redox gradient, NOM plays an important role as reaction partner or binding site in the peatland and thus may also be an important factor for Sb retention.

Antimony Solid-Phase Speciation. Figure 4 shows Sb K-edge XANES and EXAFS spectra from selected peat samples as well as Sb reference compounds identified as peat compounds during spectra evaluation. The edge positions of XANES spectra varied between 30 492.5 and 30 493.8 eV and showed a clear decreasing trend with increasing peat depth within each peat profile (Figure 4a). Edge positions of sample spectra fell between Sb(III) and Sb(V) reference compounds indicating mixtures of Sb species (Figure 4e).

Similar to Fe solid-phase analyses, we used PCA-TT followed by LCF of EXAFS spectra to elucidate the coordination environment of Sb in peat samples. Best LCF models revealed the presence of five major Sb species, specifically Sb(III) and Sb(V) inorganically associated with Fe, Sb(III) associated with O-bearing groups of NOM ($\text{Sb(III)-O-C}_{\text{org}}$), Sb(III) associated with thiol groups of NOM ($\text{Sb(III)-S-C}_{\text{org}}$) and an amorphous Sb(III) sulfide phase. All LCF results are illustrated in Figure 4d and summarized in Table SI-19.

Several similar Sb depth trends were observed in all peat profiles. With fractions of 22–25%, Sb(V) associated with Fe solely existed in the uppermost peat layers and only in profile B1 at 40 cm, a significant fraction of Sb(III) associated with Fe (18%) could be fitted; despite the general correlation between down-core total Sb and Fe contents and a minimum molar Fe:Sb ratio of 64 in all profiles described before (Figure 1). A similar observation was made by Mikutta and Rothwell⁶⁷ in British peat bogs, where a correlation between As and Fe contents was observed, but contribution of As–Fe associations was only moderate.

The exact Sb–O–Fe binding mechanisms hereby remain elusive, since our best-fit references “Sb(III)/(V)-ferrihydrite” have to be considered as proxies for Fe coordination environments previously described as Fe (oxyhydr)oxides, Fe containing phyllosilicates and/or Fe(II)/Fe(III)-NOM complexes. The Fe(II)/Fe(III)-NOM complexes can provide Fe as bridging cation for ternary complex formation (as e.g., described for As^{68–70}). Despite up to 100% of Fe-NOM complexes found, no ternary As–Fe–OM complex formation was observed in an earlier EXAFS study on As binding in peatlands.⁶⁷ These results suggest that ternary Sb–Fe–NOM complexes tend to be of minor importance, which is underlined by the fact that up to 62% (Figure 2) of Fe-NOM complexes were found in the studied peatland while a maximal of only 25% of Sb was associated with Fe (Figure 4). Despite their demonstrated low abundances, Fe (oxyhydr)-oxides seemed to be the main controlling phase for Sb(V) binding in shallow peat layers, because of their high affinity for Sb(V).¹

With 63–100% ($\bar{x} = 82\%$), organically coordinated Sb(III) was found to be the dominant fraction in every peat profile and across all depths (Figure 4, Table SI-19). Hereby, Sb(III) associated with O-bearing groups, abundant in peat NOM, had the highest percentages (52–64%, $\bar{x} = 60\%$). High affinity of antimonite to O-bearing groups of microbial extracellular polymeric substances and solid model peat NOM has just recently been shown.^{37,72} Although Sb–C distances proposed by Besold et al.³⁷ were slightly longer (2.90 Å) than the fitted Sb–C distance of our best-fit reference compound “Sb(III) complexed with Aldrich humic acid” (2.83 Å, Figure SI-8, Table SI-20), both reside in the range of published Sb–C distances of $\sim 2.85 - \sim 2.92$ Å,^{73,74} indicative for phenol groups.

We further verified the presence of an Sb–C(O) backscatter in peat samples (1) by shell-by-shell fitting of the Sb–C(O) path and (2) by systematic exclusion of the $\text{Sb(III)-O-C}_{\text{org}}$ reference within linear combination test fits. The test fits without the $\text{Sb(III)-O-C}_{\text{org}}$ reference lead to clearly worse fit qualities in all peat samples (Table SI-21) and therefore suggest the $\text{Sb(III)-O-C}_{\text{org}}$ referenceto be a true (and important) component. Further, our shell-fitting approach revealed an Sb–C(O) path at a distance of 2.82 Å (Figure SI-9 and Table SI-22), a similar distance as in our LCF reference “Sb(III) complexed with Aldrich humic acid” with 2.83 Å. Both lines of evidence therefore corroborate the high contributions of O-bearing groups for Sb(III) complexation in peat.

The LCF results further revealed that with increasing depth, Sb(III) was increasingly bound to thiol groups of NOM (14–37%, $x = 22\%$) and therefore showed a similar depth pattern as the exocyclic/elemental S fraction fitted to the S XANES spectra as described earlier (Figure SI-6). In one case, an Sb(III) sulfide phase composing 37% of the spectrum was

fitted to sample B2 60 cm (Figure 4, Table SI-19). Shell-by-shell fitting of Sb–S distances of 2.45 ± 0.01 Å for thiol-bonds and a fitted Sb–S distance of 2.48 Å for the Sb(III) sulfide containing sample confirmed our LCF results (Figure SI-10 and Table SI-23). Formation of Sb(III)–S surface associations on FeS phases in peat samples (Figure 2) with similar Sb–S distances of 2.46 Å⁶⁶ cannot be fully excluded, however, in a previous study³⁷ we demonstrated that spectral differences between organic thiols and inorganic Sb(III) on FeS phases exist and during our LCF analysis we found no model fit where the latter significantly contributed to or improved fit quality (Table SI-19). Interestingly, sample B2 60 cm, where the redox potential was lowest (148 mV) and the Sb(III) sulfide phase was detected, also exhibited the highest contribution of inorganic (mono) sulfides within all S XANES spectra (Figure SI-6), indicating required natural conditions for inorganic Sb–S sequestration in our system.

In summary, our Sb speciation results suggest that organically complexed Sb dominates solid-phase Sb in all peat samples even in the presence of Fe phases and formation of thiol-bound Sb with increasing depth correlates with the thiol group content in peat.

Geochemical Factors Leading to Low Current Sb Removal Efficiency in the Studied Peatland. The Sb solid-phase speciation results of the present study showed high affinities of Sb(III) toward organic functional groups of peat and recent results from Besold et al.³⁷ demonstrated high sorption capacities of model peat NOM for Sb under reducing conditions, both indicating a high Sb removal potential of peatlands. Yet, the actual current removal efficiency in the investigated peatland is low (~30%).¹⁹

The peatland received high Sb inflow concentrations (1884 ± 876 nmol L⁻¹) over the past 10 years combined with high hydrological loads (41 ± 20 mm d⁻¹) (Table SI-2) which lead to a permanent free-water column on top of the peatland surface of about 20 cm. Therefore, a large part of the Sb-laden water that enters the peatland does not even infiltrate but just overflows the peatland surface with a very short overall residence time.

However, next to pure hydrological reasons, geochemical factors also have to be regarded to obtain a comprehensive understanding of this system. The peatland is located close to the arctic circle with mean annual temperatures of minus 0.5 °C¹⁹ leading to general decreased microbial activities.^{75,76} Our aqueous Sb speciation revealed solely the presence of antimonate in surface waters and only in profile B2, we observed a little increase in the proportion of antimonite with increasing depth (Figure SI-11). Additionally, Pourbaix diagrams for the Sb–O–H–S system were calculated with PhreePlot using peatland Sb and S concentrations (Figure SI-12). Plotting respective pH–E_h-values from B1–B3 (Table SI-1) in the Pourbaix diagram confirmed that all surface water samples were located in the predominance field of antimonate. Further, all samples from profile B1 and upper layers of B3 were located in the predominance field of antimonate and only samples from B2 and deeper layers of B3 lay at the boundary between antimonate and antimonite, generally supporting our results from aqueous Sb speciation.

Thus, thermodynamic calculations are consistent with the measured aqueous Sb speciation and both approaches confirm that the majority of aqueous Sb was present in form of the negatively charged antimonate oxyanion (Sb(OH)₆⁻). Little binding of antimonate to NOM is plausible as NOM has a net

negative surface charge which further increases with increasing thiol group content and increasing pH;⁷⁷ thus, probably leading to electrostatic repulsions with the negatively charged antimonate at pH > 4.^{78,79} This repulsion is considered as a main factor for overall low Sb retention in the studied peatland.⁸⁰

Additionally, dissolved organic matter in the peatland may have a negative effect on antimonate sorption capacity to metal (oxyhydr)oxides (e.g., ferrihydrite and/or lepidocrocite) by competitive sorption and through organic-mineral interactions. These interactions in turn can lead to a loss of sorption sites as well as steric and electrostatic repulsions toward other species like arsenate or antimonate^{81–83} and may partly explain the low affinity of antimonate toward Fe surfaces in our system. This effect is probably supported by the relatively high pH of ~7 in the peatland and points of zero charge of naturally existing (oxyhydr)oxides being usually lower than the ones in synthetic precipitates (e.g., 5.3–7.5 vs 8.0–8.3 for ferrihydrite^{61,62}). Therefore, lowered outer-sphere complexation of Sb with metal (oxyhydr)oxides through less protonated surface sites is also suspected.⁸⁴

Overall, we propose that (microbially catalyzed) antimonate reduction kinetics probably is a key limiting factor in this system. Low reduction rates, together with the high Sb inflow concentrations, may explain why antimonate dominates aqueous Sb speciation in most peat layers despite sulfate-reducing conditions, as verified by FeS formation (Figure 2 and Figure 3). Almost identical sulfate inflow–outflow concentrations (Table SI-2) and low dissolved sulfide concentration in peat profiles (Table SI-1) further show that the peatland chemistry was substantially governed by the inflow water chemistry.

Abiotic reduction of Sb(V) to Sb(III) in the solid as well as in the aqueous phase, as shown for different Fe phases under the influence of Fe(II) before,^{58,66,85,86} are possible but are considered of minor importance since organic matter seems to effectively hinder Sb(V) reduction by inactivating reactive Fe(II) at pH ≈ 6⁶¹ (Figure 2).

Sufficient residence times for (microbially mediated) transformation of antimonate to antimonite in the peatland would certainly increase total Sb retention on NOM surfaces. Slightly acidic inflow conditions (pH 5–6) then could probably further increase Sb(III) thiol-binding or even lead to Sb(III) sulfide precipitation as described in the literature for As.⁴¹

In summary, our study reveals geochemical conditions under which peatlands can act as sinks for Sb. Despite an often observed correlation between solid phase Sb and Fe contents, binding of Sb to Fe minerals seems to be of minor importance, even at the surface of wetlands since peat NOM acts as the main governing factor for both, Sb and Fe species. Precipitation of Sb(III)S minerals also does not seem to be the dominant process in NOM-rich environments, because binding to NOM typically impedes high dissolved sulfide concentrations which would be required to achieve supersaturation with regard to Sb(III)S mineral phases.

Instead, organic functional groups of NOM were shown to be a dominant controlling factor for Sb, Fe, and S biogeochemistry. Key to an efficient sequestration is the reduction of antimonate to antimonite in the aqueous phase since only Sb(III) showed binding via O-bearing and thiol groups of NOM. Our results highlight the complex interplay of metal(loid)s such as Sb in wetlands, where NOM not only

serves as carbon source for Sb redox dynamics⁸⁷ or competing molecule (DOM) for Sb sorption on mineral surfaces,²⁰ but also acts as efficient sorption site for Sb(III) sequestration.

■ ASSOCIATED CONTENT

📄 Supporting Information

The Supporting Information is available free of charge on the ACS Publications website at DOI: 10.1021/acs.est.9b03924.

Field site characteristics and sampling, General geochemical characterization, Scanning Electron Microscopy/Energy Dispersive X-ray Spectroscopy analyses and results, Iron solid-phase speciation analyses and results, Sulfur solid-phase speciation analyses and results, Antimony solid-phase speciation analyses and results, Aqueous Sb speciation results (PDF)

■ AUTHOR INFORMATION

Corresponding Author

*Phone: +49-921-553999; fax: +49-921-552334; e-mail: b.planer-friedrich@uni-bayreuth.de.

ORCID

Vincent Noël: 0000-0002-5387-8664

Andreas C. Scheinost: 0000-0002-6608-5428

Scott Fendorf: 0000-0002-9177-1809

Britta Planer-Friedrich: 0000-0002-0656-4283

Notes

The authors declare no competing financial interest.

■ ACKNOWLEDGMENTS

This work was funded by the German Research Foundation Grant PL 302/20-1, a PhD student short-time stipend to Stanford University for J.B. (DAAD 57314604) as well as a mobility grant (DAAD 57315737) to B.P.-F. Sampling in Finland was supported by a BayIntAn mobility grant (BayIntAn_UBT_2017_23) awarded to B.P.-F. and an Academy of Finland grant (project 287397) awarded to K.K. We acknowledge help for field-sampling from Constantin Heitzer and for SEM-EDS analyses from Dorothea Wiesner (BGI Bayreuth). Antimony, iron, and sulfur K-edge XAS experiments were performed at the Stanford Synchrotron Radiation Lightsource (SSRL), a Directorate of SLAC National Accelerator Laboratory and an Office of Science User Facility operated for the US Department of Energy, Office of Science, Office of Basic Energy Sciences under Contract No. DE-AC02-76SF00515. V.N. and J.L.P. were supported by the U.S. Department of Energy, Office of Biological and Environmental Research (BER), Subsurface Biogeochemical Research (SBR) program under subcontract DE-AC02-76SF00515. We would like to thank Ryan Davis for his support in using beamline 11-2 and 4-1 as well as Matthew Latimer and Eric Nelson for help at beamline 4-3.

■ REFERENCES

- (1) Reddy, K.; DeLaune, R. D. *Biogeochemistry of Wetlands: Science and Applications*; CRC Press: Boca Raton, 2008.
- (2) Rydin, H.; Jeglum, J. K. Peatlands around the world. In *The Biology of Peatlands*; Oxford University Press: Oxford, 2006; p 216–238.
- (3) Reddy, K. R.; DeLaune, R. D. Metals/Metalloids. In *Biogeochemistry of Wetlands: Science and Applications*; CRC Press-Taylor & Francis: Boca Raton, FL, 2008.

- (4) Mikutta, C.; Langner, P.; Bargar, J. R.; Kretzschmar, R. Tetra- and Hexavalent Uranium Forms Bidentate-Mononuclear Complexes with Particulate Organic Matter in a Naturally Uranium-Enriched Peatland. *Environ. Sci. Technol.* **2016**, *50* (19), 10465–10475.

- (5) Skyllberg, U.; Xia, K.; Bloom, P. R.; Nater, E. A.; Bleam, W. F. Binding of Mercury(II) to Reduced Sulfur in Soil Organic Matter along Upland-Peat Soil Transects. *J. Environ. Qual.* **2000**, *29* (3), 855–865.

- (6) Gündoğan, R.; Acemioğlu, B.; Alma, M. H. Copper (II) adsorption from aqueous solution by herbaceous peat. *J. Colloid Interface Sci.* **2004**, *269* (2), 303–309.

- (7) González A, Z. I.; Krachler, M.; Cheburkin, A. K.; Shoty, W. Spatial Distribution of Natural Enrichments of Arsenic, Selenium, and Uranium in a Minerotrophic Peatland, Gola di Lago, Canton Ticino, Switzerland. *Environ. Sci. Technol.* **2006**, *40* (21), 6568–6574.

- (8) Brown, T. J.; Idoine, N. E.; Raycraft, E. R.; Shaw, R. A.; Deady, E. A.; Rippingale, J.; Bide, T.; Wrighton, C. E.; Rodley, J., World Mineral Production 2008–2012. *British Geological Survey* **2014**.

- (9) Brown, A. A.; Davies, R. K.; Treverton, A. C. World Mineral Production 2012–2016. *Geol. Soc. Spec. Publ.* **2018**, *459*, 79.

- (10) Krachler, M.; Emons, H.; Zheng, J. Speciation of antimony for the 21st century: promises and pitfalls. *TrAC, Trends Anal. Chem.* **2001**, *20* (2), 79–90.

- (11) Scheinost, A. C.; Rossberg, A.; Vantelon, D.; Xifra, I.; Kretzschmar, R.; Leuz, A.-K.; Funke, H.; Johnson, C. A. Quantitative antimony speciation in shooting-range soils by EXAFS spectroscopy. *Geochim. Cosmochim. Acta* **2006**, *70* (13), 3299–3312.

- (12) Filella, M.; Belzile, N.; Chen, Y.-W. Antimony in the environment: a review focused on natural waters: I. Occurrence. *Earth-Sci. Rev.* **2002**, *57* (1), 125–176.

- (13) Zhang, D.; Pan, X.; Mu, G.; Wang, J. Toxic effects of antimony on photosystem II of *Synechocystis* sp. as probed by in vivo chlorophyll fluorescence. *J. Appl. Phycol.* **2010**, *22* (4), 479–488.

- (14) Verdugo, M.; Ogra, Y.; Quiroz, W. Mechanisms underlying the toxic effects of antimony species in human embryonic kidney cells (HEK-293) and their comparison with arsenic species. *J. Toxicol. Sci.* **2016**, *41* (6), 783–792.

- (15) Filella, M.; Belzile, N.; Chen, Y.-W. Antimony in the environment: a review focused on natural waters: II. Relevant solution chemistry. *Earth-Sci. Rev.* **2002**, *59* (1), 265–285.

- (16) Planer-Friedrich, B.; Scheinost, A. C. Formation and Structural Characterization of Thioantimony Species and Their Natural Occurrence in Geothermal Waters. *Environ. Sci. Technol.* **2011**, *45* (16), 6855–6863.

- (17) Ye, L.; Chen, H.; Jing, C. Sulfate-Reducing Bacteria Mobilize Adsorbed Antimonate by Thioantimonate Formation. *Environ. Sci. Technol. Lett.* **2019**, *6* (7), 418–422.

- (18) Olsen, N. J.; Mountain, B. W.; Seward, T. M. Antimony(III) sulfide complexes in aqueous solutions at 30°C: A solubility and XAS study. *Chem. Geol.* **2018**, *476*, 233–247.

- (19) Palmer, K.; Ronkanen, A.-K.; Kløve, B. Efficient removal of arsenic, antimony and nickel from mine wastewaters in Northern treatment peatlands and potential risks in their long-term use. *Ecol. Eng.* **2015**, *75*, 350–364.

- (20) Hockmann, K.; Schulin, R. Leaching of Antimony from Contaminated Soils. In *Competitive Sorption and Transport of Heavy Metals in Soils*, **2012**, 119.

- (21) Wilson, S. C.; Lockwood, P. V.; Ashley, P. M.; Tighe, M. The chemistry and behaviour of antimony in the soil environment with comparisons to arsenic: A critical review. *Environ. Pollut.* **2010**, *158* (5), 1169–1181.

- (22) Shoty, W.; Krachler, M.; Chen, B. Antimony in recent, ombrotrophic peat from Switzerland and Scotland: Comparison with natural background values (5,320 to 8,020 14C yr BP) and implications for the global atmospheric Sb cycle. *Global Biogeochem. Cycles* **2004**, *18* (1), 1–13.

- (23) Cloy, J. M.; Farmer, J. G.; Graham, M. C.; MacKenzie, A. B. Retention of As and Sb in Ombrotrophic Peat Bogs: Records of As,

Sb, and Pb Deposition at Four Scottish Sites. *Environ. Sci. Technol.* **2009**, *43* (6), 1756–1762.

(24) Cloy, J. M.; Farmer, J. G.; Graham, M. C.; MacKenzie, A. B.; Cook, G. T. A comparison of antimony and lead profiles over the past 2500 years in Flanders Moss ombrotrophic peat bog, Scotland. *J. Environ. Monit.* **2005**, *7* (12), 1137–1147.

(25) Rothwell, J. J.; Taylor, K. G.; Chenery, S. R. N.; Cundy, A. B.; Evans, M. G.; Allott, T. E. H. Storage and Behavior of As, Sb, Pb, and Cu in Ombrotrophic Peat Bogs under Contrasting Water Table Conditions. *Environ. Sci. Technol.* **2010**, *44* (22), 8497–8502.

(26) Arsic, M.; Teasdale, P. R.; Welsh, D. T.; Johnston, S. G.; Burton, E. D.; Hockmann, K.; Bennett, W. W. Diffusive Gradients in Thin Films Reveals Differences in Antimony and Arsenic Mobility in a Contaminated Wetland Sediment during an Oxidation-Anoxic Transition. *Environ. Sci. Technol.* **2018**, *52* (3), 1118–1127.

(27) Warnken, J.; Ohlsson, R.; Welsh, D. T.; Teasdale, P. R.; Chelsky, A.; Bennett, W. W. Antimony and arsenic exhibit contrasting spatial distributions in the sediment and vegetation of a contaminated wetland. *Chemosphere* **2017**, *180*, 388–395.

(28) Fawcett, S. E.; Jamieson, H. E.; Nordstrom, D. K.; McCleskey, R. B. Arsenic and antimony geochemistry of mine wastes, associated waters and sediments at the Giant Mine, Yellowknife, Northwest Territories, Canada. *Appl. Geochem.* **2015**, *62*, 3–17.

(29) Bennett, W. W.; Hockmann, K.; Johnston, S. G.; Burton, E. D. Synchrotron X-ray absorption spectroscopy reveals antimony sequestration by reduced sulfur in a freshwater wetland sediment. *Environ. Chem.* **2017**, *14* (6), 345–349.

(30) Tighe, M.; Lockwood, P.; Wilson, S. Adsorption of antimony(v) by floodplain soils, amorphous iron(III) hydroxide and humic acid. *J. Environ. Monit.* **2005**, *7* (12), 1177–1185.

(31) Schwertmann, U. Solubility and dissolution of iron oxides. *Plant Soil* **1991**, *130* (1), 1–25.

(32) Petrunic, B. M.; MacQuarrie, K. T. B.; Al, T. A. Reductive dissolution of Mn oxides in river-recharged aquifers: a laboratory column study. *J. Hydrol.* **2005**, *301* (1), 163–181.

(33) Hockmann, K.; Lenz, M.; Tandy, S.; Nachttegaal, M.; Janousch, M.; Schulin, R. Release of antimony from contaminated soil induced by redox changes. *J. Hazard. Mater.* **2014**, *275*, 215–221.

(34) Kulp, T. R.; Miller, L. G.; Braiotta, F.; Webb, S. M.; Kocar, B. D.; Blum, J. S.; Oremland, R. S. Microbiological Reduction of Sb(V) in Anoxic Freshwater Sediments. *Environ. Sci. Technol.* **2014**, *48* (1), 218–226.

(35) Nguyen, V. K.; Lee, J.-U. Antimony-Oxidizing Bacteria Isolated from Antimony-Contaminated Sediment - A Phylogenetic Study. *Geomicrobiol. J.* **2015**, *32* (1), 50–58.

(36) Webb; McGinness; Lappin-Scott. Metal removal by sulphate-reducing bacteria from natural and constructed wetlands. *J. Appl. Microbiol.* **1998**, *84* (2), 240–248.

(37) Besold, J.; Kumar, N.; Scheinost, A. C.; Lezama Pacheco, J.; Fendorf, S.; Planer-Friedrich, B. Antimonite Complexation with Thiol and Carboxyl/Phenol Groups of Peat Organic Matter. *Environ. Sci. Technol.* **2019**, *53* (9), 5005–5015.

(38) Spratt, H. G.; Morgan, M. D. Sulfur cycling in a cedar-dominated, freshwater wetland. *Limnol. Oceanogr.* **1990**, *35* (7), 1586–1593.

(39) Steinmann, P.; Shoty, W. Ion chromatography of organic-rich natural waters from peatlands IV. Dissolved free sulfide and acid-volatile sulfur. *J. Chromatogr. A* **1995**, *706* (1), 287–292.

(40) Shoty, W. Review of the inorganic geochemistry of peats and peatland waters. *Earth-Sci. Rev.* **1988**, *25* (2), 95–176.

(41) Besold, J.; Biswas, A.; Suess, E.; Scheinost, A. C.; Rossberg, A.; Mikutta, C.; Kretzschmar, R.; Gustafsson, J. P.; Planer-Friedrich, B. Monothioarsenate Transformation Kinetics Determining Arsenic Sequestration by Sulfhydryl Groups of Peat. *Environ. Sci. Technol.* **2018**, *52* (13), 7317–7326.

(42) Yu, Z.-G.; Göttlicher, J.; Steininger, R.; Knorr, K.-H. Organic sulfur and organic matter redox processes contribute to electron flow in anoxic incubations of peat. *Environ. Chem.* **2016**, *13* (5), 816–825.

(43) Werne, J. P.; Hollander, D. J.; Lyons, T. W.; Sinninghe Damsté, J. S., Organic sulfur biogeochemistry: Recent advances and future research directions. *Special Paper Geological Society of America* **2004**, *379*, (135), 135

(44) Hesslein, R. H. An in situ sampler for close interval pore water studies. *Limnol. Oceanogr.* **1976**, *21* (6), 912–914.

(45) Steinmann, P.; Shoty, W. Sampling anoxic pore waters in peatlands using “peepers” for in situ-filtration. *Anal. Bioanal. Chem.* **1996**, *354* (5), 709–713.

(46) Osborne, T. Z.; DeLaune, R. D., Soil and Sediment Sampling of Inundated Environments. In *Methods in Biogeochemistry of Wetlands*; DeLaune, R. D., Reddy, K. R., Richardson, C. J., Megonigal, J. P., Eds.; Soil Science Society of America: Madison, WI, 2013; pp 21–40.

(47) Cline, J. D. Spectrophotometric determination of hydrogen sulfide in natural waters. *Limnol. Oceanogr.* **1969**, *14* (3), 454–458.

(48) Fortune, W.; Mellon, M. Determination of iron with o-phenanthroline: a spectrophotometric study. *Ind. Eng. Chem., Anal. Ed.* **1938**, *10* (2), 60–64.

(49) Ji, Y.; Sarret, G.; Schulin, R.; Tandy, S. Fate and chemical speciation of antimony (Sb) during uptake, translocation and storage by rye grass using XANES spectroscopy. *Environ. Pollut.* **2017**, *231*, 1322–1329.

(50) Hohmann, C.; Morin, G.; Ona-Nguema, G.; Guigner, J.-M.; Brown, G. E.; Kappler, A. Molecular-level modes of As binding to Fe(III) (oxyhydr)oxides precipitated by the anaerobic nitrate-reducing Fe(II)-oxidizing *Acidovorax* sp. strain BoFeN1. *Geochim. Cosmochim. Acta* **2011**, *75* (17), 4699–4712.

(51) Pantke, C.; Obst, M.; Benzerara, K.; Morin, G.; Ona-Nguema, G.; Dippon, U.; Kappler, A. Green Rust Formation during Fe(II) Oxidation by the Nitrate-Reducing *Acidovorax* sp. Strain BoFeN1. *Environ. Sci. Technol.* **2012**, *46* (3), 1439–1446.

(52) Ravel, B.; Newville, M. ATHENA, ARTEMIS, HEPHAESTUS: data analysis for X-ray absorption spectroscopy using IFEFFIT. *J. Synchrotron Radiat.* **2005**, *12* (4), 537–541.

(53) Webb, S. M. SIXpack: a graphical user interface for XAS analysis using IFEFFIT. *Phys. Scr.* **2005**, *2005* (T115), 1011.

(54) Wyche, N. L.; Eilu, P.; Koppström, K.; Kortelainen, V. J.; Niiranen, T.; Välimaa, J. Chapter 5.2—The Suurikuusikko Gold Deposit (Kittilä Mine), Northern Finland. In *Mineral Deposits of Finland*; Maier, W. D., Lahtinen, R., O'Brien, H., Eds.; Elsevier: 2015; pp 411–433.

(55) Karlsson, T.; Persson, P. Coordination chemistry and hydrolysis of Fe(III) in a peat humic acid studied by X-ray absorption spectroscopy. *Geochim. Cosmochim. Acta* **2010**, *74* (1), 30–40.

(56) Cornell, R. M.; Schwertmann, U. *The Iron Oxides: Structure, Properties, Reactions, Occurrences and Uses*; John Wiley & Sons: 2003.

(57) Sung, W.; Morgan, J. J. Kinetics and product of ferrous iron oxygenation in aqueous systems. *Environ. Sci. Technol.* **1980**, *14* (5), 561–568.

(58) Burton, E. D.; Hockmann, K.; Karimian, N.; Johnston, S. G. Antimony mobility in reducing environments: The effect of microbial iron(III)-reduction and associated secondary mineralization. *Geochim. Cosmochim. Acta* **2019**, *245*, 278–289.

(59) ThomasArrigo, L. K.; Byrne, J. M.; Kappler, A.; Kretzschmar, R. Impact of Organic Matter on Iron(II)-Catalyzed Mineral Transformations in Ferrihydrite-Organic Matter Coprecipitates. *Environ. Sci. Technol.* **2018**, *52* (21), 12316–12326.

(60) ThomasArrigo, L. K.; Mikutta, C.; Byrne, J.; Kappler, A.; Kretzschmar, R. Iron(II)-Catalyzed Iron Atom Exchange and Mineralogical Changes in Iron-rich Organic Freshwater Flocs: An Iron Isotope Tracer Study. *Environ. Sci. Technol.* **2017**, *51* (12), 6897–6907.

(61) Karimian, N.; Burton, E. D.; Johnston, S. G.; Hockmann, K.; Choppala, G. Humic acid impacts antimony partitioning and speciation during iron(II)-induced ferrihydrite transformation. *Sci. Total Environ.* **2019**, *683*, 399–410.

(62) Catrouillet, C.; Davranche, M.; Dia, A.; Bouhnik-Le Coz, M.; Marsac, R.; Pourret, O.; Gruau, G. Geochemical modeling of Fe(II) binding to humic and fulvic acids. *Chem. Geol.* **2014**, *372*, 109–118.

- (63) Lee, J.-H.; Fredrickson, J. K.; Kukkadapu, R. K.; Boyanov, M. I.; Kemner, K. M.; Lin, X.; Kennedy, D. W.; Bjornstad, B. N.; Konopka, A. E.; Moore, D. A.; Resch, C. T.; Phillips, J. L. Microbial Reductive Transformation of Phyllosilicate Fe(III) and U(VI) in Fluvial Subsurface Sediments. *Environ. Sci. Technol.* **2012**, *46* (7), 3721–3730.
- (64) Wu, T.; Shelobolina, E.; Xu, H.; Konishi, H.; Kukkadapu, R.; Roden, E. E. Isolation and Microbial Reduction of Fe(III) Phyllosilicates from Subsurface Sediments. *Environ. Sci. Technol.* **2012**, *46* (21), 11618–11626.
- (65) Manceau, A.; Nagy, K. L. Quantitative analysis of sulfur functional groups in natural organic matter by XANES spectroscopy. *Geochim. Cosmochim. Acta* **2012**, *99*, 206–223.
- (66) Kirsch, R.; Scheinost, A. C.; Rossberg, A.; Banerjee, D.; Charlet, L. Reduction of antimony by nano-particulate magnetite and mackinawite. *Mineral. Mag.* **2008**, *72* (1), 185–189.
- (67) Mikutta, C.; Rothwell, J. J. Peat Bogs as Hotspots for Organoarsenical Formation and Persistence. *Environ. Sci. Technol.* **2016**, *50* (8), 4314–4323.
- (68) Mikutta, C.; Frommer, J.; Voegelin, A.; Kaegi, R.; Kretzschmar, R. Effect of citrate on the local Fe coordination in ferrihydrite, arsenate binding, and ternary arsenate complex formation. *Geochim. Cosmochim. Acta* **2010**, *74* (19), 5574–5592.
- (69) Hoffmann, M.; Mikutta, C.; Kretzschmar, R. Arsenite Binding to Natural Organic Matter: Spectroscopic Evidence for Ligand Exchange and Ternary Complex Formation. *Environ. Sci. Technol.* **2013**, *47* (21), 12165–12173.
- (70) Hiemstra, T.; van Riemsdijk, W. H. Adsorption and surface oxidation of Fe(II) on metal (hydr)oxides. *Geochim. Cosmochim. Acta* **2007**, *71* (24), 5913–5933.
- (71) Mitsunobu, S.; Takahashi, Y.; Terada, Y.; Sakata, M. Antimony(V) Incorporation into Synthetic Ferrihydrite, Goethite, and Natural Iron Oxyhydroxides. *Environ. Sci. Technol.* **2010**, *44* (10), 3712–3718.
- (72) Zhou, L.; Li, A.; Ma, F.; Yang, J.; Pi, S.; Tang, A. Sb(V) Reduced to Sb(III) and More Easily Adsorbed in the Form of Sb(OH)₃ by Microbial Extracellular Polymeric Substances and Core-Shell Magnetic Nanocomposites. *ACS Sustainable Chem. Eng.* **2019**, *7* (11), 10075–10083.
- (73) Horley, G. A.; Mahon, M. F.; Molloy, K. C.; Venter, M. M.; Haycock, P. W.; Myers, C. P. Structures of Sb(OC₆H₃Me₂-2,6)₃ and Sb(OEt)₅NH₃: The First Authenticated Monomeric Sb(OR)_n (n = 3, 5). *Inorg. Chem.* **2002**, *41* (6), 1652–1657.
- (74) Tella, M.; Pokrovski, G. S. Antimony(III) complexing with O-bearing organic ligands in aqueous solution: An X-ray absorption fine structure spectroscopy and solubility study. *Geochim. Cosmochim. Acta* **2009**, *73* (2), 268–290.
- (75) Werker, A. G.; Dougherty, J. M.; McHenry, J. L.; Van Loon, W. A. Treatment variability for wetland wastewater treatment design in cold climates. *Ecol. Eng.* **2002**, *19* (1), 1–11.
- (76) Kadlec, R. H.; Reddy, K. R. Temperature Effects in Treatment Wetlands. *Water Environ. Res.* **2001**, *73* (5), 543–557.
- (77) Catrouillet, C.; Davranche, M.; Dia, A.; Bouhnik-Le Coz, M.; Pédrot, M.; Marsac, R.; Gruau, G. Thiol groups controls on arsenite binding by organic matter: New experimental and modeling evidence. *J. Colloid Interface Sci.* **2015**, *460*, 310–320.
- (78) Tella, M.; Pokrovski, G. S. Antimony(V) complexing with O-bearing organic ligands in aqueous solution: an X-ray absorption fine structure spectroscopy and potentiometric study. *Mineral. Mag.* **2008**, *72* (1), 205–209.
- (79) Li, X.; Reich, T.; Kersten, M.; Jing, C. Low-Molecular-Weight Organic Acid Complexation Affects Antimony(III) Adsorption by Granular Ferric Hydroxide. *Environ. Sci. Technol.* **2019**, *53* (9), 5221–5229.
- (80) Verbeeck, M.; Warrinnier, R.; Gustafsson, J. P.; Thiry, Y.; Smolders, E. Soil organic matter increases antimonate mobility in soil: An Sb(OH)₆ sorption and modelling study. *Appl. Geochem.* **2019**, *104*, 33–41.
- (81) Kaiser, K.; Guggenberger, G.; Haumaier, L.; Zech, W. Dissolved organic matter sorption on sub soils and minerals studied by ¹³C-NMR and DRIFT spectroscopy. *Eur. J. Soil Sci.* **1997**, *48* (2), 301–310.
- (82) Filius, J. D.; Meeussen, J. C. L.; Lumsdon, D. G.; Hiemstra, T.; van Riemsdijk, W. H. Modeling the binding of fulvic acid by goethite: the speciation of adsorbed FA molecules. *Geochim. Cosmochim. Acta* **2003**, *67* (8), 1463–1474.
- (83) Gustafsson, J. P. Arsenate adsorption to soils: Modelling the competition from humic substances. *Geoderma* **2006**, *136* (1), 320–330.
- (84) Leuz, A.-K.; Mönch, H.; Johnson, C. A. Sorption of Sb(III) and Sb(V) to Goethite: Influence on Sb(III) Oxidation and Mobilization. *Environ. Sci. Technol.* **2006**, *40* (23), 7277–7282.
- (85) Mitsunobu, S.; Takahashi, Y.; Sakai, Y. Abiotic reduction of antimony(V) by green rust (Fe₄(II)Fe₂(III)(OH)₁₂SO₄·3H₂O). *Chemosphere* **2008**, *70* (5), 942–947.
- (86) Ilgen, A. G.; Foster, A. L.; Trainor, T. P. Role of structural Fe in nontronite NAu-1 and dissolved Fe(II) in redox transformations of arsenic and antimony. *Geochim. Cosmochim. Acta* **2012**, *94*, 128–145.
- (87) Borch, T.; Kretzschmar, R.; Kappler, A.; Cappellen, P. V.; Ginder-Vogel, M.; Voegelin, A.; Campbell, K. Biogeochemical Redox Processes and their Impact on Contaminant Dynamics. *Environ. Sci. Technol.* **2010**, *44* (1), 15–23.

Supporting Information to

**“Antimonite Binding to Natural Organic Matter:
Spectroscopic Evidence from a Mine Water Impacted
Peatland”**

*Johannes Besold¹, Anne Eberle¹, Vincent Noël², Katharina Kujala³, Naresh Kumar^{4,5}, Andreas C. Scheinost⁶, Juan Lezama Pacheco⁷, Scott Fendorf⁷ and Britta Planer-Friedrich^{*1}*

¹ Department of Environmental Geochemistry, Bayreuth Center for Ecology and Environmental Research (BAYCEER), Bayreuth University, 95440 Bayreuth, Germany

² Stanford Synchrotron Radiation Lightsource, SLAC National Accelerator Laboratory, Menlo Park, CA 94025, United States

³ Water Resources and Environmental Engineering Research Unit, University of Oulu, FI-90014, Oulu, Finland

⁴ Department of Geological Sciences, School of Earth, Energy, and Environmental Sciences, Stanford University, Stanford, CA 94305, USA.

⁵ Department of Environmental Geosciences, Centre for Microbiology and Environmental Systems Science, University of Vienna, 1090 Vienna, Austria.

⁶ The Rossendorf Beamline (ROBL) at ESRF, 38043 Grenoble, France and Helmholtz-Zentrum Dresden-Rossendorf (HZDR), Institute of Resource Ecology, Bautzner Landstraße 400, 01328 Dresden, Germany

⁷ Department of Earth System Science, School of Earth, Energy, and Environmental Sciences, Stanford University, Stanford, CA 94305, USA

(46 pages, 23 tables, 12 figures)

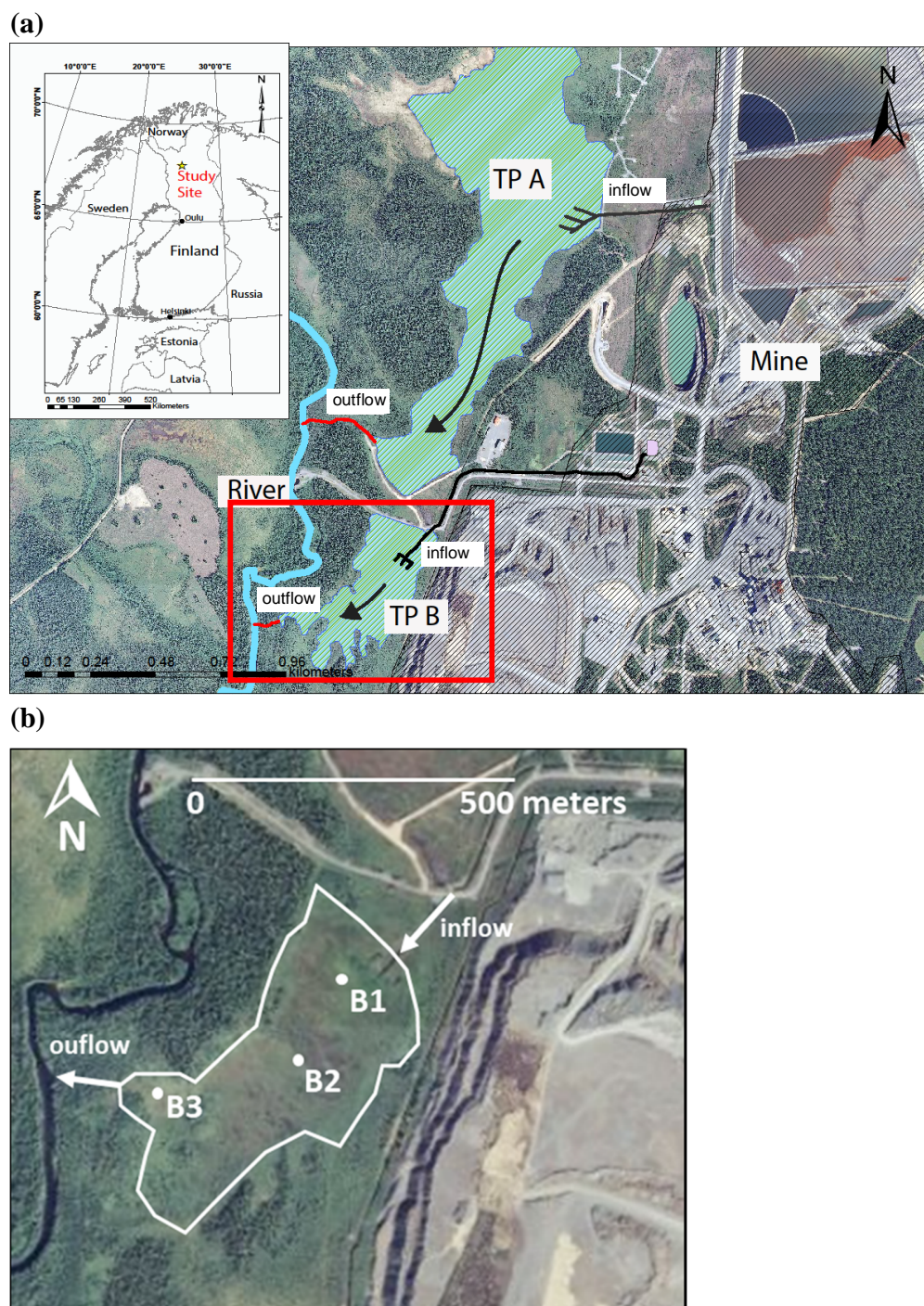
1. Field site location, characteristics and sampling.....	2
2. General geochemical characterization of pore water and peat solid phase	5
3. Scanning Electron Microscopy/Energy Dispersive X-Ray Spectroscopy (SEM/EDS) analyses and results	9
4. Iron solid-phase speciation analyses and results.....	15
5. Sulfur solid-phase speciation analyses and results.....	25
6. Antimony solid-phase speciation analyses and results.....	33
7. Aqueous Sb speciation results	42

* Corresponding author's email: b.planer-friedrich@uni-bayreuth.de

Phone: +49-921-553999; Fax: +49-921-552334

S1

1. Field site location, characteristics and sampling



General field-site characteristics

According to Palmer *et al.*¹ the peatland is characterized as a poor fen where the vegetation cover mainly consists of mosses (e.g., *Sphagnum* sp.), *Eriophorum angustifolium*, *Carex* sp. and *Trichophorum cespitosum*. Peat depth varies from 0 to 150 cm. Hydraulic conductivity of the peat at 0–100 cm depth varies from $<1.8 \times 10^{-7}$ to 7.1×10^{-4} m s⁻¹ and is highest between 20–70 cm depth. Mean annual temperature and precipitation are -0.5°C and 500–600 mm, respectively. The peatland is generally snow-covered from October to May and the main run-off event occurs after the snow-melt in May. The average slope of the area is 0.3–0.5%.

Pore water sampling and field-site analyses

For in-situ porewater sampling, equilibrium dialysis samplers (so-called peepers) of type Hesslein^{2,3} made of acrylic glass were used. They were designed for a depth profile of 80 cm with a depth resolution of 5 cm for the first 20 cm and a resolution of 10 cm for the 20 to 80 cm range (total volume was 15 mL). The peepers were filled with N₂-purged, deionized (DI) water, covered with polyether sulfone membrane (0.2 µm, Supor®200, PALL) and stored in N₂-purged DI water for transport. In mid-May 2017, when the snow was molten and the peat was mostly thawed, the peepers were installed at the three sampling points (B1-B3). They were left in the peat for four weeks to equilibrate with the pore water.³ In mid-June the peepers were collected, instantly wrapped tightly with polyethylene foil, and sealed with a rubber layer and plastic board clamps on top. For transport to a provisional field laboratory close-by and until sample processing, the peepers were stored anoxically in an argon filled bag. In the provisional field laboratory the pore water was sampled from the chambers of the peepers using syringe (Injekt 20 mL, Braun) and needle (Ø 0.60 mm, Gr.14, Sterican®). All samples were filtered (0.2 µm, CA) before further stabilization or measurement. For all depths sulfide, ferrous iron (Fe(II)) and total dissolved iron (Fe(tot)) were quantified using a mobile laboratory photometer (LASA 100, Dr. Lange). Electrical conductivity (EC) and pH were measured for each depth, redox potential only for selected depths. To be able to measure pH and redox potential with a sample volume of only about 1.5 mL each, the electrode was placed in a 5 mL syringe (Injekt 5 mL, Braun) instead of the plunger, which fit tightly around the electrode, and the sample was introduced from below by injecting it through a three way stopcock (Figure SI-2). To measure electrical conductivity in only 3 mL sample, a small plastic bag containing the sample was fitted tightly around the electrode.

Peat core sampling

Peat cores were sampled using a Russian Peat Borer up to 80 cm depth, starting from the peat surface, which

was defined as the start of dead plant material. The cores were separated in 10 cm sections from the peat surface up to 80 cm to match the pore water information from the peepers. Each depth section was transferred to a separate argon filled glass bottle (50 mL, LABSOLUTE® with plastic screw caps with aperture and PTFE-protected silicone rubber seals, DURAN®) and purged again with argon before closing. The bottles were then stored in the refrigerator at 4°C to minimize microbially induced sample change and transported back to Bayreuth under cooled conditions on ice-packs.

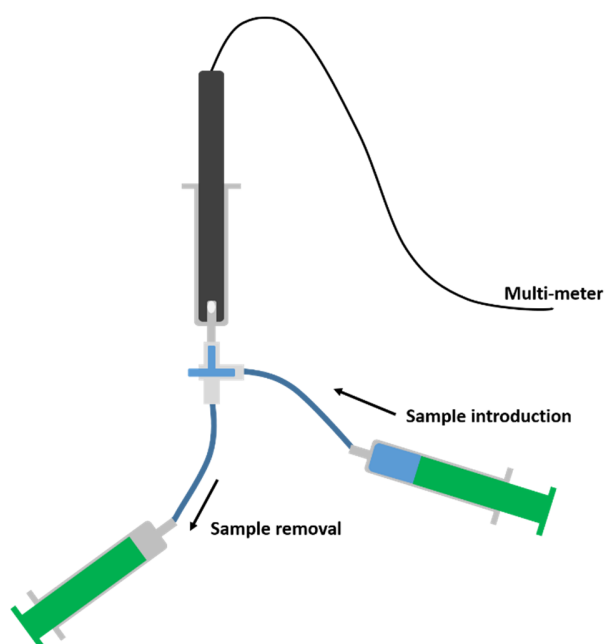


Figure SI-2: Setup for measurement of pH or redox potential with 1.5 mL sample volume. This setup was installed twice, one for the pH and one for the redox electrode, for simultaneous measurement.

2. General geochemical characterization of pore water and peat solid phase

Table SI-1: Vertical distribution of major chemical parameters in peat pore water profiles.

Sample	Depth	Aqueous S	Sulfide	Fe(II)	Fe(tot)	pH	E _h	EC
	[cm]	[mmol L ⁻¹]	[μmol L ⁻¹]	[μmol L ⁻¹]	[μmol L ⁻¹]	-	[mV]	[mS cm ⁻¹]
B1								
Surface		9.78	-	-	-	7.09	431	2.10
5 cm	0-5	11.9	< 0.3	< 0.01	0.64	7.02	341	2.01
10 cm	5-10	13.4	0.49	< 0.01	0.80	6.70	341	2.19
15 cm	10-15	13.9	0.68	1.53	0.64	6.66	334	2.19
20 cm	10-20	13.1	< 0.3	0.15	0.32	6.77	315	2.14
30 cm	20-30	11.8	3.59	8.15	7.20	6.93	258	2.04
40 cm	30-40	10.9	< 0.3	6.62	7.68	6.89	265	2.04
50 cm	40-50	10.5	< 0.3	8.31	8.80	6.86	273	2.03
60 cm	50-60	9.12	< 0.3	27.7	25.8	6.74	244	1.75
70 cm	60-70	7.21	< 0.3	1.38	1.60	6.70	285	2.00
80 cm	70-80	6.99	< 0.3	45.4	48.5	6.55	282	2.38
B2								
Surface		9.83	-	-	-	7.22	455	2.10
5 cm	0-5	13.7	< 0.3	206	216	6.75	-	2.16
10 cm	5-10	12.9	< 0.3	226	277	6.76	165	2.12
15 cm	10-15	12.2	0.77	237	262	6.73	-	2.06
20 cm	10-20	12.0	< 0.3	275	295	6.79	-	2.05
30 cm	20-30	12.1	< 0.3	423	447	6.77	-	2.04
40 cm	30-40	11.4	0.39	477	487	6.62	148	2.03
50 cm	40-50	9.88	< 0.3	853	861	6.21	-	1.67
60 cm	50-60	7.17	< 0.3	828	844	5.80	-	1.34
70 cm	60-70	6.55	1.07	1190	1162	6.08	213	1.28
80 cm	70-80	7.05	1.84	1908	2065	6.50	210	1.53
B3								
Surface		9.77	-	-	-	7.41	449	2.11
5 cm	0-5	11.9	< 0.3	<0.01	1.60	7.23	-	1.99
10 cm	5-10	13.1	< 0.3	<0.01	6.72	7.03	265	2.17
15 cm	10-15	13.5	0.38	9.00	13.7	6.92	-	2.21
20 cm	10-20	13.0	< 0.3	16.5	18.7	6.86	-	2.19
30 cm	20-30	11.3	0.78	118	118	6.72	-	2.04
40 cm	30-40	10.8	2.91	164	164	6.59	155	1.99
50 cm	40-50	10.2	0.48	66.3	63.3	6.46	-	1.88
60 cm	50-60	8.17	< 0.3	425	456	6.04	-	1.67

Table SI-2: Composition of inlet and outlet waters of the treatment peatland from monitoring data.

Parameter	Inflow		Outflow	
		2008-2018		2007-2017
pH		7.5 ±0.2		7.3 ±0.3
EC	[mS cm ⁻¹]	1.62±0.60		1.64±0.79
Alkalinity	[mmol L ⁻¹]	*2.73		*1.84
O ₂	[mmol L ⁻¹]	0.30±0.19		0.22±0.09
Cl ⁻	[mmol L ⁻¹]	0.73±0.58		0.72±0.59
COD	[mmol O ₂ L ⁻¹]	0.88±0.25		0.88±0.25
SO ₄ ²⁻	[mmol L ⁻¹]	7.85±3.58		7.95±4.73
Total N	[mmol L ⁻¹]	0.93±0.29		0.79±0.29
Sb	[µmol L ⁻¹]	1.87±0.87		1.48±0.80
Mn	[µmol L ⁻¹]	5.50±4.11		†3.17±8.65
As	[µmol L ⁻¹]	0.43±0.29		0.16±0.16
Ni	[µmol L ⁻¹]	1.09±0.72		0.61±1.01
Fe	[µmol L ⁻¹]	1.16±2.47		1.67±4.91
Mg	[mmol L ⁻¹]	**3.74 ±0.29		**3.25±1.11
Na	[mmol L ⁻¹]	**3.04±0.35		**2.96±0.43
Ca	[mmol L ⁻¹]	**7.24±0.35		**7.46±1.05
K	[mmol L ⁻¹]	**0.31±0.05		**0.28±0.04

*single measurement

**Calculated from less than 20 measurements

†One measurement omitted from calculations as outlier

Table SI-3: Vertical distribution of the water content as well as major and trace elements in peat profiles based on dry mass and analyzed by XRF spectrometry^a.

Sample	Depth	Na	Mg	Al	Si	P	Cl	K	Ca	Ti	V	Cr	Mn	Co	Ni	Cu	Zn	As	Se	Pb	Water content	
	[cm]	[g/kg]	[mg/kg]	[mg/kg]	[mg/kg]	[g/kg]	[mg/kg]	[wt%]														
B1																						
10 cm	0-10	2.9	8.7	8.6	43	1.5	1.6	2.3	31	1126	61	38	4.5	70	341	20	67	251	1.5	10	92.3	
20 cm	10-20	2.4	7.2	2.5	31	1.3	2.2	1.7	35	934	53	33	4.0	62	275	18	54	217	1.3	7.0	91.3	
30 cm	20-30	<0.2	4.4	<2.0	16	1.5	2.5	0.8	43	286	22	18	1.1	21	138	10	21	63	0.9	4.1	90.9	
40 cm	30-40	1.4	8.7	<2.0	35	2.2	4.4	1.5	55	627	42	28	4.6	54	388	23	45	161	1.1	8.7	90.7	
50 cm	40-50	0.2	2.2	<2.0	12	1.9	1.9	0.6	44	231	17	21	1.3	17	92	11	15	28	0.9	2.0	89.0	
60 cm	50-60	3.0	2.3	<2.0	8.8	1.5	1.2	0.4	33	165	12	13	0.9	17	74	9.0	12	24	0.8	3.5	88.7	
70 cm	60-70	<0.2	3.7	<2.0	16	2.8	2.4	0.7	59	255	19	23	1.3	17	169	20	23	64	0.8	4.4	88.6	
80 cm	70-80	4.5	5.4	<2.0	11	2.5	2.2	0.8	61	318	26	26	1.7	28	180	25	24	97	0.8	< 3.0	88.0	
B2																						
10 cm	0-10	<0.2	7.2	11.3	80	1.7	2.1	3.9	38	1461	74	39	4.1	70	541	40	105	151	2.6	25	91.0	
20 cm	10-20	<0.2	5.6	<2.0	93	3.6	3.8	2.2	63	557	39	24	4.6	71	328	28	65	112	1.5	38	91.5	
30 cm	20-30	<0.2	2.6	<2.0	53	2.3	2.2	0.9	43	207	20	14	1.5	33	101	13	23	49	0.7	11	91.0	
40 cm	30-40	<0.2	4.0	<2.0	55	2.9	3.4	0.9	51	218	25	16	1.8	29	153	21	25	71	0.8	10	91.2	
50 cm	40-50	4.1	4.4	<2.0	27	2.9	3.4	1.0	52	159	21	17	1.1	18	89	14	22	41	0.5	5.3	90.2	
60 cm	50-60	2.2	3.4	<2.0	21	2.4	2.7	0.7	44	133	17	10	1.4	12	122	13	22	60	0.4	5.2	91.1	
70 cm	60-70	7.0	5.0	<2.0	21	2.3	3.2	0.9	53	278	24	18	0.9	19	147	22	27	70	1.0	5.7	89.6	
80 cm	70-80	6.0	2.9	<2.0	8.2	1.8	2.0	0.5	42	139	15	14	1.0	12	84	15	15	22	0.6	3.6	87.0	
B3																						
10 cm	0-10	2.0	5.1	9.5	88	3.8	3.0	3.5	51	1733	67	47	0.6	36	255	47	44	55	1.4	20	91.5	
20 cm	10-20	5.7	5.4	9.0	80	2.8	3.4	2.9	46	1352	59	38	0.3	12	132	39	35	53	1.1	9.0	92.4	
30 cm	20-30	2.7	5.2	12.1	85	3.5	3.3	3.2	47	1587	59	40	0.3	< 10	82	31	24	20	0.6	8.2	91.2	
40 cm	30-40	3.6	4.2	9.6	61	3.6	3.0	2.8	43	1352	52	38	0.3	13	65	34	21	14	0.7	6.4	90.4	
50 cm	40-50	5.8	4.9	15.2	87	3.5	2.6	3.1	43	1810	66	43	0.4	17	86	31	24	17	0.9	6.1	87.1	
60 cm	50-60	1.8	3.0	19.2	67	3.4	1.3	3.5	28	3016	126	57	0.4	21	52	27	17	9.3	0.8	5.1	81.9	

^aFreeze-dried, homogenized, and ground peat samples (~0.5 g) were analyzed with a XEPOSTM (Spectro X Lab) energy dispersive X-ray fluorescence spectrometer (XRF) equipped with a Pd cathode and operating at 50 kV and 40 mA. Each concentration presented is an average of 3 analyses and a NIST 2711 certified reference material was intercalated during the analysis.

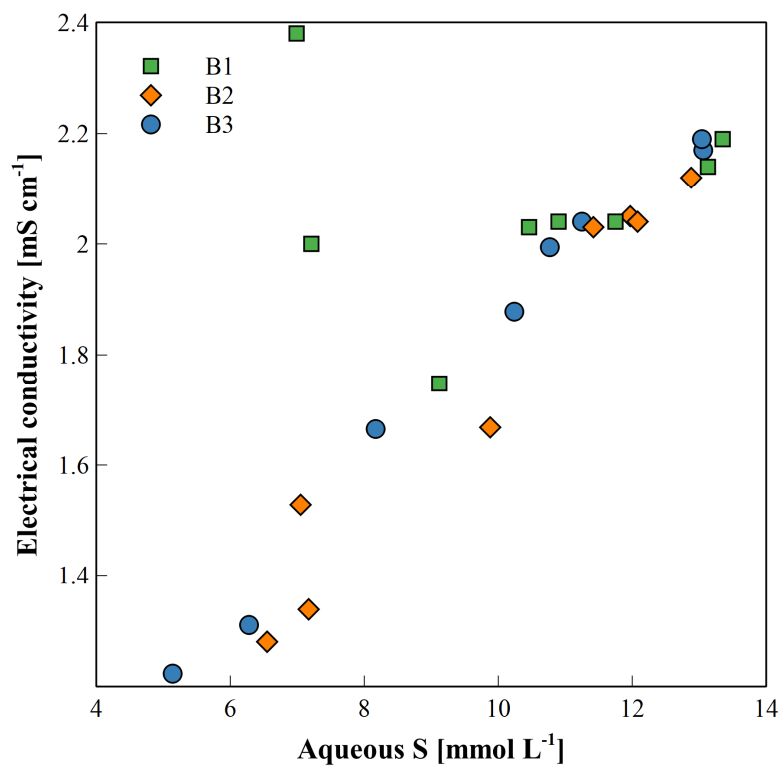
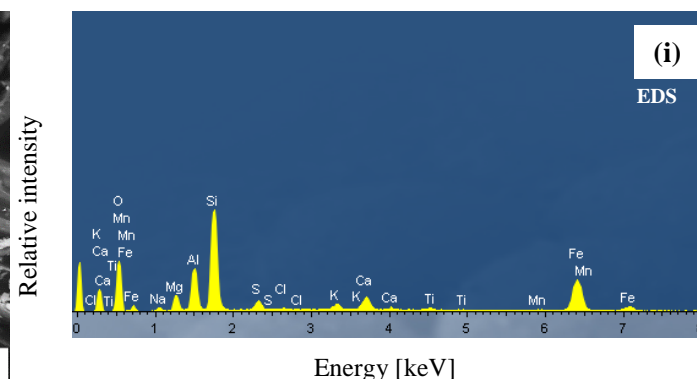
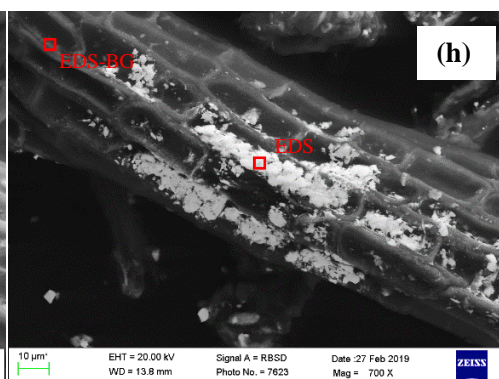
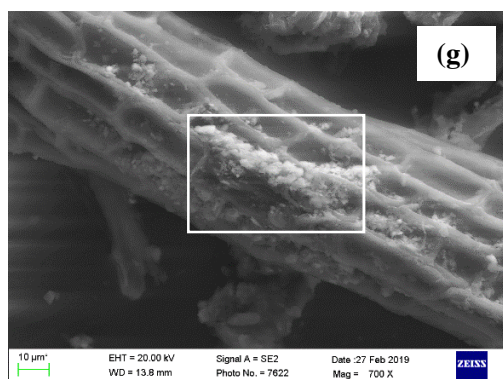
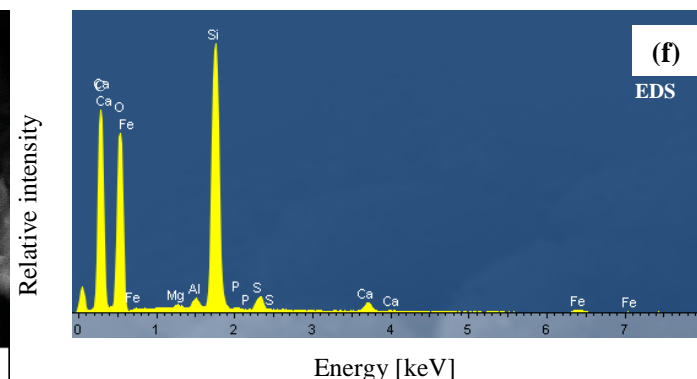
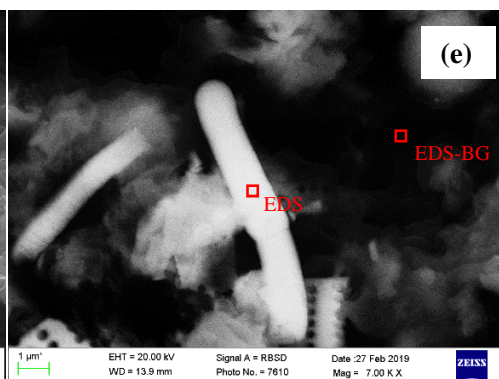
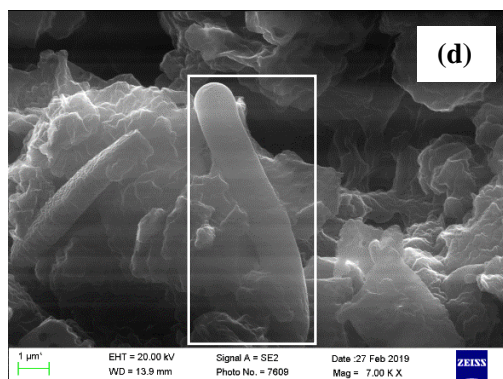
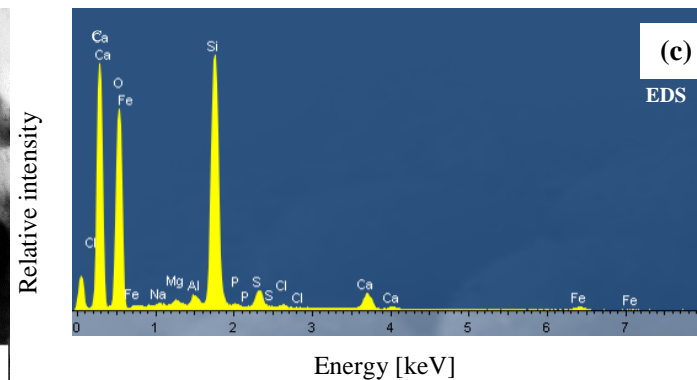
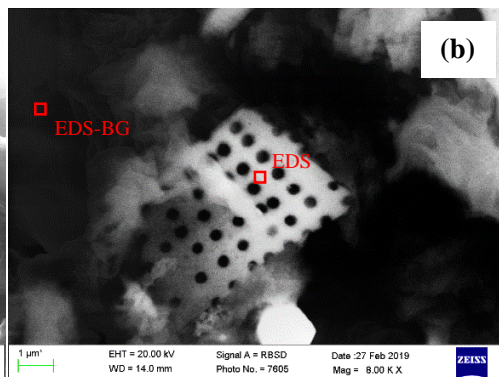
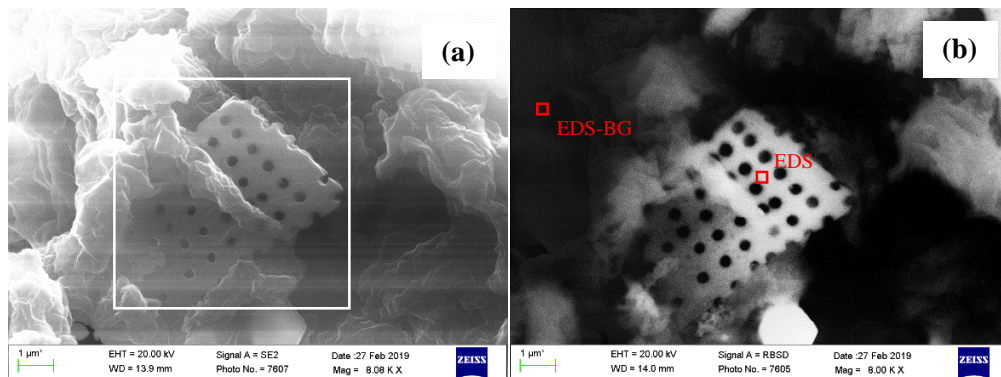
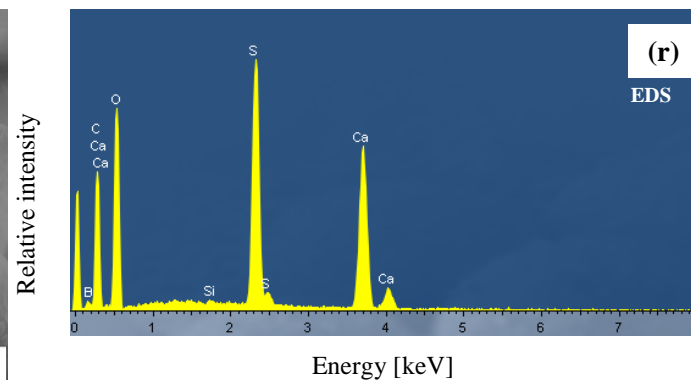
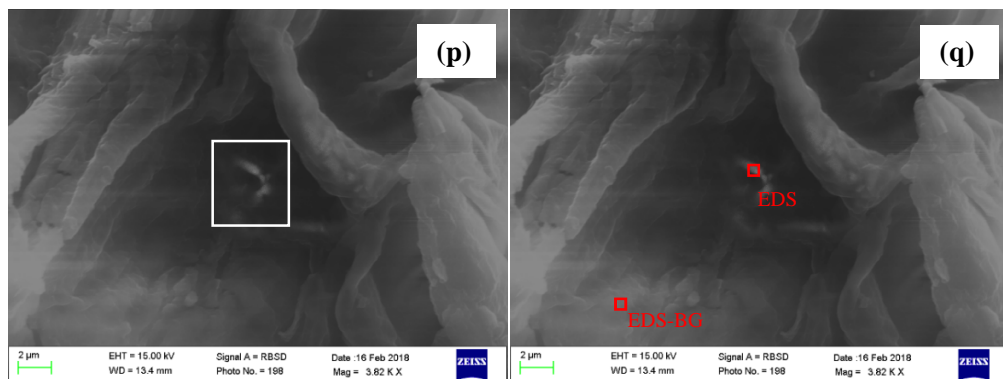
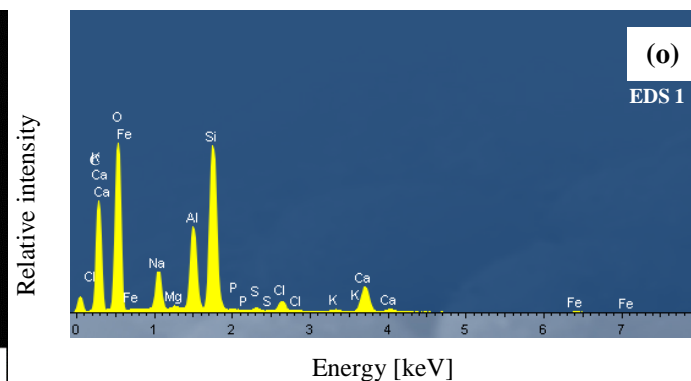
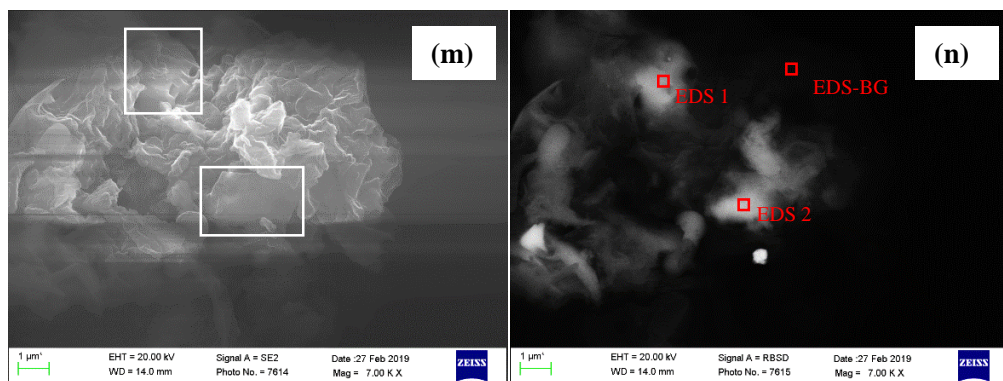
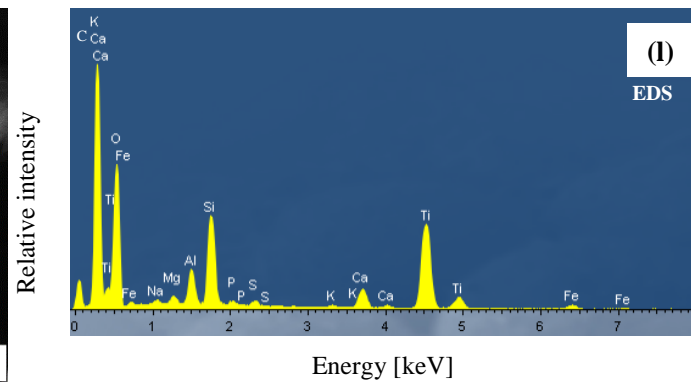
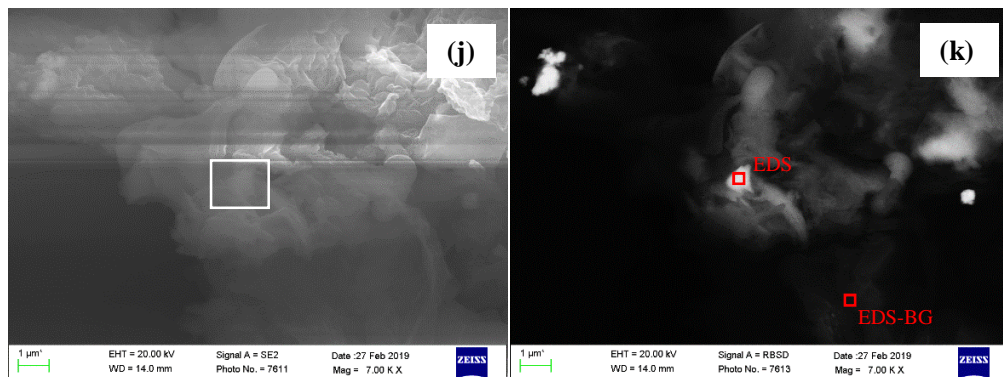


Figure SI-3: Relation between aqueous S concentration and electrical conductivity in the treatment peatland.

3. Scanning Electron Microscopy/Energy Dispersive X-Ray Spectroscopy (SEM/EDS) analyses and results

Selected freeze-dried peat samples were homogenized and fixed on adhesive carbon tape, coated with carbon, and analyzed by scanning electron microscopy (SEM) using a Leo Gemini 1530 (Carl Zeiss, Germany) with a Schottky emitter. An accelerating voltage of 20.0 keV was used to produce images with a secondary electron as well as a backscatter electron detector. Elemental composition analysis was conducted by energy-dispersive X-ray spectrometry (EDS, Oxford X-Max 20, Oxford Instruments).





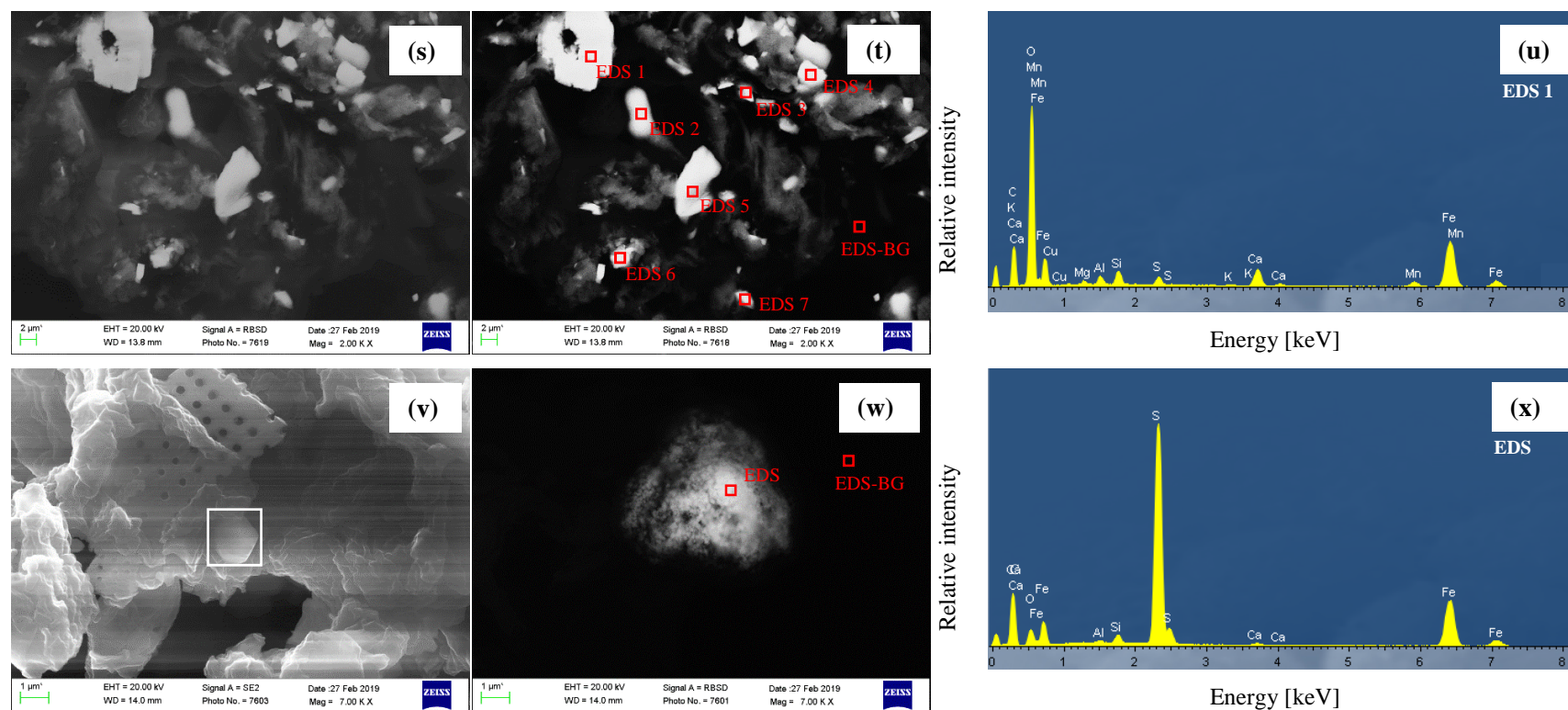


Figure SI-4: Secondary electron images (a, d, g, j, m, p, s, v), backscattered electron images (b, e, h, k, n, q, t, w) and respective (selected) energy dispersive X-ray spectroscopy analyses (EDS, c, f, i, l, o, r, u, x) of selected peat samples. Backscattered electron images were partly overlaid with secondary electron images for better visual identification. Red squares in backscattered electron images represent positions where EDS spectra were taken. Additionally to EDS spectra on a point of interest, EDS spectra from the background were taken for comparison (EDS-BG). Semi-quantitative results of all EDS analyses are displayed in **Table SI-4**.

Identified phases:

(a-c) and (d-f): Silica containing diatoms or bacteria. (g-i): Al-Fe (phyllo)silicate phases. (j-l): TiO phases. (m-o): platy Al-silicates (phyllosilicates or clay minerals). (p-r): probably artificial precipitates of CaSO₄. (s-u): EDS 1: probably a γ -FeO(OH) (lepidocrocite) phase; EDS 2-7: Al-Fe (phyllo)silicate phases in varying compositions. (v-x): FeS (mackinawite) precipitate.

Table SI-4: Semi-quantitative results of all EDS analyses from Figure SI-4. Calculations are based on respective *K* shell electron emission lines. Since samples were coated with carbon, the respective *CK* lines were not used for calculations.

Spectrum	B	O	Na	Mg	Al	Si	P	S	Cl	K	Ca	Ti	Mn	Fe	Total
	[wt%]	[wt%]	[wt%]	[wt%]	[wt%]	[wt%]	[wt%]	[wt%]	[wt%]	[wt%]	[wt%]	[wt%]	[wt%]	[wt%]	[wt%]
(b) EDS	-	65.5	0.47	0.60	0.88	25.6	0.34	2.40	0.35	-	2.71	-	-	1.22	100
(b) EDS-BG	-	65.6	0.92	1.85	3.51	9.76	1.34	4.50	1.03	-	8.46	-	-	2.99	100
(e) EDS	-	64.0	-	0.51	0.90	29.1	0.35	2.21	-	-	1.58	-	-	1.28	100
(e) EDS-BG	-	58.7	-	1.95	4.71	11.0	0.78	5.12	0.84	0.59	11.27	0.78	-	4.96	100
(h) EDS	-	32.4	1.05	3.60	8.09	20.9	-	2.33	0.33	1.27	3.74	0.81	0.41	25.01	100
(h) EDS-BG	-	79.1	1.28	1.46	-	-	-	4.63	3.28	-	8.48	-	-	1.77	100
(k) EDS	-	64.9	0.70	0.92	3.08	8.22	0.52	0.56	-	0.23	2.46	16.9	-	1.43	100
(k) EDS-BG	-	59.0	1.81	1.45	3.05	12.3	1.19	5.48	0.96	-	11.4	-	-	3.38	100
(n) EDS 1	-	60.0	6.08	0.27	8.30	18.6	0.19	0.32	1.49	0.25	4.27	-	-	0.32	100
(n) EDS 2	-	60.9	5.24	0.29	7.81	18.9	0.18	0.45	1.46	0.19	4.32	-	-	0.26	100
(n) EDS-BG	-	75.6	8.37	-	-	4.28	-	11.8	-	-	-	-	-	-	100
(q) EDS	14.7	64.5	-	-	-	0.15	-	10.8	-	-	9.9	-	-	-	100
(q) EDS-BG	-	61.2	16.9	-	4.80	3.67	-	12.9	-	-	-	-	-	-	100
(t) EDS 1	-	56.5	-	0.76	1.46	2.39	-	1.39	-	0.11	3.86	-	2.81	30.3	100
(t) EDS 2	-	59.8	-	0.17	-	38.4	-	-	-	-	0.63	-	-	0.32	100
(t) EDS 3	-	31.9	-	6.97	1.52	28.0	0.38	2.33	0.28	-	11.5	-	0.54	16.5	100
(t) EDS 4	-	51.4	0.61	6.26	2.84	19.9	-	0.54	-	0.33	6.84	0.42	0.26	10.2	100
(t) EDS 5	-	57.1	-	7.54	9.37	12.5	0.18	0.39	-	0.12	0.63	-	0.33	11.5	100
(t) EDS 6	-	62.7	5.67	0.95	6.26	17.4	0.88	1.1	-	1.04	2	-	-	2.0	100
(t) EDS 7	-	27.3	-	4.6	10.19	19.5	0.54	3.32	0.49	2.47	4.58	-	0.91	26.1	100
(t) EDS-BG	-	41.2	-	1.77	-	6.2	-	8.81	1.73	-	22.5	-	-	13.5	100

Table SI-4: *Continued*

Spectrum	B	O	Na	Mg	Al	Si	P	S	Cl	K	Ca	Ti	Mn	Fe	Total
	[wt%]	[wt%]	[wt%]	[wt%]	[wt%]	[wt%]	[wt%]	[wt%]	[wt%]	[wt%]	[wt%]	[wt%]	[wt%]	[wt%]	[wt%]
(w) EDS	-	15.7			0.42	1.57		46.0			0.58			35.7	100
(w) EDS-BG	-	61.8	1.48	1.99	3.11	7.18	0.99	7.64	1.21		10.7			3.87	100

4. Iron solid-phase speciation analyses and results

For Fe *K*-edge XAS analyses, homogenized, anoxic samples were filled into aluminum sample holders, sealed with Kapton tape and analyzed at beamline 4-1 at Stanford Synchrotron Radiation Lightsource (SSRL). The beamline was equipped with a Si(220) double crystal monochromator, which was calibrated to the *K*-edge of an Fe foil (energy: 7,112 eV). The absorption edge of the Fe foil was monitored during all sample scans. To reduce higher-order harmonics, we detuned the monochromator to 50% of the maximum beam intensity. All sample measurements were performed in fluorescence mode using a 32-element Ge array fluorescence detector (Canberra) and a He cryostat at 10 K to minimize beam damage and thermal disorder. For each sample, 3-4 scans were recorded, depending on concentration and speciation of Fe. No beam damage has been observed between each scan.

All spectra were processed using the software Athena⁴ and SIXpack⁵ and a home-made software.^{6,7} Normalization was performed by subtracting a linear function fit to the pre-edge region (-150 to -30 eV) and subsequently dividing by a quadratic polynomial fit to the post-edge region (150 to 590 eV). The edge position was defined as maximum of the first derivative of the normalized spectrum. For EXAFS analysis, E_0 was fixed to 7,122 eV. EXAFS spectra were then background-subtracted from the normalized data using the XAFS code (k-range 0.5–12 Å⁻¹).⁸ Spectra were tested for the minimum number of components by principal component analysis (PCA) based on the empirical indicator function⁹ and target-transform testing (TT) was done for the significant components against the references library using the program SIXpack.⁵ SPOIL-, R_{fTT} - and $NSSR_{TT}$ -values as well as visual confirmation were used to evaluate whether a target was acceptable.^{9,10} The spectra were then fitted by a linear combination fitting procedure using a home-made software based on the Levenberg–Marquardt minimization algorithm.^{6,7} Radial distribution functions around the Fe absorber were obtained by Fast-Fourier-transformation of the k^3 -weighted experimental function using a Kaiser-Bessel apodization window with the Bessel weight fixed to 2.5. Linear coefficients were only constrained to be positive. The accuracy of this fitting procedure ranges between $\pm 25\%$ and $\pm 5\%$ of the stated values for each individual contribution and the detection limit for minor species is estimated to be $\geq 10\%$.¹¹

Principle components analysis, target-transform testing and linear combination fitting of Fe *K*-edge XANES and EXAFS data

The suitability of reference spectra for LCF was determined by TT using the first four components (XANES and EXAFS data) calculated by PCA (based on minimum of the Malinowski indicator value⁹, Table SI-7 and Table SI-9). The quality of the transformation was evaluated by the empirical SPOIL value categorized by Malinowski¹²: 0-1.5 excellent, 1.5-3 good, 3-4.5 fair, 4.5-6 acceptable, and >6 for an unacceptable reference spectrum. All spectra with SPOIL-values <6 were used for further LCF analyses. However, the

obtained number of Fe reference spectra suitable for LCF analysis based on TT (31 out of 39 for EXAFS, 35 out of 39 for XANES) was larger than the number of principal components determined by PCA (4, XANES and EXAFS). This may be due to (i) similar local Fe coordination environments in reference compounds identified by TT or (ii) the occurrence of several species in constant proportions in all analyzed spectra¹³. Since we could not exclude the latter effect, LCF analyses were performed using all 31 Fe EXAFS and 35 Fe XANES reference spectra determined as suitable. Each experimental spectrum was least-squares simulated by calculating all single- to five-component fits. The number of components included in the fit was successively increased and each additional component was retained in the fit when the reduced chi-square value decreased at least by 10% and when the Hamilton test (following descriptions in Bennett *et al.*¹⁴) showed that the number of fitted components in one fit (N) is significantly different from fits with N-1 components and not significantly different from fits with N+1 components ($p < 0.05$). Biogeochemically reasonable models with lowest NSSR-value and closest to 100% fit sum were finally chosen as best fits (Table SI-10 and Table SI-11).

Iron reference compounds

Supplementary Table SI-5 provides an alphabetic list and details about the origin of Fe reference compounds that were analyzed by XAS and used in the PCA/TT and LCF (XANES and EXAFS) analyses of the peat samples.

Table SI-5: Iron reference compounds analyzed by XAS.

Compound	Chemical formula	Source/synthesis	Reference
2-line ferrihydrite	$(\text{Fe}^{3+})_2\text{O}_3 \cdot 0.5\text{H}_2\text{O}^{a,b}$	synthetic	Maillot <i>et al.</i> 2011 ¹⁵
6-line ferrihydrite	$(\text{Fe}^{3+})_2\text{O}_3 \cdot 0.5\text{H}_2\text{O}^{a,b}$	synthetic	Maillot <i>et al.</i> 2011 ¹⁵
Akaganeite	$\beta\text{-FeOOH}^{a,b}$	synthetic	Hohmann <i>et al.</i> 2011 ⁶
Ambient-temperature synthetic pyrite	$\text{FeS}_2^{a,b}$	synthetic	Morin <i>et al.</i> 2017 ¹⁶
Biotite	not determined	natural, Mineralogy Collection of IMPMC, Paris, France	Othmane <i>et al.</i> , 2013 ¹⁷
Chukanovite	$\text{Fe}_2(\text{CO}_3)(\text{OH})_2^{a,b}$	synthetic ^c	Azoulay <i>et al.</i> 2012 ¹⁸
Cl-Green Rust	not determined		LBL database
Crystallized goethite	$\alpha\text{-FeOOH}^{a,b}$	synthetic	Maillot <i>et al.</i> 2011 ¹⁵
Fe(II) hydroxide	$\text{Fe}(\text{OH})_2^{a,b}$	synthetic	Ona-Nguema <i>et al.</i> 2009 ¹⁹

^a estimated by XAS

^b XRD confirmed

^c Compound synthesized for this study

Table SI-5: *Continued.*

Compound	Chemical formula	Source/synthesis	Reference
Fe(II)-DOM (Suwannee River Fulvic Acid (SRFA))	not determined	Synthetic	Trusiak et al. 2018 ²⁰
Fe(II)-oxide	FeO ^{a,b}		LBL database
Fe(III)-humate (solid OM)	not determined	purified colloidal material from Rio Negro River (Brazil)	Allard et al. 2011 ²¹ Cosmidis et al. 2014 ²²
Fe(III)-phosphate	FePO ₄ ^{a,b}	natural	Cosmidis et al. 2014 ²²
Ferrosmeectite	not determined		LBL database
Goethite	α -FeOOH ^{a,b}	synthetic	Maillot et al. 2011 ¹⁵
Greigite	Fe ₃ S ₄ ^{a,b}		Noël et al, 2014 ²³
Hematite	α -Fe ₂ O ₃ ^{a,b}	synthetic	Hohmann et al. 2011 ⁶
Illite	not determined	natural, Le Puy-en-Velay, France	Noël et al. 2014 ²³
Iron(II) sulfate heptahydrate	FeSO ₄ · 7H ₂ O ^{a,b}	Sigma	Kumar et al. 2018 ²⁴
Lepidocrocite	χ -FeOOH ^{a,b}	synthetic	Ona-Nguema et al. 2005 ²⁵
Mackinawite_abio_Fe(II)	FeS ^{a,b}	Synthesized with Fe(II)	Bone et al. 2014 ²⁶
Mackinawite_abio_Fe(III)	FeS ^{a,b}	Synthesized with abiotic reduction of Fe(III)	Morin et al. 2017 ¹⁶
Mackinawite_bio_Fe(III)	FeS ^{a,b}	synthesized from microbial reduction of Fe(III)	Ikogou et al. 2017 ²⁷
Maghemite	χ -Fe ₂ O ₃ ^{a,b}	synthetic	Hohmann et al. 2011 ⁶
Magnetite	Fe ₃ O ₄ ^{a,b}	synthetic (biogenic)	Wang et al. 2008 ²⁸
Marcassite	FeS ₂ ^{a,b}	synthetic ^c	This study
Mg-rich chlorite	not determined	natural, by D. Beaufort, Université de Poitiers, France	Othmane et al., 2013 ¹⁷
Minimally oxidized mackinawite	FeS ^{a,b}	synthetic	Noël et al. 2017 ²⁹
Nano-goethite	FeOOH ^{a,b}	synthetic	Kumar et al. 2018 ²⁴
Natural pyrite	FeS ₂ ^{a,b}	Natural	This study

^a estimated by XAS^b XRD confirmed^c Compound synthesized for this study

Table SI-5: *Continued.*

Compound	Chemical formula	Source/synthesis	Reference
Nontronite	not determined	natural, Garfield nontronite (Washington, USA)	Noël et al. 2014 ²³
Phlogopite	not determined	natural	Mineral collection, IMPMC, Paris VI, France
Pyrrhotite	FeS ^{a,b}	synthetic ^c	This study
Schwertmannite	Fe ₈ O ₈ (OH) ₆ SO ₄ ^{a,b}	synthetic	Maillot et al. 2013 ³⁰
Serpentine	not determined	natural, New Idria Mining District (California, USA)	Noël et al. 2014 ²³
Siderite	Fe(CO ₃) ^{a,b}	synthetic	Dublet et al. 2012 ³¹
SO ₄ -Green Rust	not determined	synthetic	LBL database, Pantke et al. 2012 ⁷
Vermiculite	not determined	natural	Mineral collection, IMPMC, Paris VI, France
Vivianite	Fe ₃ (PO ₄) ₂ •8H ₂ O ^{a,b}	synthetic	Cosmidis et al. 2014 ²²

^aestimated by XAS^bXRD confirmed^cCompound synthesized for this study**Table SI-6:** Results from PCA of 7 *k*³-weighted peat sample Fe EXAFS spectra ($E_0 = 7122$ eV, *k*-range 2–12 Å⁻¹).

Compound	PCA EXAFS		
	Eigenvalue	Cum. Var. ^a	IND ^b
1	47.657	0.920	0.02750
2	2.703	0.960	0.02251
3	1.088	0.981	0.01975
4	0.595	0.993	0.01360
5	0.170	0.996	0.02221
6	0.112	0.998	0.05600
7	0.056	1.0	NA

^acumulative variance^bindicator function⁹

Table SI-7: Results of Fe EXAFS TT analysis (against 4 PCs). Compounds with SPOIL > 6.0 (*in italic*) were not considered for further analysis.

Name of reference compound	SPOIL-value ^a	Rf _{TT} ^b	NSSR _{TT}
Fe(III)-humate	0.84	0.07	127
Iron(II) sulfate heptahydrate	1.10	0.13	186
Fe(II)-DOM (Suwannee River Fulvic Acid (SRFA))	1.21	0.12	186
Fe(III)-phosphate	1.28	0.14	282
Illite	1.94	0.17	425
Minimally oxidized mackinawite	2.15	0.06	138
Biotite	2.21	0.26	326
Mackinawite_bio	2.24	0.09	289
Mackinawite_abio	2.44	0.08	201
Ferrosmeectite	2.58	0.30	487
Vivianite	2.60	0.31	346
Phlogopite	2.89	0.34	570
Vermiculite	2.94	0.20	374
2-line ferrihydrite	3.10	0.38	444
Nontronite	3.31	0.39	917
Schwertmannite	3.40	0.38	627
6-line ferrihydrite	3.55	0.43	538
Lepidocrocite	4.04	0.49	2008
Serpentine	4.50	0.29	247
Fe(II) hydroxide	4.52	0.64	1333
Chukanovite*	4.53	0.62	745
Siderite	4.75	0.65	2704

^a SPOIL classification (Malinowski 1978)¹²: 0–1.5, excellent; 1.5– 3, good; 3–4.5, fair; 4.5–6, acceptable; and >6, unacceptable reference

^b Calculated as $\Sigma(k^3\chi_{\text{exp}} - k^3\chi_{\text{fit}})^2 / \Sigma(k^3\chi_{\text{exp}})^2$

Table SI-7: Continued.

Name of reference compound	SPOIL-value ^a	Rf _{TT} ^b	NSSR _{TT}
Goethite	4.78	0.48	1086
Hematite	5.23	0.73	5524
Pyrrhothite	5.33	0.24	449
Mackinawite from Fe ²⁺	5.44	0.55	3034
Cl-Green Rust	5.46	0.58	817
Marcassite	5.47	0.40	1917
Fe(II)-oxide	5.70	0.65	1164
Nano-Goethite	5.88	0.57	1279
Mg-rich chlorite	5.99	0.42	607
<i>Akaganeite</i>	6.08	0.55	813
<i>Ambiant-temperature synthetic pyrite</i>	6.10	0.39	3920
<i>SO₄-Green Rust</i>	6.34	0.63	532
<i>Greigite</i>	6.44	0.59	600
<i>Cristallized goethite</i>	6.54	0.60	1362
<i>Maghemite</i>	7.50	0.77	1820
<i>Natural pyrite</i>	7.78	0.53	8035
<i>Magnetite</i>	9.56	0.71	1145

^a SPOIL classification (Malinowski 1978)¹²: 0–1.5, excellent; 1.5– 3, good; 3–4.5, fair; 4.5–6, acceptable; and >6, unacceptable reference

^b Calculated as $\Sigma(k^3\chi_{\text{exp}}-k^3\chi_{\text{fit}})^2/\Sigma(k^3\chi_{\text{exp}})^2$

Table SI-8: Results from PCA of 7 peat sample Fe XANES spectra (7102-7152 eV).

Compound	PCA XANES		
	Eigenvalue	Cum. Var. ^a	IND ^b
1	48.142	0.919	0.02848
2	1.955	0.956	0.02822
3	1.462	0.984	0.01851
4	0.575	0.995	0.00901
5	0.121	0.998	0.01245
6	0.064	0.999	0.02751
7	0.027	1	NA

^acumulative variance^bindicator function⁹**Table SI-9:** Results of Fe XANES TT analysis (against 4 PCs). Compounds with SPOIL > 6.0 (*in italic*) were not considered for further analysis.

Name of reference compound	SPOIL-value ^a	Rf _{TT} ^b	NSSR _{TT}
Mackinawite_abio	1.06	0.00008	0.02
Mackinawite_bio	1.09	0.00015	0.04
Fe(III)-humate	1.26	0.0002	0.08
Iron(II) sulfate heptahydrate	1.56	0.00051	0.20
Phlogopite	1.83	0.00118	0.47
Fe(III)-phosphate	1.91	0.0007	0.27
Goethite	1.91	0.0005	0.19
Cristallized goethite	2.42	0.00052	0.18
Fe(II)-DOM (Suwannee River Fulvic Acid (SRFA))	2.48	0.00077	0.30
Biotite	2.51	0.0003	0.11
Lepidocrocite	2.56	0.00096	0.36
Nano-Goethite	2.57	0.00062	0.21
Pyrrhothite	2.64	0.00033	0.10
Serpentine	2.67	0.00053	0.19

^a SPOIL classification (Malinowski 1978)¹²: 0–1.5, excellent; 1.5– 3, good; 3–4.5, fair; 4.5–6, acceptable; and >6, unacceptable reference^b Calculated as $\Sigma(k^3\chi_{\text{exp}}-k^3\chi_{\text{fit}})^2/\Sigma(k^3\chi_{\text{exp}})^2$

Table SI-9: *Continued.*

Name of reference compound	SPOIL-value ^a	Rf _{TT} ^b	NSSR _{TT}
Minimally oxidized mackinawite	2.70	0.00049	0.15
Mackinawite from Fe ²⁺	2.81	0.00083	0.24
Schwertmannite	3.19	0.0016	0.60
2-line ferrihydrite	3.25	0.00097	0.34
Vivianite	3.30	0.00105	0.40
6-line ferrihydrite	3.82	0.00133	0.48
Greigite	3.97	0.00057	0.18
Akaganeite	4.05	0.00068	0.26
Hematite	4.08	0.00142	0.51
Ferrosmeectite	4.19	0.00155	0.50
Ambiant-temperature synthetic pyrite	4.23	0.00203	0.62
Marcassite	4.24	0.00188	0.57
Nontronite	4.31	0.00302	1.20
Mg-rich chlorite	4.61	0.00197	0.74
Siderite	4.66	0.00888	3.50
Fe(II) hydroxide	4.86	0.0008	0.27
Cl-Green Rust	4.87	0.00034	0.12
Natural pyrite	5.26	0.0032	1.04
Illite	5.52	0.00366	1.37
Chukanovite	5.35	0.00139	0.48
Fe(II)-oxide	5.89	0.00173	0.59
<i>Maghemite</i>	<i>6.40</i>	<i>0.00283</i>	<i>1.01</i>

^a SPOIL classification (Malinowski 1978)¹²: 0–1.5, excellent; 1.5– 3, good; 3–4.5, fair; 4.5–6, acceptable; and >6, unacceptable reference

^b Calculated as $\Sigma(k^3\chi_{\text{exp}} - k^3\chi_{\text{fit}})^2 / \Sigma(k^3\chi_{\text{exp}})^2$

Table SI-9: *Continued.*

Name of reference compound	SPOIL-value ^a	Rf _{TT} ^b	NSSR _{TT}
<i>Magnetite</i>	6.49	0.00146	0.51
<i>SO₄-Green Rust</i>	6.80	0.00063	0.21
<i>Vermiculite</i>	8.66	0.00706	2.81

^a SPOIL classification (Malinowski 1978)¹²: 0–1.5, excellent; 1.5– 3, good; 3–4.5, fair; 4.5–6, acceptable; and >6, unacceptable reference

^b Calculated as $\Sigma(k^3\chi_{\text{exp}}-k^3\chi_{\text{fit}})^2/\Sigma(k^3\chi_{\text{exp}})^2$

Table SI-10: Linear Combination Fit results for *k*³-weighted Fe *K*-edge EXAFS spectra of the studied peat samples.^a

Sample	Fe [mmol kg ⁻¹]	Edge position ^b [eV]	Phyllosilicates ^c [atomic%]	Fe(III)-NOM ^d [atomic%]	Fe(II)- NOM ^e [atomic%]	FeS ^f [atomic%]	Initial fit sums [atomic%]	NSSR ^g [%]
B1 20 cm	152	7,120.4	32 (12/10/10)	23	24	21	100	2.4
B1 40 cm	59	7,120.8	43 (16/10/17)	-	25	31	106	4.1
B1 60 cm	127	7,120.5	-	-	47	53	95	3.2
B2 20 cm	58	7,120.6	-	47	15	37	99	3.0
B2 60 cm	59	7,120.7	-	10	42	48	96	4.9
B3 10 cm	61	7,120.0	22 (0/11/11)	12	48	18	93	3.5
B3 50 cm	95	7,120.9	-	-	29	71	103	4.0

^aFit range: 2–12 Å⁻¹, E₀ = 7122 eV. Fitted fractions were normalized to a component sum of 100%. Fitted fractions are accurate within ±10 atom% at best. Number of fitted components in one fit (N) is significantly different from fits with N-1 components and not significantly different from fits with N+1 components (Hamilton test, p < 0.05). Biogeochemically reasonable models with lowest NSSR and closest to 100% fit sum were chosen as best fits. ^bThe edge position is defined as maximum of the first derivative of the normalized XANES spectrum. Fit references: ^cPhyllosilicates; values in parentheses: (Biotite/Nontronite/Phlogopite). ^dFe(III)-NOM = Fe(III)-humate. ^eFe(II)-NOM = Fe(II)-DOM (Suwannee River Fulvic Acid (SRFA)). ^fFeS = Mackinawite_bio. ^gNormalized sum of squared residuals ($100 \times \Sigma_i(\text{data}_i - \text{fit}_i)^2 / \Sigma_i \text{data}_i^2$).

Table SI-11: Linear Combination Fit results for normalized Fe *K*-edge XANES spectra of the studied peat samples.^a

Sample	Fe [mmol kg ⁻¹]	Edge position ^b [eV]	Phyllosilicates ^c [atomic%]	Fe(III)-NOM ^d [atomic%]	Fe(II)- NOM ^e [atomic%]	FeS ^f [atomic%]	Initial fit sums [atomic%]	NSSR ^g [%]
B1 20 cm	152	7,120.4	35 (10/15/10)	18	20	26	99	3.9
B1 40 cm	59	7,120.8	45 (14/10/21)	-	18	37	100	2.2
B1 60 cm	127	7,120.5	10 (0/0/10)	-	40	49	99	11
B2 20 cm	58	7,120.6	-	41	20	39	93	2.9
B2 60 cm	59	7,120.7	-	10	36	54	97	9.7
B3 10 cm	61	7,120.0	25 (0/11/14)	10	38	27	104	17
B3 50 cm	95	7,120.9	12 (0/0/12)	-	13	76	94	7.1

^aFit range: 7102-7152 eV. Fitted fractions were normalized to a component sum of 100%. Fitted fractions are accurate within ± 10 atom% at best. Number of fitted components in one fit (N) is significantly different from fits with N-1 components and not significantly different from fits with N+1 components (Hamilton test, $p < 0.05$). Biogeochemically reasonable models with lowest NSSR and closest to 100% fit sum were chosen as best fits. ^bThe edge position is defined as maximum of the first derivative of the normalized XANES spectrum. Fit references: ^cPhyllosilicates; values in parentheses: (Biotite/Nontronite/Phlogopite). ^dFe(III)-NOM = Fe(III)-humate. ^eFe(II)-NOM = Fe(II)-DOM (Suwannee River Fulvic Acid (SRFA)). ^fFeS = Mackinawite_bio. ^gNormalized sum of squared residuals ($100 \times \sum_i (\text{data}_i - \text{fit}_i)^2 / \sum_i \text{data}_i^2$).

Table SI-12: Average deviation between fitted Fe XANES and Fe EXAFS fractions from Table SI-10 and Table SI-11.

Deviation average [Fe XANES - Fe EXAFS fractions]	
Phyllosilicates	± 6.0
Fe(III)-NOM	± 3.3
Fe(II)-NOM	± 7.8
FeS	± 5.3

5. Sulfur solid-phase speciation analyses and results

For S *K*-edge XANES analysis, homogenized peat samples were filled into multi-slot sample holders and sealed with Kapton tape. If necessary, the S concentration was adjusted to $\leq 1,800 \text{ mg kg}^{-1}$ with boron nitride in order to reduce self-absorption effects.³² Spectra were collected at beamline 4-3 at the Stanford Synchrotron Radiation Lightsource (SSRL), Stanford, USA. The Si(111) double crystal monochromator was calibrated relative to the white-line energy of a sodium thiosulfate standard (2,472.02 eV) which was constantly monitored between two sample runs. All measurements were performed at room temperature under constant He stream ($<0.1\%$ (v/v) O₂) in fluorescence mode using a 4-element solid-state Si drift detector (HTA Hitachi).

Between 3 and 4 scans per sample were recorded, averaged and normalized. Normalization was performed by subtracting a linear function fit to the pre-edge region (-32 to -7 eV) and subsequently dividing by another linear function fit to the post-edge region (38 to 275 eV) in Athena.⁴ Normalized S *K*-edge XANES spectra were then deconvoluted in Athena following the fitting approach recommended by Manceau and Nagy.³³ Deconvolution of the spectra was performed in the energy range 2,465-2,490 eV using two arctan functions (edge steps of reduced and oxidized S species) and seven Gaussian functions representing S *s* → *p* transition peaks of inorganic (mono) sulfide, exocyclic/elemental S, heterocyclic S, sulfoxide S, sulfone S, sulfonate S, and sulfate S. The step heights of the arctan functions were fitted, whereby their positions (energy of center) and widths were fixed in all model fits. Likewise, the positions (except for inorganic (mono) sulfide) and areas of all Gaussians were fit, while keeping the sigma values (standard deviation of Gaussian) fixed in all model fits to values determined beforehand. Following the approach of Manceau and Nagy³³, the position of the arctan (reduced species) was constrained to be located close to the Gaussian functions of the reduced sulfur functionalities (before the center of the sulfoxide Gaussian function) in order to obtain correct sulfur fractions. The fitted peak areas were corrected for the oxidation state dependent absorption cross-section of S using the generic equation of Manceau and Nagy.³³ The atomic fraction of each S species in the peat samples was then calculated by dividing its corrected peak area by the total peak area sum. Please note that the intermediate oxidized fractions (sulfoxide and sulfone S) are likely to be overestimated due to post-edge absorption features of reduced S species.³³ Figure SI-5 illustrates the Gaussian fit envelopes and experimental spectra, Table SI-13 summarizes the detailed fit results and Figure SI-6 gives a visual overview of the corrected atomic fractions.

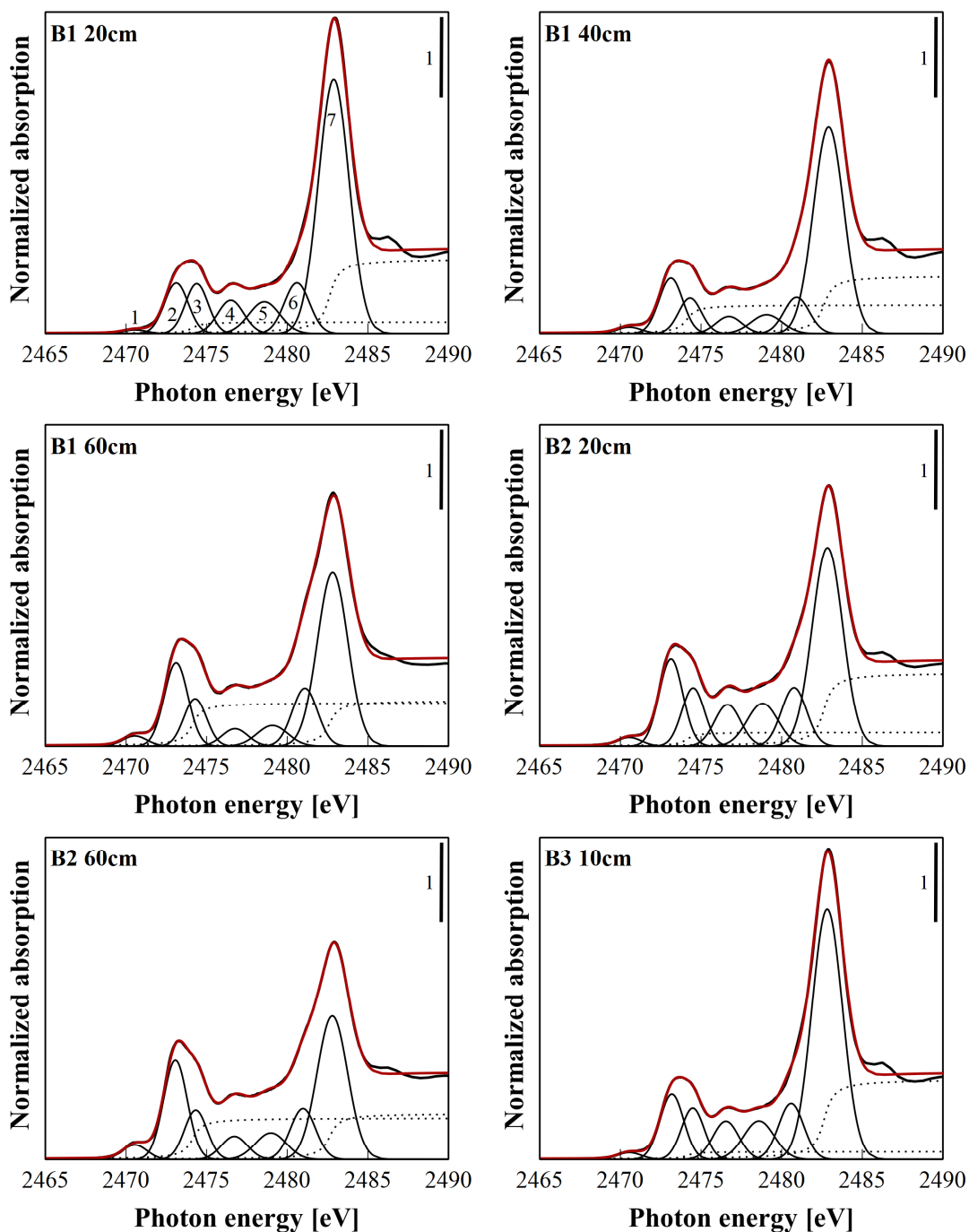


Figure SI-5: Gaussian curve fits of peat spectra. Experimental data is shown as black and fit envelopes as red lines. The two arctan functions are shown as dotted lines and the Gaussian peaks correspond to (from 1 to 7) inorganic (mono) sulfide (1), exocyclic/elemental S (2), heterocyclic S (3), sulfoxide S (4), sulfone S (5), sulfonate S (6), and sulfate S (7). The fit parameters for all samples are reported in Table SI-13. Misfit after ca. 2,485 eV depends on post-edge absorption features of the dominant sulfate peak (particularly gypsum, please compare with Figure SI-7).

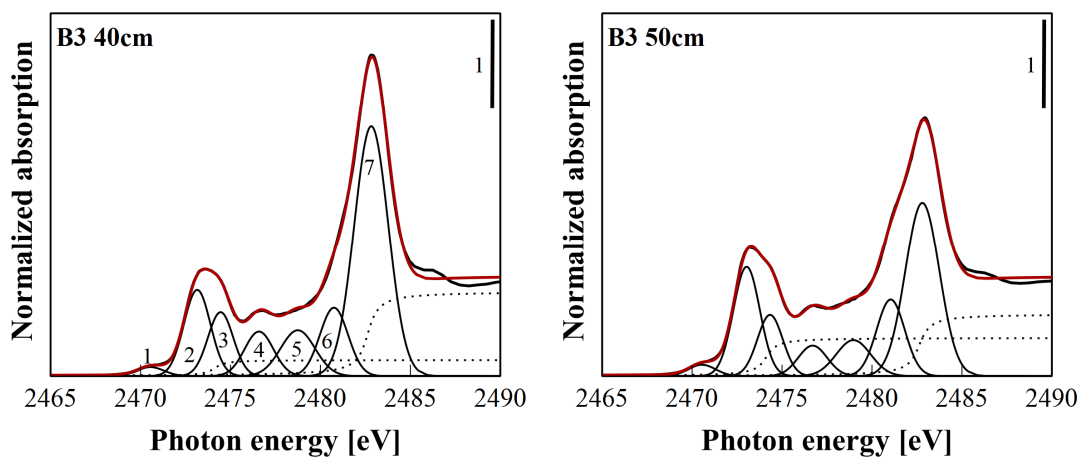


Figure SI-5: *Continued.* Gaussian curve fits of peat spectra. Experimental data is shown as black and fit envelopes as red lines. The two arctan functions are shown as dotted lines and the Gaussian peaks correspond to (from 1 to 7) inorganic (mono) sulfide (1), exocyclic/elemental S (2), heterocyclic S (3), sulfoxide S (4), sulfone S (5), sulfonate S (6), and sulfate S (7). The fit parameters for all samples are reported in Table SI-13. Misfit after ca. 2,485 eV depends on post-edge absorption features of the dominant sulfate peak (particularly gypsum, please compare with Figure SI-7).

Table SI-13: Gaussian deconvolution of normalized S *K*-edge XANES spectra of peat samples.

Sample	Fitted functions	Energy ^a (center) [eV]	Width (arctan)		Corrected area ^b	Fraction [atomic%]	NSSR ^c [*10 ⁴]
			or sigma (Gaussian)	Step (arctan) or area (Gaussian)			
B1 20 cm	Arctan (reduced S species)	2,474.03	0.45	0.15	-	-	4.06
	Arctan (oxidized S species)	2,482.53	0.45	0.98	-	-	
	Inorganic (mono) sulfide	2,470.65	0.76	0.09	0.45	9	
	Exocyclic/elemental S	2,473.12	0.73	1.21	1.09	22	
	Heterocyclic S	2,474.39	0.70	1.14	0.72	14	
	Sulfoxide S	2,476.50	0.80	0.87	0.37	7	
	Sulfone S	2,478.58	0.96	0.99	0.32	6	
	Sulfonate S	2,480.60	0.78	1.29	0.33	7	
	Sulfate S	2,482.79	0.95	7.91	1.69	34	
	B1 40 cm	Arctan (reduced S species)	2,474.03	0.45	0.40	-	
Arctan (oxidized S species)		2,482.53	0.45	0.72	-	-	
Inorganic (mono) sulfide		2,470.65	0.76	0.16	0.77	19	
Exocyclic/elemental S		2,473.12	0.73	1.30	1.16	29	
Heterocyclic S		2,474.27	0.70	0.80	0.52	13	
Sulfoxide S		2,476.71	0.80	0.38	0.16	4	
Sulfone S		2,479.03	0.96	0.51	0.16	4	
Sulfonate S		2,480.91	0.78	0.89	0.22	6	
Sulfate S		2,482.82	0.95	4.65	0.99	25	
B1 60 cm		Arctan (reduced S species)	2,474.03	0.45	0.57	-	-
	Arctan (oxidized S species)	2,482.53	0.45	0.60	-	-	
	Inorganic (mono) sulfide	2,470.65	0.76	0.25	1.23	22	
	Exocyclic/elemental S	2,473.10	0.73	2.00	1.80	32	
	Heterocyclic S	2,474.27	0.70	1.12	0.73	13	
	Sulfoxide S	2,476.75	0.80	0.46	0.19	3	
	Sulfone S	2,479.07	0.96	0.66	0.20	4	
	Sulfonate S	2,481.09	0.78	1.50	0.37	7	
	Sulfate S	2,482.82	0.95	5.39	1.15	20	

^aEnergy of the white-line maximum. Parameters with identical numbers (in italic) were fixed during fitting. ^bArea after correction for the oxidation state-dependent absorption cross-section of S with the “generic equation” of Manceau and Nagy.³³ ^cNormalized sum of squared residuals ($10^5 \times \sum_i (\text{data}_i - \text{fit}_i)^2 / \sum_i \text{data}_i^2$).

Table SI-13: *Continued.*

Sample	Fitted functions	Energy ^a	Width (arctan)	Step (arctan) or area (Gaussian)	Corrected area ^b	Fraction	NSSR ^c
		(center) [eV]	or sigma (Gaussian)				
B2 20 cm	Arctan (reduced S species)	2,474.03	0.45	0.19	-	-	2.45
	Arctan (oxidized S species)	2,482.53	0.45	0.96	-	-	
	Inorganic (mono) sulfide	2,470.65	0.76	0.22	1.06	17	
	Exocyclic/ elemental S	2,473.14	0.73	2.10	1.87	30	
	Heterocyclic S	2,474.51	0.70	1.35	0.83	13	
	Sulfoxide S	2,476.65	0.80	1.09	0.45	7	
	Sulfone S	2,478.82	0.96	1.34	0.42	7	
	Sulfonate S	2,480.77	0.78	1.50	0.38	6	
	Sulfate S	2,482.74	0.95	6.16	1.32	21	
B2 60 cm	Arctan (reduced S species)	2,474.03	0.45	0.53	-	-	1.72
	Arctan (oxidized S species)	2,482.53	0.45	0.62	-	-	
	Inorganic (mono) sulfide	2,470.65	0.76	0.36	1.77	27	
	Exocyclic/ elemental S	2,473.07	0.73	2.41	2.19	34	
	Heterocyclic S	2,474.35	0.70	1.14	0.73	11	
	Sulfoxide S	2,476.74	0.80	0.64	0.26	4	
	Sulfone S	2,478.99	0.96	0.87	0.26	4	
	Sulfonate S	2,480.98	0.78	1.32	0.33	5	
	Sulfate S	2,482.80	0.95	4.46	0.95	15	
B3 10 cm	Arctan (reduced S species)	2,474.03	0.45	0.10	-	-	4.29
	Arctan (oxidized S species)	2,482.53	0.45	1.05	-	-	
	Inorganic (mono) sulfide	2,470.65	0.76	0.17	0.82	14	
	Exocyclic/ elemental S	2,473.19	0.73	1.57	1.38	24	
	Heterocyclic S	2,474.49	0.70	1.18	0.73	13	
	Sulfoxide S	2,476.54	0.80	1.01	0.43	7	
	Sulfone S	2,478.60	0.96	1.21	0.39	7	
	Sulfonate S	2,480.59	0.78	1.44	0.37	6	
	Sulfate S	2,482.73	0.95	7.75	1.67	29	

^aEnergy of the white-line maximum. Parameters with identical numbers (in italic) were fixed during fitting. ^bArea after correction for the oxidation state-dependent absorption cross-section of S with the “generic equation” of Manceau and Nagy.³³ ^cNormalized sum of squared residuals ($10^5 \times \sum_i (\text{data}_i - \text{fit}_i)^2 / \sum_i \text{data}_i^2$).

Table SI-13: *Continued.*

Sample	Fitted functions	Energy ^a	Width (arctan)	Step (arctan) or area (Gaussian)	Corrected area ^b	Fraction	NSSR ^c
		(center) [eV]	or sigma (Gaussian)				
B3 40 cm	Arctan (reduced S species)	2,474.03	0.45	0.13	-	-	2.97
	Arctan (oxidized S species)	2,482.53	0.45	1.04	-	-	
	Inorganic (mono) sulfide	2,470.65	0.76	0.21	1.01	16	
	Exocyclic/ elemental S	2,473.19	0.73	1.91	1.67	27	
	Heterocyclic S	2,474.52	0.70	1.31	0.80	13	
	Sulfoxide S	2,476.60	0.80	1.14	0.47	8	
	Sulfone S	2,478.76	0.96	1.40	0.44	7	
	Sulfonate S	2,480.76	0.78	1.63	0.41	7	
	Sulfate S	2,482.72	0.95	6.92	1.49	24	
B3 50 cm	Arctan (reduced S species)	2,474.03	0.45	0.43	-	-	1.95
	Arctan (oxidized S species)	2,482.53	0.45	0.73	-	-	
	Inorganic (mono) sulfide	2,470.65	0.76	0.25	1.23	20	
	Exocyclic/ elemental S	2,473.04	0.73	2.34	2.15	35	
	Heterocyclic S	2,474.35	0.70	1.24	0.79	13	
	Sulfoxide S	2,476.70	0.80	0.72	0.30	5	
	Sulfone S	2,478.97	0.96	1.02	0.31	5	
	Sulfonate S	2,481.04	0.78	1.74	0.43	7	
	Sulfate S	2,482.80	0.95	4.78	1.02	16	

^aEnergy of the white-line maximum. Parameters with identical numbers (in italic) were fixed during fitting. ^bArea after correction for the oxidation state-dependent absorption cross-section of S with the “generic equation” of Manceau and Nagy.³³ ^cNormalized sum of squared residuals ($10^5 \times \sum_i (\text{data}_i - \text{fit}_i)^2 / \sum_i \text{data}_i^2$).

Table SI-14: Fitted atomic fractions of Gaussian deconvolutions of normalized S K-edge XANES spectra of peat samples grouped to reduced S (oxidation states -II to +I): inorganic (mono) sulfide, exocyclic/elemental S, heterocyclic S; intermediate oxidized S (oxidation states >+I to +III): sulfoxide S, sulfone S and oxidized S (oxidation states >+III to +VI): sulfonate S, sulfate S.

Sample	Intermediate		
	Reduced S	oxidized S	Oxidized S
	[%]	[%]	[%]
B1 20 cm	45	14	41
B1 40 cm	62	8	31
B1 50 cm	66	7	27
B2 20 cm	59	14	27
B2 60 cm	72	8	20
B3 10 cm	51	14	35
B3 40 cm	55	14	30
B3 50 cm	67	10	23

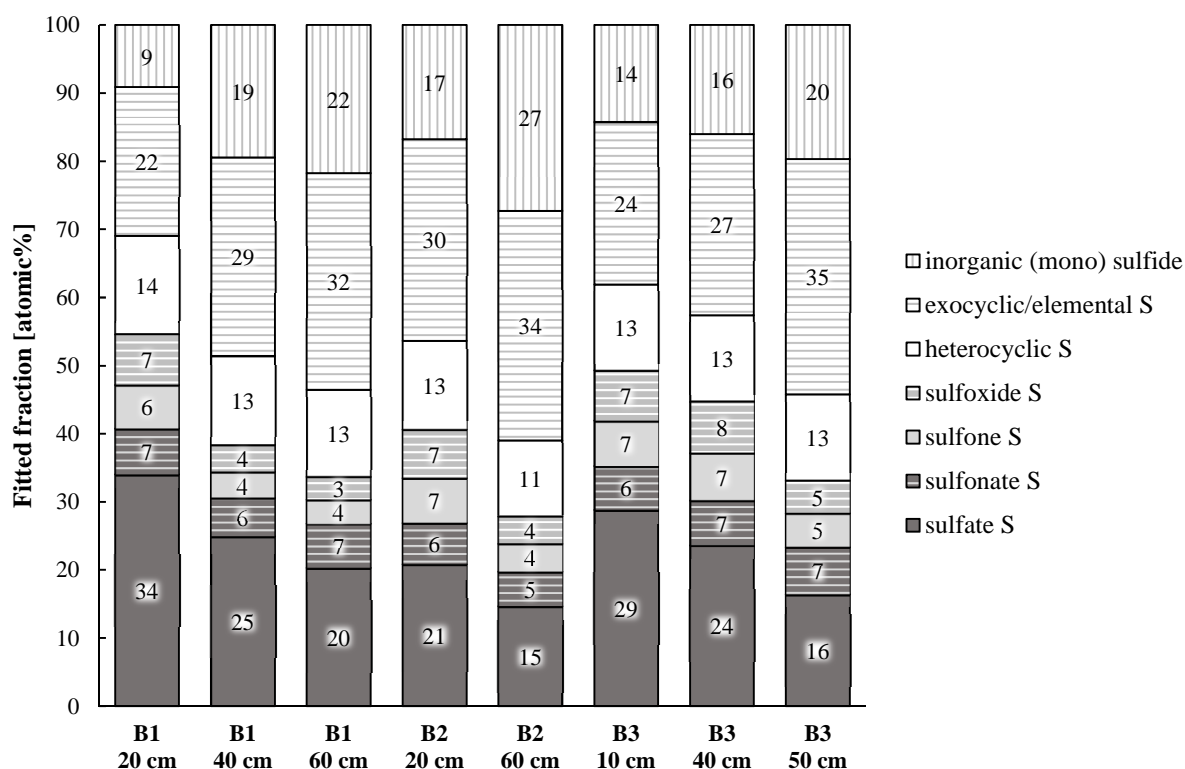


Figure SI-6: Corrected atomic fractions of Gaussian deconvolutions of normalized S K-edge XANES spectra of peat samples. Please note that the intermediate oxidized fractions (sulfoxide and sulfone S) are likely to be overestimated due to post-edge absorption features of reduced S species.³³ The detection limit of this method is ~10atomic%, so fractions <10atomic% may be questionable. However, we suppose the occurrence of components inferior to 10% as legitimate components if the occurrence of these S species are visually distinguished by the occurrence of its main edge (1s-4p)

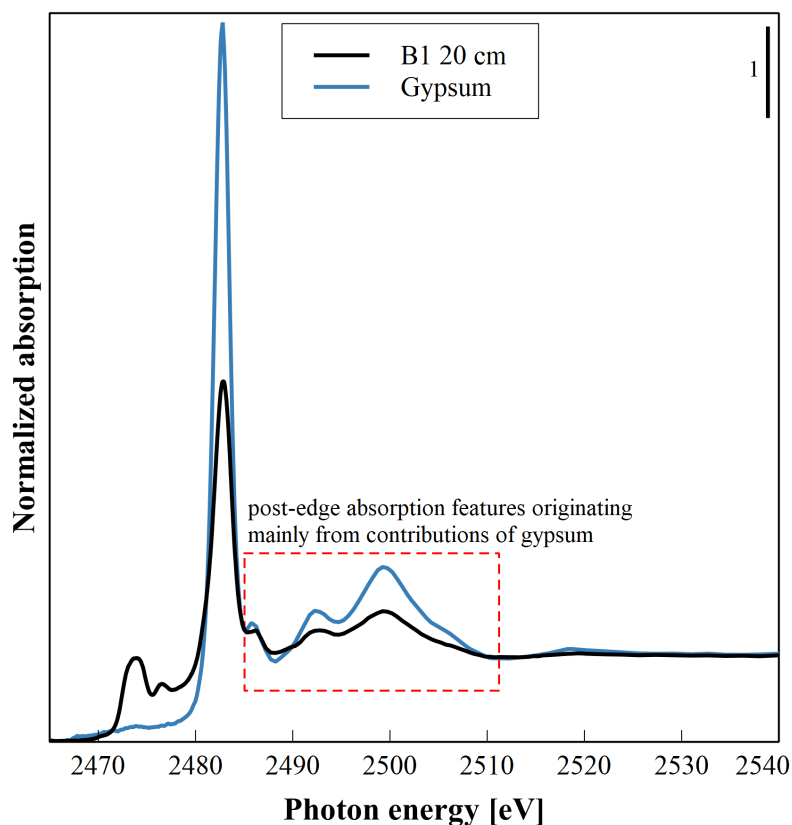


Figure SI-7: Similar significant post-edge absorption features of peat samples with high sulfate-peak contribution and the gypsum spectrum. Gypsum formation is most probably an artifact of the sample drying procedure. The post-edge feature explains the mismatch between normalized S *K*-edge peat spectra and the Gaussian curve fits in the 2485-2490 eV energy region. No other spectrum from the comprehensive spectral database of Manceau and Nagy³³ showed these features. The gypsum spectrum was also taken from Manceau and Nagy.³³

Table SI-15: Comparison of FeS content determined by Fe *K*-edge XANES/EXAFS and inorganic (mono) sulfide content determined by S *K*-edge XANES (assumed to be mainly FeS, but can comprise also other X-S phases).

Sample	Content of FeS	Content of FeS	Content of Inorganic sulfide	Deviation S XANES/ Fe EXAFS	Deviation S XANES/ Fe XANES
	(Fe EXAFS)	(Fe XANES)	(S XANES)	[%]	[%]
	[mmol kg ⁻¹]	[mmol kg ⁻¹]	[mmol kg ⁻¹]		
B1 20cm	32	40	24	25	39
B1 40 cm	39	47	57	46	22
B1 60 cm	31	29	61	96	112
B2 20 cm	96	101	49	49	51
B2 60 cm	40	45	64	61	43
B3 10 cm	28	42	44	54	3
B3 50 cm	44	47	44	2	5

6. Antimony solid-phase speciation analyses and results

For Sb *K*-edge XAS analyses, homogenized, anoxic samples were filled into aluminum sample holders, sealed with Kapton tape and analyzed at beamline 11-2 (SSRL). The beamline was equipped with a "double double" Si(220) LN₂-cooled monochromator, which was calibrated to the *K*-edge of an Sb foil (energy: 30,491 eV). The absorption edge of the Sb foil was monitored before and after every sample. To reduce higher-order harmonics, we detuned the monochromator to 80% of the maximum beam intensity. All sample measurements were performed in fluorescence mode using a 100-element Ge array fluorescence detector (Canberra) and a He cryostat at 10 K to minimize beam damage and thermal disorder. For each sample, 3-15 scans were recorded, depending on concentration and speciation of Sb.

All spectra were processed using the software Athena⁴ and SIXpack.⁵ Normalization was performed by subtracting a linear function fit to the pre-edge region (-100 to -75 eV) and subsequently dividing by a quadratic polynomial fit to the post-edge region (150 to 600-1600 eV). The edge position was defined as maximum of the first derivative of the normalized spectrum. For EXAFS analysis, E_0 was fixed to 30,491 eV. The background spline was adjusted using the Autobk algorithm (Rbkg=1.0; k -weight=2; k -range 0.5–12.5 Å⁻¹). Spectra were tested for the minimum number of components by principal component analysis (PCA) based on the empirical indicator function⁹ and target-transform testing (TT) was done for the significant components against the references library using the program SIXpack.⁵ SPOIL-, Rf_{TT}- and NSSR_{TT}-values as well as visual confirmation were used to evaluate whether a target was acceptable.^{9,10} Linear combination fitting (LCF) of the k^2 -weighted EXAFS spectra in the k -range 2–12 Å⁻¹ was done in Athena.

Principle components analysis, target-transform testing and linear combination fitting of Sb *K*-edge EXAFS data

The suitability of reference spectra for LCF was determined by TT using the first three components calculated by PCA (based on minimum of the Malinowski indicator value⁹, Table SI-18). The quality of the transformation was evaluated by the empirical SPOIL value categorized by Malinowski¹²: 0-1.5 excellent, 1.5-3 good, 3-4.5 fair, 4.5-6 acceptable, and >6 for an unacceptable reference spectrum. All spectra with SPOIL-values <6 were used for further LCF analyses. However, the obtained number of Sb reference spectra suitable for LCF analysis based on TT (18 out of 22) was larger than the number of principal components determined by PCA (3). This may be due to (i) similar local Sb coordination environments in reference compounds identified by TT or (ii) the occurrence of several species in constant proportions in all analyzed spectra¹³. Since we could not exclude the latter effect, LCF analyses were performed using all 18 Sb EXAFS reference spectra determined as suitable. Each experimental spectrum was least-squares simulated in Athena by calculating all single- to five-component fits. The number of components included in the fit was

successively increased and each additional component was retained in the fit when the reduced chi-square value decreased by at least by 10% and when the Hamilton test (following descriptions in Bennett *et al.*¹⁴) showed that the number of fitted components in one fit (N) is significantly different from fits with N-1 components and not significantly different from fits with N+1 components ($p < 0.05$). Biogeochemically reasonable models with lowest NSSR-value and closest to 100% fit sum were finally chosen as best fits (Table SI-19). Shell-fit analysis of k^3 -weighted EXAFS spectra were performed in R-space employing the software Artemis. A Kaiser-Bessel window with a sill width of 3 \AA^{-1} was used for Fourier transformation. Theoretical scattering paths were calculated with FEFF6 based on the crystal structures of a modified kermesite model ($\text{Sb}_2\text{S}_2\text{O}$)³⁴ and $\text{Sb}(\text{OC}_6\text{H}_3\text{Me}_{2-2,6})_3$.³⁵

Antimony reference compounds

Supplementary Table SI-16 provides an alphabetic list and details about the origin of Sb reference compounds that were analyzed by XAS and used in the PCA/TT and LCF (EXAFS) analyses of the peat samples.

Table SI-16: Antimony reference compounds analyzed by XAS.

Compound	Chemical formula	Source/synthesis	Reference
Berthierite	$\text{FeSb}_2\text{S}_4^b$	natural	By courtesy of Kerstin Hockmann
Bindheimite	$\text{Pb}_2(\text{Sb}_2\text{O}_6)\text{O}^{a,b}$	synthetic	Scheinost <i>et al.</i> 2006 ³⁶
Cervantite	Sb_2O_4 orthorhombic ^{a,b}	natural (Crystal and Mineral Centre, Lisboa)	Scheinost <i>et al.</i> 2006 ³⁶
Roméite	$\text{Ca}_2(\text{Sb}_2\text{O}_6)\text{O}^{a,b}$	synthetic	Scheinost <i>et al.</i> 2006 ³⁶
Sb sulfide (amorphous)	$\text{SbS}_{3.6}^{a,b}$	synthetic	Besold <i>et al.</i> 2019 ³⁷
Sb(III) oxide	Sb_2O_3 cubic ^{a,b}	Fluka	Scheinost <i>et al.</i> 2006 ³⁶
Sb(III) on FeS	SbS_3^a	synthetic	Scheinost <i>et al.</i> 2006 ³⁶
Sb(III)-AHA (Aldrich humic acid)	$\text{SbO}_{3.4}(\text{C}_{0.9})_R^a$	synthetic	Scheinost <i>et al.</i> 2006 ³⁶ and this study, see Figure SI-8, Table SI-20
Sb(III)-ferrihydrite	not determined	synthetic	Burton <i>et al.</i> 2019 ³⁸
Sb(III)-goethite	$\text{SbO}_{3.7}(\text{Fe}_{1.9})_R^a$	synthetic	Scheinost <i>et al.</i> 2006 ³⁶
Sb(III)-GSH (L-glutathione)	$\text{SbO}_{0.4}\text{S}_{3.5}(\text{C}_{S,2.1})_R^a$	synthetic	Besold <i>et al.</i> 2019 ³⁷
Sb(III)-OM (model peat)	$\text{SbO}_{3.0}\text{S}_{0.4}(\text{C}_{0.2,8})_R^a$	synthetic	Besold <i>et al.</i> 2019 ³⁷
Sb(III)-S-Resin (Ambersep GT74)	$\text{SbS}_{3.4}(\text{C}_{S,4.1})_R^a$	synthetic	Besold <i>et al.</i> 2019 ³⁷

^a estimated by XAS

^b XRD confirmed

_R Rest in sorption complex

Table SI-16: *Continued.*

Compound	Chemical formula	Source/synthesis	Reference
Sb(V) oxide	Sb ₂ O ₅ cubic ^{a,b}	Aldrich	Scheinost et al. 2006 ³⁶
Sb(V)-ferrihydrite	not determined	synthetic	According to Scheinost et al. 2006 ³⁶ for goethite
Sb(V)-goethite	SbO ₆ (Fe _{1.0}) _R ^a	synthetic	Scheinost et al. 2006 ³⁶
Senarmontite	Sb ₂ O ₃ cubic ^{a,b}	natural (Crystal and Mineral Centre, Lisboa)	Scheinost et al. 2006 ³⁶
Stibiconite	Sb ₂ O ₄ cubic ^{a,b}	natural (Crystal and Mineral Centre, Lisboa)	Scheinost et al. 2006 ³⁶
Stibnite	Sb ₂ S ₃ ^a	Aldrich	Planer-Friedrich & Scheinost 2011 ³⁹
Tetrahedrite	Cu ₁₂ [S(SbS ₃) ₄] ^b	natural	Benett et al. 2017 ¹⁴
Tripuhyite	FeSbO ₄ ^{a,b}	synthetic	Scheinost et al. 2006 ³⁶
Valentinite	Sb ₂ O ₃ orthorhombic ^{a,b}	natural (Crystal and Mineral Centre, Lisboa)	Scheinost et al. 2006 ³⁶

^a estimated by XAS^b XRD confirmed_R Rest in sorption complex**Table SI-17:** Results from PCA of 7 *k*²-weighted peat sample Sb EXAFS spectra (*k*-range 2–12 Å⁻¹, E₀ = 30,491 eV).

Compound	PCA EXAFS		
	Eigenvalue	Cum. Var. ^a	IND ^b
1	1.063	0.866	0.00143
2	0.124	0.967	0.00042
3	0.021	0.985	0.00030
4	0.007	0.992	0.00037
5	0.004	0.995	0.00071
6	0.003	0.998	0.00239
7	0.002	1.0	N.A.

^aCumulative variance^bIndicator function⁹

Table SI-18: Results of Sb EXAFS TT analysis (against 3 PCs). Compounds with SPOIL > 6.0 (*in italic*) were not considered for further analysis.

Name of reference compound	SPOIL-value ^a	Rf _{TT} ^b	NSSR _{TT}
Sb(V)-ferrihydrite	1.44	0.05	5.93
Sb sulfide (amorphous)	1.54	0.37	8.91
Sb(V)-goethite	1.61	0.07	7.08
Sb(III) on FeS	1.68	0.40	11.02
Sb(III)-GSH	1.70	0.38	11.78
Sb(V) oxide	1.75	0.06	2.80
Sb(III)-AHA	1.75	0.04	1.60
Sb(III)-S-Resin (GT74)	1.77	0.41	12.62
Sb(III)-goethite	1.81	0.06	2.56
Tetrahedrite	2.36	0.52	19.17
Sb(III)-ferrihydrite	2.38	0.10	3.02
Berthierite	2.49	0.58	10.65
Bindheimite	2.57	0.11	13.33
Tripuhyite	2.76	0.15	16.17
Valentinite	3.63	0.19	17.39
Roméite	3.77	0.21	30.67
Stibiconite	4.54	0.11	4.22
Sb(III)-NOM (model peat)	4.91	0.29	6.69
<i>Cervantite</i>	<i>8.08</i>	<i>0.23</i>	<i>19.27</i>
<i>Senarmontite</i>	<i>11.12</i>	<i>0.52</i>	<i>29.83</i>
<i>Stibnite</i>	<i>11.33</i>	<i>0.39</i>	<i>3.76</i>
<i>Sb(III) oxide</i>	<i>12.85</i>	<i>0.63</i>	<i>59.24</i>

^a SPOIL classification (Malinowski 1978)¹²: 0–1.5, excellent; 1.5– 3, good; 3–4.5, fair; 4.5–6, acceptable; and >6, unacceptable reference

^b Calculated as $\Sigma(k^3\chi_{\text{exp}} - k^3\chi_{\text{fit}})^2 / \Sigma(k^3\chi_{\text{exp}})^2$

Table SI-19: Linear Combination Fit results for k^2 -weighted Sb *K*-edge EXAFS spectra of the studied peat samples.^a

Sample	Sb [$\mu\text{mol kg}^{-1}$]	Edge position ^b [eV]	Sb(V)-O- Fe ^c [atomic%]	Sb(III)-O- Fe ^d [atomic%]	Sb(III)-O- C _{org} ^e [atomic%]	Sb(III)-S- C _{org} ^f [atomic%]	Sb sulfide (amorph.) ^g [atomic%]	Initial fit sums [atomic%]	NSSR ^h [%]
B1 20 cm	1092	30,493.8	22	-	64	14 (14/0)	-	100	1.8
B1 40 cm	916	30,492.9	-	18	60	22 (0/22)	-	99	2.0
B1 60 cm	375	30,492.7	-	-	64	36 (36/0)	-	92	6.9
B2 20 cm	1536	30,493.2	25	-	54	21 (21/0)	-	96	3.6
B2 60 cm	256	30,492.8	-	-	63	-	37	99	7.6
B3 10 cm	756	30,493.8	24	-	52	24 (24/0)	-	90	2.4
B3 50 cm	66	30,492.5	-	-	63	37 (37/0)	-	85	16.7

^aFit range: 2–12 \AA^{-1} , $E_0 = 30,491$ eV. Fitted fractions were normalized to a component sum of 100%. Fitted fractions are accurate within ± 10 atom% at best. Number of fitted components in one fit (N) is significantly different from fits with N-1 components and not significantly different from fits with N+1 components (Hamilton test, $p < 0.05$). Biogeochemically reasonable models with lowest NSSR and closest to 100% fit sum were chosen as best fits. ^bThe edge position is defined as maximum of the first derivative of the normalized XANES spectrum. Fit references: ^cSb(V)-O-Fe = Sb(V) adsorbed to ferrihydrite, ^dSb(III)-O-Fe = Sb(III) adsorbed to ferrihydrite, ^eSb(III)-O-C_{org} = Sb(III) complexed with alcoholic groups of OM (Sb(III)-AHA), ^fSb(III)-S-C_{org} = Sb(III) complexed with thiol groups of OM; values in parentheses: (Sb(III)-S-Resin (GT74)/Sb(III)-GSH), ^gSb sulfide (amorph.) = amorphous Sb(III) sulfide, ^hNormalized sum of squared residuals ($100 \times \sum_i (\text{data}_i - \text{fit}_i)^2 / \sum_i \text{data}_i^2$).

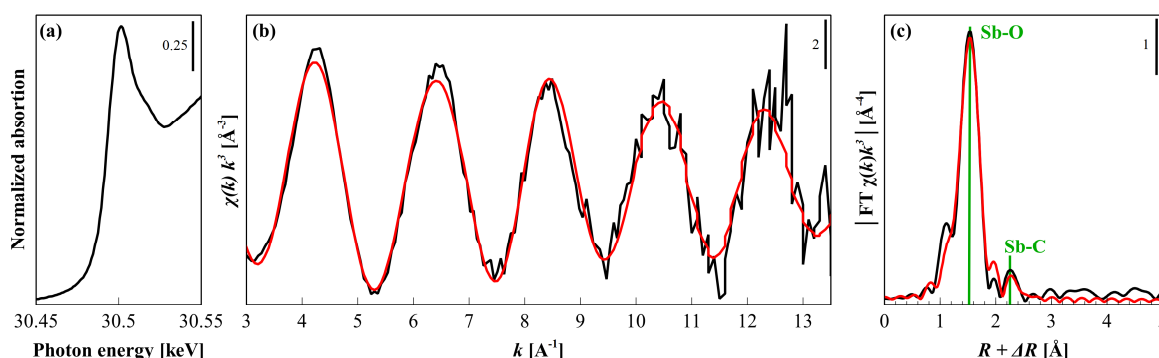


Figure SI-8: Antimony *K*-edge XANES-spectrum (a), k^2 -weighted EXAFS spectrum (b) and Fourier-transform magnitude of Sb(III) complexed with Aldrich humic acid (Sb(III)-AHA). Black lines represent experimental data and the best fit is shown as red lines. Single scattering paths of Sb-O and Sb-C(O) are marked with green lines at the respective positions in the FT.

Table SI-20: EXAFS parameters determined by shell-fitting of Sb *K*-edge EXAFS spectra of antimonite complexed with Aldrich humic acid (Sb(III)-AHA).^a

Sample	Path	CN ^b	R [Å] ^c	σ^2 [Å ²] ^d	ΔE_0 [eV] ^e	NSSR [%] ^f
Sb(III)-AHA	Sb-O	3.4	1.98	0.0021	9.7	8.2
	Sb-C(O)	0.9	2.83	0.0026		

^aThe amplitude reduction factor was set to 1.0 for all fits. Fits were carried out in R-space over an $R + \Delta R$ -range of 1.5–3.0 \AA using a k -range of 3–13.5. ^bCoordination number (path degeneracy), error $\pm 25\%$. ^cMean half path length, error ± 0.01 \AA . ^dDebye–Waller parameter, error ± 0.002 \AA^2 . ^eEnergy-shift parameter. ^fNSSR = $\sum_i (\text{data}_i - \text{fit}_i)^2 / \sum_i \text{data}_i^2$.

Table SI-21: Comparison between LCF fits with and without reference compound Sb(III)-O-C_{org}.

		With Sb(III)-O-C_{org}	Without Sb(III)-O-C_{org}
B1 20 cm	NSSR [%]	1.77	3.67
	Fit sum [atomic%]	98.6	123.0
B1 40 cm	NSSR [%]	2.00	3.79
	Fit sum [atomic%]	98.9	108.9
B1 60 cm	NSSR [%]	6.51	9.57
	Fit sum [atomic%]	93.7	76.9
B2 20 cm	NSSR [%]	3.74	3.99
	Fit sum [atomic%]	95.2	88.8
B2 60 cm	NSSR [%]	7.23	10.65
	Fit sum [atomic%]	98.0	74.6
B3 10 cm	NSSR [%]	2.28	3.81
	Fit sum [atomic%]	89.0	76.7
B3 50 cm ^a	NSSR [%]	24.43	24.09
	Fit sum [atomic%]	86.9	95.0

^aSample B3 50 cm is an exception because of (1) small k-range recorded (k=10) with lower information content and (2) still high shot noise, both related to the low Sb concentration of ~5 ppm.

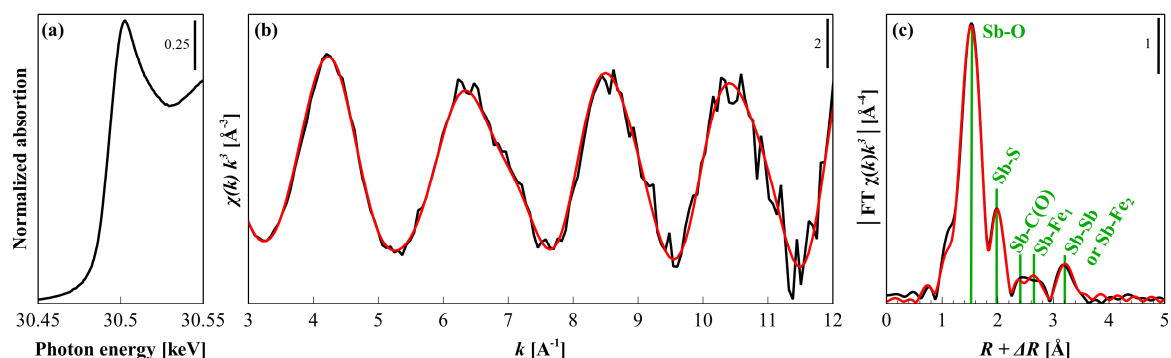


Figure SI-9: Antimony *K*-edge XANES-spectrum (a), k^3 -weighted EXAFS spectrum (b) and Fourier-transform magnitude of peat sample B2 20 cm. Black lines represent experimental data and the best fit is shown as red lines. Single scattering paths of Sb-O, Sb-S, Sb-C(O), Sb-Fe₁ and Sb-Sb or alternatively Sb-Fe₂ (see Table SI-22) are marked with green lines at the respective positions in the FT.

Table SI-22: EXAFS parameters determined by shell-fitting of Sb *K*-edge EXAFS spectra of peat sample B2 20 cm with two alternative shell-fit models.^a

Sample	Path	CN ^b	R [Å] ^c	σ^2 [Å ²] ^d	ΔE_0 [eV] ^e	NSSR [%] ^f
B2 20 cm	Sb-O	3.1	1.97	0.0011	10.4	4.3
	Sb-S	0.4	2.43	0.0010		
	Sb-C(O)	1.3	2.82	0.0010		
	Sb-Fe	0.3	3.07	0.0010		
	Sb-Sb	0.7	3.36	0.0045		
B2 20 cm, alternative	Sb-O	3.0	1.97	0.0010	10.3	4.3
	Sb-S	0.4	2.42	0.0010		
	Sb-C(O)	1.5	2.81	0.0010		
	Sb-Fe ₁	0.3	3.03	0.0055		
	Sb-Fe ₂	0.5	3.58	0.0010		

^aThe amplitude reduction factor was set to 0.8 for all fits. Fits were carried out in *R*-space over an $R+\Delta R$ -range of 1.1-3.6 Å using a *k*-range of 2-12.4. ^bCoordination number (path degeneracy), error $\pm 25\%$. ^cMean half path length, error ± 0.01 Å. ^dDebye-Waller parameter, error ± 0.002 Å². ^eEnergy-shift parameter. ^fNSSR = $\sum_i (\text{data}_i - \text{fit}_i)^2 / \sum_i (\text{data}_i)$.

The presence of an Sb-C(O) backscatterer could be verified by our shell-by-shell fitting approach of peat sample B2 20 cm. The sample was exemplarily chosen because of (1) the high quality of the sample spectra, necessary to reveal small Sb-C contributions, and (2) the relatively low contribution of the neighboring S backscatterer, which could partly overlap with the C(O) feature.

Two alternative shell-fit models (Table SI-22) with equal quality were developed, which both revealed the Sb-C(O) contribution, but showed differences regarding the feature at ~ 3.3 - 3.6 Å. This feature either could be fitted as a second Fe backscatterer at a distance of 3.58 Å, indicative for a corner-sharing complex with Fe (oxyhydr)oxides³⁶ or as an Sb-Sb path at 3.36 Å, suggesting small contributions of (particulate) metallic Sb or Sb(V)-oxide³⁶, probably a relict originating from the mining process.

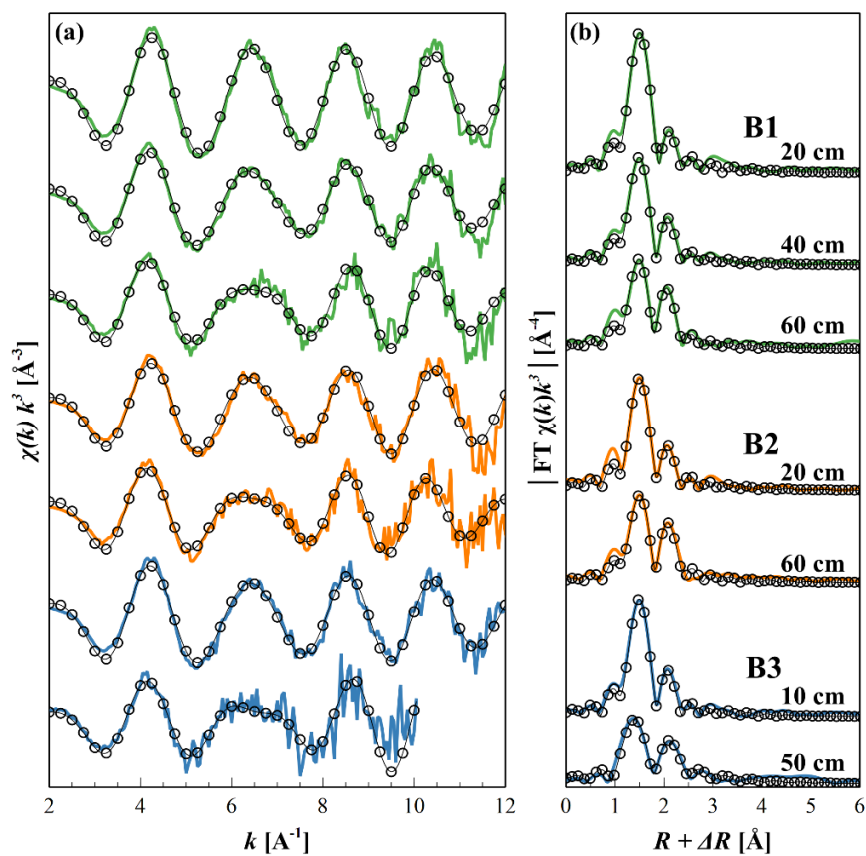


Figure SI-10: Shell fits of k^3 -weighted Sb K -edge EXAFS spectra and the respective Fourier-transform magnitudes of peat samples from B1-B3. Solid lines represent experimental data and the best fits for the first coordination shell are shown as dotted black lines.

Table SI-23: EXAFS parameters determined by shell-fitting of Sb *K*-edge EXAFS spectra of peat samples from B1-B3.^a

Sample	Path	CN ^b	R [Å] ^c	σ^2 [Å ²] ^d	ΔE_0 [eV] ^e	NSSR [%] ^f
B1 20 cm	Sb-O	3.7	1.98	0.0026	6.6	1.4
	Sb-S	0.4	2.47	0.0047		
B1 40 cm	Sb-O	2.7	1.98	0.0019	6.3	2.1
	Sb-S	1.1	2.45	0.0083		
B1 60 cm	Sb-O	2.2	1.98	0.0014	6.7	3.5
	Sb-S	1.5	2.46	0.0070		
B2 20 cm	Sb-O	2.3	1.97	0.0010	6.9	1.6
	Sb-S	1.0	2.43	0.0104		
B2 60 cm	Sb-O	2.4	1.99	0.0032	7.3	3.3
	Sb-S	1.3	2.48	0.0044		
B3 10 cm	Sb-O	2.9	1.98	0.0023	6.9	1.9
	Sb-S	0.8	2.46	0.0060		
B3 50 cm	Sb-O	1.9	1.98	0.0021	6.4	5.4
	Sb-S	2.0	2.45	0.0104		

^aThe amplitude reduction factor was set to 1.0 for all fits. Fits were carried out in *R*-space over an *R*+ ΔR -range of 1.0-3.0 Å using a *k*-range of 3-12 except for sample B3 50 cm: *k* = 3-9.5. ^bCoordination number (path degeneracy), error $\pm 25\%$. ^cMean half path length, error ± 0.01 Å. ^dDebye-Waller parameter, error ± 0.002 Å². ^eEnergy-shift parameter. ^fNSSR = $\sum_i (\text{data}_i - \text{fit}_i)^2 / \sum_i (\text{data}_i)^2$.

7. Aqueous Sb speciation results

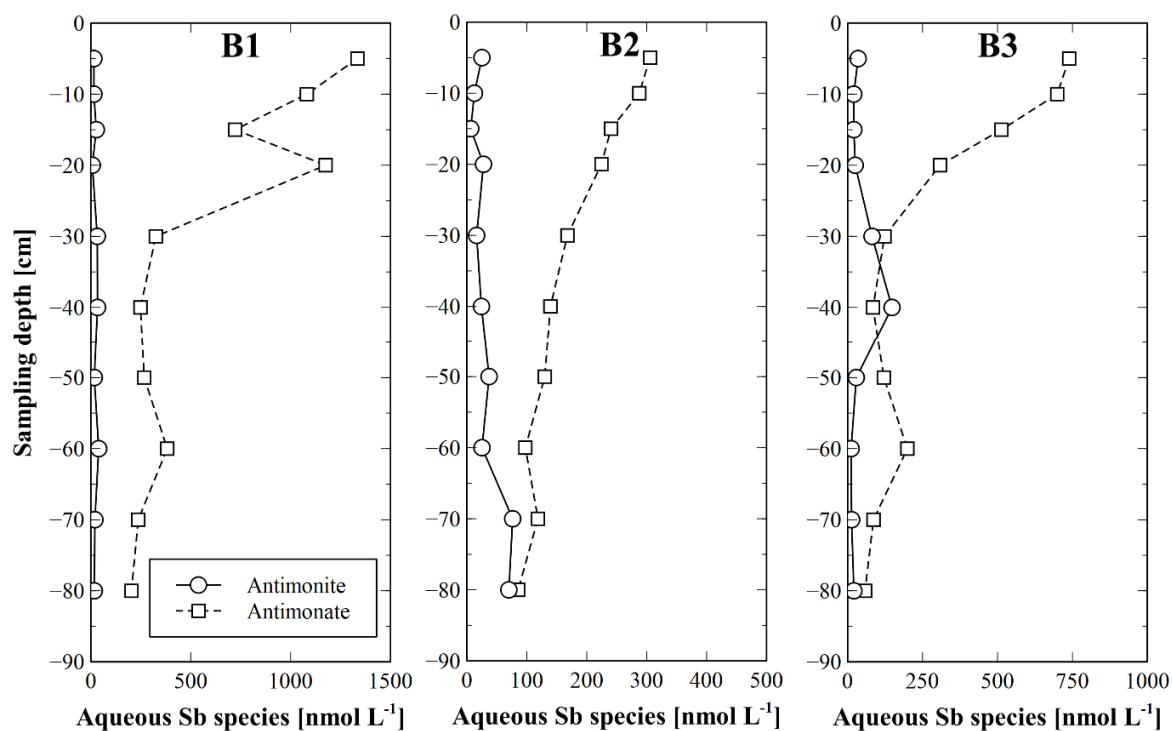


Figure SI-11: Aqueous antimony speciation of peat profiles B1-B3. Aqueous Sb species recovery ($(\text{Sum Sb species} / \text{Sb totals}) \times 100\%$): $\bar{x} = 79\%$ (35–156%). Please note that scales of x-axis differ to emphasize species changes.

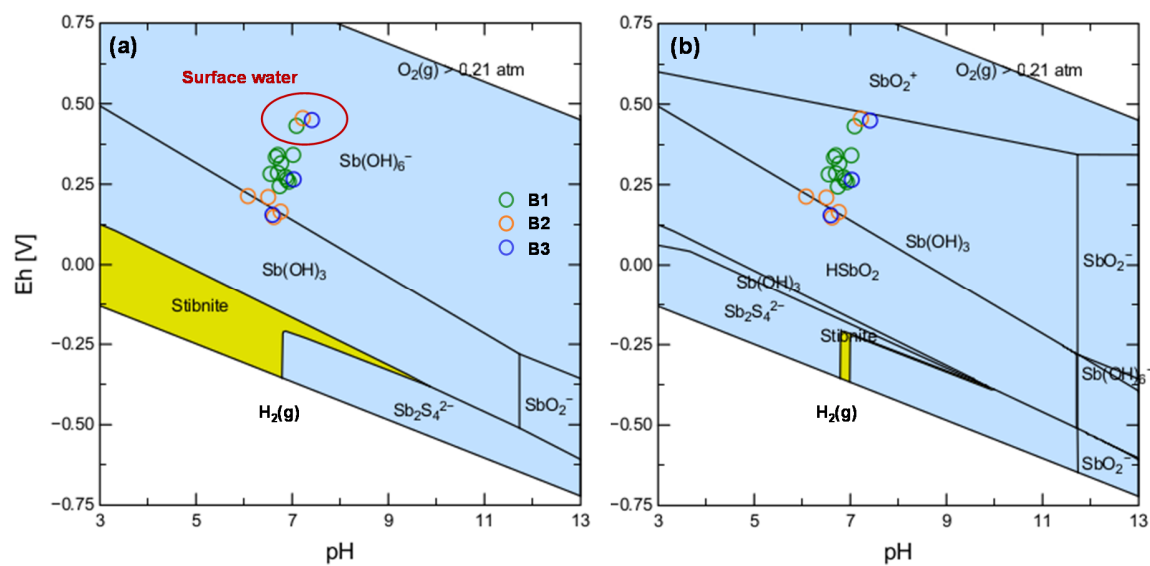


Figure SI-12: Pourbaix diagrams (25°C, 1 bar) calculated with input values of 0.002 mmol L⁻¹ Sb and 10 mmol L⁻¹ S for the Sb-O-H-S system using the WATEQ4F database extended with Sb data from the MINTEQ database. (a) shows the most-abundant Sb species and (b) the second-most-abundant species. Circles illustrate measured pH-Eh values from sampling profiles B1-B3.

References

- Palmer, K.; Ronkanen, A.-K.; Kløve, B., Efficient removal of arsenic, antimony and nickel from mine wastewaters in Northern treatment peatlands and potential risks in their long-term use. *Ecol. Eng.* 2015, 75, 350-364.
- Hesslein, R. H., An in situ sampler for close interval pore water studies. *Limnol. Oceanogr.* 1976, 21, (6), 912-914.
- Steinmann, P.; Shotyk, W., Sampling anoxic pore waters in peatlands using “peepers” for in situ-filtration. *Fresenius' Journal of Analytical Chemistry* 1996, 354, (5), 709-713.
- Ravel, B.; Newville, M., ATHENA, ARTEMIS, HEPHAESTUS: data analysis for X-ray absorption spectroscopy using IFEFFIT. *J. Synchrotron Rad.* 2005, 12, (4), 537-541.
- Webb, S., SIXpack: a graphical user interface for XAS analysis using IFEFFIT. *Phys. Scr.* 2005, 2005, (T115), 1011.
- Hohmann, C.; Morin, G.; Ona-Nguema, G.; Guigner, J.-M.; Brown, G. E.; Kappler, A., Molecular-level modes of As binding to Fe(III) (oxyhydr)oxides precipitated by the anaerobic nitrate-reducing Fe(II)-oxidizing *Acidovorax* sp. strain BoFeN1. *Geochim. Cosmochim. Acta* 2011, 75, (17), 4699-4712.
- Pantke, C.; Obst, M.; Benzerara, K.; Morin, G.; Ona-Nguema, G.; Dippon, U.; Kappler, A., Green Rust Formation during Fe(II) Oxidation by the Nitrate-Reducing *Acidovorax* sp. Strain BoFeN1. *Environ. Sci. Technol.* 2012, 46, (3), 1439-1446.
- Winterer, M., XAFS-A data analysis program for materials science. *Le Journal de Physique IV* 1997, 7, (C2), C2-243-C2-244.
- Malinowski, E. R., Determination of the number of factors and the experimental error in a data matrix. *Anal. Chem.* 1977, 49, (4), 612-617.
- Beauchemin, S.; Hesterberg, D.; Beauchemin, M., Principal component analysis approach for modeling sulfur K-XANES spectra of humic acids. *Soil Sci. Soc. Am. J.* 2002, 66, (1), 83-91.
- Cancès, B.; Juillot, F.; Morin, G.; Laperche, V.; Alvarez, L.; Proux, O.; Hazemann, J. L.; Brown, G. E.; Calas, G., XAS Evidence of As(V) Association with Iron Oxyhydroxides in a Contaminated Soil at a Former Arsenical Pesticide Processing Plant. *Environ. Sci. Technol.* 2005, 39, (24), 9398-9405.
- Malinowski, E. R., Theory of error for target factor analysis with applications to mass spectrometry and nuclear magnetic resonance spectrometry. *Anal. Chim. Acta* 1978, 103, (4), 339-354.
- Mancaeu, A.; Marcus, M. A.; Tamura, N., Quantitative Speciation of Heavy Metals in Soils and Sediments by Synchrotron X-ray Techniques. *Rev. Mineral. Geochem.* 2002, 49, (1), 341-428.
- Bennett, W. W.; Hockmann, K.; Johnston, S. G.; Burton, E. D., Synchrotron X-ray absorption spectroscopy reveals antimony sequestration by reduced sulfur in a freshwater wetland sediment. *Environ. Chem.* 2017, 14, (6), 345-349.
- Maillot, F.; Morin, G.; Wang, Y.; Bonnin, D.; Ildfonse, P.; Chaneac, C.; Calas, G., New insight into the structure of nanocrystalline ferrihydrite: EXAFS evidence for tetrahedrally coordinated iron(III). *Geochim. Cosmochim. Acta* 2011, 75, (10), 2708-2720.
- Morin, G.; Noël, V.; Menguy, N.; Brest, J.; Baptiste, B.; Tharaud, M.; Ona-Nguema, G.; Ikogou, M.; Viollier, E.; Juillot, F., Nickel accelerates pyrite nucleation at ambient temperature. *Geochem. Perspect. Lett.* 2017, 5, 6-11.
- Othmane, G.; Allard, T.; Morin, G.; Sélo, M.; Brest, J.; Llorens, I.; Chen, N.; Bargar, J. R.; Fayek, M.; Calas, G., Uranium Association with Iron-Bearing Phases in Mill Tailings from Gunnar, Canada.

- Environ. Sci. Technol. 2013, 47, (22), 12695-12702.
18. Azoulay, I.; Rémazeilles, C.; Refait, P., Determination of standard Gibbs free energy of formation of chukanovite and Pourbaix diagrams of iron in carbonated media. *Corros. Sci.* 2012, 58, 229-236.
 19. Ona-Nguema, G.; Morin, G.; Wang, Y.; Menguy, N.; Juillot, F.; Olivi, L.; Aquilanti, G.; Abdelmoula, M.; Ruby, C.; Bargar, J. R.; Guyot, F.; Calas, G.; Brown, G. E., Arsenite sequestration at the surface of nano-Fe(OH)₂, ferrous-carbonate hydroxide, and green-rust after bioreduction of arsenic-sorbed lepidocrocite by *Shewanella putrefaciens*. *Geochim. Cosmochim. Acta* 2009, 73, (5), 1359-1381.
 20. Trusiak, A.; Treibergs, L. A.; Kling, G. W.; Cory, R. M., The role of iron and reactive oxygen species in the production of CO₂ in arctic soil waters. *Geochim. Cosmochim. Acta* 2018, 224, 80-95.
 21. Allard, T.; Weber, T.; Bellot, C.; Damblans, C.; Bardy, M.; Bueno, G.; Nascimento, N. R.; Fritsch, E.; Benedetti, M. F., Tracing source and evolution of suspended particles in the Rio Negro Basin (Brazil) using chemical species of iron. *Chem. Geol.* 2011, 280, (1), 79-88.
 22. Cosmidis, J.; Benzerara, K.; Morin, G.; Busigny, V.; Lebeau, O.; Jézéquel, D.; Noël, V.; Dublet, G.; Othmane, G., Biomineralization of iron-phosphates in the water column of Lake Pavin (Massif Central, France). *Geochim. Cosmochim. Acta* 2014, 126, 78-96.
 23. Noël, V.; Marchand, C.; Juillot, F.; Ona-Nguema, G.; Viollier, E.; Marakovic, G.; Olivi, L.; Delbes, L.; Gelebart, F.; Morin, G., EXAFS analysis of iron cycling in mangrove sediments downstream a lateritized ultramafic watershed (Vavouto Bay, New Caledonia). *Geochim. Cosmochim. Acta* 2014, 136, 211-228.
 24. Kumar, N.; Lezama Pacheco, J.; Noel, V.; Dublet, G.; Brown, G. E., Sulfidation mechanisms of Fe(III)-(oxyhydr)oxide nanoparticles: a spectroscopic study. *Environ. Sci.: Nano* 2018, 5, (4), 1012-1026.
 25. Ona-Nguema, G.; Morin, G.; Juillot, F.; Calas, G.; Brown, G. E., EXAFS Analysis of Arsenite Adsorption onto Two-Line Ferrihydrite, Hematite, Goethite, and Lepidocrocite. *Environ. Sci. Technol.* 2005, 39, (23), 9147-9155.
 26. Bone, S. E.; Bargar, J. R.; Sposito, G., Mackinawite (FeS) Reduces Mercury(II) under Sulfidic Conditions. *Environ. Sci. Technol.* 2014, 48, (18), 10681-10689.
 27. Ikogou, M.; Ona-Nguema, G.; Juillot, F.; Le Pape, P.; Menguy, N.; Richeux, N.; Guigner, J.-M.; Noël, V.; Brest, J.; Baptiste, B.; Morin, G., Long-term sequestration of nickel in mackinawite formed by *Desulfovibrio capillatus* upon Fe(III)-citrate reduction in the presence of thiosulfate. *Appl. Geochem.* 2017, 80, 143-154.
 28. Wang, S.; Mulligan, C. N., Speciation and surface structure of inorganic arsenic in solid phases: A review. *Environ. Int.* 2008, 34, (6), 867-879.
 29. Noël, V.; Boye, K.; Kukkadapu, R. K.; Bone, S.; Lezama Pacheco, J. S.; Cardarelli, E.; Janot, N.; Fendorf, S.; Williams, K. H.; Bargar, J. R., Understanding controls on redox processes in floodplain sediments of the Upper Colorado River Basin. *Sci. Total Environ.* 2017, 603-604, 663-675.
 30. Maillot, F.; Morin, G.; Juillot, F.; Bruneel, O.; Casiot, C.; Ona-Nguema, G.; Wang, Y.; Lebrun, S.; Aubry, E.; Vlais, G.; Brown, G. E., Structure and reactivity of As(III)- and As(V)-rich schwertmannites and amorphous ferric arsenate sulfate from the Carnoulès acid mine drainage, France: Comparison with biotic and abiotic model compounds and implications for As remediation. *Geochim. Cosmochim. Acta* 2013, 104, 310-329.
 31. Dublet, G.; Juillot, F.; Morin, G.; Fritsch, E.; Fandeur, D.; Ona-Nguema, G.; Brown, G. E., Ni speciation in a New Caledonian lateritic regolith: A quantitative X-ray absorption spectroscopy investigation. *Geochim. Cosmochim. Acta* 2012, 95, 119-133.
 32. Prietzel, J.; Botzaki, A.; Tyufekchieva, N.; Brettholle, M.; Thieme, J.; Klysubun, W., Sulfur Speciation in Soil by S K-Edge XANES Spectroscopy: Comparison of Spectral Deconvolution and Linear

- Combination Fitting. *Environ. Sci. Technol.* 2011, 45, (7), 2878-2886.
33. Manceau, A.; Nagy, K. L., Quantitative analysis of sulfur functional groups in natural organic matter by XANES spectroscopy. *Geochim. Cosmochim. Acta* 2012, 99, (Supplement C), 206-223.
 34. Hybler, J.; Durovic, S., Kermesite, Sb₂S₂O: crystal structure revision and order-disorder interpretation. *Acta Crystallogr. Sect. B-Struct. Sci.* 2013, 69, 570-583.
 35. Horley, G. A.; Mahon, M. F.; Molloy, K. C.; Venter, M. M.; Haycock, P. W.; Myers, C. P., Structures of Sb(OC₆H₃Me_{2-2,6})₃ and Sb(OEt)₅·NH₃: The First Authenticated Monomeric Sb(OR)_n (n = 3, 5). *Inorg. Chem.* 2002, 41, (6), 1652-1657.
 36. Scheinost, A. C.; Rossberg, A.; Vantelon, D.; Xifra, I.; Kretzschmar, R.; Leuz, A.-K.; Funke, H.; Johnson, C. A., Quantitative antimony speciation in shooting-range soils by EXAFS spectroscopy. *Geochim. Cosmochim. Acta* 2006, 70, (13), 3299-3312.
 37. Besold, J., Antimonite complexation with thiol and carboxyl/phenol groups of peat organic matter. *Environ. Sci. Technol.* 2019.
 38. Burton, E. D.; Hockmann, K.; Karimian, N.; Johnston, S. G., Antimony mobility in reducing environments: The effect of microbial iron(III)-reduction and associated secondary mineralization. *Geochim. Cosmochim. Acta* 2019, 245, 278-289.
 39. Planer-Friedrich, B.; Scheinost, A. C., Formation and Structural Characterization of Thioantimony Species and Their Natural Occurrence in Geothermal Waters. *Environ. Sci. Technol.* 2011, 45, (16), 6855-6863.

List of Publications

The following papers have been published during the work on this thesis:

Besold, J.; Biswas, A.; Suess, E.; Scheinost, A. C.; Rossberg, A.; Mikutta, C.; Kretzschmar, R.; Gustafsson, J. P.; Planer-Friedrich, B., Monothioarsenate transformation kinetics determining arsenic sequestration by sulfhydryl groups of peat. *Environ. Sci. Technol.* **2018**, 52, (13), 7317-7326.

Besold, J.; Kumar, N.; Scheinost, A. C.; Lezama Pacheco, J.; Fendorf, S.; Planer-Friedrich, B., Antimonite complexation with thiol and carboxyl/phenol groups of peat organic matter. *Environ. Sci. Technol.* **2019**, 53, (9), 5005-5015.

Besold, J.; Eberle, A.; Noël, V.; Kujala, K.; Kumar, N.; Scheinost, A. C.; Pacheco, J. L.; Fendorf, S.; Planer-Friedrich, B., Antimonite binding to natural organic matter: spectroscopic evidence from a mine water impacted peatland. *Environ. Sci. Technol.* **2019**, 53, (18), 10792-10802.

Biswas, A.; Besold, J.; Sjöstedt, C.; Gustafsson, J. P.; Scheinost, A. C.; Planer-Friedrich, B., Complexation of arsenite, arsenate, and monothioarsenate with oxygen-containing functional groups of natural organic matter: An XAS Study. *Environ. Sci. Technol.* **2019**, 53, (18), 10723-10731.

Eberle, A.; Besold, J.; Kerl, C. F.; Lezama Pacheco, J.; Fendorf, S.; Planer-Friedrich, B., Arsenic fate in peat controlled by pH-dependent role of reduced sulfur. *Environ. Sci. Tech.* **2020**, 54, (11), 6682-6692.

Kumar, N.; Noël, V.; Planer-Friedrich, B.; Besold, J.; Lezama Pacheco, J.; Bargar, J. R.; Brown, G. E. Jr.; Fendorf, S.; Boye, K., Redox heterogeneities promote thioarsenate formation and release into groundwater from low arsenic sediments. *Environ. Sci. Tech.* **2020**, 54, (6), 3237-3244.

Other publications realized during the time as PhD student:

Mehlhorn, J.; Besold, J.; Lezama Pacheco, J. S.; Gustafsson, J. P.; Kretzschmar, R.; Planer-Friedrich, B., Copper mobilization and immobilization along an organic matter and redox gradient—insights from a mofette site. *Environ. Sci. Technol.* **2018**, 52, (23), 13698-13707.

Kujala, K.; Besold, J.; Mikkonen, A.; Tirola, M.; Planer-Friedrich, B., Abundant and diverse arsenic-metabolizing microorganisms in peatlands treating arsenic-contaminated mining wastewaters. *Environ. Microbiol.* **2020**, 22, (4), 1572-1587.

Supervised Bachelor and Master Theses

The following theses have been co-supervised during the work on this thesis:

Bachelor thesis:

Heitzer, C. (2017): Complexation of monothioarsenate to different size fractions of particulate and dissolved natural organic matter, Bachelor Thesis, University of Bayreuth, Environmental Geochemistry.

Steeb, M. (2019): An environmental-geochemistry background analysis of photographs by J. Henry Fair, Bachelor Thesis, University of Bayreuth, Environmental Geochemistry.

Master thesis:

Eberle, A. (2018): Sulfur-induced remobilization of arsenic from natural organic matter, Master Thesis, University of Bayreuth, Environmental Geochemistry.

Results of this project are included in study 3 of this thesis.

(Eidesstattliche) Versicherungen und Erklärungen

(§ 9 Satz 2 Nr. 3 PromO BayNAT)

Hiermit versichere ich eidesstattlich, dass ich die Arbeit selbstständig verfasst und keine anderen als die von mir angegebenen Quellen und Hilfsmittel benutzt habe (vgl. Art. 64 Abs. 1 Satz 6 BayHSchG).

(§ 9 Satz 2 Nr. 3 PromO BayNAT)

Hiermit erkläre ich, dass ich die Dissertation nicht bereits zur Erlangung eines akademischen Grades eingereicht habe und dass ich nicht bereits diese oder eine gleichartige Doktorprüfung endgültig nicht bestanden habe.

(§ 9 Satz 2 Nr. 4 PromO BayNAT)

Hiermit erkläre ich, dass ich Hilfe von gewerblichen Promotionsberatern bzw. -vermittlern oder ähnlichen Dienstleistern weder bisher in Anspruch genommen habe noch künftig in Anspruch nehmen werde.

(§ 9 Satz 2 Nr. 7 PromO BayNAT)

Hiermit erkläre ich mein Einverständnis, dass die elektronische Fassung meiner Dissertation unter Wahrung meiner Urheberrechte und des Datenschutzes einer gesonderten Überprüfung unterzogen werden kann.

(§ 9 Satz 2 Nr. 8 PromO BayNAT)

Hiermit erkläre ich mein Einverständnis, dass bei Verdacht wissenschaftlichen Fehlverhaltens Ermittlungen durch universitätsinterne Organe der wissenschaftlichen Selbstkontrolle stattfinden können.

.....

Ort, Datum, Unterschrift